Title

Development of Non-Traditional Bioanalytical Methods for the Study of Pharmacokinetics and Protein Complexes

Author

Ferguson, Carly Nicole

Publication Date

2014

Peer reviewed|Thesis/dissertation

UNIVERSITY OF CALIFORNIA

Los Angeles

Development of Non-Traditional Bioanalytical Methods for the Study of Pharmacokinetics and Protein Complexes

A dissertation submitted in partial satisfaction of the requirements for the degree of Doctor of Philosophy in Biochemistry and Molecular Biology

by

Carly Nicole Ferguson

2014

(This page intentionally left blank.)

ABSTRACT OF THE DISSERTATION

Development of Non-Traditional Bioanalytical Methods for the Study of Pharmacokinetics and Protein Complexes

by

Carly Nicole Ferguson

Doctor of Philosophy in Biochemistry and Molecular Biology

University of California, Los Angeles 2014

Professor Joseph A. Loo, Chair

While proteomics, mass spectrometry and their combination have seen great advancements since their inception, there is room for improvement in many areas, including increased sensitivity, specificity, and applicability. Mass spectrometry-based imaging (MSI) is a relatively new technology that has found application in the medical sciences. Spatially measuring proteins, lipids, and other biomolecules in clinically relevant tissues is a powerful tool for disease biomarker studies and for disease pathology. An improved tissue imaging method has been developed that employs a series of wash steps to decrease the complexity of the lower mass range in order to better observe tissue distribution of targeted drug molecules and their metabolites. This was previously unstudied due to the common belief that any solvent would delocalize analytes of interest; however, we have shown that attention to solubility properties of these molecules allows for non-disruptive solvent selection. This method was utilized to determine the biodistribution of small molecule read-through (SMRT) compounds that are potential treatment molecules for premature termination codon (PTC) genetic disorders. MSI experiments revealed that one compound in particular, BZ16, crossed

the blood-brain barrier (BBB) and entered the cerebellum. MSI was also utilized to study the distribution of a molecular tweezer (MT) compound, CLR01, which is a potential treatment for amyloid-based diseases. After administration to animal subjects, CLR01 was observed in the ventral portion of the brain, confirming the compound's ability to cross the BBB.

One area that has not been well addressed by these newer technologies is the study of protein-ligand interactions. The development of improved ambient ionization methods for mass spectrometry provides a complementary technique for the study of small molecules and their interactions with proteins and other biomolecules. Protein-ligand binding studies are crucial in the development of drug molecules; such techniques as reactive desorption electrospray ionization (DESI) allow for the study of large proteins and protein complexes in their native states.

DESI-related work has resulted in an improved protein soft ionization method, enabling the characterization of large native protein complexes (> 150 kDa). Our reactive DESI method employs two solvent capillaries: one containing buffer to maintain native conformation, and another containing electrospray-compatible solvent to more efficiently ionize proteins at higher resolution. Additionally, we have shown that we can probe protein-ligand binding stoichiometry, selectivity, and kinetics by including a small molecule in our electrospray-compatible solvent.

The dissertation of Carly Nicole Ferguson is approved.

Robin L. Garrell

James A. Wohlschlegel

Joseph A. Loo, Committee Chair

University of California, Los Angeles

2014

I would like to dedicate this work to my family. To my mother (Lissa), father (Scott), sister (Lindsay), fiancé (Matt), and to all friends and family for the love and support over the years.

Additionally, I would like to dedicate this to my undergraduate mentors: Dr. John Eyler, Dr. Ron Heeren, and Dr. Rick Yost and their passion for the fields of analytical chemistry and mass spectrometry, and their excellent mentorship. Thank you for allowing an undergraduate with no mass spec experience to participate in a once-in-a-lifetime opportunity through the MSPIRE fellowship.

TABLE OF CONTENTS

LIST OF FIGURES

LIST OF TABLES

ACKNOWLEDGMENTS

I would first and foremost like to thank my mentor, Professor Joe Loo, for his constant support and guidance throughout my graduate studies. Joe's encouragement and direction inspire confidence in each of his students; and, his warm demeanor fosters an environment of open discussions and collaborative thinking. I am forever thankful for the opportunity to be so involved in the set-up of our imaging equipment, and for his enthusiasm and support that made for a great setting to come with new project ideas. It has been a privilege to become a member of the Loo lab family.

Additionally, I would also like to express my gratitude to Dr. Rachel Loo for her guidance and expertise, especially for her thoughtful and thorough responses to the hundreds of organic chemistry, physics, and trypsin digest questions I have asked over the years.

To my undergraduate students, Joe Fowler and Jon Waxer, I would like to thank them for all of their hard work and dedication during our time together at UCLA.

For past and present Loo lab members, I would like to say thank you for the help and support, especially Hong Nguyen, Sean Shen, Pete Wongkongkathep, and Drs. Jonathan Erde, Huilin Li, Eric Pang, Dyna Shirasaki, and Jiang Zhang.

Finally, I would like to thank my committee members, Drs. Robin Garrell, Jing Huang, Emily Reisler, James Wohlschlegel, and Joe Loo for their guidance and advice over these past five years.

The work presented in this dissertation was supported by the Cellular and Molecular Biology Training Grant, the Audree Fowler Fellowship, the UCLA Chemistry Association Fellowship, and the UCLA Faculty Women's Club Fellowship.

CHAPTER one of this dissertation is a version of Ferguson, C.N., Fowler, J.M., Waxer, J.A., Gatti, R.A., Loo, J.A. Mass Spectrometry-Based Tissue Imaging of Small Molecules in *Advancements of Mass Spectrometry in Medicine*; Woods, A. G., Darie, C. C., Eds.; Springer International Publishing: 2014, Vol. 806, p 283, reprinted with permissions. Copyright 2014 Springer International Publishing Switzerland. I would like to acknowledge my co-authors Joseph W.M. Fowler, Jonathan F. Waxer, and Drs. Richard A. Gatti, and Joseph A. Loo.

CHAPTER two of this dissertation is a manuscript in preparation entitled “Mass Spectrometry Imaging of Small Drug Molecules: Ionization and Sample Preparation.” I would like to acknowledge Joseph W.M. Fowler and Jonathan F. Waxer for their assistance in tissue sample preparation and MSI analysis for each molecular study; Sean Shen, Robert Ortiz, and Drs. Michael Hall, and Jean Lee for their help and guidance with benzodiazepenes; Drs. Ewa Micewicz, Dorthe Schaue, William H. McBride, and Richard A. Gatti for their expertise in mouse models, as well as providing exciting, novel drug compounds to study; and, Dr. Joseph A. Loo for his guidance and expertise throughout the course of each study.

CHAPTER three of this dissertation is a manuscript in preparation entitled “Biodistribution of Small Molecule Read-Through (SMRT) Compounds in a Mouse Model as Determined by Matrix-Assisted Laser Desorption/Ionization-Mass Spectrometry Imaging (MALDI-MSI).” I would like to acknowledge Joseph W.M. Fowler Fowler and Jonathan F. Waxer for their assistance in tissue sample preparation and MSI analysis for each molecular study; Sean Shen for his assistance in LC-MS/MS experiments; Ewa Micewicz and William H. McBride for their expertise in mouse

models; Richard A. Gatti for providing an exciting, novel compound class to study; and, Joseph A. Loo for his guidance and expertise throughout the course of the study.

CHAPTER four of this dissertation is a manuscript in preparation entitled “Protein Coronae Composition of Mesoporous Silica Nanoparticles Dependent Upon Surface Modifications and Biological Material.“ I would like to acknowledge Dr. Rolando E. Yanes for conducting all of the cell culture and nanoparticle incubation protocols; Angela A. Hwang for synthesizing all nanoparticles; Dr. Jie Lu for conducting Western blot experiments; Dr. Dyna Shirasaki for her assistance with LC-MS/MS experiments; and, Drs. Jeffrey I. Zink, Fuyu Tamanoi, and Joseph A. Loo for their guidance and expertise throughout the course of the study.

CHAPTER five of this dissertation is reprinted with permissions from Ferguson, C. N.; Benchaar, S. A.; Miao, Z.; Loo, J. A.; and Chen, H. Direct Ionization of Large Proteins and Protein Complexes by Desorption Electrospray Ionization-Mass Spectrometry. *Analytical Chemistry* **2011** *83* (17), 6468-6473. Copyright 2014 American Chemical Society. I would like to acknowledge Dr. Sabrina Benchaar for her assistance with ion mobility experiments; Dr. Zhixin Miao for her assistance in writing; Dr. Hao Chen for his guidance in liquid DESI, as well as providing an exciting study; and Dr. Joseph A. Loo for his guidance and expertise throughout the course of the study.

CHAPTER six of this dissertation is reprinted with permission from Liu, P.; Zhang, J.; Ferguson, C. N.; Chen, H.; and Loo, J.A. Measuring Protein-Ligand Interactions Using Liquid Sample Desorption Electrospray Ionization Mass Spectrometry. *Analytical Chemistry* **2013** *85* (24), 11966-11972. Copyright 2014 American Chemical Society. I would like to acknowledge Pengyuan Liu for conducting

the DESI experiments; Dr. Jiang Zhang for his assistance with instrument operations; Dr. Hao Chen for his guidance in liquid DESI; and Dr. Joseph A. Loo for his guidance and expertise throughout the course of the study.

VITA

2005-2009	Bachelors of Science, University of Florida Chemistry
2007-2008	National Science Foundation Research Experience for Undergraduates Fellowship: Assembling the Tree of Life
2008	National Science Foundation Mass Spectrometry Partnership for International Research Experience Fellowship
2008-2009	University of Florida University Scholars Program
2009-2010	Teaching Assistant, University of California, Los Angeles Department of Chemistry and Biochemistry
2010-2013	Cellular and Molecular Biology Training Grant
2013-2014	Teaching Assistant, University of California, Los Angeles Department of Chemistry and Biochemistry
2013-2014	UCLA Audree Fowler Fellowship in Protein Science
2013-2014	UCLA Faculty Women's Club Fellowship
2014	UCLA Chemistry Association Fellowship

PUBLICATIONS

Ferguson, C.N., Fowler, J.M., Waxer, J.A., Gatti, R.A., Loo, J.A. "Mass Spectrometry-Based Tissue Imaging of Small Molecules." In *Advancements of Mass Spectrometry in Medicine*; Woods, A. G., Darie, C. C., Eds.; Springer International Publishing: 2014, Vol. 806, p 283.

Liu, P., Zhang, J., **Ferguson, C.N.**, Loo, J.A., Chen, H. 2013. Measuring Protein-Ligand Interactions Using Liquid Sample Desorption Electrospray Ionization Mass Spectrometry. *Analytical Chemistry* 85 (24), 11966-11972.

Kimball, R.T., Wang, N., Heimer-McGinn, V., **Ferguson, C.N.**, Braun, E.L. 2013. Identifying Localized Biases in Large Datasets: A Case Study Using the Avian Tree of Life. *Molecular Phylogenetics and Evolution* 69, 1021-1032.

Ferguson, C.N., Benchaar, S.A., Loo, J.A., Miao, Z., Chen, H. 2011. Direct Ionization of Large Proteins and Protein Complexes by Desorption Electrospray Ionization-Mass Spectrometry. *Analytical Chemistry* 83 (17), 6468-6473.

SELECT PRESENTATIONS

Ferguson, C.N., Yanes, R.E., Hwang, A.A., Thomas, C.R., Zink, J.I., Tamanoi, F., Loo, J.A. January 2014. Surface-Modified Nanoparticles as a Proteomics-Based Diagnostic Tool. UCLA Molecular Biology Institute Annual Research Conference, Los Angeles, CA.

Ferguson, C.N., Fowler, J.M., Waxer, J.F., Micewicz, E., Headley, A., McBride, W.H., Gatti, R.A., Loo, J.A. October 2012. Analysis of Nonaminoglycoside Distribution in Tissue via MALDI-Mass Spectrometry Imaging (MALDI-MSI). UCLA Molecular Biology Institute Annual Research Conference, Lake Arrowhead, CA.

Ferguson, C.N., Micewicz, E., Headley, A., McBride, W.H., Gatti, R.A., Loo, J.A. September 2012. Analysis of Nonaminoglycoside Distribution in Tissue via MALDI-Mass Spectrometry Imaging (MALDI-MSI). Ourense Conference on Imaging Mass Spectrometry, Ourense, Spain.

Ferguson, C.N., Kobzeff, F., Micewicz, E., Headley, A., McBride, W.H., Gatti, R.A., Loo, J.A. May 2012. Biodistribution in Tissue of Novel Drug Molecules via MALDI-Imaging Mass Spectrometry (MALDI-IMS). American Society for Mass Spectrometry Annual Conference, Vancouver, British Columbia, Canada.

Ferguson, C.N., Liu, P., Zhang, J., Benchaar, S.A., Miao, Z., Loo, J.A., Chen, H. January 2012. Direct Ionization of Large Proteins and Protein Complexes by Desorption Electrospray Ionization-Mass Spectrometry (DESI-MS). Conference on Ion Chemistry and Mass Spectrometry, Lake Arrowhead, CA.

CHAPTER 1

Mass Spectrometry-Based Tissue Imaging of Small Molecules

Mass Spectrometry-Based Tissue Imaging of Small Molecules

Carly N. Ferguson, Joseph W.M. Fowler, Jonathan F. Waxer, Richard A. Gatti, and Joseph A. Loo

ABSTRACT

Mass spectrometry imaging (MSI) of tissue samples is a promising analytical tool that has quickly become associated with biomedical and pharmacokinetic studies. It eliminates several labor-intensive protocols associated with more classical imaging techniques, and provides accurate, histological data at a rapid pace. Because mass spectrometry is used as the readout, MSI can be applied to almost any molecule, especially those that are biologically relevant. Many examples of its utility in the study of peptides and proteins have been reported; here we discuss its value in the mass range of small molecules. We explore its success and potential in the analysis of lipids, medicinals, and metal-based compounds by featuring representative studies from mass spectrometry imaging laboratories around the globe.

INTRODUCTION

Mass spectrometry-based imaging of tissue samples and surfaces is a relatively new technology with a significant function in medicinal development [1]. MSI was developed in the laboratory of Dr. Richard Caprioli, and has continued to garner interest in labs around the world as its applications expand [1,2]. The methodology essentially provides a chemical map of a surface by incorporating mass spectrometry instrumentation and assigning spatially relevant coordinates [1]. The specificity of analyte detection is provided by the mass spectrometry readout.

MSI is most often coupled with matrix-assisted laser desorption/ionization (MALDI), although we will briefly discuss an alternative ionization method. MALDI utilizes a matrix compound that is mixed and crystallized with the analyte of interest followed by desorption/ionization with a laser beam. MALDI matrices absorb efficiently at the wavelength of the specified laser. In MSI, the fundamentals of MALDI are utilized in a spatially relevant manner. A thin surface (for our purposes, a thin tissue section) is evenly coated in a MALDI matrix, and this surface is subsequently analyzed by rastering across it with a MALDI laser irradiation. The spatial resolution is controlled by the operator and is limited by the laser spot size (e.g., typically 100 μm or less), and thousands of spectra are collected at specific X-Y coordinates covering the surface of interest. After collection, all spectra are compiled into one, average spectrum, wherein masses of interest can be selectively highlighted and their spatial distribution depicted in a virtual image [1]. This workflow is shown in Figure 1. Tissue samples (whole organs) are typically sliced on a cryotome at 10 – 20 mm thickness and thaw-mounted onto glass slides coated with conductive material. Matrix is applied via any one of a number

of automated mechanisms, typically consisting of a nebulizer that evenly coats the entire slide with a thin layer of matrix crystals [1-3].

There are several benefits of implementing mass spectrometry imaging. Traditional protein and peptide imaging methods, such as immunohistochemistry (IHC) staining, require the use of a specific antibody [4]. Additionally, these staining methods only allow for a small number of molecules of interest to be analyzed on any given tissue section [5,6]. MSI does not require antibodies, and the use of a mass spectrometer's analyzer and detector also allow for the visualization of thousands of molecules of interest simultaneously as all ionized molecules are non-specifically detected. Similar benefits are true of MSI experiments for detection of small molecules. The mass accuracy of the MS analyzer, e.g., time-of-flight (TOF) analyzers most often applied for MSI, often allows for the identification of the molecule of interest, and advanced MS methods, such as tandem mass spectrometry (MS/MS), yield additional molecular information to derive identification.

A recent study by the Caprioli group demonstrates the functionality of MSI in a pathological sense. This work probed proteomic differences between two dermatological conditions: Spitz nevus (SN) and Spitzoid malignant melanoma (SMM). These two conditions are virtually indistinguishable by traditional pathology methods; however, an MSI study was able to identify a key proteomic difference that distinguishes the benign SN from the malignant SMM with 97% accuracy. This study showcases the ability of MSI to complement existing histopathology methods for more confident diagnoses [7].

In addition to interest in proteins and peptides, small molecules of all types are compounds of interest in many clinically relevant studies. Herein we discuss the advances of mass spectrometry imaging in three classes of small molecules: lipids, drug compounds, and nanoparticles. Combined, these studies broadly indicate the bright future MSI holds in the biomedical field.

LIPIDS

Lipids have considerable diversity in chemical structure and biological function, and comprise the external lipid bilayer as well as subcellular organelles, including the mitochondria and surrounding nuclear membrane [8]. Due to this diversity in structure and localization, techniques that pinpoint specific lipids within tissues, while not delocalizing the compound of interest, are of great interest. The techniques generally used to identify lipids, however, involve the extraction of the lipids prior to analysis, which destroys relevant information regarding its overall spatial distribution [9]. These traditional procedures for lipid analysis utilize destructive assays, which are subsequently coupled with mass spectrometry and/or liquid chromatography [10-14]. Fluorescence imaging could theoretically overcome these challenges, as fluorescent tagging procedures preserve location, reveal the exact position of lipids, and allow researchers to observe the rapid and dynamic changes in the location and structure of lipids [15]. However, most fluorescent tags are as large as the lipid molecules themselves, which would likely cause changes to the overall location and metabolism of the lipid. Therefore, in order to successfully study lipids within a biological system, analytical techniques must be able to overcome two major challenges: (i) preservation of the structural and locational information of individual lipids, and (ii) provide a high level of molecular specificity to

differentiate the diversity in lipid structure [16]. Modern mass spectrometry, due to its excellent sensitivity and molecular specificity, is arguably a method of choice for lipid analysis. The mass spectrometric analysis of lipids is traditionally achieved through lipid extraction from a sample and subsequent analysis by electrospray ionization (ESI), with or without prior chromatographic separation [16]. Although this method provides detailed structural information, it is not useful for measuring the spatial distribution of specific lipids. Therefore, new mass spectrometry approaches have been developed that provide direct surface analysis capabilities.

MALDI-MSI of Lipids. Recently, advances in MALDI-MSI have allowed for in-depth qualitative, quantitative, and spatial analyses of several types of lipid species. Although the preparation and specific parameters needed to map lipids varies between specific species, MALDI-MSI has been shown to be a more efficient and convenient technique to detect lipids compared to traditional methods. Techniques, such as fluorescence confocal microscopy and fluorescent tagging of molecules are poor in lipid characterization because of the relatively small size of lipids as well as their ubiquity throughout many cell types [17]. The abundance of lipids in various cell structures, such as internal and external membranes, is beneficial to MALDI IMS because it allows for the direct visualization of these various compounds on a tissue section. Furthermore, the sensitivity of MS for molecular weight ranges under 1000 Da is especially high [18].

MALDI generates two-dimensional molecular maps by ionizing molecules on a tissue sample through direct exposure to a laser. This is ideal for analysis of lipid compounds because of their inherent ability to ionize and produce positive or negative

ions. Lipid molecules are amphipathic molecules comprised of either phosphate anions or nitrogen-centered cations that readily ionize during MALDI [8,19].

Several techniques exist to prepare various types of lipid species in order to obtain good quality mass spectra. Generally, washing the mounted tissue slides with aqueous, volatile salt solutions simplifies the spectra to lipid compounds, such as phosphotidylcholine, that generate an abundance of positive ions through MALDI [20]. This will remove interfering salts and generate well-resolved mass spectra by taking out interfering chemical noise. Lipid species that form a high abundance of negative ions during the MALDI process, such as phosphatidylenolamine, naturally produce simpler spectra because they do not form alkali metal attachment ions [17].

A final advantage of MALDI-MSI of lipids is that it can be used in combination with other techniques. For example, MALDI can be used after thin layer chromatography (TLC) allowing for precise isolation of lipid compounds directly on the TLC plate, versus a more labor-intensive extraction process [17]. MALDI-MSI has also been used in conjunction with structural information obtained from ESI experiments, immunoblotting, and histological information obtained from staining to provide a multimodal model of lipid localization in the brain [21]. MALDI-MSI analysis of lipids has also allowed advancements in forensic investigation as well as diagnosis of diseases such as breast cancer and traumatic brain injury [17,22]. MALDI-MSI has proven invaluable in the growth of lipid research and continues to spread into other avenues of biochemistry and analytical chemistry.

DESI of Lipid Compounds. MALDI-MSI is often used for peptide and protein analysis, and has been used for lipid analysis as well [23]. MALDI-MSI utilizes a

preparative step that evenly covers the tissue with an organic matrix, assisting with ionization of the sample [24,25]. The type of matrix used, however, greatly influences the efficiency of ionization for different classes of molecules, and experimental conditions used for lipid imaging are different from those used for proteins in terms of matrix used, mass-to-charge (m/z) range, and the acquisition mode when using TOF analyzers [24-28].

Desorption electrospray ionization (DESI) is an ambient desorption/ionization technique that is based on the direct examination of unprepared, unmodified samples in the open environment, and is commonly used for drug, metabolite, and lipid imaging. Recently, the development of dimethylformamide (DMF)-based solvent combinations has minimized the destructive nature of the technique, and has enabled DESI-MSI to be performed with preservation of morphological features [23,29]. By preserving morphological features, histological and immunohistochemical analysis can be performed after MSI [26]. The ability to preserve tissue morphology for histological examination, while assessing the lipid and protein profiles on the same section of tissue, provides an opportunity to correlate findings [29]. Eberlin and Liu *et al* demonstrated that a single tissue section initially used for DESI-MSI of lipids can then be used for protein MSI, and subsequently hemotoxylin and eosin (H&E) staining to acquire morphological information [29].

By combining the techniques of DESI-MSI, MALDI-MSI, and H&E staining, Eberlin, et al. (2011b) unambiguously matched the morphological and chemical features of mouse brain and human brain cancer tissue samples. They found that, prior to DESI-MSI of lipids, using either acetonitrile (ACN):DMF (1:1) or ethanol:DMF (1:1) solvent systems did not disturb the native protein localization, as ion images of control tissue

sections showed similar protein spatial distributions, as well as similar co-localization of lipids and proteins [29]. Furthermore, results were able to be obtained from a sample of human glioma grade III, having first undergone DESI-MSI, followed by MALDI-MSI, and finally optical imaging after H&E staining [29]. In addition, their analysis of a control tissue section, which had not been subjected to DESI-MSI, revealed similar spatial distributions of their select proteins of interest [29]. This new approach combines the unique strengths of DESI and MALDI for lipid and protein MSI, and allows the unambiguous matching of morphological and chemical features. Eberlin, et al. (2011b) conclude that the combined methods of DESI, MALDI, and H&E on the same tissue section enables a more complete evaluation; and, is expected to not only enhance diagnostic capabilities, but allow insights into the pathophysiology of disease.

These capabilities were further demonstrated by the same group in a study that employed ambient ionization-based MSI for characterization of tumor borders. Several brain tumors were analyzed via DESI-MSI to develop lipid-based classifiers to distinguish between tumor and healthy tissue. This technique provides fast classification, and remains promising for intraoperative use to differentiate visibly indistinguishable tumor borders [30].

MSI with FT-ICR MS for Lipid Analysis. MALDI-MSI with TOF analyzers does not provide the ultra-high resolution and mass accuracy necessary for direct identification of low molecular weight compounds. However, MALDI can be coupled with Fourier transform ion cyclotron resonance (FT-ICR) MS in order to obtain high mass accuracy and identify compounds of interest with a high degree of confidence in tissue [31].

Vidova, et al. (2010) characterized the major lipid components of the ocular lens using MALDI-TOF-MSI. They found that the major lipid components were mainly long chain phosphatidylcholines (PC) and sphingomyelins (SM) [32]. However, MALDI-TOF-MSI did not provide the proper degree of resolution and mass accuracy to determine the exact masses of the lipid components in order to produce accurate spatial distribution results of compounds close in molecular weight. Therefore, Vidova, et al. (2010) used MALDI-FT-ICR-MSI in order to determine the masses of the specific PC and SM species within the ocular lens. Sections of porcine eyes were prepared and analyzed with MALDI-FT-ICR-MSI in positive ion mode. An example of the usefulness of FT-ICR MS in this specific study was in the analysis of a lipid compound with a mass of 787 Da. The study found that the lipid aggregated in its protonated form at m/z 787.6685 and also found an unknown molecule at m/z 787.6042. Ultra-high resolution MS allowed for the discrimination between these two peaks, whereas a lower resolution MS instrument would not be able to resolve the two, and would disrupt quantitative, qualitative, and spatial distribution analyses. By utilizing the high mass accuracy of FT-ICR MS, Vidova, et al. (2010) was able to find spatial and concentration-dependent distributions of various species of lipids within the ocular lens.

Lipids in Traumatic Brain Injury. MALDI-MSI is also an important tool that can be used to develop molecular biomarkers of disease. Recently, Woods, et al. (2013) used MALDI-MSI to characterize and quantify the spatial distribution of ganglioside species in mouse brains after being subjected to low level explosive detonations. This study set out to find a biochemical connection between exposure to explosive blasts and traumatic brain imagery (TBI). Gangliosides account for 6% of total brain mass and are

included in several biochemical and metabolic pathways [33]. Ceramides are the scaffold molecules that form gangliosides, and the effects of proximity blasts from explosions may cause a disruption in the various pathways of these two lipids [34]. Woods, et al. (2013) studied the changes in the amount and spatial distribution of gangliosides and ceramides in mouse model brains exposed to blast explosions. Ceramides were found to be present at higher concentrations in TBI brains; however, this was determined via ESI due to insufficient MALDI ionization efficiency. It was found that exposure to explosive blasts increases the amounts of a ganglioside GM2 in several portions of the brain and causes a subsequent decrease in the concentration of ceramide species (Figure 2). This was the first successful study to display an increase in GM2 from a non-genetic cause [22]. The findings of Woods, et al. (2013) point towards the possibility of using gangliosides and ceramides as biomarkers in the detection and analysis traumatic brain injury in patients, and, furthermore, implicate MALDI-MSI as a useful strategy for biomarker discovery.

MEDICINAL DEVELOPMENT

For the discovery and development of new drug entities, knowledge of a given compound's biodistribution is a critical factor. To where does a new drug compound distribute in the body? What are the metabolites of this new drug and where do these metabolites accumulate? What are the quantitative measures of their distribution? These questions must be answered in order to move from an *in vivo* animal model to human clinical trials. Because the approval process of a novel therapeutic is long, arduous, and very costly, areas in which technology can speed the acquisition of this information are open to modification [35]. The majority of these technology-driven areas

throughout the drug development timeline occur within the pre-clinical stage. Traditionally, these early questions are answered via methods such as autoradiography and fluorescent tagging, each with its own set of limitations [36,37]. Both methods require labor-intensive synthesis efforts to apply the necessary tags. Autoradiography involves the use of radioactive materials, and thus comes with its own set of regulatory issues. When radiolabeled versions of novel compounds are delivered to an animal, an autoradiograph is produced; however, there is little to no indication of whether the observed image is the result of an intact compound or a metabolic fragment [36,37]. Conversely, in a metabolite study, only metabolites containing radiolabeled atoms will be detected and observed. Fluorescence tags are significantly larger than radioactive labels, and require a significant amount of testing due to the possibility that the tag may interfere with the compound's membrane penetrance and efficacy [38]. Compounds are often less than 500 Da, meaning even the smallest dye molecule can have a large effect on the uptake and subsequent biodistribution of the compounds of interest. Images are further complicated by molecules exhibiting autofluorescence, and difficulties similar to radiolabeling, such as difficulty attributing a signal to intact or fragmented compound [38]. The synthesis of a pure compound itself provides a challenge.

These issues can be circumvented by MSI, as its non-targeted nature means all molecules on a given surface are chemically mapped, and no tag is required. With proper controls in place, previously unknown metabolites can be uncovered by utilizing tandem mass spectrometry (MS/MS) capabilities, essentially determining the structure of an unknown peak. Below we discuss a few case studies that have utilized MSI in drug development [35,39].

Fosdevirine. MALDI-MSI has already found success in the pharmaceutical industry, as evidenced by the recent study by Castellino, et al. (2013). Human immunodeficiency virus (HIV) is a widespread disease with limited treatments available. It is primarily an autoimmune disorder that develops when viral strains display varying resistance to the available treatments. It remains an active area of research in the pharamaceutical industry [40].

The group of Castellino conducted experiments on a non-nucleoside reverse transcriptase inhibitor that had passed all pre-clinical testing and entered into Phase IIb clinical trials. Fosdevirine was developed by GlaxoSmithKline to treat a wide range of HIV-1 strains, the most common subtype as well as the most lethal. Many of these strains have become resistant to other forms of existing treatment, such as Efavirenz [40]. Rigorous pre-clinical testing identified Fosdevirine as a promising drug due to its efficacy in low doses, and its effectiveness against both single and double mutants of reverse transcriptase that confer remarkable resistance against other drugs. The drug moved into a human model, with Phase I testing conducted on healthy individuals indicating no observable toxicity or side effects. Further testing on HIV-1-infected individuals that had not previously received treatment confirmed earlier findings from healthy individuals. However, Phase IIb trials involving HIV-1-infected individuals that had undergone alternative treatments resulted in 25% of all subjects experiencing seizures, with no link to neurological problems in medical histories [40].

MSI was employed to study its biodistribution and metabolism in rabbit, minipig, and monkey brain tissue in order to evaluate potential differences associated with adverse neurological symptoms. This was done in conjunction with liquid

chromatography-MS (LC-MS) analyses of cerebral spinal fluid (CSF) from seizure patients as well as animal models. LC-MS analyses of CSF found two cysteine adduct metabolites, M22 and M16, to be present in seizure patients as well as rabbits and minipigs that exhibited central nervous system (CNS) toxicity due to Fosveridine treatment. While these results indicate M22 and M16 as potential effectors of CNS toxicity, they do not provide spatial distribution information within the tissues themselves. MSI studies further indicated a potential mechanism for this CNS toxicity, providing important localization information. M22 was observed to localize to the white matter portion of the brain in minipig and rabbit, both of which exhibited Fosveridine-induced CNS toxicity. In monkeys, where no such toxicity was observed, Fosveridine was found to localize to the gray matter portion of the brain. It is hypothesized that binding of M22 and M16 to the GABAa receptor could be the cause of this CNS toxicity. With MSI's capability to multiplex with other modes of imaging, it is possible to utilize a technique such as immunohistochemical staining in order to observe that M22 colocalizes with the GABAa receptor in rabbit and minipig brain, but not monkey brain [40]. Together, this localization to the white matter and colocalization with the GABAa receptor in model organisms exhibiting Fosveridine CNS toxicity show the advantages of combining MSI with traditional staining protocols [35,39,40].

Paclitaxel. Optimized sample preparation protocols are important in the field of MSI. One such step is the matrix selection, both type and application method can be varied in order to optimize ionization of specific molecules [2,41]. This optimization is especially crucial in small drug molecule studies due to the ion suppression effects that are observed in the low m/z range of the spectrum. Because traditional MALDI matrices

are, themselves, small molecules, they contribute a number of interfering, intense ion peaks in a mass spectrum. This can often suppress signal from target drug molecules that are present in much lower levels than the saturated matrix solutions. Additionally, the spatial resolution of any given imaging run can be limited by the size of the crystallized matrix particles themselves, often exceeding the size of the laser spot and thus decreasing the resolution of the data [2,35,39,41].

One common solution to these problems is the use of nanoparticle-assisted laser desorption/ionization (NALDI). Nanoparticles are typically composed of an inorganic material, and exhibit such desirable characteristics as low heat capacity and efficient photo-adsorption. They are also smaller in size than matrix crystals, and thus do not interfere with spatial resolution as readily; additionally, they have a large surface area that allows for maximum adsorption of the desired analytes [42].

Morosi, et al. (2013) employed NALDI for analysis of the biodistribution of a small drug molecule used for cancer treatments, Paclitaxel, in solid tumors. This group utilized MSI in organs excised from mice injected with Paclitaxel, and further utilized MSI in the study of human xenograft tumors excised from mice injected with Paclitaxel. MSI served two major advantages in the detection of Paclitaxel: negative ion mode and tandem mass spectrometry. Paclitaxel ionizes more efficiently in negative ion mode, and is typically suppressed by abundant lipids in positive ion mode over the m/z 800-1000 range (Paclitaxel MW 853.9 m/z). Thus, MSI allows for the option of collecting data for observation of a negatively charged ion of Paclitaxel, specifically a fragment ion at m/z 284.2. MS/MS coupled to MSI experiments allowed for the confirmation of this peak by observing the transition from m/z 284.2 to m/z 72.6 [42].

This group also employed quantitative MSI by utilizing a deuterated internal standard, D5-Paclitaxel. The internal standard was spotted onto control tissues, a calibration curve was constructed, and Paclitaxel signal was measured and compared to the internal standard signal in a specific region of interest. The success of this quantitative method was further shown by the differences in normalized intensities in liver when mice were treated with different levels of the drug. This group indicates that their success with quantitative MSI was likely due to the homogeneity of the nanoparticles used, versus the traditional heterogeneous MALDI matrix crystals [42].

Read-Through Compounds. The treatment and management of genetic disorders are major target areas in the drug development field since no such drugs are yet of proven efficacy. One common genotype is caused by nonsense mutations, resulting in a malformed or unstable protein. Such nonsense mutations create a premature termination codon (PTC). Instead of translating a gene sequence in its entirety, the mRNA falls off the ribosome resulting in a truncated form of the protein. This protein fragment is subsequently degraded, and thus no full length, functional protein is produced by the patients' cells [43].

Examples of PTC disorders include Duchenne muscular dystrophy (MD), cystic fibrosis, and ataxia-telangiectasia (A-T). A-T is often caused by a single point mutation in the ataxia-telangiectasia mutated (ATM) gene encoding for ATM protein. This serine/threonine kinase is active in DNA repair, mainly by phosophorylation of a large number of proteins involved in DNA repair and cancer. Individuals deficient in ATM exhibit such symptoms as impaired cerebellum development, increased risk of cancer

(one-third of all A-T patients develop cancer), and enhanced susceptibility to radiation [44-46].

Aminoglycosides, such as Gentamicin, could potentially be used to treat PTC disorders by binding to the small ribosomal subunit at the decoding site and inducing translational read-through of the stop codon [47]. While this has been successful in laboratory studies in "proof of concept," it would engender adverse side effects such as toxicity and potential deafness [48-50]. Treating neurological diseases like A-T would also require that the aminoglycoside cross the blood-brain barrier. Due to their large and rigid structure, aminoglycosides do not penetrate a healthy blood-brain barrier. A new class of small molecule read-through (SMRT) compounds has recently been developed that overcomes most of these issues [43-51].

Although SMRT compounds have shown promise *in vitro*, there has been little information concerning the biodistribution of these compounds. In a mouse model, we determined the biodistribution of a derivative of RTC13 utilizing MSI [51,52]. The compound was administered intraperitoneally to mice, and its biodistribution was studied in all major organs at various time points. The SMRT compound was found to cross the blood-brain barrier without any off-target build-up. These results were confirmed by MS/MS, and tissue structure was elucidated by H&E staining, as shown in Figure 3 (in prepration). These results highlight the utility of MSI as an initial biodistribution screening technique due to its speed and direct analysis of unmodified, novel compounds.

METALS AND NANOPARTICLES

A newer area of MSI being investigated is the imaging of nanoparticles and other metal elements. Metal analysis is typically done using inductively coupled plasma MS (ICP-MS), which uses a plasma flame to ionize metal particles wherein they are detected by a mass spectrometer [53,54]. While ICP-MS is often coupled with liquid samples in an electrospray-like set-up, recent studies have utilized laser ablation ICP-MS (LA-ICP-MS) to study dried samples, such as droplets, tissues, and other surfaces. The coupling of ICP-MS to laser ablation has allowed for spatially relevant images to be collected, and thus MSI of metal elements is possible. We will discuss two examples of LA-ICP-MSI analyses of metals in tissue [53,54].

Aside from the study of innate metal composition of tissues, there is growing interest in metal- and non-metal-based nanoparticle biodistribution. This stems from the recent development of nanoparticles as drug delivery vehicles [55]. Nanoparticles are promising due to their small, biocompatible nature and their ability to package many varieties of molecules, from proteins to small drug compounds, and deliver them to specific areas of a cell or organism. We will discuss a recent study that further stretched the capabilities of MALDI-MSI for the purposes of imaging nanoparticles in tissue [56].

Endogenous Metal Ions. LA-ICP-MS has long been used for the analysis of trace metals in samples; however, LA-ICP-MSI is a more recent application of this useful technique [53,54]. Many metal ions play key roles in biological processes, thus it is of interest to study their distribution in tissue samples. Lear, et al. (2012) further improved the LA-ICP-MSI protocols in order to allow for the detection of traditionally undetectable metal ions by altering the reaction gas contents in a typical experiment.

Tissue surfaces are extremely complex, with thousands of different compounds present in a 1 mm^2 pixel, thus it is advantageous to develop techniques that will allow for enhanced signal intensity of particular molecules of interest. Specifically in LA-ICP-MSI, argon gas is employed to provide electrons as well as assist in the nebulizing process of ions of interest; however, this use of Ar significantly interferes with a number of signal regions, most notably that of iron (Fe). Additional impurities in the Ar gas source can lead to further eclipsing of signals of interest. This group employed the use of an H_2 reaction gas to dissociate ArO clusters and other interfering compounds while maintaining sensitivity in the detection of several metal ions, including: Mn, Fe, Cu, and Zn [57].

Mouse brain was used to study the distribution of each of the above mentioned metal ions. For Cu and Zn ions, specifically ^{63}Cu and ^{66}Zn, there are no known interferences and thus it was shown that use of H_2 reaction gas did not improve signal intensity during an LA-ICP-MSI experiment; however, both ions were able to be mapped at a 30 mm spatial resolution. The success of the H_2 reaction gas was evident in the analysis of the ^{56}Fe and ^{57}Fe ions, as well as the ^{55}Mn ion, both of which experience heavy interference with Ar gas clusters and impurities. Background signal was reduced after introduction of the reaction gas, and thus a much clearer ^{56}Fe image was produced at a spatial resolution of 6 mm. This improvement was even more pronounced in the analysis of ^{57}Fe, which is more heavily suppressed by interfering signals due to its lower abundance. The adaptability of this technique for analysis of important metal ions indicates its promise as an analytical tool for analysis of all biologically relevant molecules, from metal ions to proteins [57].

Platinum from cis-*platin drug.* Drug toxicity studies are imperative in advancing novel compounds into clinical trials. *Cis*-platin is a commonly used drug complex in the treatment of many types of cancers; however, it is known to exhibit nephrotoxicity when given in larger doses. It is of great interest to observe the biodistribution of platinum (Pt) in *cis*-platin-treated individuals, as well as the differential distributions of copper and zinc (Cu and Zn), two important metal ions involved in biological processes [53].

Traditionally, Pt has been tracked in tissue via neutron activation analysis and autoradiography. These techniques, while sensitive, require labor-intensive techniques further complicated by the need for a nuclear reactor to produce neutrons. Less expensive alternatives to nuclear reactors often result in lower sensitivity, and still involve the use of radioactive materials. Zoriy, et al. (2007) turned to LA-ICP-MSI to study the biodistribution of Pt, a technique that does not require the use of radioactive materials and is capable of whole-tissue analysis. This technique had been previously employed to show a correlation between the Alzheimer's disease-related amyloid beta protein (Ab) and trace element concentration [58].

This group was able to image the biodistribution of Pt, Cu, and Zn in mouse kidney derived from *cis*-platin-dosed animals. Hemotoxylin and eosin staining was used to distinguish specific kidney structures, with LA-ICP-MSI experiments utilizing a spatial resolution of 50 mm. Zoriy, et al. (2007) were also able to employ internal standards for quantitative purposes. They observed a higher concentration of Cu in the capsule and external cortex (glomeruli), and a higher concentration of Zn in the inner cortex (tubules). Pt concentration was highest in the medulla, decreased in the inner cortex, and was lowest along the periphery of the kidney. The Pt gradient reflected the typical

primary urine gradient found in the kidney structures. This is thought to be the first alternative imaging method for Pt that did not require the use of radioactive materials, and thus shows the versatility of MSI [53].

Nanoparticles. A growing problem in medicine is the treatment of drug-resistant diseases, especially drug-resistant cancers. These cancers often require a combination of drugs working synergistically to effectively kill the fast-growing cells. Determining the perfect treatment cocktail can be a daunting task for physicians and researchers, and further prescribing of a large number of medications can create a variety of burdens for the patient in question. This also leads to complications in FDA investigational new drug (IND) studies. Nanoparticle drug delivery vehicles are a promising solution to these woes for a number of reasons [55].

Nanoparticles are typically small, biocompatible molecules on the scale of nanometers. Their surfaces are easily modified via various synthesis routes, and this allows for specific targeting of nanoparticles to desired cell types [55]. Additionally, their mostly hollow cores allow for packaging of a variety of molecules. Recent studies have indicated nanoparticles as effective delivery vehicles to carry molecules to specific drug-resistant cancer cells and subsequently release them, in this particular case these molecules included siRNA and a small drug compound [55].

Traditional nanoparticle imaging methods require the use of a large dye molecule, which can interfere with the activity and resulting biodistribution of the nanoparticles in question. Nanoparticles, such as gold or silica, are often used as MALDI matrices due to their limited background noise contributions in a mass spectrum [42]. However, they are not commonly detected using LDI-based methods due to their

variation in size, the fact that they often contain fixed charges, and the lack of a predictive spectral profile.

Yan, et al. (2013) have circumvented these limitations by establishing a spectral profile, or 'barcode,' of the nanoparticles involved via attachment of a ligand molecule to the surface of the nanoparticle. These ligands are smaller in size than traditional dyes, and serve the added function of modifying the surface properties of the nanoparticles. This study was able to identify a molecular ion attributed to the gold nanoparticle core, as well as three distinct molecular ions attributed to each of the ligands attached, as shown in Figure 4. This illustrates a promising future for the use of LDI-MS-based imaging methods for the detection of such nontraditional molecules as nanoparticles [56].

CONCLUSIONS

Since its inception nearly two decades ago, the field of mass spectrometry imaging has grown rapidly. New developments in sample preparation protocols, desorption/ionization methods, instrumentation (e.g., mass spectrometry analyzers and detectors), and data processing and data display have aided in its incorporation into bioanalytical chemistry and even medicine. We have discussed a number of applications in the realm of small molecules, and many more examples of MSI's utility can be found in the study of peptides and proteins. Going forward, it is likely that MSI will become a permanent fixture in biomedical research. Further advancements in software and instrumentation are already aiding its incorporation into clinical settings, and the continued, collaborative goal towards standardized protocols will aid in its development as a pharmaceutical and clinical tool.

ACKNOWLEDGMENTS

This work was supported by the Ruth L. Kirschstein National Research Service Award (Grant GM007185, UCLA Cellular and Molecular Biology Training Grant, for C.N.F.) and the US National Institutes of Health Shared Instrumentation Program (Grant S10 RR025600 to J.A.L.).

FIGURES

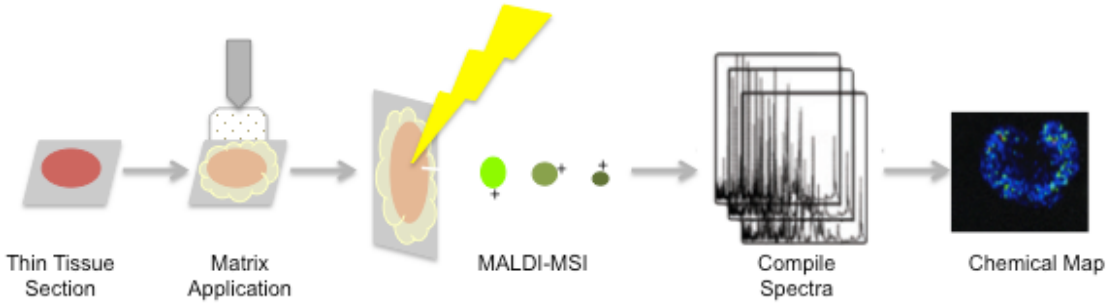

Figure 1. Schematic of a MALDI-MSI experiment shows a typical tissue sample preparation protocol. A laser then rasters across the tissue surface. At each point, or pixel, a mass spectrum is collected. These spectra are averaged, and individual masses are selected to create maps, such as the one shown on the right (kidney tissue of a small molecule metabolite).

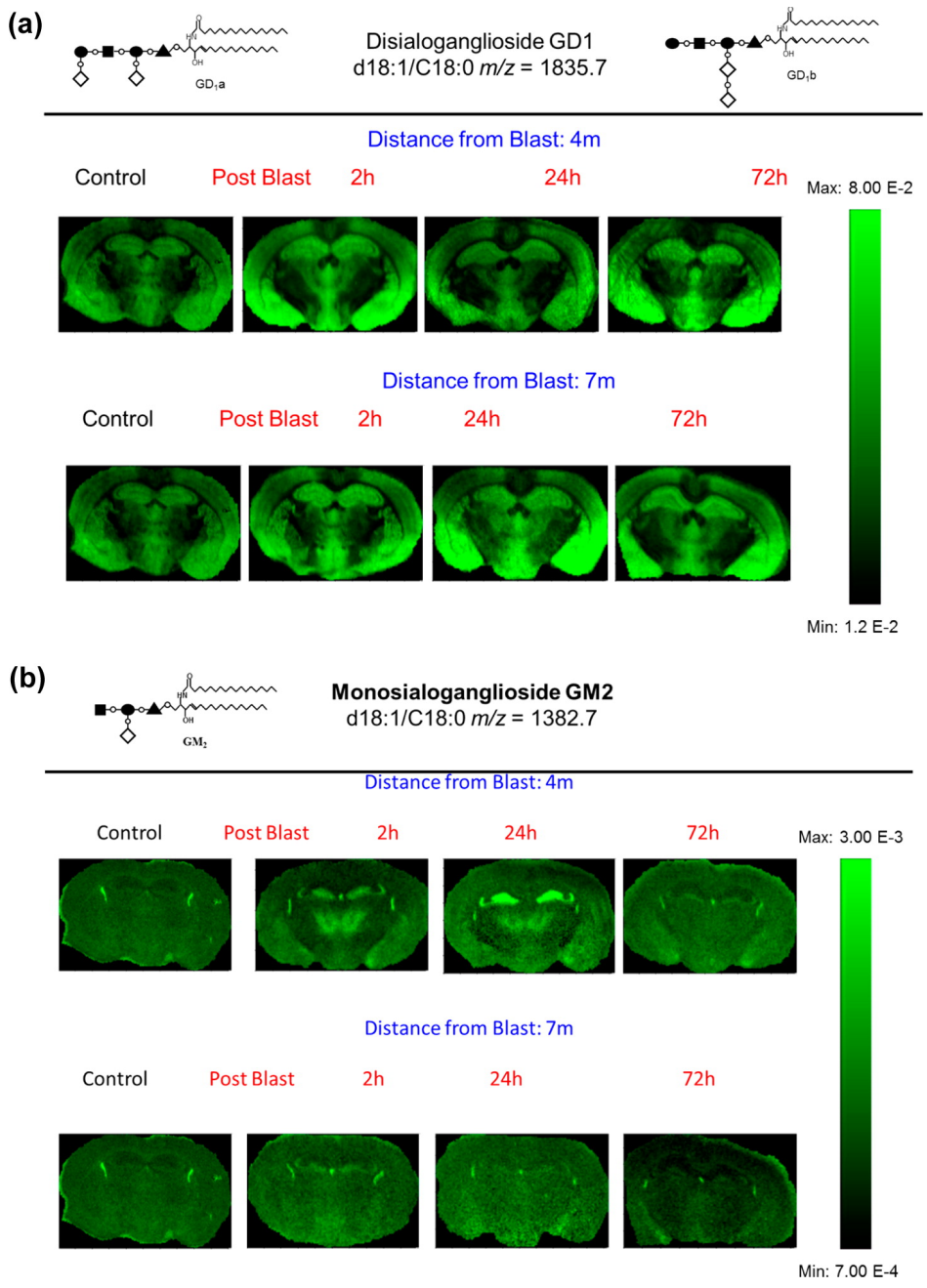

Figure 2. MALDI-MSI of two gangliosides: (a) GD1d18:1/C18:0 and (b) GM2 d18:1/C18:0 in brains of control mice and mice 2, 24, and 72 h after open field blast exposure at 4 and 7 m. In panel a, GD1 is present mainly in gray matter areas (hippocampus, cortex, and hypothalamus), and there is no observable change in the distribution of GD1 between control and blast groups. In panel b, for the controls, the

GM2 peak was highly localized in the lateral and the dorsal third ventricles while increases were observed in the hippocampus and thalamus for blast exposure, especially for 4 m 2 and 24 h postblast samples. Reprinted with permission from the *Journal of the American Chemical Society*. Copyright © 2013 American Chemical Society [22].

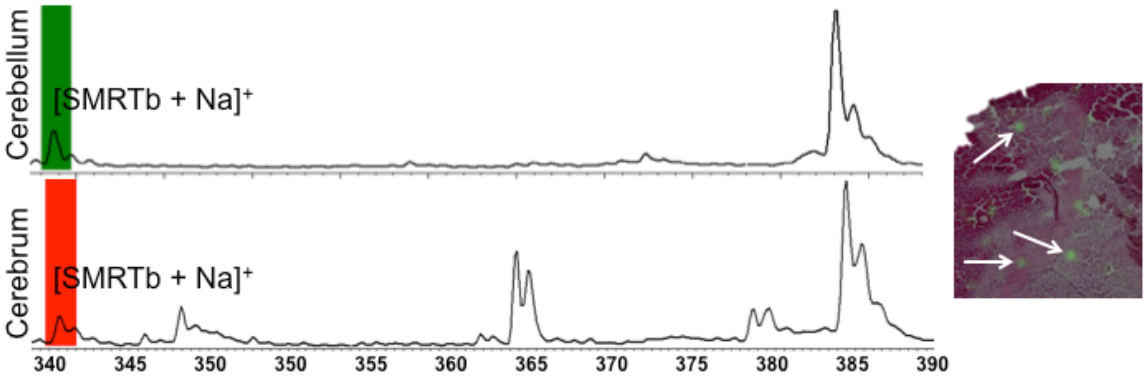

Figure 3. MALDI-MSI of brains from SMRT-treated mice. The top panel shows a sodiated adduct found in cerebellum, imaging shown on right: green spots (white arrows) correspond to signal. Tissue was H&E stained following MSI. The bottom panel shows a sodiated adduct found in the cerebrum.

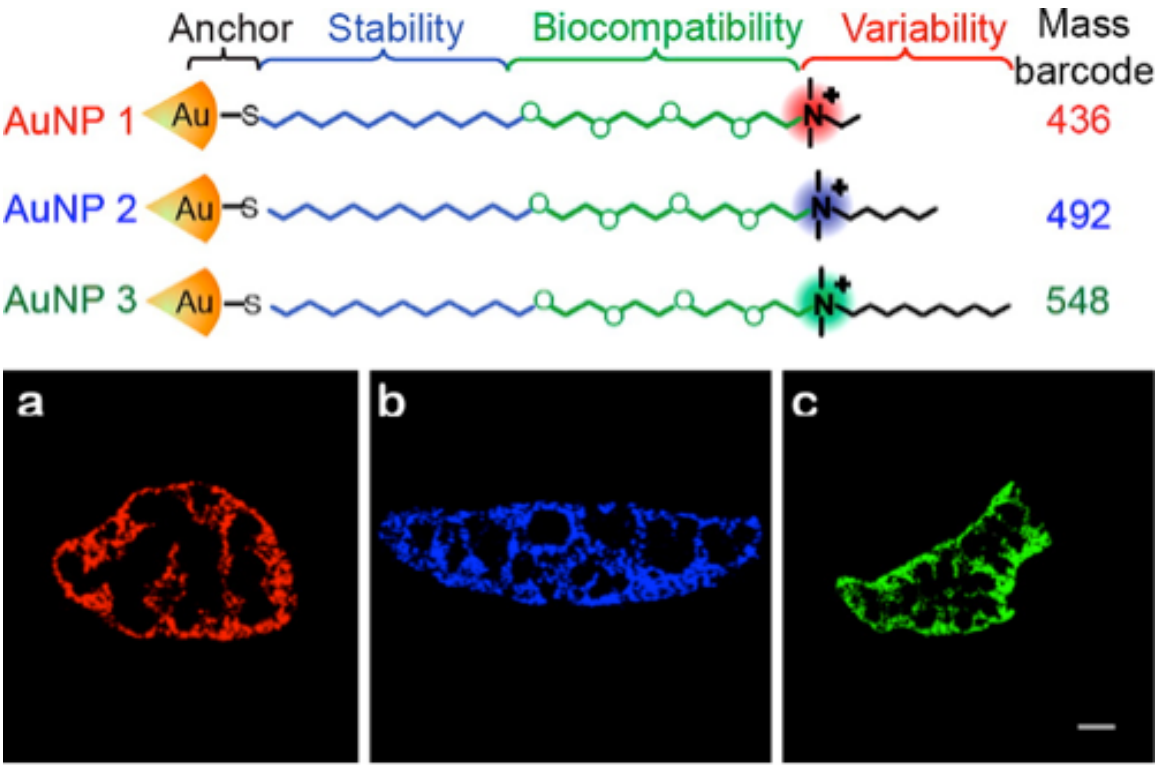

Figure 4. Structures of the surface monolayers on the AuNPs: the "mass barcode" is the *m*/*z* of the AuNP surface ligand. LDI-MS images of AuNPs in mouse spleens. The biodistributions of AuNPs are shown in panel (a) (AuNP 1), (b) (AuNP 2), and (c) (AuNP 3). Reprinted and adapted with permission from the *Journal of the American Chemical Society*. Copyright © 2013 American Chemical Society [56].

REFERENCES

ANDERSSON, M., GROSECLOSE, M. R., DEUTCH, A. Y. & CAPRIOLI, R. M. 2008. Imaging mass spectrometry of proteins and peptides: 3D volume reconstruction. *Nat Meth,* 5, 101-108.

BARTON-DAVIS, E. R., SHOTURMA, D. I. & SWEENEY, H. L. 1999. Contribution of satellite cells to IGF-I induced hypertrophy of skeletal muscle. *Acta Physiol Scand,* 167, 301-5.

BÖRNER, K., MALMBERG, P., MÅNSSON, J.-E. & NYGREN, H. 2007. Molecular imaging of lipids in cells and tissues. *International Journal of Mass Spectrometry,* 260, 128-136.

BUCCOLIERO, R. & FUTERMAN, A. H. 2003. The roles of ceramide and complex sphingolipids in neuronal cell function. *Pharmacological Research,* 47, 409-419.

BULLEY, N. R., FATTORI, M., MEISEN, A. & MOYLS, L. 1984. Supercritical fluid extraction of vegetable oil seeds. *Journal of the American Oil Chemists' Society,* 61, 1362-1365.

CASTELLINO, S. 2012. MALDI imaging MS analysis of drug distribution in tissue: the right time!(?). *Bioanalysis,* 4, 2549-2551.

CASTELLINO, S., GROSECLOSE, M. R., SIGAFOOS, J., WAGNER, D., DE SERRES, M., POLLI, J. W., ROMACH, E., MYER, J. & HAMILTON, B. 2013. Central Nervous System Disposition and Metabolism of Fosdevirine (GSK2248761), a Non-Nucleoside Reverse Transcriptase Inhibitor: An LC-MS and Matrix-Assisted Laser Desorption/Ionization Imaging MS Investigation into Central Nervous System Toxicity. *Chemical Research in Toxicology,* 26, 241-251.

CASTELLINO, S., GROSECLOSE, M. R. & WAGNER, D. 2011. MALDI imaging mass spectrometry: bridging biology and chemistry in drug development. *Bioanalysis,* 3, 2427-41.

CHAURAND, P., CORNETT, D. S. & CAPRIOLI, R. M. 2006. Molecular imaging of thin mammalian tissue sections by mass spectrometry. *Current Opinion in Biotechnology,* 17, 431-436.

CHUN, H. H. & GATTI, R. A. 2004. Ataxia-telangiectasia, an evolving phenotype. *DNA Repair (Amst),* 3, 1187-96.

CHUN, H. H., SUN, X., NAHAS, S. A., TERAOKA, S., LAI, C.-H., CONCANNON, P. & GATTI, R. A. 2003. Improved diagnostic testing for ataxia–telangiectasia by immunoblotting of nuclear lysates for ATM protein expression. *Molecular Genetics and Metabolism,* 80, 437-443.

COLSCH, B., JACKSON, S. N., DUTTA, S. & WOODS, A. S. 2011. Molecular Microscopy of Brain Gangliosides: Illustrating their Distribution in Hippocampal Cell Layers. *ACS Chemical Neuroscience,* 2, 213-222.

CONTE, E., MILANI, R., MORALI, G. & ABBALLE, F. 1997. Comparison between accelerated solvent extraction and traditional extraction methods for the analysis of the herbicide diflufenican in soil. *Journal of Chromatography A,* 765, 121-125.

COONS, A. H., CREECH, H. J., JONES, R. N. & BERLINER, E. 1942. The demonstration of pneumococcal antigen in tissues by the use of fluorescent antibody. *J. Immunol,* 45, 159-70.

DU, L., DAMOISEAUX, R., NAHAS, S., GAO, K., HU, H., POLLARD, J. M., GOLDSTINE, J., JUNG, M. E., HENNING, S. M., BERTONI, C. & GATTI, R. A.

2009. Nonaminoglycoside compounds induce readthrough of nonsense mutations. *J Exp Med,* 206, 2285-97.

DU, L., JUNG, M. E., DAMOISEAUX, R., COMPLETO, G., FIKE, F., KU, J. M., NAHAS, S., PIAO, C., HU, H. & GATTI, R. A. 2013. A New Series of Small Molecular Weight Compounds Induce Read Through of All Three Types of Nonsense Mutations in the ATM Gene. *Mol Ther*.

EBERLIN, L. S., FERREIRA, C. R., DILL, A. L., IFA, D. R., CHENG, L. & COOKS, R. G. 2011a. Nondestructive, Histologically Compatible Tissue Imaging by Desorption Electrospray Ionization Mass Spectrometry. *ChemBioChem,* 12, 2129-2132.

EBERLIN, L. S., LIU, X., FERREIRA, C. R., SANTAGATA, S., AGAR, N. Y. R. & COOKS, R. G. 2011b. Desorption Electrospray Ionization then MALDI Mass Spectrometry Imaging of Lipid and Protein Distributions in Single Tissue Sections. *Analytical Chemistry,* 83, 8366-8371.

EBERLIN, L. S., NORTON, I., ORRINGER, D., DUNN, I. F., LIU, X., IDE, J. L., JARMUSCH, A. K., LIGON, K. L., JOLESZ, F. A., GOLBY, A. J., SANTAGATA, S., AGAR, N. Y. R. & COOKS, R. G. 2013. Ambient mass spectrometry for the intraoperative molecular diagnosis of human brain tumors. *Proceedings of the National Academy of Sciences,* 110, 1611-1616.

ELLIS, S. R., BROWN, S. H., IN HET PANHUIS, M., BLANKSBY, S. J. & MITCHELL, T. W. 2013. Surface analysis of lipids by mass spectrometry: More than just imaging. *Progress in Lipid Research,* 52, 329-353.

FAHY, E., SUBRAMANIAM, S., BROWN, H. A., GLASS, C. K., MERRILL, A. H., MURPHY, R. C., RAETZ, C. R. H., RUSSELL, D. W., SEYAMA, Y., SHAW, W.,

SHIMIZU, T., SPENER, F., VAN MEER, G., VANNIEUWENHZE, M. S., WHITE, S. H., WITZTUM, J. L. & DENNIS, E. A. 2005. A comprehensive classification system for lipids. *Journal of Lipid Research,* 46, 839-862.

FERGUSON, L., BRADSHAW, R., WOLSTENHOLME, R., CLENCH, M. & FRANCESE, S. 2011. Two-Step Matrix Application for the Enhancement and Imaging of Latent Fingermarks. *Analytical Chemistry,* 83, 5585-5591.

FUCHS, B., SÜS, R. & SCHILLER, J. 2010. An update of MALDI-TOF mass spectrometry in lipid research. *Progress in Lipid Research,* 49, 450-475.

GARCÍA-AYUSO, L. E., VELASCO, J., DOBARGANES, M. C. & LUQUE DE CASTRO, M. D. 2000. Determination of the oil content of seeds by focused microwave-assisted soxhlet extraction. *Chromatographia,* 52, 103-108.

GATTI, R. A. 2012. SMRT compounds correct nonsense mutations in primary immunodeficiency and other genetic models. *Ann N Y Acad Sci,* 1250, 33-40.

HOLTHUIS, J. C. M., POMORSKI, T., RAGGERS, R. J., SPRONG, H. & VAN MEER, G. 2001. The Organizing Potential of Sphingolipids in Intracellular Membrane Transport. *Physiological Reviews,* 81, 1689-1723.

HUTCHINSON, R. W., COX, A. G., MCLEOD, C. W., MARSHALL, P. S., HARPER, A., DAWSON, E. L. & HOWLETT, D. R. 2005. Imaging and spatial distribution of β-amyloid peptide and metal ions in Alzheimer's plaques by laser ablation–inductively coupled plasma–mass spectrometry. *Analytical Biochemistry,* 346, 225-233.

LAI, C. H., CHUN, H. H., NAHAS, S. A., MITUI, M., GAMO, K. M., DU, L. & GATTI, R. A. 2004. Correction of ATM gene function by aminoglycoside-induced read-

through of premature termination codons. *Proc Natl Acad Sci U S A,* 101, 15676-81.

LAZOVA, R., SEELEY, E. H., KEENAN, M., GUEORGUIEVA, R. & CAPRIOLI, R. M. 2012. Imaging Mass Spectrometry—A New and Promising Method to Differentiate Spitz Nevi From Spitzoid Malignant Melanomas. *The American Journal of Dermatopathology,* 34, 82-90.

LEAR, J., HARE, D. J., FRYER, F., ADLARD, P. A., FINKELSTEIN, D. I. & DOBLE, P. A. 2012. High-Resolution Elemental Bioimaging of Ca, Mn, Fe, Co, Cu, and Zn Employing LA-ICP-MS and Hydrogen Reaction Gas. *Analytical Chemistry,* 84, 6707-6714.

MARSHALL, A. G., HENDRICKSON, C. L. & JACKSON, G. S. 1998. Fourier transform ion cyclotron resonance mass spectrometry: A primer. *Mass Spectrometry Reviews,* 17, 1-35.

MCCOMBIE, G. & KNOCHENMUSS, R. 2004. Small-Molecule MALDI Using the Matrix Suppression Effect To Reduce or Eliminate Matrix Background Interferences. *Analytical Chemistry,* 76, 4990-4997.

MCDONNELL, L. A. & HEEREN, R. M. 2007a. Imaging mass spectrometry. *Mass Spectrom Rev,* 26, 606-43.

MCDONNELL, L. A. & HEEREN, R. M. A. 2007b. Imaging mass spectrometry. *Mass Spectrometry Reviews,* 26, 606-643.

MENG, H., LIONG, M., XIA, T., LI, Z., JI, Z., ZINK, J. I. & NEL, A. E. 2010. Engineered design of mesoporous silica nanoparticles to deliver doxorubicin and P-

glycoprotein siRNA to overcome drug resistance in a cancer cell line. *ACS Nano,* 4, 4539-50.

MOROSI, L., SPINELLI, P., ZUCCHETTI, M., PRETTO, F., CARRÀ, A., D'INCALCI, M., GIAVAZZI, R. & DAVOLI, E. 2013. Determination of Paclitaxel Distribution in Solid Tumors by Nano-Particle Assisted Laser Desorption Ionization Mass Spectrometry Imaging. *PLoS ONE,* 8, e72532.

MURPHY, R. C., HANKIN, J. A. & BARKLEY, R. M. 2009. Imaging of lipid species by MALDI mass spectrometry. *Journal of Lipid Research,* 50, S317-S322.

RASEY, J. S., KROHN, K. A., GRUNBAUM, Z., SPENCE, A. M., MENARD, T. W. & WADE, R. A. 1986. Synthesis, biodistribution, and autoradiography of radiolabeled S-2-(3-methylaminopropylamino)ethylphosphorothioic acid (WR-3689). *Radiat Res,* 106, 366-79.

REYZER, M. & CAPRIOLI, R. 2011. Imaging Mass Spectrometry. *In:* BANOUB, J. (ed.) *Detection of Biological Agents for the Prevention of Bioterrorism.* Springer Netherlands.

RUBAKHIN, S. S., JURCHEN, J. C., MONROE, E. B. & SWEEDLER, J. V. 2005. Imaging mass spectrometry: fundamentals and applications to drug discovery. *Drug Discovery Today,* 10, 823-837.

RUDIN, M. & WEISSLEDER, R. 2003. Molecular imaging in drug discovery and development. *Nat Rev Drug Discov,* 2, 123-131.

RUJOI, M., ESTRADA, R. & YAPPERT, M. C. 2004. In Situ MALDI-TOF MS Regional Analysis of Neutral Phospholipids in Lens Tissue. *Analytical Chemistry,* 76, 1657-1663.

SANCHEZ-CARBAYO, M. 2006. Antibody Arrays: Technical Considerations and Clinical Applications in Cancer. *Clinical Chemistry,* 52, 1651-1659.

SCHULTZ, C., NEEF, A. B., GADELLA, T. W. & GOEDHART, J. 2010. Imaging Lipids in Living Cells. *Cold Spring Harbor Protocols,* 2010, pdb.top83.

SCHWAMBORN, K. & CAPRIOLI, R. M. 2010. MALDI Imaging Mass Spectrometry – Painting Molecular Pictures. *Molecular Oncology,* 4, 529-538.

SOLON, E. G., SCHWEITZER, A., STOECKLI, M. & PRIDEAUX, B. 2009. Autoradiography, MALDI-MS, and SIMS-MS Imaging in Pharmaceutical Discovery and Development. *The AAPS Journal,* 12, 11-26.

SWIFT, M., MORRELL, D., CROMARTIE, E., CHAMBERLIN, A. R., SKOLNICK, M. H. & BISHOP, D. T. 1986. The incidence and gene frequency of ataxia-telangiectasia in the United States. *Am J Hum Genet,* 39, 573-83.

TAYLOR, S., KING, J. & LIST, G. 1993. Determination of oil content in oilseeds by analytical supercritical fluid extraction. *Journal of the American Oil Chemists' Society,* 70, 437-439.

WANG, H.-Y. J., LIU, C. B. & WU, H.-W. 2011. A simple desalting method for direct MALDI mass spectrometry profiling of tissue lipids. *Journal of Lipid Research,* 52, 840-849.

WATROUS, J. D., ALEXANDROV, T. & DORRESTEIN, P. C. 2011. The evolving field of imaging mass spectrometry and its impact on future biological research. *Journal of Mass Spectrometry,* 46, 209-222.

WENK, M. R. 2005. The emerging field of lipidomics. *Nat Rev Drug Discov,* 4, 594-610.

WOODS, A. S., COLSCH, B., JACKSON, S. N., POST, J., BALDWIN, K., ROUX, A., HOFFER, B., COX, B. M., HOFFER, M., RUBOVITCH, V., PICK, C. G., SCHULTZ, J. A. & BALABAN, C. 2013. Gangliosides and Ceramides Change in a Mouse Model of Blast Induced Traumatic Brain Injury. *ACS Chemical Neuroscience,* 4, 594-600.

YAN, B., KIM, S. T., KIM, C. S., SAHA, K., MOYANO, D. F., XING, Y., JIANG, Y., ROBERTS, A. L., ALFONSO, F. S., ROTELLO, V. M. & VACHET, R. W. 2013. Multiplexed Imaging of Nanoparticles in Tissues Using Laser Desorption/Ionization Mass Spectrometry. *Journal of the American Chemical Society,* 135, 12564-12567.

YOSHIZAWA, S., FOURMY, D. & PUGLISI, J. D. 1998. Structural origins of gentamicin antibiotic action. *EMBO J,* 17, 6437-48.

ZEMSKI BERRY, K. A., HANKIN, J. A., BARKLEY, R. M., SPRAGGINS, J. M., CAPRIOLI, R. M. & MURPHY, R. C. 2011. MALDI Imaging of Lipid Biochemistry in Tissues by Mass Spectrometry. *Chemical Reviews,* 111, 6491-6512.

ZINGMAN, L. V., PARK, S., OLSON, T. M., ALEKSEEV, A. E. & TERZIC, A. 2007. Aminoglycoside-induced translational read-through in disease: overcoming nonsense mutations by pharmacogenetic therapy. *Clin Pharmacol Ther,* 81, 99-103.

ZORIY, M., MATUSCH, A., SPRUSS, T. & BECKER, J. S. 2007. Laser ablation inductively coupled plasma mass spectrometry for imaging of copper, zinc, and platinum in thin sections of a kidney from a mouse treated with cis-platin. *International Journal of Mass Spectrometry,* 260, 102-106.

ZORIY, M. V., DEHNHARDT, M., MATUSCH, A. & BECKER, J. S. 2008. Comparative imaging of P, S, Fe, Cu, Zn and C in thin sections of rat brain tumor as well as control tissues by laser ablation inductively coupled plasma mass spectrometry. *Spectrochimica Acta Part B: Atomic Spectroscopy,* 63, 375-382.

CHAPTER 2

Mass Spectrometry Imaging of Small Drug Molecules: Ionization and Sample Preparation

Mass Spectrometry Imaging of Small Drug Molecules: Ionization and Sample Preparation

Carly N. Ferguson, Joseph W.M. Fowler, Jonathan F. Waxer, Christine Fontanilla, Sean Shen, Roberto Ortiz, Ewa Micewicz, Dorthe Schaue, William H. McBride, Gal Bitan, Michael Hall, Jean Lee, Richard A. Gatti, Joseph A. Loo

ABSTRACT

Mass spectrometry imaging (MSI) is a powerful tool for the analysis of biodistribution of small drug compounds. However, in tissue this lower molecular weight range is complicated by innate small molecules, lipids, salts, and MALDI matrices. Ion suppression plays a large role due to the high abundance of these innate compounds compared to the relatively low abundance of dosed drug compounds. We utilized solvents of varying polarities to assess the effectiveness of a tissue wash step to enhance small drug molecule signal by studying compound types: benzodiazepines, small molecule read through (SMRT) compounds, molecular tweezers (MT), radiomitigators (RM) and mesoporous silica nanoparticles (MSNP). Wash steps were found to enhance signal without delocalization in benzodiazepine, SMRT, and MSNP experiments; however, only SMRT was present in high enough concentrations to be detected in dosed animals. Wash steps did not have any added benefit in MT and RM experiments, though MT was detected in dosed animals without the use of a wash step. Wash steps can be utilized to enhance sensitivity, though optimization is key.

INTRODUCTION

Matrix-assisted laser desorption/ionization mass spectrometry imaging (MALDI-MSI) is a useful tool in visualizing small molecule and drug distribution within animal tissue as it is a label-free method that allows for high spatial resolution.[3] A tandem time-of-flight mass spectrometer (TOF/TOF-MS) is typically used such that observed molecules (or peaks) can be fragmented in order to confirm identification. One of the drawbacks of MALDI-MSI on small molecules is the complex nature of the lower mass range of a spectrum, largely due to matrix molecules that fall within the same mass range as a drug compound (<1,000 Daltons). However, this limitation can be overcome by optimization of the ionization source or by optimization of tissue preparation protocols to enhance sensitivity of the MSI methods.[59] Taken together, these indicate that MSI is a powerful method for visualizing drugs and resulting metabolite distributions in tissue. Here, we will discuss DESI, LESA, and LAESI ionization techniques, as well as solvent optimization by pH and polarity.

Desoprtion Electrospray Ionization (DESI) is the first mass spectrometry (MS) method to operate in an ambient environment.[60] This technique allows samples to be subjected to processing actions and/or testing conditions while the mass spectra are being recorded. This method has high sensitivity, is virtually instantaneous in response time, and is applicable to small-molecule organic compounds.[60] DESI combines features of electrospray ionization (ESI) with those of the family of desorption ionization (DI) methods.[61] An electrospray emitter is used to create gas-phase solvent ions, ionic clusters, and charged microdroplets which are directed at the sample. An electrical potential of several kilovolts is applied to the spray solution and pneumatic nebulization

is used to assist in desolvation.[60] All of the DI methods (plasma desorption, PD; laser desorption ionization, LDI; matrix assisted laser desorption ionization, MALDI; secondary ion mass spectrometry, SIMS; fast atom bombardment, FAB) involve the impact on condensed-phase samples of projectiles, however, the principal feature that distinguishes DESI from other DI methods is its independence from high-vacuum environments.[60]

Another unique feature of DESI is its ability to analyze organic molecules at sample surfaces by MS without any sample preparation. In order to achieve ionization, the sample is first sprayed with an electrically charged aqueous mist by directing a pneumatically assisted electrospray at the surface of the sample.[60] This releases ions from the surface and allows them to travel through air, at atmospheric pressure, to the atmospheric interface of the mass spectrometer. DESI ion sources are readily connected to any mass spectrometer equipped with an atmospheric pressure interface, and, depending on the capabilities of the mass spectrometer, tandem MS, selected ion monitoring, exact mass, and other types of measurement are possible.[60] Although sample preparations are not necessary for DESI analysis, elected chemicals can be added to the spray solution to provide specificity for the ionization of particular types of analytes. In all cases, the sample remains fully accessible to observation as well as additional physical and chemical processing during analysis.[60]

When imaging surfaces, spatial resolution becomes an important performance parameter. Parameters which influence DESI's spatial resolution include the incident angle (α), the spray tip-to-surface distance (d_1), the spray tip diameter, the solvent flow

rate, the nebulizing gas flow rate, and the orifice diameter of the entrance capillary into the mass spectrometer.[60]

Beyond the instrumental parameters, several other surface factors should be considered as well. The electrical conductivity of the surface, for example, is particularly important with regard to DESI ionization. Since the DESI mechanism involves the landing and release of charged particles at a surface, neutralization at the surface must be avoided.[60] Neutralization is most likely to occur in the case of conductive materials, such as metals or graphite, which must either be carefully isolated or floated at a potential that is equal to or lower than the spray voltage.[60] Secondly, the electrostatic properties of the surface are also important to consider. The stability of the signal is largely dependent on the surface's preference for the polarity of the spray. For instance, polytetrafluoroethylene (PTFE) is a highly electronegative polymer and gives excellent signal stability in the negative-ion mode, while poly(methyl methacrylate) (PMMA) gives better performance in the positive-ion mode.[60]

Furthermore, the chemical nature of the surface is also an important parameter. In order to avoid an uneven distribution of the analyte on the surface, one must consider the surface's affinity towards the analyte, for the nature of the surface may affect crystallization of the analyte when the sample is deposited from solution.[60] This is a necessary precaution because a loss of sensitivity occurs in cases of high affinity of analyte molecules to the surface substrate. PTFE is a generally applicable surface, in part because of its low affinity toward most analytes.[60]

Finally, surface roughness was observed by Takáts *et al.* (2005) to have an effect on ionization efficiency. Microscope glass slides were used as DESI substrate

before and after high frequency (HF) etching. Etching was found to dramatically increase signal stability and to eliminate 'sweet spot' effects. Therefore, rough surfaces like paper give high sensitivity and are often the substrates of choice for DESI.[60]

The potential of MS for chemical imaging is well recognized and it is now increasingly being used to image specific biological compounds in biological tissue.[62] SIMS and MALDI-TOF are the two main methods being used for these experiments, unfortunately, both methods are demanding with regard to sample preparation.[60] DESI, on the other hand, requires no destructive matrix and little or no sample preparation. In the realm of small molecule imaging, the absence of matrix ions provide major advantages due to the mixed analyte-matrix clusters crowding the low-mass range.[63]

DESI provides a significant advantage when considering the flexibility of sample preparation. The fact that the sample is fully accessible to manipulation during the imaging experiment makes the imaging of living systems conceivable. This feature makes *in vivo* analysis possible, and a few examples have already been reported, including the analysis of skin and wound surfaces.[64]

The major challenge in developing a DESI-imaging capability is to achieve the appropriate spot sizes. Unlike MALDI-TOF and SIMS which offer much higher spatial resolution on the cellular and subcellular levels,[63] spot sizes of 50 μm in circular area can be reached using fine capillaries.[60] To improve resolution further it will be necessary to use new approaches, such as new hybrid methods. In these methods, DESI is used to define a larger area of sample and to provide a mechanism for ionization and ion transport from this region. Subsequently, a fine laser spot, or needlepoint, is used to

define a region by its unique thermal or electrical potential, as well as to distinguish ions arising from the target subarea for study within the sample.[60]

Two methods of ionization, Liquid Extraction Surface Analysis (LESA) and Laser Ablation Electrospray Ionization (LAESI), have been coupled with mass spectrometry to visualize molecules in various tissues *in situ*. Recent findings have shown the applicability of these techniques to characterize and localize small molecules in tissue. Biodistribution of small molecules through mass spectrometry has been challenging due to their small size and diversity of chemical properties. However, LESA and LAESI offer two useful approaches towards small molecule analysis.

LESA combines micro-liquid extraction with nano-electrospray to ionize surface molecules on a tissue sample.[65] An automated system dispenses a small volume of extraction solvent over targeted areas in a given tissue section. A liquid junction forms over the tissue and a static extraction occurs. After a defined length of time, the solvent is aspirated and put in contact with an electrospray ionization (ESI) source. The ionized molecules within the extraction solvent are then coupled with a mass spectrometer.[65,66] Mass spectra are then obtained for each placement of extraction solvent, allowing the production of a map of specific analytes within a system. For example, studies have been able to profile small molecules, such as terfenadine and its metabolite fexofenadine, within mouse organs, as well as produce relative quantification data.[66]

LAESI utilizes a mid-infrared laser beam to ablate molecules on tissue and ionize them through an electrospray ionization source.[67] Tissue sections are thaw-mounted onto a microscope slide. Defined regions of analysis are mapped out and the sample is then exposed to a mid-infrared laser beam at a wavelength of 2.94 μm. The laser beam

excites the O-H in water molecules within the sample, causing phase explosion and microscale ablation.[68] The laser beam is focused so that the ejected molecules pass downstream to an electrospray emitter. The intercepting electrospray plume of charged droplets produces gas phase ions that are then sent directly into a coupled mass spectrometer.[67] Current studies using LAESI have been able to localize small drug molecules and lipids in rat brain, small analytes in plant seedlings, and small molecules in single cells.[67-69]

As with all forms of MSI, LESA-MSI and LAES-MSI have their advantages and disadvantages in small molecule analysis. Both overcome the boundary of needing pretreatment or a matrix coating.[70] LESA employs a type of “soft ionization” that allows fragile molecules *in situ* to remain intact and enter the mass spectrometer.[66] Moreover, LAESI is an advantageous technique because it can map metabolites in tissue in an atmospheric environment. Where other MSI techniques ionize molecules in vacuums, LAESI has the ability to analyze tissues in an environment that is more congruent to native conditions. In LESA, the type of extraction solvent and time of extraction and aspiration are all variables that need to be optimized to each tissue and analyte. This variation makes it difficult to perform whole body relative quantification of a small molecule. LAESI also has a large disadvantage because ionization of molecules depends on a water rich target. Therefore, dehydration is a common problem with LAESI, though steps have been taken to overcome it.

In this study, we optimized small molecule ionization by MALDI and a polarity-based solvent wash step for 5 molecules or molecule classes: benzodiazepines, small molecule read-through (SMRT) compounds, a tweezer compound (CLR01), a

radiomitigator (RM512), and mesoporous silica nanoparticles (MSNP). Diazepam is currently used as treatment, and thus served as a standard for study, and its structure is shown in Figure 1C. The remaining compounds are each studied for potential medical significance, as will be discussed below.

The treatment and management of genetic disorders are major target areas in the drug development field. Genetic disorders caused by single-nucleotide polymorphisms (SNPs), specifically those caused by premature termination codons (PTCs), comprise over 30% of all genetic disorders. PTCs halt read-through of the genetic code, resulting in truncated forms of proteins.[43] Of particular interest is Ataxia-telangiectasia (A-T), a PTC disorder caused by a SNP in the gene coding for AT-mutated (ATM) protein.[46] Aminoglycosides are drugs traditionally used to treat PTC disorders; however, they have shown to be toxic and their large, rigid structures make blood-brain barrier penetration unlikely. Crossing of the blood-brain barrier is imperative in the treatment of A-T, as one of the disorder's hallmarks is impaired cerebellum development. SMRT compounds are a promising treatment option, and were studied by MALDI-MSI, with structures shown in Figure 2.

Neurodegenerative disorders are another key area of medicine, and a major target area in the drug development field. Amyloid-associated diseases, such as Alzheimers and Parkinsons, account for a significant amount of medical care cost and are increasing issues in the aging population. Though the mechanisms of the diseases are still unclear, therapies to combat amyloid plaque formation are a popular area of development.[71] One such therapy, termed molecular tweezers, has shown success both *in vitro* and *in vivo* rat studies as it successfully disrupts amyloid fibrils.[72,73] Two

questions remain: do these compounds (specifically tweezer CLR01, structure shown in Figure 1A) cross the blood-brain barrier, and do they colocalize with amyloid plaques? Preliminary autoradiography data indicates that CLR01 crosses the blood-brain barrier at 1-3% efficiency.

Recent world events have created another area of interest in the field of drug development: the need for radiomitigator compounds. The Fukushima nuclear disaster following the earthquake and subsequent tsunami in Japan during 2011 created a large population of people exposed to high doses of radiation. Radiation exposure has several adverse side effects due to DNA breakage and includes increased cancer susceptibility.[74] There are two compound types to consider: radioprotectors and radiomitigators. Radioprotectors function typically as free radical scavengers, and thus must be administered prior to radiation exposure or at the exact moment of exposure.[75] Radiomitigators, on the other hand, function by activating a series of cascading pathways that play a role in DNA repair. These compounds can then be administered after exposure, as they are able to assist in mitigating downstream effects. Two classes of antibiotics were previously indicated as having success *in vivo* when administered to mice post-radiation exposure.[75]

While these antibiotic classes are promising, their large, rigid structures make penetration of the blood-brain barrier unlikely.[75] High-throughput screens were utilized to identify a new class of radiomitigators (RM) with a smaller, more flexible structure. One such compound, RM512 (structure shown in Figure 1B), was shown to extend survival of treated mice out to 100 days post-exposure. While the effects of RM512

have been positive, the distribution of the compound in tissue was thus far unknown and was studied by MALDI-MSI.

A growing problem in the medical field is that of drug-resistant cancers. Recently, synergistic treatment of such cancer cells via siRNA and small molecules utilizing a novel drug delivery vehicle, mesoporous silica nanoparticles (MSNPs), has been developed by Dr. Jeff Zink, and were shown to be effective *in vitro*.[55] We sought to further explore their biodistribution via MALDI-MSI.

In this study, we examined the effects of wash solvents on the above-mentioned molecules by MALDI-MSI. Additionally, we studied the biodistribution of these same molecules in treated animals via MALDI-MSI. While the wash solvents were successful for some of the molecules, they were not universally applicable. Biodistribution was possible for some of the molecules, but LC-MS/MS analysis of the extracted tissue homogenates indicate there are still sensitivity issues associated with MALDI-MSI.

METHODS

Materials. Diazepam, D5-diazepam, oxazepam, D5-oxazepam, temazepam, and desmethyldiazepam were provided by Dr. Michael Hall (Amgen). SMRTs RTC13, BZ6, BZ16, 216, 216-3, 216-3 salt, 216-4, 216-5, and 216-6 were synthesized by the lab of Dr. Michael Jung (UCLA). Mesoporous silica nanoparticles (MSNP) were synthesized by the lab of Dr. Jeffrey Zink (UCLA). RM512 was provided by the lab of Dr. Bill McBride (UCLA). CLR01 was provided by the lab of Dr. Gal Bitan. Eosin Y, hematoxylin, and VectaShield hardset mounting medium were purchased from Fisher Scientific. Acetonitrile (ACN), α-Cyano-4-hydroxycinnamic acid (CHCA), 2,5-dihydroxybenzoic acid (DHB), dimethyl sulfoxide (DMSO), ethanol, formic acid (FA), glacial acetic acid,

norharmane (NHM), titanium dioxide (TiO_2), trifluoroacetic acid (TFA), and xylene were purchased from Sigma-Aldrich.

Diazepam Animal Dosing. Male CD-1 mice (6-8 weeks) were used. Diazepam was administered at a single dosage of 15 mg/kg as intraperitoneal injections. A total of 24 CD-1 mice were used: 6 vehicle controls 18 diazepam-dosed. Mice were bred and maintained in a strict defined-flora, pathogen-free environment in the American Association of Laboratory Animal Care–accredited animal facilities of the Amgen. The Amgen Animal Care and Use Committee approved all experiments, which were done in accordance with all local and national guidelines for the care and use of animals.

Diazepam Organ Extraction. Mice were sacrificed at 0 h (vehicle), 0.1 h, 1 h, and 6 h using isofluorane, with 6 mice sacrificed at each timepoint. Additionally, at each of the 0.1 h, 1 h, and 6 h timepoints 3 different perfusion techniques were employed, with 2 mice per technique: minimal blood removal, light exsanguination by cardiocentesis, and transcardio perfusion. Vehicle-treated mice were perfused with minimal blood removal. Brains were excised, and each was flash frozen in -50 ^{o}C isopentane before being stored at -80 ^{o}C until further experiments.

Diazepam Blood Collection. Approximately 0.07 mL of whole blood were collected per mouse via retro-orbital sinus puncture vein or cardiac puncture. Blood was allowed to clot for 20 mins at room temperature, and subsequently centrifuged for serum (approximately 0.040 mL per mouse). All specimens were stored at -80 ^{o}C until further experiments.

BZ6 and BZ16 Animal Dosing. C57/Black 6 (BL6) and severe compromised immunodeficiency (SCID) mice were used. SMRTs BZ6 and BZ16 were administered at

a dosage of 30 mg/kg over the course of 8 weeks for a total of 6 intraperitoneal injections. A total of 8 C57BL/6 and 8 SCID mice were used for each of the 3 treatment groups (vehicle, BZ6, and BZ16). Mice were bred and maintained in a strict defined-flora, pathogen-free environment in the American Association of Laboratory Animal Care–accredited animal facilities of the Department of Radiation Oncology, University of California Los Angeles. The University of California at Los Angeles Animal Care and Use Committee approved all experiments, which were done in accordance with all local and national guidelines for the care and use of animals.

BZ6 and BZ16 Organ Extraction. Mice were sacrificed using isofluorane, and the following organs were excised: brain, heart, kidney, liver, lung, and spleen. Each organ was excised and flash frozen in -50 ^{o}C isopentane before being stored at -80 ^{o}C until further experiments.

RTC13, 216, and 216-3 Animal Dosing. C57/Black 6 (BL6) mice were used. SMRTs RTC13, 216, and 216-3 were administered a single dosage of 30 mg/kg as intraperitoneal injections. A total of 20 C57BL/6 mice were used: 2 vehicle controls, 6 RTC13-dosed, 6 216-dosed, and 6 216-3-dosed. Mice were bred and maintained in a strict defined-flora, pathogen-free environment in the American Association of Laboratory Animal Care–accredited animal facilities of the Department of Radiation Oncology, University of California Los Angeles. The University of California at Los Angeles Animal Care and Use Committee approved all experiments, which were done in accordance with all local and national guidelines for the care and use of animals.

RTC13, 216, and 216-3 Organ Extraction. Mice were sacrificed at 0 h (vehicle), 2 h, 8 h, and 24 h using isofluorane, with 2 mice per drug sacrificed at each timepoint. The

following organs were excised: brain, heart, kidney, liver, lung, and spleen. Each organ was excised and flash frozen in -50 ^{o}C isopentane before being stored at -80 ^{o}C until further experiments.

RM512 Animal Dosing. C3H mice were used. RM512 was administered at a single dosage of 5 mg/kg as intraperitoneal injections. A total of 8 C3H mice were used: 2 vehicle controls and 6 RM512-dosed. Mice were bred and maintained in a strict defined-flora, pathogen-free environment in the American Association of Laboratory Animal Care–accredited animal facilities of the Department of Radiation Oncology, University of California Los Angeles. The University of California at Los Angeles Animal Care and Use Committee approved all experiments, which were done in accordance with all local and national guidelines for the care and use of animals.

RM512 Organ Extraction. Mice were sacrificed at 0 h (vehicle), 2 h, 4 h, and 24 h using isofluorane, with 2 mice sacrificed at each timepoint. The following organs were excised: brain, gut, heart, kidney, liver, lung, and spleen. Each organ was excised and flash frozen in -50 ^{o}C isopentane before being stored at -80 ^{o}C until further experiments.

CLR01 Animal Dosing. Triple transgenic neurodegenerative (Alzheimer's disease) mice (older than 1 year) were used due to their 3XTg tau, APP, and PS1 gene mutations that induce amyloid plaque formation. CLR01 was administered at a dosage of 10 mg/kg once per day over the course of 5 days as intraperitoneal injections. A total of 4 mice were used: 1 vehicle control and 3 CLR01. Mice were bred and maintained in a strict defined-flora, pathogen-free environment in the American Association of Laboratory Animal Care–accredited animal facilities of the Department of Neurology, University of California Los Angeles. The University of California at Los Angeles Animal

Care and Use Committee approved all experiments, which were done in accordance with all local and national guidelines for the care and use of animals.

CLR01 Organ Extraction. Mice were sacrificed using isofluorane. The following organs were excised: brain, liver, and spinal chord. Each organ was excised and flash frozen in -50 ^{o}C isopentane before being stored at -80 ^{o}C until further experiments.

Tissue Preparation. Organs were sectioned on a Leica CM1850 Cryostat at a thickness of 16 μm. Brain, gut, heart, kidney, liver, and spleen were sectioned at a temperature of -21 ^{o}C, while lung was sectioned at a temperature of -34 ^{o}C. All sections were thaw-mounted onto a glass slide, dried under vacuum at room temperature for 10 minutes, and subjected to a wash step (where applicable). Slides were subsequently coated in either a DHB or CHCA matrix at a concentration of 40 mg/mL or 7 mg/mL, respectively, in 50% ACN, 50% H_2O, and 0.1% TFA utilizing a Bruker ImagePrep or an HTX Technologies TM Sprayer.

Mass Spectrometry Imaging. All mass spectrometry (MS) and mass spectrometry imaging (MSI) were conducted on a Bruker Daltonics AutoFlex MALDI tandem time-of-flight (TOF/TOF) mass spectrometer equipped with a Smartbeam-II^{TM} Nd:YAG UV laser. A small molecule method was employed, covering the range of 0 to 1,000 m/z, operating in the linear positive mode. MSI experiments were run at a spatial resolution of 200 to 400 μm, averaging 500 spectra at each raster point. All experiments were run utilizing Bruker Daltonics software Compass package: FlexControl and FlexImaging. Additional MS experiments were conducted on a Bruker Daltonics SolariX Fourier-transform ion cyclotron resonance mass spectrometer (FT-ICR-MS) equipped with a

Smartbeam-II™ Nd:YAG UV Laser. All FT-ICR-MS data were collected using Bruker Daltonics software, SolariXControl.

Data Analysis. All MALDI-TOF/TOF-MS data analysis was conducted manually using Bruker Daltonics software, FlexAnalysis. All MALDI-TOF/TOF-MSI data analysis was conducted manually using Bruker Daltonics software, FlexImaging. All MALDI-FT-ICR-MS data analysis was conducted manually using Bruker Daltonics software, DataAnalysis.

Tissue Homogenization and Extraction. Organs from each treatment group and timepoint (where applicable) were homogenized using a 5 mL hand-held glass homogenizer. A tissue to water ratio of 1 g to 4 mL was used. Tissues were suspended in a given amount of water and pulverized for 30 s. From each homogenate stock, 50 μL were mixed with 150 μL of either 10 μM BZ6 (for BZ16, 512 2 h brain, 216 2 h brain, 216-3 2 h brain, and RTC13 2 h brain) or 10 μM 216-5 standard in ACN (all other organs, treatment groups, and timepoints), vortexed, and centrifuged for 10 min at 4,000 rpm. Supernatant was collected for future MS analysis. Brains from each treatment group and timepoint in the diazepam study were homogenized using QIAGEN TissueLyser II. The same extraction protocol was followed post-homogenization. Both D5-diazepam and D5-oxazepam were spiked into homogenates at a concentration of 0.1 μM for quantitative analyses.

Diazepam Serum Extraction. Plasma from each perfusion group and timepoint was extracted by combining 100 μL of plasma with 300 μL of 100% ACN, vortexing, and centrifuging for 10 min at 4000 rpm at room temperature. The supernatant was collected

for future MS analysis. Both D5-diazepam and D5-oxazepam were spiked into serum extracts at a concentration of 0.1 μM for quantitative analyses.

LC-MS/MS Validation. Samples were run on a Proxeon ThermoScientific EASY nano liquid chromatography (nLC) system equipped with an Acclaim PepMap100 C18 76 μm x 2 cm NanoViper trap column with 3 μm particle size and 100 Å pore size and a PepMapRSLC C18 75 μm x 15 cm analytical column with 2 μm particle size and 100 Å pore size. An aqueous mobile phase (A) was made up of 0.1% FA in H_2O, and an organic mobile phase (B) was made up of 0.1% FA in ACN. For each sample, 2 μL were injected onto the trap column, washed with 100% A for 5 minutes, and small molecules were eluted from the column with a gradient of 5-100% B over 5 minutes, and held at 100% B for 10 minutes at a flow rate of 5 μL/min. The nLC system is interfaced with a ThermoScientific Q Exactive™ hybrid quadrupole-orbitrap mass spectrometer.

LC-MS/MS Data Analysis. Data were analyzed and quantified using Thermo Xcalibur Qual and Quan Browser software. The molecular ions, $[M+H]^+$, for Diazepam (285.0794 m/z) and deuterated d-Diazepam (290.1108 m/z) were extracted within 10 ppm mass accuracy using Qual Browser to confirm their presence in plasma and determine approximate retention time (RT) windows for elution. Oxazepam (287.0587 m/z), a metabolite of Diazepam was also examined along with a deuterated d5-Oxazepam (292.0901 m/z) internal standard.

Qualitative analysis of Diazepam and Oxazepam in various mouse plasma samples was performed using Thermo Quan Browser. All analyte ions were extracted by their molecular ion m/z from the full MS scan of 200-2,000 m/z. Diazepam and d5-Diazepam was integrated at RT 13.49 min. with a 60 sec. elution window. Oxazepam

and d5-Oxazepam was integrated at 11.77 min. with a 60 sec. elution window. Peaks were integrated using the ICIS integration algorithm with the following parameters: peak detection: highest peak, smoothing points: 7, baseline window: 100, area noise factor: 2, peak noise factor: 10, minimum peak height (S/N): 3. Plasma concentrations for Diazepam and Oxazepam were determined in relation to the peak areas of their respective deuterated standards (0.01 μM). All samples were analyzed in triplicate.

RESULTS AND DISCUSSION

Wash Solvent Selection. Solvents were selected based on relative polarity. Water was selected as the most polar solvent. Ethanol was selected for its high polarity, though lower than that of water. Chloroform was selected for its mild polarity (lower than that of ethanol and water). Xylene was selected for its low polarity. Ethanol was utilized at a percentage of 70% in water. For washing procedures, slides were prepared with 8 thin control tissue sections. The top 4 sections were spotted with drugs and used as unwashed sections. The bottom 4 sections were spotted with the same drugs and used as washed sections. Slides were submerged half-way into the wash solvent, allowed to sit for 30 seconds, removed, and allowed to dry under vacuum prior to matrix coating and MALDI-MSI analysis.

Diazepam Wash Solvents. Prior to wash analysis, diazepam was spotted onto a ground steel plate in serial dilutions of 100 μM, 10 μM, 1 μM, 0.1 μM, and 0.01 μM in ethanol. It was observed with detectable signal, and identified within the signal-to-noise ratio cutoff at 1 μM, as shown in Figure 3. Though peaks were observed at 0.1 μM and 0.01 μM, they were not within the signal-to-noise range acceptable for peak identification, as shown in Figure 3D-E. MS/MS data was collected, as shown in Figure

3 inset. When this experiment was repeated on thin tissue sections thaw-mounted to a glass slide, the detection limit was 10 μM, with no identifiable peaks at 1 μM or below as shown in Figure 4. Because diazepam is soluble in ethanol, it was not expected that an ethanol wash would allow for maintenance of diazepam localization. Wash experiments with water, chloroform, and xylene indicated that water resulted in a 2-fold increase in intensity of the diazepam peak when spotted on tissue, as shown in Figure 5B. Chloroform and xylene washed diazepam from the tissue sections, resulting in no detection of the spotted compound, as shown in Figure 5C-D. Known diazepam metabolites oxazepam, temazepam, and desmethyldiazepam were studied as well (structures shown in Figure 1D-F). Oxazepam was spotted onto a ground steel plate in serial dilutions of 100 μM, 10 μM, 1 μM, 0.1 μM, and 0.01 μM in DMSO. It was observed with detectable signal, and identified within the signal-to-noise ratio cutoff at 100 μM, as shown in Figure 6. Though peaks were observed at 10 μM, 1 μM, 0.1 μM and 0.01 μM, they were not within the signal-to-noise range acceptable for peak identification, as shown in Figure 6B-E. MS/MS data was collected, as shown in Figure 6 inset. Desmethyldiazepam was spotted onto a ground steel plate in serial dilutions of 100 μM, 10 μM, 1 μM, 0.1 μM, and 0.01 μM in DMSO. It was observed with detectable signal, and identified within the signal-to-noise ratio cutoff at 100 μM, as shown in Figure 7. Though peaks were observed at 10 μM, 1 μM, 0.1 μM, and 0.01 μM, they were not within the signal-to-noise range acceptable for peak identification, as shown in Figure 7B-E. MS/MS data was collected, as shown in Figure 7 inset. Temazepam was spotted onto a ground steel plate in serial dilutions of 100 μM, 10 μM, 1 μM, 0.1 μM, and 0.01 μM in DMSO. It was observed with detectable signal, and identified within the signal-to-

noise ratio cutoff at 10 μM, as shown in Figure 8. Though peaks were observed at 1 μM, 0.1 μM, and 0.01 μM, they were not within the signal-to-noise range acceptable for peak identification, as shown in Figure 8C-E. MS/MS data was collected, as shown in Figure 8 inset.

Diazepam Biodistribution in Brain by MALDI-MSI. The distribution of diazepam was observed in treated CD-1 mice at 3 varied timepoints: 0.1 h, 1 h, and 6 h. For each diazepam-treated mouse, 3 perfusion methods were tested: minimal perfusion (standard pharmacokinetic perfusion), light exsanguination by cardiocentesis, and full transcardio perfusion. It is known from previous studies that diazepam is able to cross the blood-brain barrier.

Diazepam-treated 0.1 h Minimal Perfusion. Diazepam was not detected in the brain at 0.1 h post-dose. Briefly, 2 intact brains from diazepam-treated, minimally perfused CD-1 mice sacrificed at 0.1 h post-dose were compared to 2 intact brains excised from vehicle-treated CD-1 minimally perfused mice sacrificed at 0.1 h. No unique peaks were observed.

Diazepam-treated 1 h Minimal Perfusion. Diazepam was not detected in the brain at 1 h post-dose. Briefly, 2 intact brains from diazepam-treated, minimally perfused CD-1 mice sacrificed at 1 h post-dose were compared to 2 intact brains excised from vehicle-treated CD-1 minimally perfused mice sacrificed at 1 h. No unique peaks were observed.

Diazepam-treated 6 h Minimal Perfusion. Diazepam was not detected in the brain at 6 h post-dose. Briefly, 2 intact brains from diazepam-treated, minimally perfused CD-1 mice sacrificed at 6 h post-dose were compared to 2 intact brains excised from vehicle-

treated CD-1 minimally perfused mice sacrificed at 6 h. No unique peaks were observed.

Diazepam-treated 0.1 h Cardiocentesis. Diazepam was not detected in the brain at 0.1 h post-dose. Briefly, 2 intact brains from diazepam-treated, lightly perfused CD-1 mice sacrificed at 0.1 h post-dose were compared to 2 intact brains excised from vehicle-treated CD-1 minimally perfused mice sacrificed at 0.1 h. No unique peaks were observed.

Diazepam-treated 1 h Cardiocentesis. Diazepam was not detected in the brain at 1 h post-dose. Briefly, 2 intact brains from diazepam-treated, lightly perfused CD-1 mice sacrificed at 1 h post-dose were compared to 2 intact brains excised from vehicle-treated CD-1 minimally perfused mice sacrificed at 1 h. No unique peaks were observed.

Diazepam-treated 6 h Cardiocentesis. Diazepam was not detected in the brain at 6 h post-dose. Briefly, 2 intact brains from diazepam-treated, lightly perfused CD-1 mice sacrificed at 6 h post-dose were compared to 2 intact brains excised from vehicle-treated CD-1 minimally perfused mice sacrificed at 6 h. No unique peaks were observed.

Diazepam-treated 0.1 h Transcardio Perfusion. Diazepam was not detected in the brain at 0.1 h post-dose. Briefly, 2 intact brains from diazepam-treated, fully perfused CD-1 mice sacrificed at 0.1 h post-dose were compared to 2 intact brains excised from vehicle-treated CD-1 minimally perfused mice sacrificed at 0.1 h. No unique peaks were observed.

Diazepam-treated 1 h Transcardio Perfusion. Diazepam was not detected in the brain at 1 h post-dose. Briefly, 2 intact brains from diazepam-treated, fully perfused CD-1 mice sacrificed at 1 h post-dose were compared to 2 intact brains excised from vehicle-treated CD-1 minimally perfused mice sacrificed at 1 h. No unique peaks were observed.

Diazepam-treated 6 h Transcardio Perfusion. Diazepam was not detected in the brain at 6 h post-dose. Briefly, 2 intact brains from diazepam-treated, fully perfused CD-1 mice sacrificed at 6 h post-dose were compared to 2 intact brains excised from vehicle-treated CD-1 minimally perfused mice sacrificed at 6 h. No unique peaks were observed.

Diazepam Biodistribution in Brain by LC-MS/MS. Diazepam was not observed in the brain via MALDI-MSI. Extracted brain tissue homogenates were analyzed via LC-MS/MS for diazepam content, and roughly quantitated using D5-diazepam as a standard. Concentration was calculated based on relative intensities of the 0.1 μM D5-diazepam peak compared to that of the diazepam peak, assuming a mass of 0.5 g for each mouse brain. Additionally, concentration of a diazepam metabolite, oxazepam, was calculated based on relative intensities of the 0.1 μM D5-oxazepam peak.

Diazepam-treated 0.1 h Minimal Perfusion. Diazepam was not detected in the brain at 0.1 h post-dose via MALDI-MSI; however, it was observed via LC-MS/MS. The D5-diazepam standard eluted at 13.09 min, and the diazepam peak eluted at 13.21 min at 285.0769 m/z, as shown in Figure 9. The D5-oxazepam eluted at 11.65 min, and the oxazepam peak eluted at 11.70 min at 287.0749 m/z, as shown in Figure 10. A brain sample taken from a diazepam-treated CD-1 mouse that was minimally perfused at 0.1

h post-dose was compared to a brain sample taken from a vehicle-treated CD-1 mouse that was minimally perfused at 0.1 h. This was confirmed by MS/MS analysis of the diazepam peak. Diazepam was detected at a concentration of 985.59 nM (1.12 μg/g) as shown in Table 1. Oxazepam was detected at a concentration of 296.32 nM (0.31 μg/g) as shown in Table 2.

Diazepam-treated 1 h Minimal Perfusion. Diazepam was not detected in the brain at 1 h post-dose via MALDI-MSI; however, it was observed via LC-MS/MS. The D5-diazepam standard eluted at 13.10 min, and the diazepam peak eluted at 13.21 min at 285.2964 m/z, as shown in Figure 11. The D5-oxazepam eluted at 11.59 min, and the oxazepam peak eluted at 11.70 min at 287.0749 m/z, as shown in Figure 12. A brain sample taken from a diazepam-treated CD-1 mouse that was minimally perfused at 1 h post-dose was compared to a brain sample taken from a vehicle-treated CD-1 mouse that was minimally perfused at 1 h. This was confirmed by MS/MS analysis of the diazepam peak. Diazepam was detected at a concentration of 66.03 nM (0.08 μg/g), as shown in Table 1. Oxazepam was detected at a concentration of 296.82 nM (0.41 μg/g), as shown in Table 2.

Diazepam-treated 6 h Minimal Perfusion. Diazepam was not detected in the brain at 6 h post-dose via MALDI-MSI; however, it was observed via LC-MS/MS. The D5-diazepam standard eluted at 13.14 min, and the diazepam peak eluted at 13.23 285.2963 min at m/z, as shown in Figure 13. The D5-oxazepam eluted at 11.62 min, and the oxazepam peak eluted at 11.68 min at 287.0567 m/z, as shown in Figure 14. A brain sample taken from a diazepam-treated CD-1 mouse that was minimally perfused at 6 h post-dose was compared to a brain sample taken from a vehicle-treated CD-1 mouse that was

minimally perfused at 6 h. This was confirmed by MS/MS analysis of the diazepam peak. Diazepam was detected at a concentration of 4.25 nM (0.00 μg/g), as shown in Table 1. Oxazepam was detected at a concentration of 289.82 nM (0.46 μg/g), as shown in Table 2.

Diazepam-treated 0.1 h Cardiocentesis. Diazepam was not detected in the brain at 0.1 h post-dose via MALDI-MSI; however, it was observed via LC-MS/MS. The D5-diazepam standard eluted at 13.17 min, and the diazepam peak eluted at 13.28 min at 285.0775 m/z, as shown in Figure 15. The D5-oxazepam eluted at 11.63 min, and the oxazepam peak eluted at 11.69 min at 287.0746 m/z, as shown in Figure 16. A brain sample taken from a diazepam-treated CD-1 mouse that was lightly perfused at 0.1 h post-dose was compared to a brain sample taken from a vehicle-treated CD-1 mouse that was minimally perfused at 0.1 h. This was confirmed by MS/MS analysis of the diazepam peak. Diazepam was detected at a concentration of 743.50 nM (0.84 μg/g), as shown in Table 1. Oxazepam was detected at a concentration of 565.77 nM (1.15 μg/g), as shown in Table 2.

Diazepam-treated 1 h Cardiocentesis. Diazepam was not detected in the brain at 1 h post-dose via MALDI-MSI; however, it was observed via LC-MS/MS. The D5-diazepam standard eluted at 13.24 min, and the diazepam peak eluted at 13.32 min at 285.0776 m/z, as shown in Figure 17. The D5-oxazepam eluted at 11.62 min, and the oxazepam peak eluted at 11.68 min at 287.0747 m/z, as shown in Figure 18. A brain sample taken from a diazepam-treated CD-1 mouse that was lightly perfused at 1 h post-dose was compared to a brain sample taken from a vehicle-treated CD-1 mouse that was minimally perfused at 1 h. This was confirmed by MS/MS analysis of the diazepam

peak. Diazepam was detected at a concentration of 88.95 nM (0.10 μg/g), as shown in Table 1. Oxazepam was detected at a concentration of 408.61 nM (0.67 μg/g), as shown in Table 2.

Diazepam-treated 6 h Cardiocentesis. Diazepam was not detected in the brain at 6 h post-dose via MALDI-MSI; however, it was observed via LC-MS/MS. The D5-diazepam standard eluted at 13.32 min, and the diazepam peak eluted at 13.41 min, though no distinguishable diazepam peak was detected in the mass spectrum, as shown in Figure 19. The D5-oxazepam eluted at 11.68 min, and the oxazepam peak eluted at 11.71 min at 287.06 m/z, as shown in Figure 20. A brain sample taken from a diazepam-treated CD-1 mouse that was lightly perfused at 6 h post-dose was compared to a brain sample taken from a vehicle-treated CD-1 mouse that was minimally perfused at 6 h. This was confirmed by MS/MS analysis of the diazepam peak. Diazepam was detected at a concentration of 3.06 nM (0.00 μg/g), as shown in Table 1. Oxazepam was detected at a concentration of 5.09 nM (0.01 μg/g), as shown in Table 2.

Diazepam-treated 0.1 h Transcardio Perfusion. Diazepam was not detected in the brain at 0.1 h post-dose via MALDI-MSI; however, it was observed via LC-MS/MS. The D5-diazepam standard eluted at 13.39 min, and the diazepam peak eluted at 13.46 min at 285.0775 m/z, as shown in Figure 21. The D5-oxazepam eluted at 11.68 min, and the oxazepam peak eluted at 11.74 min at 287.0747 m/z, as shown in Figure 22. A brain sample taken from a diazepam-treated CD-1 mouse that was fully perfused at 0.1 h post-dose was compared to a brain sample taken from a vehicle-treated CD-1 mouse that was minimally perfused at 0.1 h. This was confirmed by MS/MS analysis of the diazepam peak. Diazepam was detected at a concentration of 1466.42 nM (1.67 μg/g),

as shown in Table 1. Oxazepam was detected at a concentration of 532.41 nM (1.16 μg/g), as shown in Table 2.

Diazepam-treated 1 h Transcardio Perfusion. Diazepam was not detected in the brain at 1 h post-dose via MALDI-MSI; however, it was observed via LC-MS/MS. The D5-diazepam standard eluted at 13.38 min, and the diazepam peak eluted at 13.46 min at 285.2971 m/z, as shown in Figure 23. The D5-oxazepam eluted at 11.67 min, and the oxazepam peak eluted at 11.70 min at 287.0747 m/z, as shown in Figure 24. A brain sample taken from a diazepam-treated CD-1 mouse that was fully perfused at 1 h post-dose was compared to a brain sample taken from a vehicle-treated CD-1 mouse that was minimally perfused at 1 h. This was confirmed by MS/MS analysis of the diazepam peak. Diazepam was detected at a concentration of 74.22 nM (0.08 μg/g), as shown in Table 1. Oxazepam was detected at a concentration of 1355.24 nM (3.40 μg/g), as shown in Table 2.

Diazepam-treated 6 h Transcardio Perfusion. Diazepam was not detected in the brain at 6 h post-dose via MALDI-MSI; however, it was observed via LC-MS/MS. The D5-diazepam standard eluted at 13.41 min, and the diazepam peak eluted at 13.50 min at 285.2963 m/z, as shown in Figure 25. The D5-oxazepam eluted at 11.70 min, and the oxazepam peak eluted at 11.74 min at 287.0747 m/z, as shown in Figure 26. A brain sample taken from a diazepam-treated CD-1 mouse that was fully perfused at 6 h post-dose was compared to a brain sample taken from a vehicle-treated CD-1 mouse that was minimally perfused at 6 h. This was confirmed by MS/MS analysis of the diazepam peak. Diazepam was detected at a concentration of 99.09 nM (0.11 μg/g), as shown in

Table 1. Oxazepam was detected at a concentration of 650.98 nM (0.70 μg/g), as shown in Table 2.

Diazepam Presence in Serum by LC-MS/MS. Diazepam was not observed in the brain via MALDI-MSI. Extracted serum samples were analyzed via LC-MS/MS for diazepam content to assess entry into the bloodstream, and roughly quantitated using D5-diazepam as a standard. Concentration was calculated based on relative intensities of the 0.1 μM D5-diazepam peak compared to that of the diazepam peak, assuming a mass of 0.5 g for each mouse brain. Additionally, concentration of a diazepam metabolite, oxazepam, was calculated based on relative intensities of the 0.1 μM D5-oxazepam peak.

Diazepam-treated 0.1 h Minimal Perfusion. Diazepam was observed via LC-MS/MS. The D5-diazepam standard eluted at 13.46 min, and the diazepam peak eluted at 13.55 min at 285.2958 m/z, as shown in Figure 27. The D5-oxazepam eluted at 11.77 min, and the oxazepam peak eluted at 11.82 min at 287.0745 m/z, as shown in Figure 28. A serum sample taken from a diazepam-treated CD-1 mouse that was minimally perfused at 0.1 h post-dose was compared to a serum sample taken from a vehicle-treated CD-1 mouse that was minimally perfused at 0.1 h. This was confirmed by MS/MS analysis of the diazepam peak. Diazepam was detected at a concentration of 269.52 nM (0.78 μg/g), as shown in Table 3. Oxazepam was detected at a concentration of 684.86 nM (0.34 μg/g), as shown in Table 4.

Diazepam-treated 1 h Minimal Perfusion. Diazepam was observed via LC-MS/MS. The D5-diazepam standard eluted at 13.45 min, and the diazepam peak eluted at 13.53 min at 285.0082 m/z, as shown in Figure 29. The D5-oxazepam peak eluted at 11.72 min,

and the oxazepam peak eluted at 11.75 min at 287.0746 m/z, as shown in Figure 30. A serum sample taken from a diazepam-treated CD-1 mouse that was minimally perfused at 1 h post-dose was compared to a serum sample taken from a vehicle-treated CD-1 mouse that was minimally perfused at 1 h. This was confirmed by MS/MS analysis of the diazepam peak. Diazepam was detected at a concentration of 362.36 nM (0.07 μg/g), as shown in Table 3. Oxazepam was detected at a concentration of 684.86 nM (0.34 μg/g), as shown in Table 4.

Diazepam-treated 6 h Minimal Perfusion. Diazepam was observed via LC-MS/MS. The D5-diazepam standard eluted at 13.48 min, and the diazepam peak eluted at 13.51 min at 285.2213 m/z, as shown in Figure 31. The D5-oxazepam peak eluted at 11.72 min, and the oxazepam peak eluted at 11.77 min at 287.06 m/z, as shown in Figure 32. A serum sample taken from a diazepam-treated CD-1 mouse that was minimally perfused at 6 h post-dose was compared to a serum sample taken from a vehicle-treated CD-1 mouse that was minimally perfused at 6 h. This was confirmed by MS/MS analysis of the diazepam peak. Diazepam was detected at a concentration of 7.88 nM (0.01 μg/g), as shown in Table 3. Oxazepam was detected at a concentration of 401.50 nM (0.33 μg/g), as shown in Table 4.

Diazepam-treated 0.1 h Cardiocentesis. Diazepam was observed via LC-MS/MS. The D5-diazepam standard eluted at 13.47 min, and the diazepam peak eluted at 13.55 min at 285.0086 m/z, as shown in Figure 33. The D5-oxazepam peak eluted at 11.74 min, and the oxazepam peak eluted at 11.79 min at 287.0746 m/z, as shown in Figure 34. A serum sample taken from a diazepam-treated CD-1 mouse that was lightly perfused at 0.1 h post-dose was compared to a serum sample taken from a vehicle-treated CD-1

mouse that was minimally perfused at 0.1 h. This was confirmed by MS/MS analysis of the diazepam peak. Diazepam was detected at a concentration of 615.26 nM (0.70 μg/g), as shown in Table 3. Oxazepam was detected at a concentration of 1009.21 nM (0.64 μg/g), as shown in Table 4.

Diazepam-treated 1 h Cardiocentesis. Diazepam was observed via LC-MS/MS. The D5-diazepam standard eluted at 13.46 min, and the diazepam peak eluted at 13.51 min at 285.2980 m/z, as shown in Figure 35. The D5-oxazepam peak eluted at 11.71 min, and the oxazepam peak eluted at 11.76 min at 287.0746 m/z, as shown in Figure 36. A serum sample taken from a diazepam-treated CD-1 mouse that was lightly perfused at 1 h post-dose was compared to a serum sample taken from a vehicle-treated CD-1 mouse that was minimally perfused at 1 h. This was confirmed by MS/MS analysis of the diazepam peak. Diazepam was detected at a concentration of 65.90 nM (0.07 μg/g), as shown in Table 3. Oxazepam was detected at a concentration of 590.42 nM (0.46 μg/g), as shown in Table 4.

Diazepam-treated 6 h Cardiocentesis. Diazepam was observed via LC-MS/MS. The D5-diazepam standard eluted at 13.44 min, and the diazepam peak eluted at 13.55 min at 285.0081 m/z, as shown in Figure 37. The D5-oxazepam peak eluted at 11.74 min, and the oxazepam peak eluted at 11.80 min at 287.0567 m/z, as shown in Figure 38. A serum sample taken from a diazepam-treated CD-1 mouse that was lightly perfused at 6 h post-dose was compared to a serum sample taken from a vehicle-treated CD-1 mouse that was minimally perfused at 6 h. This was confirmed by MS/MS analysis of the diazepam peak. Diazepam was detected at a concentration of 6.55 nM (0.01 μg/g),

as shown in Table 3. Oxazepam was detected at a concentration of 11.51 nM (0.01 μg/g), as shown in Table 4.

Diazepam-treated 0.1 h Transcardio Perfusion. Diazepam was observed via LC-MS/MS. The D5-diazepam standard eluted at 13.45 min, and the diazepam peak eluted at 13.56 min at 285.2969 m/z, as shown in Figure 39. The D5-oxazepam peak eluted at 11.74 min, and the oxazepam peak eluted at 11.79 min at 287.0747 m/z, as shown in Figure 40. A serum sample taken from a diazepam-treated CD-1 mouse that was fully perfused at 0.1 h post-dose was compared to a serum sample taken from a vehicle-treated CD-1 mouse that was minimally perfused at 0.1 h. This was confirmed by MS/MS analysis of the diazepam peak. Diazepam was detected at a concentration of 806.41 nM (0.92 μg/g), as shown in Table 3. Oxazepam was detected at a concentration of 1023.29 nM (0.60 μg/g), as shown in Table 4.

Diazepam-treated 1 h Transcardio Perfusion. Diazepam was observed via LC-MS/MS. The D5-diazepam standard eluted at 13.46 min, and the diazepam peak eluted at 13.55 min at 285.0081 m/z, as shown in Figure 41. The D5-oxazepam peak eluted at 11.72 min, and the oxazepam peak eluted at 11.76 min at 287.0748 m/z, as shown in Figure 42. A serum sample taken from a diazepam-treated CD-1 mouse that was fully perfused at 1 h post-dose was compared to a serum sample taken from a vehicle-treated CD-1 mouse that was minimally perfused at 1 h. This was confirmed by MS/MS analysis of the diazepam peak. Diazepam was detected at a concentration of 32.02 nM (0.04 μg/g), as shown in Table 3. Oxazepam was detected at a concentration of 2995.41 nM (1.54 μg/g), as shown in Table 4.

Diazepam-treated 6 h Transcardio Perfusion. Diazepam was observed via LC-MS/MS. The D5-diazepam standard eluted at 13.45 min, and the diazepam peak eluted at 13.53 min at 285.0092 m/z, as shown in Figure 43. The D5-oxazepam peak eluted at 11.72 min, and the oxazepam peak eluted at 11.76 min at 287.06 m/z, as shown in Figure 44. A serum sample taken from a diazepam-treated CD-1 mouse that was fully perfused at 6 h post-dose was compared to a serum sample taken from a vehicle-treated CD-1 mouse that was minimally perfused at 6 h. This was confirmed by MS/MS analysis of the diazepam peak. Diazepam was detected at a concentration of 5.19 nM (0.01 μg/g), as shown in Table 3. Oxazepam was detected at a concentration of 614.49 nM (0.74 μg/g), as shown in Table 4.

SMRT Wash Solvents. Prior to wash analysis, SMRT compounds were spotted onto thin tissue sections in serial dilutions of 500 μM, 50 μM, 5 μM, 0.5 μM, and 0.05 μM in DMSO for BZ6 and BZ16. BZ6 had an additional dilution at 50 mM in DMSO. RTC13 and 216 had an additional dilution at 1 mM in DMSO. All SMRT compounds had high intensity peaks corresponding to their sodiated forms. These sodiated peaks were present at much higher amounts than the protonated peaks. BZ16 was observed with detectable signal, and identified within the signal-to-noise ratio cutoff at 0.05 μM, though a mass shift was observed. BZ6 was observed with detectable signal, and identified within the signal-to-noise ratio cutoff at 500 μM, a sharp increase compared to the detection limit of BZ16. RTC13 and 216 were observed with detectable signal, and identified within the signal-to-noise ratio cutoff at 100 μM.

Overall, wash experiments showed a lowered baseline in tissue average spectra, as shown in Figure 45. Wash experiments with water, chloroform, and xylene indicated

that ethanol resulted in an increase in intensity of the BZ6 and BZ16 peaks when spotted on tissue, and did not cause delocalization, as shown in Figure 46. Water, chloroform and xylene washed BZ6 and BZ16 from the tissue sections, resulting in no detection of the spotted compound. Potential adducts of 216 and 216-3 were observed at 345 and 326 m/z, respectively, in water washed tissue sections with little delocalization. Ethanol, xylene, and chloroform washed 216 and 216-3 from the tissue sections, resulting in no detection of the spotted compound. Water, ethanol, chloroform, and xylene washed RTC13 from the tissue sections, resulting in no detection of the spotted compound.

SMRT Biodistribution by MALDI-MSI. SMRT biodistribution via MALDI-MSI is reported in Chapter 3. Ultimately, the 70% ethanol wash enhanced signal and allowed for the detected of the sodiated BZ16 peak in treated brain.

BZ6-treated SCID mice exhibited several unique peaks. A peak at 84 m/z was detected in both the cerebrum and the cerebellum. Washed and unwashed images of the cerebellum in Figure 47A-B show that delocalization did not occur after the 70% ethanol wash step; and, signal not detected in the unwashed sections was observed in the periphery, likely due to the elimination of salts and other interfering compounds. Figure 48A-B, Figure 49A-B, Figure 50A-B, and Figure 51A-B show the same trend in BZ6-treated SCID brain, but for a peak at 183 m/z, 736 m/z, 763 m/z, and 801 m/z respectively.

BZ16-treated C57BL/6 mice exhibited several unique peaks, as well. BZ16 was detected, in its monosodiated form, in cerebrum and cerebellum sections. Figure 52A shows that the BZ16 peak was not observed in unwashed tissue sections; however, as

shown in Figure 52B, a 70% ethanol wash was able to enhance this signal to allow for the detected of BZ16.

SMRT Biodistribution by LC-MS/MS. SMRT biodistribution via LC-MS/MS is reported in Chapter 3.

CLR01 Wash Solvents. Prior to wash analysis, CLR01 was spotted onto thin tissue sections to observe spectral peaks. Protonated, mono-sodiated, and di-sodiated peaks from CLR01 were observed. Water, ethanol, chloroform, and xylene washed CLR01 from the tissue sections, resulting in no detection of the spotted compound.

CLR01 Biodistribution in Brain by MALDI-MSI. Biodistribution of CLR01 was assessed in triple transgenic mice. This group consisted of three mice treated with CLR01. This particular strain of laboratory mouse was considered a control, with no investigation of therapeutic effects associated with CLR01 treatment. A peak corresponding to the protonated form of CLR01 726 m/z observed in standard MALDI analysis was observed in treated brains, at the base of the brains, as shown in Figure 53. This mass was observed in both positive and negative modes. MS/MS analysis of the 726 m/z peak yielded fragment ions at 580, 581, 582, 583, and 584 m/z with the same localization, as shown in Figure 54. These fragments did not correspond to previously observed fragments in standard MALDI analyses.

CLR01 Biodistribution in Brain by LC-MS/MS. Excised organs from 1 CLR01-treated triple transgenic rat (specimen R1) was individually homogenized with water, proteins were crashed out with ACN, and resulting supernatant was run via LC-MS/MS using previously mentioned methods. BZ6 (239.0233 m/z) or 216-5 (419.1284 m/z) was utilized as an internal standard, spiked in during homogenization and prior to extraction.

Extracted ion chromatograms (XIC) were obtained for the transition observed from 725.3➔158.7 m/z, with the standard shown in Figure 55. The peak eluted at approximately 50 min at very low abundance, as shown in Figure 56.

RM512 Wash Solvents. Prior to wash analysis, RM512 was spotted onto thin tissue sections to observe spectral peaks. Protonated RM512 was observed. Water, ethanol, chloroform, and xylene washed RM512 from the tissue sections, resulting in no detection of the spotted compound. While RM512 was readily observed by MALDI when spotted on a groundsteel plate, as well as a thin tissue section, as shown in Figure 57A-B, it was not observed when spotted on a tissue section with a mixture of other small drug compounds, as shown in Figure 57C. This suggests RM512 is susceptible to the effects of ion suppression in complex matrices.

RM512 Biodistribution by MALDI-MSI. Biodistribution of RM512 was assessed in C3H mice. This group consisted of eight mice treated with RM512. This particular strain of laboratory mouse was considered a control, with no investigation of therapeutic effects associated with RM512 treatment.

2 h Brain. RM512 analyses of brains excised at 2 h post-dose yielded 2 unique peaks. Two intact brain samples taken from RM512-treated C3H mice were compared to 2 brains excised from vehicle-treated C3H mice. Peaks were observed at 260 and 298 m/z, as shown in Figure 58. A peak corresponding to the protonated form of RM512 observed in standard MALDI runs was not detected via MSI.

2 h Gut. No unique peaks were detected in gut samples at 2 h post-dose. Two gut samples excised from RM512-treated C3H mice were compared to 2 gut samples excised from vehicle-treated C3H mice.

2 h Heart. RM512 analyses of hearts excised at 2 h post-dose yielded 3 unique peaks. Two heart samples taken from RM512-treated C3H mice were compared to 2 hearts excised from vehicle-treated C3H mice. Peaks were observed at 64, 334, and 339 m/z, as shown in Figure 59B-D. A peak corresponding to the protonated form of RM512 observed in standard MALDI runs was not detected via MSI.

2 h Kidney. RM512 analyses of kidneys excised at 2 h post-dose yielded 1 unique peak. Four kidney samples taken from RM512-treated C3H mice were compared to 4 kidneys excised from vehicle-treated C3H mice. A peak was observed at 185 m/z, as shown in Figure 60B. A peak corresponding to the protonated form of RM512 observed in standard MALDI runs was not detected via MSI.

2 h Liver. No unique peaks were detected in liver samples at 2 h post-dose. Two liver samples excised from RM512-treated C3H mice were compared to 2 liver samples excised from vehicle-treated C3H mice.

2 h Lung. RM512 analyses of lungs excised at 2 h post-dose yielded 1 unique peak. Four lung samples taken from RM512-treated C3H mice were compared to 4 lungs excised from vehicle-treated C3H mice. A peak was observed at 621 m/z, as shown in Figure 61. A peak corresponding to the protonated form of RM512 observed in standard MALDI runs was not detected via MSI.

2 h Spleen. RM512 analyses of spleen excised at 2 h post-dose yielded 1 unique peak. Two spleen samples taken from RM512-treated C3H mice were compared to 2 spleen samples excised from vehicle-treated C3H mice. A peak was observed at 185 m/z, as shown in Figure 62. A peak corresponding to the protonated form of RM512 observed in standard MALDI runs was not detected via MSI.

4 h Brain. RM512 analyses of brains excised at 4 h post-dose yielded 1 unique peak. Two intact brain samples taken from RM512-treated C3H mice were compared to 2 brains excised from vehicle-treated C3H mice. A peak was observed at 260 m/z, as shown in Figure 58A. A peak corresponding to the protonated form of RM512 observed in standard MALDI runs was not detected via MSI.

4 h Gut. No unique peaks were detected in gut samples at 4 h post-dose. Two gut samples excised from RM512-treated C3H mice were compared to 2 gut samples excised from vehicle-treated C3H mice.

4 h Heart. RM512 analyses of hearts excised at 4 h post-dose yielded 5 unique peaks. Two heart samples taken from RM512-treated C3H mice were compared to 2 hearts excised from vehicle-treated C3H mice. Peaks were observed at 50, 64, 79, 334, and 339 m/z, as shown in Figure 59. A peak corresponding to the protonated form of RM512 observed in standard MALDI runs was not detected via MSI.

4 h Kidney. RM512 analyses of kidneys excised at 4 h post-dose yielded 1 unique peak. Four kidney samples taken from RM512-treated C3H mice were compared to 4 kidneys excised from vehicle-treated C3H mice. A peak was observed at 185 m/z, as shown in Figure 60B. A peak corresponding to the protonated form of RM512 observed in standard MALDI runs was not detected via MSI.

4 h Liver. No unique peaks were detected in liver samples at 4 h post-dose. Two liver samples excised from RM512-treated C3H mice were compared to 2 liver samples excised from vehicle-treated C3H mice.

4 h Lung. RM512 analyses of lungs excised at 4 h post-dose yielded 1 unique peak. Four lung samples taken from RM512-treated C3H mice were compared to 4 lungs

excised from vehicle-treated C3H mice. A peak was observed at 621 m/z, as shown in Figure 61. A peak corresponding to the protonated form of RM512 observed in standard MALDI runs was not detected via MSI.

4 h Spleen. No unique peaks were detected in spleen samples at 4 h post-dose. Two spleen samples excised from RM512-treated C3H mice were compared to 2 spleen samples excised from vehicle-treated C3H mice.

24 h Brain. No unique peaks were detected in brain samples at 24 h post-dose. Two intact brain samples taken from RM512-treated C3H mice were compared to 2 brains excised from vehicle-treated C3H mice.

24 h Gut. No unique peaks were detected in gut samples at 24 h post-dose. Two gut samples excised from RM512-treated C3H mice were compared to 2 gut samples excised from vehicle-treated C3H mice.

24 h Heart. RM512 analyses of hearts excised at 24 h post-dose yielded 4 unique peaks. Two heart samples taken from RM512-treated C3H mice were compared to 2 hearts excised from vehicle-treated C3H mice. Peaks were observed at 50, 64, 79, and 334 m/z, as shown in Figure 59. A peak corresponding to the protonated form of RM512 observed in standard MALDI runs was not detected via MSI.

24 h Kidney. RM512 analyses of kidneys excised at 2 h post-dose yielded 2 unique peaks. Four kidney samples taken from RM512-treated C3H mice were compared to 4 kidneys excised from vehicle-treated C3H mice. Peaks were observed at 163 and 185 m/z, as shown in Figure 60. A peak corresponding to the protonated form of RM512 observed in standard MALDI runs was not detected via MSI.

24 h Liver. No unique peaks were detected in liver samples at 24 h post-dose. Two liver samples excised from RM512-treated C3H mice were compared to 2 liver samples excised from vehicle-treated C3H mice.

24 h Lung. RM512 analyses of lungs excised at 24 h post-dose yielded 1 unique peak. Four lung samples taken from RM512-treated C3H mice were compared to 4 lungs excised from vehicle-treated C3H mice. A peak was observed at 621 m/z, as shown in Figure 61. A peak corresponding to the protonated form of RM512 observed in standard MALDI runs was not detected via MSI.

24 h Spleen. RM512 analyses of spleen excised at 24 h post-dose yielded 2 unique peaks. Two spleen samples taken from RM512-treated C3H mice were compared to 2 spleen samples excised from vehicle-treated C3H mice. Peaks were observed at 185 and 621 m/z, as shown in Figure 62. A peak corresponding to the protonated form of RM512 observed in standard MALDI runs was not detected via MSI.

RM512 Biodistribution by LC-MS/MS. Excised organs from 3 RM512-treated C3H mouse (specimen 2hM1, 4hM1, and 24hM1) and 1 vehicle-treated C3H mouse (specimen 0hM1) were individually homogenized with water, proteins were crashed out with ACN, and resulting supernatant was run via LC-MS/MS using previously mentioned methods. BZ6 (239.0233 m/z) or 216-5 (419.1284 m/z) was utilized as an internal standard, spiked in during homogenization and prior to extraction. Extracted ion chromatograms (XIC) were obtained for the intact, protonated masses of each compound.

2 h Brain. . Intact RM512 was not detected in the brain using MALDI-MSI, but it was detected in extracted brain homogenate. The BZ6 standard eluted at 6.95 min, and the

RM512 peak eluted at 10.26 min at 348.1003 m/z, as shown in Figure 63. A brain sample taken from RM512-treated C3H mouse 2hM1 was compared to a spleen sample taken from vehicle-treated C3H mouse 0hM1. The observed mass was well within a mass accuracy of 10 ppm, as was confirmed by MS/MS.

2 h Gut. Intact RM512 was not detected in the gut via MALDI-MSI, and was not detected in extracted gut homogenate, as well. The 216-5 standard eluted at 8.73 min. While several peaks were observed during the chromatographic run, RM512 was not, as shown in the XIC and the lack of an accurate mass in the mass spectrum. A gut sample taken from RM512-treated C3H mouse 2hM1 was compared to a gut sample taken from vehicle-treated C3H mouse 0hM1.

2 h Heart. Intact RM512 was not detected in the heart via MALDI-MSI, and was not detected in extracted heart homogenate, as well. The 216-5 standard eluted at 8.73 min. While several peaks were observed during the chromatographic run, RM512 was not, as shown in the XIC and the lack of an accurate mass in the mass spectrum. A heart sample taken from RM512-treated C3H mouse 2hM1 was compared to a heart sample taken from vehicle-treated C3H mouse 0hM1.

2 h Kidney. Intact RM512 was not detected in the kidney via MALDI-MSI, and was not detected in extracted kidney homogenate, as well. The 216-5 standard eluted at 8.74 min. While several peaks were observed during the chromatographic run, RM512 was not, as shown in the XIC and the lack of an accurate mass in the mass spectrum. A kidney sample taken from RM512-treated C3H mouse 2hM1 was compared to a kidney sample taken from vehicle-treated C3H mouse 0hM1.

2 h Liver. Intact RM512 was not detected in the liver via MALDI-MSI, and was not detected in extracted liver homogenate, as well. The 216-5 standard eluted at 8.74 min. While several peaks were observed during the chromatographic run, RM512 was not, as shown in the XIC and the lack of an accurate mass in the mass spectrum. A liver sample taken from RM512-treated C3H mouse 2hM1 was compared to a liver sample taken from vehicle-treated C3H mouse 0hM1.

2 h Lung. Intact RM512 was not detected in the lung via MALDI-MSI, and was not detected in extracted lung homogenate, as well. The 216-5 standard eluted at 8.74 min. While several peaks were observed during the chromatographic run, RM512 was not, as shown in the XIC and the lack of an accurate mass in the mass spectrum. A lung sample taken from RM512-treated C3H mouse 2hM1 was compared to a lung sample taken from vehicle-treated C3H mouse 0hM1.

2 h Spleen. Intact RM512 was not detected in the spleen via MALDI-MSI, and was not detected in extracted spleen homogenate, as well. The 216-5 standard eluted at 8.75 min. While several peaks were observed during the chromatographic run, RM512 was not, as shown in the XIC and the lack of an accurate mass in the mass spectrum. A spleen sample taken from RM512-treated C3H mouse 2hM1 was compared to a spleen sample taken from vehicle-treated C3H mouse 0hM1.

4 h Brain. Intact RM512 was not detected in the brain via MALDI-MSI, and was not detected in extracted brain homogenate, as well. The 216-5 standard eluted at 8.74 min. While several peaks were observed during the chromatographic run, RM512 was not, as shown in the XIC and the lack of an accurate mass in the mass spectrum. A

brain sample taken from RM512-treated C3H mouse 4hM1 was compared to a brain sample taken from vehicle-treated C3H mouse 0hM1.

4 h Gut. Intact RM512 was not detected in the gut via MALDI-MSI, and was not detected in extracted gut homogenate, as well. The 216-5 standard eluted at 8.75 min. While several peaks were observed during the chromatographic run, RM512 was not, as shown in the XIC and the lack of an accurate mass in the mass spectrum. A gut sample taken from RM512-treated C3H mouse 4hM1 was compared to a gut sample taken from vehicle-treated C3H mouse 0hM1.

4 h Heart. Intact RM512 was not detected in the heart via MALDI-MSI, and was not detected in extracted heart homogenate, as well. The 216-5 standard eluted at 8.76 min. While several peaks were observed during the chromatographic run, RM512 was not, as shown in the XIC and the lack of an accurate mass in the mass spectrum. A heart sample taken from RM512-treated C3H mouse 4hM1 was compared to a heart sample taken from vehicle-treated C3H mouse 0hM1.

4 h Kidney. Intact RM512 was not detected in the kidney via MALDI-MSI, and was not detected in extracted kidney homogenate, as well. The 216-5 standard eluted at 8.75 min. While several peaks were observed during the chromatographic run, RM512 was not, as shown in the XIC and the lack of an accurate mass in the mass spectrum. A kidney sample taken from RM512-treated C3H mouse 4hM1 was compared to a kidney sample taken from vehicle-treated C3H mouse 0hM1.

4 h Liver. Intact RM512 was not detected in the liver via MALDI-MSI, and was not detected in extracted liver homogenate, as well. The 216-5 standard eluted at 8.75 min. While several peaks were observed during the chromatographic run, RM512 was not,

as shown in the XIC and the lack of an accurate mass in the mass spectrum. A liver sample taken from RM512-treated C3H mouse 4hM1 was compared to a liver sample taken from vehicle-treated C3H mouse 0hM1.

4 h Lung. Intact RM512 was not detected in the lung via MALDI-MSI, and was not detected in extracted lung homogenate, as well. The 216-5 standard eluted at 8.76 min. While several peaks were observed during the chromatographic run, RM512 was not, as shown in the XIC and the lack of an accurate mass in the mass spectrum. A lung sample taken from RM512-treated C3H mouse 4hM1 was compared to a lung sample taken from vehicle-treated C3H mouse 0hM1.

4 h Spleen. Intact RM512 was not detected in the spleen via MALDI-MSI, and was not detected in extracted spleen homogenate, as well. The 216-5 standard eluted at 8.77 min. While several peaks were observed during the chromatographic run, RM512 was not, as shown in the XIC and the lack of an accurate mass in the mass spectrum. A spleen sample taken from RM512-treated C3H mouse 4hM1 was compared to a spleen sample taken from vehicle-treated C3H mouse 0hM1.

24 h Brain. Intact RM512 was not detected in the brain via MALDI-MSI, and was not detected in extracted brain homogenate, as well. The 216-5 standard eluted at 8.77 min. While several peaks were observed during the chromatographic run, RM512 was not, as shown in the XIC and the lack of an accurate mass in the mass spectrum. A brain sample taken from RM512-treated C3H mouse 24hM1 was compared to a brain sample taken from vehicle-treated C3H mouse 0hM1.

24 h Gut. Intact RM512 was not detected in the gut via MALDI-MSI, and was not detected in extracted gut homogenate, as well. The 216-5 standard eluted at 8.75 min.

While several peaks were observed during the chromatographic run, RM512 was not, as shown in the XIC and the lack of an accurate mass in the mass spectrum. A gut sample taken from RM512-treated C3H mouse 24hM1 was compared to a gut sample taken from vehicle-treated C3H mouse 0hM1.

24 h Heart. Intact RM512 was not detected in the heart via MALDI-MSI, and was not detected in extracted heart homogenate, as well. The 216-5 standard eluted at 8.76 min. While several peaks were observed during the chromatographic run, RM512 was not, as shown in the XIC and the lack of an accurate mass in the mass spectrum. A heart sample taken from RM512-treated C3H mouse 24hM1 was compared to a heart sample taken from vehicle-treated C3H mouse 0hM1.

24 h Kidney. Intact RM512 was not detected in the kidney via MALDI-MSI, and was not detected in extracted kidney homogenate, as well. The 216-5 standard eluted at 8.75 min. While several peaks were observed during the chromatographic run, RM512 was not, as shown in the XIC and the lack of an accurate mass in the mass spectrum. A kidney sample taken from RM512-treated C3H mouse 24hM1 was compared to a kidney sample taken from vehicle-treated C3H mouse 0hM1.

24 h Liver. Intact RM512 was not detected in the liver via MALDI-MSI, and was not detected in extracted liver homogenate, as well. The 216-5 standard eluted at 8.75 min. While several peaks were observed during the chromatographic run, RM512 was not, as shown in the XIC and the lack of an accurate mass in the mass spectrum. A liver sample taken from RM512-treated C3H mouse 24hM1 was compared to a liver sample taken from vehicle-treated C3H mouse 0hM1.

24 h Lung. Intact RM512 was not detected in the lung via MALDI-MSI, and was not detected in extracted lung homogenate, as well. The 216-5 standard eluted at 8.77 min. While several peaks were observed during the chromatographic run, RM512 was not, as shown in the XIC and the lack of an accurate mass in the mass spectrum. A lung sample taken from RM512-treated C3H mouse 24hM1 was compared to a lung sample taken from vehicle-treated C3H mouse 0hM1.

24 h Spleen. Intact RM512 was not detected in the spleen via MALDI-MSI, and was not detected in extracted spleen homogenate, as well. The 216-5 standard eluted at 8.76 min. While several peaks were observed during the chromatographic run, RM512 was not, as shown in the XIC and the lack of an accurate mass in the mass spectrum. A spleen sample taken from RM512-treated C3H mouse 24hM1 was compared to a spleen sample taken from vehicle-treated C3H mouse 0hM1.

MSNP Wash Solvents. Prior to wash analysis, MSNP and MSNP-Phos were spotted onto thin tissue sections to observe spectral peaks. Unique peaks were observed at 284 and 205 m/z, respectively. Water, ethanol, chloroform, and xylene washed MSNP from the tissue sections, resulting in no detection of the spotted compound. Ethanol resulted in a delocalization of MSNP-Phos, while water, chloroform, and xylene did not. Figure 64A shows the average spectrum for an MSNP-Phos associated peak at 205 m/z, with a slight increase in signal intensity after a water wash, shown in Figure 64B. Figure 65A shows the average spectrum for an MSNP-Phos associated peak at 205 m/z after xylene wash, with no observable delocalization, though no enhancement of signal intensity was observed. Figure 66A shows the average spectrum for an MSNP-Phos

associated peak at 205 m/z, with a slight increase in signal intensity after a chloroform wash, shown in Figure 66B.

MSNP Biodistribution in Kidney by MALDI-MSI. Despite the ability of water, chloroform, and xylene washes to enhance MSNP-Phos signal without delocalization, attempts to image the distribution of MSNP-Phos in kidneys excised from MSNP-Phos-treated rats were unsuccessful.

CONCLUSIONS

MSI is a useful technique for the analysis of small drug molecules due to it label-free methodology. Washing lowered the baseline and eliminated some interfering peaks, as shown in Figure 67, with xylene and chloroform resulting in the most drastic changes. Diazepam experiments indicted that water washing was able to enhance the protonated peak signal. Ethanol-washed tissue sections had much cleaner spectra, higher intensity peaks, and a flatter baseline in BZ6-treated and BZ16-treated tissue sections. Additionally, the ethanol wash allowed for previously undetectable peaks from BZ16-treated brain to be observed. A wash step was not useful in all experiments. CLR01 was delocalized by wash solvents, however, it was still observed in MSI experiments. These experiments indicated localization to the lower portion of the brain, and further staining experiments will indicate whether this localization is related to the location of amyloid plaques. RM512 was delocalized by wash solvents, as well, but was not observed in MSI experiments. This is likely due to the susceptibility of RM512 to ion suppression effects, although it was also confirmed via LC-MS/MS experiments that RM512 was not present in any organs other than brain at 2 h post-dose. Finally, MSNP was not delocalized by wash solvents, and signal was enhanced by xylene and

chloroform washes; however, MSNP was not detected in dosed kidney. This could be due to rapid clearance or low abundance.

Overall, MSI is a promising method for biodistribution studies, as it is fast and label-free. MSI can serve as a fast first scan, and the optimization of MSI can be done quickly and efficiently. Selecting appropriate ionization methods for spatial resolution and sensitivity, as well as selecting appropriate sample preparation methods (such as wash steps and perfusion conditions) can enhance the capabilities of MSI in the study of novel drug compounds.

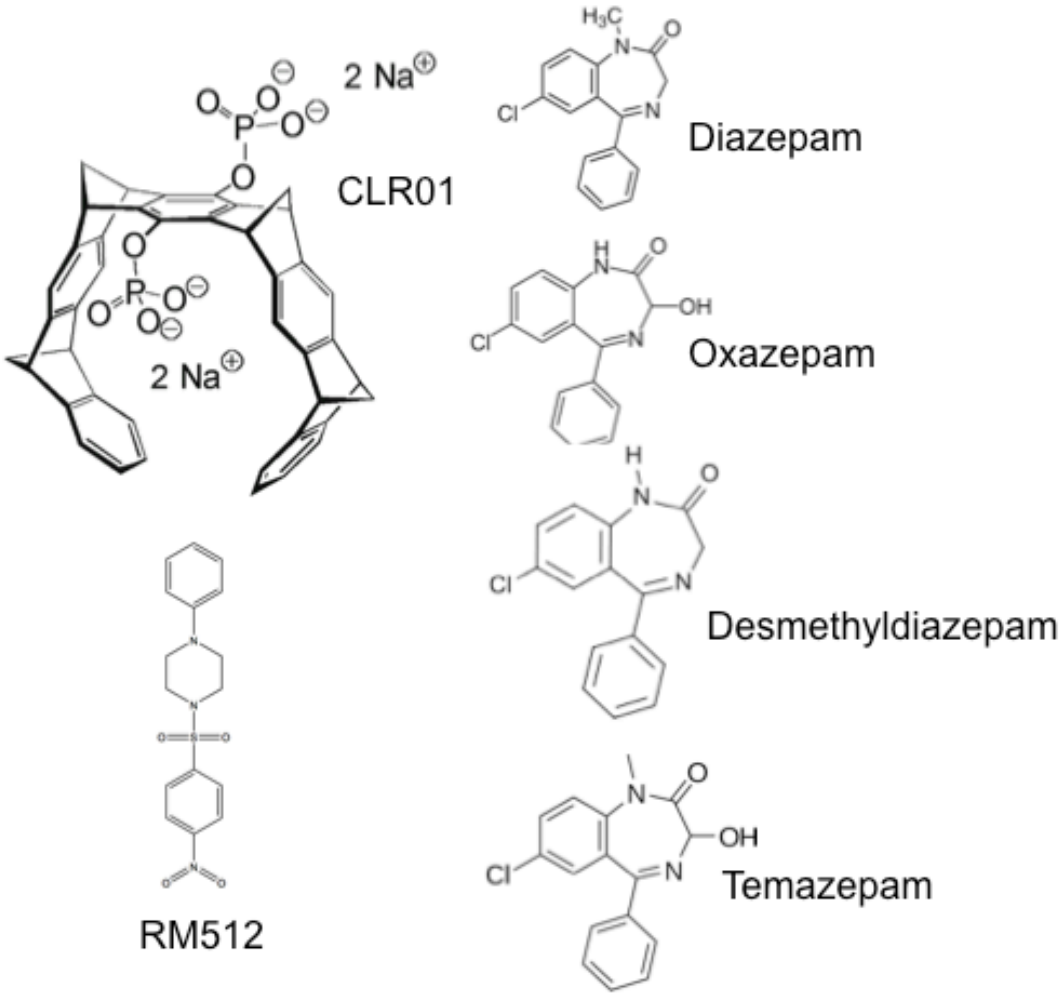

Figure 1. The structures of drug compounds analyzed are depicted: (A) CLR01 (B) RM512 (C) Diazepam (D) Oxazepam (E) Desmethyldiazepam (F) Temazepam.

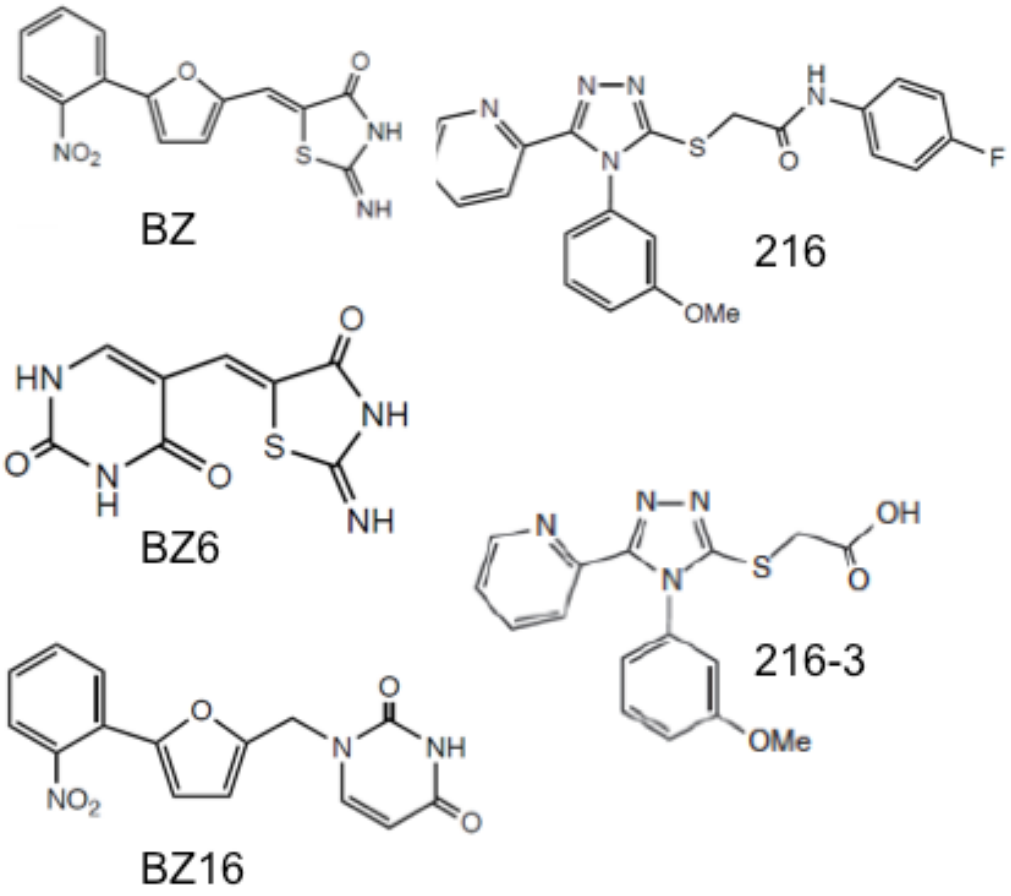

Figure 2. The structures of SMRT compounds are depicted. (A) RTC13 (B) BZ6 (C) BZ16 (D) 216 (E) 216-3.

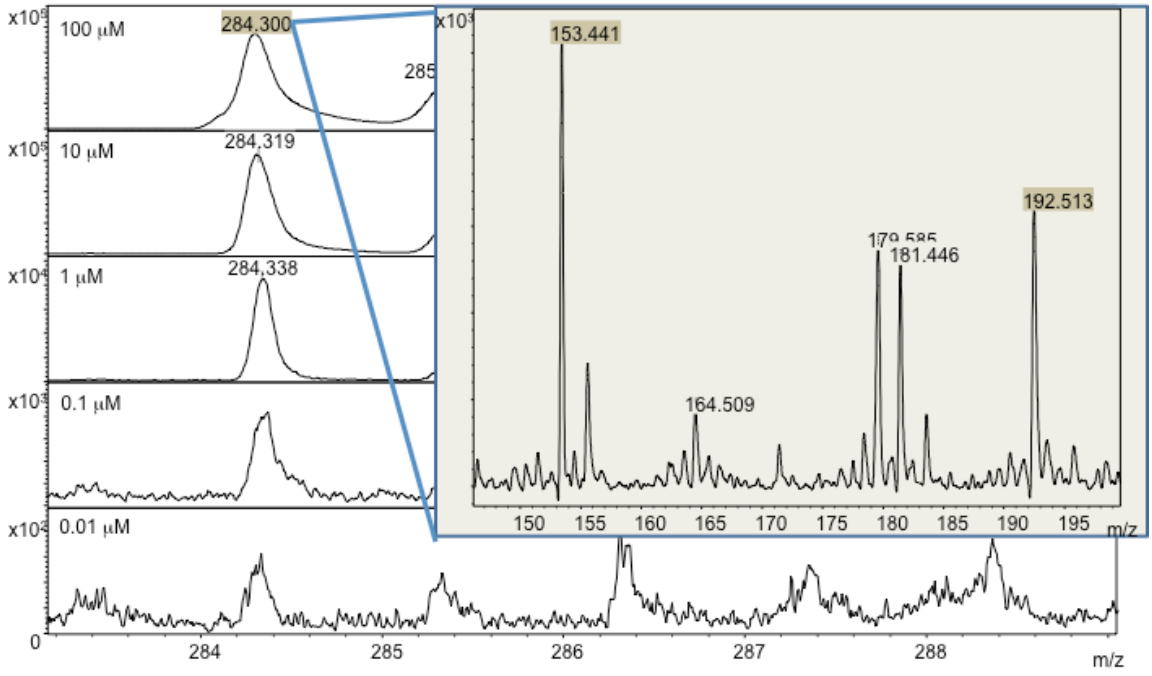

Figure 3. Diazepam dilutions were spotted onto a MALDI plate, with spectra shown. (A) 100 μM diazepam in ethanol (B) 10 μM diazepam in ethanol (C) 1 μM diazepam in ethanol (D) 0.1 μM diazepam in ethanol (E) 0.01 μM diazepam in ethanol (F) MS/MS of protonated diazepam.

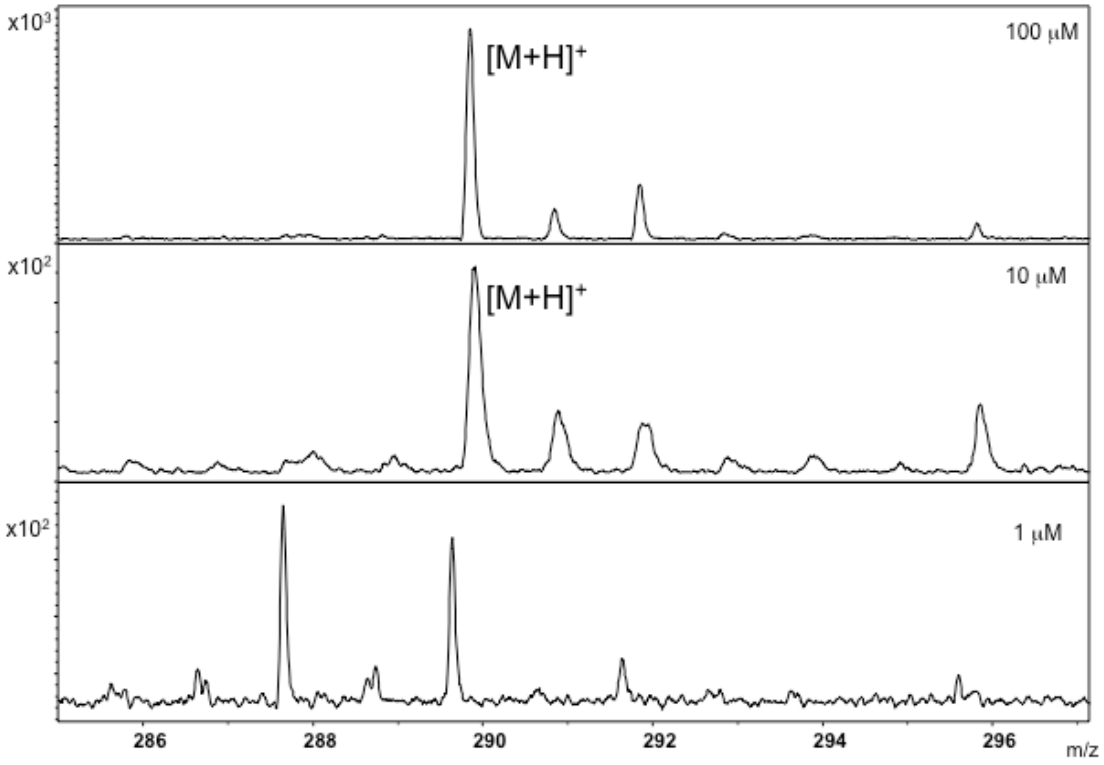

Figure 4. Diazepam dilutions were spotted onto tissue sections, with spectra shown. (A) 100 μM diazepam in ethanol (B) 10 μM diazepam in ethanol (C) 1 μM diazepam in ethanol.

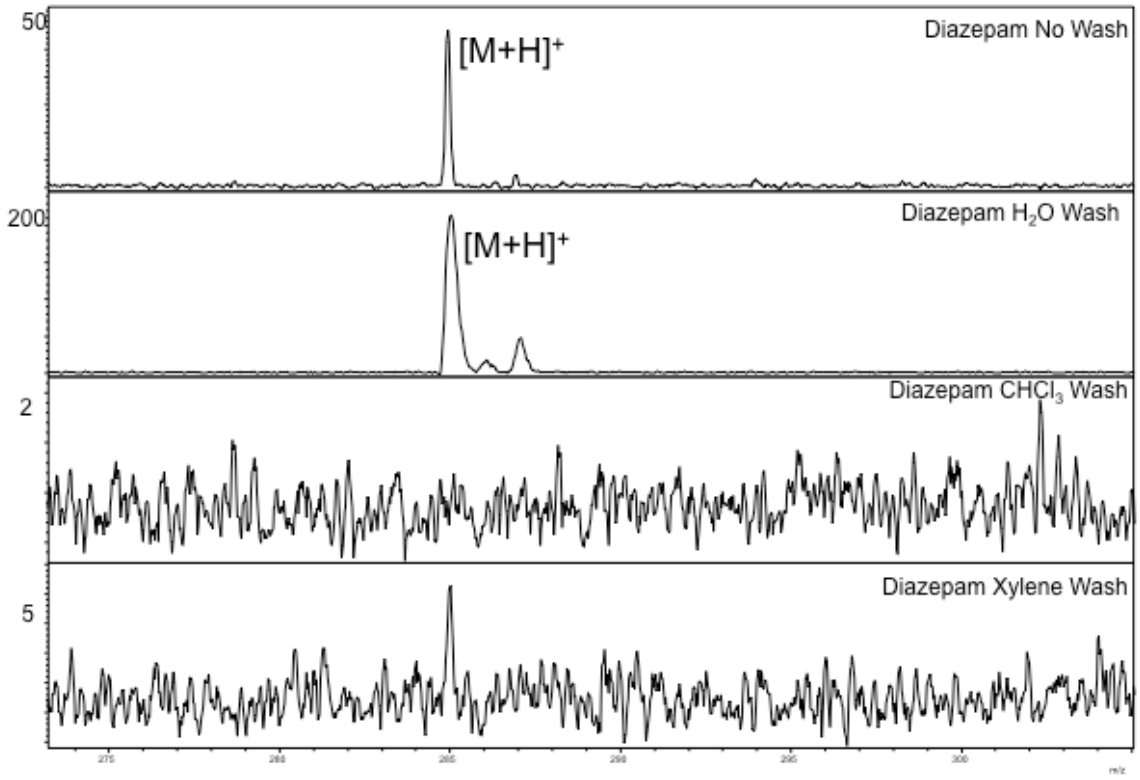

Figure 5. Diazepam dilutions were spotted onto a MALDI plate, with spectra shown. (A) 100 μM diazepam in ethanol (B) 10 μM diazepam in ethanol (C) 1 μM diazepam in ethanol (D) 0.1 μM diazepam in ethanol (E) 0.01 μM diazepam in ethanol.

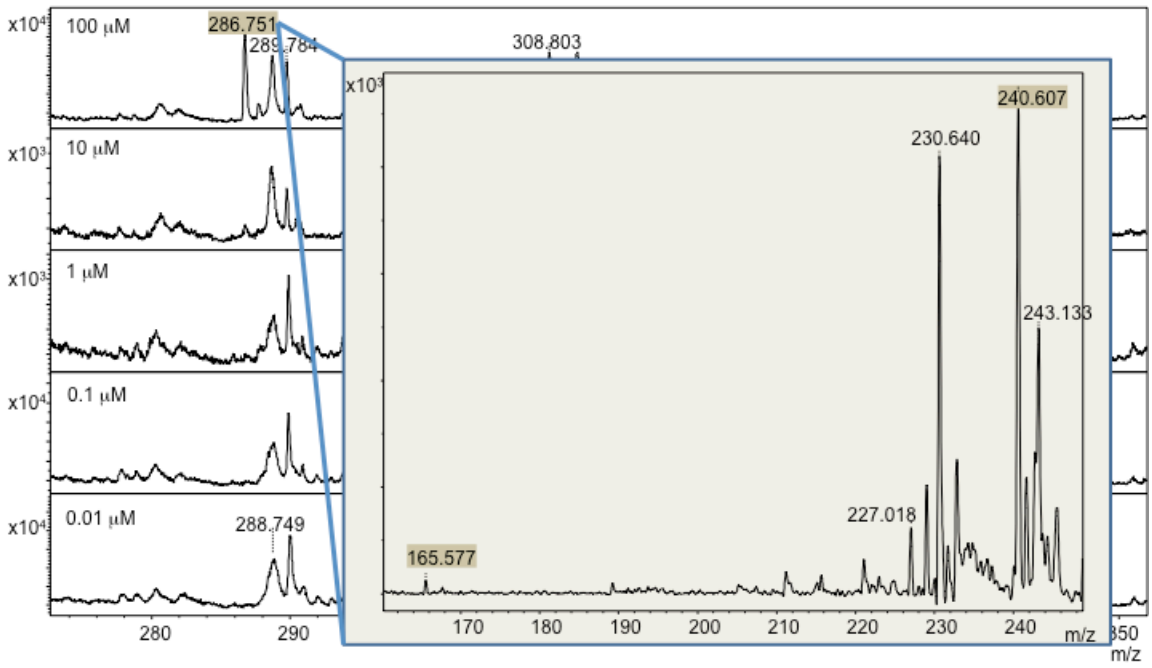

Figure 6. Oxazepam dilutions were spotted onto a MALDI plate, with spectra shown. (A) 100 μM oxazepam in DMSO (B) 10 μM oxazepam in DMSO (C) 1 μM oxazepam in DMSO (D) 0.1 μM oxazepam in DMSO (E) 0.01 μM oxazepam in DMSO (F) MS/MS of protonated oxazepam.

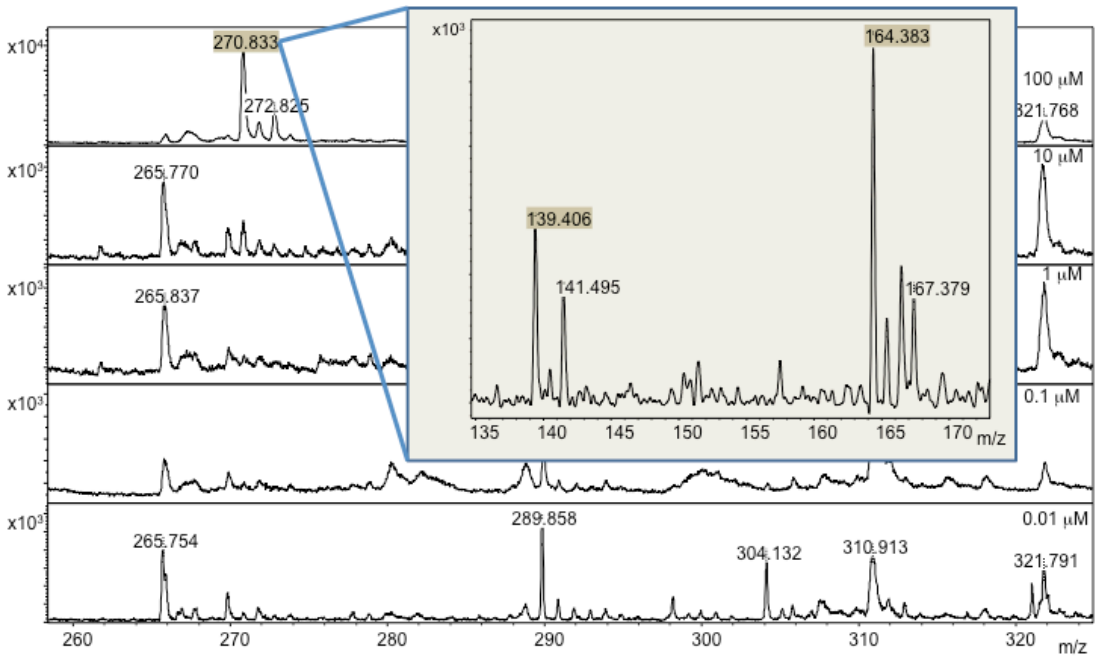

Figure 7. Desmethyldiazepam dilutions were spotted onto a MALDI plate, with spectra shown. (A) 100 μM desmethyldiazepam in DMSO (B) 10 μM desmethyldiazepam in DMSO (C) 1 μM desmethyldiazepam in DMSO (D) 0.1 μM desmethyldiazepam in DMSO (E) 0.01 μM desmethyldiazepam in DMSO (F) MS/MS of protonated desmethyldiazepam.

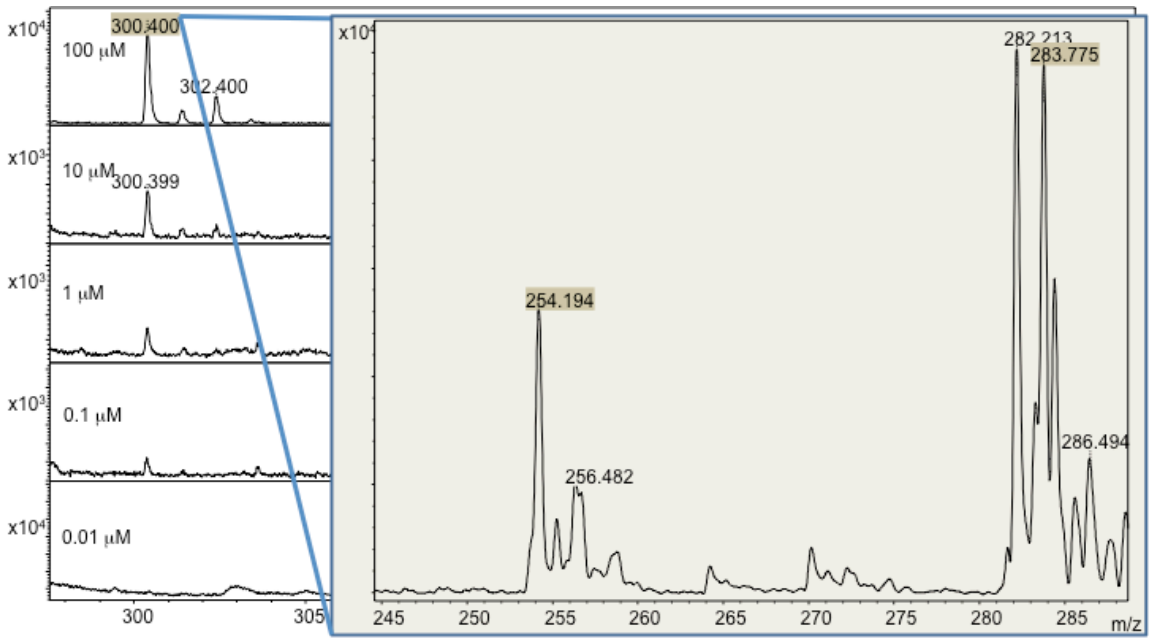

Figure 8. Temazepam dilutions were spotted onto a MALDI plate, with spectra shown. (A) 100 μM temazepam in DMSO (B) 10 μM temazepam in DMSO (C) 1 μM temazepam in DMSO (D) 0.1 μM temazepam in DMSO (E) 0.01 μM temazepam in DMSO (F) MS/MS of protonated temazepam.

Diazepam Brain Tissue Concentration			
Condition	**Timepoint (Hr)**	**Calculated [Diazepam] (nM)**	**Calcaulted [Diazepam] ug/g***
Vehicle	0.1	2.87	0.00
	1	0.74	0.00
	6	0.53	0.00
Diazepam, Standard PK	0.1	985.59	**1.12**
	1	66.03	0.08
	6	4.25	0.00
Diazepam, cardiocentesis	0.1	743.50	**0.84**
	1	88.95	0.10
	6	3.06	0.00
Diazepam, Transcardio perfusion	0.1	1466.42	**1.67**
	1	74.22	0.08
	6	99.09	0.11

Table 1. Diazepam concentrations in homogenized brain extracts were calculated for each perfusion group and time point, and are reported in nM and μg/g.

Oxazepam Brain Tissue Concentration			
Condition	**Timepoint (Hr)**	**Calculated [Oxazepam] (nM)**	**Calcaulted [Oxazepam] ug/g**
Vehicle	0.1	6.26	0.01
	1	2.86	0.00
	6	512.48	0.58
Diazepam, Standard PK	0.1	269.52	**0.31**
	1	362.36	0.41
	6	401.50	0.46
Diazepam, cardiocentesis	0.1	1009.21	**1.15**
	1	590.42	0.67
	6	11.51	0.01
Diazepam, Transcardio perfusion	0.1	1023.29	**1.16**
	1	2995.41	3.40
	6	614.49	0.70

Table 2. Oxazepam concentrations in homogenized brain extracts were calculated for each perfusion group and time point, and are reported in nM and μg/g.

Diazepam Serum Concentration			
Condition	**Timepoint (Hr)**	**Calculated [Diazepam] (nM)**	**Calcaulted [Diazepam] ug/g***
Vehicle	0.1	1.85	0.00
	1	0.73	0.00
	6	3.69	0.00
Diazepam, Standard PK	0.1	684.86	**0.78**
	1	64.31	0.07
	6	7.88	0.01
Diazepam, cardiocentesis	0.1	615.26	**0.70**
	1	65.90	0.07
	6	6.55	0.01
Diazepam, Transcardio perfusion	0.1	806.41	**0.92**
	1	32.02	0.04
	6	5.19	0.01

Table 3. Diazepam concentrations in serum extracts were calculated for each perfusion group and time point, and are reported in nM and μg/g.

Oxazepam Serum Concentration			
Condition	**Timepoint (Hr)**	**Calculated [Oxazepam] (nM)**	**Calcaulted [Oxazepam] ug/g**
Vehicle	0.1	5.91	0.01
	1	4.68	0.01
	6	662.64	0.75
Diazepam, Standard PK	0.1	296.32	**0.34**
	1	296.65	0.34
	6	289.82	0.33
Diazepam, cardiocentesis	0.1	565.77	**0.64**
	1	408.61	0.46
	6	5.09	0.01
Diazepam, Transcardio perfusion	0.1	532.41	**0.60**
	1	1355.24	1.54
	6	650.98	0.74

Table 4. Oxazepam concentrations in serum extracts were calculated for each perfusion group and time point, and are reported in nM and μg/g.

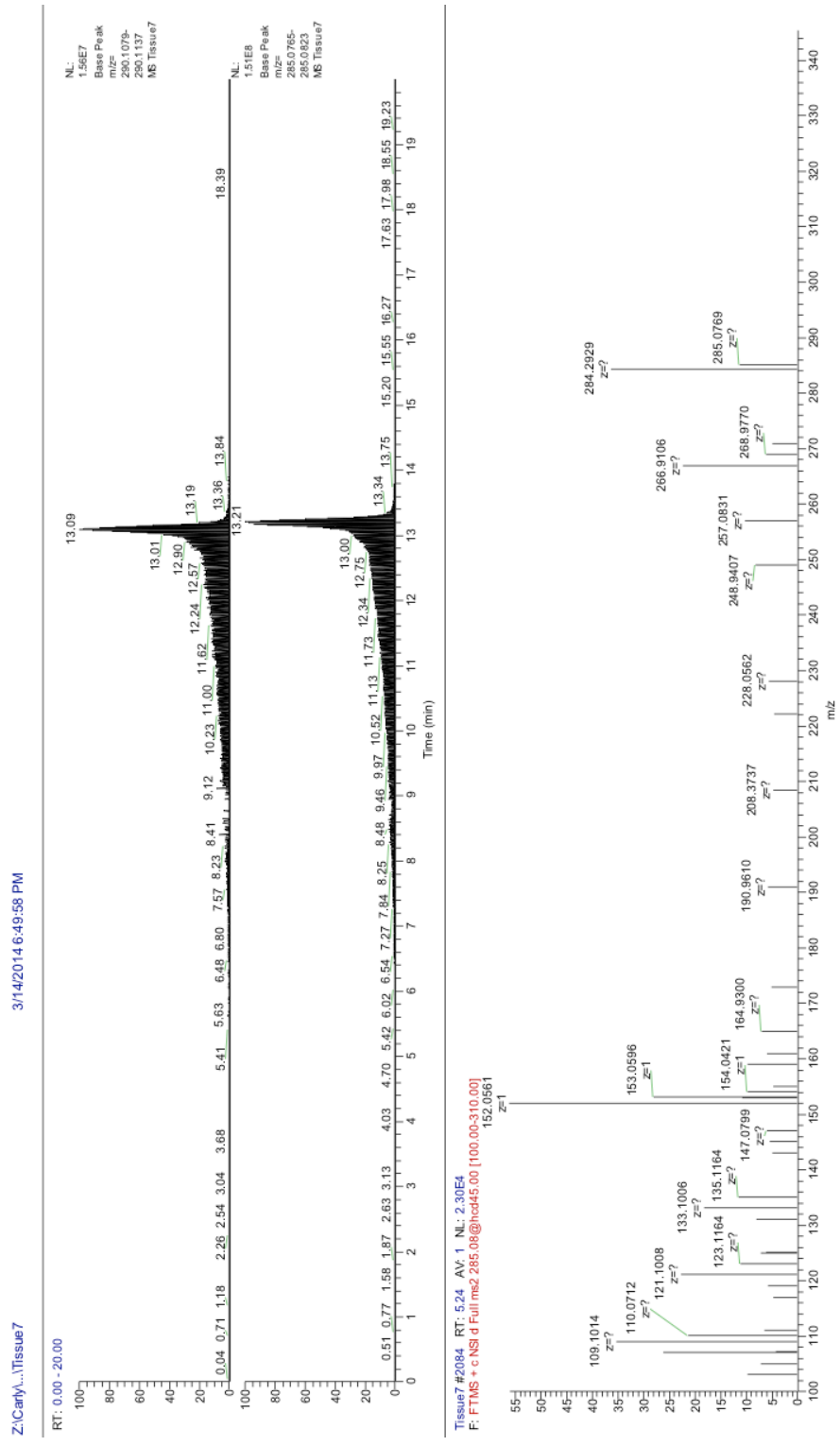

Figure 9. Diazepam was detected in an extracted, minimally perfused brain homogenate from a diazepam-treated CD1 mouse sacrificed at 0.1 h post-dose. (A) XIC

of a d5-diazepam spiked standard. (B) XIC of diazepam. (C) Mass spectrum of diazepam.

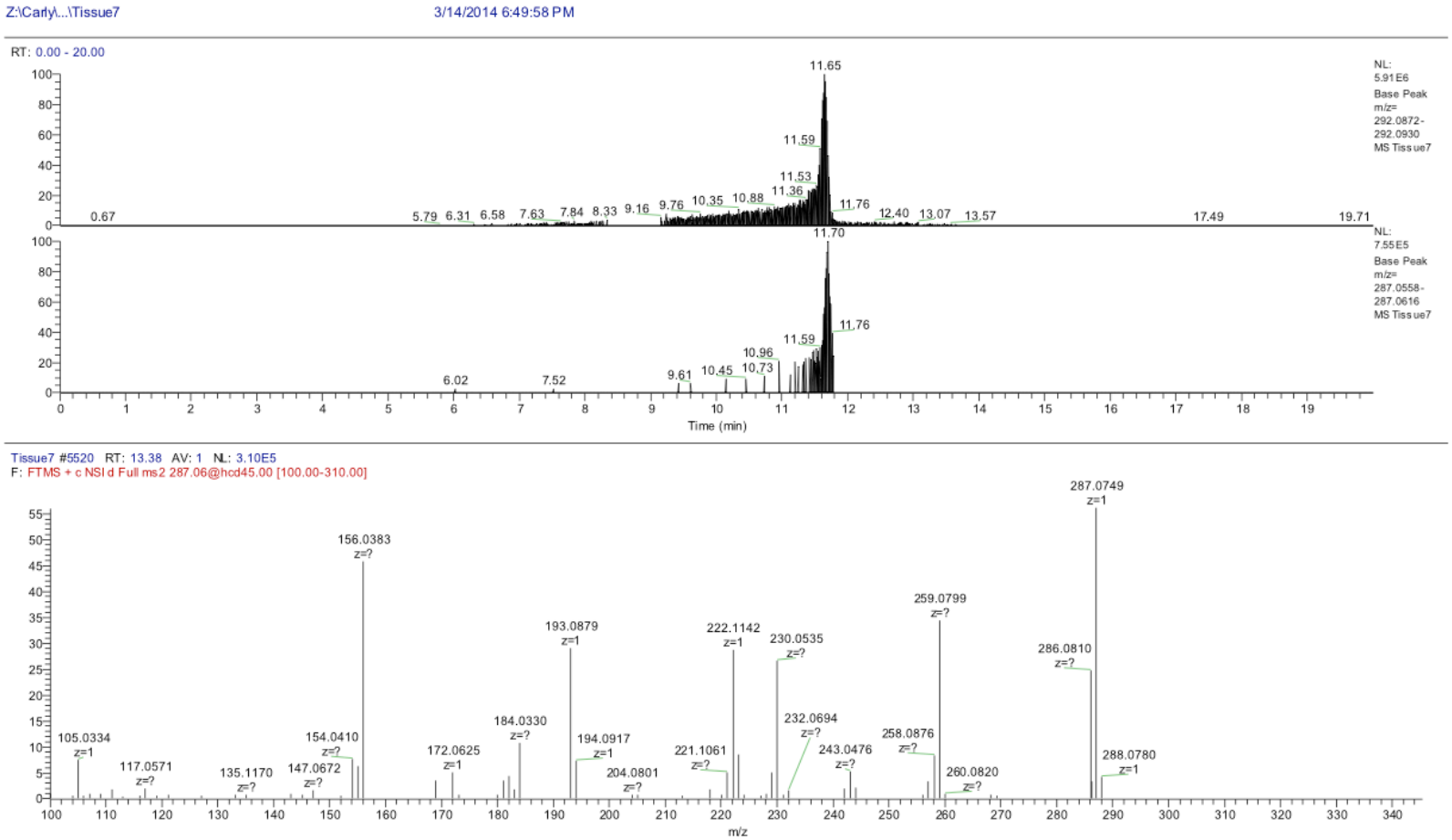
Z:\Carly\...\Tissue7
3/14/2014 6:49:58 PM
RT: 0.00 - 20.00
NL: 5.91E6 Base Peak m/z= 292.0872-292.0930 MS Tissue7
NL: 7.55E5 Base Peak m/z= 287.0558-287.0616 MS Tissue7
Time (min)
Tissue7 #5520 RT: 13.38 AV: 1 NL: 3.10E5
F: FTMS + c NSI d Full ms2 287.06@hcd45.00 [100.00-310.00]
m/z

Figure 10. Oxazepam was detected in an extracted, minimally perfused brain homogenate from a diazepam-treated CD1 mouse sacrificed at 0.1 h post-dose. (A) XIC of a d5-oxazepam spiked standard. (B) XIC of oxazepam. (C) Mass spectrum of oxazepam.

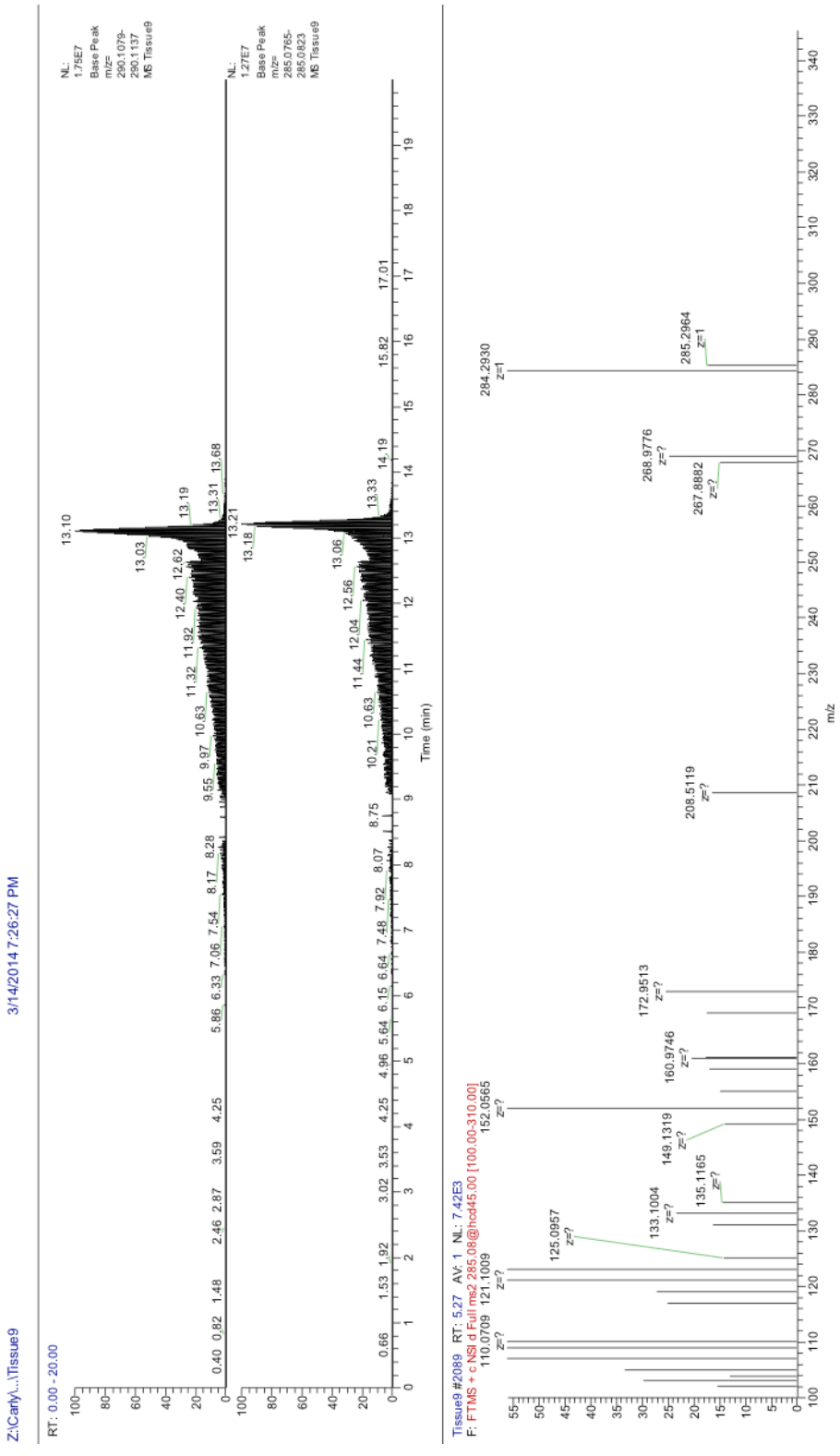

Figure 11. Diazepam was detected in an extracted, minimally perfused brain homogenate from a diazepam-treated CD1 mouse sacrificed at 1 h post-dose. (A) XIC

of a d5-diazepam spiked standard. (B) XIC of diazepam. (C) Mass spectrum of diazepam.

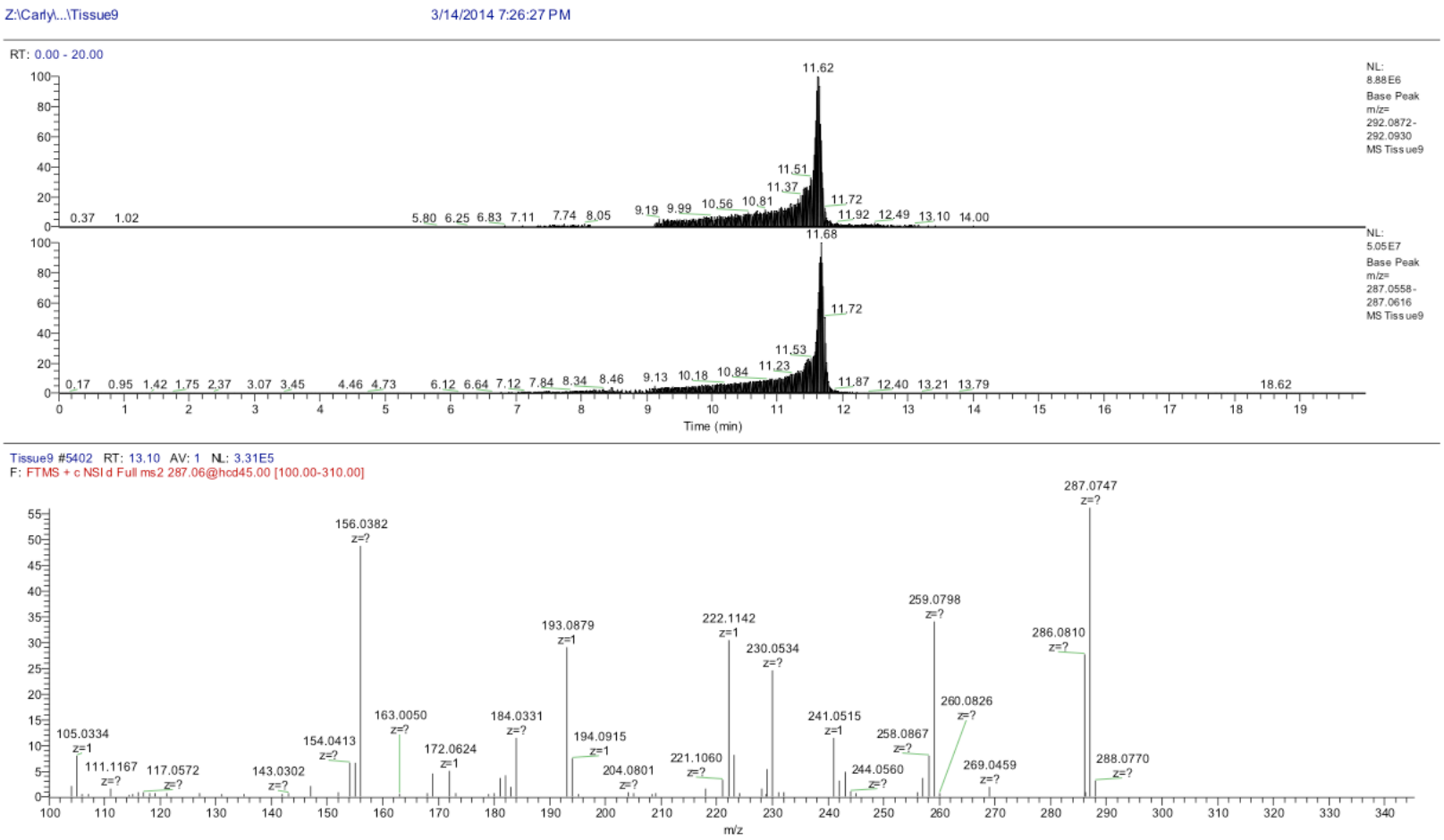
Z:\Carly\...\Tissue9
3/14/2014 7:26:27 PM
RT: 0.00 - 20.00
NL: 8.88E6 Base Peak m/z= 292.0872-292.0930 MS Tissue9
NL: 5.05E7 Base Peak m/z= 287.0558-287.0616 MS Tissue9
Time (min)
Tissue9 #5402 RT: 13.10 AV: 1 NL: 3.31E5
F: FTMS + c NSI d Full ms2 287.06@hcd45.00 [100.00-310.00]
m/z

Figure 12. Oxazepam was detected in an extracted, minimally perfused brain homogenate from a diazepam-treated CD1 mouse sacrificed at 1 h post-dose. (A) XIC of a d5-oxazepam spiked standard. (B) XIC of oxazepam. (C) Mass spectrum of oxazepam.

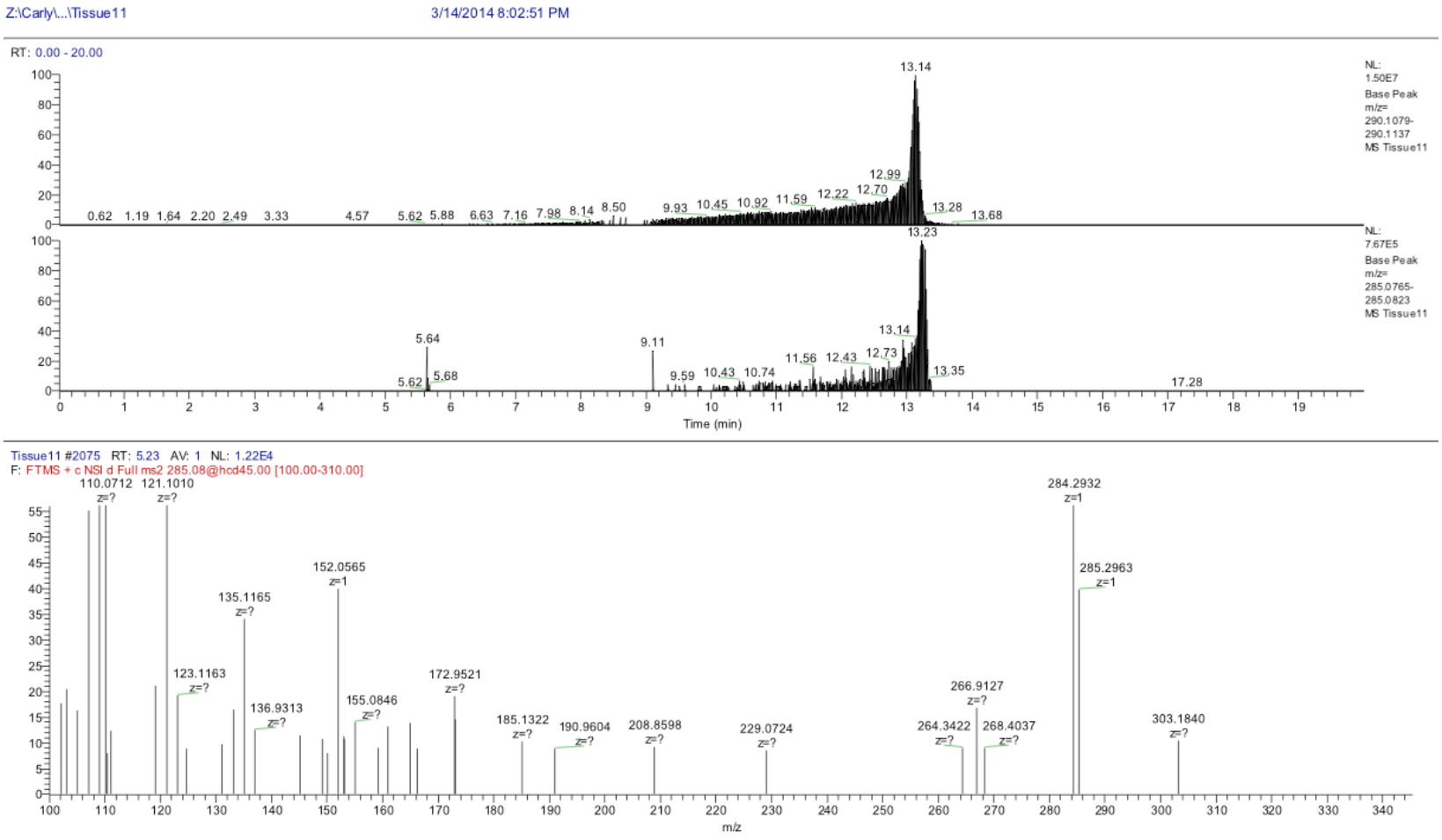
Z:\Carly\...\Tissue11
3/14/2014 8:02:51 PM
RT: 0.00 - 20.00
NL: 1.50E7 Base Peak m/z= 290.1079-290.1137 MS Tissue11
NL: 7.67E5 Base Peak m/z= 285.0765-285.0823 MS Tissue11
Time (min)
Tissue11 #2075 RT: 5.23 AV: 1 NL: 1.22E4
F: FTMS + c NSI d Full ms2 285.08@hcd45.00 [100.00-310.00]
m/z

Figure 13. Diazepam was detected in an extracted, minimally perfused brain homogenate from a diazepam-treated CD1 mouse sacrificed at 6 h post-dose. (A) XIC of a d5-diazepam spiked standard. (B) XIC of diazepam. (C) Mass spectrum of diazepam.

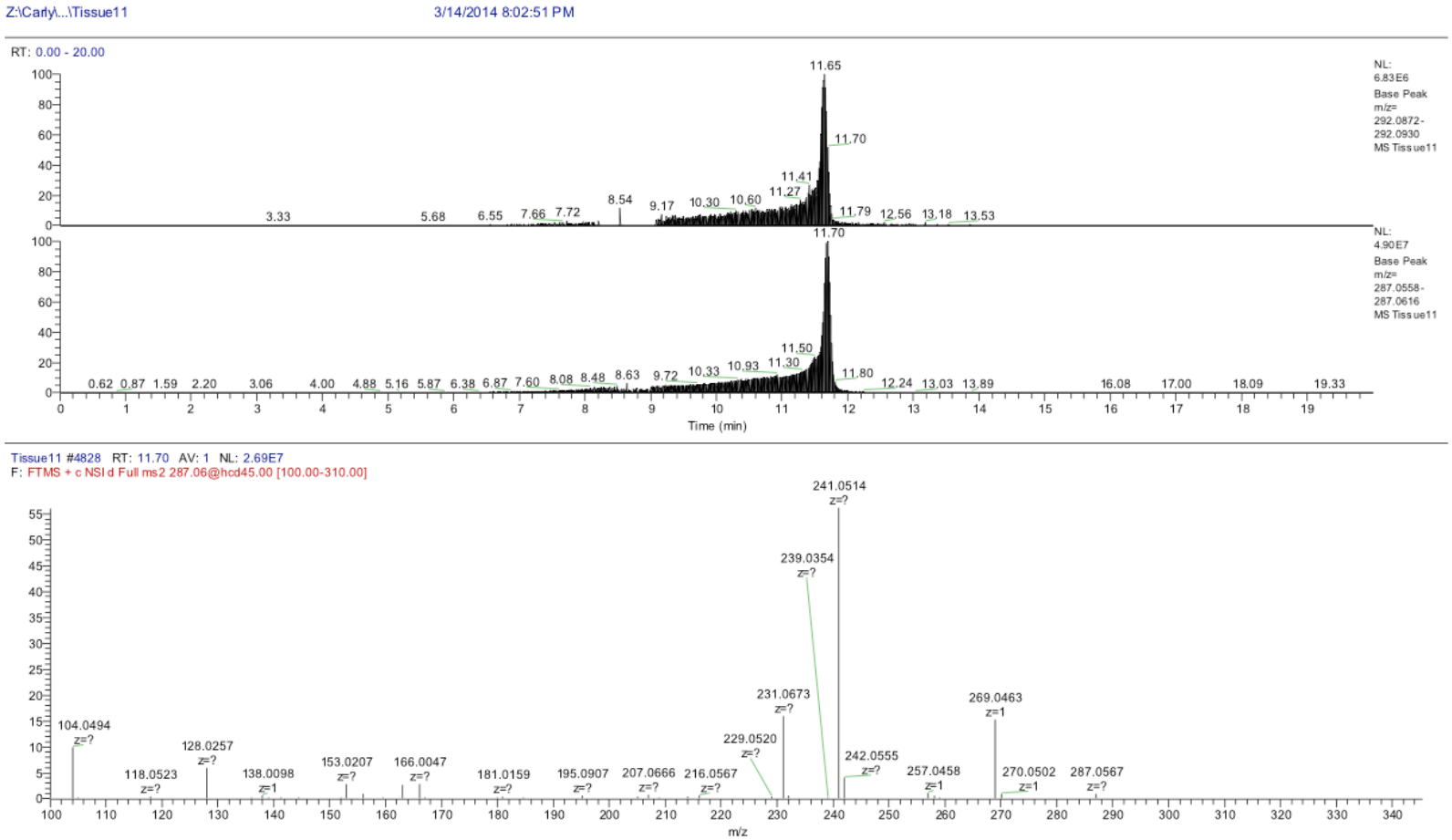
Z:\Carly\...\Tissue11
3/14/2014 8:02:51 PM
RT: 0.00 - 20.00
NL: 6.83E6 Base Peak m/z= 292.0872-292.0930 MS Tissue11
NL: 4.90E7 Base Peak m/z= 287.0558-287.0616 MS Tissue11
Time (min)
Tissue11 #4828 RT: 11.70 AV: 1 NL: 2.69E7
F: FTMS + c NSI d Full ms2 287.06@hcd45.00 [100.00-310.00]
m/z

Figure 14. Oxazepam was detected in an extracted, minimally perfused brain homogenate from a diazepam-treated CD1 mouse sacrificed at 6 h post-dose. (A) XIC of a d5-oxazepam spiked standard. (B) XIC of oxazepam. (C) Mass spectrum of oxazepam.

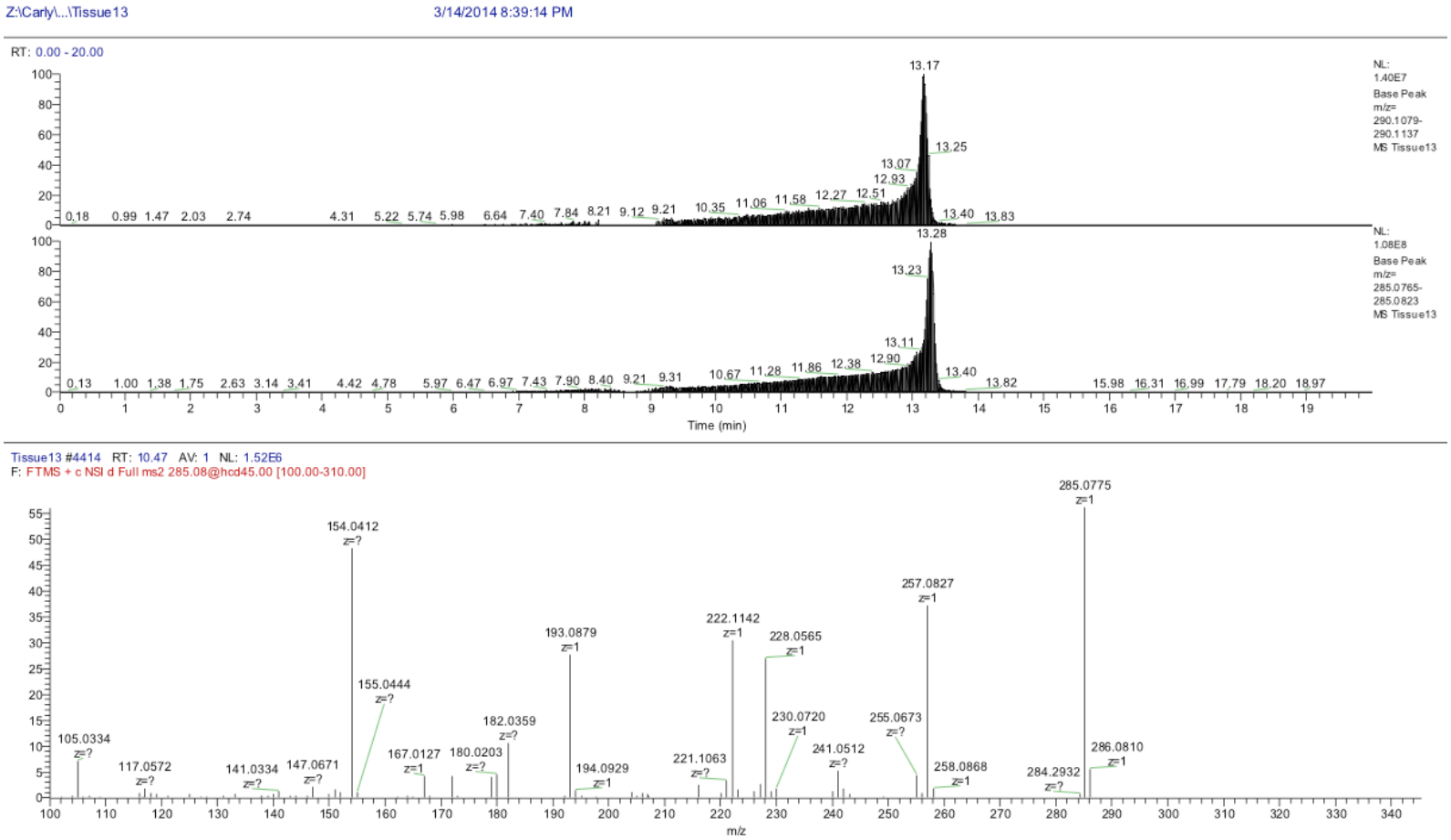
Z:\Carly\...\Tissue13
3/14/2014 8:39:14 PM
RT: 0.00 - 20.00
NL: 1.40E7 Base Peak m/z= 290.1079-290.1137 MS Tissue13
NL: 1.08E8 Base Peak m/z= 285.0765-285.0823 MS Tissue13
Time (min)
Tissue13 #4414 RT: 10.47 AV: 1 NL: 1.52E6
F: FTMS + c NSI d Full ms2 285.08@hcd45.00 [100.00-310.00]
m/z

Figure 15. Diazepam was detected in an extracted brain homogenate from a lightly exsanguinated (via cardiocentesis) diazepam-treated CD1 mouse sacrificed at 0.1 h post-dose. (A) XIC of a d5-diazepam spiked standard. (B) XIC of diazepam. (C) Mass spectrum of diazepam.

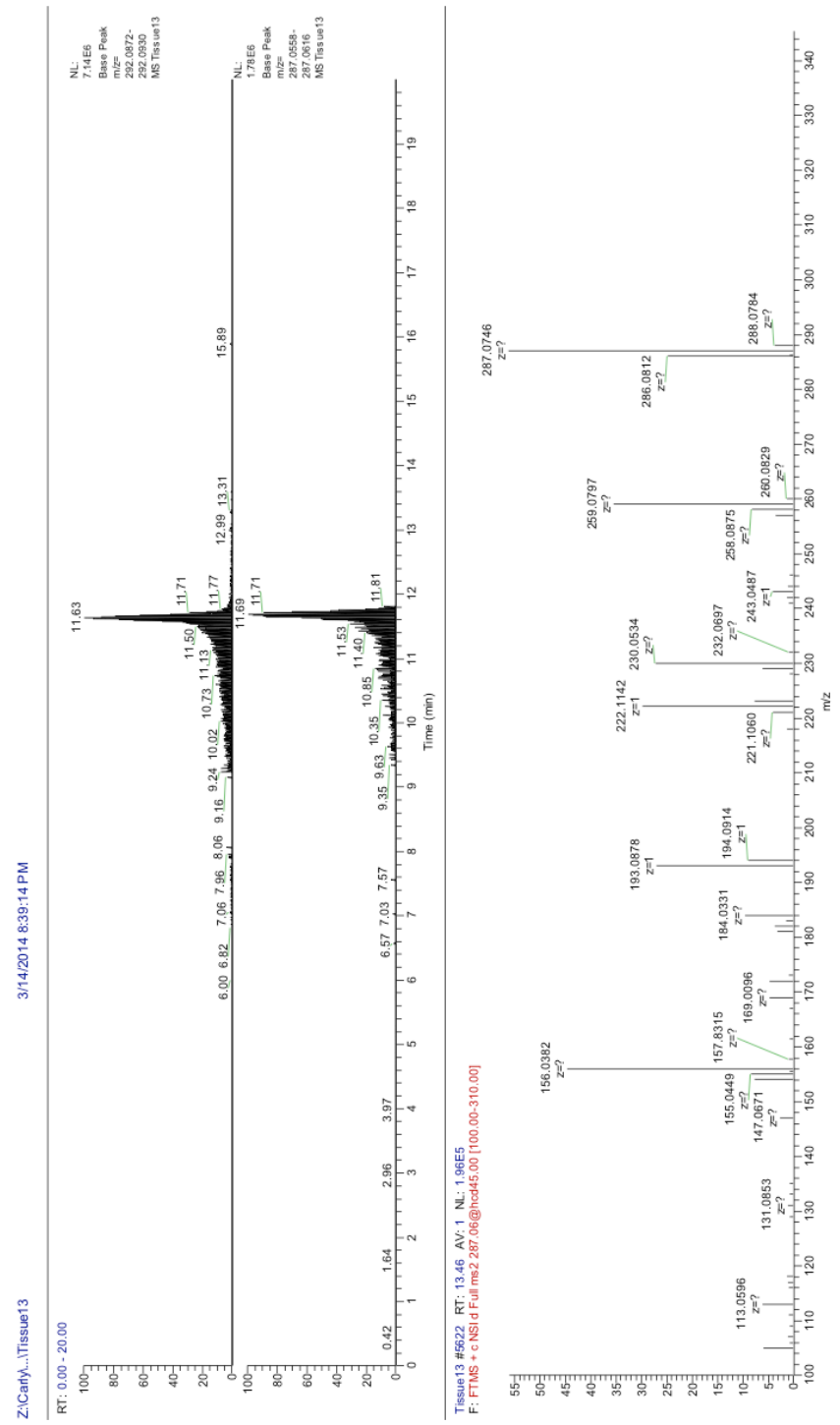

Figure 16. Oxazepam was detected in an extracted brain homogenate from a lightly exsanguinated (via cardiocentesis) diazepam-treated CD1 mouse sacrificed at 0.1 h post-dose. (A) XIC of a d5-oxazepam spiked standard. (B) XIC of oxazepam. (C) Mass spectrum of oxazepam.

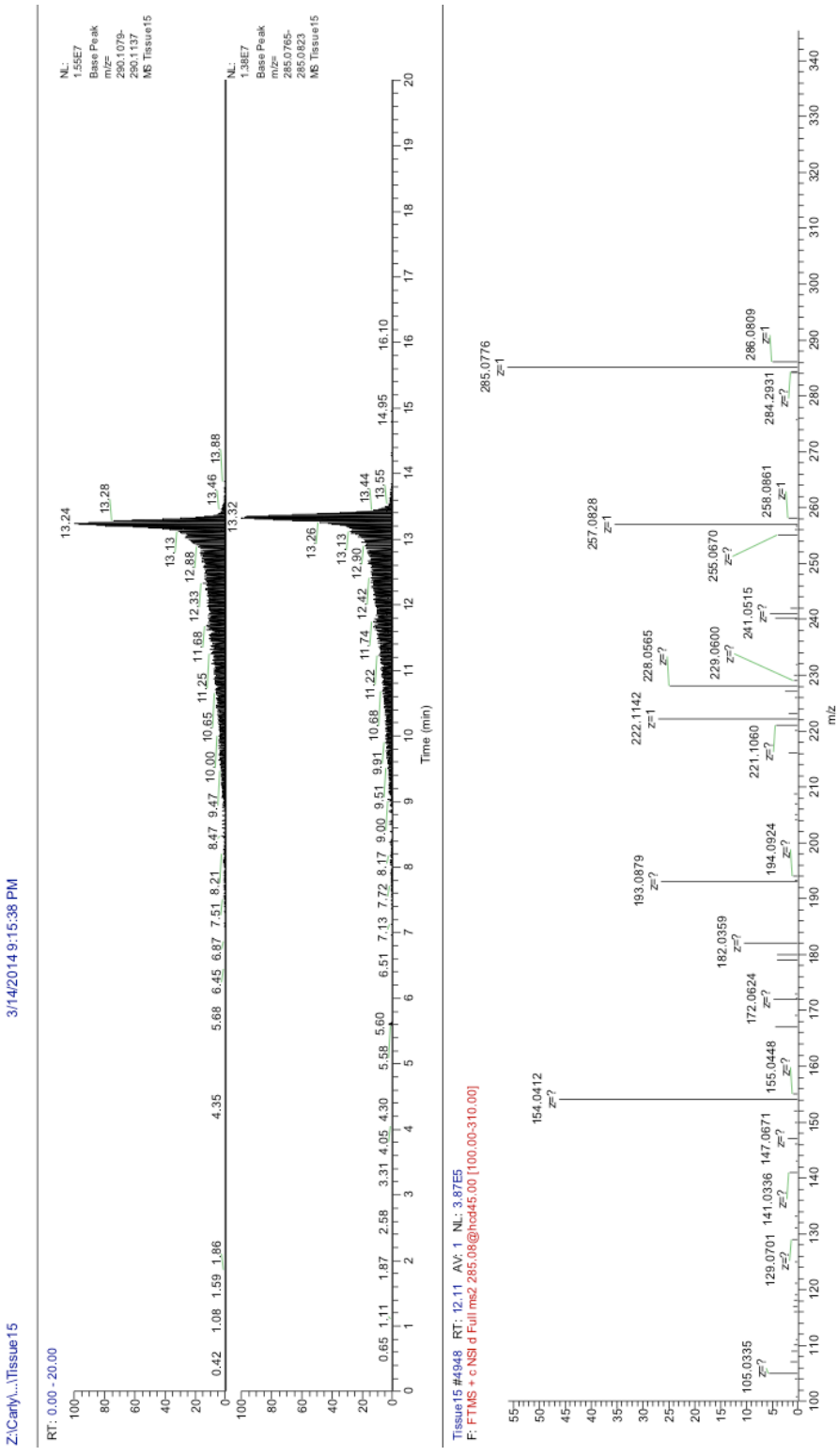

Figure 17. Diazepam was detected in an extracted brain homogenate from a lightly exsanguinated (via cardiocentesis) diazepam-treated CD1 mouse sacrificed at 1 h post-

dose. (A) XIC of a d5-diazepam spiked standard. (B) XIC of diazepam. (C) Mass spectrum of diazepam.

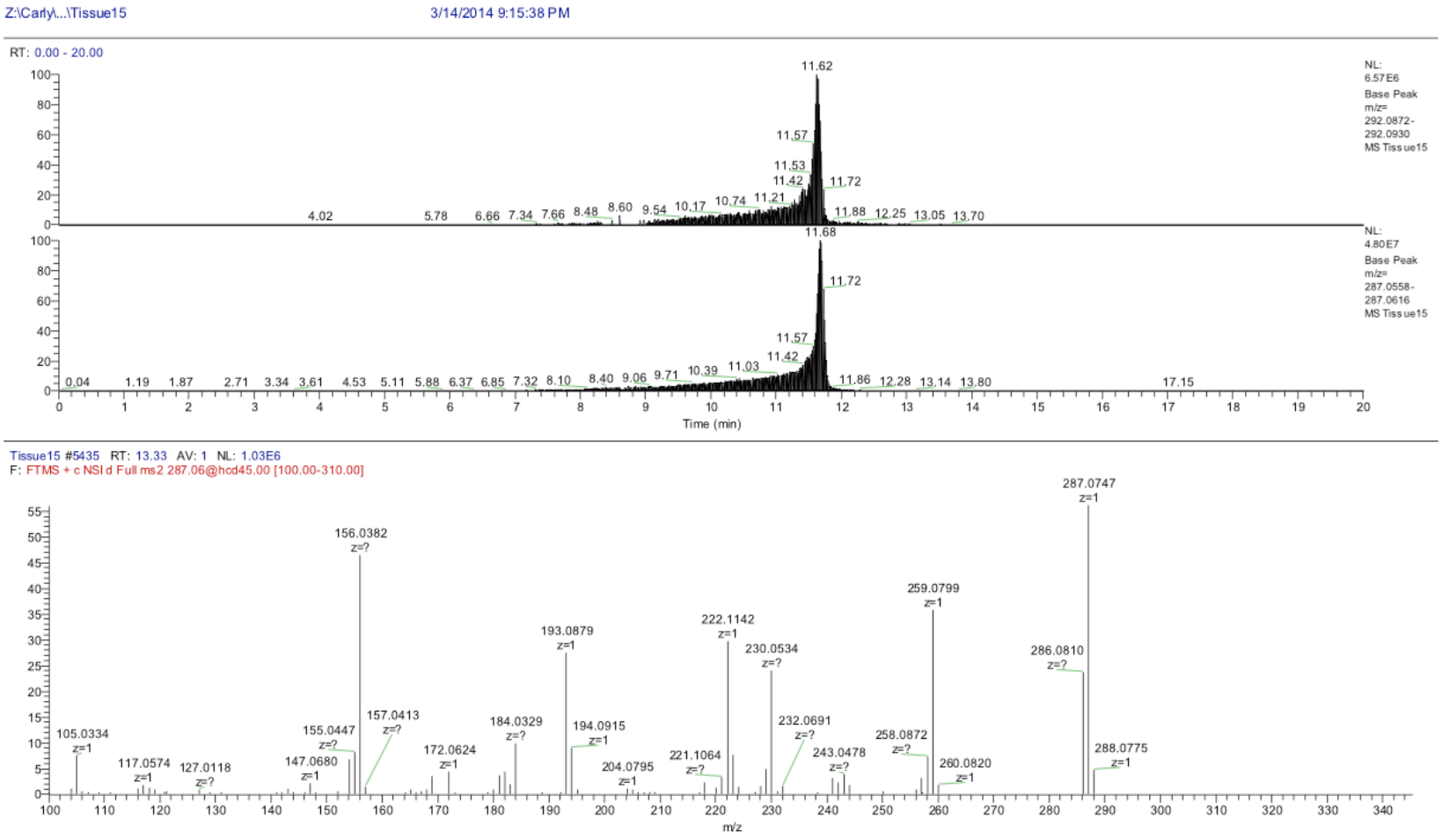
Z:\Carly\...\Tissue15
3/14/2014 9:15:38 PM
RT: 0.00 - 20.00
NL: 6.57E6
Base Peak m/z= 292.0872-292.0930 MS Tissue15
NL: 4.80E7
Base Peak m/z= 287.0558-287.0616 MS Tissue15
Time (min)
Tissue15 #5435 RT: 13.33 AV: 1 NL: 1.03E6
F: FTMS + c NSI d Full ms2 287.06@hcd45.00 [100.00-310.00]
m/z

Figure 18. Oxazepam was detected in an extracted brain homogenate from a lightly exsanguinated (via cardiocentesis) diazepam-treated CD1 mouse sacrificed at 1 h post-dose. (A) XIC of a d5-oxazepam spiked standard. (B) XIC of oxazepam. (C) Mass spectrum of oxazepam.

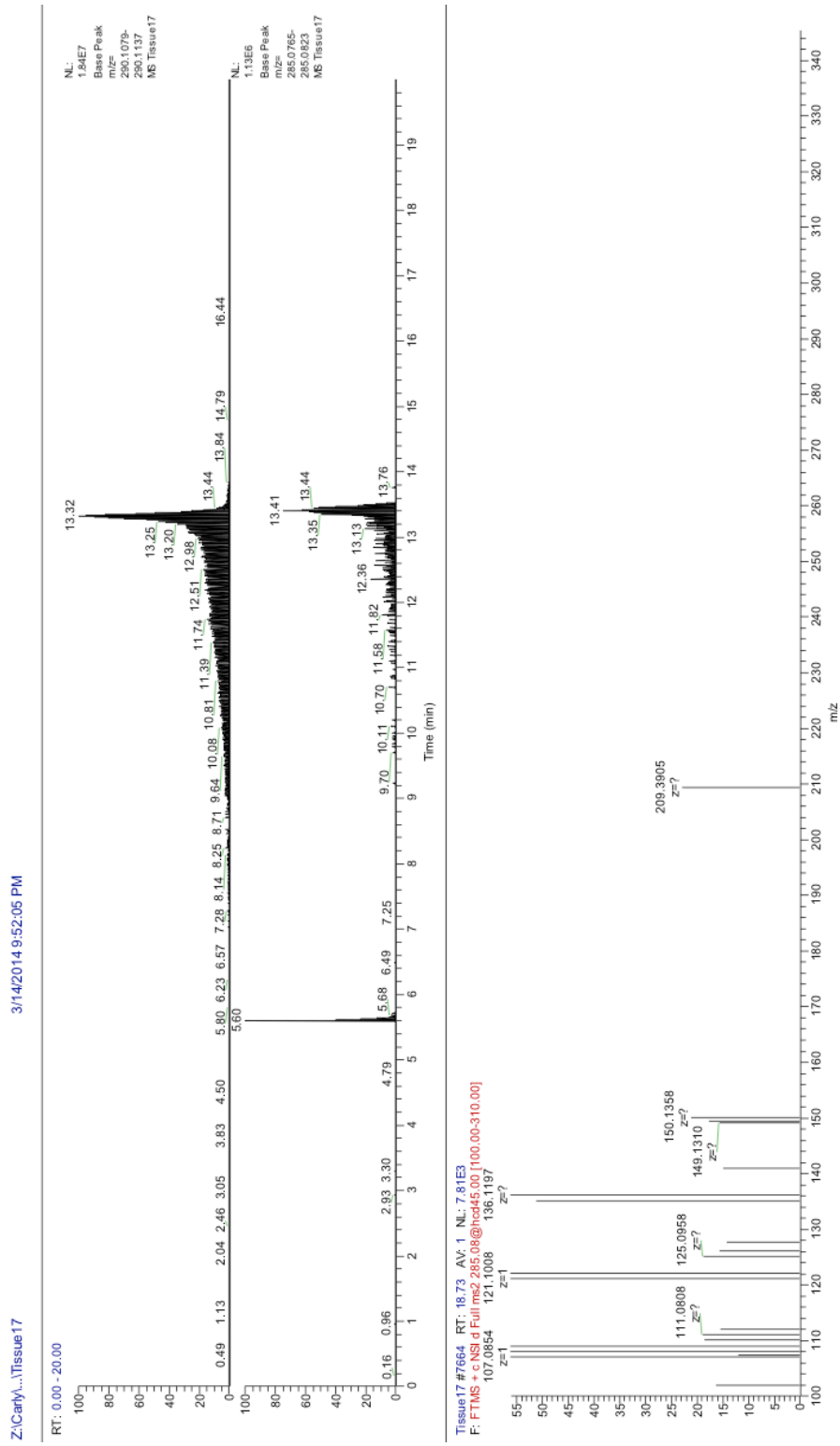

Figure 19. Diazepam was detected in an extracted brain homogenate from a lightly exsanguinated (via cardiocentesis) diazepam-treated CD1 mouse sacrificed at 6 h post-

dose. (A) XIC of a d5-diazepam spiked standard. (B) XIC of diazepam. (C) Mass spectrum of diazepam.

Z:\Carly\...\Tissue17 3/14/2014 9:52:05 PM

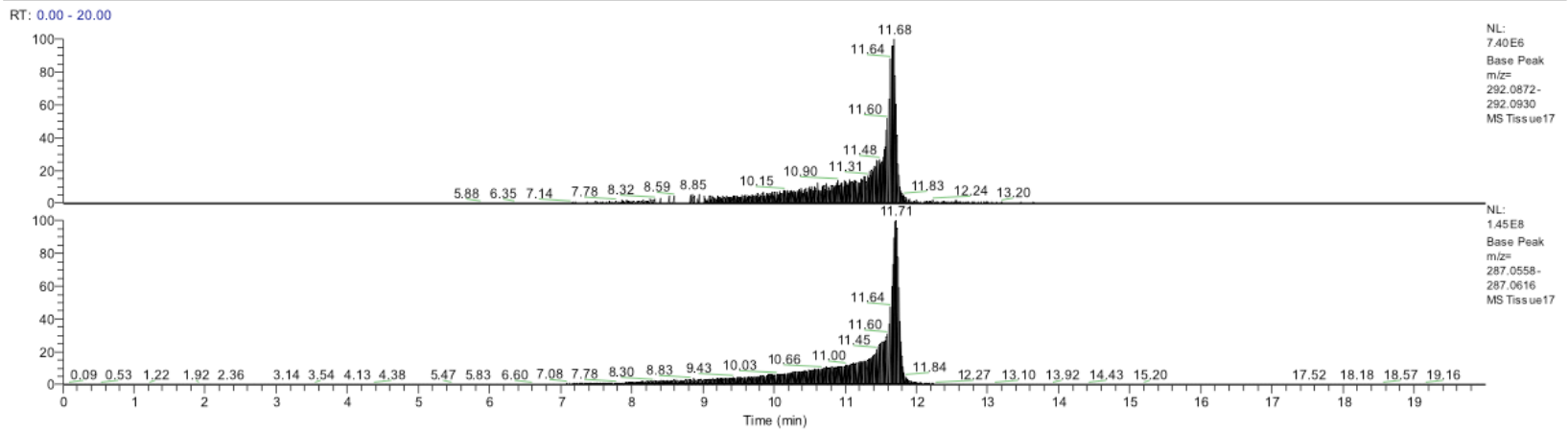

Tissue17 #4938 RT: 12.04 AV: 1 NL: 8.09E5
F: FTMS + c NSI d Full ms2 287.06@hcd45.00 [100.00-310.00]

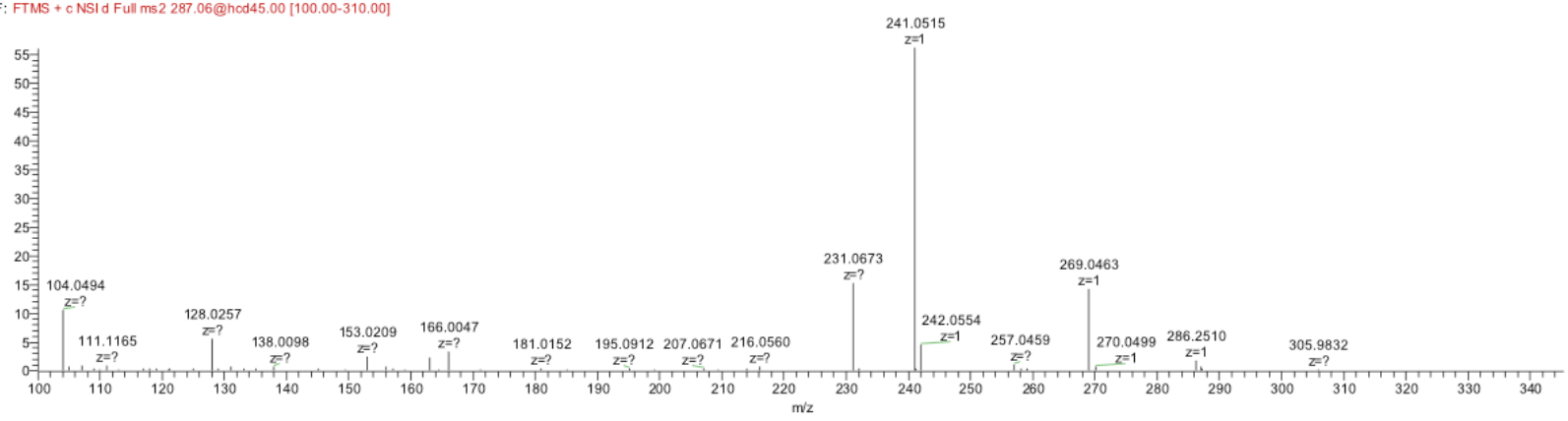

Figure 20. Oxazepam was detected in an extracted brain homogenate from a lightly exsanguinated (via cardiocentesis) diazepam-treated CD1 mouse sacrificed at 1 h post-dose. (A) XIC of a d5-oxazepam spiked standard. (B) XIC of oxazepam. (C) Mass spectrum of oxazepam.

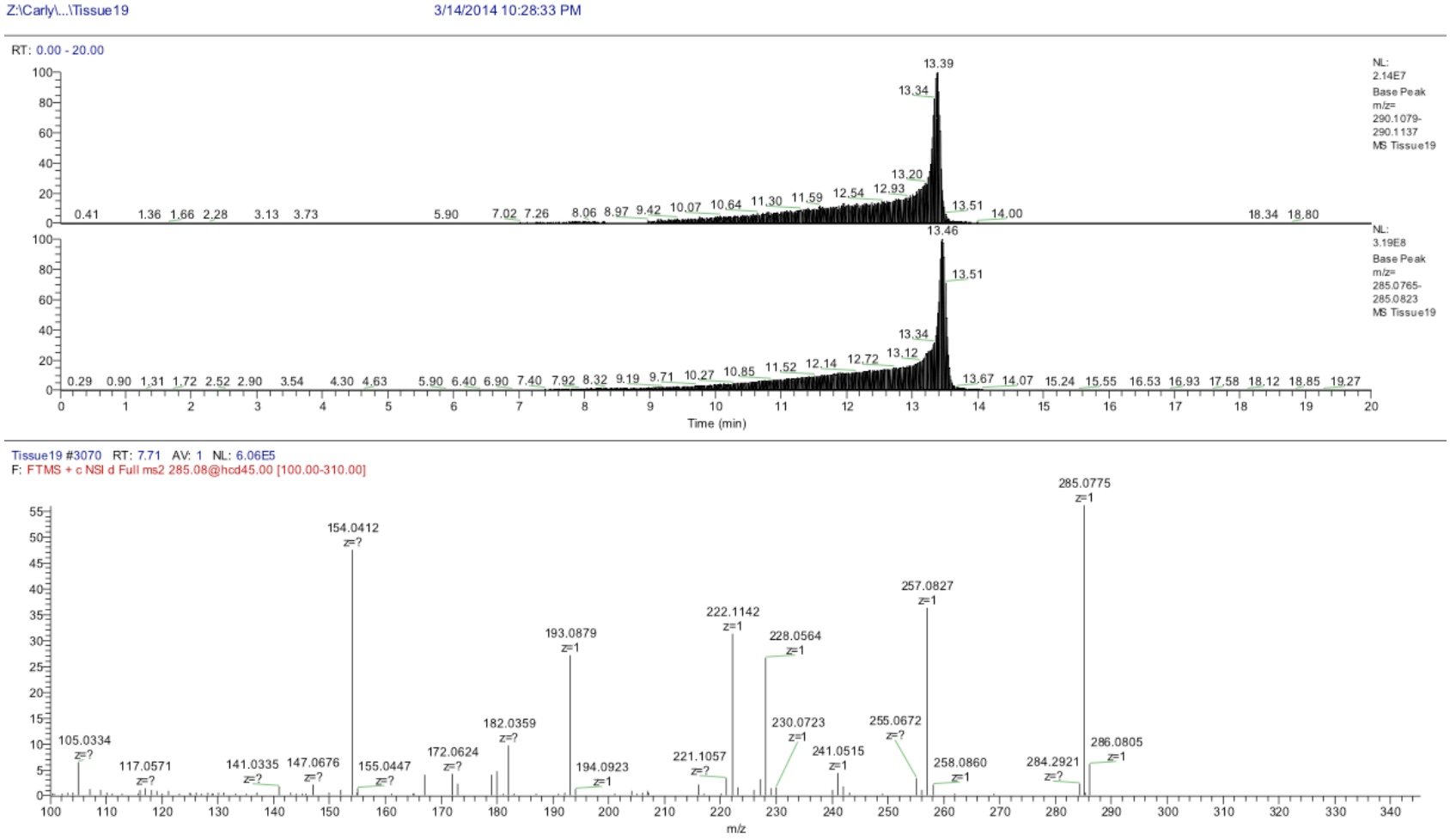
Z:\Carly\...\Tissue19
3/14/2014 10:28:33 PM
RT: 0.00 - 20.00
NL: 2.14E7
Base Peak m/z= 290.1079-290.1137 MS Tissue19
NL: 3.19E8
Base Peak m/z= 285.0765-285.0823 MS Tissue19
Time (min)
Tissue19 #3070 RT: 7.71 AV: 1 NL: 6.06E5
F: FTMS + c NSI d Full ms2 285.08@hcd45.00 [100.00-310.00]
m/z
285.0775 z=1
154.0412 z=?
257.0827 z=1
222.1142 z=1
193.0879 z=1
228.0564 z=1
182.0359 z=?
230.0723 z=1
255.0672 z=?
105.0334 z=?
172.0624 z=?
241.0515 z=1
286.0805 z=1
117.0571 z=?
141.0335 z=?
147.0676 z=?
155.0447 z=?
194.0923 z=1
221.1057 z=?
258.0860 z=1
284.2921 z=?

Figure 21. Diazepam was detected in an extracted brain homogenate from a transcardially perfused diazepam-treated CD1 mouse sacrificed at 0.1 h post-dose. (A) XIC of a d5-diazepam spiked standard. (B) XIC of diazepam. (C) Mass spectrum of diazepam.

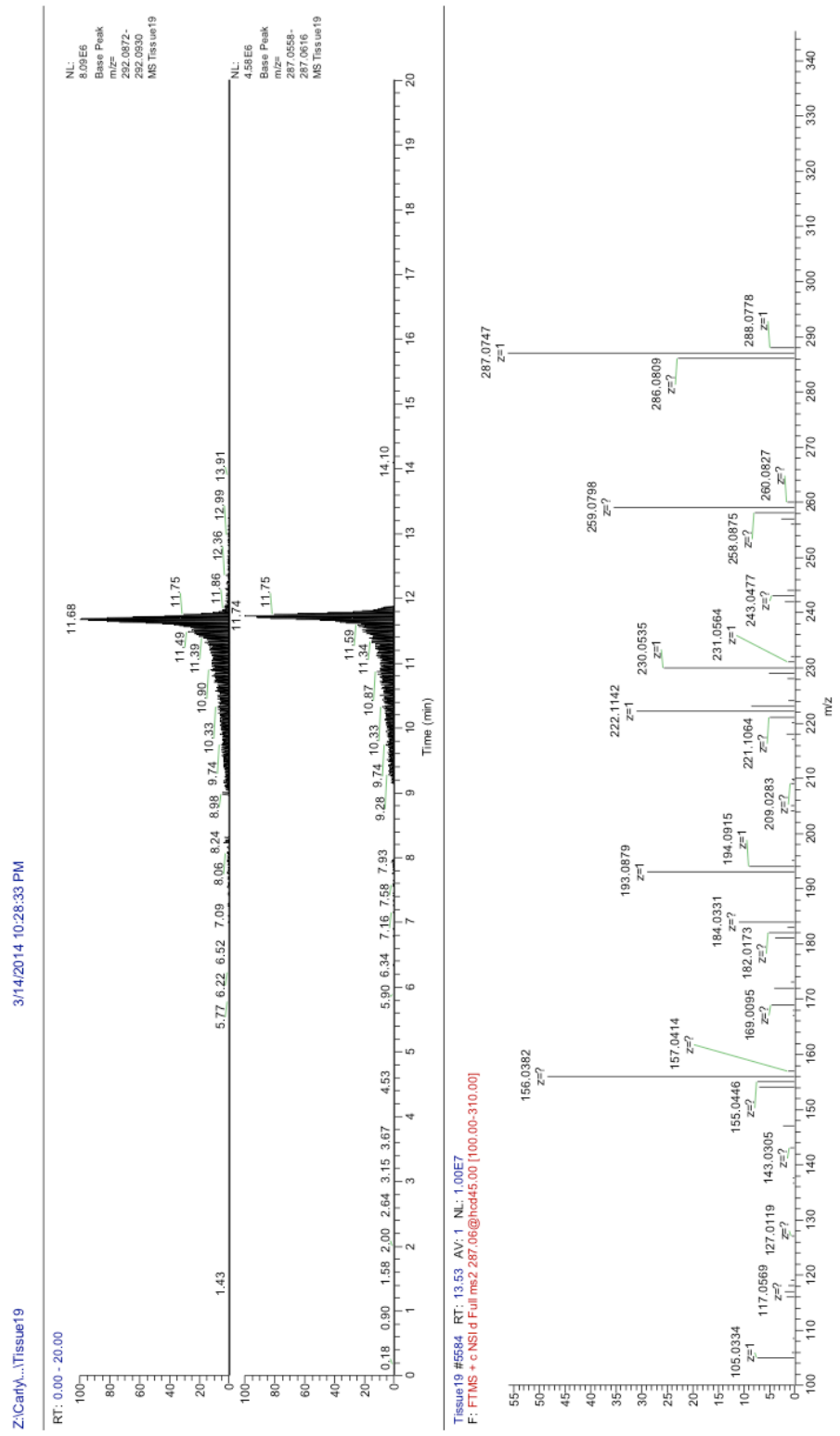

Figure 22. Oxazepam was detected in an extracted brain homogenate from a transcardially perfused diazepam-treated CD1 mouse sacrificed at 0.1 h post-dose. (A)

XIC of a d5-oxazepam spiked standard. (B) XIC of oxazepam. (C) Mass spectrum of oxazepam.

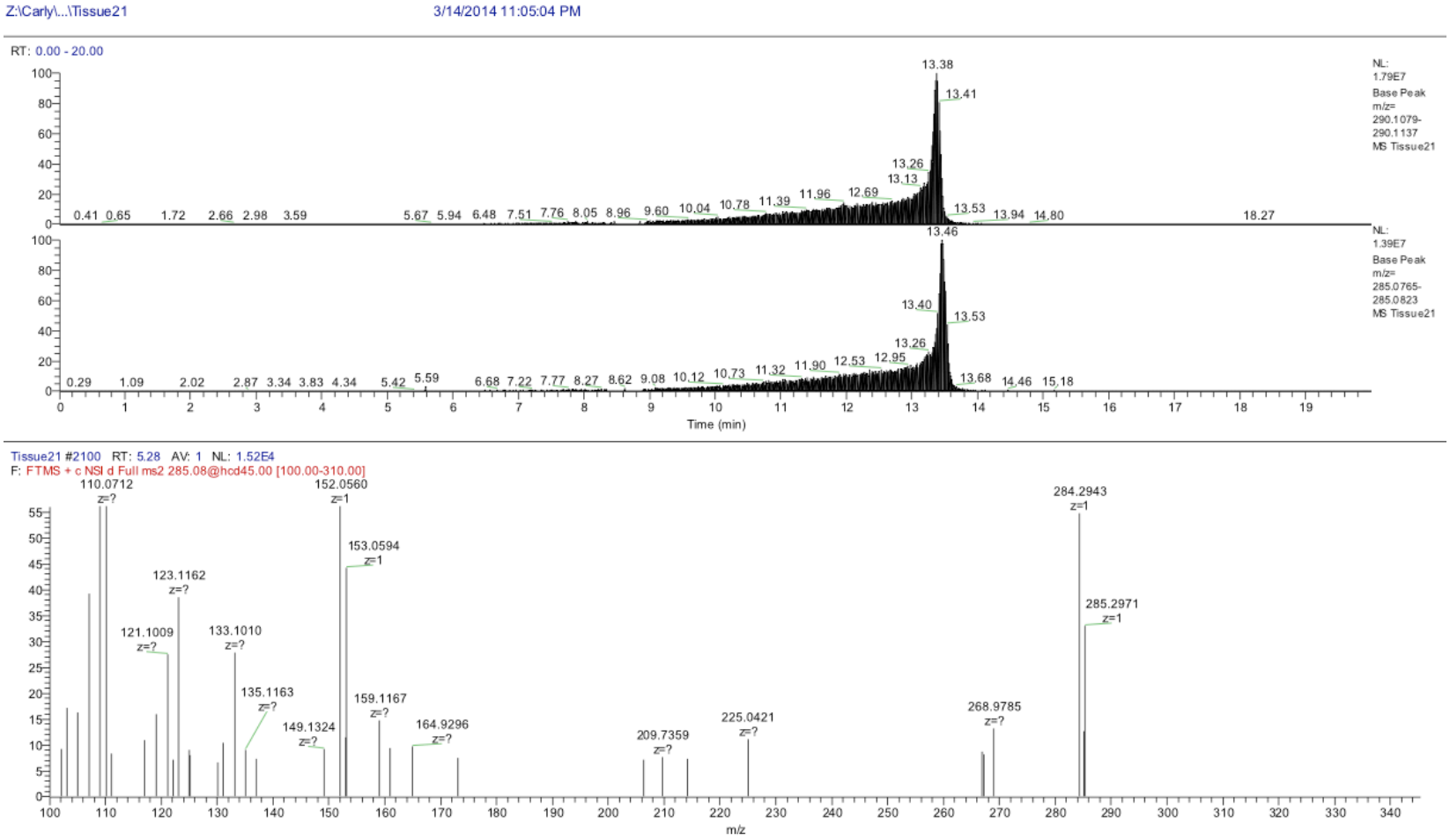
Z:\Carly\...\Tissue21
3/14/2014 11:05:04 PM
RT: 0.00 - 20.00
NL: 1.79E7 Base Peak m/z= 290.1079-290.1137 MS Tissue21
NL: 1.39E7 Base Peak m/z= 285.0765-285.0823 MS Tissue21
Time (min)
Tissue21 #2100 RT: 5.28 AV: 1 NL: 1.52E4
F: FTMS + c NSI d Full ms2 285.08@hcd45.00 [100.00-310.00]
110.0712 z=?
152.0560 z=1
284.2943 z=1
153.0594 z=1
123.1162 z=?
285.2971 z=1
121.1009 z=?
133.1010 z=?
135.1163 z=?
159.1167 z=?
149.1324 z=?
164.9296 z=?
209.7359 z=?
225.0421 z=?
268.9785 z=?
m/z

Figure 23. Diazepam was detected in an extracted brain homogenate from a transcardially perfused diazepam-treated CD1 mouse sacrificed at 1 h post-dose. (A) XIC of a d5-diazepam spiked standard. (B) XIC of diazepam. (C) Mass spectrum of diazepam.

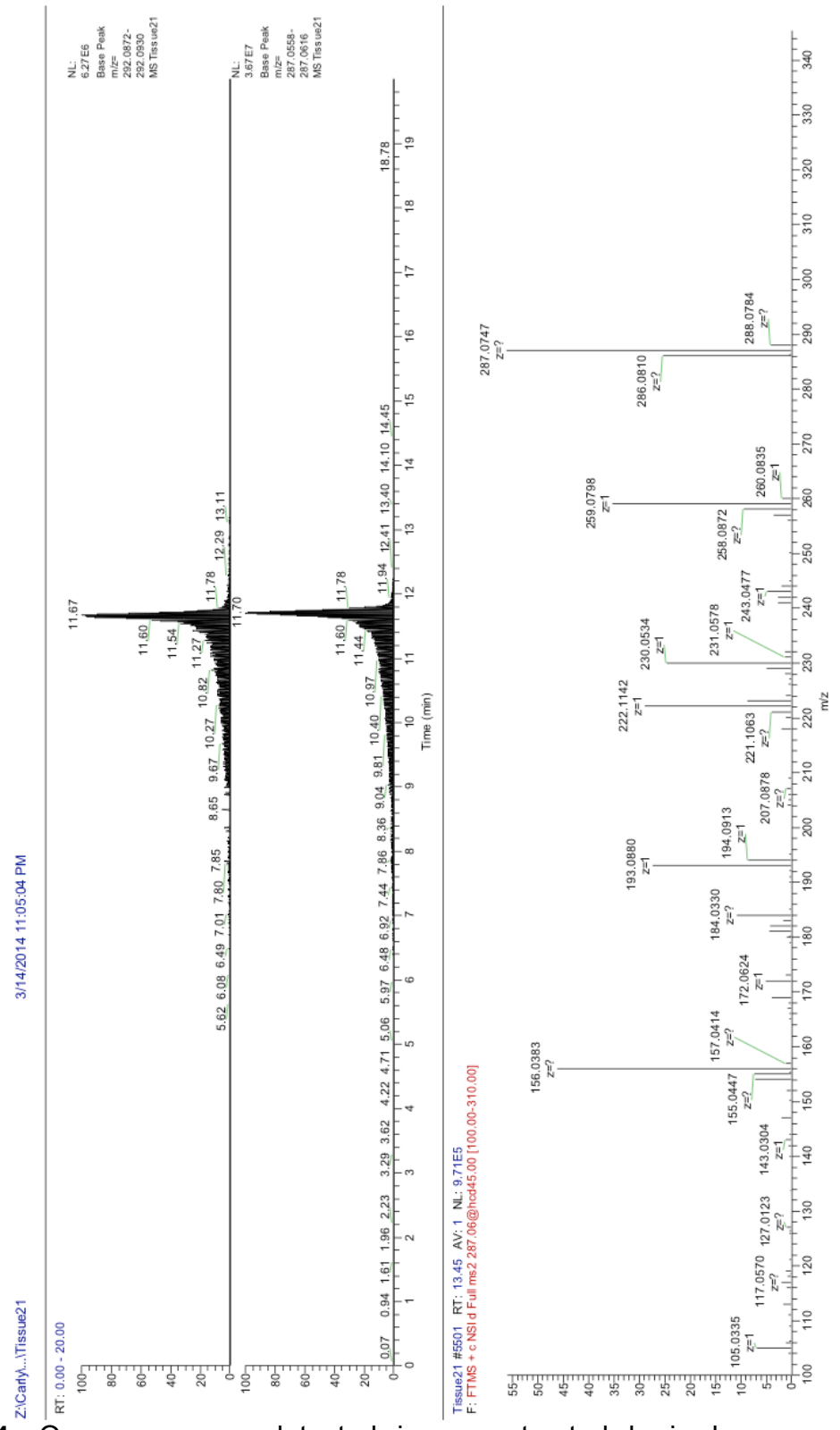

Figure 24. Oxazepam was detected in an extracted brain homogenate from a transcardially perfused diazepam-treated CD1 mouse sacrificed at 1 h post-dose. (A)

XIC of a d5-oxazepam spiked standard. (B) XIC of oxazepam. (C) Mass spectrum of oxazepam.

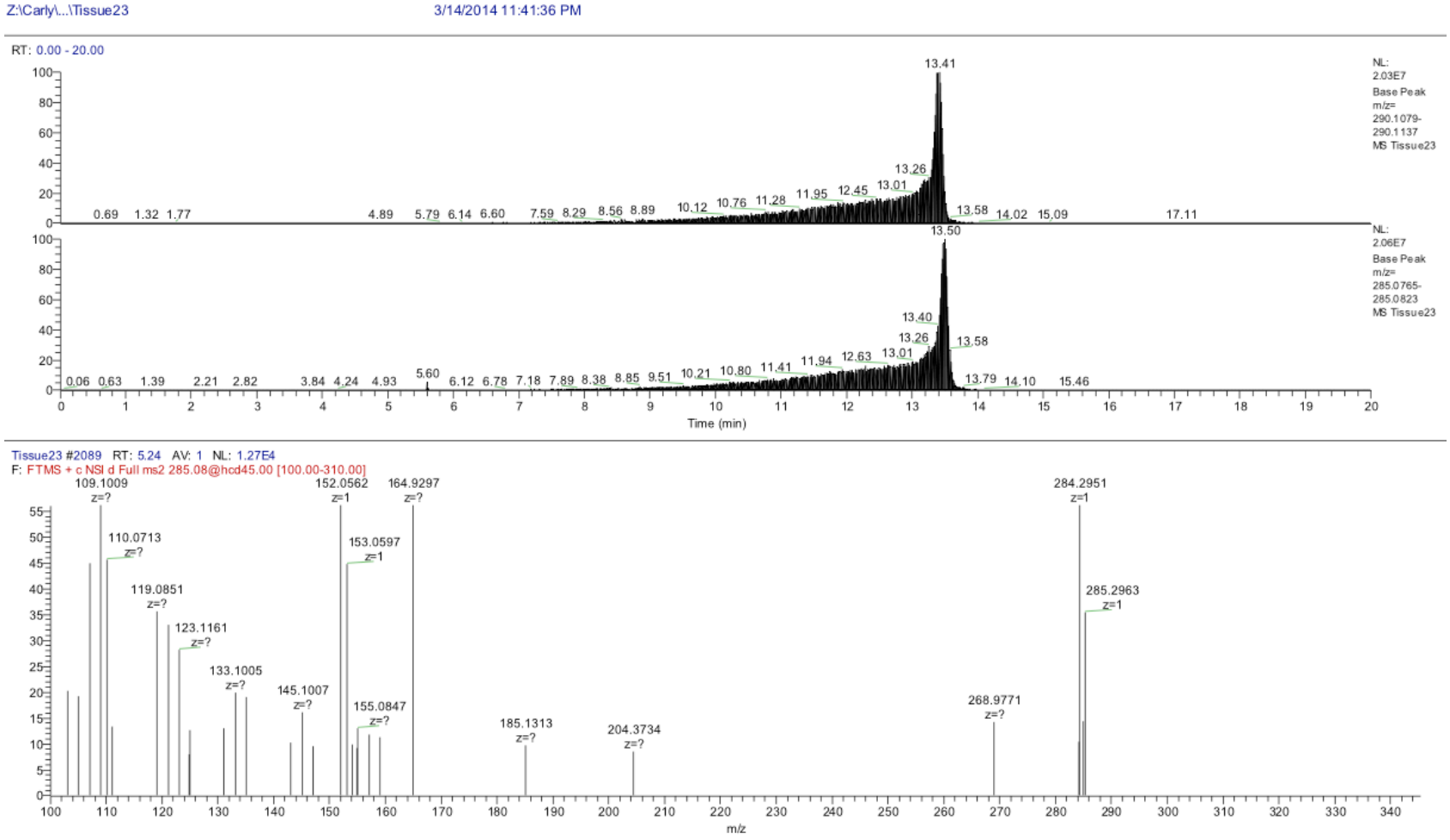
Z:\Carly\...\Tissue23
3/14/2014 11:41:36 PM
RT: 0.00 - 20.00
NL: 2.03E7 Base Peak m/z= 290.1079-290.1137 MS Tissue23
NL: 2.06E7 Base Peak m/z= 285.0765-285.0823 MS Tissue23
Time (min)
Tissue23 #2089 RT: 5.24 AV: 1 NL: 1.27E4
F: FTMS + c NSI d Full ms2 285.08@hcd45.00 [100.00-310.00]
109.1009 z=?
110.0713 z=?
119.0851 z=?
123.1161 z=?
133.1005 z=?
145.1007 z=?
152.0562 z=1
153.0597 z=1
155.0847 z=?
164.9297 z=?
185.1313 z=?
204.3734 z=?
268.9771 z=?
284.2951 z=1
285.2963 z=1
m/z

Figure 25. Diazepam was detected in an extracted brain homogenate from a transcardially perfused diazepam-treated CD1 mouse sacrificed at 6 h post-dose. (A) XIC of a d5-diazepam spiked standard. (B) XIC of diazepam. (C) Mass spectrum of diazepam.

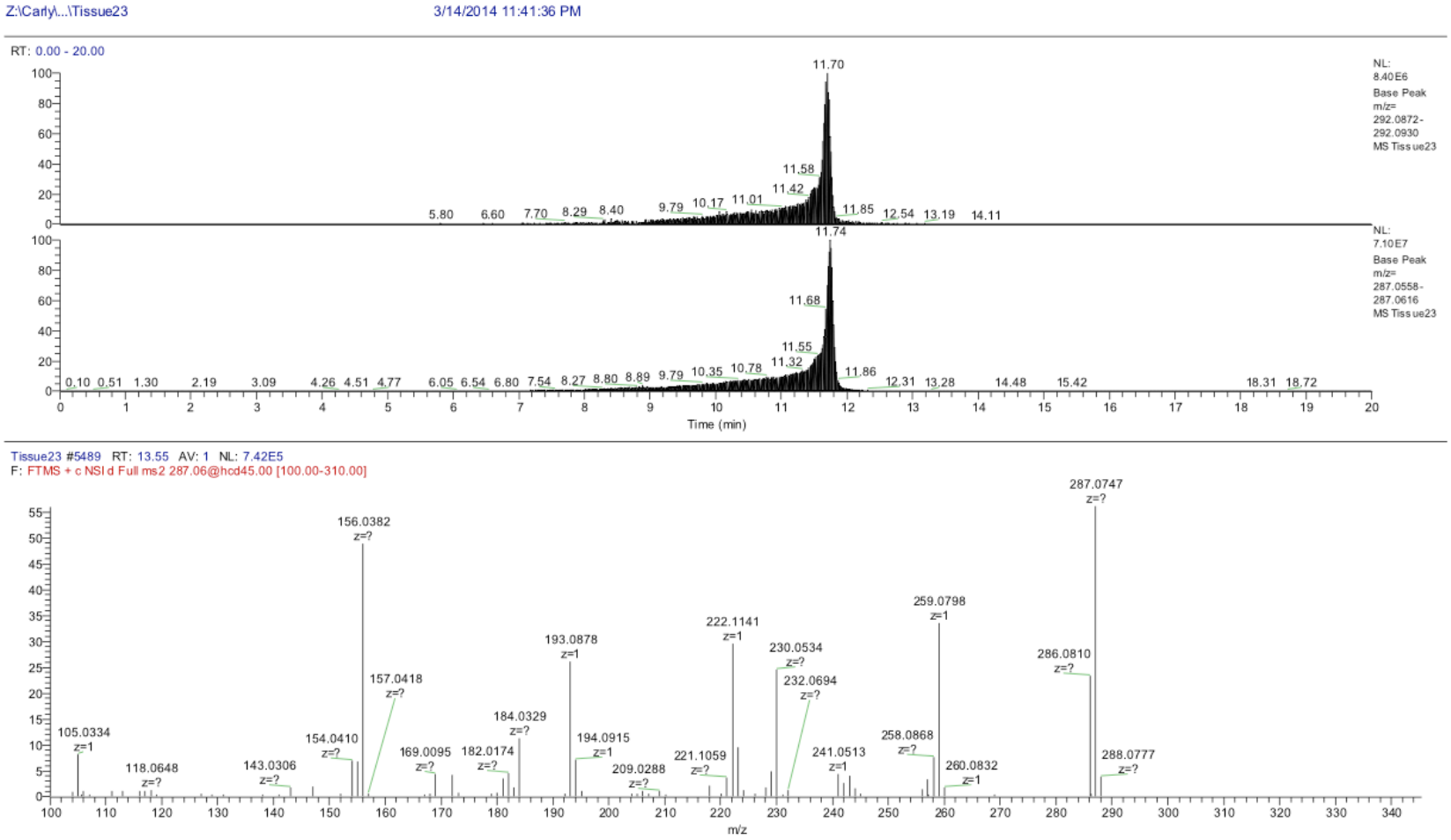
Z:\Carly\...\Tissue23
3/14/2014 11:41:36 PM
RT: 0.00 - 20.00
NL: 8.40E6
Base Peak m/z= 292.0872-292.0930 MS Tissue23
NL: 7.10E7
Base Peak m/z= 287.0558-287.0616 MS Tissue23
Time (min)
Tissue23 #5489 RT: 13.55 AV: 1 NL: 7.42E5
F: FTMS + c NSI d Full ms2 287.06@hcd45.00 [100.00-310.00]
m/z

Figure 26. Oxazepam was detected in an extracted brain homogenate from a transcardially perfused diazepam-treated CD1 mouse sacrificed at 6 h post-dose. (A) XIC of a d5-oxazepam spiked standard. (B) XIC of oxazepam. (C) Mass spectrum of oxazepam.

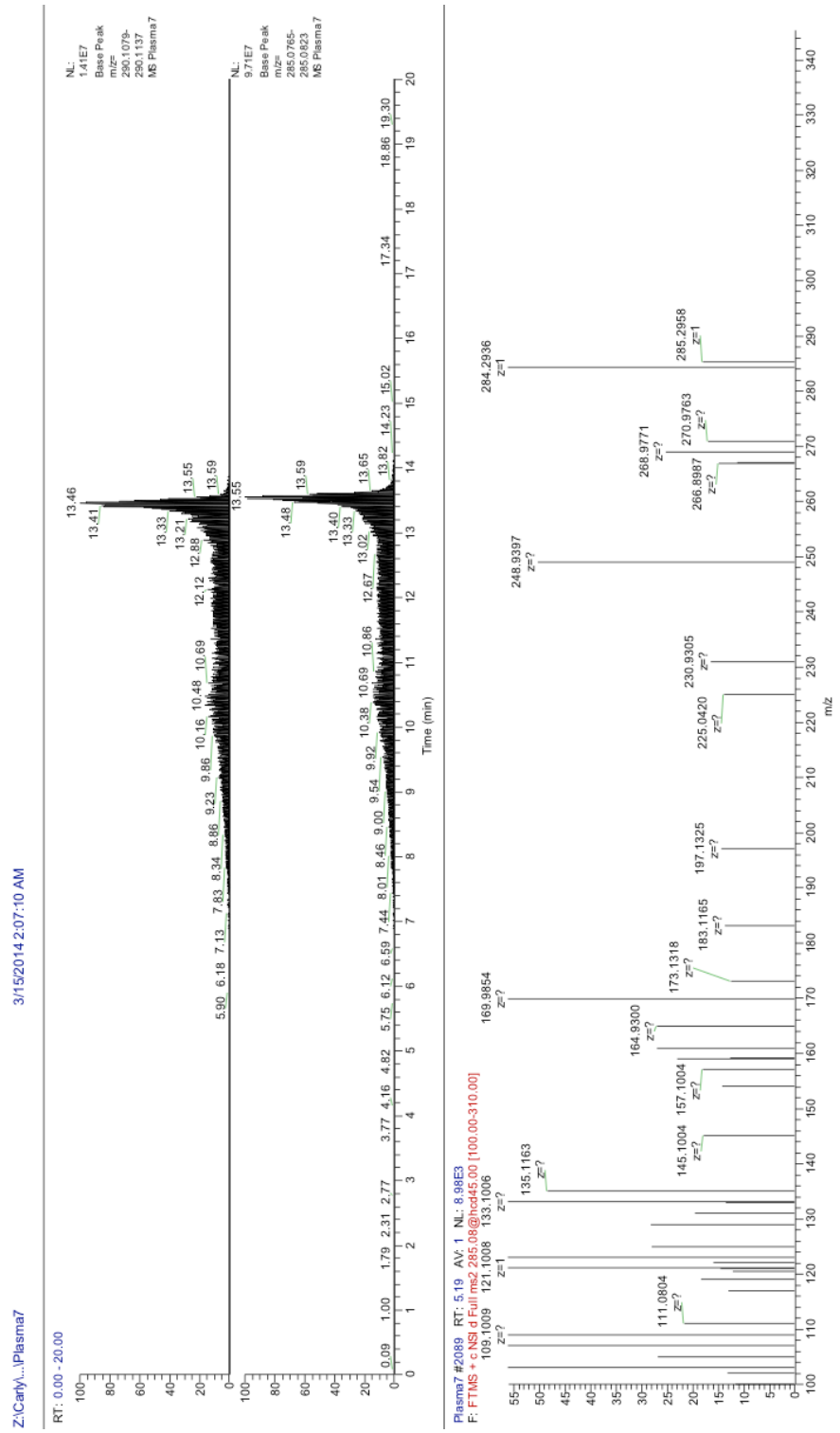

Figure 27. Diazepam was detected in extracted serum from a minimally perfused diazepam-treated CD1 mouse sacrificed at 0.1 h post-dose. (A) XIC of a d5-diazepam spiked standard. (B) XIC of diazepam. (C) Mass spectrum of diazepam.

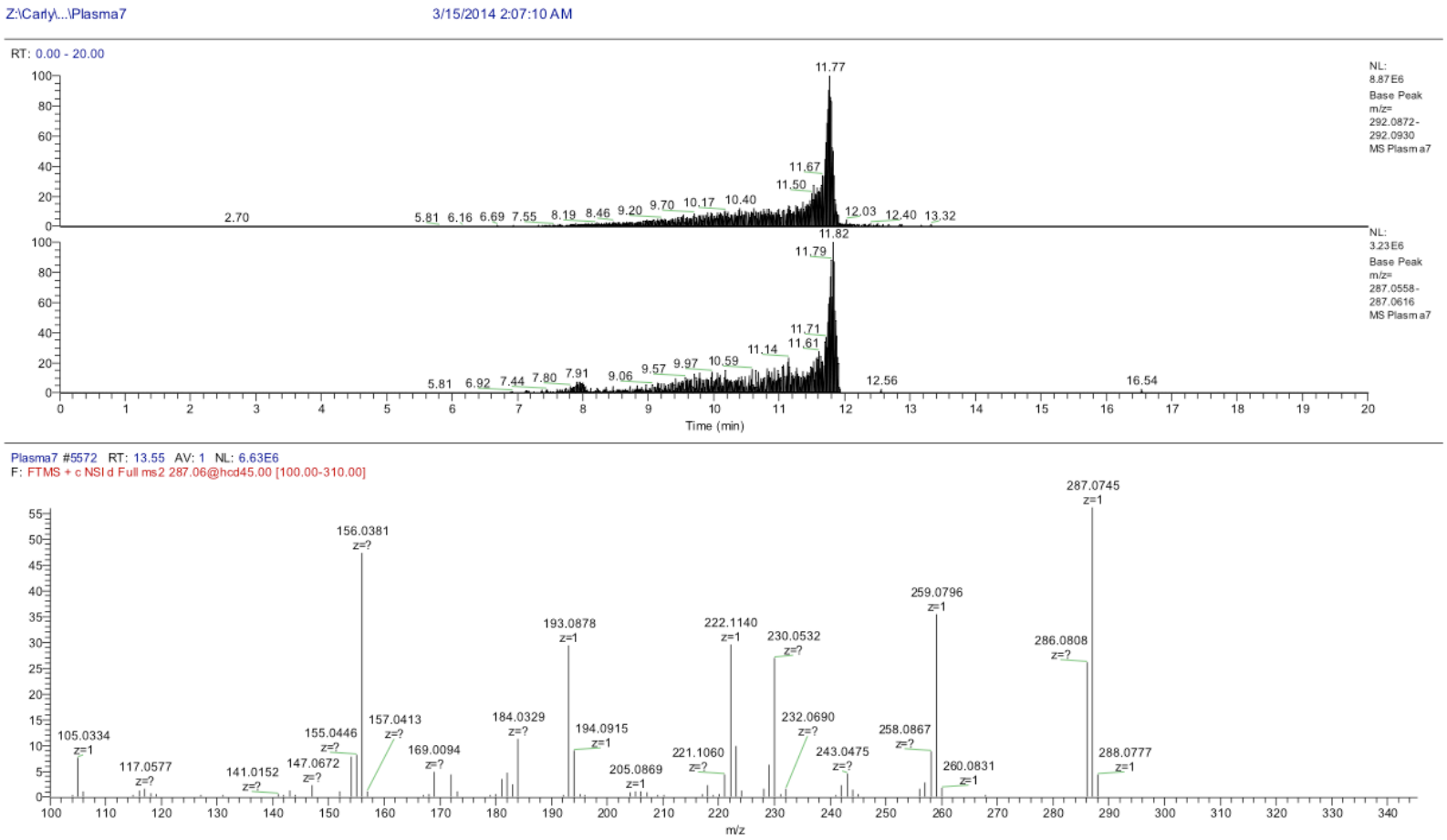
Z:\Carly\...\Plasma7
3/15/2014 2:07:10 AM
RT: 0.00 - 20.00
NL: 8.87E6 Base Peak m/z= 292.0872-292.0930 MS Plasma7
NL: 3.23E6 Base Peak m/z= 287.0558-287.0616 MS Plasma7
Time (min)
Plasma7 #5572 RT: 13.55 AV: 1 NL: 6.63E6
F: FTMS + c NSI d Full ms2 287.06@hcd45.00 [100.00-310.00]
m/z

Figure 28. Oxazepam was detected in extracted serum from a minimally perfused diazepam-treated CD1 mouse sacrificed at 0.1 h post-dose. (A) XIC of a d5-oxazepam spiked standard. (B) XIC of oxazepam. (C) Mass spectrum of oxazepam.

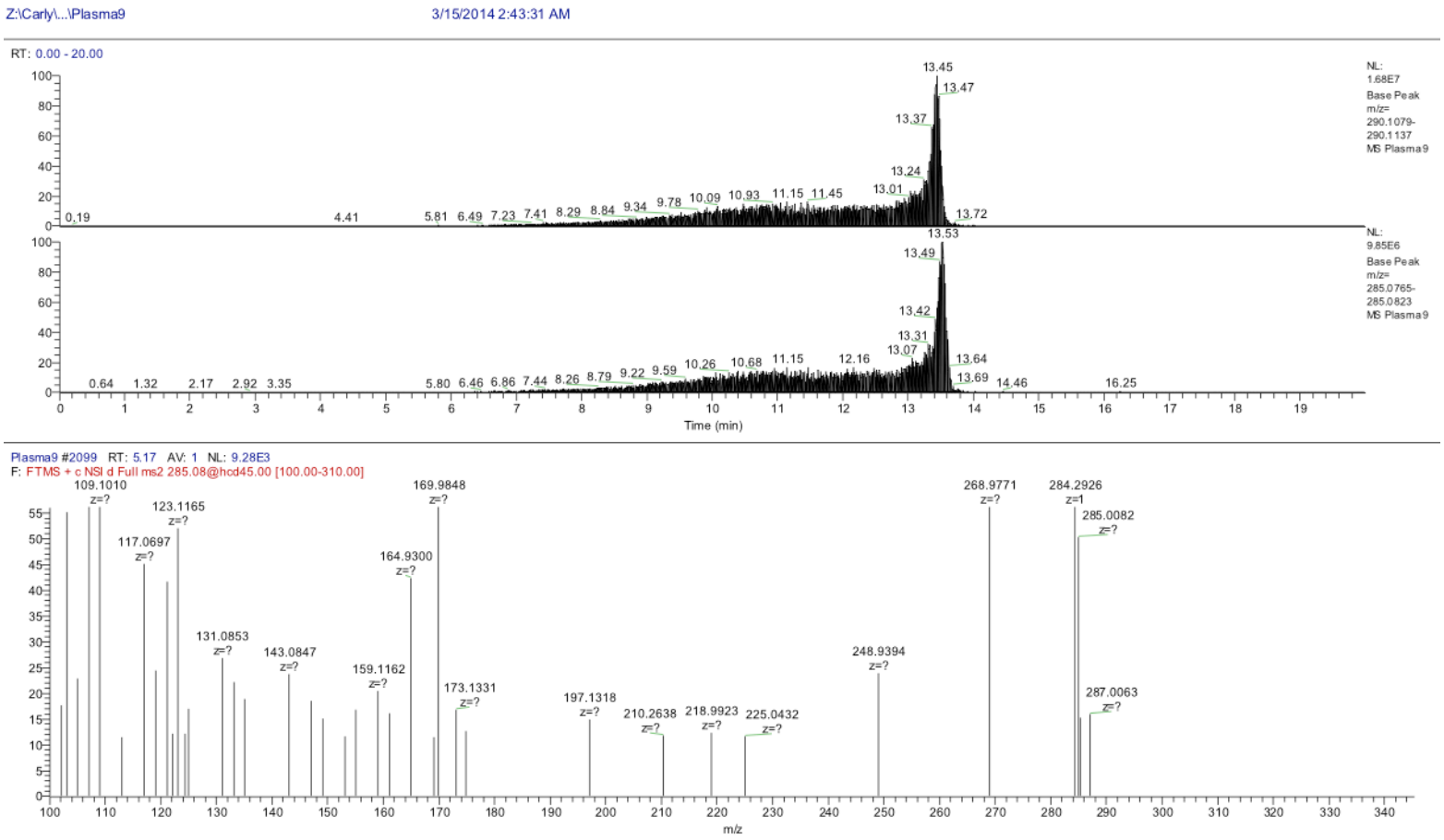
Z:\Carly\...\Plasma9
3/15/2014 2:43:31 AM
RT: 0.00 - 20.00
NL: 1.68E7 Base Peak m/z= 290.1079-290.1137 MS Plasma9
NL: 9.85E6 Base Peak m/z= 285.0765-285.0823 MS Plasma9
Time (min)
Plasma9 #2099 RT: 5.17 AV: 1 NL: 9.28E3
F: FTMS + c NSI d Full ms2 285.08@hcd45.00 [100.00-310.00]
m/z

Figure 29. Diazepam was detected in extracted serum from a minimally perfused diazepam-treated CD1 mouse sacrificed at 1 h post-dose. (A) XIC of a d5-diazepam spiked standard. (B) XIC of diazepam. (C) Mass spectrum of diazepam.

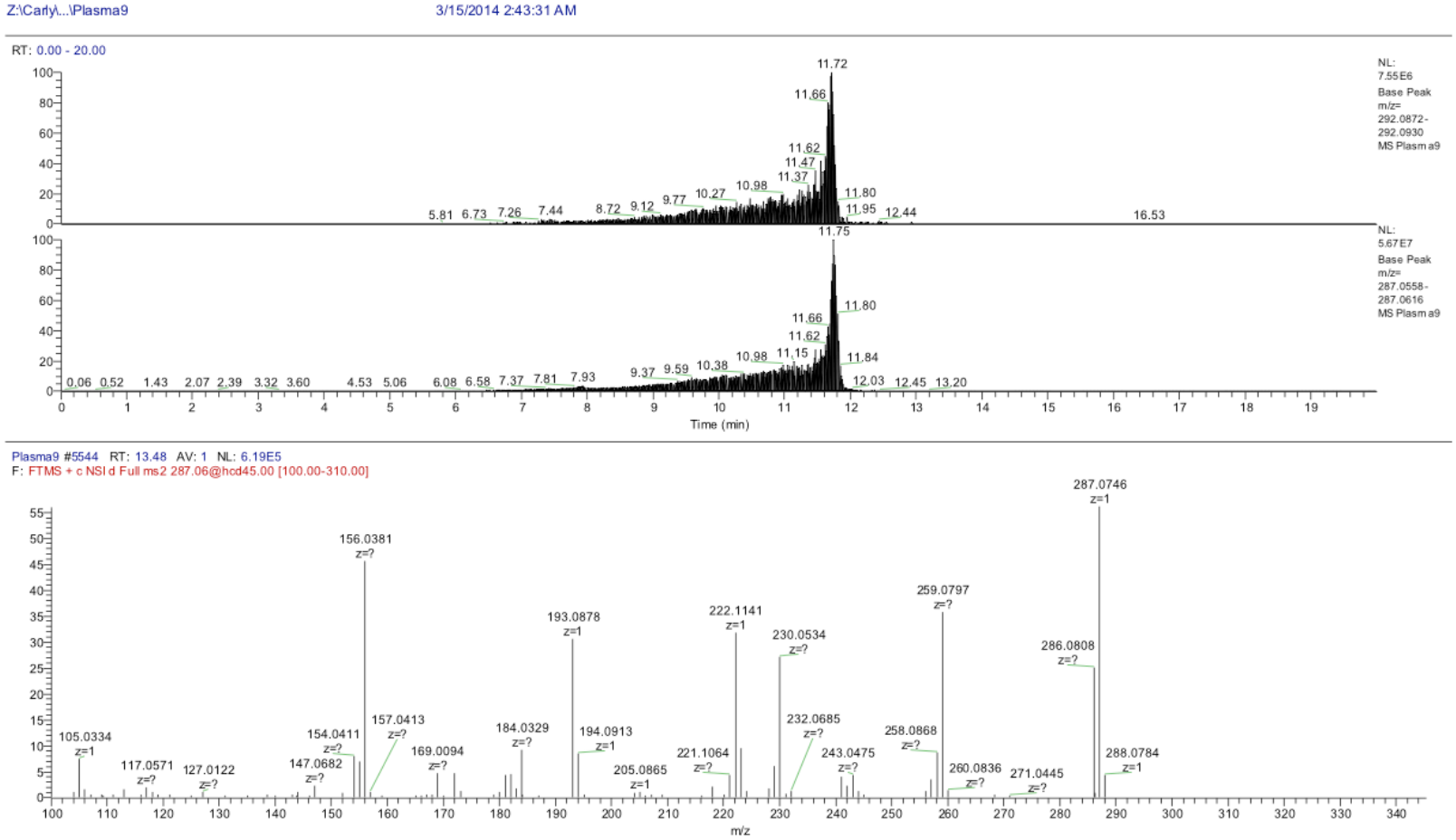
Z:\Carly\...\Plasma9
3/15/2014 2:43:31 AM
RT: 0.00 - 20.00
NL: 7.55E6 Base Peak m/z= 292.0872-292.0930 MS Plasma9
NL: 5.67E7 Base Peak m/z= 287.0558-287.0616 MS Plasma9
Time (min)
Plasma9 #5544 RT: 13.48 AV: 1 NL: 6.19E5
F: FTMS + c NSI d Full ms2 287.06@hcd45.00 [100.00-310.00]
m/z

Figure 30. Oxazepam was detected in extracted serum from a minimally perfused diazepam-treated CD1 mouse sacrificed at 1 h post-dose. (A) XIC of a d5-oxazepam spiked standard. (B) XIC of oxazepam. (C) Mass spectrum of oxazepam.

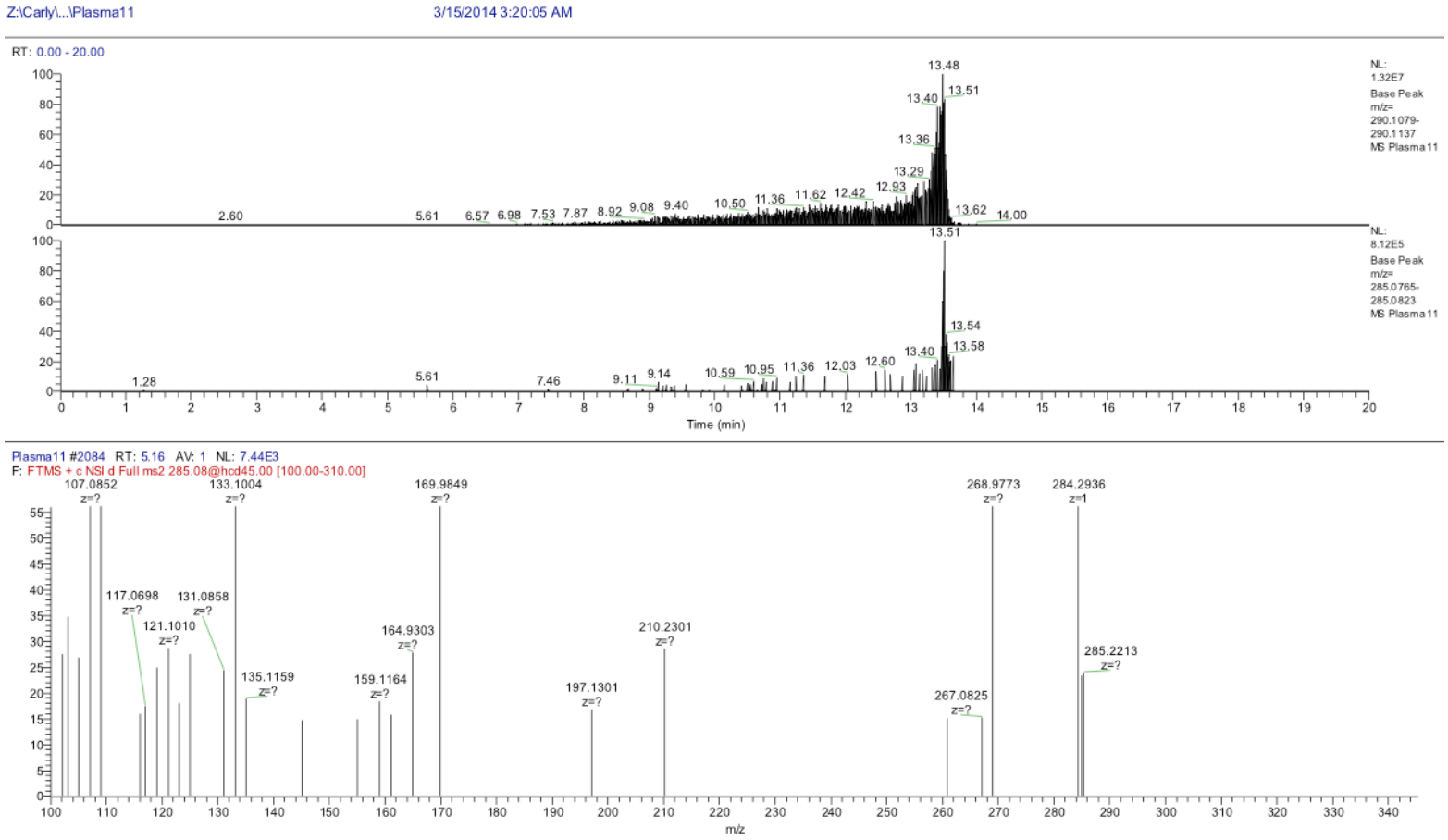
Z:\Carly\...\Plasma11
3/15/2014 3:20:05 AM
RT: 0.00 - 20.00
NL: 1.32E7 Base Peak m/z= 290.1079-290.1137 MS Plasma11
NL: 8.12E5 Base Peak m/z= 285.0765-285.0823 MS Plasma11
Time (min)
Plasma11 #2084 RT: 5.16 AV: 1 NL: 7.44E3
F: FTMS + c NSI d Full ms2 285.08@hcd45.00 [100.00-310.00]
m/z

Figure 31. Diazepam was detected in extracted serum from a minimally perfused diazepam-treated CD1 mouse sacrificed at 6 h post-dose. (A) XIC of a d5-diazepam spiked standard. (B) XIC of diazepam. (C) Mass spectrum of diazepam.

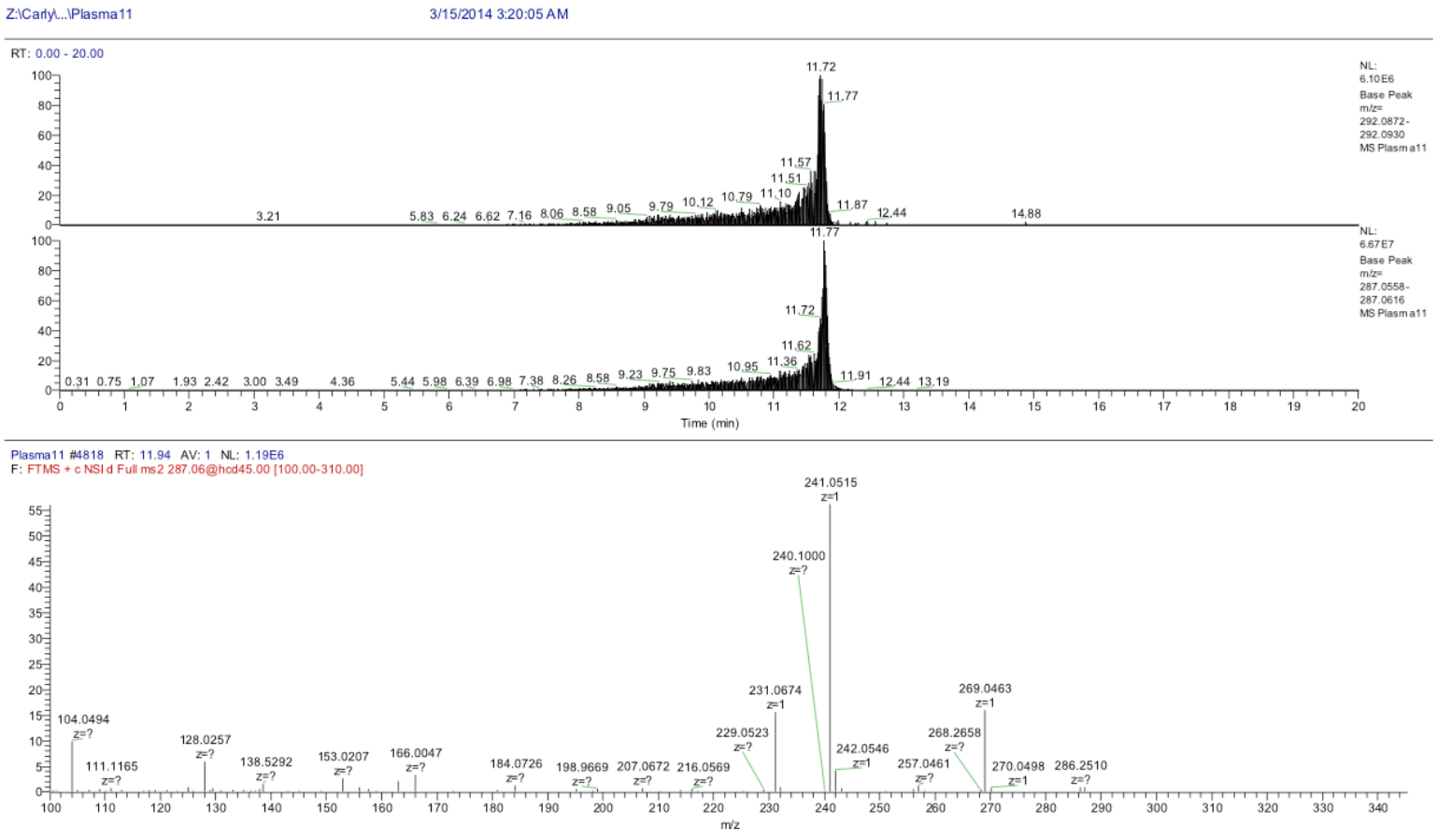
Z:\Carly\...\Plasma11
3/15/2014 3:20:05 AM
RT: 0.00 - 20.00
NL: 6.10E6 Base Peak m/z= 292.0872-292.0930 MS Plasma11
NL: 6.67E7 Base Peak m/z= 287.0558-287.0616 MS Plasma11
Time (min)
Plasma11 #4818 RT: 11.94 AV: 1 NL: 1.19E6
F: FTMS + c NSI d Full ms2 287.06@hcd45.00 [100.00-310.00]
m/z

Figure 32. Oxazepam was detected in extracted serum from a minimally perfused diazepam-treated CD1 mouse sacrificed at 1 h post-dose. (A) XIC of a d5-oxazepam spiked standard. (B) XIC of oxazepam. (C) Mass spectrum of oxazepam.

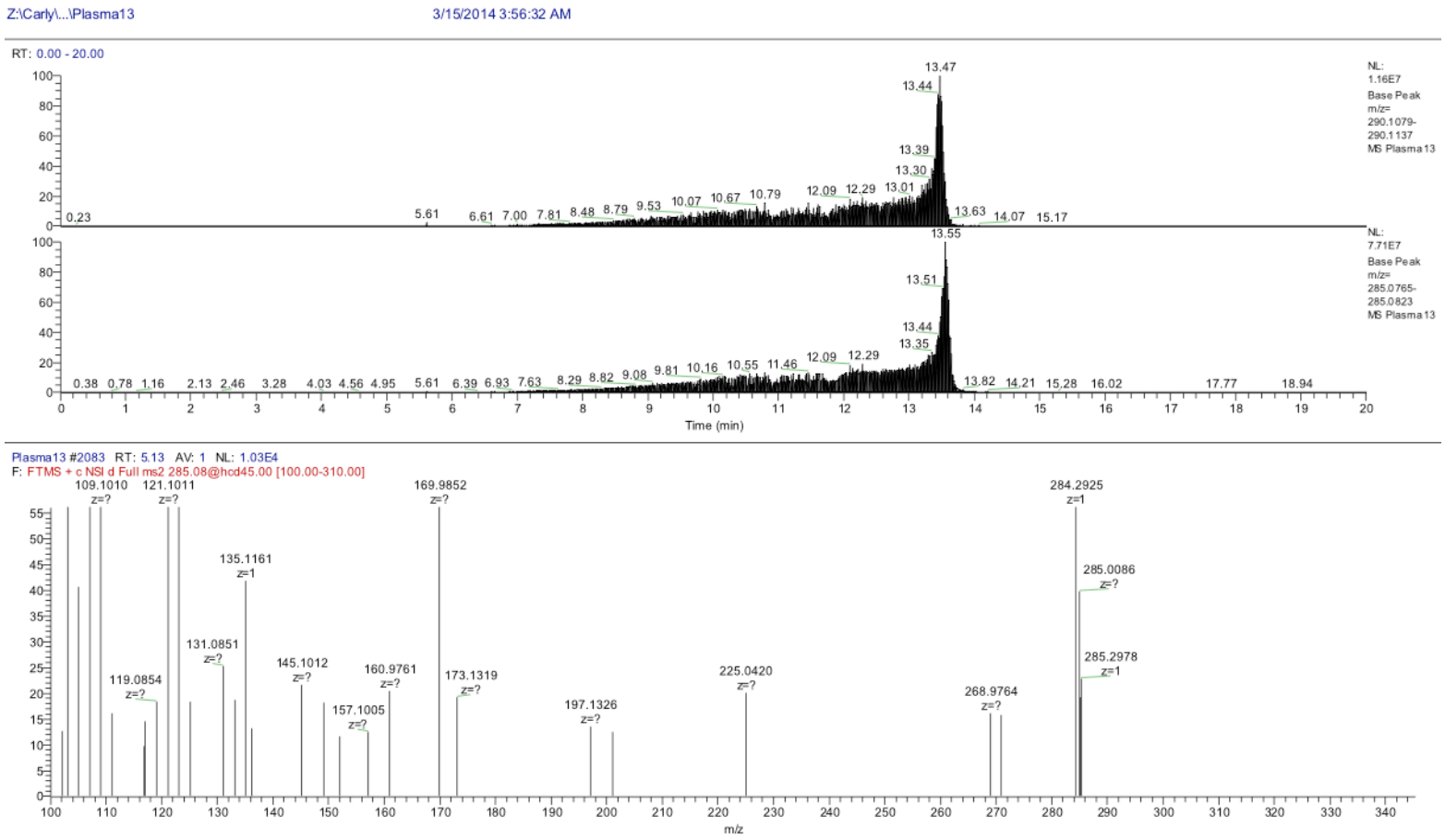
Z:\Carly\...\Plasma13
3/15/2014 3:56:32 AM
RT: 0.00 - 20.00
NL: 1.16E7 Base Peak m/z= 290.1079-290.1137 MS Plasma13
NL: 7.71E7 Base Peak m/z= 285.0765-285.0823 MS Plasma13
Time (min)
Plasma13 #2083 RT: 5.13 AV: 1 NL: 1.03E4
F: FTMS + c NSI d Full ms2 285.08@hcd45.00 [100.00-310.00]
109.1010 z=?
121.1011 z=?
169.9852 z=?
284.2925 z=1
135.1161 z=1
285.0086 z=?
131.0851 z=?
285.2978 z=1
145.1012 z=?
160.9761 z=?
119.0854 z=?
173.1319 z=?
225.0420 z=?
157.1005 z=?
197.1326 z=?
268.9764 z=?
m/z

Figure 33. Diazepam was detected in extracted serum from a lightly exsanguinated (via cardiocentesis) diazepam-treated CD1 mouse sacrificed at 0.1 h post-dose. (A) XIC of a d5-diazepam spiked standard. (B) XIC of diazepam. (C) Mass spectrum of diazepam.

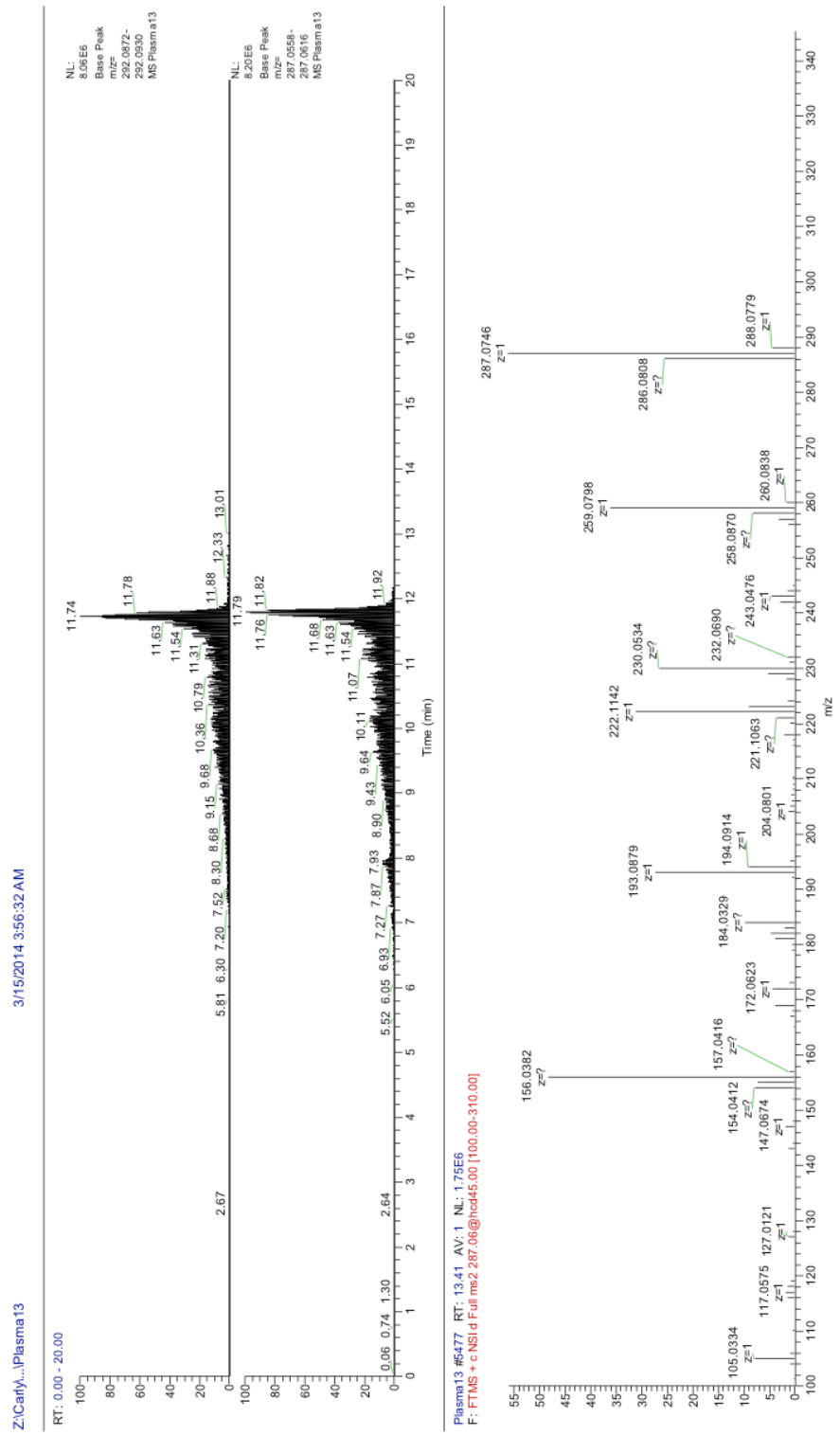

Figure 34. Oxazepam was detected in extracted serum from a lightly exsanguinated (via cardiocentesis) diazepam-treated CD1 mouse sacrificed at 0.1 h post-dose. (A) XIC

of a d5-oxazepam spiked standard. (B) XIC of oxazepam. (C) Mass spectrum of oxazepam.

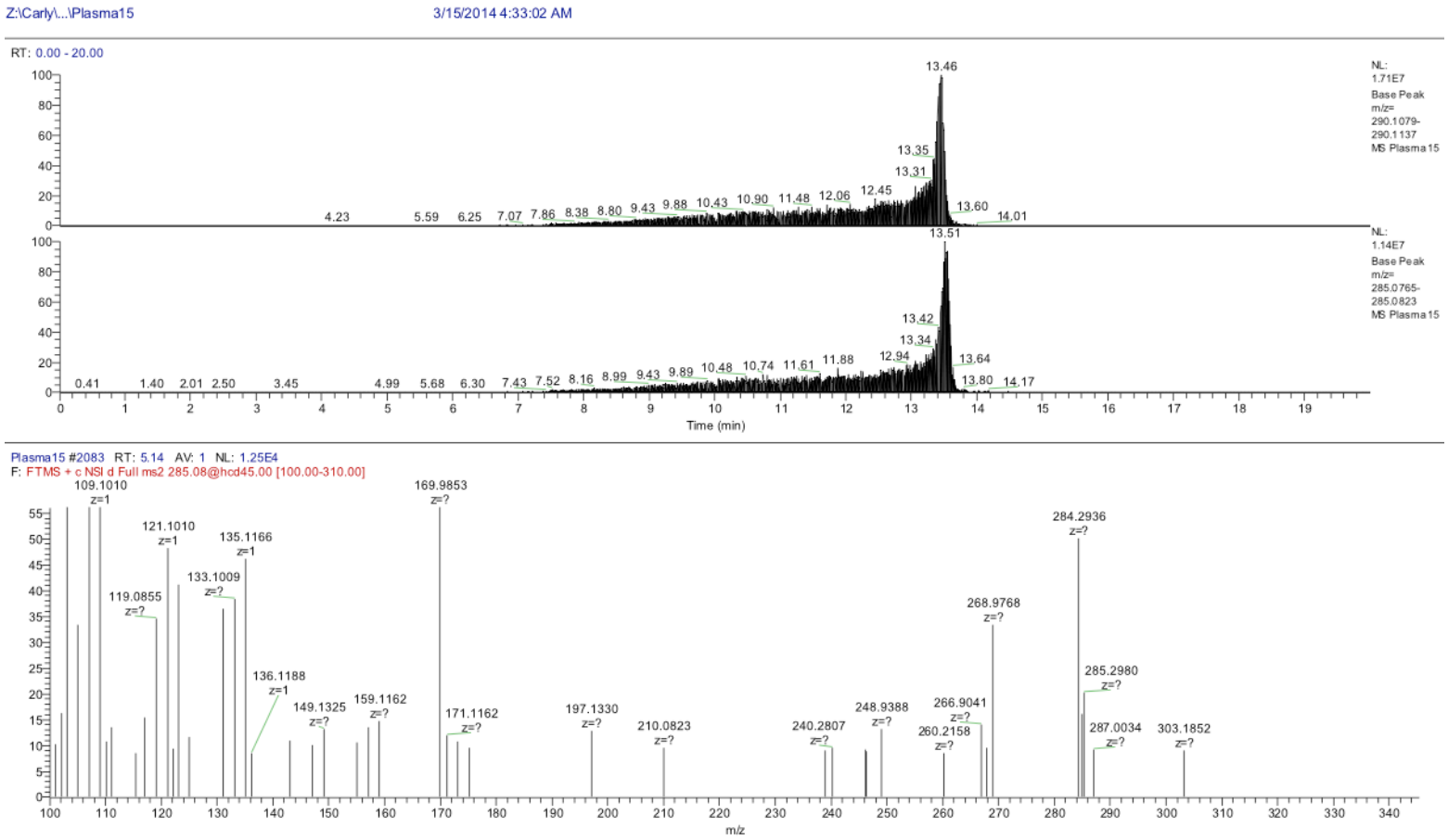
Z:\Carly\...\Plasma15
3/15/2014 4:33:02 AM
RT: 0.00 - 20.00
NL: 1.71E7 Base Peak m/z= 290.1079-290.1137 MS Plasma15
NL: 1.14E7 Base Peak m/z= 285.0765-285.0823 MS Plasma15
Time (min)
Plasma15 #2083 RT: 5.14 AV: 1 NL: 1.25E4
F: FTMS + c NSI d Full ms2 285.08@hcd45.00 [100.00-310.00]
m/z

Figure 35. Diazepam was detected in extracted serum from a lightly exsanguinated (via cardiocentesis) diazepam-treated CD1 mouse sacrificed at 1 h post-dose. (A) XIC of a d5-diazepam spiked standard. (B) XIC of diazepam. (C) Mass spectrum of diazepam.

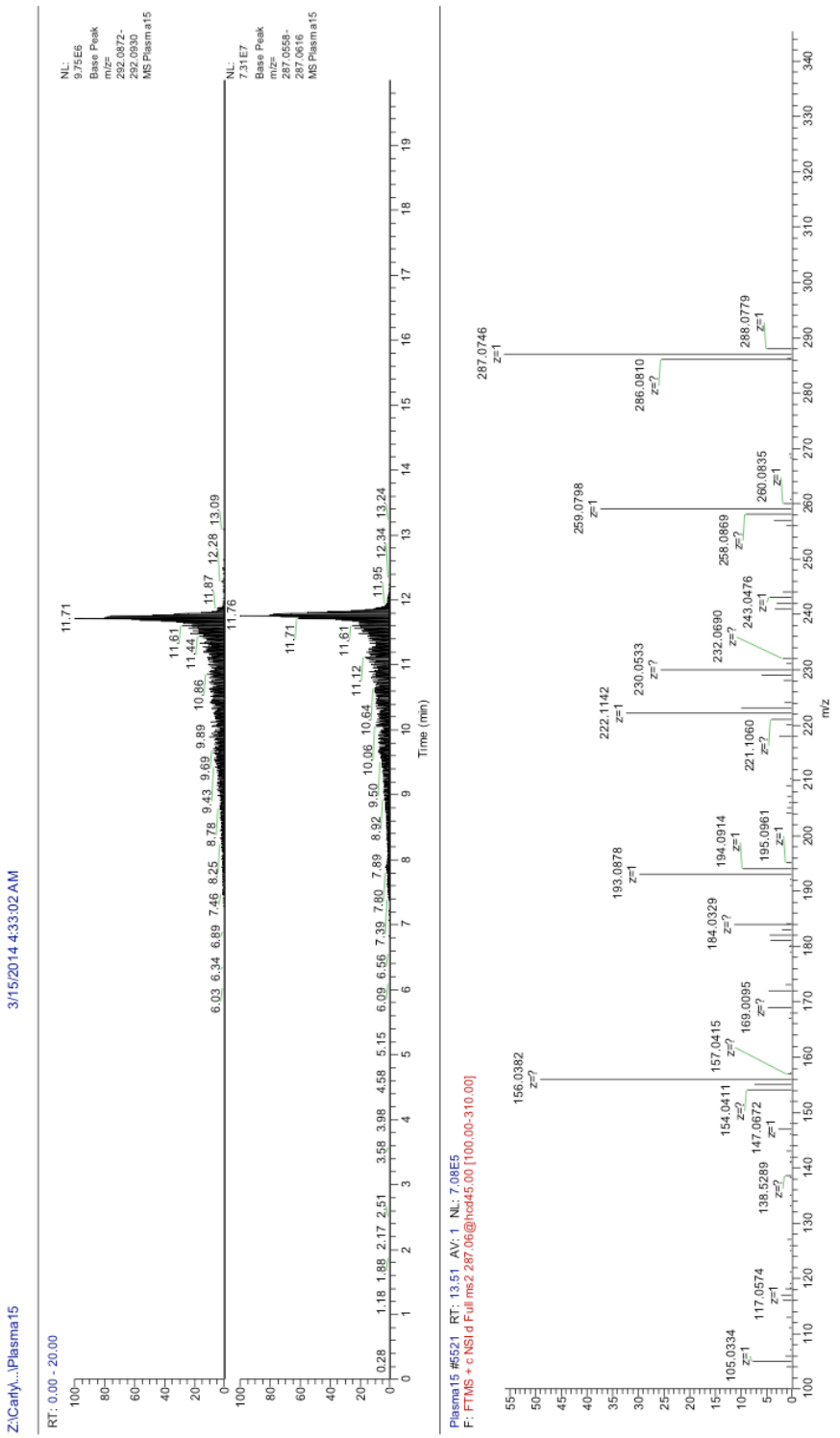

Figure 36. Oxazepam was detected in extracted serum from a lightly exsanguinated (via cardiocentesis) diazepam-treated CD1 mouse sacrificed at 1 h post-dose. (A) XIC

of a d5-oxazepam spiked standard. (B) XIC of oxazepam. (C) Mass spectrum of oxazepam.

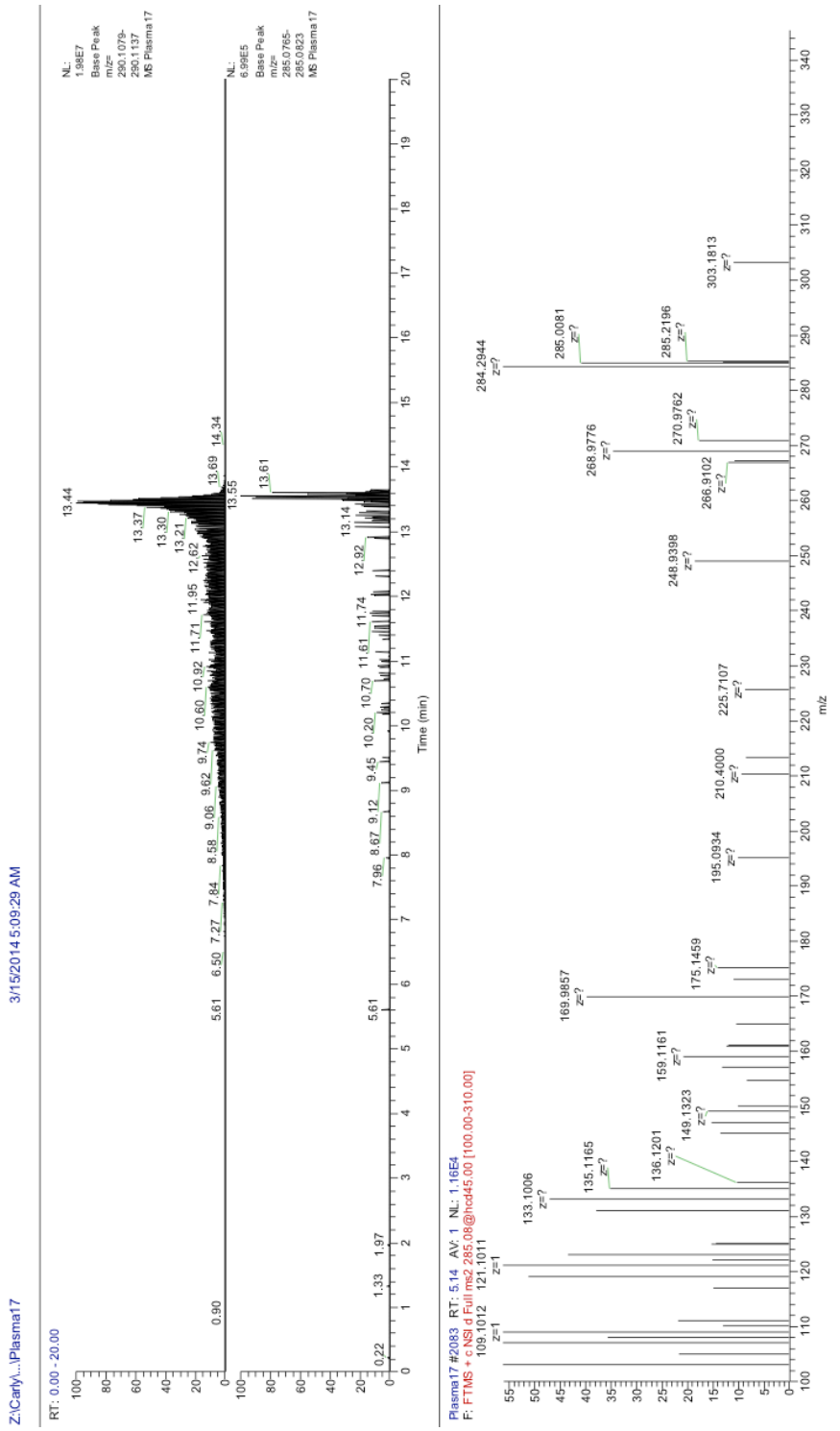

Figure 37. Diazepam was detected in extracted serum from a lightly exsanguinated (via cardiocentesis) diazepam-treated CD1 mouse sacrificed at 6 h post-dose. (A) XIC of a d5-diazepam spiked standard. (B) XIC of diazepam. (C) Mass spectrum of diazepam.

Z:\Carly\...\Plasma17 3/15/2014 5:09:29 AM

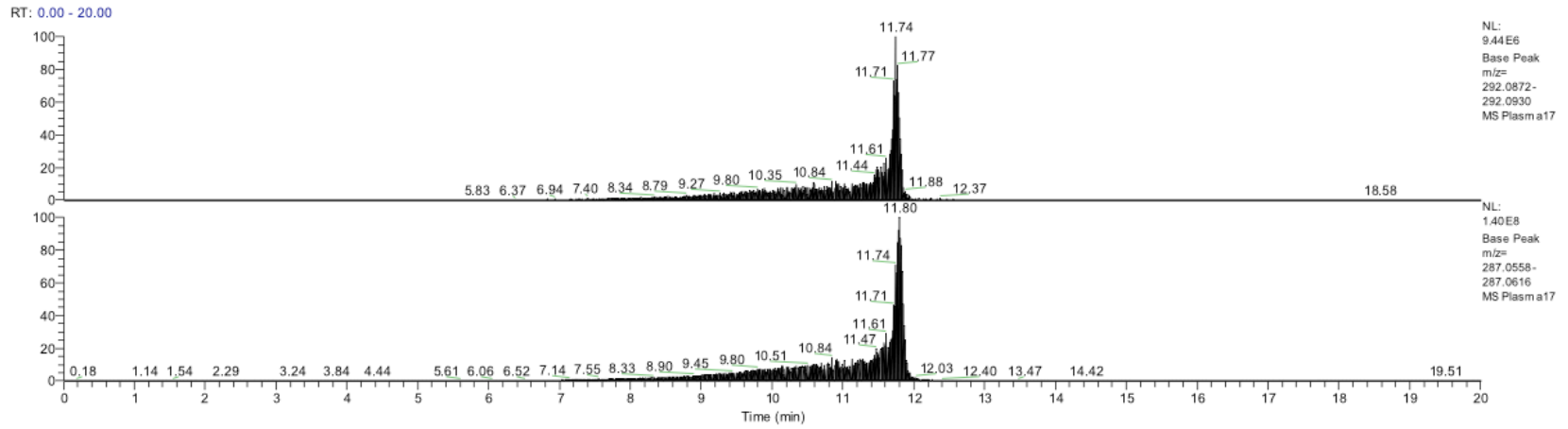

Plasma17 #4750 RT: 11.73 AV: 1 NL: 3.33E7
F: FTMS + c NSI d Full ms2 287.06@hcd45.00 [100.00-310.00]

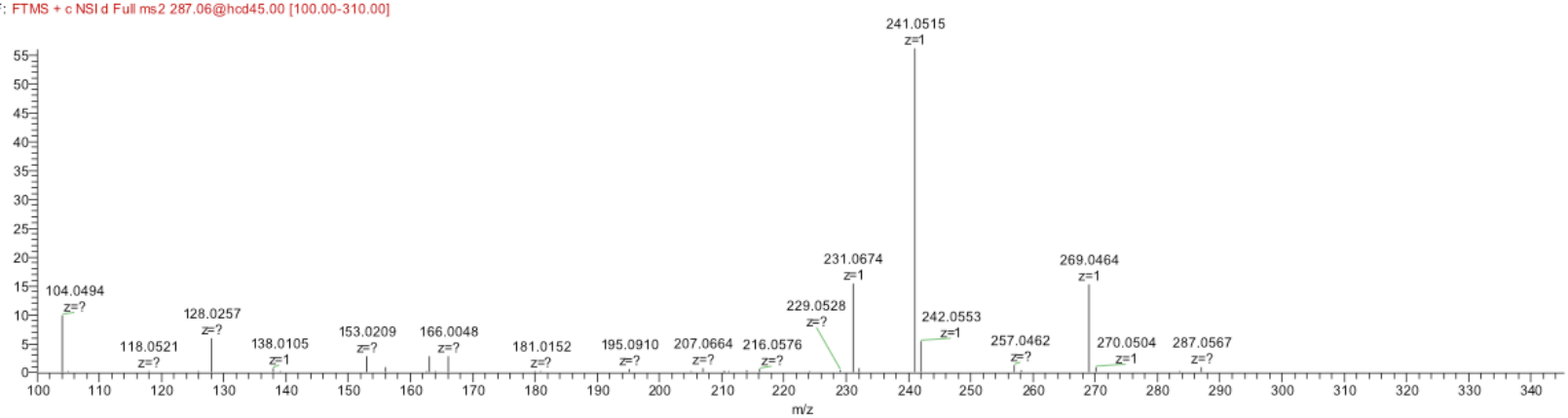

Figure 38. Oxazepam was detected in extracted serum from a lightly exsanguinated (via cardiocentesis) diazepam-treated CD1 mouse sacrificed at 6 h post-dose. (A) XIC of a d5-oxazepam spiked standard. (B) XIC of oxazepam. (C) Mass spectrum of oxazepam.

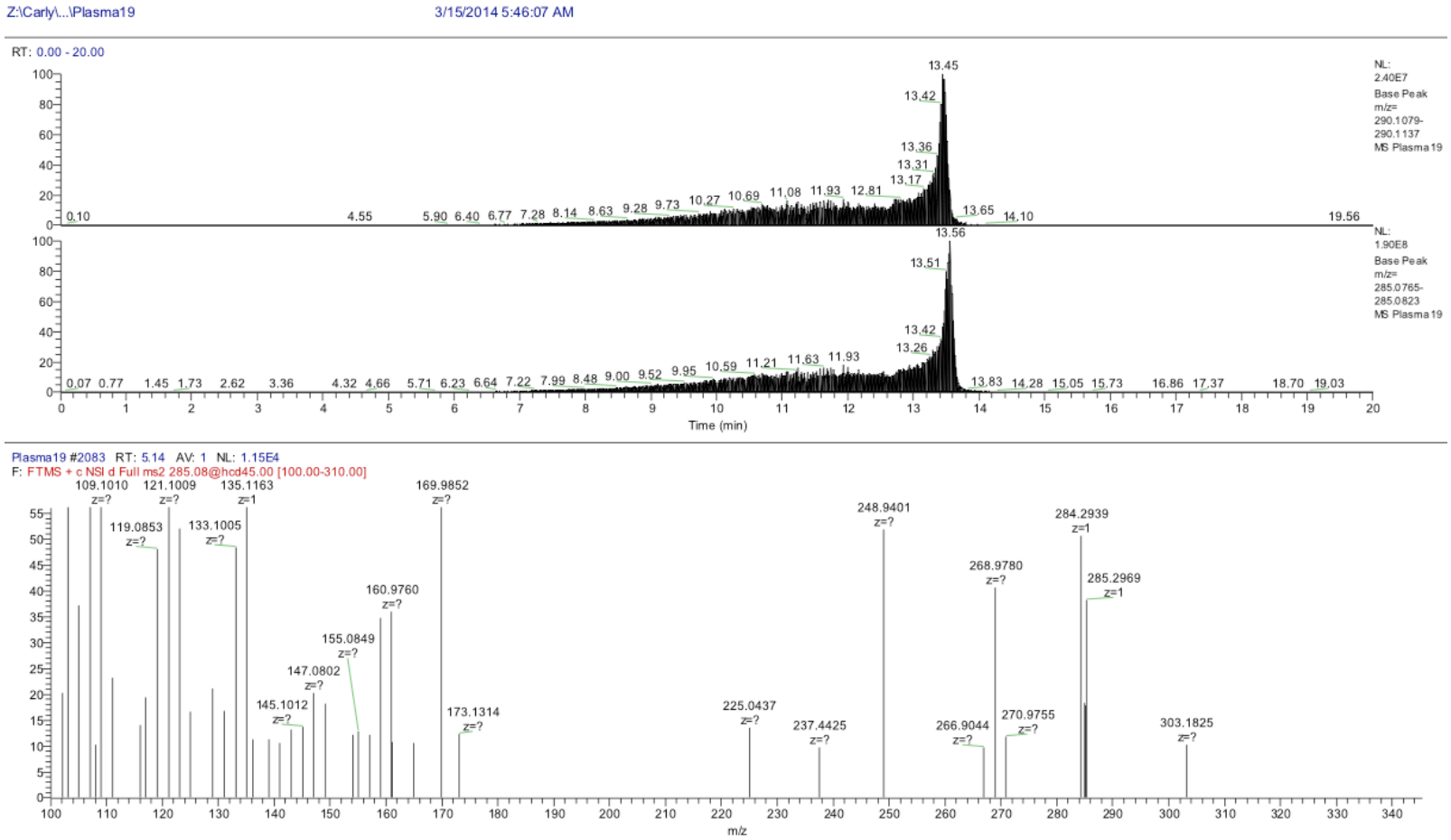
Z:\Carly\...\Plasma19
3/15/2014 5:46:07 AM
RT: 0.00 - 20.00
NL: 2.40E7 Base Peak m/z= 290.1079-290.1137 MS Plasma19
NL: 1.90E8 Base Peak m/z= 285.0765-285.0823 MS Plasma19
Time (min)
Plasma19 #2083 RT: 5.14 AV: 1 NL: 1.15E4
F: FTMS + c NSI d Full ms2 285.08@hcd45.00 [100.00-310.00]
m/z

Figure 39. Diazepam was detected in extracted serum from a transcardially perfused diazepam-treated CD1 mouse sacrificed at 0.1 h post-dose. (A) XIC of a d5-diazepam spiked standard. (B) XIC of diazepam. (C) Mass spectrum of diazepam.

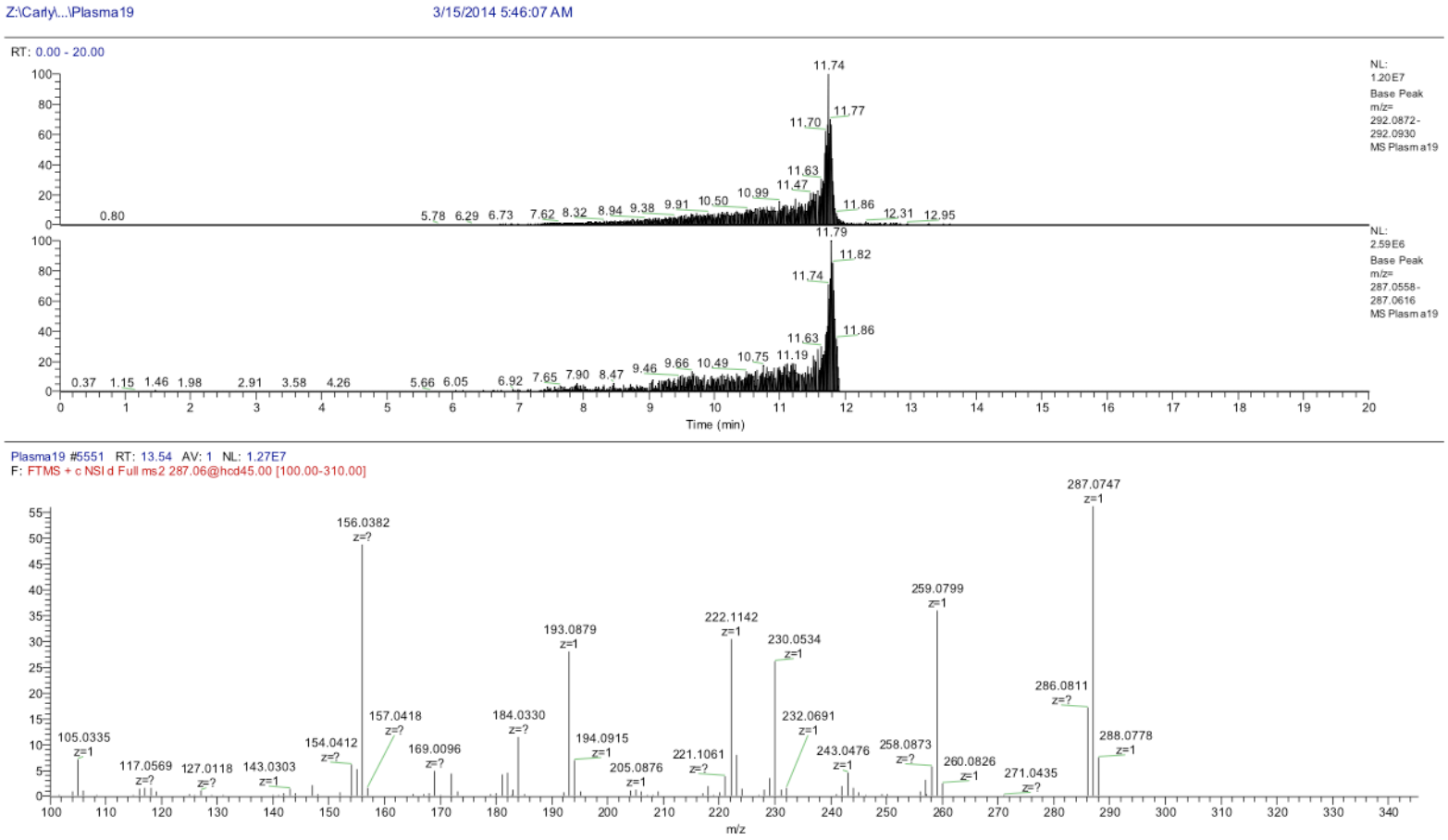
Z:\Carly\...\Plasma19
3/15/2014 5:46:07 AM
RT: 0.00 - 20.00
NL: 1.20E7
Base Peak m/z= 292.0872-292.0930 MS Plasma19
NL: 2.59E6
Base Peak m/z= 287.0558-287.0616 MS Plasma19
Time (min)
Plasma19 #5551 RT: 13.54 AV: 1 NL: 1.27E7
F: FTMS + c NSI d Full ms2 287.06@hcd45.00 [100.00-310.00]
m/z

Figure 40. Oxazepam was detected in extracted serum from a transcardially perfused diazepam-treated CD1 mouse sacrificed at 0.1 h post-dose. (A) XIC of a d5-oxazepam spiked standard. (B) XIC of oxazepam. (C) Mass spectrum of oxazepam.

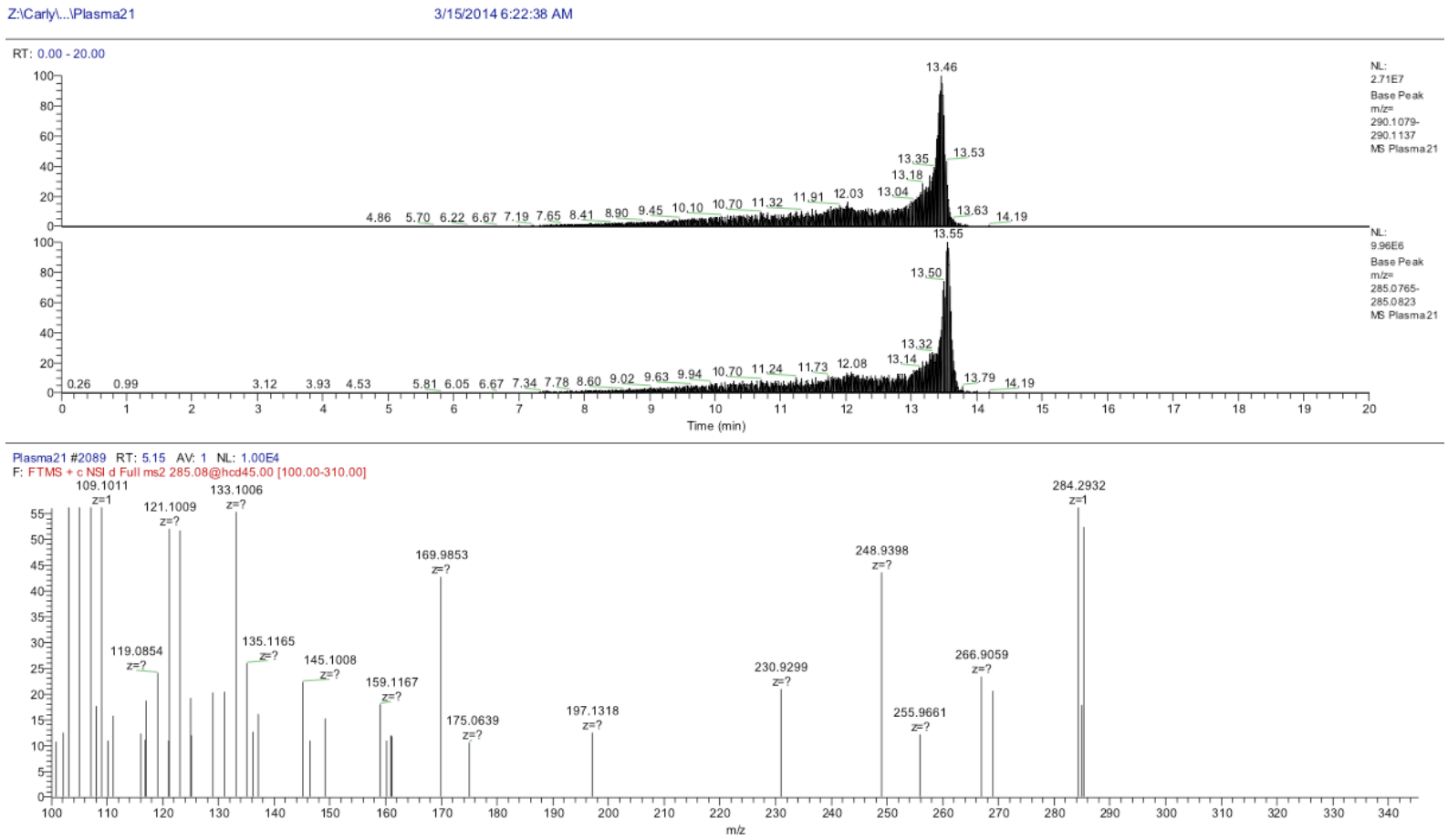
Z:\Carly\...\Plasma21
3/15/2014 6:22:38 AM
RT: 0.00 - 20.00
NL: 2.71E7 Base Peak m/z= 290.1079-290.1137 MS Plasma21
NL: 9.96E6 Base Peak m/z= 285.0765-285.0823 MS Plasma21
Time (min)
Plasma21 #2089 RT: 5.15 AV: 1 NL: 1.00E4
F: FTMS + c NSI d Full ms2 285.08@hcd45.00 [100.00-310.00]
m/z

Figure 41. Diazepam was detected in extracted serum from a transcardially perfused diazepam-treated CD1 mouse sacrificed at 1 h post-dose. (A) XIC of a d5-diazepam spiked standard. (B) XIC of diazepam. (C) Mass spectrum of diazepam.

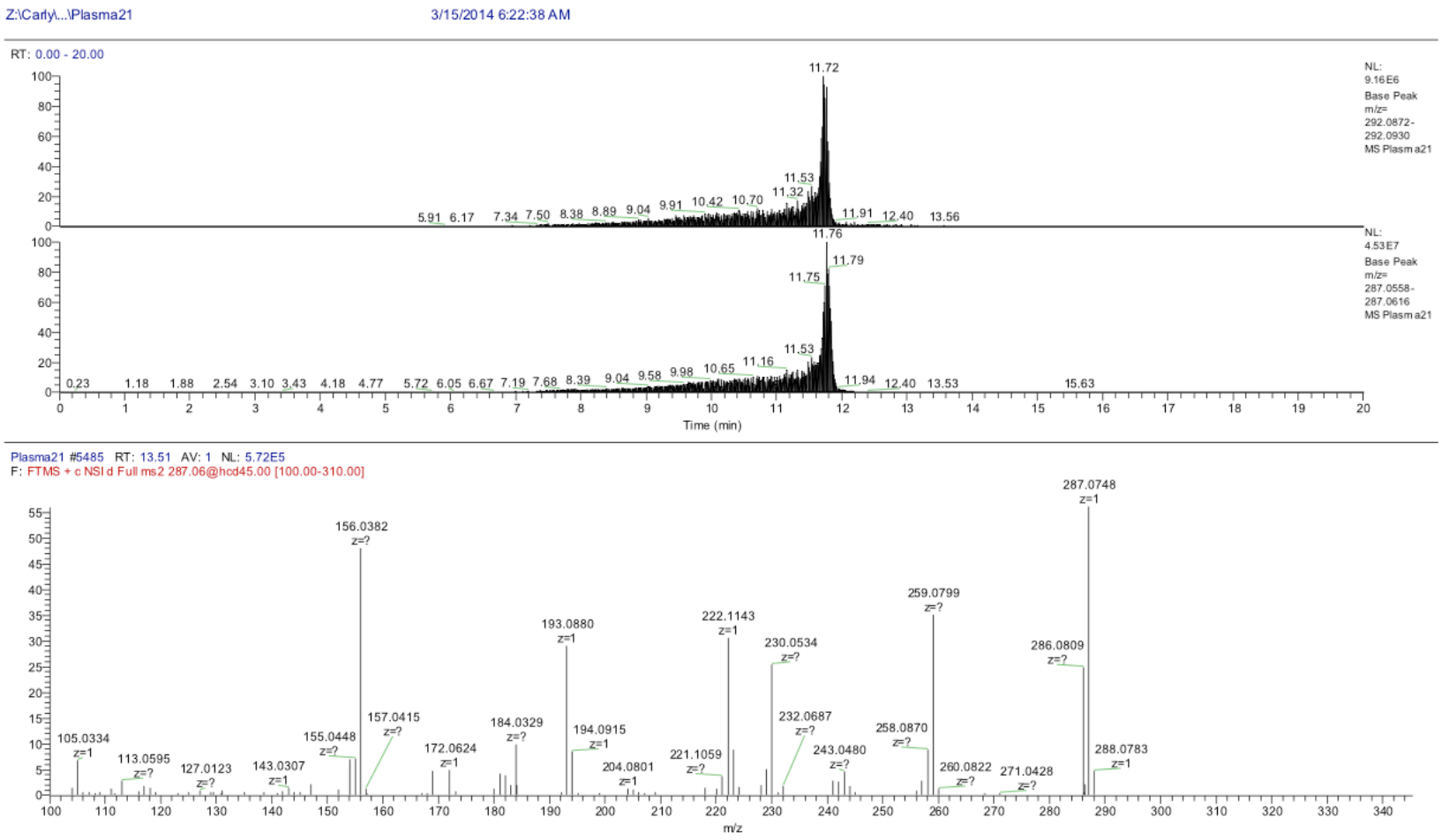
Z:\Carly\...\Plasma21
3/15/2014 6:22:38 AM
RT: 0.00 - 20.00
NL: 9.16E6 Base Peak m/z= 292.0872-292.0930 MS Plasma21
NL: 4.53E7 Base Peak m/z= 287.0558-287.0616 MS Plasma21
Time (min)
Plasma21 #5485 RT: 13.51 AV: 1 NL: 5.72E5
F: FTMS + c NSI d Full ms2 287.06@hcd45.00 [100.00-310.00]
m/z

Figure 42. Oxazepam was detected in extracted serum from a transcardially perfused diazepam-treated CD1 mouse sacrificed at 1 h post-dose. (A) XIC of a d5-oxazepam spiked standard. (B) XIC of oxazepam. (C) Mass spectrum of oxazepam.

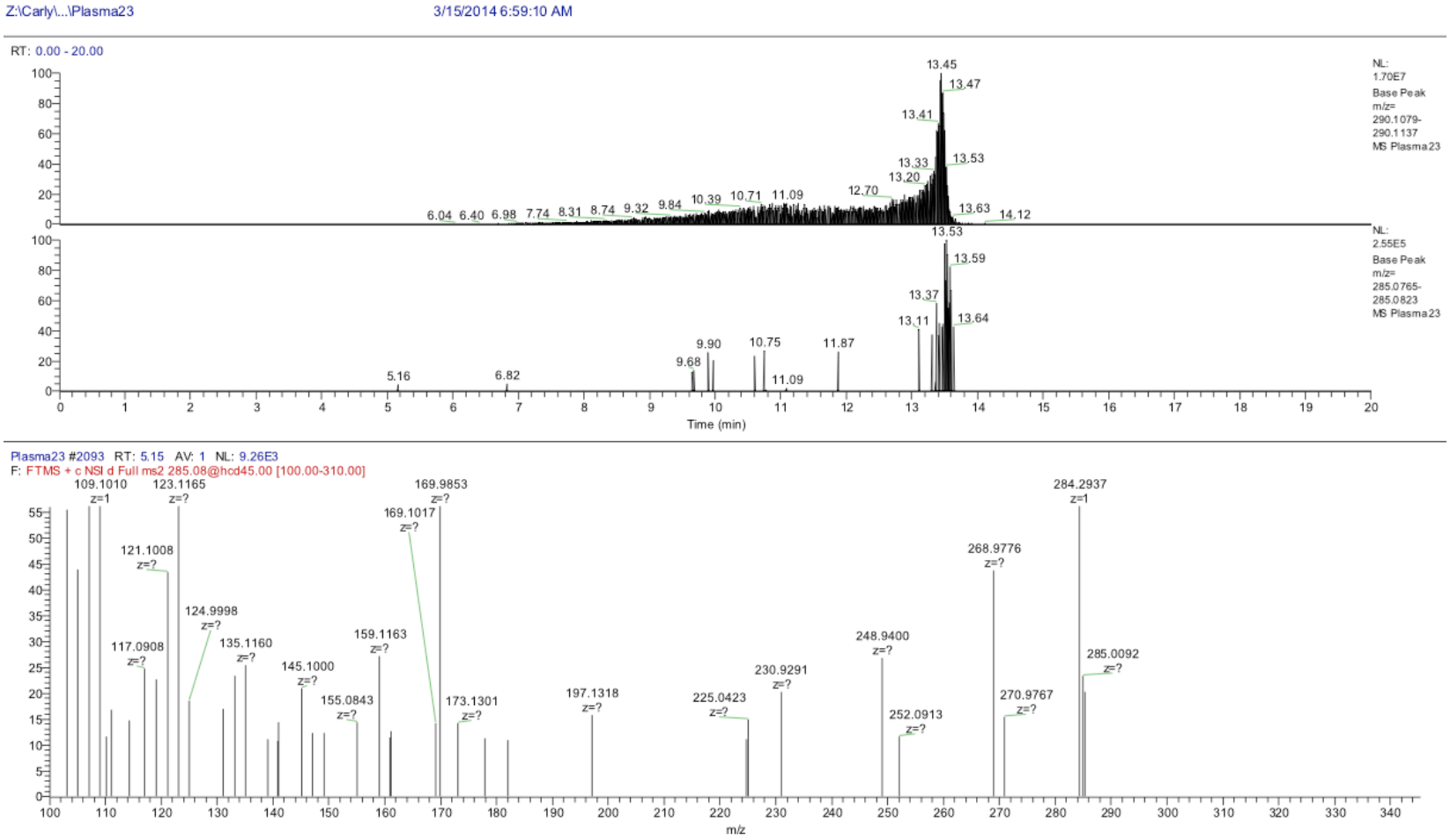
Z:\Carly\...\Plasma23
3/15/2014 6:59:10 AM
RT: 0.00 - 20.00
NL: 1.70E7 Base Peak m/z= 290.1079-290.1137 MS Plasma23
NL: 2.55E5 Base Peak m/z= 285.0765-285.0823 MS Plasma23
Time (min)
Plasma23 #2093 RT: 5.15 AV: 1 NL: 9.26E3
F: FTMS + c NSI d Full ms2 285.08@hcd45.00 [100.00-310.00]
m/z

Figure 43. Diazepam was detected in extracted serum from a transcardially perfused diazepam-treated CD1 mouse sacrificed at 6 h post-dose. (A) XIC of a d5-diazepam spiked standard. (B) XIC of diazepam. (C) Mass spectrum of diazepam.

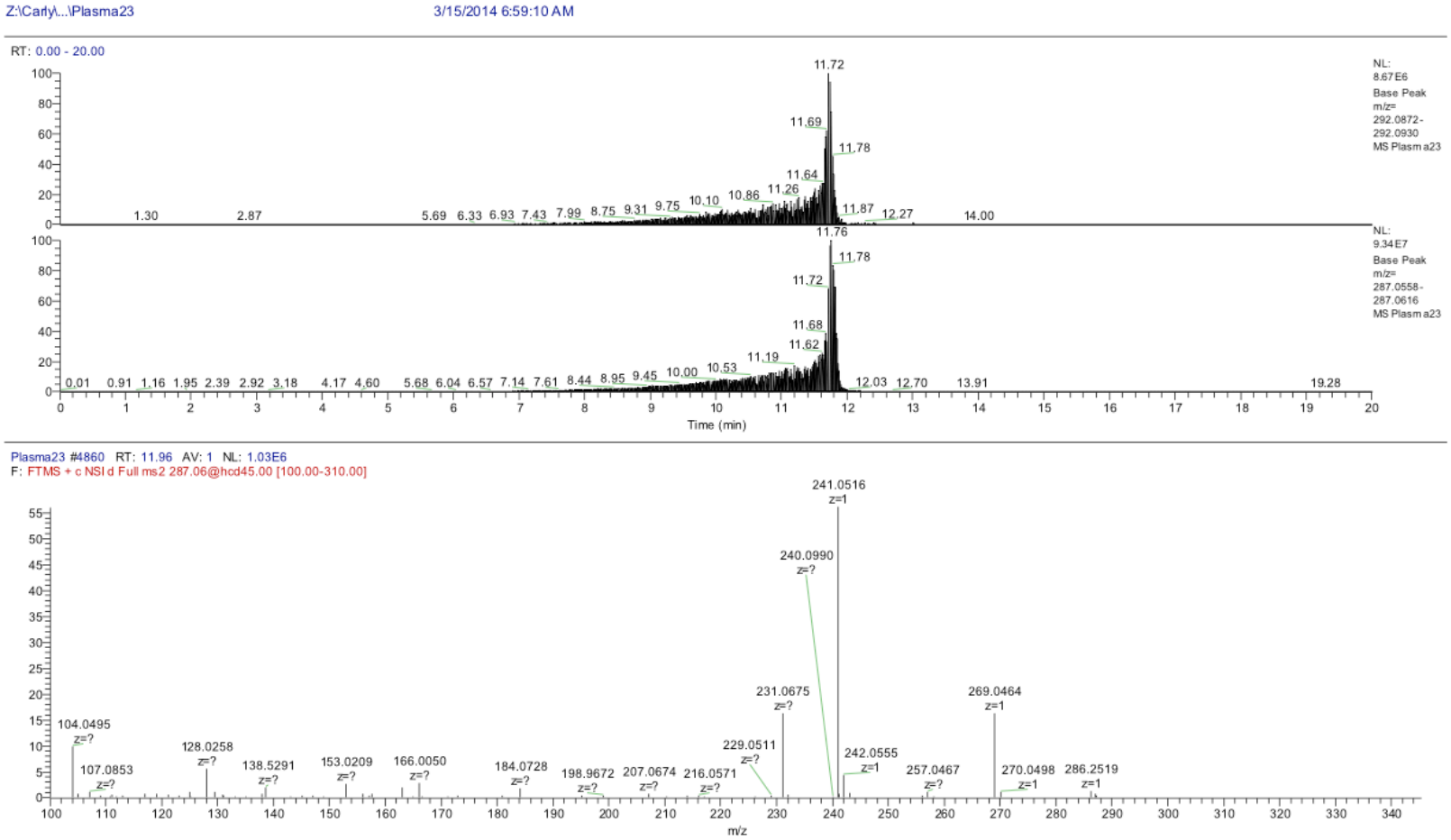
Z:\Carly\...\Plasma23
3/15/2014 6:59:10 AM
RT: 0.00 - 20.00
NL: 8.67E6 Base Peak m/z= 292.0872-292.0930 MS Plasma23
NL: 9.34E7 Base Peak m/z= 287.0558-287.0616 MS Plasma23
Time (min)
Plasma23 #4860 RT: 11.96 AV: 1 NL: 1.03E6
F: FTMS + c NSI d Full ms2 287.06@hcd45.00 [100.00-310.00]
241.0516 z=1
240.0990 z=?
231.0675 z=?
269.0464 z=1
229.0511 z=?
242.0555 z=1
104.0495 z=?
128.0258 z=?
107.0853 z=?
138.5291 z=?
153.0209 z=?
166.0050 z=?
184.0728 z=?
198.9672 z=?
207.0674 z=?
216.0571 z=?
257.0467 z=?
270.0498 z=1
286.2519 z=1
m/z

Figure 44. Oxazepam was detected in extracted serum from a transcardially perfused diazepam-treated CD1 mouse sacrificed at 6 h post-dose. (A) XIC of a d5-oxazepam spiked standard. (B) XIC of oxazepam. (C) Mass spectrum of oxazepam.

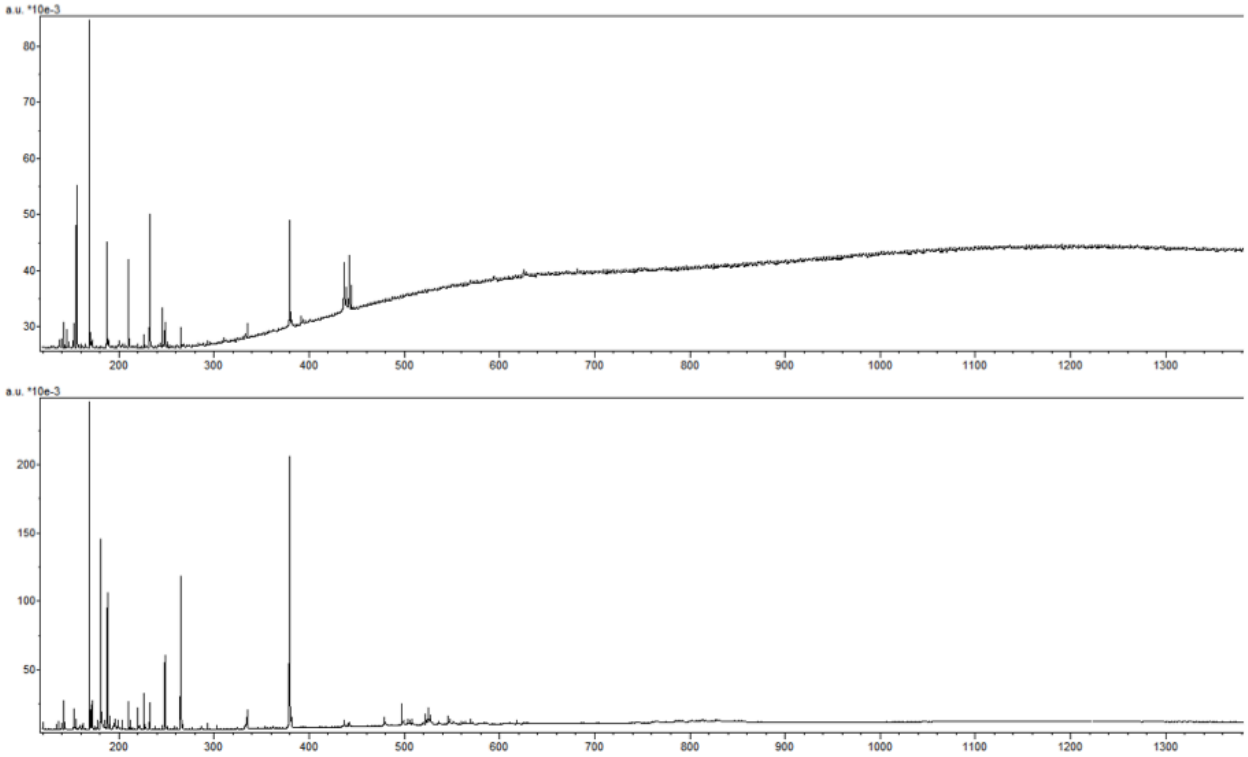

Figure 45. In general, a 30 s 70% ethanol wash lowered the baseline rise observed in a liver tissue imaging experiments. (A) Shows the average spectrum for a given tissue section prior to washing. (B) Shows the average spectrum for the same given tissue section post-washing.

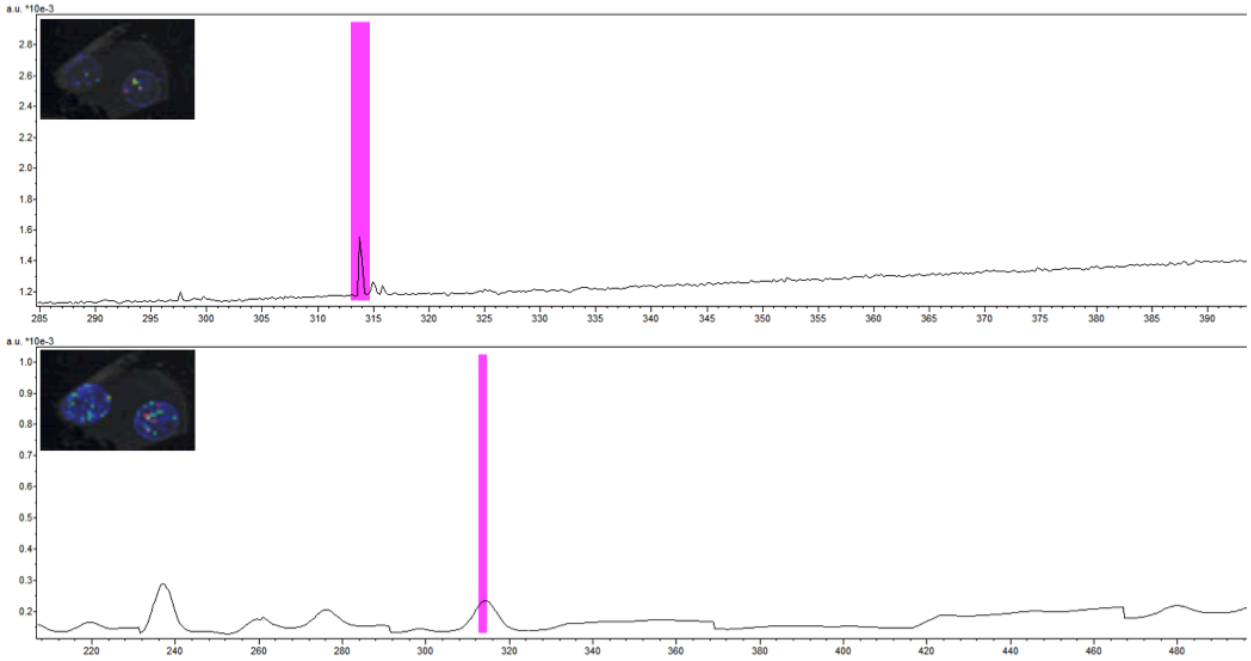

Figure 46. BZ16 was spotted onto a control brain tissue section, with no matrix added, and imaged prior to washing, and after washing for 30 s with 70% ethanol. Differences in mass accuracy were miniscule, though washing enhanced the signal intensity and detection capabilities with no delocalization. (A) Shows the average spectrum and image for an unwashed tissue section. (B) Shows the average spectrum and image for a washed tissue section.

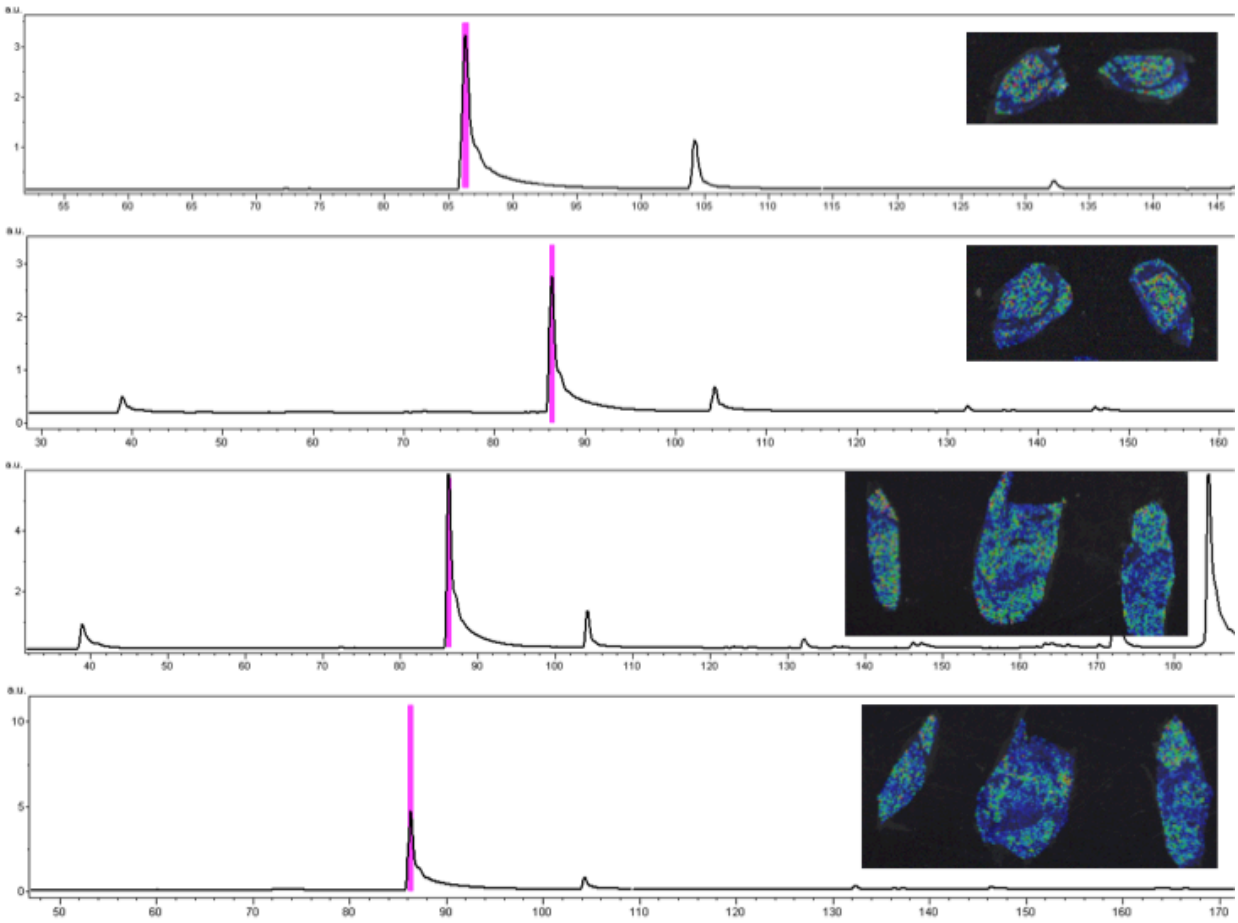

Figure 47. A unique peak was observed in brain excised from BZ6-treated SCID mice. (A) Shows the average spectrum from an unwashed cerebellum section, with the unique peak at 84 m/z highlighted in pink, and the virtual image shown to the right. (B) Shows the average spectrum from a washed cerebellum section, with the unique peak at 84 m/z highlighted in pink, and the virtual image shown to the right. (C) Shows the average spectrum from an unwashed cerebrum section, with the unique peak at 84 m/z highlighted in pink, and the virtual image shown to the right. (D) Shows the average spectrum from a washed cerebrum section, with the unique peak at 84 m/z highlighted in pink, and the virtual image shown to the right.

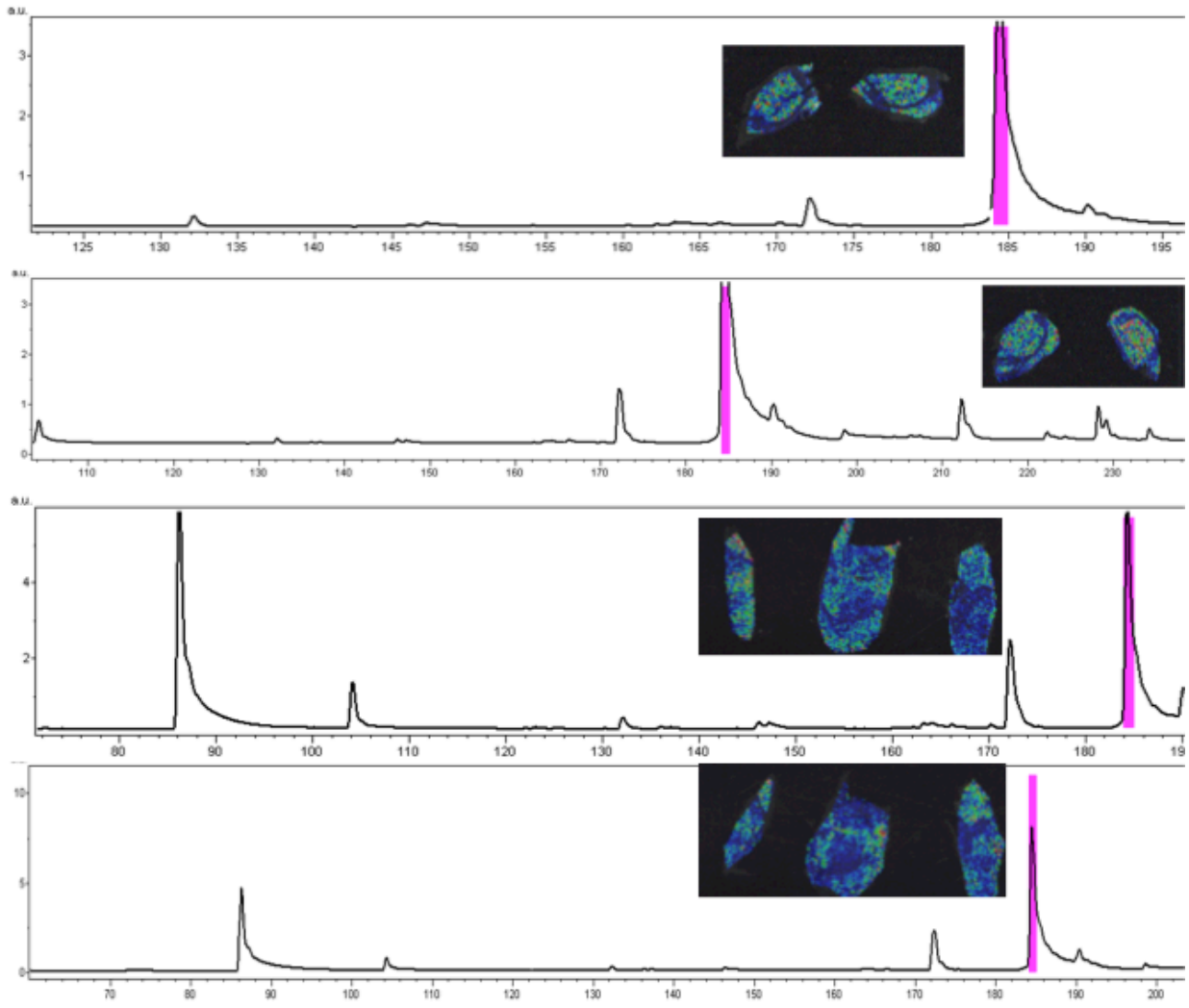

Figure 48. A unique peak was observed in brain excised from BZ6-treated SCID mice. (A) Shows the average spectrum from an unwashed cerebellum section, with the unique peak at 183 m/z highlighted in pink, and the virtual image shown to the right. (B) Shows the average spectrum from a washed cerebellum section, with the unique peak at 183 m/z highlighted in pink, and the virtual image shown to the right. (C) Shows the average spectrum from an unwashed cerebrum section, with the unique peak at 183 m/z highlighted in pink, and the virtual image shown to the right. (D) Shows the average

spectrum from a washed cerebrum section, with the unique peak at 183 m/z highlighted in pink, and the virtual image shown to the right.

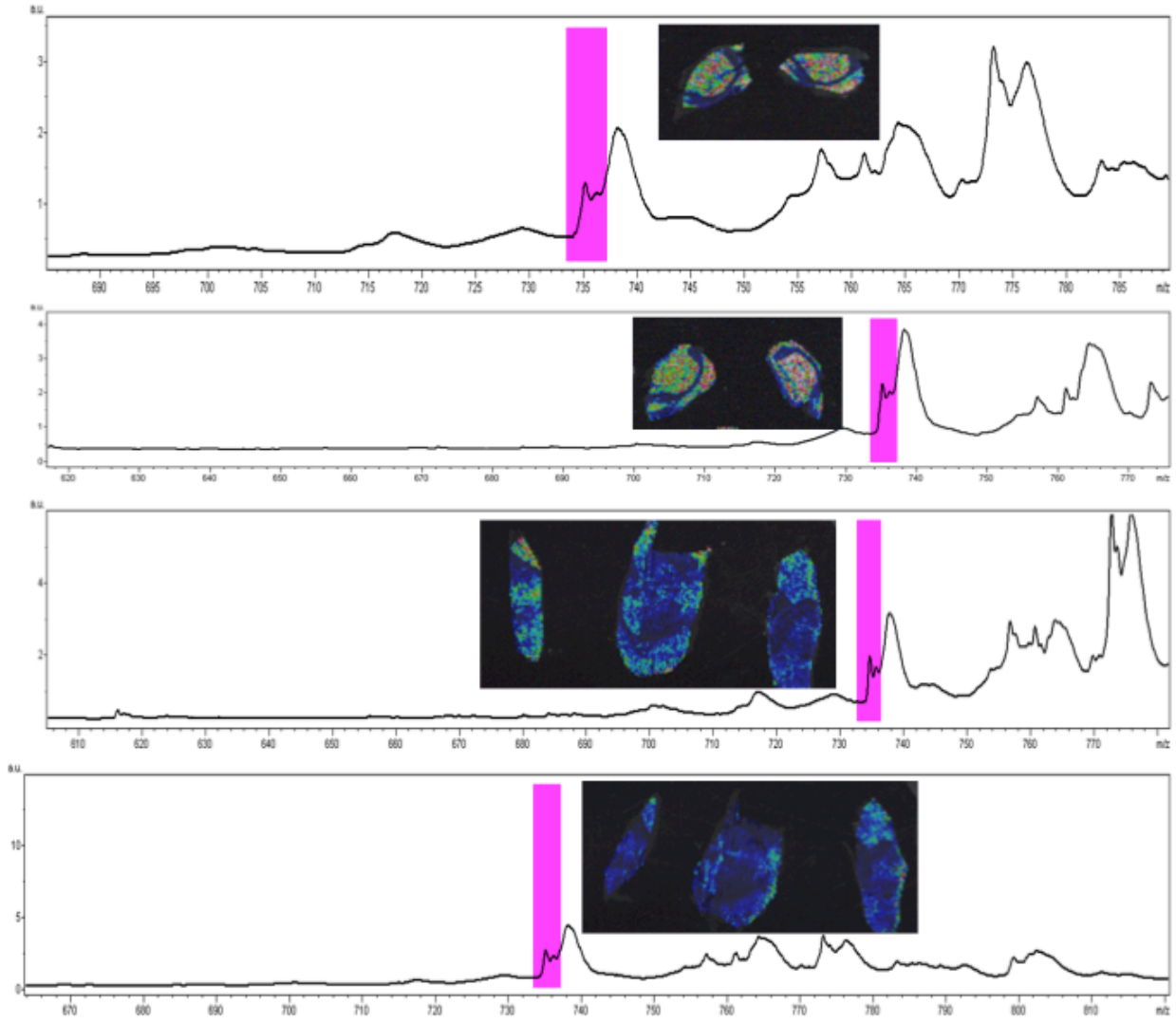

Figure 49. A unique peak was observed in brain excised from BZ6-treated SCID mice. (A) Shows the average spectrum from an unwashed cerebellum section, with the unique peak at 736 m/z highlighted in pink, and the virtual image shown to the right. (B) Shows the average spectrum from a washed cerebellum section, with the unique peak at 736 m/z highlighted in pink, and the virtual image shown to the right. (C) Shows the average spectrum from an unwashed cerebrum section, with the unique peak at 736 m/z highlighted in pink, and the virtual image shown to the right. (D) Shows the average

spectrum from a washed cerebrum section, with the unique peak at 736 m/z highlighted in pink, and the virtual image shown to the right.

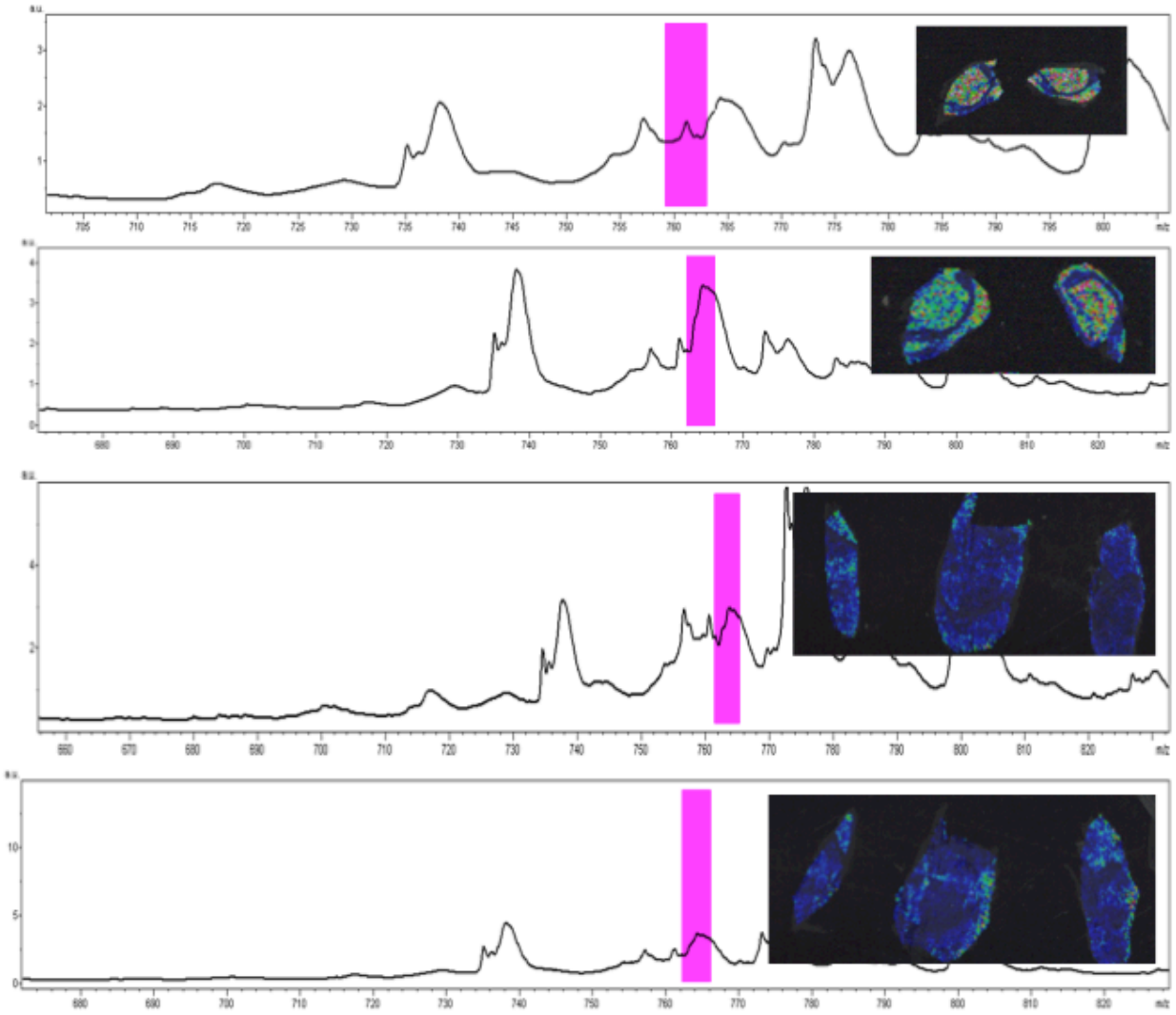

Figure 50. A unique peak was observed in brain excised from BZ6-treated SCID mice. (A) Shows the average spectrum from an unwashed cerebellum section, with the unique peak at 763 m/z highlighted in pink, and the virtual image shown to the right. (B) Shows the average spectrum from a washed cerebellum section, with the unique peak at 763 m/z highlighted in pink, and the virtual image shown to the right. (C) Shows the average spectrum from an unwashed cerebrum section, with the unique peak at 763 m/z highlighted in pink, and the virtual image shown to the right. (D) Shows the average

spectrum from a washed cerebrum section, with the unique peak at 763 m/z highlighted in pink, and the virtual image shown to the right.

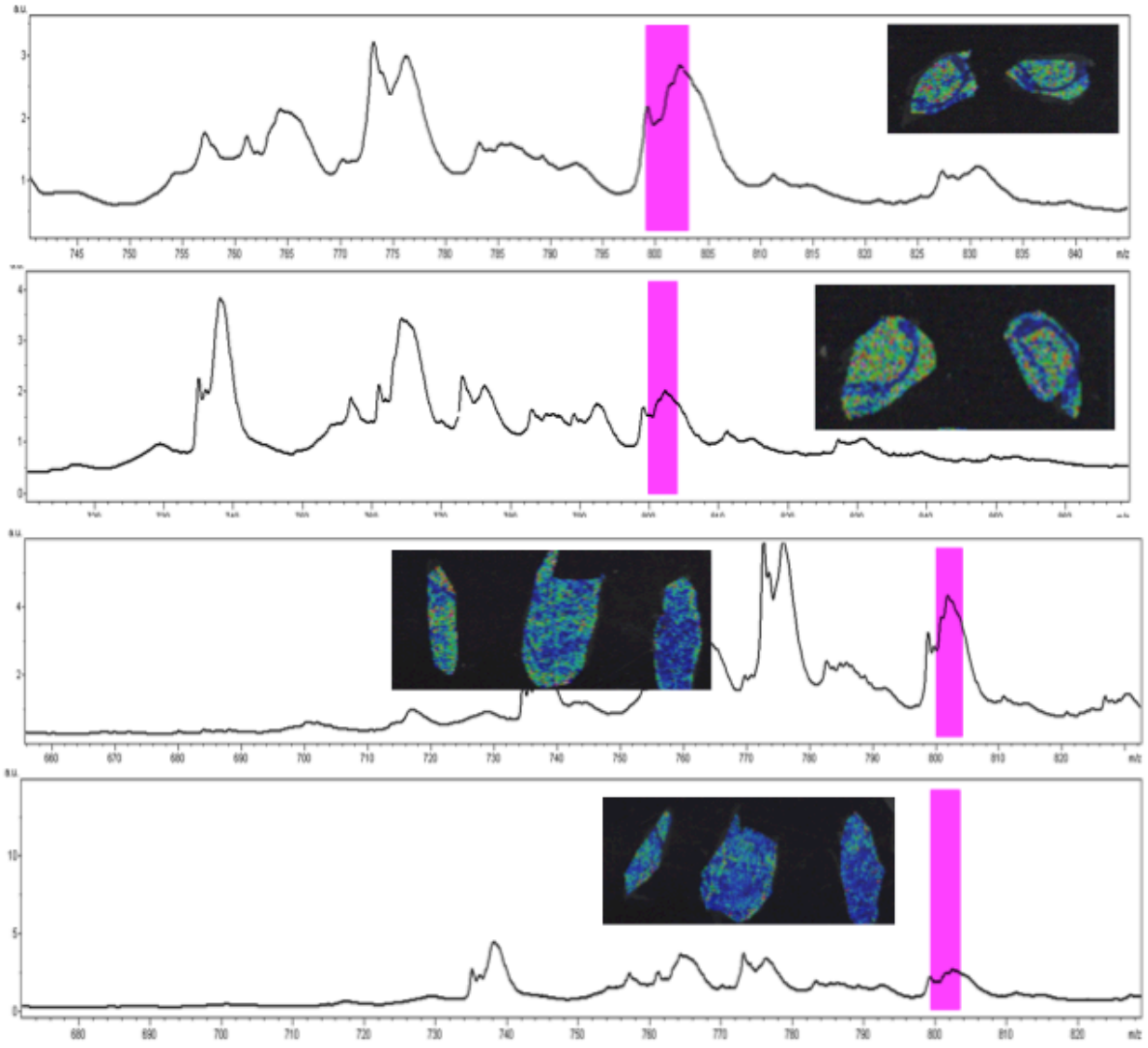

Figure 51. A unique peak was observed in brain excised from BZ6-treated SCID mice. (A) Shows the average spectrum from an unwashed cerebellum section, with the unique peak at 801 m/z highlighted in pink, and the virtual image shown to the right. (B) Shows the average spectrum from a washed cerebellum section, with the unique peak at 801 m/z highlighted in pink, and the virtual image shown to the right. (C) Shows the average spectrum from an unwashed cerebrum section, with the unique peak at 801 m/z highlighted in pink, and the virtual image shown to the right. (D) Shows the average

spectrum from a washed cerebrum section, with the unique peak at 801 m/z highlighted in pink, and the virtual image shown to the right.

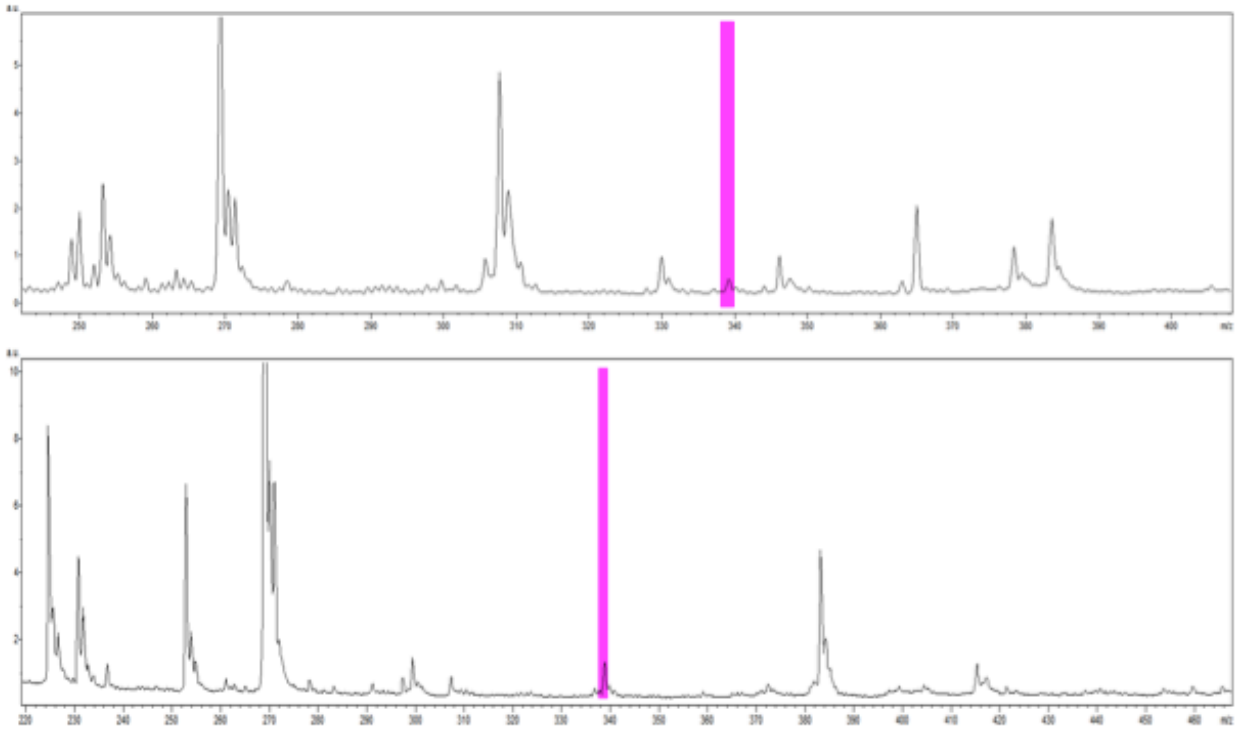

Figure 52. BZ16 was found to cross the blood-brain barrier and enter the cerebellum. (A) Shows the average spectrum from an unwashed cerebellum section, with the unique peak at 338 m/z highlighted in pink. (B) Shows the average spectrum from a washed cerebellum section, with the unique peak at 338 m/z highlighted in pink.

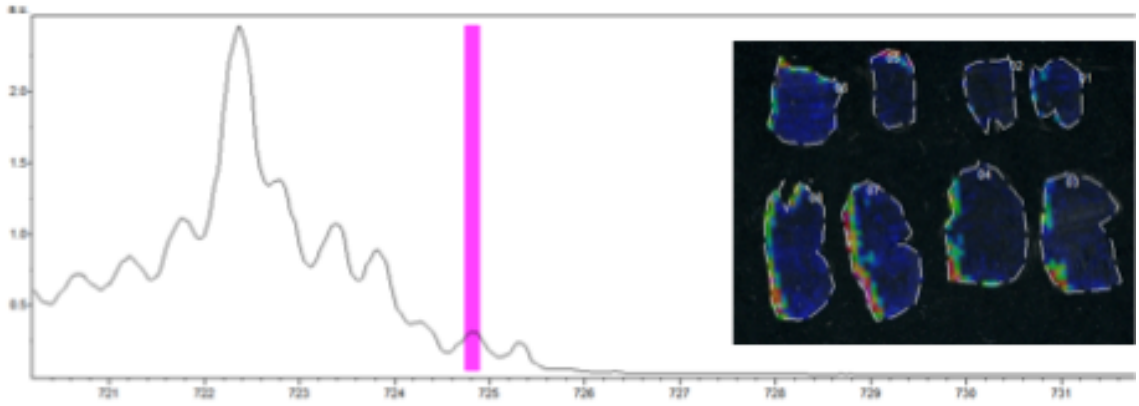

Figure 53. A negative mode image of CLR01-treated rat brain was collected, and a small peak was observed at 726 m/z, localized to the lower portion of the brain. The average spectrum is shown, with the unique peak at 726 m/z highlighted in pink, and the virtual image shown to the right.

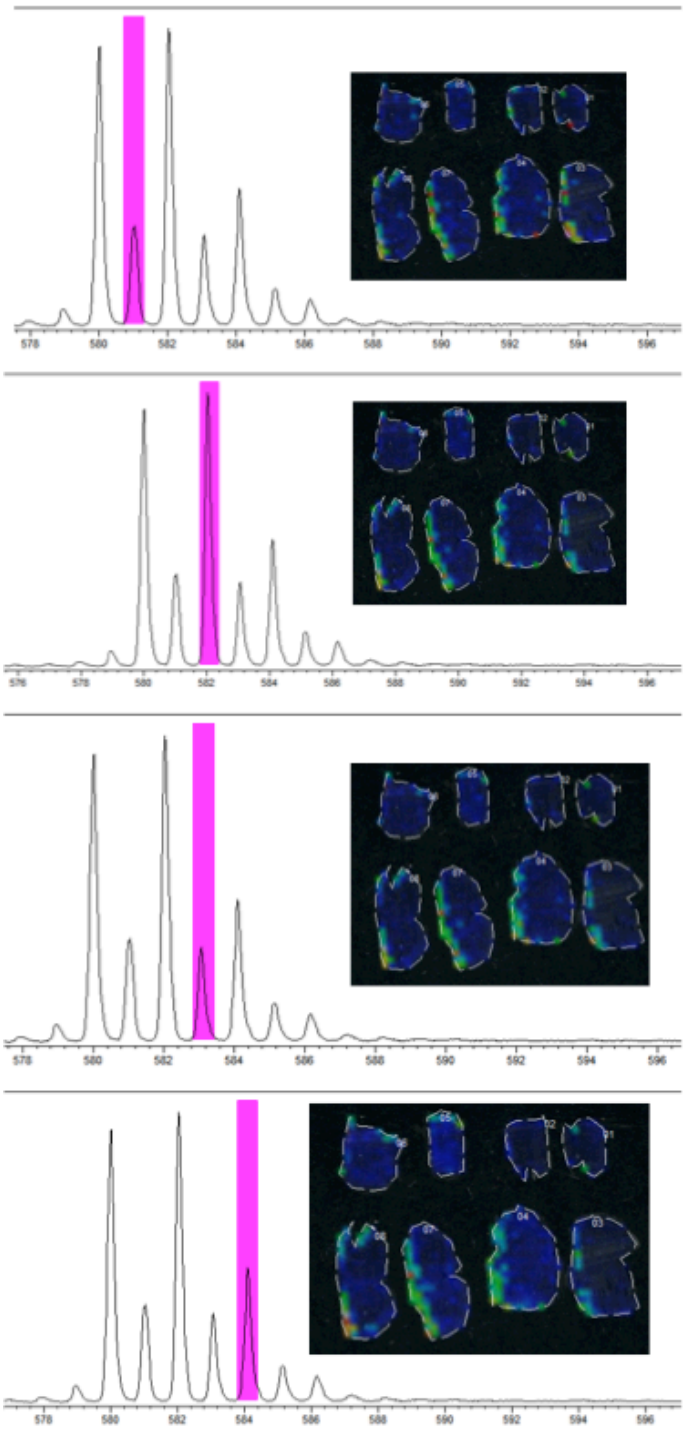

Figure 54. A negative mode MS/MS (726 m/z) image of CLR01-treated rat brain was collected, and a series of fragments were observed to localize to the lower portion of the brain. (A) Average spectrum is shown for 581 m/z, with the unique peak highlighted in

pink, and the virtual image shown to the right. (B) Average spectrum is shown for 582 m/z, with the unique peak highlighted in pink, and the virtual image shown to the right. (3) Average spectrum is shown for 583 m/z, with the unique peak highlighted in pink, and the virtual image shown to the right. (D) Average spectrum is shown for 584 m/z, with the unique peak highlighted in pink, and the virtual image shown to the right.

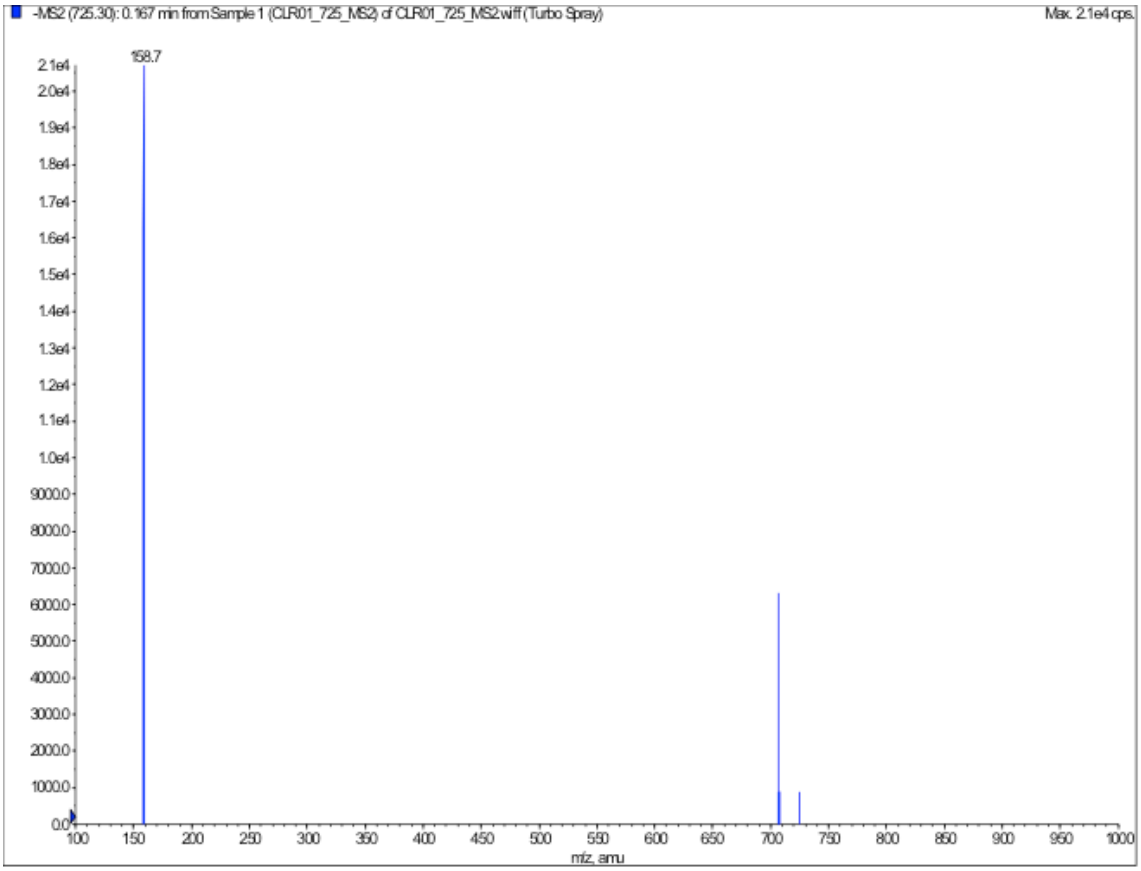

Figure 55. An LC-MS/MS spectrum is shown from a QTrap, utilizing SRM to monitor the transition in negative mode of 725.3 m/z ➔ 158.7 m/z for a standard 10 μM CLR01 infusion.

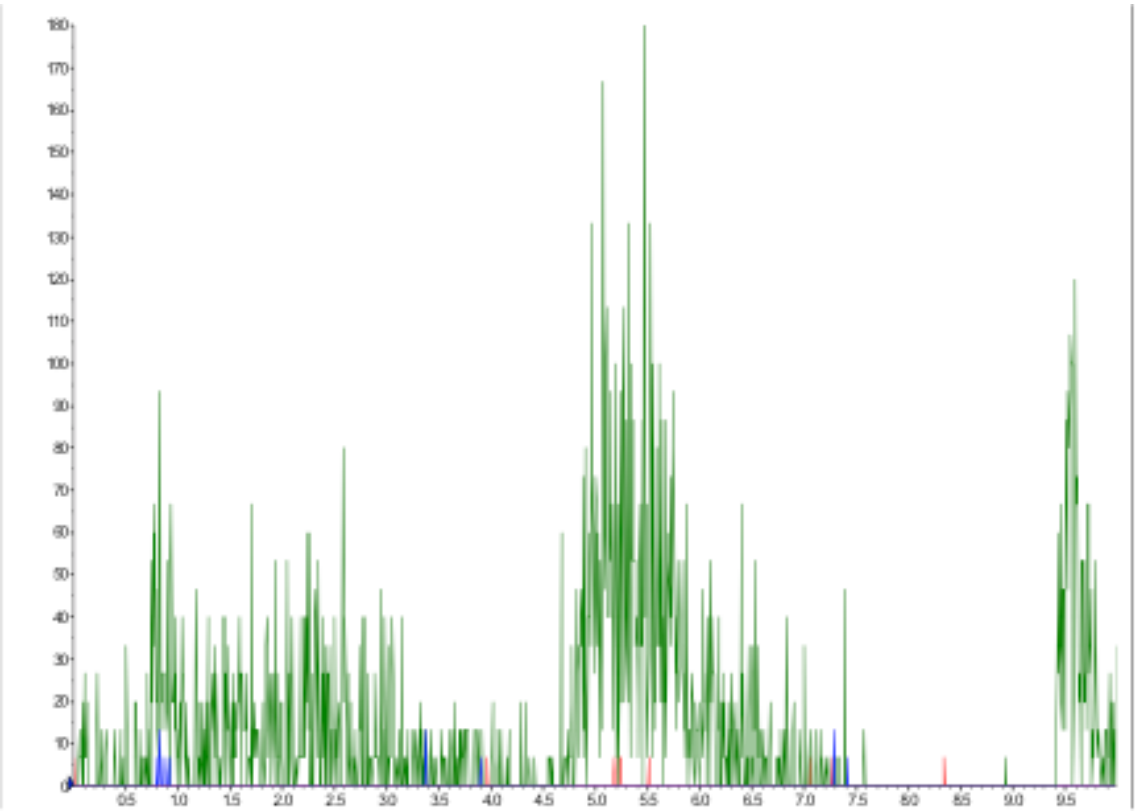

Figure 56. An LC-MS/MS spectrum is shown from a QTrap, utilizing SRM to monitor the transition in negative mode of 725.3 m/z ➔ 158.7 m/z for a homogenized brain extract excised from CLR01-treated triple transgenic rat.

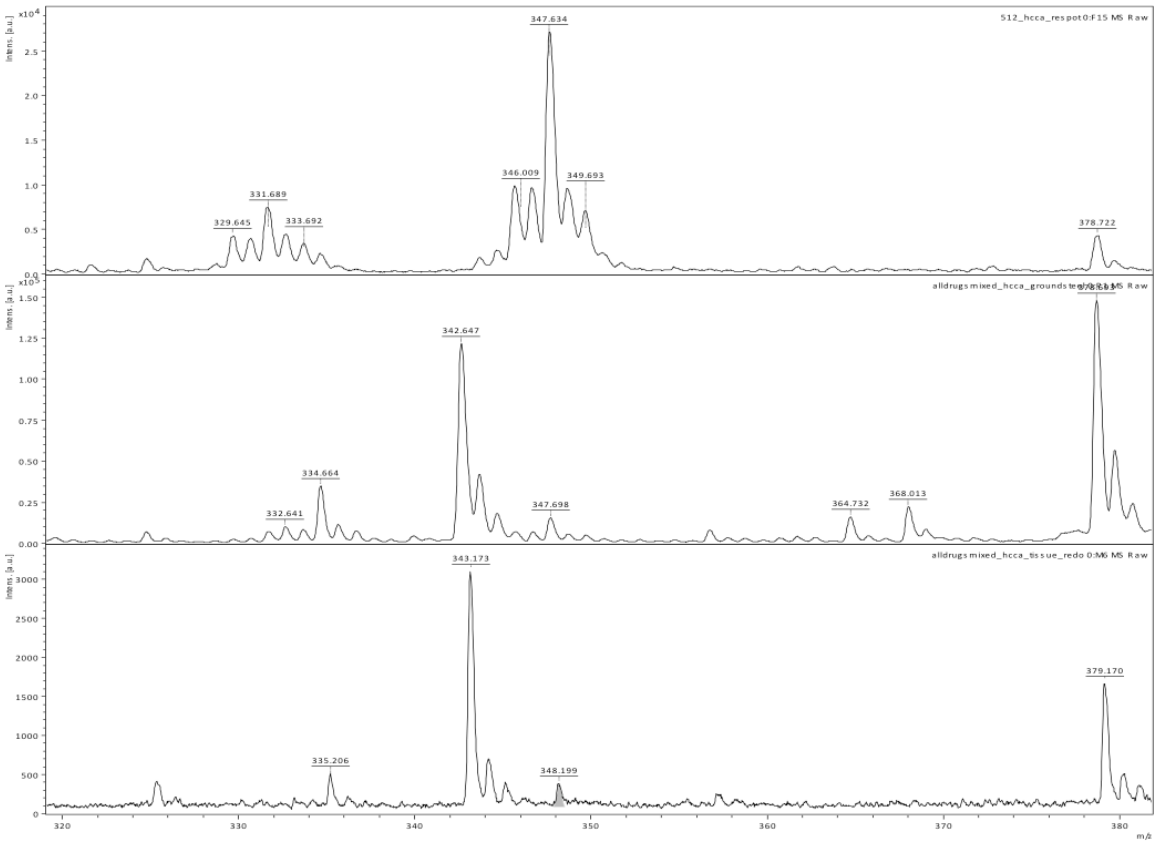

Figure 57. (A) RM512 ionization at 500 μM. (B) RM512 ionization at 500 μM when spotted on a MALDI plate with a mixture of drugs. (C) RM512 ionization at 500 μM when spotted on a tissue section with a mixture of drugs.

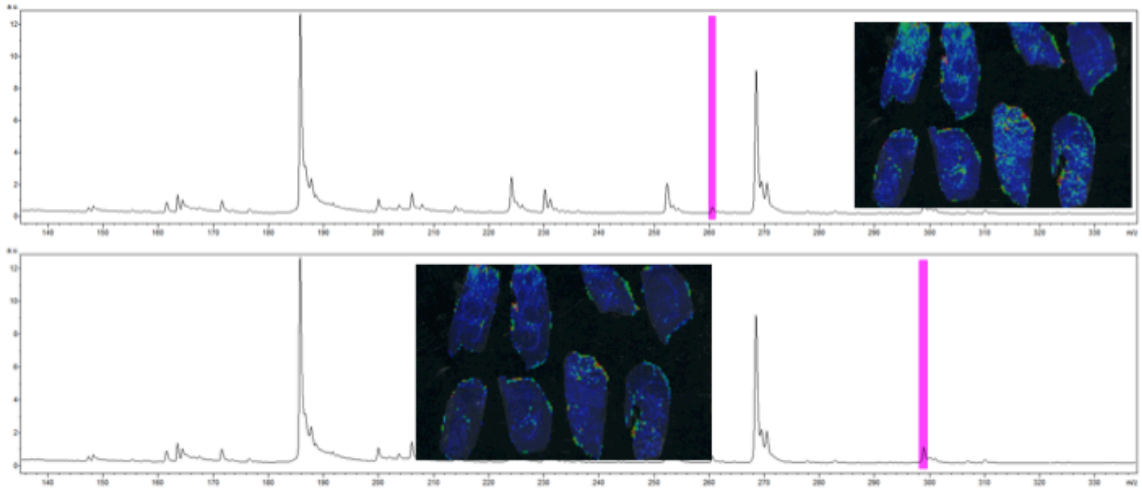

Figure 58. Several unique peaks were detected in brains excised from RM512-treated C3H mice. (A) Shows the average spectrum from a brain section, with the unique peak at 260 m/z highlighted in pink, and the virtual image shown to the right (detected in 2 h and 4 h post-dose mice). (B) Shows the average spectrum from a brain section, with the unique peak at 298 m/z highlighted in pink, and the virtual image shown to the right (detected in 2 h post-dose mice).

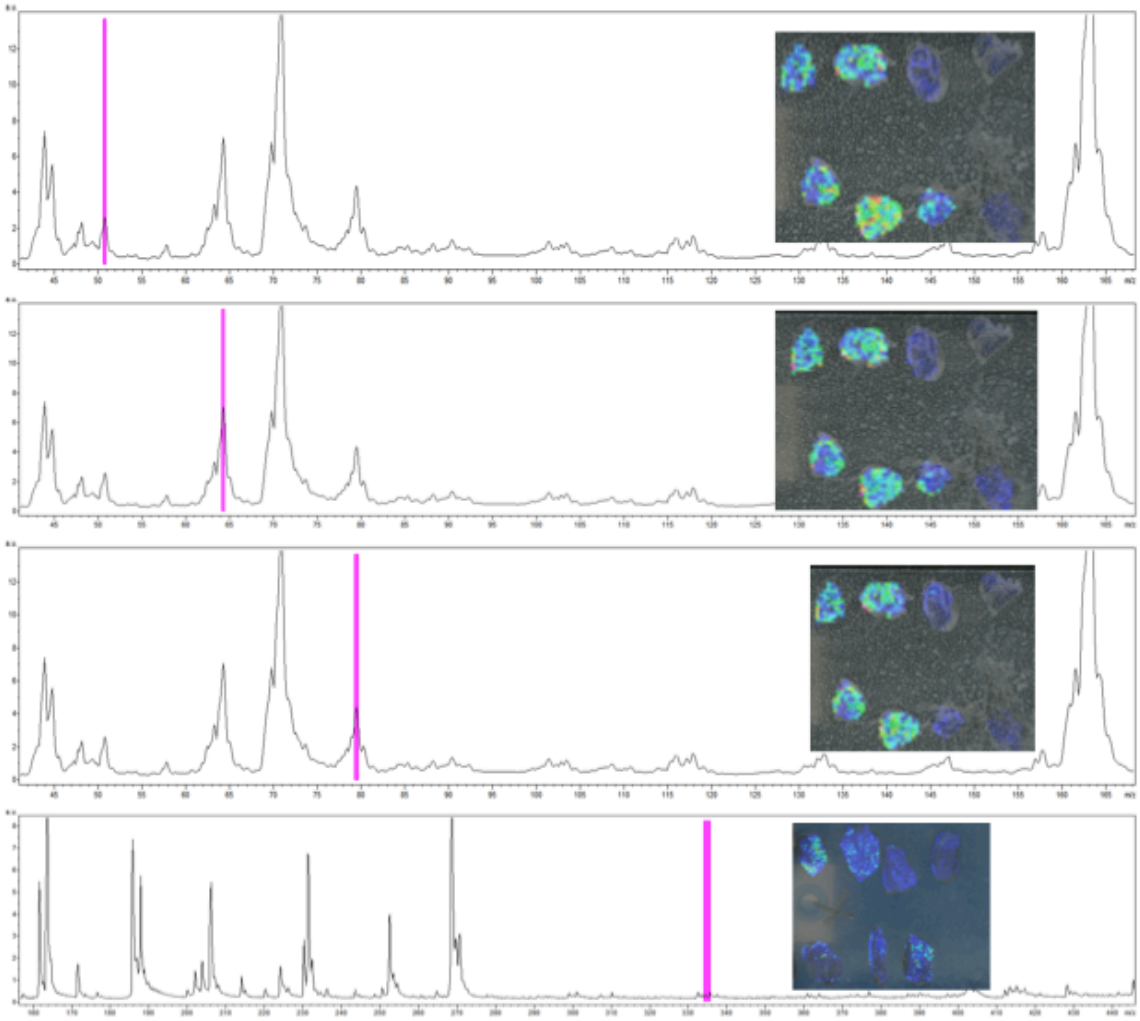

Figure 59. Several unique peaks were detected in hearts excised from RM512-treated C3H mice. (A) Shows the average spectrum from a heart section, with the unique peak at 50 m/z highlighted in pink, and the virtual image shown to the right (detected in 4 h and 24 h post-dose mice). (B) Shows the average spectrum from a heart section, with the unique peak at 64 m/z highlighted in pink, and the virtual image shown to the right (detected in 2 h, 4 h, and 24 h post-dose mice). (C) Shows the average spectrum from a heart section, with the unique peak at 79 m/z highlighted in pink, and the virtual image shown to the right (detected in 4 h and 24 h post-dose mice). (D) Shows the average

spectrum from a heart section, with the unique peak at 344 m/z highlighted in pink, and the virtual image shown to the right (detected in 2 h and 4 h post-dose mice).

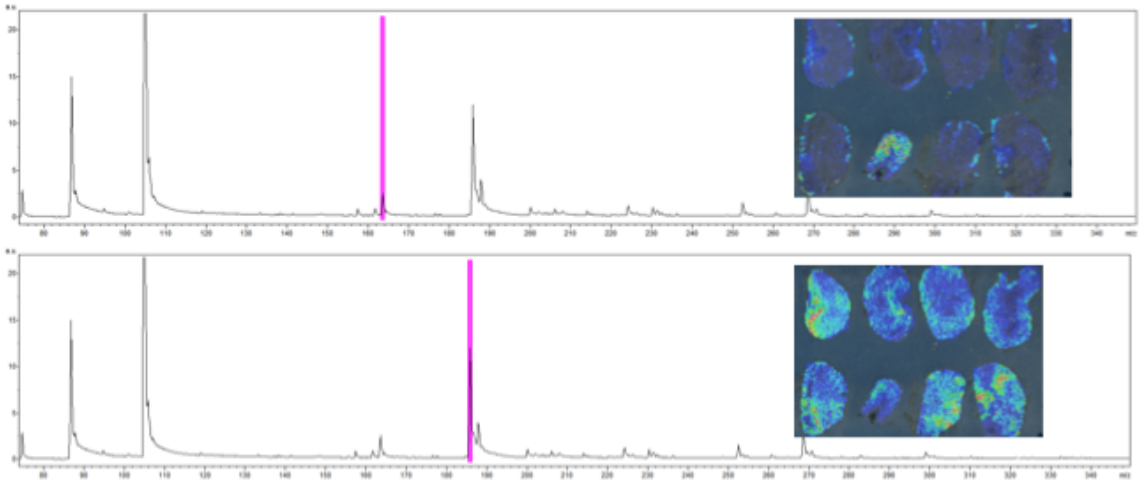

Figure 60. Several unique peaks were detected in kidneys excised from RM512-treated C3H mice. (A) Shows the average spectrum from a kidney section, with the unique peak at 163 m/z highlighted in pink, and the virtual image shown to the right (detected in 24 h post-dose mice). (B) Shows the average spectrum from a kidney section, with the unique peak at 185 m/z highlighted in pink, and the virtual image shown to the right (detected in 2 h, 4 h, and 24 h post-dose mice).

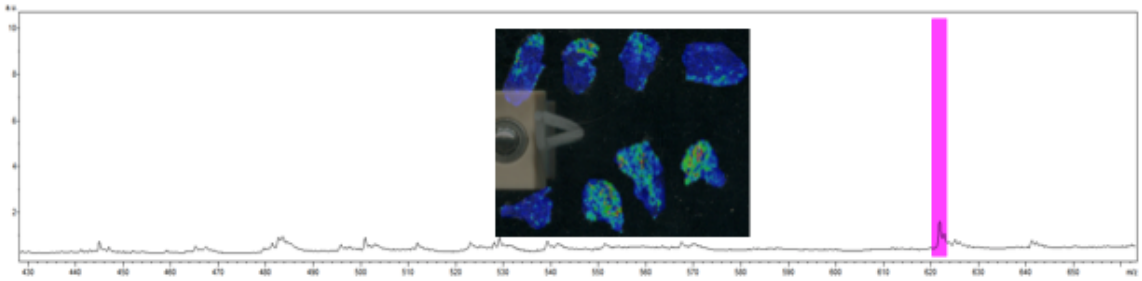

Figure 61. One unique peak was detected in lungs excised from RM512-treated C3H mice. The average spectrum is shown from a lung section, with the unique peak at 621 m/z highlighted in pink, and the virtual image shown to the left (detected in 2 h, 4 h, and 24 h post-dose mice).

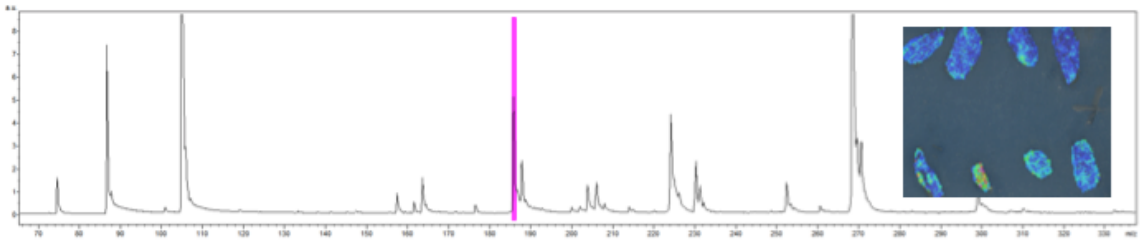

Figure 62. One unique peak was detected in spleen excised from RM512-treated C3H mice. The average spectrum is shown from a lung section, with the unique peak at 185 m/z highlighted in pink, and the virtual image shown to the right (detected in 2 h and 24 h post-dose mice).

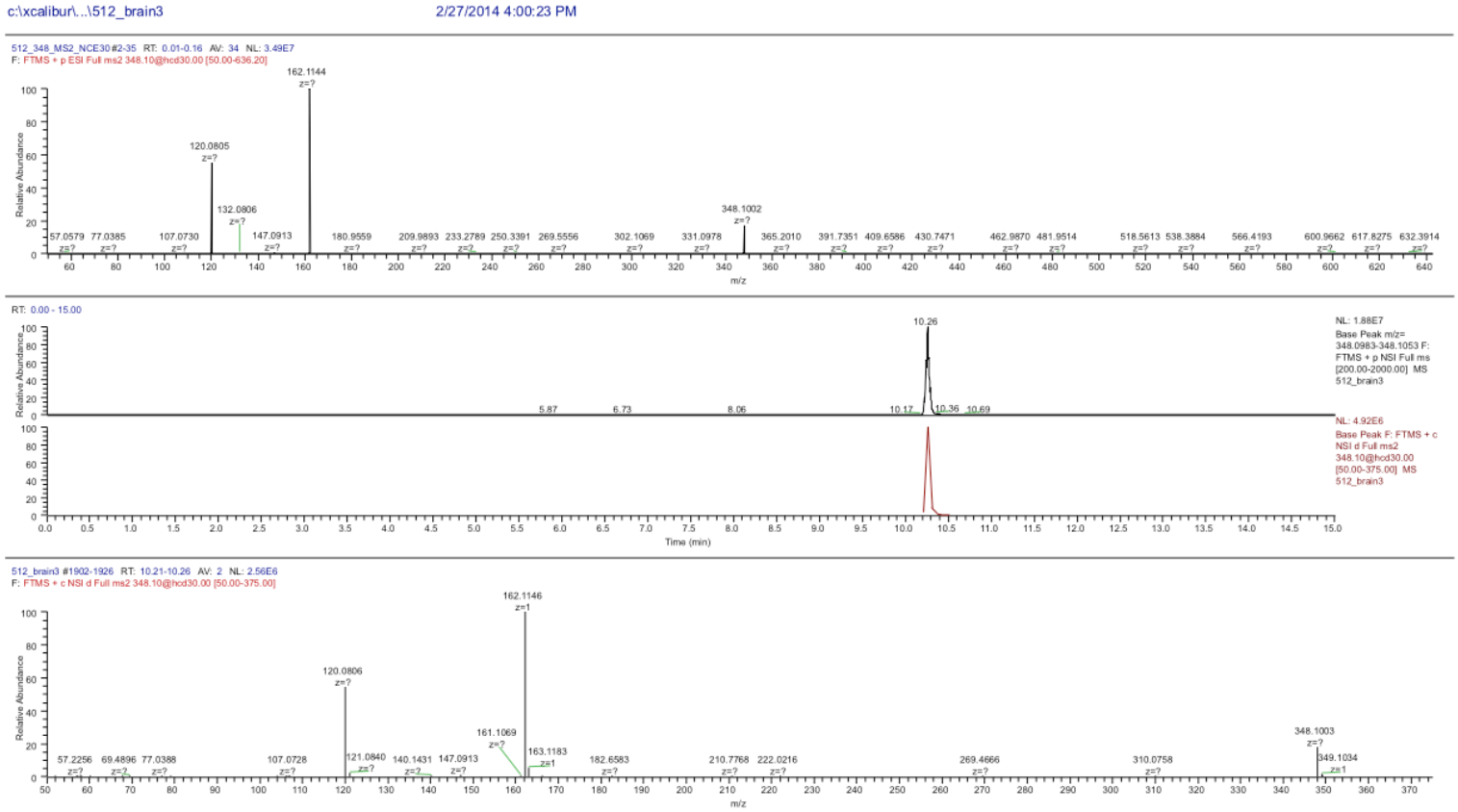
c:\xcalibur\...\512_brain3
2/27/2014 4:00:23 PM
512_348_MS2_NCE30 #2-35 RT: 0.01-0.16 AV: 34 NL: 3.49E7
F: FTMS + p ESI Full ms2 348.10@hcd30.00 [50.00-636.20]
Relative Abundance
m/z
RT: 0.00 - 15.00
10.26
NL: 1.88E7
Base Peak m/z= 348.0983-348.1053 F: FTMS + p NSI Full ms [200.00-2000.00] MS 512_brain3
NL: 4.92E6
Base Peak F: FTMS + c NSI d Full ms2 348.10@hcd30.00 [50.00-375.00] MS 512_brain3
Time (min)
512_brain3 #1902-1926 RT: 10.21-10.26 AV: 2 NL: 2.56E6
F: FTMS + c NSI d Full ms2 348.10@hcd30.00 [50.00-375.00]
Relative Abundance
m/z

Figure 63. RM512 was detected in extracted brain homogenate from a C3H mouse sacrificed at 2 h post-dose. (A) MS/MS spectrum of RM512 standard (B) XIC of RM512 in extracted brain homogenate. (B) XIC of MS/MS of RM512 in extracted brain homogenate. (C) Mass spectrum of RM512 in extracted brain homogenate.

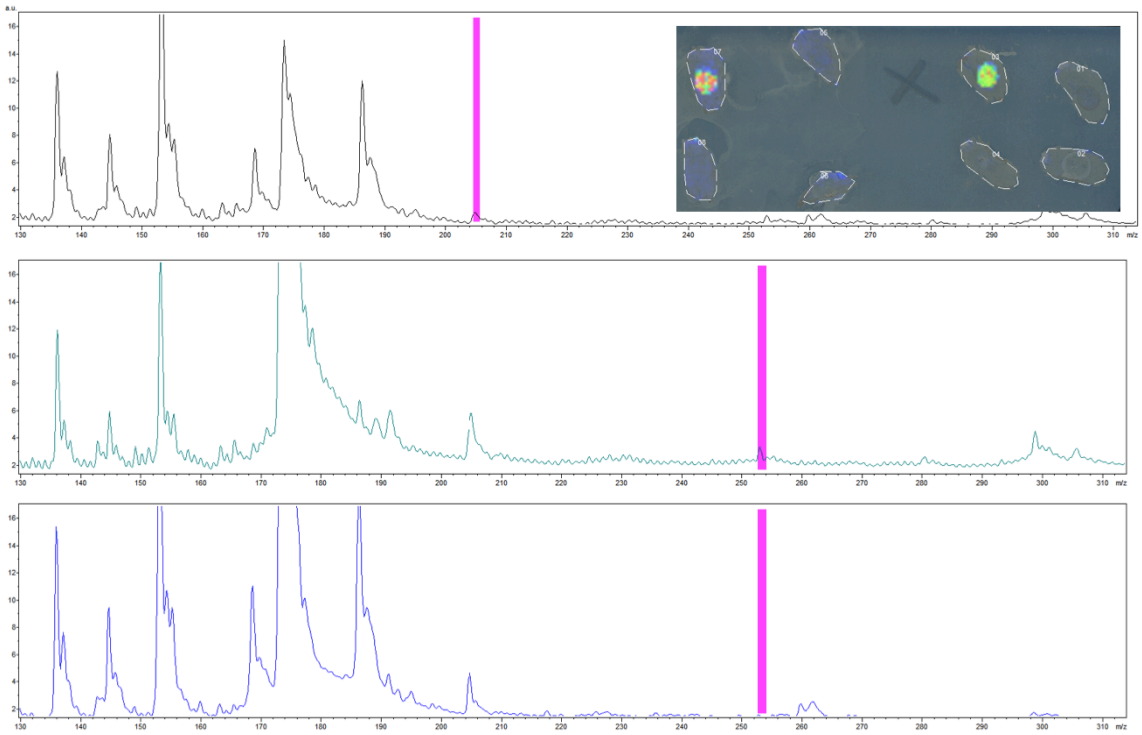

Figure 64. (A) Average spectrum of Phos-MSNP (205 m/z) spotted onto tissue sections, with virtual image to the right. Indicates no delocalization by H_2O washing. (B) Average spectrum of Phos-MSNP H_2O washed tissue section. (C) Average spectrum of Phos-MSNP unwashed tissue section.

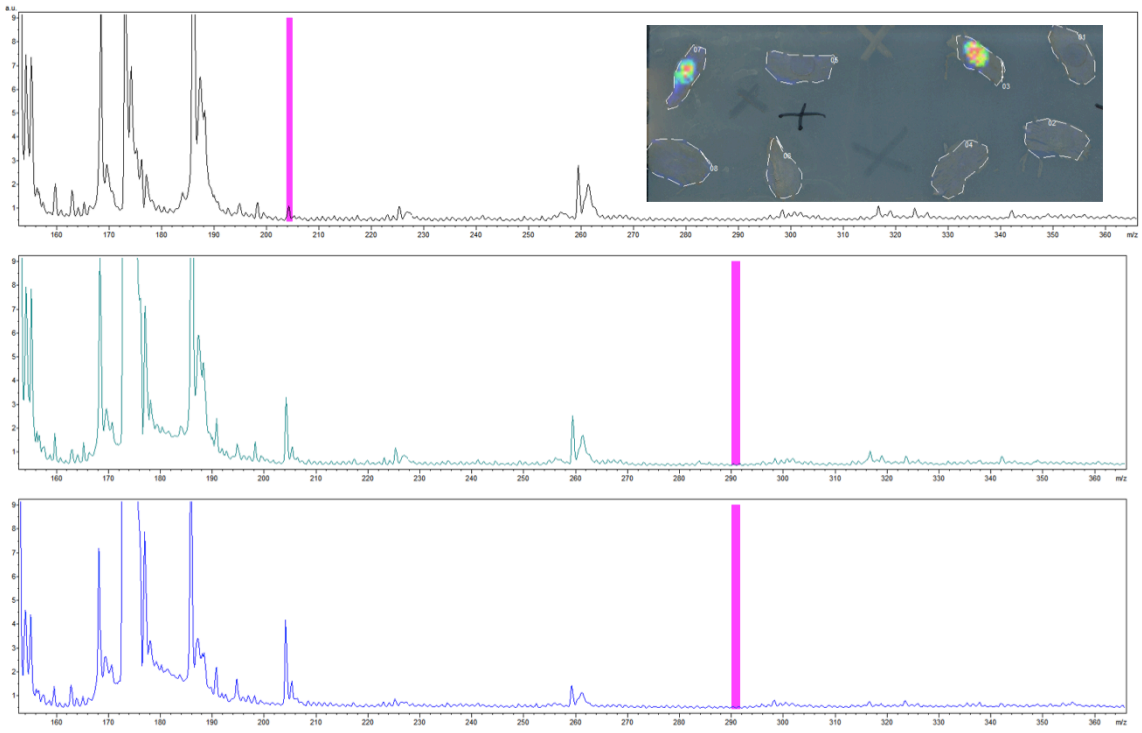

Figure 65. (A) Average spectrum of Phos-MSNP spotted onto tissue sections, with virtual image to the right. Indicates no delocalization by Xylene washing. (B) Average spectrum of Phos-MSNP Xylene washed tissue section. (C) Average spectrum of Phos-MSNP unwashed tissue section.

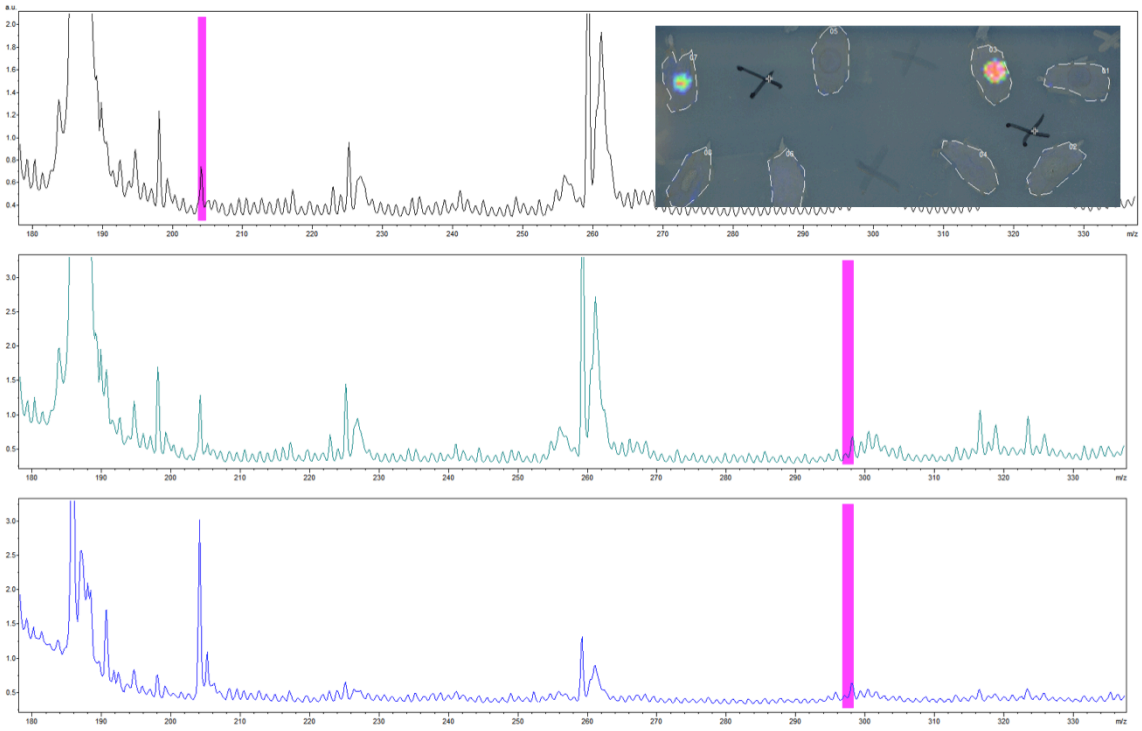

Figure 66. (A) Average spectrum of Phos-MSNP spotted onto tissue sections, with virtual image to the right. Indicates no delocalization by chloroform washing. (B) Average spectrum of Phos-MSNP chloroform washed tissue section. (C) Average spectrum of Phos-MSNP unwashed tissue section.

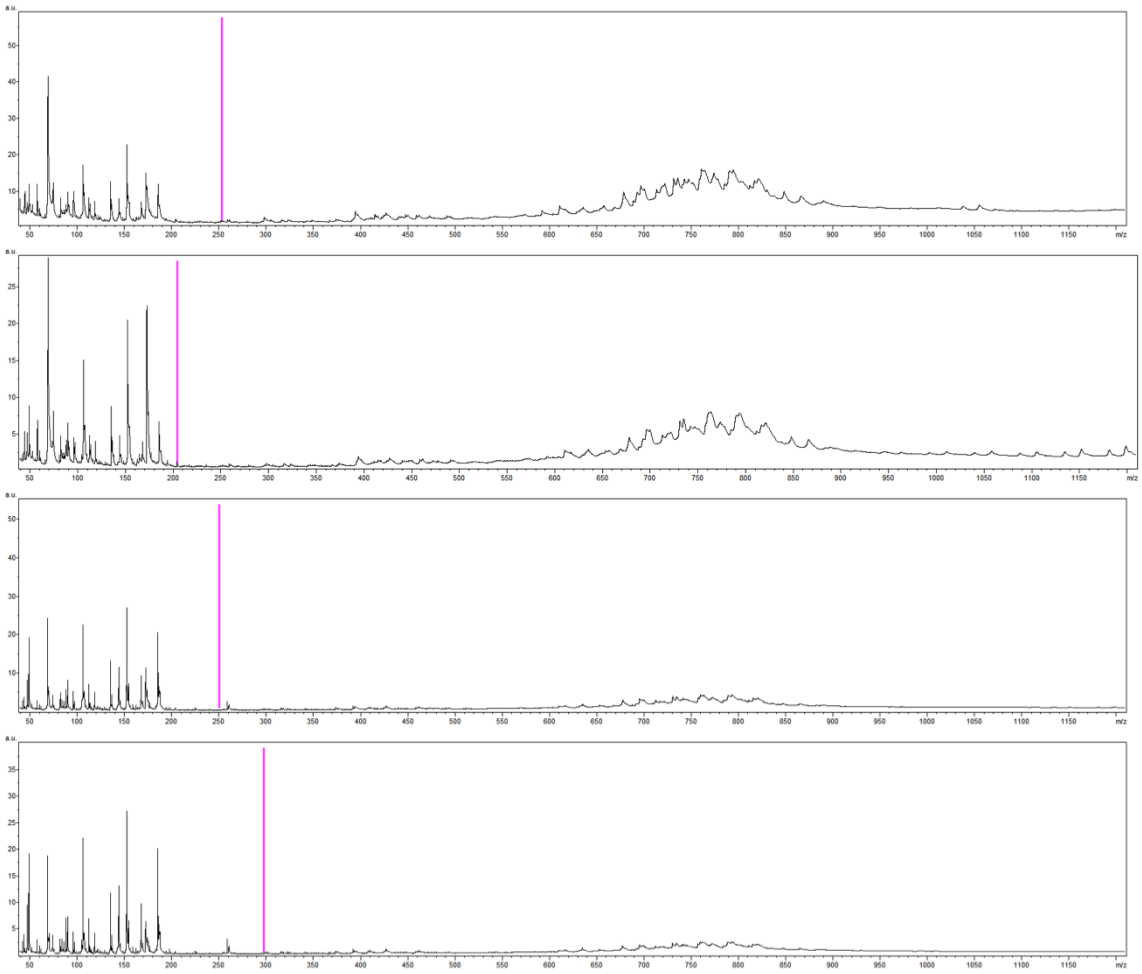

Figure 67. The baseline from tissue is affected depending on the solvent utilized. (A) Water. (B) Ethanol. (C) Xylene. (D) Chloroform.

REFERENCES

1. McDonnell, L. A.; Heeren, R. M., Imaging mass spectrometry. *Mass spectrometry reviews* **2007,** *26* (4), 606-43.

2. Reyzer, M. L.; Hsieh, Y.; Ng, K.; Korfmacher, W. A.; Caprioli, R. M., Direct analysis of drug candidates in tissue by matrix-assisted laser desorption/ionization mass spectrometry. *Journal of mass spectrometry : JMS* **2003,** *38* (10), 1081-92.

3. Takats, Z.; Wiseman, J. M.; Cooks, R. G., Ambient mass spectrometry using desorption electrospray ionization (DESI): instrumentation, mechanisms and applications in forensics, chemistry, and biology. *Journal of mass spectrometry : JMS* **2005,** *40* (10), 1261-75.

4. Karas, M.; Hillenkamp, F., Laser desorption ionization of proteins with molecular masses exceeding 10,000 daltons. *Analytical chemistry* **1988,** *60* (20), 2299-301.

5. Todd, P. J.; Schaaff, T. G.; Chaurand, P.; Caprioli, R. M., Organic ion imaging of biological tissue with secondary ion mass spectrometry and matrix-assisted laser desorption/ionization. *Journal of mass spectrometry : JMS* **2001,** *36* (4), 355-69.

6. Wiseman, J. M.; Ifa, D. R.; Zhu, Y.; Kissinger, C. B.; Manicke, N. E.; Kissinger, P. T.; Cooks, R. G., Desorption electrospray ionization mass spectrometry: Imaging drugs and metabolites in tissues. *Proceedings of the National Academy of Sciences of the United States of America* **2008,** *105* (47), 18120-5.

7. Takats, Z.; Wiseman, J. M.; Gologan, B.; Cooks, R. G., Mass spectrometry sampling under ambient conditions with desorption electrospray ionization. *Science* **2004,** *306* (5695), 471-3.

8. Kertesz, V.; Van Berkel, G. J., Fully automated liquid extraction-based surface sampling and ionization using a chip-based robotic nanoelectrospray platform. *Journal of mass spectrometry : JMS* **2010,** *45* (3), 252-60.

9. Eikel, D.; Vavrek, M.; Smith, S.; Bason, C.; Yeh, S.; Korfmacher, W. A.; Henion, J. D., Liquid extraction surface analysis mass spectrometry (LESA-MS) as a novel profiling tool for drug distribution and metabolism analysis: the terfenadine example. *Rapid communications in mass spectrometry : RCM* **2011,** *25* (23), 3587-96.

10. Nemes, P.; Woods, A. S.; Vertes, A., Simultaneous imaging of small metabolites and lipids in rat brain tissues at atmospheric pressure by laser ablation electrospray ionization mass spectrometry. *Analytical chemistry* **2010,** *82* (3), 982-8.

11. Nemes, P.; Vertes, A., Laser ablation electrospray ionization for atmospheric pressure, in vivo, and imaging mass spectrometry. *Analytical chemistry* **2007,** *79* (21), 8098-106.

12. Shrestha, B.; Vertes, A., In situ metabolic profiling of single cells by laser ablation electrospray ionization mass spectrometry. *Analytical chemistry* **2009,** *81* (20), 8265-71.

13. Chaurand, P.; Norris, J. L.; Cornett, D. S.; Mobley, J. A.; Caprioli, R. M., New developments in profiling and imaging of proteins from tissue sections by MALDI mass spectrometry. *Journal of proteome research* **2006,** *5* (11), 2889-900.

14. Gatti, R. A., SMRT compounds correct nonsense mutations in primary immunodeficiency and other genetic models. *Annals of the New York Academy of Sciences* **2012,** *1250*, 33-40.

15. Swift, M.; Morrell, D.; Cromartie, E.; Chamberlin, A. R.; Skolnick, M. H.; Bishop, D. T., The incidence and gene frequency of ataxia-telangiectasia in the United States. *American journal of human genetics* **1986,** *39* (5), 573-83.

16. Attar, A.; Rahimi, F.; Bitan, G., Modulators of amyloid protein aggregation and toxicity: EGCG and CLR01. *Translat.Neurosci.* **2013,** *4* (4), 385-409.

17. Prabhudesai, S.; Sinha, S.; Attar, A.; Kotagiri, A.; Fitzmaurice, A. G.; Lakshmanan, R.; Ivanova, M. I.; Loo, J. A.; Klarner, F. G.; Schrader, T.; Stahl, M.; Bitan, G.; Bronstein, J. M., A novel "molecular tweezer" inhibitor of alpha-synuclein neurotoxicity in vitro and in vivo. *Neurotherapeutics : the journal of the American Society for Experimental NeuroTherapeutics* **2012,** *9* (2), 464-76.

18. Sinha, S.; Lopes, D. H. J.; Du, Z.; Pang, E. S.; Shanmugam, A.; Lomakin, A.; Talbiersky, P.; Tennstaedt, A.; McDaniel, K.; Bakshi, R.; Kuo, P.-Y.; Ehrmann, M.; Benedek, G. B.; Loo, J. A.; Klärner, F.-G.; Schrader, T.; Wang, C.; Bitan, G., Lysine-Specific Molecular Tweezers Are Broad-Spectrum Inhibitors of Assembly and Toxicity of Amyloid Proteins. *Journal of the American Chemical Society* **2011,** *133* (42), 16958-16969.

19. Einstein, A. J.; Henzlova, M. J.; Rajagopalan, S., Estimating risk of cancer associated with radiation exposure from 64-slice computed tomography coronary angiography. *JAMA : the journal of the American Medical Association* **2007,** *298* (3), 317-23.

20. Kim, K.; Pollard, J. M.; Norris, A. J.; McDonald, J. T.; Sun, Y.; Micewicz, E.; Pettijohn, K.; Damoiseaux, R.; Iwamoto, K. S.; Sayre, J. W.; Price, B. D.; Gatti, R. A.; McBride, W. H., High-throughput screening identifies two classes of antibiotics as

radioprotectors: tetracyclines and fluoroquinolones. *Clinical cancer research : an official journal of the American Association for Cancer Research* **2009,** *15* (23), 7238-45.

21. Meng, H.; Liong, M.; Xia, T.; Li, Z.; Ji, Z.; Zink, J. I.; Nel, A. E., Engineered design of mesoporous silica nanoparticles to deliver doxorubicin and P-glycoprotein siRNA to overcome drug resistance in a cancer cell line. *ACS nano* **2010,** *4* (8), 4539-50.

CHAPTER 3

Biodistribution of Small Molecule Read-Through (SMRT) Compounds in a Mouse Model as Determined by Matrix-Assisted Laser Desorption/Ionization-Mass Spectrometry Imaging (MALDI-MSI)

Biodistribution of Small Molecule Read-Through (SMRT) Compounds in a Mouse Model as Determined by Matrix-Assisted Laser Desorption/Ionization-Mass Spectrometry Imaging (MALDI-MSI)

Carly N. Ferguson, Jonathan F. Waxer, Joseph W.M. Fowler, Ewa Micewicz, William H. McBride, Richard A. Gatti, Joseph A. Loo

ABSTRACT

The biodistribution of drug compounds is an important factor in studying potential therapeutics. Any off-target effects, or build-up, must be assessed, as well as confirmation of entry into desired organs and regions of the body. This is often done using labor-intensive, tag-based methodologies; or, a full-organ homogenization and extraction are utilized, losing spatial information. While each method has its advantages, we proposed the use of mass spectrometry imaging (MSI) for the study of a set of potential therapeutics: small molecule read-through (SMRT) compounds. These compounds have been found to effectively induce read-through in an Ataxia-Telangiectasia (AT) premature termination codon (PTC) disorder model *in vitro*. With a target organ of the brain, and a target localization of the cerebellum, MSI was able to determine that one SMRT compound, BZ16, crossed the blood-brain barrier (BBB) and entered the cerebellum. The addition of a solvent wash step in tissue pre-treatment allowed for enhancement of signal; however, LC-MS/MS was needed to determine BBB penetration ability of two of the five additional SMRT compounds, RTC13 and 216, due to their low abundance. This suggests that BZ16 crossed the BBB with greater efficiency, and indicates the complementary nature of these methods: while MSI preserves spatial distribution, LC-MS/MS gives a greater depth of sensitivity.

INTRODUCTION

Over 1,800 inherited human diseases are the result of an alteration in the genetic code that prematurely stop the translation of proteins. These mutations that result in a premature termination codon (PTC) are coined “nonsense mutations” and make-up approximately 30% of all heritable disorders.[76] Different classes of mutations, including frameshift insertions/deletions, splice-site intron inclusions, or, as shown in Figure 1A, single nucleotide polymorphisms (SNPs) of a normal codon with UAA, UAG, or UGA codons, can all introduce a PTC, thus arresting protein synthesis.[77] Only the latter, which constitutes primary PTC mutations, however, would have a potential for therapeutic benefits.[49]

One therapeutic approach for overcoming nonsense mutations is gene therapy. Its potential for targeted repair would make it the treatment of choice, but, to date, several limitations have precluded clinical success.[78] A pharmacological approach, on the other hand, can modify gene expression by blocking nonsense mediated mRNA destruction, without correcting the underlying gene defect.[50] The notion that even such limited expression of a mutated gene could result in the production of a partially or fully functional protein, sufficient for therapeutic benefit, is the rationale supporting such emerging pharmacogenetic strategies.[76-79]

Aminoglycosides are widely used in clinical practice as bacterial antibiotics with established effects on translational accuracy or efficiency due to their high-affinity binding to prokaryotic ribosomal RNA (rRNA) at the decoding center.[50,80] The conformation of rRNA becomes altered in the presence of an aminoglycoside which induces codon misreading. This misreading has two potential effects. It either leads to

the incorporation of an erroneous amino acid (mis-incorporation) at a sense codon, or to the failure of recognition of the stop codon, resulting in a translational read-through rather than chain termination.[47,81,82] Due to the structural differences between prokaryotic and eukaryotic ribosomes, the effects of aminoglycosides on protein translation in eukaryotic cells have been demonstrated at concentrations 10 to 15 times higher than the typical therapeutic antibacterial concentrations.[50] Although this partial susceptibility of eukaryotic ribosomes toward aminoglycoside interaction has traditionally been viewed as the underlying mechanism of drug toxicity, this side effect may provide the opportunity for the treatment of human genetic diseases associated with translational defects.[50]

In 1999, the ability of aminoglycosides to promote protein translation, despite the presence of a PTC mutation, was first demonstrated *in vivo* in a model of Duchenne muscular dystrophy.[83] Although the efficiency of read-through has varied from 1% to 25% in human cell lines, even a low amount of produced protein in the presence of a nonsense PTC mutation may be functionally significant.[84,85] This is especially the case in recessive disorders, where protein expression is essentially absent. In such cases, even 1% of normal protein function may restore a near-normal or clinically less severe phenotype.[76-79] Accordingly, it is primarily in recessive disorders that aminoglycosides have provided the greatest promise in both cell culture experiments and clinical trials.

Ataxia-telangiectasia (A-T) is one such example of an autosomal recessive disorder. This neuro-degenerative disorder has an onset in early childhood and results from mutations in the A-T mutated (ATM) gene.[86] The ATM protein is a hierarchical serine-threonine kinase, phosphorylating many substrates involved in repair of double-

stranded DNA breaks, control of cell cycle checkpoints, and responses to oxidative stress as well as in radiosensitivity, cancer susceptibility, immune function, and neurological development.[87] Using protein truncation testing (PTT) driven by plasmid templates containing PTC mutations in the ATM gene, Lai *et al* observed *in vitro* read-through effects of various magnitudes with three or four aminoglycosides.[49,88] Full-length ATM protein was also documented *ex vivo* by immunoprecipitation.[49] Finally, the correction of radioresistant DNA synthesis and radiosensitivity, as well as autophosphorylation of ATM, suggested that this read-through produced functional ATM protein.[49]

Although aminoglycosides have provided some promise for a pharmacological approach in gene expression, some disadvantages threaten its effectiveness as a long-term treatment for autosomal recessive disorders. The high concentrations of aminoglycosides needed to sufficiently interfere with human ribosomes is one such limitation, for these concentrations run the risk of systemic drug toxicity. Furthermore, a high cellular concentration of aminoglycosides could interfere with other aspects of normal protein synthesis, causing a series of adverse effects on the individual. Thus, the clinical success to date has been observed with local aminoglycoside delivery, for the systemic delivery of currently available aminoglycosides at clinically approved doses has failed, as in the case of McArdle disease and Duchenne muscular dystrophy.[89,90] With specific consideration to A-T, aminoglycosides are further troubled by the water-soluble nature of the compounds, resulting in an inability to penetrate the blood-brain barrier.[91] These shortcomings of aminoglycoside compounds allow for further

exploration of potential read-through compounds that do not exhibit toxicity and overcome the impermeability of the blood-brain barrier.

Recently the laboratory of Dr. Richard Gatti screened 34,000 compounds utilizing a non-fluorescent, ATM-based transcription/translation assay to identify low molecular weight read-through compounds.[51] Twelve hits, termed small molecule read-through compounds (SMRTs), produced functional ATM protein from ATM-deficient cells, and displayed high read-through activity of three A-T associated PTCs at levels <10 μM. Two leading SMRTs, RTC13 and RTC14 displayed read-through of nonsense-mutated Duchenne muscular dystrophy mouse myotubes, effectively restoring dystrophin protein.[92] Further studies treated a Duchenne muscular dystrophy mouse model with RTC13. Both restoration of dystrophin protein and improved muscle function were observed.[93] While these *in vitro* and *in vivo* studies show great promise for SMRTs, further *in vivo* animal model experiments are needed to assess SMRT viability as a potential A-T therapeutic. Particularly, SMRT penetration of the blood-brain barrier is essential to be considered an effective A-T treatment option. Here, we propose the use of mass spectrometry imaging (MSI) to assess SMRT ability to cross the blood-brain barrier, and to further analyze biodistribution of these therapeutic compounds. The SMRT compounds utilized for this study are shown in Figure 1B.

MSI is a relatively new technology that has found application in the medical sciences. It employs an ionization technique, matrix-assisted laser desorption/ionization (MALDI), focusing a laser directly on a thin tissue section to ionize molecules within the tissue.[70] Each molecule is detected as a mass-to-charge ratio (m/z), with charge typically being equal to one. The user-defined m/z range allows for focus on specific

compound classes of interest, given a molecular weight range. The MALDI laser rasters across a designated sample area, in this study a thin tissue section of a mouse organ, and averages hundreds of spectra at thousands of coordinates throughout the section. The specific number of points is determined by the spatial resolution, typically in the tens-of to hundreds-of micrometer range. Software then compiles an average spectrum for the entire sample, and individual masses of interest can be selected, with their location within the sample digitally displayed. This effectively creates a chemical map of the tissue section, with the workflow shown in Figure 2. Spatially measuring proteins, lipids, and other biomolecules in clinically relevant tissues is a powerful tool for disease biomarker studies and for disease pathology.[3]

One area that has not been well addressed by these newer technologies is the study of small molecules. Important information for the development of new drug entities is biodistribution. Where does a new drug compound distribute in the body of an animal model? What are the metabolites of this new drug, and where do these metabolites accumulate? Traditional methods of visualizing biodistribution include radiolabeling or application of chemical tags to the new compounds – both strategies that require time-consuming chemical synthesis efforts.[3] MSI offers a means to circumvent these labor-intensive protocols, effectively eliminating the need for a tag or label. Here, we propose the use of MALDI-MSI for the study of SMRT distribution in an animal model, with emphasis of blood-brain barrier penetration analysis.

METHODS

Materials. SMRTs RTC13, BZ6, BZ16, 216, 216-3, 216-3 salt, 216-4, 216-5, and 216-6 were synthesized by the lab of Dr. Michael Jung (UCLA). Mesoporous silica

nanoparticles (MSNP) were synthesized by the lab of Dr. Jeffrey Zink (UCLA). Eosin Y, hematoxylin, and VectaShield hardset mounting medium were purchased from Fisher Scientific. Acetonitrile (ACN), α-Cyano-4-hydroxycinnamic acid (CHCA), 2,5-dihydroxybenzoic acid (DHB), dimethyl sulfoxide (DMSO), ethanol, formic acid (FA), glacial acetic acid, norharmane (NHM), titanium dioxide (TiO_2), trifluoroacetic acid (TFA), and xylene were purchased from Sigma-Aldrich.

BZ6 and BZ16 Animal Dosing. C57/Black 6 (BL6) and severe compromised immunodeficiency (SCID) mice were used. SMRTs BZ6 and BZ16 were administered at a dosage of 30 mg/kg over the course of 8 weeks for a total of 6 intraperitoneal injections. A total of 8 C57BL/6 and 8 SCID mice were used for each of the 3 treatment groups (vehicle, BZ6, and BZ16). Mice were bred and maintained in a strict defined-flora, pathogen-free environment in the American Association of Laboratory Animal Care–accredited animal facilities of the Department of Radiation Oncology, University of California Los Angeles. The University of California at Los Angeles Animal Care and Use Committee approved all experiments, which were done in accordance with all local and national guidelines for the care and use of animals.

BZ6 and BZ16 Organ Extraction. Mice were sacrificed using isofluorane, and the following organs were excised: brain, heart, kidney, liver, lung, and spleen. Each organ was excised and flash frozen in -50 ^{o}C isopentane before being stored at -80 ^{o}C until further experiments.

RTC13, 216, and 216-3 Animal Dosing. C57/Black 6 (BL6) mice were used. SMRTs RTC13, 216, and 216-3 were administered a single dosage of 30 mg/kg as intraperitoneal injections. A total of 20 C57BL/6 mice were used: 2 vehicle controls, 6

RTC13-dosed, 6 216-dosed, and 6 216-3-dosed. Mice were bred and maintained in a strict defined-flora, pathogen-free environment in the American Association of Laboratory Animal Care–accredited animal facilities of the Department of Radiation Oncology, University of California Los Angeles. The University of California at Los Angeles Animal Care and Use Committee approved all experiments, which were done in accordance with all local and national guidelines for the care and use of animals.

RTC13, 216, and 216-3 Organ Extraction. Mice were sacrificed at 0 h (vehicle), 2 h, 8 h, and 24 h using isofluorane, with 2 mice per drug sacrificed at each timepoint. The following organs were excised: brain, heart, kidney, liver, lung, and spleen. Each organ was excised and flash frozen in -50 ^{o}C isopentane before being stored at -80 ^{o}C until further experiments.

Tissue Preparation. Organs were sectioned on a Leica CM1850 Cryostat at a thickness of 16 μm. Brain, heart, kidney, liver, and spleen were sectioned at a temperature of -21 ^{o}C, while lung was sectioned at a temperature of -34 ^{o}C. All sections were thaw-mounted onto a glass slide, dried under vacuum at room temperature for 10 minutes, and subjected to a wash step consisting of 30 seconds suspended in a solution of 70% ethanol (where applicable). Slides were subsequently coated in a CHCA matrix at a concentration of 7 mg/mL in 50% ACN, 50% H_2O, and 0.1% TFA utilizing a Bruker ImagePrep or an HTX Technologies TM Sprayer.

Mass Spectrometry Imaging. All mass spectrometry (MS) and mass spectrometry imaging (MSI) were conducted on a Bruker Daltonics AutoFlex MALDI tandem time-of-flight (TOF/TOF) mass spectrometer equipped with a Smartbeam-II^{TM} Nd:YAG UV laser. A small molecule method was employed, covering the range of 0 to 1,000 m/z,

operating in the linear positive mode. MSI experiments were run at a spatial resolution of 200 to 400 μm, averaging 500 spectra at each raster point. All experiments were run utilizing Bruker Daltonics software Compass package: FlexControl and FlexImaging. Additional MS experiments were conducted on a Bruker Daltonics SolariX Fourier-transform ion cyclotron resonance mass spectrometer (FT-ICR-MS) equipped with a Smartbeam-II™ Nd:YAG UV Laser. All FT-ICR-MS data were collected using Bruker Daltonics software, SolariXControl.

Data Analysis. All MALDI-TOF/TOF-MS data analysis was conducted manually using Bruker Daltonics software, FlexAnalysis. All MALDI-TOF/TOF-MSI data analysis was conducted manually using Bruker Daltonics software, FlexImaging. All MALDI-FT-ICR-MS data analysis was conducted manually using Bruker Daltonics software, DataAnalysis.

Tissue Homogenization and Extraction. Organs from each treatment group and timepoint (where applicable) were homogenized using a 5 mL hand-held glass homogenizer. A tissue to water ratio of 1 g to 4 mL was used. Tissues were suspended in a given amount of water and pulverized for 30 s. From each homogenate stock, 50 μL were mixed with 150 μL of either 10 μM BZ6 (for BZ16, 512 2 h brain, 216 2 h brain, 216-3 2 h brain, and RTC13 2 h brain) or 10 μM 216-5 standard in ACN (all other organs, treatment groups, and timepoints), vortexed, and centrifuged for 10 min at 4,000 rpm. Supernatant was collected for future MS analysis.

LC-MS/MS Validation. Samples were run on a Proxeon ThermoScientific EASY nano liquid chromatography (nLC) system equipped with an Acclaim PepMap100 C18 76 μm x 2 cm NanoViper trap column with 3 μm particle size and 100 Å pore size and a

PepMapRSLC C18 75 μm x 15 cm analytical column with 2 μm particle size and 100 Å pore size. An aqueous mobile phase (A) was made up of 0.1% FA in H_2O, and an organic mobile phase (B) was made up of 0.1% FA in ACN. For each sample, 2 μL were injected onto the trap column, washed with 100% A for 5 minutes, and small molecules were eluted from the column with a gradient of 5-100% B over 5 minutes, and held at 100% B for 10 minutes at a flow rate of 5 μL/min. The nLC system is interfaced with a ThermoScientific Q Exactive™ hybrid quadrupole-orbitrap mass spectrometer.

LC-MS/MS Data Analysis. Data was analyzed and quantified using Thermo Xcalibur Qual and Quan Browser software. The molecular ions, $[M+H]^+$, for BZ6, BZ16, RTC13, 216, 216-3, and 216-5 were extracted within 10 ppm mass accuracy using Qual Broser to confirm their presence in tissue and determine approximate retention time (RT) window for elution. All analyte ions were extracted by their molecular ion m/z from the full MS scan of 200-2,000 m/z.

Histological Staining. Slides previously prepared for MSI were stained using hemotoxylin and eosin Y. Slides were washed in 2 changes of xylene for 10 mins, rehydrated in 2 changes of absolute ethanol, and placed into gradient ethanol baths of 95%, 80%, 70%, and 60% in H_2O for 2 mins per condition. Hematoxylin was applied drop-wise to cover each tissue section and allowed to stain for 3 mins. Slides were washed under flowing H_2O for 5 mins and rinsed in 95% ethanol, 10 dips per slide. Counterstain eosin Y at a concentration of 0.25% in 60% ethanol and 0.5% glacial acetic acid was added drop-wise to cover each tissue section and allowed to stain for 30 s. Slides were washed under flowing H_2O for 5 mins and rinsed in 95% ethanol, 5 s per slide, followed by washes through 2 changes of absolute ethanol for 30 s each and

2 changes of xylene for 2 min each. Slides were allowed to dry completely before placing one drop of VectaShield hardset mounting medium on each end of the slide and covering with a coverslip to permanently set the stain. Slides were air dried overnight at room temperature, and scanned at 20X or 40X resolution with an APERIO brightfield microscope.

RESULTS.

Observation of drugs on and off tissue. Prior to any dosing experiments, compound ionization was optimized both on and off tissue. Serial dilutions of RTC13, BZ6, BZ16, 216, 216-3, 216-4, 216-5, and 216-6 were spotted on a ground steel plate as well as control brain tissue sections. RTC13, BZ16, 216, 216-3, 216-4, 216-5, and 216-6 were spotted at concentrations of 50 mM, 500 μM, 50 μM, 5 μM, 500 nM, and 50 nM. BZ6 was spotted at concentrations of 10 mM, 100 μM, 10 μM, 1 μM, 100 nM, and 10 nM. Limits of detection assessed off-tissue were greater than those assessed on-tissue. SMRT compounds were also found to ionize efficiently without the need of a MALDI matrix; however, the limit of detection was severely impaired without the use of matrix and peaks were not observed below 50 mM for RTC13, BZ16, 216, 216-3, 216-4, 216-5, and 216-6 or 10 mM for BZ6. BZ6 had a lower limit of detection of 500 μM, shown in Figure 3. BZ16 had a lower limit of detection of 50 nM, shown in Figure 4. RTC13 had a lower limit of detection of 100 μM, shown in Figure 5. 216 had a lower limit of detection of 100 μM, shown in Figure 6.

Effects of tissue washing. Tissue washing in MSI experiments is highly optimized for proteins, peptides, and lipids. Water can be used to remove interfering salts and lipids, as can ethanol, resulting in enhanced signal from proteins and peptides with minimal

delocalization. While this protocol is typically reserved for protein and peptide analyses, we employed the use of a 30 s 70% ethanol in H_2O wash to remove lipids and enhance SMRT compound signals. We have previously shown this can be an effective method with small molecules if solvents of varying chemical properties are tested. We utilized the matrix-free ionization capabilities of the SMRT compounds to assess before and after mass spectrometry images of spotted standards on tissue. These data show that signal is enhanced after the washing of tissue sections with 70% ethanol for 30 s, and that delocalization of SMRT compounds does not occur, as shown in Figure 7 and Figure 8. The success of this wash step was further assessed in treated tissues. BZ16-treated tissues were analyzed both with and without a wash step. Tissues first washed with ethanol were found to have slightly higher signal intensity at the $[BZ16 + Na]^+$ peak than those that were not treated with ethanol.

BZ6 build-up at the site of injection. After sacrifice, designated organs were extracted from mice. During this extraction, we observed the build-up of a yellow substance in the abdominal cavity of all BZ6-treated mice, both C57BL/6 and SCID, as shown in Figure 9. This was likely BZ6 itself, indicating that it was not absorbed into the bloodstream. It was also determined the BZ6 exhibits extremely poor solubility in most solvents, including the commonly used DMSO. While MSI assessments for BZ6 were continued, the drug was no longer considered a viable option as a potential therapeutic. No such build-up was observed in BZ16-dosed mice.

BZ6 biodistribution in C57BL/6 mice. Biodistribution of BZ6 was first assessed in C57BL/6 mice. This group consisted of eight mice treated with BZ6. This particular

strain of laboratory mouse was considered a control, with no investigation of therapeutic effects associated with BZ6 treatment.

Brain. Due to the solubility issues associated with BZ6, as well as the build-up of the compound at the site of injection, it was likely that BZ6 did not cross the blood-brain barrier. Excised, frozen brains were divided into cerebellum and cerebrum sections, and analyzed separately. This assumption that BZ6 would not be found in the brain was confirmed via MSI experiments conducted with 8 BZ6-treated C57BL/6 brains. When compared to 8 brains from vehicle-treated C57BL/6 mice, no unique peaks were detected, indicating no differences between BZ6- and vehicle-treated brains.

Heart. The solubility and build-up issues with BZ6-treated mice similarly suggested that BZ6 did not enter the bloodstream. This assumption that BZ6 would not be found in the bloodstream, and thus not in heart tissue, though one unique peak was observed in C57BL/6 unwashed heart sections at 626 m/z. When compared to 8 hearts from vehicle-treated C57BL/6 mice, 1 unique peaks was detected, as shown in Figure 10.

Kidney. While drugs are typically found in the kidney, one of the filtering and excretory organs, BZ6 was not found to be present in kidney tissue. MSI experiments conducted with 16 BZ6-treated C57BL/6 kidneys indicated that BZ6 was absent, likely due to its inability to enter the bloodstream. When compared to 16 kidneys from vehicle-treated C57BL/6 mice, no unique peaks were detected, indicating no differences between BZ6- and vehicle-treated kidneys.

Liver. Similarly to the kidney, the liver is involved in filtering and excretion, and thus is typically a localization point for drugs given to animal models. BZ6 was not found to be present in liver tissue. MSI experiments conducted with 8 BZ6-treated C57BL/6 livers

indicated that intact BZ6 was absent, though one unique peak was observed. When compared to 8 liver samples from vehicle-treated C57BL/6 mice, one unique peak was detected at 988 m/z, shown in Figure 11.

Lung. Unless specifically targeted, the lung is an undesirable, off-target location for drug build-up. MSI experiments conducted with 8 BZ6-treated C57BL/6 lung samples indicated that intact BZ6 was absent, though one unique peak was observed. When compared to 8 lung samples from vehicle-treated C57BL/6 mice, one unique peak was detected at 749 m/z, shown in Figure 12.

Spleen. The final organ analyzed, spleen, is a filtering organ. Similarly to previously mentioned samples, BZ6 was not expected to be present in spleen. Again likely owing to its inability to enter the bloodstream, BZ6 was not found to be present in spleen tissue. When compared to 8 spleen samples from vehicle-treated C57BL/6 mice, no unique peaks were detected, indicating no differences between BZ6- and vehicle-treated spleen.

BZ6 biodistribution in SCID mice. Biodistribution of BZ6 was also assessed in severe combined immunodeficiency (SCID) mice. SCID is a genetic disorder that is characterized by an organism's compromised immune system, rendering it unable to elicit appropriate immune responses. SCID is caused by a SNP, specifically a premature termination codon in the gene coding for protein kinase, deoxyribonucleic acid (DNA)-dependent protein kinase (DNA-PK). This protein is involved in DNA repair, known to cooperate with ATM protein, and thus a deficiency results in the SCID genetic disorder in mice.

Brain. Due to the solubility issues associated with BZ6, as well as the build-up of the compound at the site of injection, it was expected that, similar to what was observed in C57BL/6 mice, BZ6 did not cross the blood-brain barrier. Excised, frozen brains were again divided into cerebellum and cerebrum sections, and analyzed separately. While the protonated or sodiated masses previously observed from BZ6 standard MALDI experiments were not observed, MSI experiments conducted with 8 BZ6-treated SCID brains did indicate several unique peaks. When compared to 8 brains from vehicle-treated SCID mice, 10 unique peaks were detected, indicating some differences between BZ6- and vehicle-treated brains. Five of these unique peaks were found in both unwashed and ethanol washed tissue sections from both cerebellum and cerebrum segments of the brain (84, 183, 736, 763, and 801 m/z), and 2 unique peaks were found in ethanol washed tissue sections from both cerebellum and cerebrum segments of the brain (357 and 371 m/z). One additional unique peak was observed in unwashed cerebrum sections (103 m/z); and, two additional unique peaks were observed in ethanol-washed cerebellum sections (169 and 789 m/z). Figures 13 through 21 show the spectra and virtual images for each of the above-mentioned peaks.

Heart. Similarly to BZ6-treated SCID brain samples, BZ6-treated SCID heart samples exhibited several unique peaks as observed by comparison of 8 hearts from BZ6-treated SCID mice to 8 vehicle-treated control SCID mice. This is in contrast to BZ6-treated C57BL/6 heart samples, although it should be noted that the protonated or sodiated masses previously observed from BZ6 standard MALDI experiments were not observed. Overall, 14 unique peaks were observed in heart sections, with 2 observed in both unwashed and ethanol-washed sections (103 and 183 m/z). An additional 5 unique

peaks were observed in ethanol-washed tissue sections (211, 249, 496, 523, and 734 m/z), and a further 7 unique peaks were observed in unwashed tissue sections (22, 71, 85, 131, 161, 221, and 616 m/z). There were no unique peaks observed in both ethanol-washed and unwashed heart sections, and no masses were found to correlate to the protonated or sodiated forms of BZ6 observed in MALDI standard runs. Figures 22 through 24 show the spectra and virtual images for each of the above-mentioned peaks.

Kidney. Despite the presence of several unique peaks in other organs, no unique peaks were observed in kidneys excised from BZ6-treated SCID mice. MSI experiments conducted with 16 BZ6-treated SCID kidneys indicated that BZ6 was absent when compared to 16 kidneys from vehicle-treated SCID mice.

Liver. BZ6-treated liver from SCID mice were found to contain unique peaks, as well, when 8 liver samples from dosed SCID mice were compared to liver samples from 8 vehicle-treated SCID mice. Unwashed sections exhibited 9 unique peaks (38, 103, 183, 249, 455, 615, 619, 764, 790, and 815 m/z), washed sections exhibited 2 unique peaks (145 and 161 m/z), and both sample preparation methods shared 2 unique peaks (85 and 103 m/z). The protonated or sodiated masses previously observed from BZ6 standard MALDI experiments were not observed. Figures 25 through 28 show the spectra and virtual images for each of the above-mentioned peaks.

Lung. A smaller number of unique peaks were observed in the lungs when compared to brain, heart, and liver samples. The 16 lung samples taken from BZ6-treated SCID mice were compared to 16 lung samples taken from vehicle-treated SCID mice. Unwashed sections exhibited 2 unique peaks (107 and 504 m/z) and washed sections were observed to have 2 unique peaks, as well (87 and 768 m/z). There were no unique

peaks observed in both ethanol-washed and unwashed lung sections, and no masses were found to correlate to the protonated or sodiated forms of BZ6 observed in MALDI standard runs. Figures 29 and 30 show the spectra and virtual images for each of the above-mentioned peaks.

Spleen. Spleen samples (8) taken from BZ6-treated SCID mice were compared to 8 spleen samples extracted from vehicle-treated SCID mice. Unwashed tissue sections were found to contain 1 unique peak at 626 m/z, and washed sections were observed to have 3 unique peaks (105, 226, and 254 m/z). There were no unique peaks observed in both ethanol-washed and unwashed spleen sections, and no masses were found to correlate to the protonated or sodiated forms of BZ6 observed in MALDI standard runs. Figure 31 show the spectra and virtual images for each of the above-mentioned peaks.

BZ16 distribution in C57BL/6 mice. Biodistribution of BZ16 was assessed in C57BL/6 mice. This group consisted of eight mice treated with BZ16. This particular strain of laboratory mouse was considered a control, with no investigation of therapeutic effects associated with BZ16 treatment.

Brain. Excised, frozen brains were divided into cerebellum and cerebrum sections, and analyzed separately. Thus, 8 cerebellum and 8 cerebrum sections from BZ16-treated C57BL/6 mice were compared to 8 cerebellum and 8 cerebrum sections from vehicle-treated C57BL/6 mice. Only 1 unique peak was observed, present in both the cerebellum and cerebrum sections of washed tissue only. This peak at 338 m/z is within the error range expected for the $[BZ16 + Na]^+$ peak, suggesting that BZ16 does cross the blood-brain barrier. Figure 32A shows localization of this peak to the cerebellum, and Figure 32B shows the average spectrum with the detected BZ16 peak.

Figures 33A-B show the slight increase in signal intensity after washing the tissue section with 70% ethanol for 30 s. Figure 34A shows localization of this peak to the cerebrum, and Figure 34B shows the average spectrum with the detected BZ16 peak.

Heart. It is suggested that BZ16 does enter the bloodstream and crosses the blood-brain barrier. This was further supported by the presence of a unique peak in unwashed heart tissue sections at 617 m/z, as shown in Figure 35. When 8 heart samples excised from BZ16-treated C57BL/6 mice were compared to 8 heart samples excised from vehicle-treated C57BL/6 mice, this unique peak observation arose. No unique peaks were observed in ethanol-washed sections. Additionally, no masses observed were found to correlate to the protonated or sodiated forms of BZ16 observed in MALDI standard runs.

Kidney. Despite the fact that the kidneys are filtering organs, no unique peaks were observed in kidneys excised from BZ16-treated C57BL/6 mice. MSI experiments conducted with 16 BZ16-treated C57BL/6 kidneys indicated that BZ16 was absent when compared to 16 kidneys from vehicle-treated C57BL/6 mice.

Liver. Unlike the kidneys, liver (a filtering organ) excised from BZ16-treated C57BL/6 mice exhibited 2 unique peaks when compared to C57BL/6 vehicle-treated mice. Ethanol-washed tissue sections were found to have peaks at 278 and 776 m/z, as shown in Figure 36. Unique peaks were not observed in unwashed liver tissue samples. None of the observed masses were found to correlate to the protonated or sodiated forms of BZ16 observed in MALDI standard runs.

Lung. Despite the presence of several unique peaks in other organs, no unique peaks were observed in lungs excised from BZ16-treated C57BL/6 mice. MSI experiments

conducted with 16 BZ16-treated C57BL/6 lungs indicated that BZ16 was absent when compared to 16 lungs from vehicle-treated C57BL/6 mice.

Spleen. Similar to the kidney, spleens excised from BZ16-treated C57BL/6 mice exhibited no unique peaks when compared to vehicle-treated C57BL/6 mice, indicating BZ16 was not present in the spleen. This is in contrast to the liver, another filtering organ.

BZ16 distribution in SCID mice. Biodistribution of BZ16 was also assessed in SCID mice. As previously mentioned, SCID is a genetic disorder that is caused by a premature termination codon in the gene coding for protein kinase, deoxyribonucleic acid (DNA)-dependent protein kinase (DNA-PK). This protein is involved in DNA repair, known to cooperate with ATM protein, and thus a deficiency results in the SCID genetic disorder in mice.

Brain. Excised, frozen brains taken from BZ6- and vehicle-treated SCID mice were again divided into cerebellum and cerebrum sections, and analyzed separately. While the protonated or sodiated masses previously observed from BZ16 standard MALDI experiments and C57 BZ16-treated brains were not observed, MSI experiments conducted with 8 BZ16-treated SCID brains did indicate several unique peaks. When compared to 8 brains from vehicle-treated SCID mice, 9 unique peaks were detected. One of these unique peaks, 224 m/z, was found in both unwashed and ethanol washed tissue sections from both cerebellum and cerebrum segments of the brain. Furthermore, 2 unique peaks were found in ethanol washed tissue sections from cerebellum (75 and 810 m/z) and no unique peaks were found in ethanol washed cerebrum segments of the brain. Two additional unique peaks were observed in unwashed cerebellum sections

(133 and 779 m/z); and, four additional unique peaks were observed in unwashed cerebrum sections (98, 126, 142, and 621 m/z). Figures 37 through 40 show the spectra and virtual images for each of the above-mentioned peaks.

Heart. BZ16-treated brains derived from SCID mice suggested that the compound entered the bloodstream. This was similarly observed in 8 heart samples excised from BZ16-treated SCID mice when compared to 8 vehicle-treated SCID mice. Overall, four unique peaks were identified. Ethanol-washed tissue sections exhibited 2 unique peaks (138 and 504 m/z), and unwashed heart sections were found to contain 2 unique peaks (116 and 165 m/z). There were no unique peaks observed in both ethanol-washed and unwashed heart sections, and no masses were found to correlate to the protonated or sodiated forms of BZ16 observed in MALDI standard runs. Figures 41 and 42 show the spectra and virtual images for each of the above-mentioned peaks.

Kidney. Although several unique peaks were detected in other filtering organs, only one unique peak was detected in kidneys excised from BZ16-treated SCID mice. After excision, 16 kidneys derived from BZ16-treated SCID mice were compared to 16 kidneys derived from vehicle-treated SCID mice. One unique peak at 149 m/z was observed in unwashed tissue sections; however, no masses observed matched to the protonated or sodiated forms of BZ16 observed in standard MALDI runs. Figure 43 shows the spectrum and virtual image for the above-mentioned peak.

Liver. Unlike kidney, several unique peaks were observed in liver samples taken from BZ16-treated SCID mice. When 8 liver samples excised from BZ16-treated SCID mice were compared to 8 liver samples excised from vehicle-treated SCID mice, 5 unique peaks were observed in unwashed tissue sections (104, 335, 463, 533, and 626 m/z).

The peak observed at 335 m/z is thought to be attributed to the sodiated form of BZ16 typically observed in standard MALDI runs; however, the protonated form was not observed. Figure 44 shows the spectra and virtual images for the above-mentioned peaks.

Lung. A smaller number of unique peaks were observed in the lungs when compared to brain, heart, and liver samples. The 16 lung samples taken from BZ16-treated SCID mice were compared to 16 lung samples taken from vehicle-treated SCID mice. Unwashed sections exhibited no unique peaks, ethanol-washed sections were observed to have 2 unique peaks (60 and 784 m/z), and both sample preparation methods shared a unique peak at 23 m/z. No detected masses corresponded to protonated or sodiated forms of BZ16 detected in MALDI standard experiments. Figures 45 and 46 show the spectra and virtual images for the above-mentioned peaks.

Spleen. Spleen sections were analyzed from SCID mice treated with BZ16. The 8 spleen samples taken from BZ16-treated mice were compared to 8 spleen samples excised from vehicle-treated SCID mice. One unique peak at 88 m/z was detected in treated mice, common to both unwashed and ethanol-washed tissue sections Unwashed sections exhibited 3 unique peaks (75, 232, and 254 m/z), while ethanol-washed tissue sections were found to have 1 unique peak at 786 m/z. No peaks were detected that corresponded to protonated or sodiated forms of BZ16 detected in MALDI standard experiments. Figures 47 and 48 show the spectra and virtual images for the above-mentioned peaks.

RTC13 biodistribution via MALDI-MSI. The distribution of RTC13 was observed in treated C57BL/6 mice at 3 varied timepoints. As seen with BZ6, some build-up of

RTC13 was observed at the site of injection within the abdominal cavity. While the amount of build-up was significantly less than that observed with BZ6, it was unclear whether this build-up indicated a lack of absorption into the bloodstream.

2 h Brain. Though RTC13 is the parent compound of BZ16, it was not detected in the brain at 2 h post-dose. Briefly, 2 intact brains from RTC13-treated C57BL/6 mice sacrificed at 2 h post-dose were compared to 2 intact brains excised from vehicle-treated C57BL/6 mice. No unique peaks were observed, indicating RTC13 did not penetrate the blood-brain barrier within 2 h of dosing.

2 h Heart. Further indication of a low bloodstream absorption came due to the absence of unique peaks detected in 2 heart samples excised from RTC13-treated C57BL/6 mice sacrificed at 2 h post-dose when compared to 2 vehicle-treated C57BL/6 mice.

2 h Kidney. Though one of the main filtering organs, RTC13 was not found in the kidneys. After analysis of 4 kidney samples from RTC13-treated mice sacrificed 2 h post-dosing compared to 4 kidney samples from vehicle-treated mice, no unique peaks were observed.

2 h Liver. Unlike kidney samples, the liver (another filtering organ) exhibited several unique peaks. At 2 h post-dosage, 4 kidneys were excised from 2 RTC13-treated C57BL/6 mice and compared to 4 kidneys excised from vehicle-treated C57BL/6 mice. A total of 4 unique peaks were observed (196, 209, 212, and 239 m/z). Peaks corresponding to the protonated and sodiated forms of RTC13 observed in standard MALDI runs were not detected via MSI. Figure 49 shows the spectra and virtual images for the above-mentioned peaks.

2 h Lung. RTC13 was not detected in the lungs at 2 h post-dose. Four lung samples excised from RTC13-treated C57BL/6 mice were compared to 4 lung samples excised from vehicle-treated C57BL/6 mice. No unique peaks were observed.

2 h Spleen. Similar to liver, unique peaks were observed in 2 spleen samples from RTC13-treated C57BL/6 mice when compared to 2 spleen samples from vehicle-treated C57BL/6 mice at 2 h post-dose. Two peaks were observed (154 and 191 m/z). Peaks corresponding to the protonated and sodiated forms of RTC13 observed in standard MALDI runs were not detected via MSI. Figure 50 shows the spectra and virtual images for the above-mentioned peaks.

8 h Brain. RTC13 was not detected in the brain at 8 h post-dose, either. As evidenced by 2 intact brains from RTC13-treated C57BL/6 mice sacrificed 8 h post-injection compared to 2 intact brains excised from vehicle-treated C57BL/6 mice. No unique peaks were observed, indicating RTC13 did not penetrate the blood-brain barrier within 8 h of dosing.

8 h Heart. At the 8 h post-dose time point, RTC13 was not detected in either of the 2 heart samples obtained from RTC13-treated C57BL/6 mice when compared to 2 heart samples excised from vehicle-treated C57BL/6 mice.

8 h Kidney. At 8 h post-dosing, no unique peaks were observed in 4 kidney samples derived from RTC13-treated C57BL/6 mice when compared to 4 kidney samples from vehicle-treated C57BL/6 mice.

8 h Liver. Similar to the 2 h time point, livers excised from 2 RTC13-treated C57BL/6 mice were compared to livers excised from 2 vehicle-treated C57BL/6 mice, and 3 unique peaks were observed (196, 212, and 239 m/z). Peaks corresponding to the

protonated and sodiated forms of RTC13 observed in standard MALDI runs were not detected via MSI. Figure 49 shows the spectra and virtual images for the above-mentioned peaks.

8 h Lung. At a sacrifice time point 8 h post-dose, RTC13 was still not detected in 4 lung samples excised from RTC13-treated C57BL/6 mice when compared to 4 lung samples excised from vehicle-treated C57BL/6 mice. No unique peaks were observed.

8 h Spleen. A unique peak was observed in 2 spleen samples from RTC13-treated C57BL/6 mice when compared to 2 spleen samples from vehicle-treated C57BL/6 mice at 8 h post-dose. One peak was detected at 191 m/z. Peaks corresponding to the protonated and sodiated forms of RTC13 observed in standard MALDI runs were not detected via MSI. Figure 50 shows the spectrum and virtual image for the above-mentioned peak.

24 h Brain. Finally, RTC13 was not detected in the brain at 24 h post-dose. As evidenced by 2 intact brains from RTC13-treated C57BL/6 mice sacrificed 24 h post-injection compared to 2 intact brains excised from vehicle-treated C57BL/6 mice. No unique peaks were observed, indicating RTC13 did not penetrate the blood-brain barrier within 24 h of dosing.

24 h Heart. After a full 24 h post-dose, RTC13 was still not detected in 2 heart samples excised from RTC13-treated C57BL/6 mice when compared to 2 heart samples from vehicle-treated C57BL/6 mice. This suggests that RTC13 does not readily enter the bloodstream.

24 h Kidney. At 24 h post-dosing, RTC13 was still not detected in 4 kidney samples taken from RTC13-treated C57BL/6 mice when compared to 4 kidney samples from

vehicle-treated C57BL/6 mice. This further suggests that RTC13 does not readily enter the bloodstream.

24 h Liver. At 24 h post-dosing, only one unique peak was detected in 2 liver samples taken from RTC13-treated C57BL/6 mice when compared to 2 liver samples from vehicle-treated C57BL/6 mice. This peak at 209 m/z was also observed in the 2 h time point, but was not observed in the 8 h time point. Peaks corresponding to the protonated and sodiated forms of RTC13 observed in standard MALDI runs were not detected via MSI. Figure 49 shows the spectrum and virtual image for the above-mentioned peak.

24 h Lung. As seen with several other organs, RTC13 was not detected in 4 lung samples excised from RTC13-treated C57BL/6 mice when compared to 4 lung samples taken from vehicle-treated C57BL/6 mice at 24 h post-dose.

24 h Spleen. Of the 2 unique peaks observed at 2 h post-dose, 154 m/z was observed in 2 spleen samples taken from RTC13-treated C57BL/6 mice when compared to 2 spleen samples from vehicle-treated C57BL/6 mice at 24 h post-dose. Peaks corresponding to the protonated and sodiated forms of RTC13 observed in standard MALDI runs were not detected via MSI. Figure 50 shows the spectrum and virtual image for the above-mentioned peak.

216 biodistribution via MALDI-MSI. The distribution of 216 was observed in treated C57BL/6 mice at 3 varied timepoints: 2 h, 8 h, and 24 h. This was assessed by MALDI-MSI of 6 different excised organs.

2 h Brain. Though 216 is similar in size and structure to the RTC-derived compounds, it was not detected in the brain at 2 h post-dose. Briefly, 2 intact brains from 216-treated

C57BL/6 mice sacrificed at 2 h post-dose were compared to 2 intact brains excised from vehicle-treated C57BL/6 mice. No unique peaks were observed, indicating 216 did not penetrate the blood-brain barrier within 2 h of dosing.

2 h Heart. No build-up at the site of injection was observed in 216-treated mice; however, no unique peaks were detected in the heart at 2 h post-dose. The 2 heart samples excised from 216-treated C57BL/6 mice were compared to 2 heart samples taken from vehicle-treated C57BL/6 mice.

2 h Kidney. No unique peaks were detected in the kidney at 2 h post-dose. The 4 kidney samples taken from 216-treated C57BL/6 mice were compared to 4 kidney samples excised from vehicle-treated C57BL/6 mice.

2 h Liver. No unique peaks were detected in the spleen at 2 h post-dose. The 2 liver samples taken from 216-treated C57BL/6 mice were compared to 2 liver samples excised from vehicle-treated C57BL/6 mice.

2 h Lung. No unique peaks were detected in the lungs at 2 h post-dose. The 4 lung samples taken from 216-treated C57BL/6 mice were compared to 4 lung samples excised from vehicle-treated C57BL/6 mice.

2 h Spleen. No unique peaks were detected in the spleen at 2 h post-dose. The 2 spleen samples taken from 216-treated C57BL/6 mice were compared to 2 spleen samples excised from vehicle-treated C57BL/6 mice.

8 h Brain. After sacrifice at 8 h post-dose, no unique peaks were observed, indicating 216 did not penetrate the blood-brain barrier within 8 h of dosing. Two intact brains from 216-treated C57BL/6 mice were compared to 2 intact brains excised from vehicle-treated C57BL/6 mice.

8 h Heart. No unique peaks were detected in the heart at 8 h post-dose. The 2 heart samples excised from 216-treated C57BL/6 mice were compared to 2 heart samples taken from vehicle-treated C57BL/6 mice.

8 h Kidney. No unique peaks were detected in the kidney at 8 h post-dose. The 4 kidney samples taken from 216-treated C57BL/6 mice were compared to 4 kidney samples excised from vehicle-treated C57BL/6 mice.

8 h Liver. No unique peaks were detected in the spleen at 8 h post-dose. The 2 liver samples taken from 216-treated C57BL/6 mice were compared to 2 liver samples excised from vehicle-treated C57BL/6 mice.

8 h Lung. No unique peaks were detected in the lungs at 8 h post-dose. The 4 lung samples taken from 216-treated C57BL/6 mice were compared to 4 lung samples excised from vehicle-treated C57BL/6 mice.

8 h Spleen. No unique peaks were detected in the spleen at 8 h post-dose. The 2 spleen samples taken from 216-treated C57BL/6 mice were compared to 2 spleen samples excised from vehicle-treated C57BL/6 mice.

24 h Brain. After sacrifice at 24 h post-dose, no unique peaks were observed. Two intact brains from 216-treated C57BL/6 mice were compared to 2 intact brains excised from vehicle-treated C57BL/6 mice. This suggested that 216 did not cross the blood-brain barrier.

24 h Heart. Finally, no unique peaks were detected in the heart at 24 h post-dose. The 2 heart samples excised from 216-treated C57BL/6 mice were compared to 2 heart samples taken from vehicle-treated C57BL/6 mice. This suggested that 216 did not effectively enter the bloodstream in a detectable amount.

24 h Kidney. No unique peaks were detected in the kidney at 24 h post-dose. The 4 kidney samples taken from 216-treated C57BL/6 mice were compared to 4 kidney samples excised from vehicle-treated C57BL/6 mice. This suggested that 216 is quickly eliminated from the body post-dose.

24 h Liver. No unique peaks were detected in the spleen at 24 h post-dose. The 2 liver samples taken from 216-treated C57BL/6 mice were compared to 2 liver samples excised from vehicle-treated C57BL/6 mice. This further suggested that 216 is quickly eliminated from the body post-dose, given its absence from the filtering organs.

24 h Lung. No unique peaks were detected in the lungs at 24 h post-dose. The 4 lung samples taken from 216-treated C57BL/6 mice were compared to 4 lung samples excised from vehicle-treated C57BL/6 mice. This further suggested that 216 did not effectively enter the bloodstream in a detectable amount.

24 h Spleen. No unique peaks were detected in the spleen at 2 h post-dose. The 2 spleen samples taken from 216-treated C57BL/6 mice were compared to 2 spleen samples excised from vehicle-treated C57BL/6 mice. This further suggested that 216 may have been quickly eliminated or excreted after dosing, given its absence from filtering organs.

216-3 biodistribution. The distribution of 216-3, a 216 derivative, was observed in treated C57BL/6 mice at 3 varied timepoints: 2 h, 8 h, and 24 h. This was assessed by MALDI-MSI of 6 different excised organs.

2 h Brain. Unlike the 216 parent compound data (which showed no unique peaks), 216-3 analyses of brains excised at 2 h post-dose yielded 3 unique peaks. Two intact brain

samples taken from 216-3-treated C57BL/6 mice were compared to 2 brains excised from vehicle-treated C57BL/6 mice. Peaks were observed at 210, 262, and 387 m/z.

2 h Heart. No build-up at the site of injection was observed in 216-3-treated mice; however, no unique peaks were detected in the heart at 2 h post-dose. The 2 heart samples excised from 216-3-treated C57BL/6 mice were compared to 2 heart samples taken from vehicle-treated C57BL/6 mice.

2 h Kidney. When 4 kidneys excised from 216-3-treated C57BL/6 mice were compared to 4 kidneys taken from vehicle-treated C57BL/6 mice, one unique peak was observed at 2 h post-dose. This peak was at 170 m/z, though peaks corresponding to the protonated and sodiated forms of 216-3 observed in standard MALDI runs were not detected via MSI.

2 h Liver. An additional peak was observed in liver samples taken from 2 216-3-treated C57BL/6 mice at 2 h post-dose when compared to 2 livers excised from vehicle-treated C57BL/6 mice. This peak was at 307 m/z, though peaks corresponding to the protonated and sodiated forms of 216-3 observed in standard MALDI runs were not detected via MSI.

2 h Lung. No unique peaks were detected in lung samples at 2 h post-dose. Four lung samples excised from 216-3-treated C57BL/6 mice were compared to 4 lung samples excised from vehicle-treated C57BL/6 mice.

2 h Spleen. Unlike kidney and liver samples, no unique peaks were detected in spleen samples. Two spleen samples excised from 216-3-treated C57BL/6 mice sacrificed at 2 h post-dose were compared to 2 spleen samples excised from vehicle-treated C57BL/6 mice.

8 h Brain. None of the peaks detected in brain at 2 h post-dose were detected in brain samples excised at 8 h post-dose. Two intact brain samples from 216-3-treated C57BL/6 mice were compared to 2 intact brain samples taken from vehicle-treated C57BL/6 mice, and no unique peaks were observed.

8 h Heart. While unique peaks were not observed in heart samples taken at 2 h post-dose, 2 unique peaks were observed when 2 heart samples excised from 216-3-treated C57BL/6 mice at 8 h post-dose were compared to 2 heart samples excised from vehicle-treated C57BL/6 mice. These peaks were detected at 179 and 350 m/z, though peaks corresponding to the protonated and sodiated forms of 216-3 observed in standard MALDI runs were not detected via MSI.

8 h Kidney. Similarly to kidneys examined at 2 h post-dose, 4 kidneys excised from 216-3-treated C57BL/6 mice were compared to 4 kidneys excised from vehicle-treated C57BL/6 mice indicated a unique peak observed at 170 m/z. Peaks corresponding to the protonated and sodiated forms of 216-3 observed in standard MALDI runs were not detected via MSI.

8 h Liver. Two liver samples excised from 216-3-treated C57BL/6 mice were compared to vehicle-treated C57BL/6 mice. A peak was detected at 307 m/z, which was also detected at 2 h post-dose. An additional unique peak was detected at 204 m/z. Peaks corresponding to the protonated and sodiated forms of 216-3 observed in standard MALDI runs were not detected via MSI.

8 h Lung. No unique peaks were detected in lung samples at 8 h post-dose. Four lung samples excised from 216-3-treated C57BL/6 mice were compared to 4 lung samples excised from vehicle-treated C57BL/6 mice.

8 h Spleen. Again unlike kidney and liver samples, no unique peaks were detected in spleen samples. Two spleen samples excised from 216-3-treated C57BL/6 mice sacrificed at 8 h post-dose were compared to 2 spleen samples excised from vehicle-treated C57BL/6 mice.

24 h Brain. While none of the unique peaks detected at 2 h post-dose were observed in 8 h post-dose mice, one of the peaks was detected in mice dosed with 216-3 and sacrificed at 24 h post-dose. Two intact brain samples taken from 216-3-treated C57BL/6 mice were compared to 2 intact brain samples excised from vehicle-treated C57BL/6 mice. A peak at 262 m/z was observed, though peaks corresponding to the protonated and sodiated forms of 216-3 observed in standard MALDI runs were not detected via MSI.

24 h Heart. Both unique peaks observed in mice sacrificed at 8 h post-dosed were observed in hearts taken from 2 216-3-treated C57BL/6 mice when compared to 2 hearts excised from vehicle-treated C57BL/6 mice. These peaks were detected at 179 and 350 m/z. An additional peak, unique to 24 h post-dose heart samples, was detected at 372 m/z. Peaks corresponding to the protonated and sodiated forms of 216-3 observed in standard MALDI runs were not detected via MSI.

24 h Kidney. Although a unique peak was observed in kidney samples at 2 h and 8 h post-dose, no unique peaks were detected at 24 h post-dose when 4 kidneys excised from 216-3-treated C57BL/6 mice were compared to 4 kidneys taken from vehicle-treated C57BL/6 mice.

24 h Liver. Although unique peaks was observed in liver samples at 2 h and 8 h post-dose, no unique peaks were detected at 24 h post-dose when 2 liver samples excised

from 216-3-treated C57BL/6 mice were compared to 2 liver samples taken from vehicle-treated C57BL/6 mice. This suggests 216-3 may be cleared prior to 24 h by the filtering organs.

24 h Lung. No unique peaks were detected in lung samples at 24 h post-dose. Four lung samples excised from 216-3-treated C57BL/6 mice were compared to 4 lung samples excised from vehicle-treated C57BL/6 mice.

24 h Spleen. No unique peaks were detected in spleen samples. Two spleen samples excised from 216-3-treated C57BL/6 mice sacrificed at 24 h post-dose were compared to 2 spleen samples excised from vehicle-treated C57BL/6 mice.

BZ6 Detection by LC-MS/MS. Excised organs from 1 BZ6-treated C57BL/6 mouse (specimen 11) and 1 vehicle-treated C57BL/6 mouse (specimen 5) were individually homogenized with water, proteins were crashed out with ACN, and resulting supernatant was run via LC-MS/MS using previously mentioned methods. 216-5 (419.1284 m/z) was utilized as an internal standard, spiked in during homogenization and prior to extraction. Extracted ion chromatograms (XIC) were obtained for the intact, protonated masses of each compound.

Brain. Intact BZ6 was not detected in the brain using MALDI-MSI, and it was also not detected in extracted brain homogenate. The 216-5 standard eluted at 8.80 min. While several peaks were observed during the chromatographic run, BZ6 was not, as shown in the XIC, and the lack of an accurate mass in the mass spectrum. A brain sample taken from BZ6-treated C57BL/6 mouse 11 was compared to a brain sample taken from vehicle-treated C57BL/6 mouse 5.

Heart. Intact BZ6 was not detected in the heart via MALDI-MSI, and was absent from extracted heart homogenate, as well. The 216-5 standard eluted at 8.80 min. While several peaks were observed during the chromatographic run, BZ6 was not, as shown in the XIC and the lack of an accurate mass in the mass spectrum. A heart sample taken from BZ6-treated C57BL/6 mouse 11 was compared to a heart sample taken from vehicle-treated C57BL/6 mouse 5.

Kidney. Intact BZ6 was not detected in the kidney via MALDI-MSI, and was not detected in extracted kidney homogenate, as well. The 216-5 standard eluted at 8.82 min. While several peaks were observed during the chromatographic run, BZ6 was not, as shown in the XIC and the lack of an accurate mass in the mass spectrum. A kidney sample taken from BZ6-treated C57BL/6 mouse 11 was compared to a kidney sample taken from vehicle-treated C57BL/6 mouse 5.

Liver. Intact BZ6 was not detected in the liver via MALDI-MSI, and was not detected in extracted liver homogenate, as well. The 216-5 standard eluted at 8.76 min. While several peaks were observed during the chromatographic run, BZ6 was not, as shown in the XIC and the lack of an accurate mass in the mass spectrum. A liver sample taken from BZ6-treated C57BL/6 mouse 11 was compared to a liver sample taken from vehicle-treated C57BL/6 mouse 5.

Lung. Intact BZ6 was not detected in the lung via MALDI-MSI, and was not detected in extracted lung homogenate, as well. The 216-5 standard eluted at 8.78 min. While several peaks were observed during the chromatographic run, BZ6 was not, as shown in the XIC and the lack of an accurate mass in the mass spectrum. A lung sample taken

from BZ6-treated C57BL/6 mouse 11 was compared to a lung sample taken from vehicle-treated C57BL/6 mouse 5.

Spleen. Intact BZ6 was not detected in the spleen via MALDI-MSI, but was detected in the extracted spleen homogenate. The 216-5 standard eluted at 8.77 min, and the BZ6 peak eluted at 8.33 min at 239.0238 m/z (2.09 ppm mass accuracy), as shown in Figure 51. A spleen sample taken from BZ6-treated C57BL/6 mouse 11 was compared to a spleen sample taken from vehicle-treated C57BL/6 mouse 5. An MS/MS spectrum was not able to be attained; however, the observed mass was well within a mass accuracy of 10 ppm.

BZ16 Detection by LC-MS/MS. Excised organs from 1 BZ16-treated C57BL/6 mouse (specimen 21) and 1 vehicle-treated C57BL/6 mouse (specimen 5) were individually homogenized with water, proteins were crashed out with ACN, and resulting supernatant was run via LC-MS/MS using previously mentioned methods. 216-5 (419.1284 m/z) was utilized as an internal standard for heart, kidney, liver, lung, and spleen samples, spiked in during homogenization and prior to extraction. BZ6 (239.0233 m/z) was utilized as an internal standard for brain samples, spiked in during homogenization and prior to extraction. Extracted ion chromatograms (XIC) were obtained for the intact, protonated masses of each compound.

Brain. Intact BZ16 was detected in the brain via MALDI-MSI in its sodiated form, and confirmed by MALDI-TOF/TOF as shown in Figure 52. BZ16 was also detected in the extracted brain homogenate, though in its protonated form, as shown in Figure 53. This was expected, as LC-MS/MS runs of the BZ16 standard indicated a strong peak corresponding to the protonated form (eluting at 7.84 min) and limited ionization of the

sodiated form. Here, BZ6 was utilized as a standard and eluted at 6.95 min. BZ16 eluted at 7.82 min with a measured mass of 314.0763 m/z (2.86 ppm mass accuracy). The observed mass was well within a mass accuracy of 10 ppm. MS/MS of this peak confirmed it as BZ16, as the characteristic fragment mass at 202.0492 m/z was observed. This mass corresponded to a loss of $C_4H_3N_2O_2$, as shown in Figure 54. A brain sample taken from BZ16-treated C57BL/6 mouse 21 was compared to a brain sample taken from vehicle-treated C57BL/6 mouse 5.

Heart. Intact BZ16 was not detected in the heart via MALDI-MSI, and was not detected in extracted heart homogenate, as well. The 216-5 standard eluted at 8.78 min. While several peaks were observed during the chromatographic run, BZ16 was not, as shown in the XIC and the lack of an accurate mass in the mass spectrum. A heart sample taken from BZ16-treated C57BL/6 mouse 21 was compared to a heart sample taken from vehicle-treated C57BL/6 mouse 5.

Kidney. Intact BZ16 was not detected in the kidney via MALDI-MSI, and was not detected in extracted kidney homogenate, as well. The 216-5 standard eluted at 8.79 min. While several peaks were observed during the chromatographic run, BZ16 was not, as shown in the XIC and the lack of an accurate mass in the mass spectrum. A kidney sample taken from BZ16-treated C57BL/6 mouse 21 was compared to a kidney sample taken from vehicle-treated C57BL/6 mouse 5.

Liver. Intact BZ16 was not detected in the liver via MALDI-MSI, and was not detected in extracted liver homogenate, as well. The 216-5 standard eluted at 8.79 min. While several peaks were observed during the chromatographic run, BZ16 was not, as shown in the XIC and the lack of an accurate mass in the mass spectrum. A low intensity peak

within 10 ppm of the expected protonated BZ16 m/z was observed; however, the lack of isotopes and a defined peak in the XIC eliminated this mass from consideration. A liver sample taken from BZ16-treated C57BL/6 mouse 21 was compared to a liver sample taken from vehicle-treated C57BL/6 mouse 5.

Lung. Intact BZ16 was not detected in the lung via MALDI-MSI, and was not detected in extracted lung homogenate, as well. The 216-5 standard eluted at 8.79 min. While several peaks were observed during the chromatographic run, BZ16 was not, as shown in the XIC and the lack of an accurate mass in the mass spectrum. A lung sample taken from BZ16-treated C57BL/6 mouse 21 was compared to a lung sample taken from vehicle-treated C57BL/6 mouse 5.

Spleen. Intact BZ16 was not detected in the spleen via MALDI-MSI, and was not detected in extracted spleen homogenate, as well. The 216-5 standard eluted at 8.75 min. While several peaks were observed during the chromatographic run, BZ16 was not, as shown in the XIC and the lack of an accurate mass in the mass spectrum. A spleen sample taken from BZ16-treated C57BL/6 mouse 21 was compared to a spleen sample taken from vehicle-treated C57BL/6 mouse 5.

RTC13 Detection by LC-MS/MS. Excised organs from 3 RTC13-treated C57BL/6 mice (specimen 2h-M1, 8h-M1, and 24h-M1) and 1 vehicle-treated C57BL/6 mouse (specimen 0h-M1) were individually homogenized with water, proteins were crashed out with ACN, and resulting supernatant was run via LC-MS/MS using previously mentioned methods. 216-5 (419.1284 m/z) was utilized as an internal standard for all heart, kidney, liver, lung, and spleen samples as well as 8 h and 24 h brain samples, spiked in during homogenization and prior to extraction. BZ6 (239.0233 m/z) was utilized as an internal

standard for 2 h brain samples, spiked in during homogenization and prior to extraction. Extracted ion chromatograms (XIC) were obtained for the intact, protonated masses of each compound.

2 h Brain. Intact RTC13 was not detected in the brain at 2 h post-dose via MALDI-MSI, but was detected in the extracted brain homogenate. The BZ6 standard eluted at 6.92 min, and the RTC13 peak eluted at 8.92 min at 316.0377 m/z (3.16 ppm mass accuracy), though the peak was broad, as shown in Figure 55. A brain sample taken from RTC13-treated C57BL/6 mouse 2h-M1 was compared to a brain sample taken from vehicle-treated C57BL/6 mouse 0h-M1. An MS/MS spectrum was not able to be attained due to low intensity of the eluted peak; however, the observed mass was well within a mass accuracy of 10 ppm.

2 h Heart. Intact RTC13 was not detected in the heart at 2 h post-dosevia MALDI-MSI, and was not detected in extracted heart homogenate, as well. The 216-5 standard eluted at 8.78 min. While several peaks were observed during the chromatographic run, RTC13 was not, as shown in the XIC and the lack of an accurate mass in the mass spectrum. A heart sample taken from RTC13-treated C57BL/6 mouse 2h-M1 was compared to a heart sample taken from vehicle-treated C57BL/6 mouse 0h-M1.

2 h Kidney. Intact RTC13 was not detected in the kidney at 2 h post-dose via MALDI-MSI, and was not detected in extracted kidney homogenate, as well. The 216-5 standard eluted at 8.77 min. While several peaks were observed during the chromatographic run, RTC13 was not, as shown in the XIC and the lack of an accurate mass in the mass spectrum. A kidney sample taken from RTC13-treated C57BL/6

mouse 2h-M1 was compared to a kidney sample taken from vehicle-treated C57BL/6 mouse 0h-M1.

2 h Liver. Intact RTC13 was not detected in the liver at 2 h post-dose via MALDI-MSI, and was not detected in extracted liver homogenate, as well. The 216-5 standard eluted at 8.78 min. While several peaks were observed during the chromatographic run, RTC13 was not, as shown in the XIC and the lack of an accurate mass in the mass spectrum. A liver sample taken from RTC13-treated C57BL/6 mouse 2h-M1 was compared to a liver sample taken from vehicle-treated C57BL/6 mouse 0h-M1.

2 h Lung. Intact RTC13 was not detected in the lung at 2 h post-dose via MALDI-MSI, and was not detected in extracted lung homogenate, as well. The 216-5 standard eluted at 8.76 min. While several peaks were observed during the chromatographic run, RTC13 was not, as shown in the XIC and the lack of an accurate mass in the mass spectrum. A lung sample taken from RTC13-treated C57BL/6 mouse 2h-M1 was compared to a lung sample taken from vehicle-treated C57BL/6 mouse 0h-M1.

2 h Spleen. Intact RTC13 was not detected in the spleen at 2 h post-dose via MALDI-MSI, and was not detected in extracted spleen homogenate, as well. The 216-5 standard eluted at 8.78 min. While several peaks were observed during the chromatographic run, RTC13 was not, as shown in the XIC and the lack of an accurate mass in the mass spectrum. A spleen sample taken from RTC13-treated C57BL/6 mouse 2h-M1 was compared to a spleen sample taken from vehicle-treated C57BL/6 mouse 0h-M1.

8 h Brain. Intact RTC13 was not detected in the brain at 8 h post-dose via MALDI-MSI, and was not detected in extracted brain homogenate, as well. The 216-5 standard

eluted at 8.78 min. While several peaks were observed during the chromatographic run, RTC13 was not, as shown in the XIC and the lack of an accurate mass in the mass spectrum. A brain sample taken from RTC13-treated C57BL/6 mouse 8h-M1 was compared to a brain sample taken from vehicle-treated C57BL/6 mouse 0h-M1.

8 h Heart. Intact RTC13 was not detected in the heart at 8 h post-dose via MALDI-MSI, and was not detected in extracted heart homogenate, as well. The 216-5 standard eluted at 8.78 min. While several peaks were observed during the chromatographic run, RTC13 was not, as shown in the XIC and the lack of an accurate mass in the mass spectrum. A heart sample taken from RTC13-treated C57BL/6 mouse 8h-M1 was compared to a heart sample taken from vehicle-treated C57BL/6 mouse 0h-M1.

8 h Kidney. Intact RTC13 was not detected in the kidney at 8 h post-dose via MALDI-MSI, however, a broad peak eluted at 10.12 min in extracted kidney homogenate. The 216-5 standard eluted at 8.73 min. A low abundance peak was observed at 316.0386 m/z (0.31 ppm mass accuracy), as shown in Figure 56, within a 10 ppm mass accuracy limit, though its lowered intensity did not allow for MS/MS confirmation. A kidney sample taken from RTC13-treated C57BL/6 mouse 8h-M1 was compared to a kidney sample taken from vehicle-treated C57BL/6 mouse 0h-M1.

8 h Liver. Intact RTC13 was not detected in the liver at 8 h post-dose via MALDI-MSI, and was not detected in extracted liver homogenate, as well. The 216-5 standard eluted at 8.76 min. While several peaks were observed during the chromatographic run, RTC13 was not, as shown in the XIC and the lack of an accurate mass in the mass spectrum. A liver sample taken from RTC13-treated C57BL/6 mouse 8h-M1 was compared to a liver sample taken from vehicle-treated C57BL/6 mouse 0h-M1.

8 h Lung. Intact RTC13 was not detected in the lung at 8 h post-dose via MALDI-MSI, and was not detected in extracted lung homogenate, as well. The 216-5 standard eluted at 8.76 min. While several peaks were observed during the chromatographic run, RTC13 was not, as shown in the XIC and the lack of an accurate mass in the mass spectrum. A lung sample taken from RTC13-treated C57BL/6 mouse 8h-M1 was compared to a lung sample taken from vehicle-treated C57BL/6 mouse 0h-M1.

8 h Spleen. Intact RTC13 was not detected in the spleen at 8 h post-dose via MALDI-MSI, and was not detected in extracted spleen homogenate, as well. The 216-5 standard eluted at 8.76 min. While several peaks were observed during the chromatographic run, RTC13 was not, as shown in the XIC and the lack of an accurate mass in the mass spectrum. A spleen sample taken from RTC13-treated C57BL/6 mouse 8h-M1 was compared to a spleen sample taken from vehicle-treated C57BL/6 mouse 0h-M1.

24 h Brain. Intact RTC13 was not detected in the brain at 24 h post-dose via MALDI-MSI, and was not detected in extracted brain homogenate, as well. The 216-5 standard eluted at 8.75 min. While several peaks were observed during the chromatographic run, RTC13 was not, as shown in the XIC and the lack of an accurate mass in the mass spectrum. A brain sample taken from RTC13-treated C57BL/6 mouse 24h-M1 was compared to a brain sample taken from vehicle-treated C57BL/6 mouse 0h-M1.

24 h Heart. Intact RTC13 was not detected in the heart at 24 h post-dose via MALDI-MSI, and was not detected in extracted heart homogenate, as well. The 216-5 standard eluted at 8.76 min. While several peaks were observed during the chromatographic run, RTC13 was not, as shown in the XIC and the lack of an accurate mass in the mass

spectrum. A heart sample taken from RTC13-treated C57BL/6 mouse 24h-M1 was compared to a heart sample taken from vehicle-treated C57BL/6 mouse 0h-M1.

24 h Kidney. Intact RTC13 was not detected in the kidney at 24 h post-dose via MALDI-MSI, and was not detected in extracted kidney homogenate, as well. The 216-5 standard eluted at 8.74 min. While several peaks were observed during the chromatographic run, RTC13 was not, as shown in the XIC and the lack of an accurate mass in the mass spectrum. A kidney sample taken from RTC13-treated C57BL/6 mouse 24h-M1 was compared to a kidney sample taken from vehicle-treated C57BL/6 mouse 0h-M1.

24 h Liver. Intact RTC13 was not detected in the liver at 24 h post-dose via MALDI-MSI, but was detected in the extracted liver homogenate. The 216-5 standard eluted at 8.76 min, and the RTC13 peak eluted at 10.14 min at 316.0382 m/z (1.58 ppm mass accuracy), though the peak was broad, as shown in Figure 57. A liver sample taken from RTC13-treated C57BL/6 mouse 24h-M1 was compared to a liver sample taken from vehicle-treated C57BL/6 mouse 0h-M1. An MS/MS spectrum was not able to be attained due to low intensity of the eluted peak; however, the observed mass was well within a mass accuracy of 10 ppm.

24 h Lung. Intact RTC13 was not detected in the lung at 24 h post-dose via MALDI-MSI, but was detected in the extracted liver homogenate. The 216-5 standard eluted at 8.76 min, and the RTC13 peak eluted at 10.17 min at 316.0380 m/z (2.21 ppm mass accuracy), though the peak was broad, as shown in Figure 58. A lung sample taken from RTC13-treated C57BL/6 mouse 24h-M1 was compared to a lung sample taken from vehicle-treated C57BL/6 mouse 0h-M1. An MS/MS spectrum was not able to be

attained due to low intensity of the eluted peak; however, the observed mass was well within a mass accuracy of 10 ppm.

24 h Spleen. Intact RTC13 was not detected in the spleen at 24 h post-dose via MALDI-MSI, but was detected in the extracted spleen homogenate. The 216-5 standard eluted at 8.74 min, and the RTC13 peak eluted at 10.14 min at 316.0381 m/z (1.89 ppm mass accuracy), though the peak was broad, as shown in Figure 59. A spleen sample taken from RTC13-treated C57BL/6 mouse 24h-M1 was compared to a spleen sample taken from vehicle-treated C57BL/6 mouse 0h-M1. An MS/MS spectrum was not able to be attained due to low intensity of the eluted peak; however, the observed mass was well within a mass accuracy of 10 ppm.

216 Detection by LC-MS/MS. Excised organs from 3 216-treated C57BL/6 mice (specimen 2h-M1, 8h-M1, and 24h-M1) and 1 vehicle-treated C57BL/6 mouse (specimen 0h-M1) were individually homogenized with water, proteins were crashed out with ACN, and resulting supernatant was run via LC-MS/MS using previously mentioned methods. 216-5 (419.1284 m/z) was utilized as an internal standard for all heart, kidney, liver, lung, and spleen samples as well as 8 h and 24 h brain samples, spiked in during homogenization and prior to extraction. BZ6 (239.0233 m/z) was utilized as an internal standard for 2 h brain samples, spiked in during homogenization and prior to extraction. Extracted ion chromatograms (XIC) were obtained for the intact, protonated masses of each compound.

2 h Brain. Intact 216 was not detected in the brain at 2 h post-dose via MALDI-MSI, but was detected in the extracted brain homogenate. The BZ6 standard eluted at 6.80 min, and the 216 peak eluted at 9.62min at 436.1220 m/z (4.12 ppm mass accuracy), as

shown in Figure 60. A brain sample taken from 216-treated C57BL/6 mouse 2h-M1 was compared to a brain sample taken from vehicle-treated C57BL/6 mouse 0h-M1. An MS/MS spectrum was not able to be attained; however, the observed mass was well within a mass accuracy of 10 ppm.

2 h Heart. Intact 216 was not detected in the heart at 2 h post-dose via MALDI-MSI, and was not detected in extracted heart homogenate, as well. The 216-5 standard eluted at 8.75 min. While several peaks were observed during the chromatographic run, 216 was not, as shown in the XIC and the lack of an accurate mass in the mass spectrum. A heart sample taken from 216-treated C57BL/6 mouse 2h-M1 was compared to a heart sample taken from vehicle-treated C57BL/6 mouse 0h-M1.

2 h Kidney. Intact 216 was not detected in the kidney at 2 h post-dose via MALDI-MSI, and was not detected in extracted kidney homogenate, as well. The 216-5 standard eluted at 8.74 min. While several peaks were observed during the chromatographic run, 216 was not, as shown in the XIC and the lack of an accurate mass in the mass spectrum. A kidney sample taken from 216-treated C57BL/6 mouse 2h-M1 was compared to a kidney sample taken from vehicle-treated C57BL/6 mouse 0h-M1.

2 h Liver. Intact 216 was not detected in the liver at 2 h post-dose via MALDI-MSI, and was not detected in extracted liver homogenate, as well. The 216-5 standard eluted at 8.76 min. While several peaks were observed during the chromatographic run, 216 was not, as shown in the XIC and the lack of an accurate mass in the mass spectrum. A liver sample taken from 216-treated C57BL/6 mouse 2h-M1 was compared to a liver sample taken from vehicle-treated C57BL/6 mouse 0h-M1.

2 h Lung. Intact 216 was not detected in the lung at 2 h post-dose via MALDI-MSI, and was not detected in extracted lung homogenate, as well. The 216-5 standard eluted at 8.73 min. While several peaks were observed during the chromatographic run, 216 was not, as shown in the XIC and the lack of an accurate mass in the mass spectrum. A lung sample taken from 216-treated C57BL/6 mouse 2h-M1 was compared to a lung sample taken from vehicle-treated C57BL/6 mouse 0h-M1.

2 h Spleen. Intact 216 was not detected in the spleen at 2 h post-dose via MALDI-MSI, and was not detected in extracted spleen homogenate, as well. The 216-5 standard eluted at 8.76 min. While several peaks were observed during the chromatographic run, 216 was not, as shown in the XIC and the lack of an accurate mass in the mass spectrum. A spleen sample taken from 216-treated C57BL/6 mouse 2h-M1 was compared to a spleen sample taken from vehicle-treated C57BL/6 mouse 0h-M1.

8 h Brain. Intact 216 was not detected in the brain at 8 h post-dose via MALDI-MSI, and was not detected in extracted brain homogenate, as well. The 216-5 standard eluted at 8.75 min. While several peaks were observed during the chromatographic run, 216 was not, as shown in the XIC and the lack of an accurate mass in the mass spectrum. A brain sample taken from 216-treated C57BL/6 mouse 8h-M1 was compared to a brain sample taken from vehicle-treated C57BL/6 mouse 0h-M1.

8 h Heart. Intact 216 was not detected in the heart at 8 h post-dose via MALDI-MSI, and was not detected in extracted heart homogenate, as well. The 216-5 standard eluted at 8.76 min. While several peaks were observed during the chromatographic run, 216 was not, as shown in the XIC and the lack of an accurate mass in the mass spectrum. A

heart sample taken from 216-treated C57BL/6 mouse 8h-M1 was compared to a heart sample taken from vehicle-treated C57BL/6 mouse 0h-M1.

8 h Kidney. Intact 216 was not detected in the kidney at 8 h post-dose via MALDI-MSI, and was not detected in extracted kidney homogenate, as well. The 216-5 standard eluted at 8.76 min. While several peaks were observed during the chromatographic run, 216 was not, as shown in the XIC and the lack of an accurate mass in the mass spectrum. A kidney sample taken from 216-treated C57BL/6 mouse 8h-M1 was compared to a kidney sample taken from vehicle-treated C57BL/6 mouse 0h-M1.

8 h Liver. Intact 216 was not detected in the liver at 8 h post-dose via MALDI-MSI, and was not detected in extracted liver homogenate, as well. The 216-5 standard eluted at 8.75 min. While several peaks were observed during the chromatographic run, 216 was not, as shown in the XIC and the lack of an accurate mass in the mass spectrum. A liver sample taken from 216-treated C57BL/6 mouse 8h-M1 was compared to a liver sample taken from vehicle-treated C57BL/6 mouse 0h-M1.

8 h Lung. Intact 216 was not detected in the lung at 8 h post-dose via MALDI-MSI, and was not detected in extracted lung homogenate, as well. The 216-5 standard eluted at 8.76 min. While several peaks were observed during the chromatographic run, 216 was not, as shown in the XIC and the lack of an accurate mass in the mass spectrum. A lung sample taken from 216-treated C57BL/6 mouse 8h-M1 was compared to a lung sample taken from vehicle-treated C57BL/6 mouse 0h-M1.

8 h Spleen. Intact 216 was not detected in the spleen at 8 h post-dose via MALDI-MSI, and was not detected in extracted spleen homogenate, as well. The 216-5 standard eluted at 8.76 min. While several peaks were observed during the chromatographic run,

216 was not, as shown in the XIC and the lack of an accurate mass in the mass spectrum. A spleen sample taken from 216-treated C57BL/6 mouse 8h-M1 was compared to a spleen sample taken from vehicle-treated C57BL/6 mouse 0h-M1.

24 h Brain. Intact 216 was not detected in the brain at 24 h post-dose via MALDI-MSI, and was not detected in extracted brain homogenate, as well. The 216-5 standard eluted at 8.75 min. While several peaks were observed during the chromatographic run, 216 was not, as shown in the XIC and the lack of an accurate mass in the mass spectrum. A brain sample taken from 216-treated C57BL/6 mouse 24h-M1 was compared to a brain sample taken from vehicle-treated C57BL/6 mouse 0h-M1.

24 h Heart. Intact 216 was not detected in the heart at 24 h post-dose via MALDI-MSI, and was not detected in extracted heart homogenate, as well. The 216-5 standard eluted at 8.77 min. While several peaks were observed during the chromatographic run, 216 was not, as shown in the XIC and the lack of an accurate mass in the mass spectrum. A heart sample taken from 216-treated C57BL/6 mouse 24h-M1 was compared to a heart sample taken from vehicle-treated C57BL/6 mouse 0h-M1.

24 h Kidney. Intact 216 was not detected in the kidney at 24 h post-dose via MALDI-MSI, and was not detected in extracted kidney homogenate, as well. The 216-5 standard eluted at 8.76 min. While several peaks were observed during the chromatographic run, 216 was not, as shown in the XIC and the lack of an accurate mass in the mass spectrum. A kidney sample taken from 216-treated C57BL/6 mouse 24h-M1 was compared to a kidney sample taken from vehicle-treated C57BL/6 mouse 0h-M1.

24 h Liver. Intact 216 was not detected in the liver at 24 h post-dose via MALDI-MSI, and was not detected in extracted liver homogenate, as well. The 216-5 standard eluted at 8.75 min. While several peaks were observed during the chromatographic run, 216 was not, as shown in the XIC and the lack of an accurate mass in the mass spectrum. A liver sample taken from 216-treated C57BL/6 mouse 24h-M1 was compared to a liver sample taken from vehicle-treated C57BL/6 mouse 0h-M1.

24 h Lung. Intact 216 was not detected in the lung at 24 h post-dose via MALDI-MSI, and was not detected in extracted lung homogenate, as well. The 216-5 standard eluted at 8.74 min. While several peaks were observed during the chromatographic run, 216 was not, as shown in the XIC and the lack of an accurate mass in the mass spectrum. A lung sample taken from 216-treated C57BL/6 mouse 24h-M1 was compared to a lung sample taken from vehicle-treated C57BL/6 mouse 0h-M1.

24 h Spleen. Intact 216 was not detected in the spleen at 24 h post-dose via MALDI-MSI, and was not detected in extracted spleen homogenate, as well. The 216-5 standard eluted at 8.76 min. While several peaks were observed during the chromatographic run, 216 was not, as shown in the XIC and the lack of an accurate mass in the mass spectrum. A spleen sample taken from 216-treated C57BL/6 mouse 24h-M1 was compared to a spleen sample taken from vehicle-treated C57BL/6 mouse 0h-M1.

216-3 Detection by LC-MS/MS. Excised organs from 3 216-3-treated C57BL/6 mice (specimen 2h-M1, 8h-M1, and 24h-M1) and 1 vehicle-treated C57BL/6 mouse (specimen 0h-M1) were individually homogenized with water, proteins were crashed out with ACN, and resulting supernatant was run via LC-MS/MS using previously mentioned

methods. 216-5 (419.1284 m/z) was utilized as an internal standard for all heart, kidney, liver, lung, and spleen samples as well as 8 h and 24 h brain samples, spiked in during homogenization and prior to extraction. BZ6 (239.0233 m/z) was utilized as an internal standard for 2 h brain samples, spiked in during homogenization and prior to extraction. Extracted ion chromatograms (XIC) were obtained for the intact, protonated masses of each compound.

2 h Brain. Intact 216-3 was not detected in the brain at 2 h post-dose via MALDI-MSI, and was not detected in extracted brain homogenate, as well. The BZ6 standard eluted at 6.82 min. While several peaks were observed during the chromatographic run, 216 was not, as shown in the XIC and the lack of an accurate mass in the mass spectrum. A brain sample taken from 216-3-treated C57BL/6 mouse 2h-M1 was compared to a brain sample taken from vehicle-treated C57BL/6 mouse 0h-M1.

Other 216-3-Treated Organs. Intact 216-3 was not detected in other organs at 2 h, 8 h, and 24 h time points via MALDI-MSI; however, it was detected in all organs (brain, heart, kidney, liver, lung, and spleen) at 8 h and 24 h, as well as heart, kidney, liver, lung, and spleen at 2 h in LC-MS/MS analyses of tissue homogenates. Upon further inspection, a mass within 10 ppm of 216-3 was detected in the organs of control mice as well. Further evaluation of 216-3 was not possible, though the initial experiments with brain extracted at 2 h post-dose suggested it did not cross the blood-brain barrier.

DISCUSSION.

Tissue Washing. The observation of BZ16 in mouse brain, as well as several potential BZ16 metabolites after tissue washing suggest that detailed pre-dosing analyses can enhance the utility of MALDI-MSI by improving sensitivity through the removal of salts

and lipids. Experimenting with solvent variation via MALDI-MSI analysis of standard-spotted thin tissue sections pre- and post-washing assisted in the MSI analyses of SMRT compounds. BZ16 was not delocalized by an optimized ethanol wash step, and this washing assisted in the visualization of BZ16 in the cerebrum and cerebellum of treated C57BL/6 mice.

C57BL/6 and SCID Mice Compared. Biodistribution of BZ6 and BZ16 were analyzed in both C57BL/6 and SCID mice. C57BL/6 mice are traditionally used as background or control mice, while SCID strains were used for immunological studies related to SMRTs. RTC13, 216, and 216-3 analyses exclusively utilized C57BL/6 mice. Though results stemming from SCID mice were analyzed, all MALDI-MSI and LC-MS/MS analyses and conclusions utilized C57BL/6-based data. In general, more unique peaks were detected in SCID mice than in C57BL/6. Several BZ6-associated peaks within SCID mouse organs displayed similar distribution patterns, though this was not true of BZ16-associated peaks. More unique peaks were detected in BZ6-treated SCID mice than BZ16-treated SCID mice, further indicating SCID mice as an unreliable data source in this experiment.

BZ6. Initial BZ6 analyses indicated a build-up at the site of injection. Intact BZ6 was not observed in any organs via MALDI-MSI. Peaks unique to BZ6-treated C57BL/6 mice were not detected, while several peaks unique to BZ6-treated SCID mice were detected. These peaks observed in SCID mice did not match protonated or sodiated forms of BZ6 observed in standard runs. Though they may be metabolites, these peaks will not be further investigated until a formal metabolic study is completed. Intact BZ6 was not observed in brain, heart, kidney, liver, or lung via LC-MS/MS analyses of

extracted tissue; however, intact BZ6 was observed in the extracted spleen homogenate LC-MS/MS analysis. The absence of BZ6 from MALDI-MSI spectra suggests its concentration may be below the limit of detection for this technique, or it is outside of the dynamic range of MSI. Physiologically, its presence in LC-MS/MS spectra of extracted homogenate suggests the spleen is an off-target build-up site. BZ6's absence from the other filtering organs, such as kidney and liver, further suggests an unwanted build-up in the spleen. These data suggest BZ6 is not a viable treatment option due to its absence from the brain and build-up in the spleen, and thus it will not be considered further.

Though SCID data were not weighted as heavily as C57BL/6, some similarities were observed among specific BZ6-associated unique peaks in MSI experiments. Peak 84 m/z was found in brain, heart, and liver. Peak 103 m/z was found in brain and liver. Peak 161 m/z was found in heart and liver. Peak 249 m/z was found in heart and liver. Peak 615 m/z was found in liver and heart. Peak 789 m/z was found in brain and liver. Peaks 84, 183, 736, 763, and 801 m/z had similar distributions in cerebellum sections, suggesting they are related to one another. Peaks 357 and 371 m/z had similar distributions in the brain, suggesting they are related to one another. Peaks 211, 249, and 496 m/z had similar distributions in heart samples, suggesting they are related. Peaks 38 and 183 m/z had similar distributions in liver, suggesting they are related. Finally, peaks 764 and 790 had similar distribution in liver, suggesting they are related. These similarities in distribution among various peaks throughout brain, heart, and liver were limited to BZ6-treated mice. Because BZ6 was not detected in organs other than

spleen via LC-MS/MS experiments, it is unlikely that these peaks are direct metabolites of BZ6. They are more likely downstream effects of BZ6 treatment.

BZ16. Unlike its BZ6 sister compound, BZ16 was not observed to build-up at the site of injection. Intact BZ16 was observed in the brain in its sodiated form, found in both the cerebrum and the cerebellum of BZ16-treated C57BL/6 mice. Peaks unique to BZ16-treated C57BL/6 mice were also detected in the liver. These peaks observed in the liver of C57BL/6 mice did not match protonated or sodiated forms of BZ16 observed in standard runs. Though they may be metabolites, these peaks will not be further investigated until a formal metabolic study is completed. Intact BZ16 was not observed in the brain, heart, kidney, lung, and spleen of BZ16-treated SCID mice; however, a peak corresponding to the sodiated form of BZ16 was detected in SCID liver. Further MALDI-MS/MS of thin tissue sections and LC-MS/MS analyses of extracted brain homogenate confirmed BZ16's presence in C57BL/6 brain; however, intact BZ16 was not detected in the liver in LC-MS/MS experiments. MALDI-MS/MS and LC-MS/MS analyses of the peak detected at 776 m/z in BZ16-treated C57BL/6 liver did not yield sufficient data for confirmation of this peak as an adduct of BZ16. These data suggest BZ16 is a viable treatment option as it was found in the brain and was not found to build-up in other organs. Its absence from kidney and liver suggest it may be cleared quickly and efficiently.

RTC13. RTC13 was observed to build-up at the site of injection, though not to the same extent of its derivative compound, BZ6. Intact RTC13 was not observed in any organs via MALDI-MSI. Peaks unique to RTC13-treated C57BL/6 mice were detected in liver and spleen. These peaks observed did not match protonated or sodiated forms of

RTC13 observed in standard runs. Though they may be metabolites, these peaks will not be further investigated until a formal metabolic study is completed. Intact RTC13 was observed in extracted brain homogenates at 2 h post-dose via LC-MS/MS analyses, indicating it did cross the blood-brain barrier; however, RTC13 was not detected in the brain at 8 h and 24 h post-dose via LC-MS/MS analyses. RTC13 was also detected in extracted kidney homogenates at 8 h post-dose and extracted liver, lung, and spleen homogenates at 24 h post-dose via LC-MS/MS experiments. Taken together, these data indicate that RTC13 is not a viable treatment option due to its short-lived presence in the brain, and its build-up in the filtering organs, as well as lung, at 8 h and 24 h after dosing; additionally, RTC13's build-up at the site of injection further indicates that it should not be pursued further.

216. While 216 was not observed to build-up at the site of injection, it was also not found in any organs at any time points via MALDI-MSI experiments. Further LC-MS/MS analysis of extracted brain homogenate at 2 h post-dose indicated 216 did cross the blood-brain barrier. LC-MS/MS analyses of extracted brain homogenates at 8 h and 24 h post-dose, as well as all other extracted tissue homogenates at all time points did not show presence of 216. This suggests that 216 is not a viable treatment option due to its short-lived presence in the brain, and further suggests that it is cleared from the body quickly.

216-3. As seen with the parent compound 216, derivative 216-3 did not build-up at the site of injection. Intact 216-3 was not observed in any organs at any time points via MALDI-MSI analyses. Initial LC-MS/MS analysis of extracted brain homogenate at 2 h post-dose indicated 216-3 did not cross the blood-brain barrier. Further LC-MS/MS

analyses of extracted brain homogenates at 8 h and 24 h post-dose, as well as all other extracted tissue homogenates at all time points (including the control) contained a contaminating peak within 10 ppm of the protonated form of 216-3. The peak intensity did not appear to be elevate in 216-3-treated organs compared to organs from control C57BL/6 mice; and, these data preliminarily suggest that 216-3 does not cross the blood-brain barrier, thus indicating it is not a viable treatment option.

CONCLUSION.

MALDI-MSI is a promising technology for the analysis of small molecules. Its advantages in speed, sample preparation, and lack of tagging over traditional methods aim to reduce time and cost in quick screening of novel therapeutics. However, improvements in sensitivity are necessary, as shown by the failure of MALDI-MSI to detect RTC13 and 216 in the brain. Though LC-MS/MS chromatograms of RTC13 extracted brain, kidney, lung, and spleen homogenates and 216 extracted brain homogenate indicated lower peak intensity compared to that of BZ16 extracted brain homogenate, the same was not true of BZ6 extracted spleen homogenate and RTC13 extracted liver homogenate. This further indicates area for improvement in MALDI-MSI analyses of small molecule therapeutics.

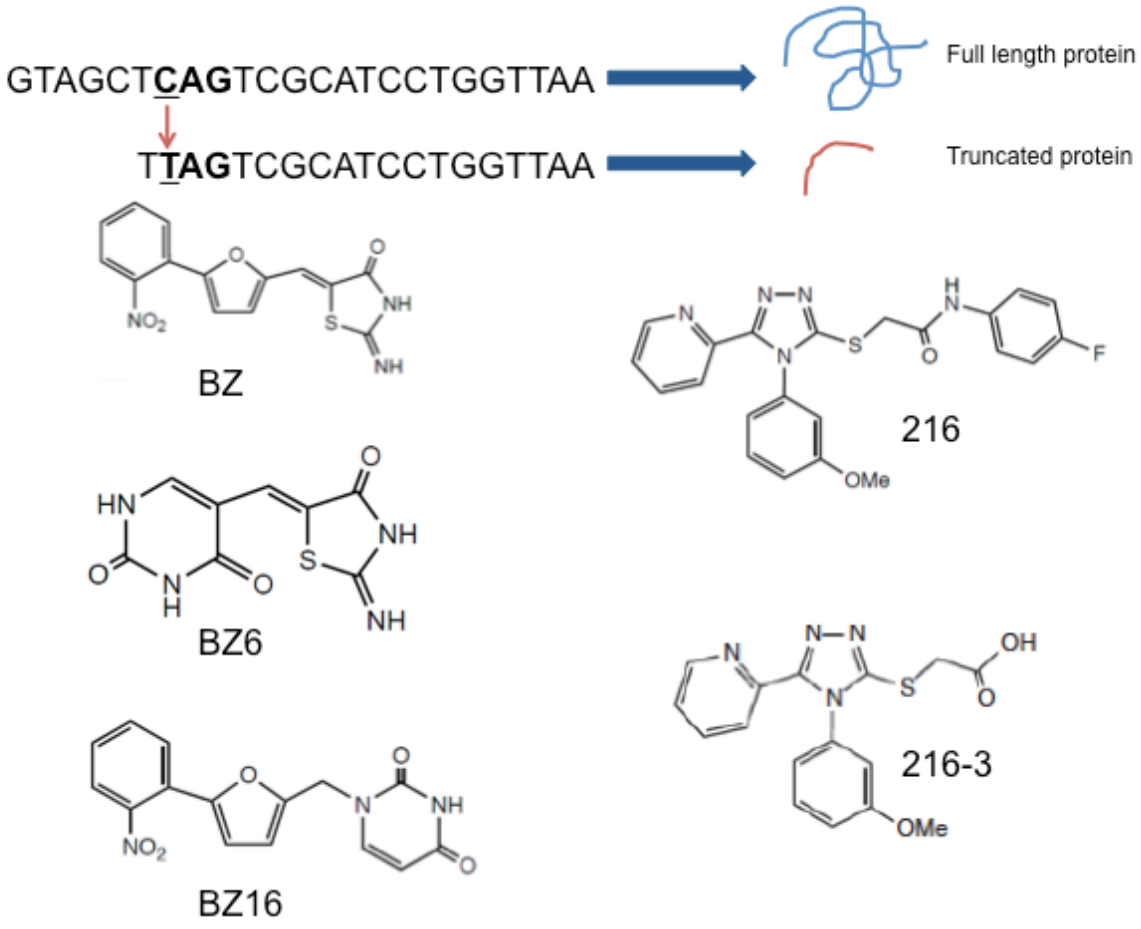

Figure 1. (A) In some AT patients, a nonsense mutation in the DNA sequence of ATM protein results in a premature TAG stop codon. Full-length ATM protein is no longer produced, resulting in a truncated form of the protein. This truncated form is typically degraded, thus functional ATM protein (involved in the repair of double stranded DNA breaks) is no longer present. Symptoms attributed to this lack of ATM protein include impaired cerebellum development, increased susceptibility to cancer, and adverse side effects due to radiation exposure.[43] (B) The 5 SMRT compounds utilized in this study are shown here.

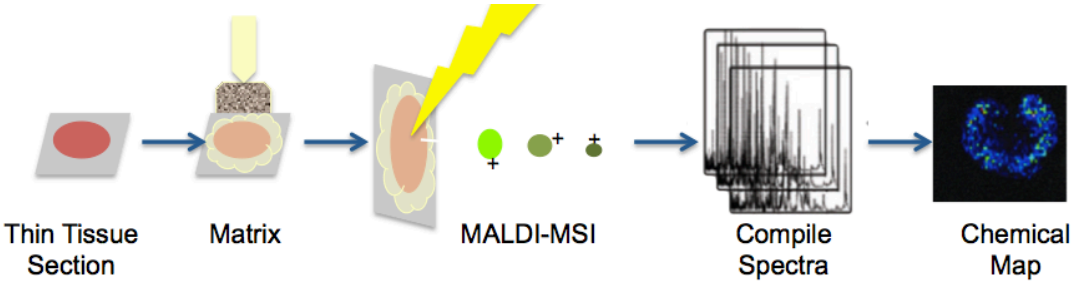

Figure 2. A typical MALDI-MSI workflow is shown. Organs, or other tissue samples, are sliced using a cryo-microtome at a thickness of 12 to 16 μm and are thaw-mounted to a slide with a conductive coating. A thin layer of matrix is applied using a fine-particle aerosol mist generator. Software is used to establish an area of analysis within the tissue section, specifying a spatial resolution. Hundreds to thousands of average spectra are collected at rastering points across the tissue are, and are assigned (x, y, z) coordinates. These spectra are compiled into one average spectrum, and the coordinates are used to create a virtual map on the tissue section image of any selected peak of interest within the average spectrum.

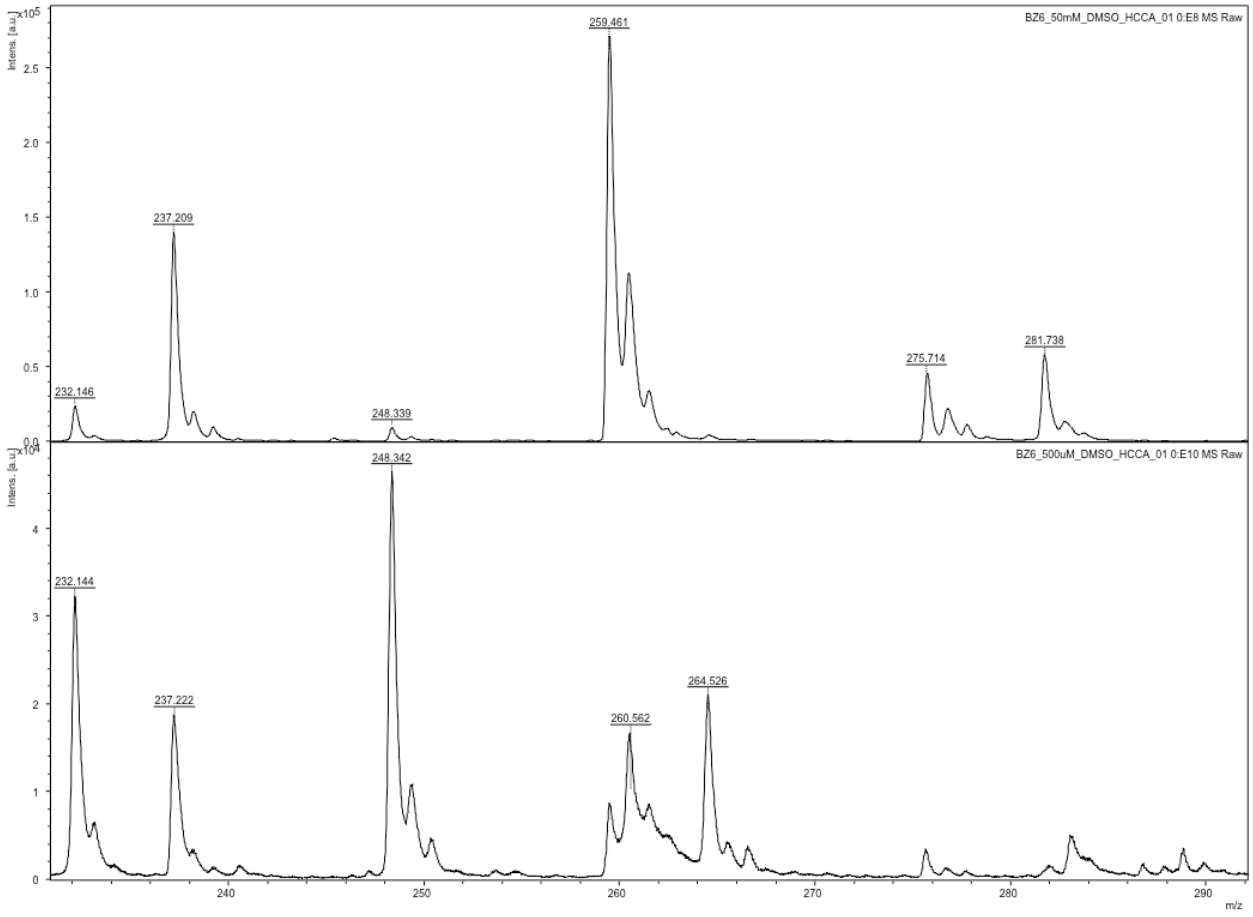

Figure 3. The limit of detection of SMRT compound BZ6 off-tissue is shown above. (A) BZ6 signal at a concentration of 50 mM in DMSO. The monosodiated form of BZ6 is the most dominant. (B) BZ6 signal at a concentration of 500 μM. The monosodiated form of BZ6 is still observed, although the signal intensity is low and the mass resolution is poor. This was considered the lower limit of detection for BZ6.

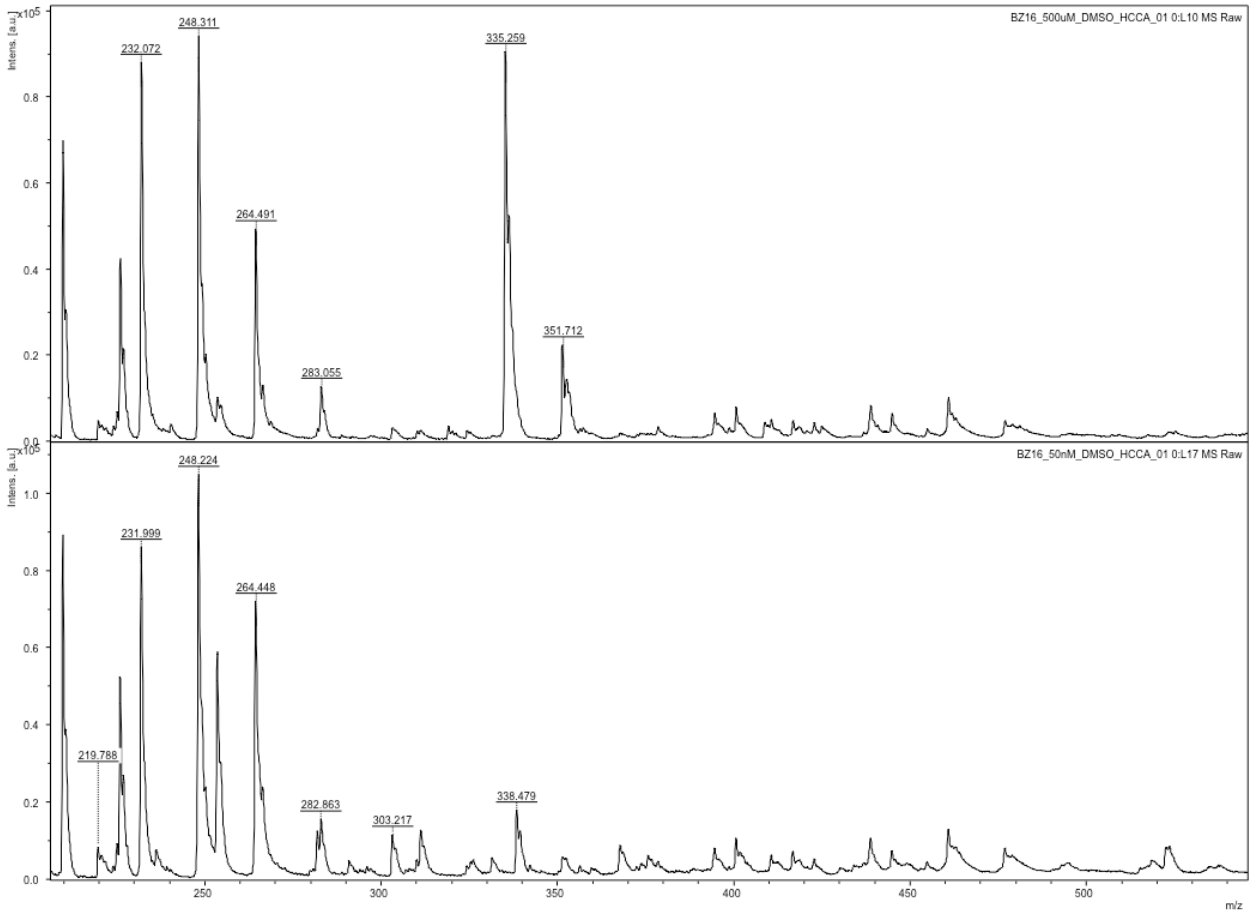

Figure 4. The limit of detection of SMRT compound BZ16 off-tissue is shown above. (A) BZ16 signal at a concentration of 500 μM in DMSO. The monosodiated form of BZ16 is the most dominant. (B) BZ16 signal at a concentration of 50 nM. The monosodiated form of BZ16 is still observed, although the signal intensity is low and the mass resolution is poor. This was considered the lower limit of detection for BZ16.

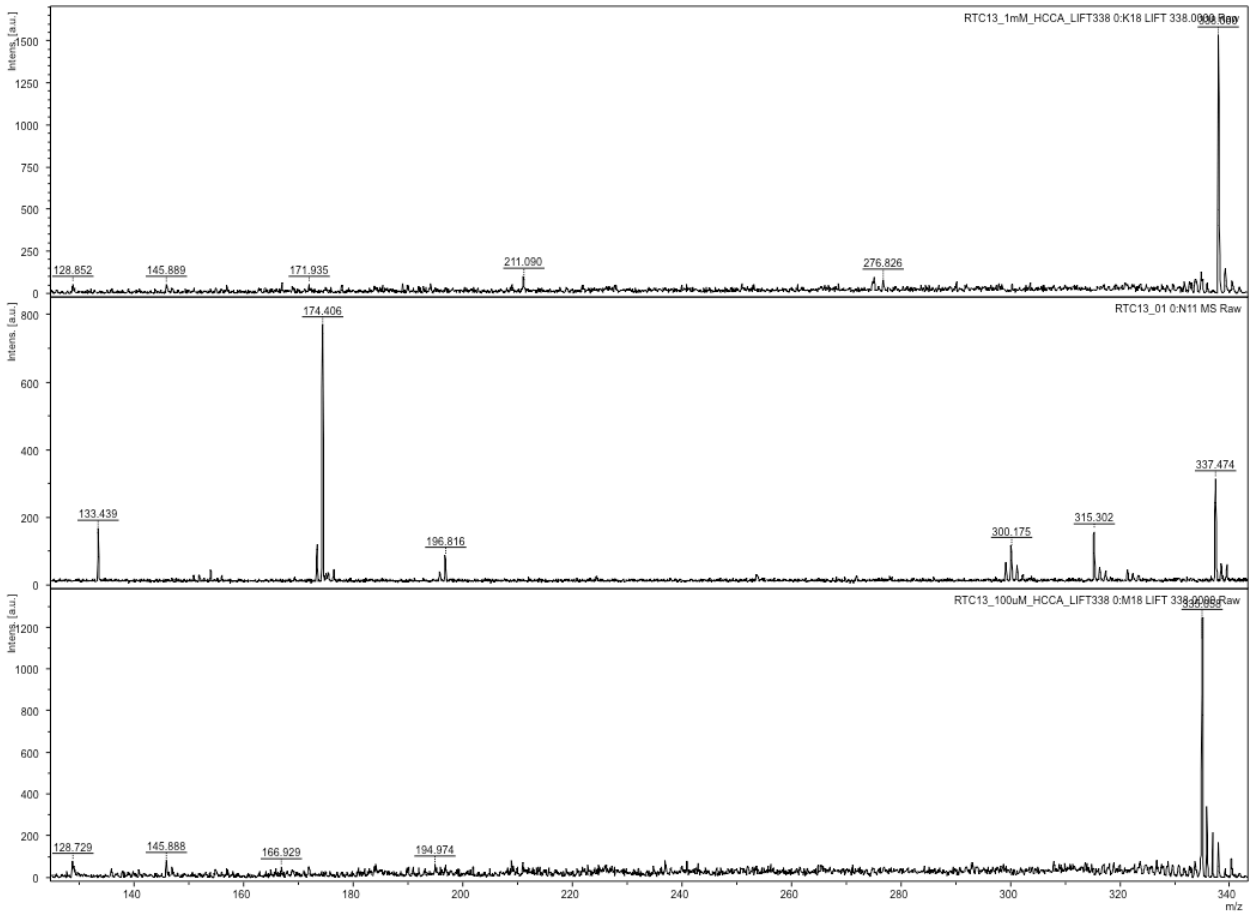

Figure 5. The limit of detection of SMRT compound RTC13 off-tissue is shown above. (A) 216 signal at a concentration of 1 mM in DMSO. The monosodiated form of RTC13 is the most dominant. (B) RTC13 signal at a concentration of 500 μM. The monosodiated form of RTC13 is still observed, although the signal intensity is lower. (C) RTC13 signal at a concentration of 100 μM. The monosodiated form of RTC13 is still observed, although the signal intensity is low and the mass accuracy has decreased. This was considered the lower limit of detection for RTC13.

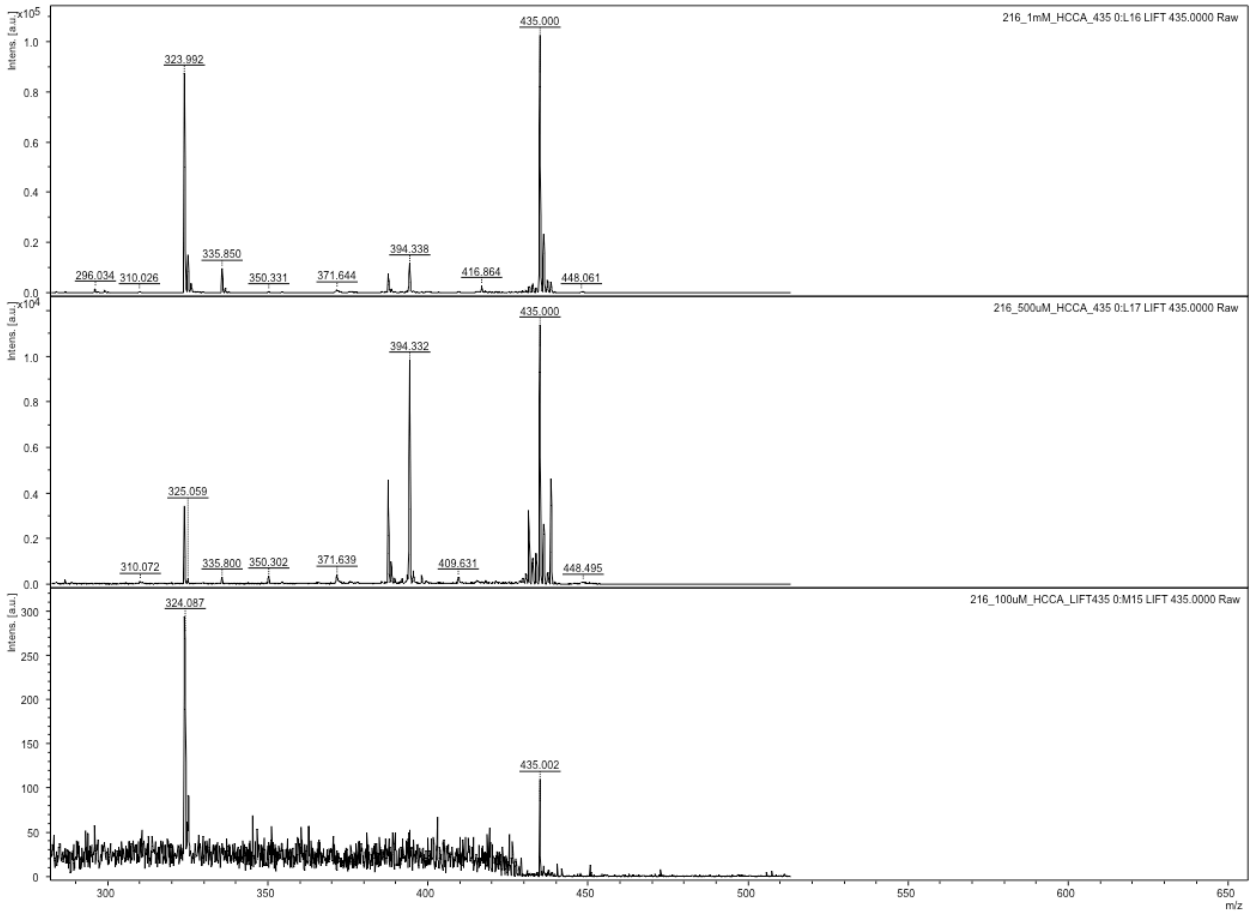

Figure 6. The limit of detection of SMRT compound 216 off-tissue is shown above. (A) 216 signal at a concentration of 1 mM in DMSO. The monosodiated form of 216 is the most dominant. (B) 216 signal at a concentration of 500 μM. The monosodiated form of 216 is still observed, although the signal intensity is lower. (C) 216 signal at a concentration of 100 μM. The monosodiated form of 216 is still observed, although the signal intensity is low. This was considered the lower limit of detection for 216.

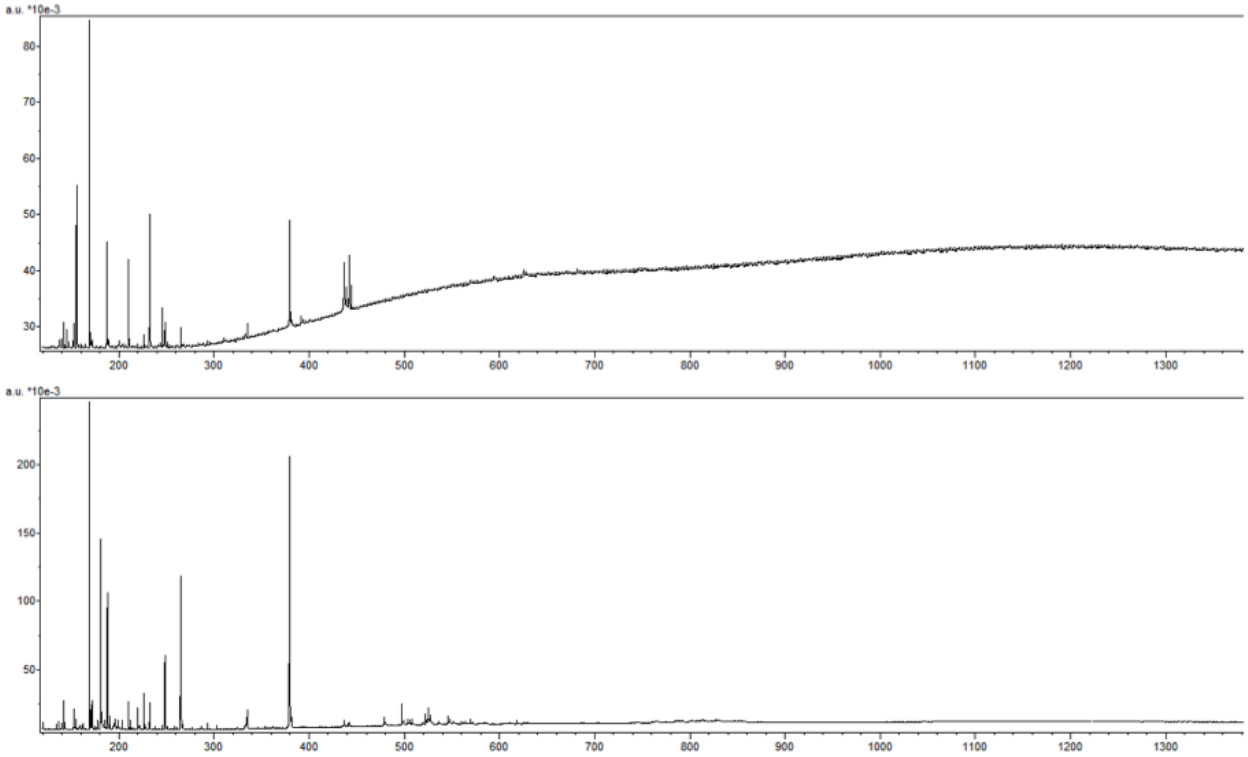

Figure 7. In general, a 30 s 70% ethanol wash lowered the baseline rise observed in a liver tissue imaging experiments. (A) Shows the average spectrum for a given tissue section prior to washing. (B) Shows the average spectrum for the same given tissue section post-washing.

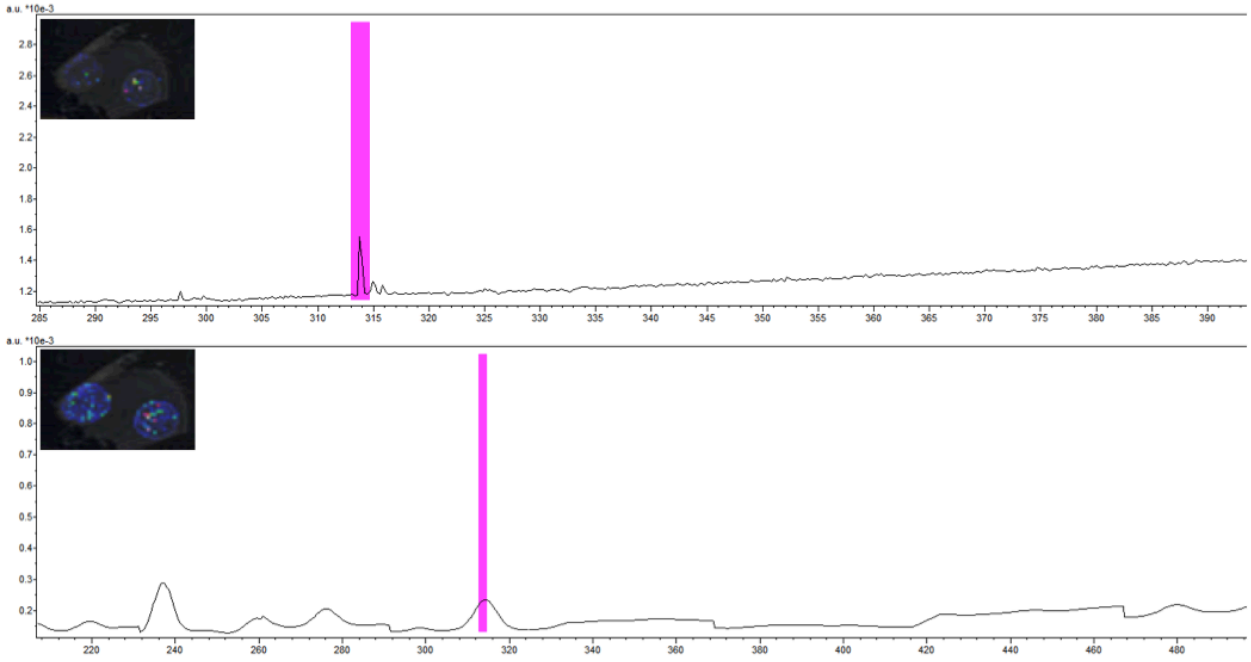

Figure 8. BZ16 was spotted onto a control brain tissue section, with no matrix added, and imaged prior to washing, and after washing for 30 s with 70% ethanol. Differences in mass accuracy were miniscule, though washing enhanced the signal intensity and detection capabilities with no delocalization. (A) Shows the average spectrum and image for an unwashed tissue section. (B) Shows the average spectrum and image for a washed tissue section.

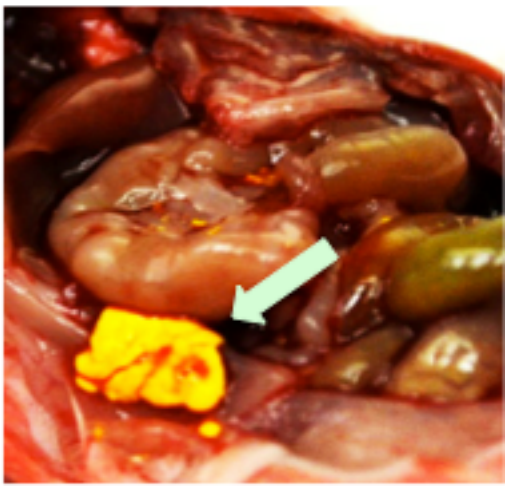

Figure 9. BZ6 was found to build-up at the site of injection. The solid yellow material throughout the abdominal cavity was indicative of BZ6 precipitation.

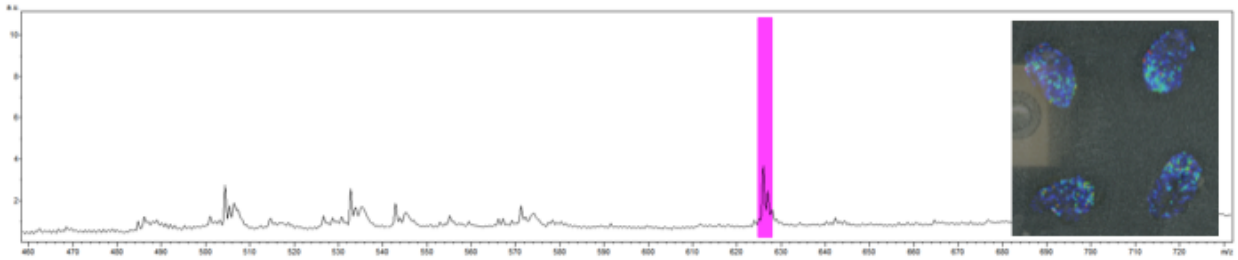

Figure 10. A unique peak was observed in heart excised from BZ6-treated C57BL/6 mice. The average spectrum is shown here, from unwashed sections, with the unique peak at 626 m/z highlighted in pink. The resulting virtual image is shown on the right.

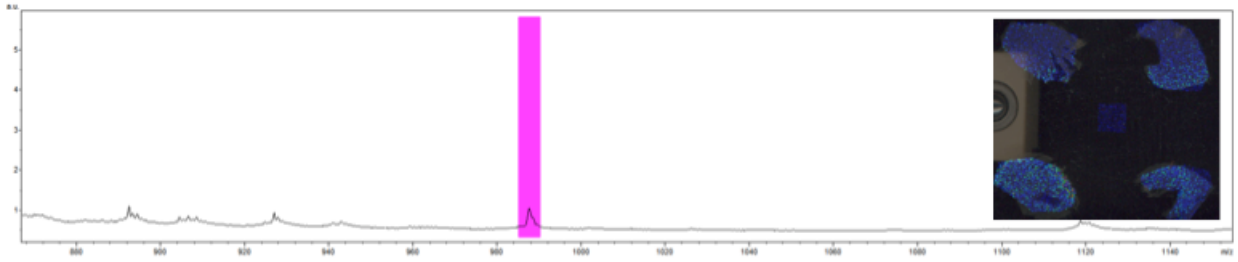

Figure 11. A unique peak was observed in liver excised from BZ6-treated C57BL/6 mice. The average spectrum is shown here, from unwashed sections, with the unique peak at 988 m/z highlighted in pink. The resulting virtual image is shown on the right.

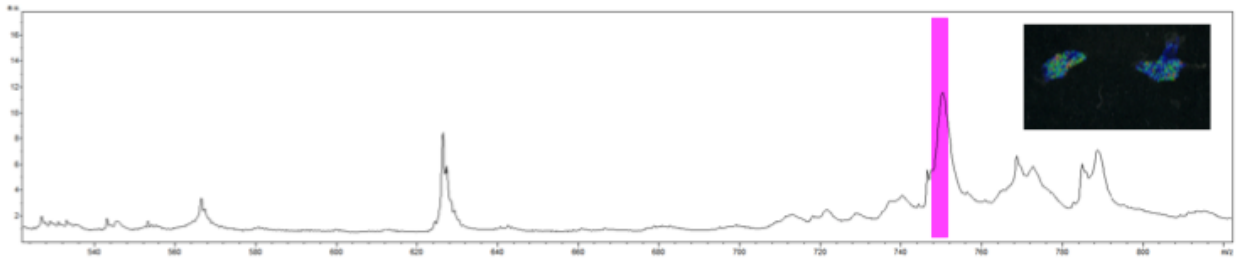

Figure 12. A unique peak was observed in lung excised from BZ6-treated C57BL/6 mice. The average spectrum is shown here, from unwashed sections, with the unique peak at 749 m/z highlighted in pink. The resulting virtual image is shown on the right.

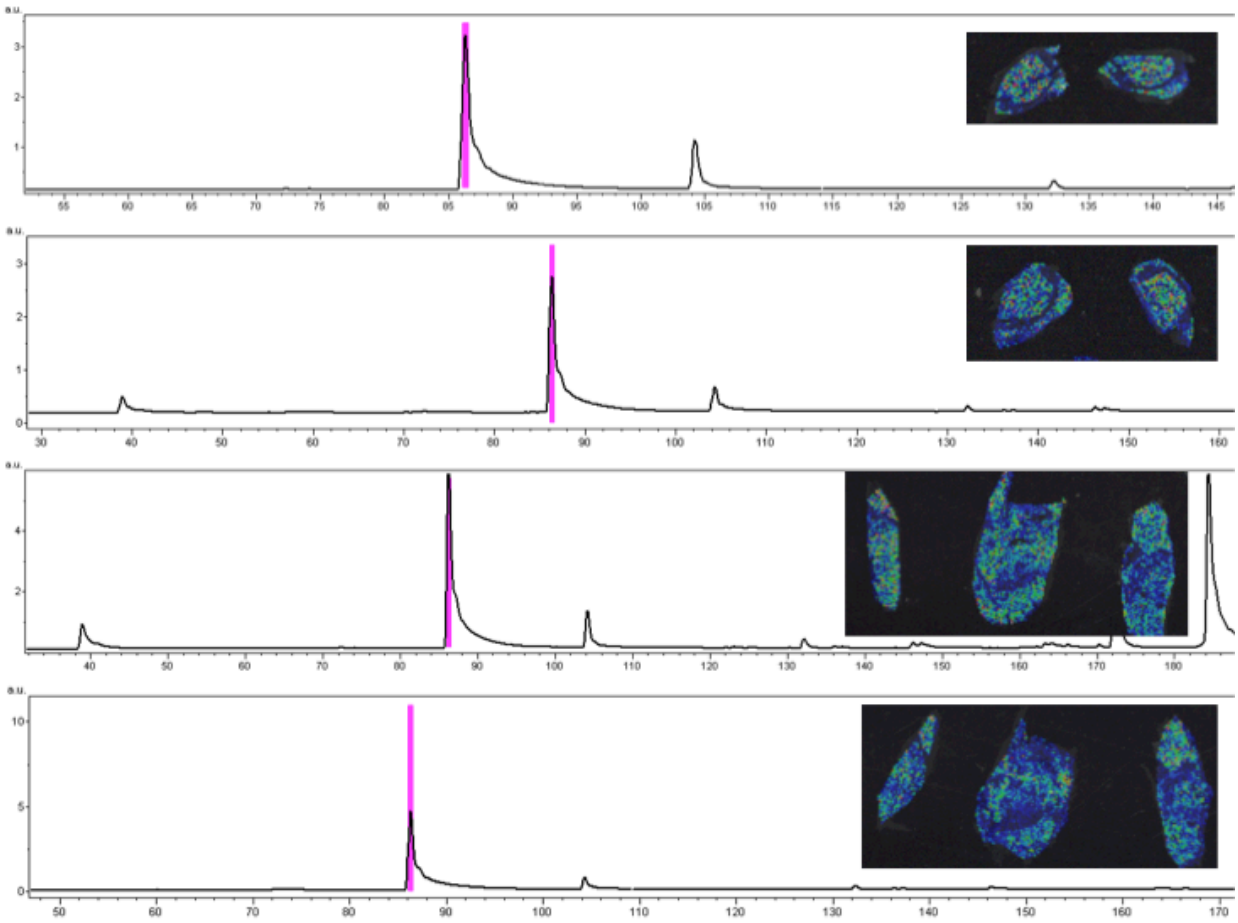

Figure 13. A unique peak was observed in brain excised from BZ6-treated SCID mice. (A) Shows the average spectrum from an unwashed cerebellum section, with the unique peak at 84 m/z highlighted in pink, and the virtual image shown to the right. (B) Shows the average spectrum from a washed cerebellum section, with the unique peak at 84 m/z highlighted in pink, and the virtual image shown to the right. (C) Shows the average spectrum from an unwashed cerebrum section, with the unique peak at 84 m/z highlighted in pink, and the virtual image shown to the right. (D) Shows the average spectrum from a washed cerebrum section, with the unique peak at 84 m/z highlighted in pink, and the virtual image shown to the right.

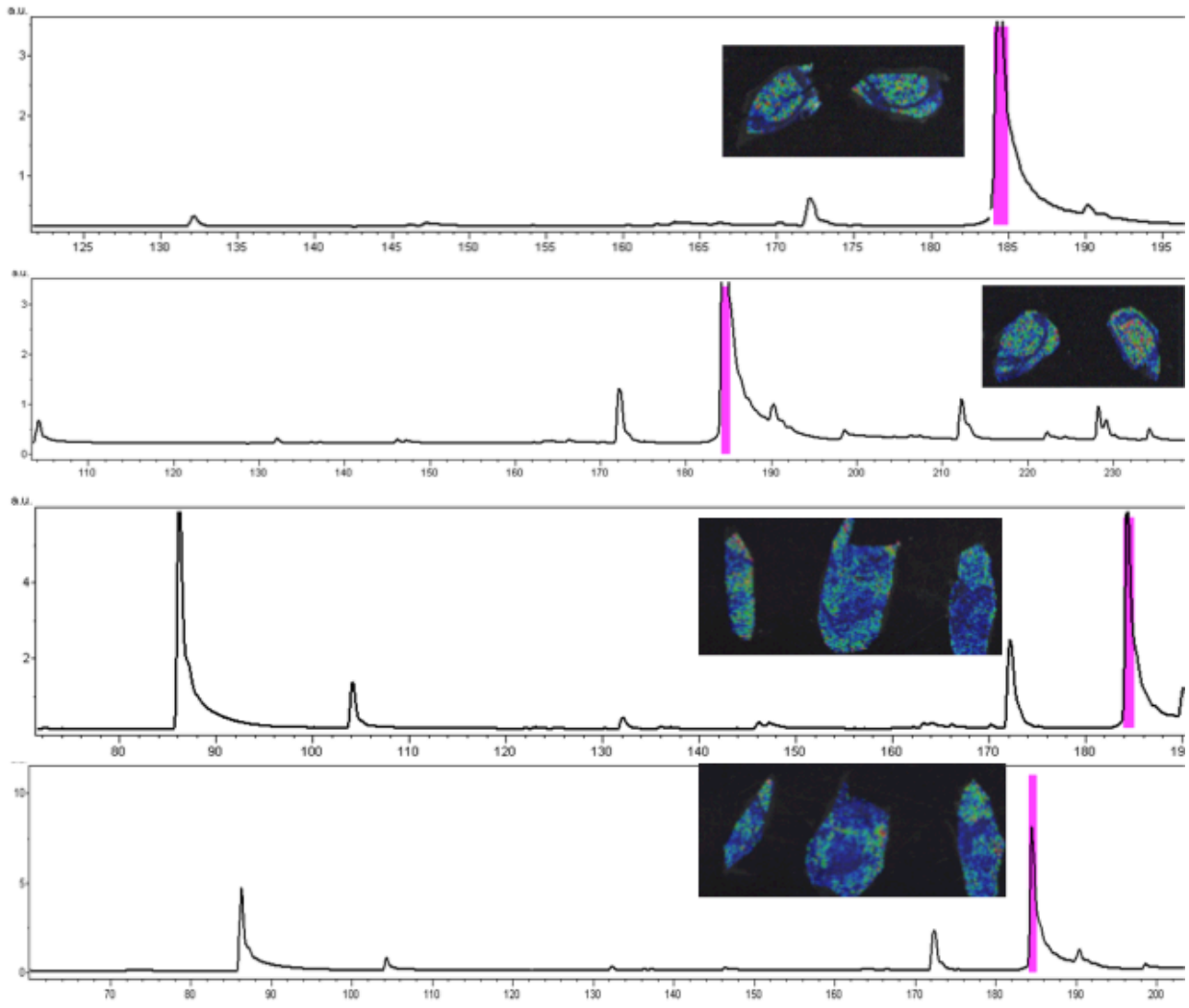

Figure 14. A unique peak was observed in brain excised from BZ6-treated SCID mice. (A) Shows the average spectrum from an unwashed cerebellum section, with the unique peak at 183 m/z highlighted in pink, and the virtual image shown to the right. (B) Shows the average spectrum from a washed cerebellum section, with the unique peak at 183 m/z highlighted in pink, and the virtual image shown to the right. (C) Shows the average spectrum from an unwashed cerebrum section, with the unique peak at 183 m/z highlighted in pink, and the virtual image shown to the right. (D) Shows the average

spectrum from a washed cerebrum section, with the unique peak at 183 m/z highlighted in pink, and the virtual image shown to the right.

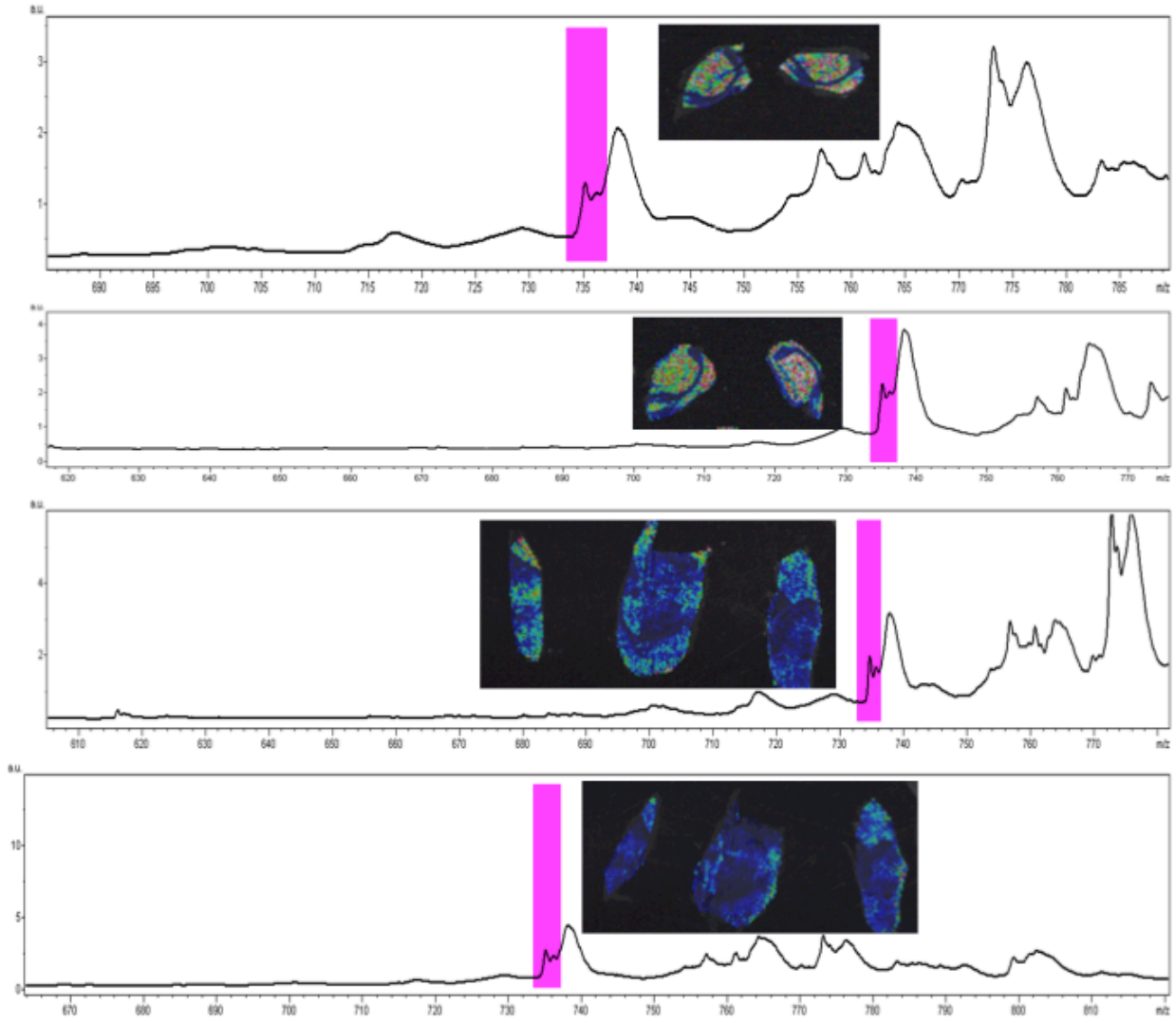

Figure 15. A unique peak was observed in brain excised from BZ6-treated SCID mice. (A) Shows the average spectrum from an unwashed cerebellum section, with the unique peak at 736 m/z highlighted in pink, and the virtual image shown to the right. (B) Shows the average spectrum from a washed cerebellum section, with the unique peak at 736 m/z highlighted in pink, and the virtual image shown to the right. (C) Shows the average spectrum from an unwashed cerebrum section, with the unique peak at 736 m/z highlighted in pink, and the virtual image shown to the right. (D) Shows the average

spectrum from a washed cerebrum section, with the unique peak at 736 m/z highlighted in pink, and the virtual image shown to the right.

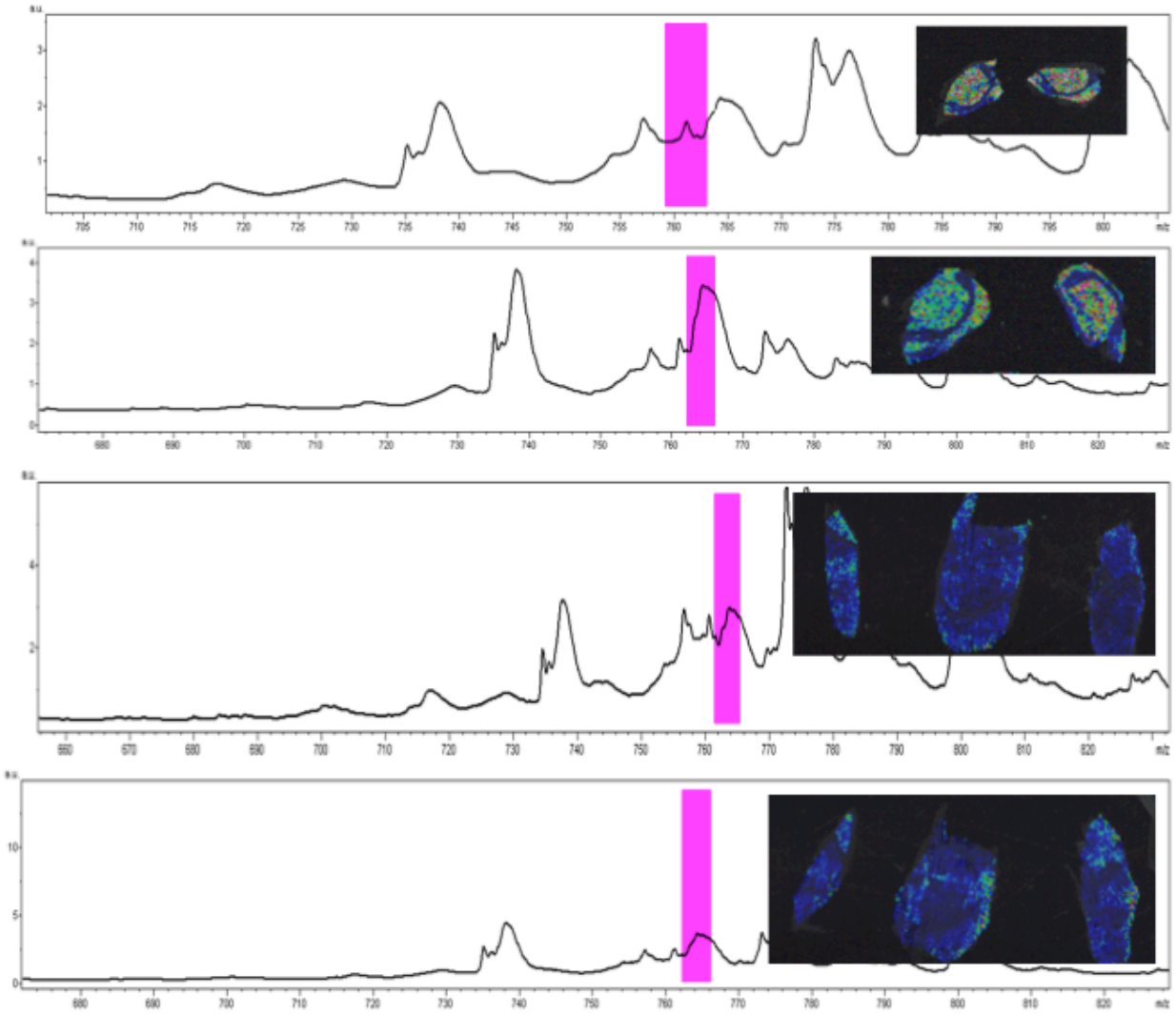

Figure 16. A unique peak was observed in brain excised from BZ6-treated SCID mice. (A) Shows the average spectrum from an unwashed cerebellum section, with the unique peak at 763 m/z highlighted in pink, and the virtual image shown to the right. (B) Shows the average spectrum from a washed cerebellum section, with the unique peak at 763 m/z highlighted in pink, and the virtual image shown to the right. (C) Shows the average spectrum from an unwashed cerebrum section, with the unique peak at 763 m/z highlighted in pink, and the virtual image shown to the right. (D) Shows the average

spectrum from a washed cerebrum section, with the unique peak at 763 m/z highlighted in pink, and the virtual image shown to the right.

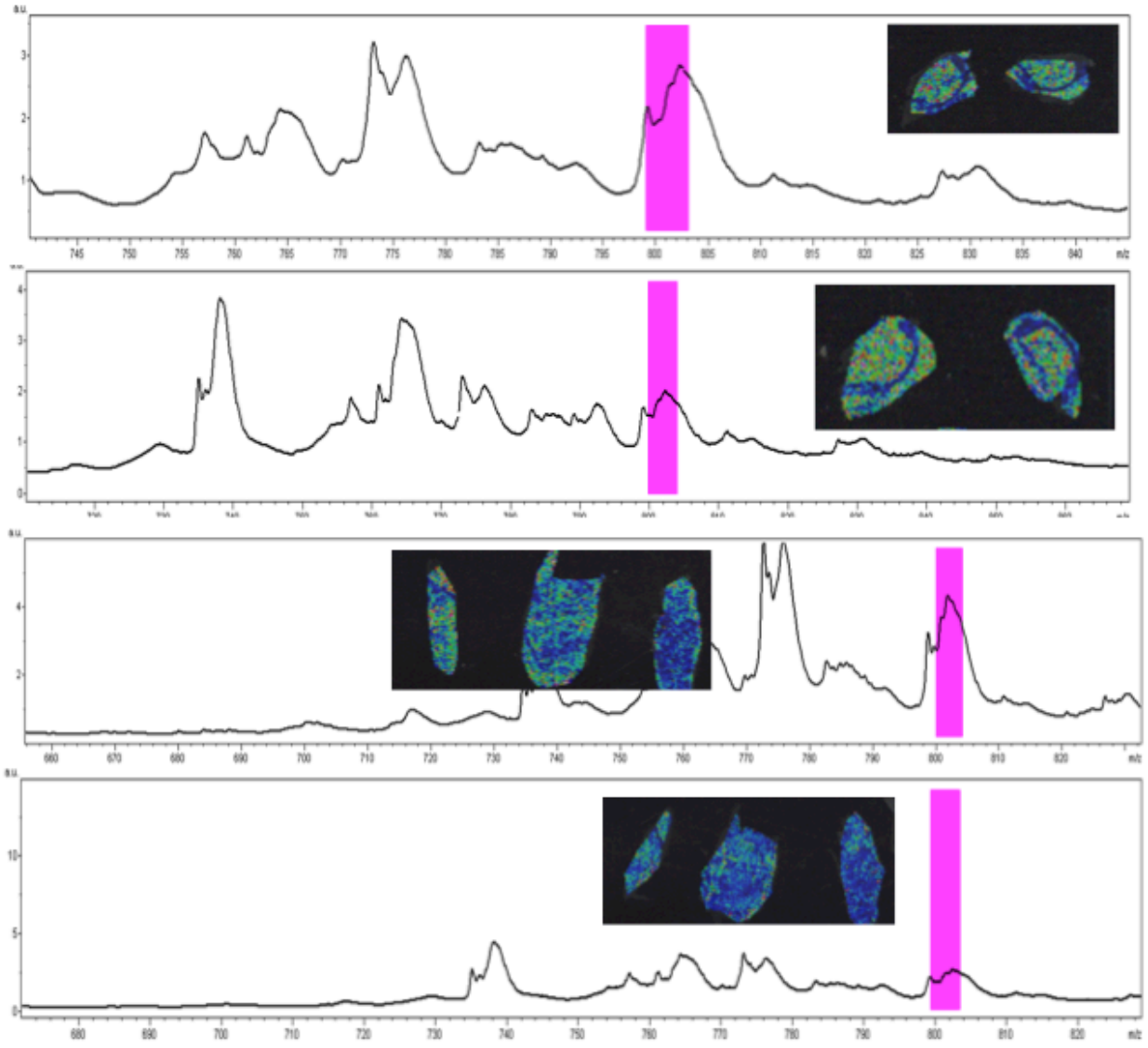

Figure 17. A unique peak was observed in brain excised from BZ6-treated SCID mice. (A) Shows the average spectrum from an unwashed cerebellum section, with the unique peak at 801 m/z highlighted in pink, and the virtual image shown to the right. (B) Shows the average spectrum from a washed cerebellum section, with the unique peak at 801 m/z highlighted in pink, and the virtual image shown to the right. (C) Shows the average spectrum from an unwashed cerebrum section, with the unique peak at 801 m/z highlighted in pink, and the virtual image shown to the right. (D) Shows the average

spectrum from a washed cerebrum section, with the unique peak at 801 m/z highlighted in pink, and the virtual image shown to the right.

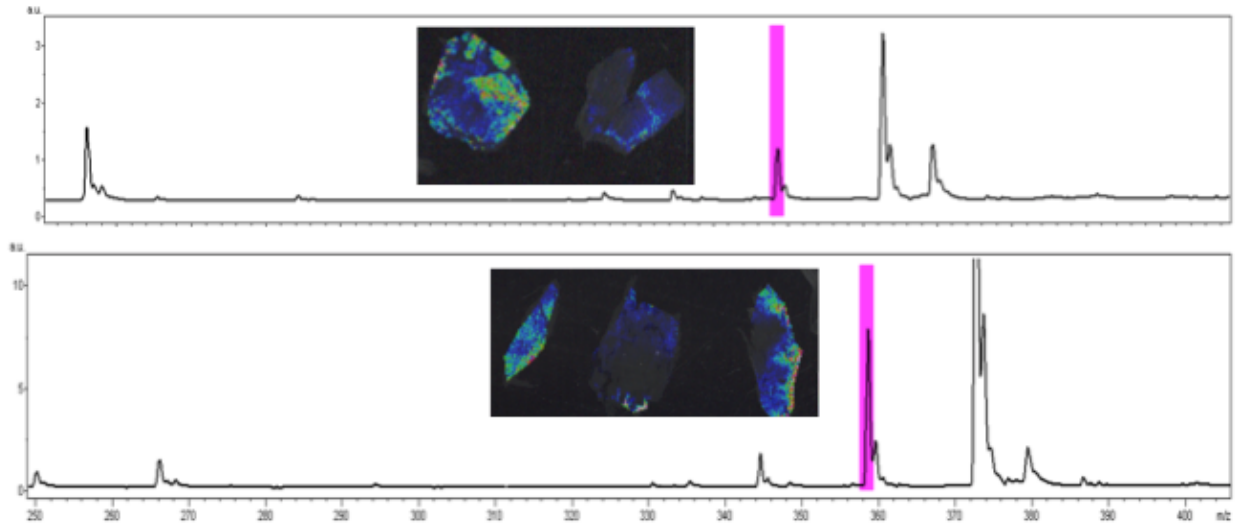

Figure 18. A unique peak was observed in brain excised from BZ6-treated SCID mice. (A) Shows the average spectrum from a washed cerebellum section, with the unique peak at 357 m/z highlighted in pink, and the virtual image shown to the right. (B) Shows the average spectrum from a washed cerebrum section, with the unique peak at 357 m/z highlighted in pink, and the virtual image shown to the right.

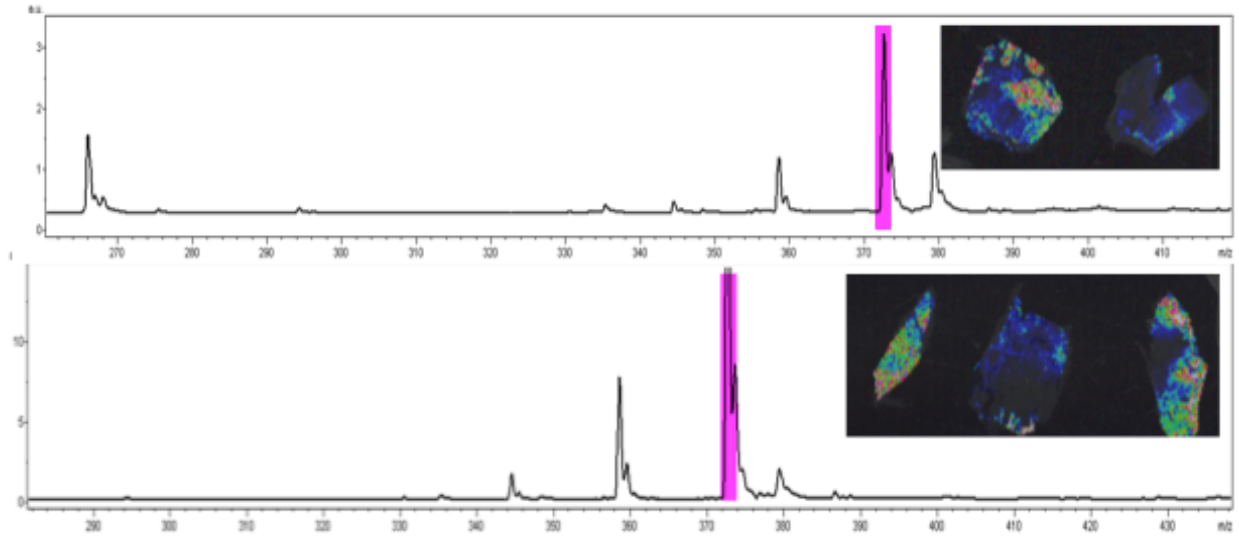

Figure 19. A unique peak was observed in brain excised from BZ6-treated SCID mice. (A) Shows the average spectrum from a washed cerebellum section, with the unique peak at 371 m/z highlighted in pink, and the virtual image shown to the right. (B) Shows the average spectrum from a washed cerebrum section, with the unique peak at 371 m/z highlighted in pink, and the virtual image shown to the right.

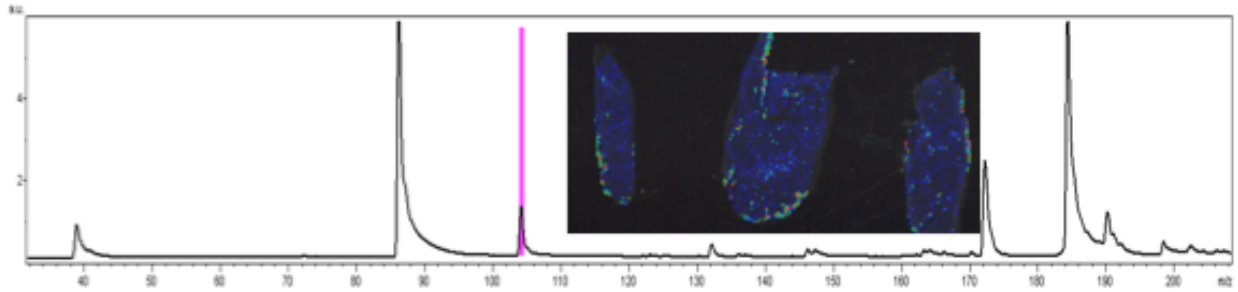

Figure 20. A unique peak was observed in brain excised from BZ6-treated SCID mice. The above shows the average spectrum from an unwashed cerebrum section, with the unique peak at 103 m/z highlighted in pink, and the virtual image shown to the right.

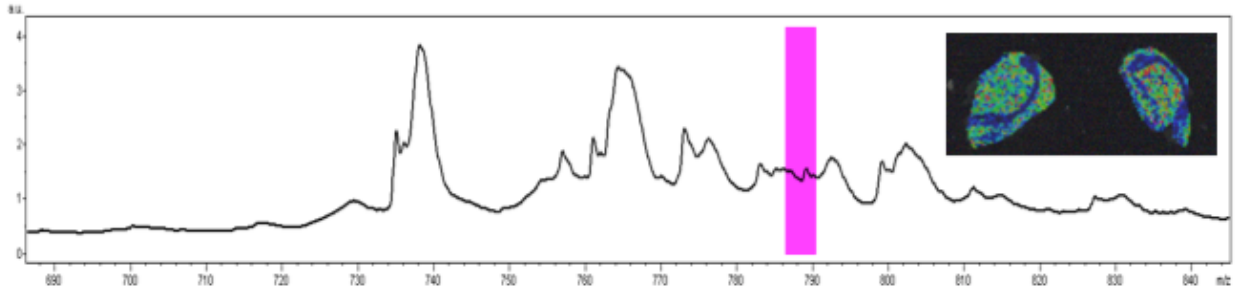

Figure 21. A unique peak was observed in brain excised from BZ6-treated SCID mice. The above shows the average spectrum from a washed cerebellum section, with the unique peak at 789 m/z highlighted in pink, and the virtual image shown to the right.

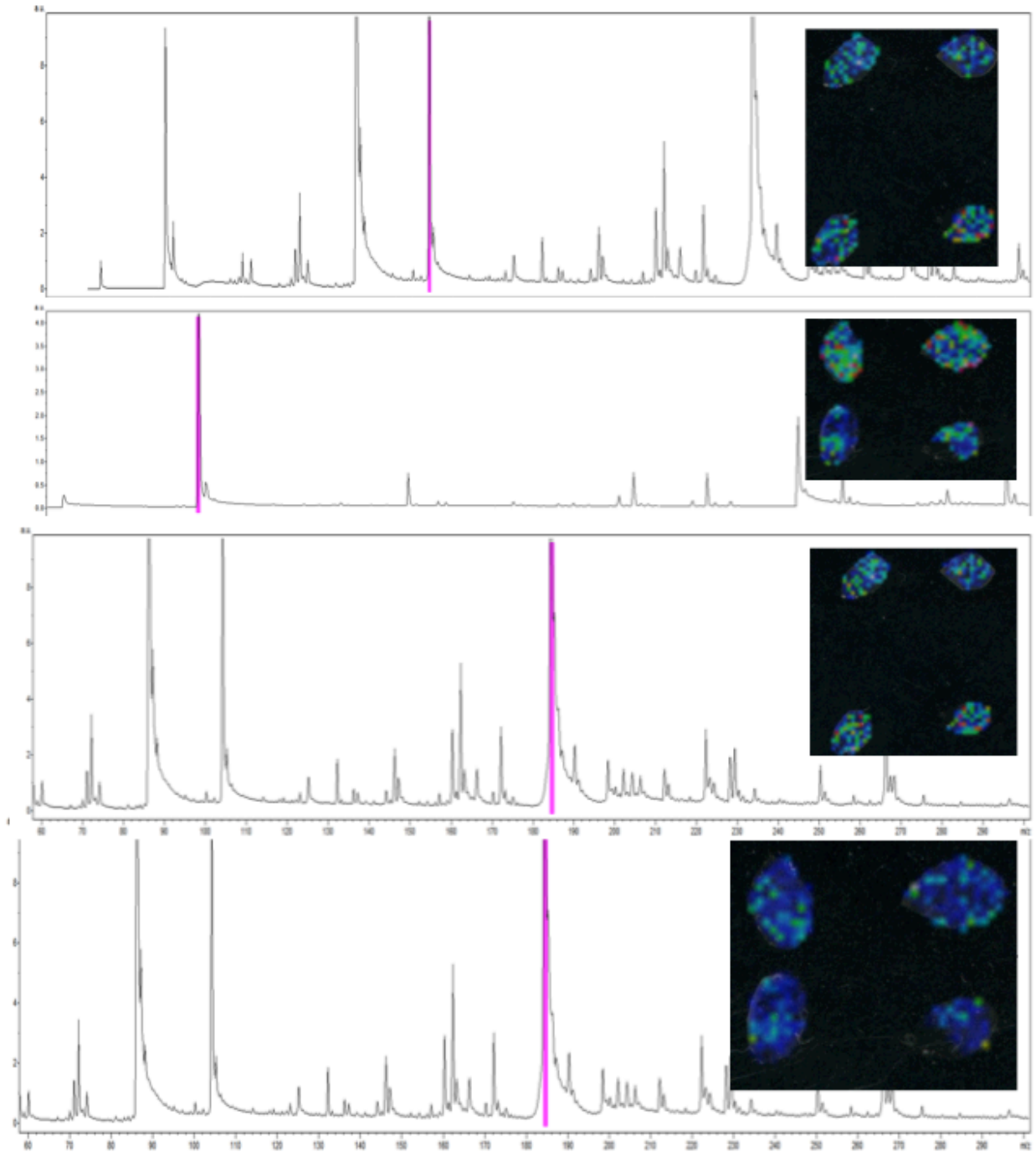

Figure 22. A unique peak was observed in heart excised from BZ6-treated SCID mice. (A) Shows the average spectrum from an unwashed heart section, with the unique peak at 103 m/z highlighted in pink, and the virtual image shown to the right. (B) Shows the average spectrum from a washed heart section, with the unique peak at 103 m/z

highlighted in pink, and the virtual image shown to the right. (C) Shows the average spectrum from an unwashed heart section, with the unique peak at 183 m/z highlighted in pink, and the virtual image shown to the right. (D) Shows the average spectrum from a washed heart section, with the unique peak at 183 m/z highlighted in pink, and the virtual image shown to the right.

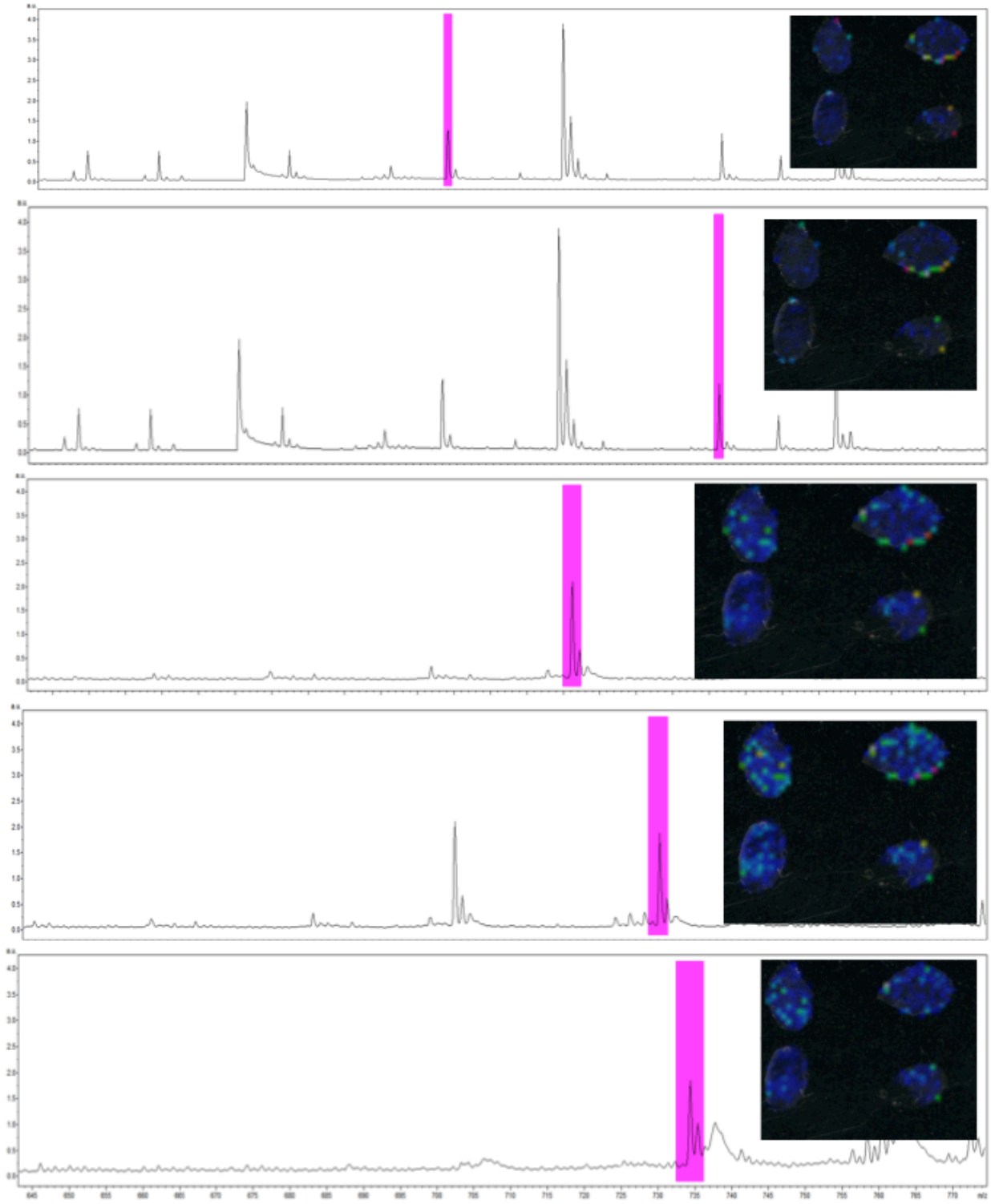

Figure 23. Several unique peaks were observed in heart excised from BZ6-treated SCID mice. (A) Shows the average spectrum from a washed heart section, with the

unique peak at 211 m/z highlighted in pink, and the virtual image shown to the right. (B) Shows the average spectrum from a washed heart section, with the unique peak at 249 m/z highlighted in pink, and the virtual image shown to the right. (C) Shows the average spectrum from a washed heart section, with the unique peak at 496 m/z highlighted in pink, and the virtual image shown to the right. (D) Shows the average spectrum from a washed heart section, with the unique peak at 523 m/z highlighted in pink, and the virtual image shown to the right. (E) Shows the average spectrum from a washed heart section, with the unique peak at 734 m/z highlighted in pink, and the virtual image shown to the right.

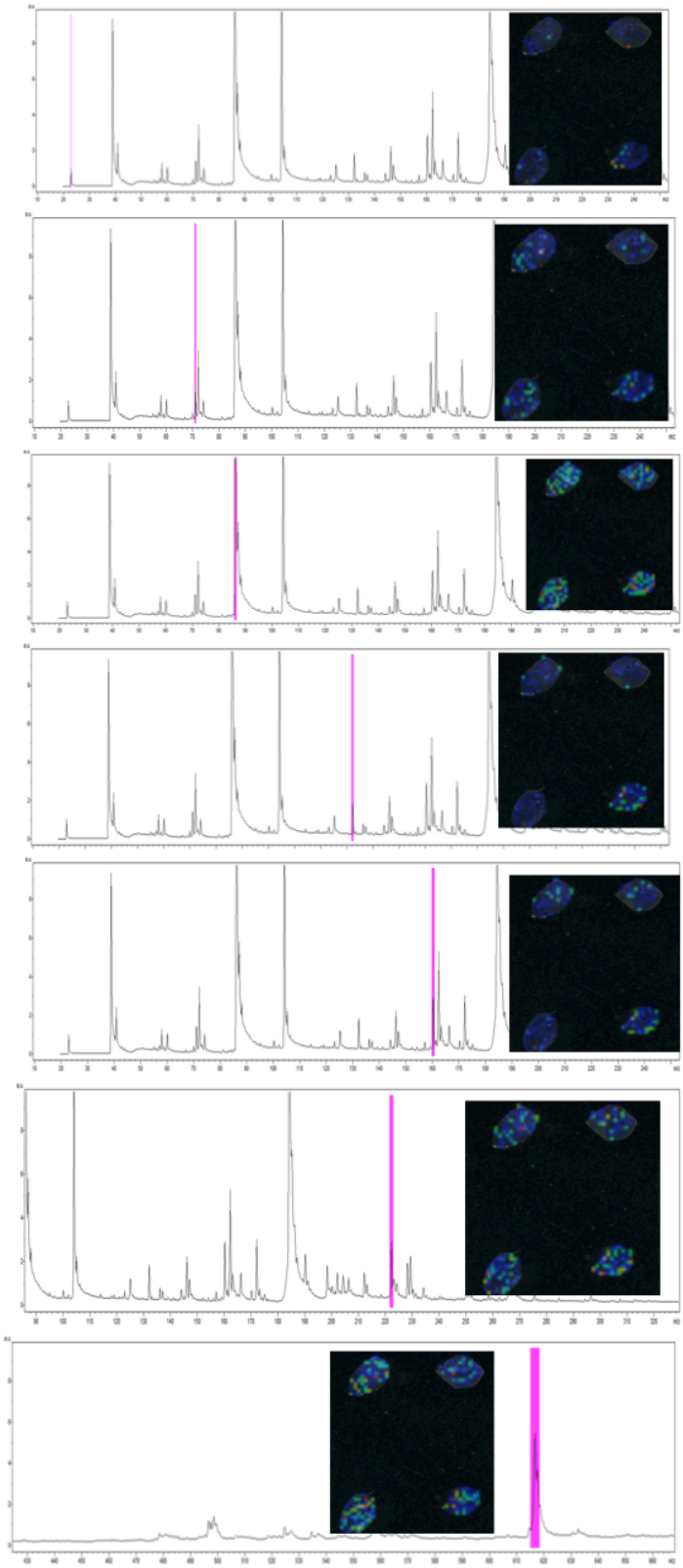

Figure 24. Several unique peaks were observed in heart excised from BZ6-treated SCID mice. (A) Shows the average spectrum from an unwashed heart section, with the unique peak at 22 m/z highlighted in pink, and the virtual image shown to the right. (B) Shows the average spectrum from an unwashed heart section, with the unique peak at 71 m/z highlighted in pink, and the virtual image shown to the right. (C) Shows the average spectrum from an unwashed heart section, with the unique peak at 85 m/z highlighted in pink, and the virtual image shown to the right. (D) Shows the average spectrum from an unwashed heart section, with the unique peak at 131 m/z highlighted in pink, and the virtual image shown to the right. (E) Shows the average spectrum from an unwashed heart section, with the unique peak at 161 m/z highlighted in pink, and the virtual image shown to the right. (F) Shows the average spectrum from an unwashed heart section, with the unique peak at 221 m/z highlighted in pink, and the virtual image shown to the right. (G) Shows the average spectrum from an unwashed heart section, with the unique peak at 616 m/z highlighted in pink, and the virtual image shown to the right.

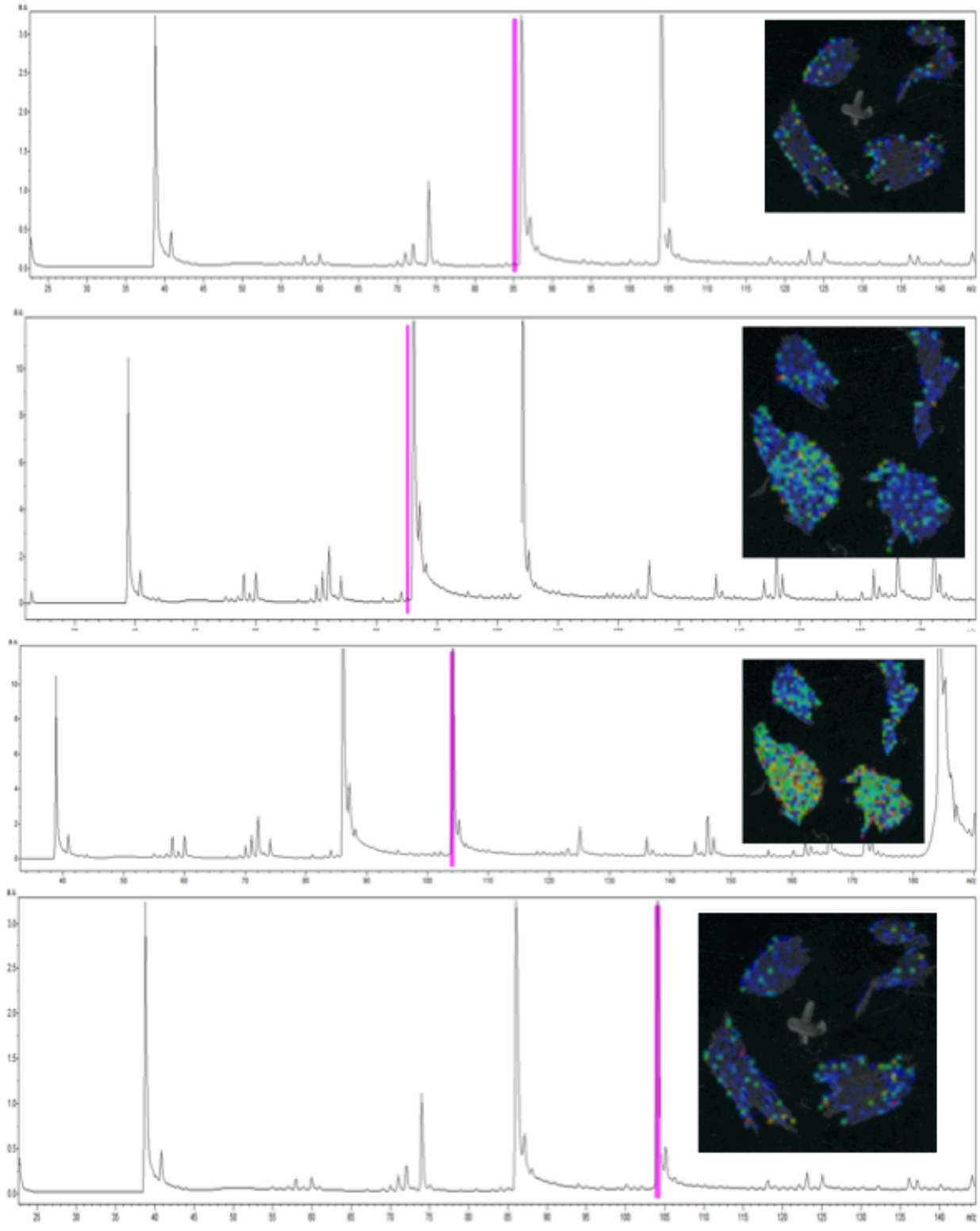

Figure 25. A unique peak was observed in liver excised from BZ6-treated SCID mice. (A) Shows the average spectrum from an unwashed liver section, with the unique peak at 85 m/z highlighted in pink, and the virtual image shown to the right. (B) Shows the average spectrum from a washed liver section, with the unique peak at 85 m/z highlighted in pink, and the virtual image shown to the right. (C) Shows the average spectrum from an unwashed liver section, with the unique peak at 103 m/z highlighted in pink, and the virtual image shown to the right. (D) Shows the average spectrum from a washed liver section, with the unique peak at 103 m/z highlighted in pink, and the virtual image shown to the right.

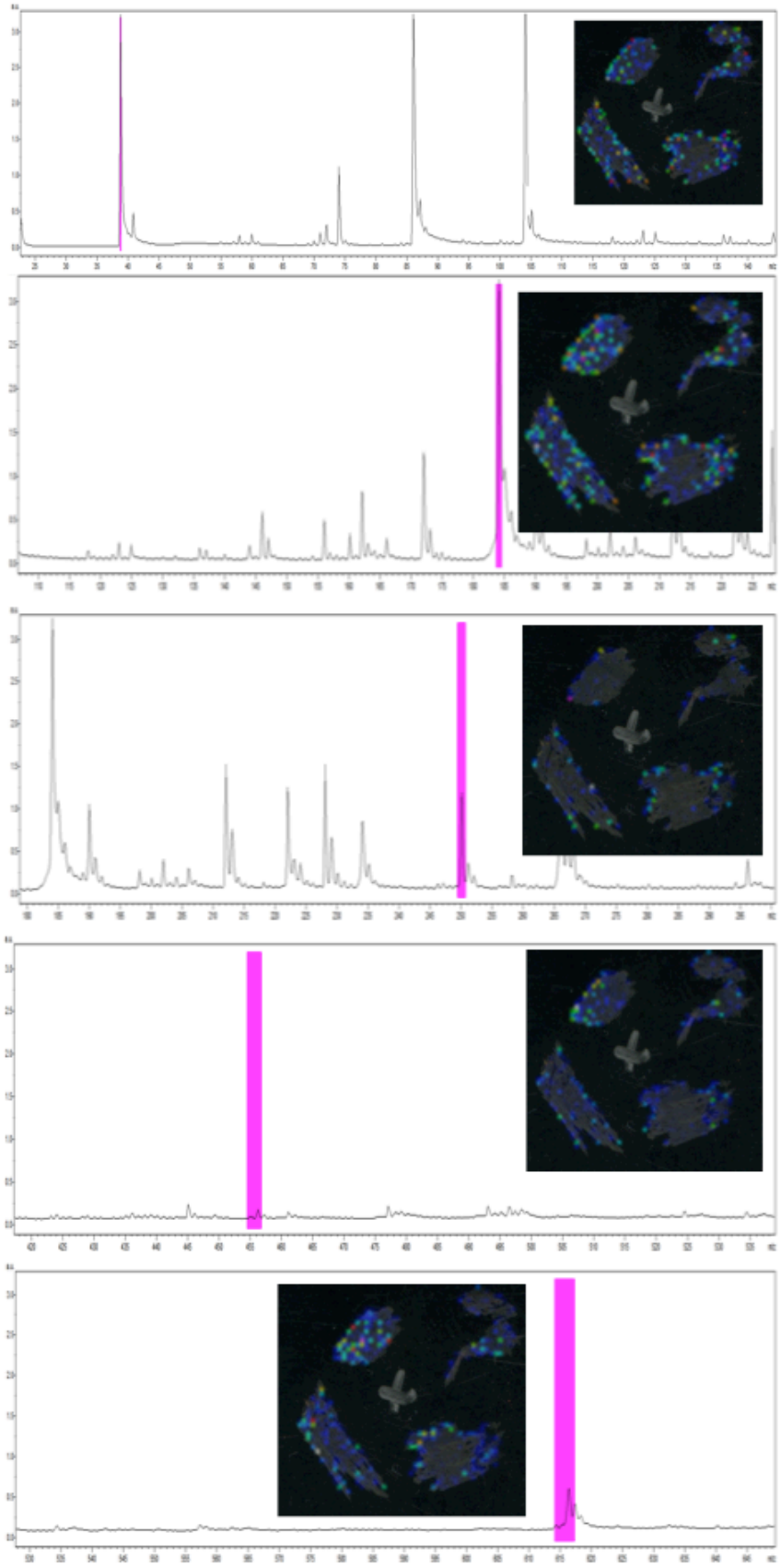

Figure 26. Several unique peaks were observed in liver excised from BZ6-treated SCID mice. (A) Shows the average spectrum from an unwashed liver section, with the unique peak at 38 m/z highlighted in pink, and the virtual image shown to the right. (B) Shows the average spectrum from an unwashed liver section, with the unique peak at 183 m/z highlighted in pink, and the virtual image shown to the right. (C) Shows the average spectrum from an unwashed liver section, with the unique peak at 249 m/z highlighted in pink, and the virtual image shown to the right. (D) Shows the average spectrum from an unwashed liver section, with the unique peak at 455 m/z highlighted in pink, and the virtual image shown to the right. (E) Shows the average spectrum from an unwashed liver section, with the unique peak at 615 m/z highlighted in pink, and the virtual image shown to the right.

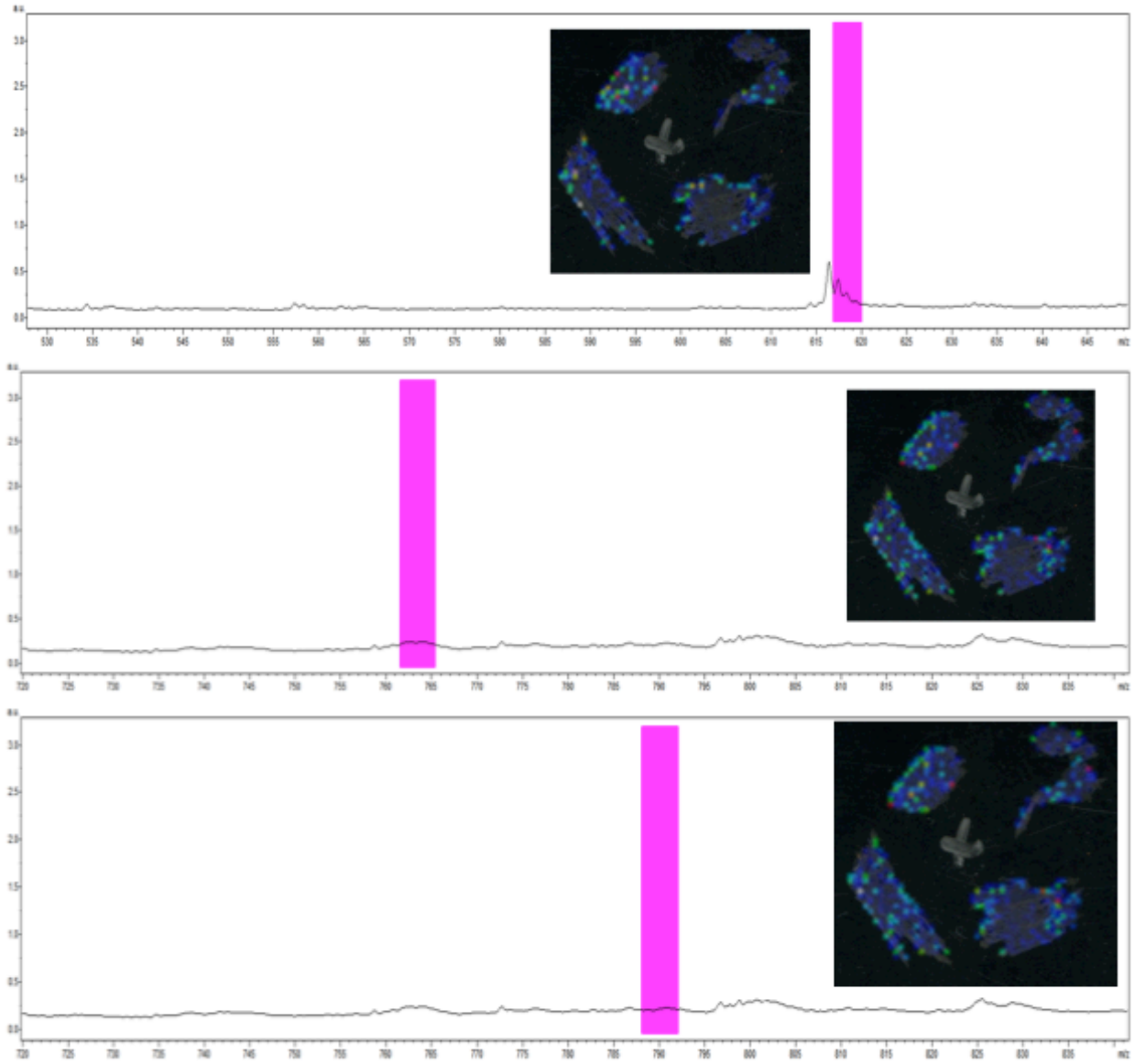

Figure 27. Several unique peaks were observed in liver excised from BZ6-treated SCID mice. (A) Shows the average spectrum from an unwashed liver section, with the unique peak at 619 m/z highlighted in pink, and the virtual image shown to the right. (B) Shows the average spectrum from an unwashed liver section, with the unique peak at 764 m/z highlighted in pink, and the virtual image shown to the right. (C) Shows the average spectrum from an unwashed liver section, with the unique peak at 790 m/z highlighted in pink, and the virtual image shown to the right.

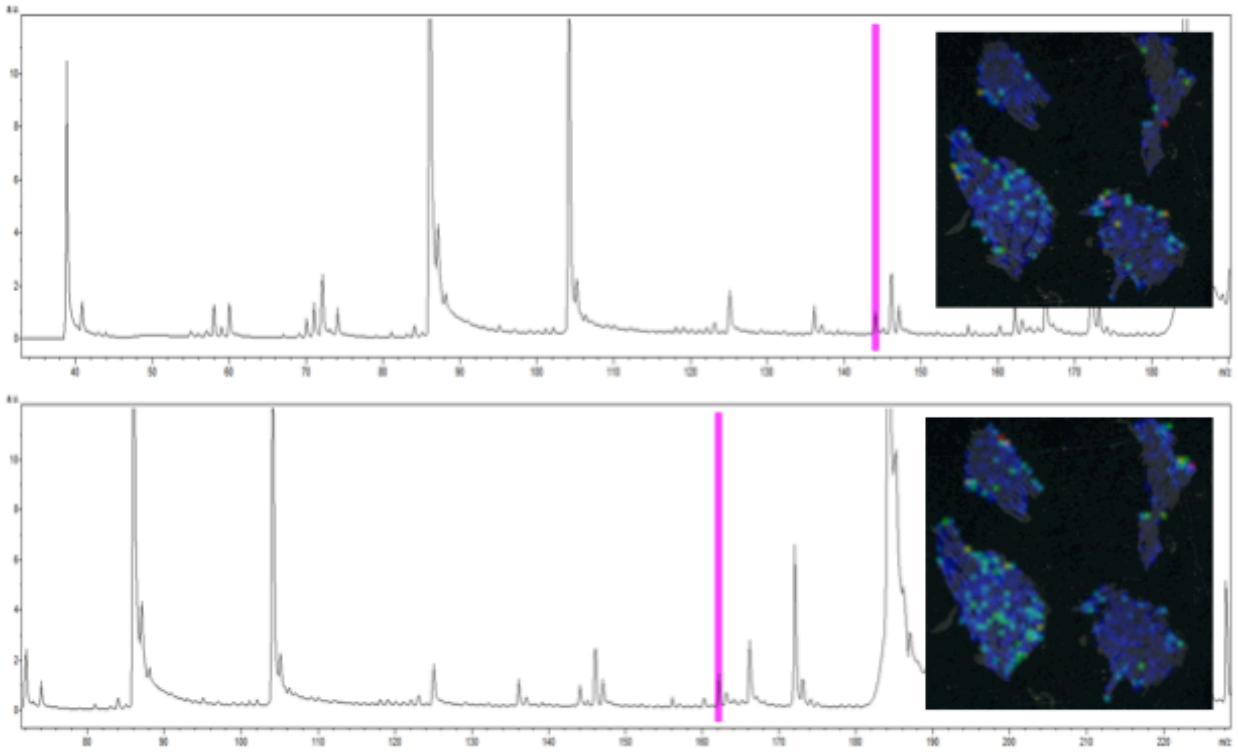

Figure 28. Several unique peaks were observed in liver excised from BZ6-treated SCID mice. (A) Shows the average spectrum from a washed liver section, with the unique peak at 145 m/z highlighted in pink, and the virtual image shown to the right. (B) Shows the average spectrum from a washed liver section, with the unique peak at 161 m/z highlighted in pink, and the virtual image shown to the right.

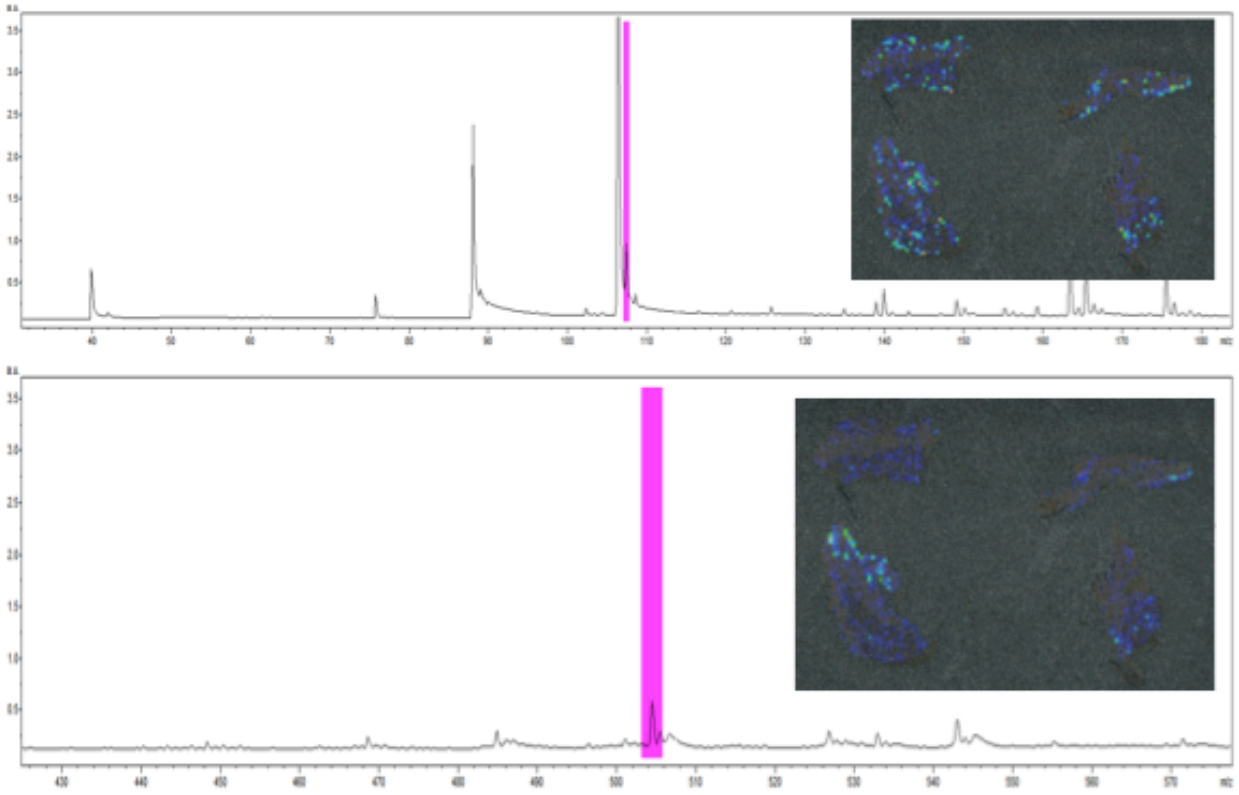

Figure 29. Several unique peaks were observed in lung excised from BZ6-treated SCID mice. (A) Shows the average spectrum from an unwashed lung section, with the unique peak at 107 m/z highlighted in pink, and the virtual image shown to the right. (B) Shows the average spectrum from an unwashed lung section, with the unique peak at 504 m/z highlighted in pink, and the virtual image shown to the right.

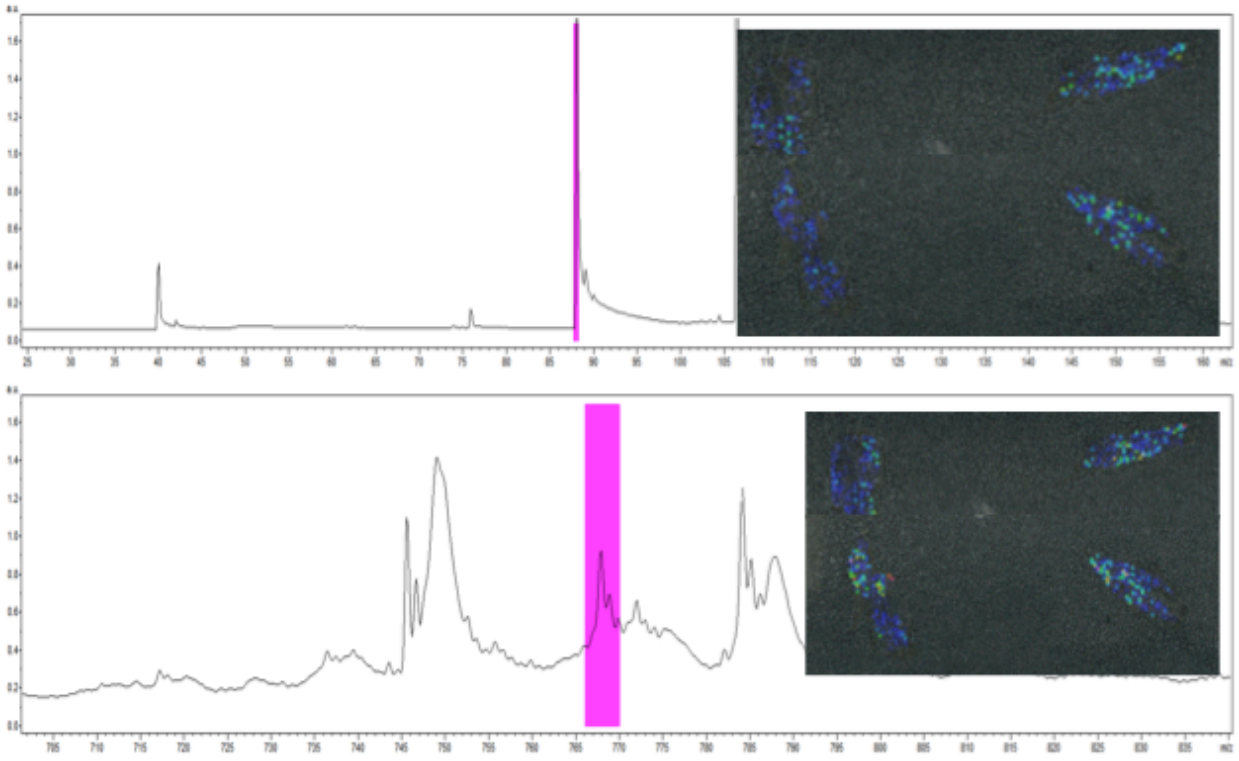

Figure 30. Several unique peaks were observed in lung excised from BZ6-treated SCID mice. (A) Shows the average spectrum from a washed lung section, with the unique peak at 87 m/z highlighted in pink, and the virtual image shown to the right. (B) Shows the average spectrum from a washed lung section, with the unique peak at 768 m/z highlighted in pink, and the virtual image shown to the right.

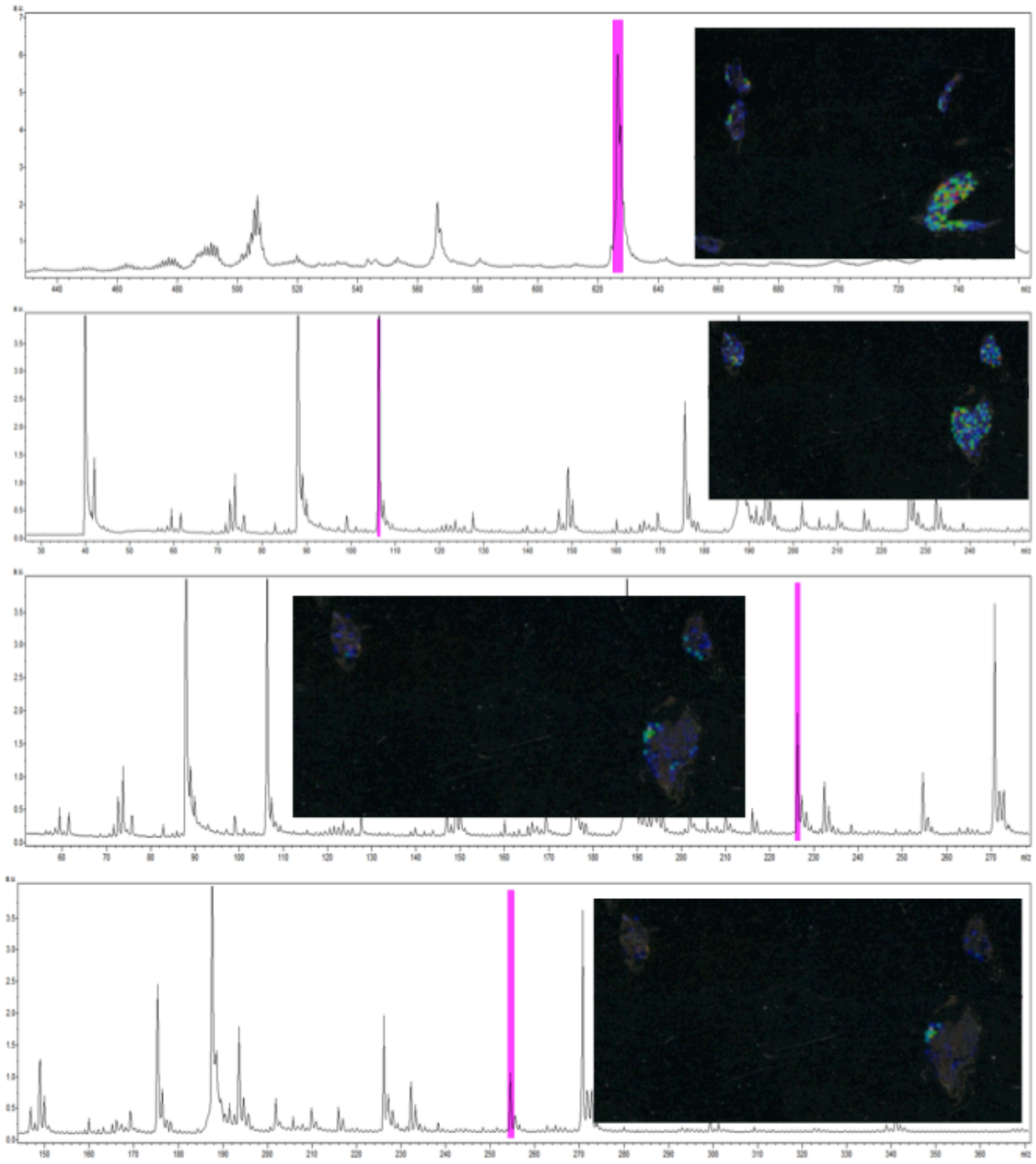

Figure 31. Several unique peaks were observed in spleen excised from BZ6-treated SCID mice. (A) Shows the average spectrum from an unwashed spleen section, with the unique peak at 626 m/z highlighted in pink, and the virtual image shown to the right. (B) Shows the average spectrum from a washed spleen section, with the unique peak at

105 m/z highlighted in pink, and the virtual image shown to the right. (C) Shows the average spectrum from a washed spleen section, with the unique peak at 226 m/z highlighted in pink, and the virtual image shown to the right. (D) Shows the average spectrum from a washed spleen section, with the unique peak at 254 m/z highlighted in pink, and the virtual image shown to the right.

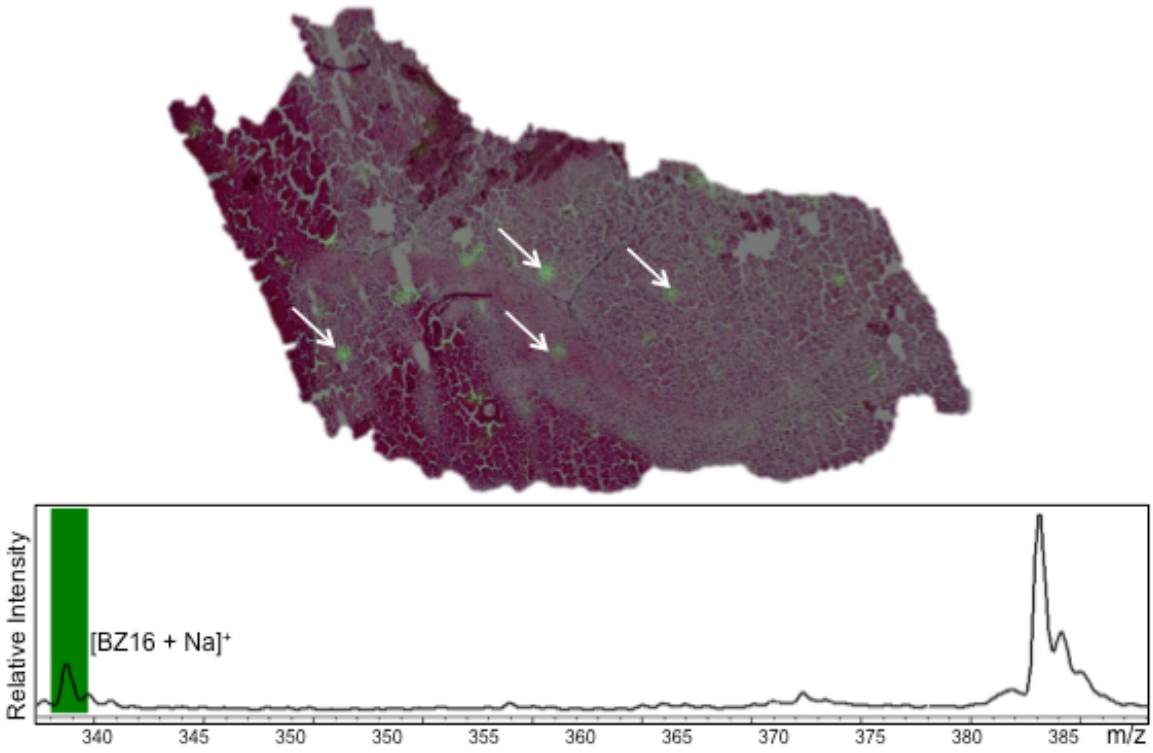

Figure 32. BZ16 was found to cross the blood-brain barrier and enter the cerebellum. (A) Shows an H&E stained cerebellum section, with BZ16 location indicated by the white arrows and green spots. (B) Shows the average spectrum collected, from washed sections, with the monosodiated BZ16 peak highlighted in green.

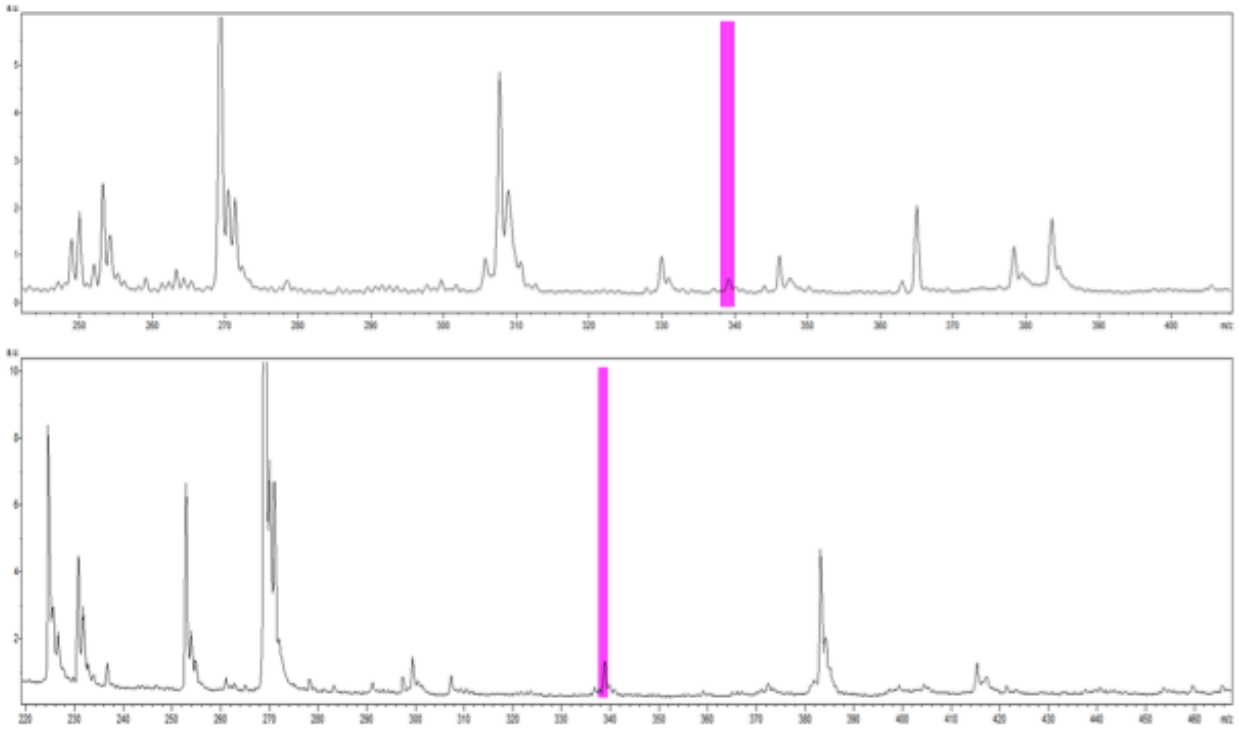

Figure 33. BZ16 was found to cross the blood-brain barrier and enter the cerebellum. (A) Shows the average spectrum from an unwashed cerebellum section, with the unique peak at 338 m/z highlighted in pink. (B) Shows the average spectrum from a washed cerebellum section, with the unique peak at 338 m/z highlighted in pink.

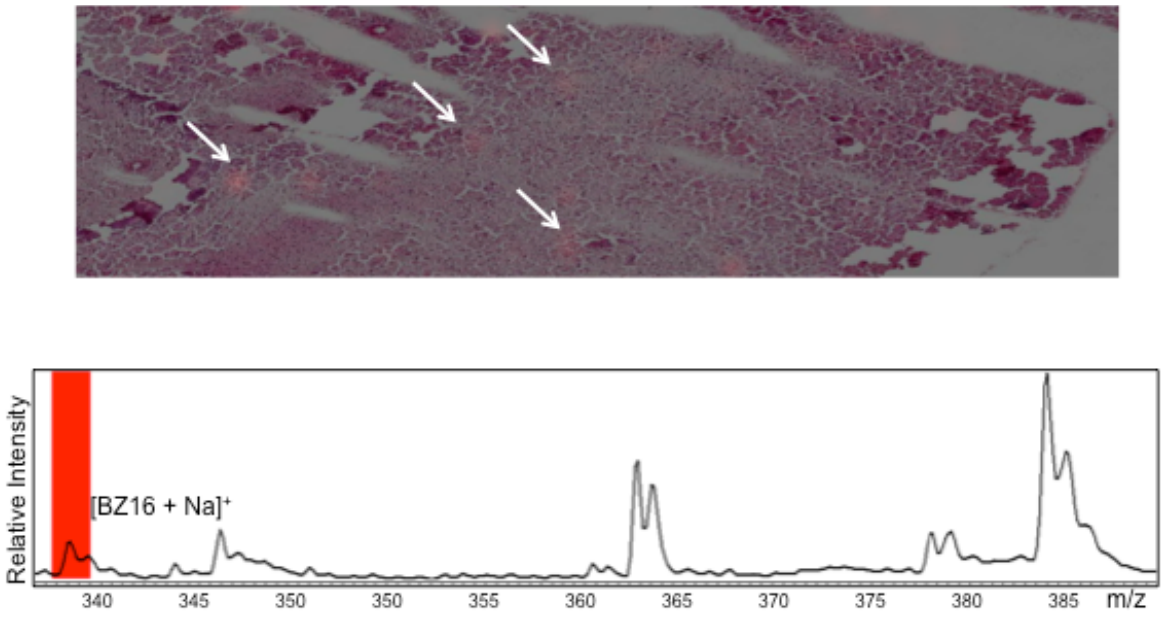

Figure 34. BZ16 was found to cross the blood-brain barrier and enter the cerebrum. (A) Shows an H&E stained cerebrum section, with BZ16 location indicated by the white arrows and red spots. (B) Shows the average spectrum collected, from washed sections, with the monosodiated BZ16 peak highlighted in red.

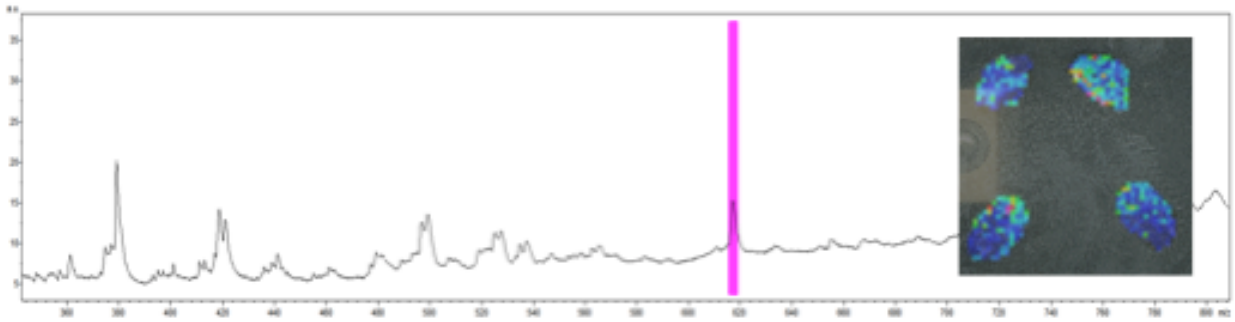

Figure 35. One unique peak was observed in heart excised from BZ16-treated C57BL/6 mice. The average spectrum from an unwashed heart section, with the unique peak at 617 m/z highlighted in pink is shown, and the virtual image shown to the right.

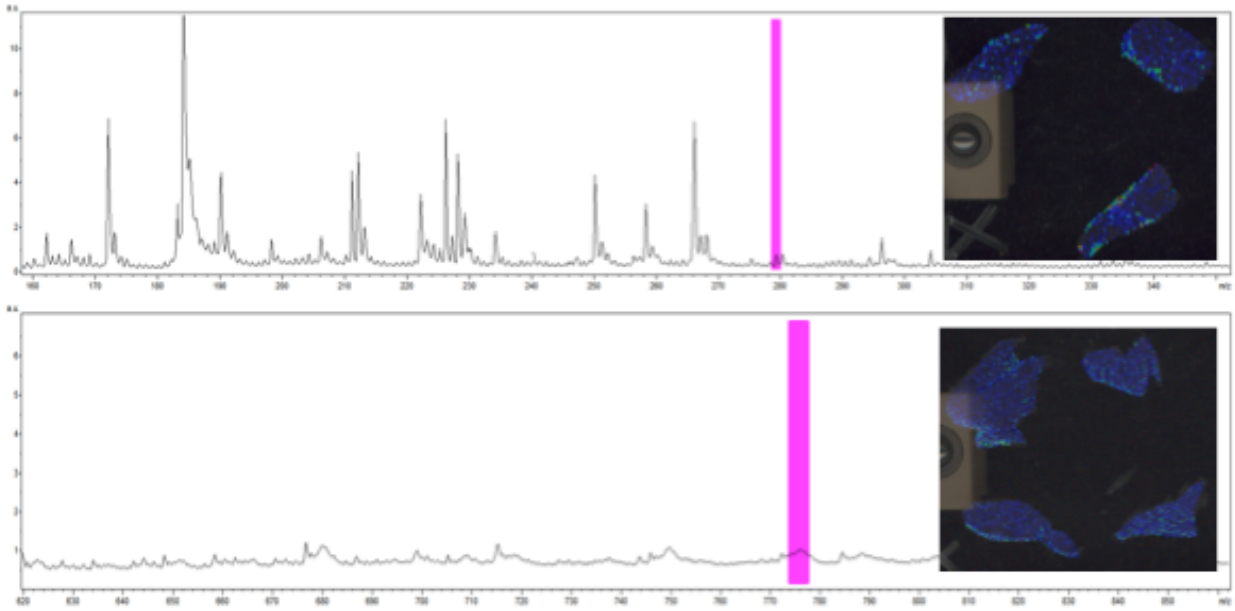

Figure 36. Several unique peaks were observed in liver excised from BZ16-treated C57BL/6 mice. (A) Shows the average spectrum from a washed liver section, with the unique peak at 278 m/z highlighted in pink, and the virtual image shown to the right. (B) Shows the average spectrum from a washed liver section, with the unique peak at 776 m/z highlighted in pink, and the virtual image shown to the right.

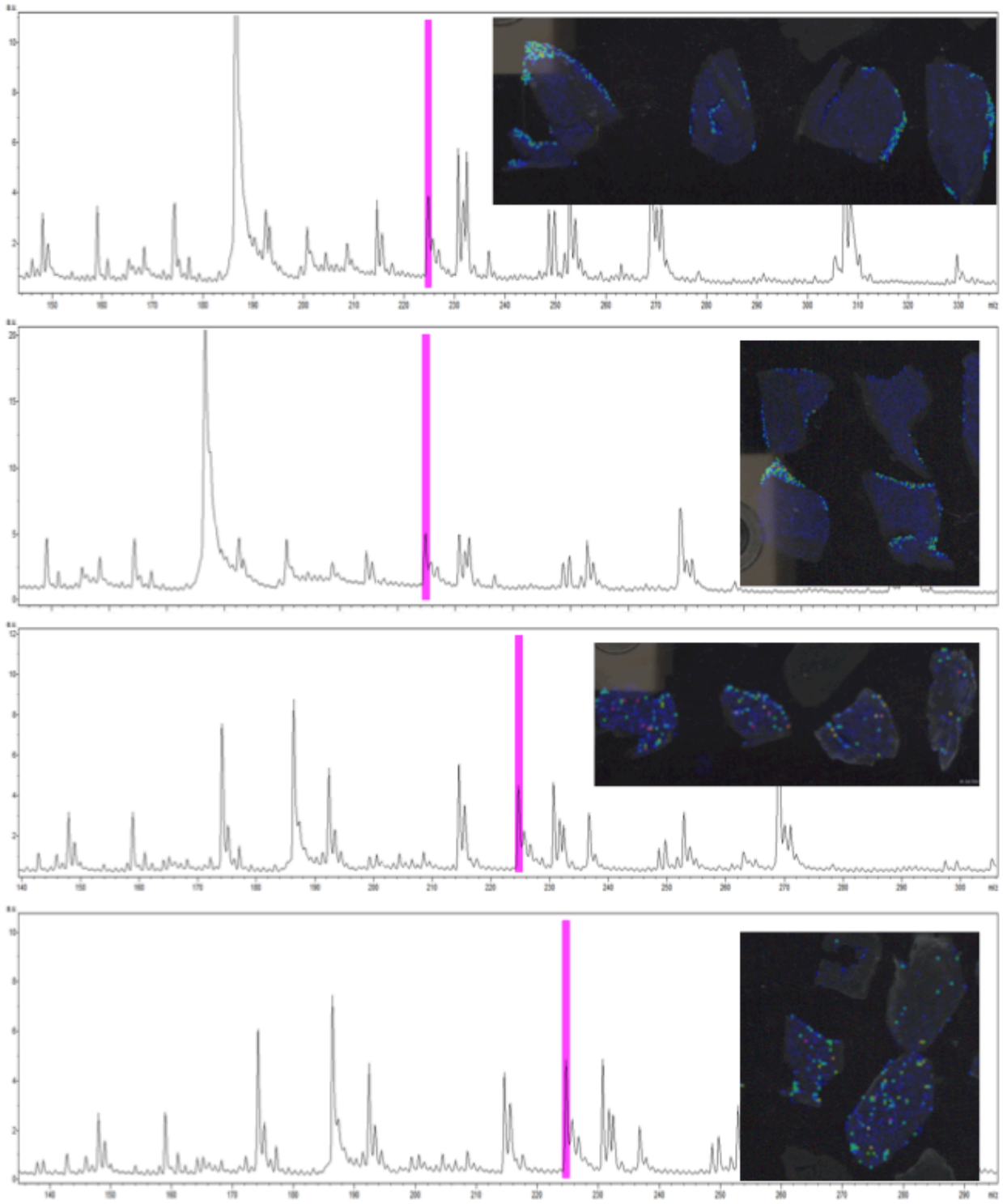

Figure 37. A unique peak was observed in brain excised from BZ16-treated SCID mice. (A) Shows the average spectrum from an unwashed cerebellum section, with the unique peak at 224 m/z highlighted in pink, and the virtual image shown to the right. (B) Shows

the average spectrum from a washed cerebellum section, with the unique peak at 224 m/z highlighted in pink, and the virtual image shown to the right. (C) Shows the average spectrum from an unwashed cerebrum section, with the unique peak at 224 m/z highlighted in pink, and the virtual image shown to the right. (D) Shows the average spectrum from a washed cerebrum section, with the unique peak at 224 m/z highlighted in pink, and the virtual image shown to the right.

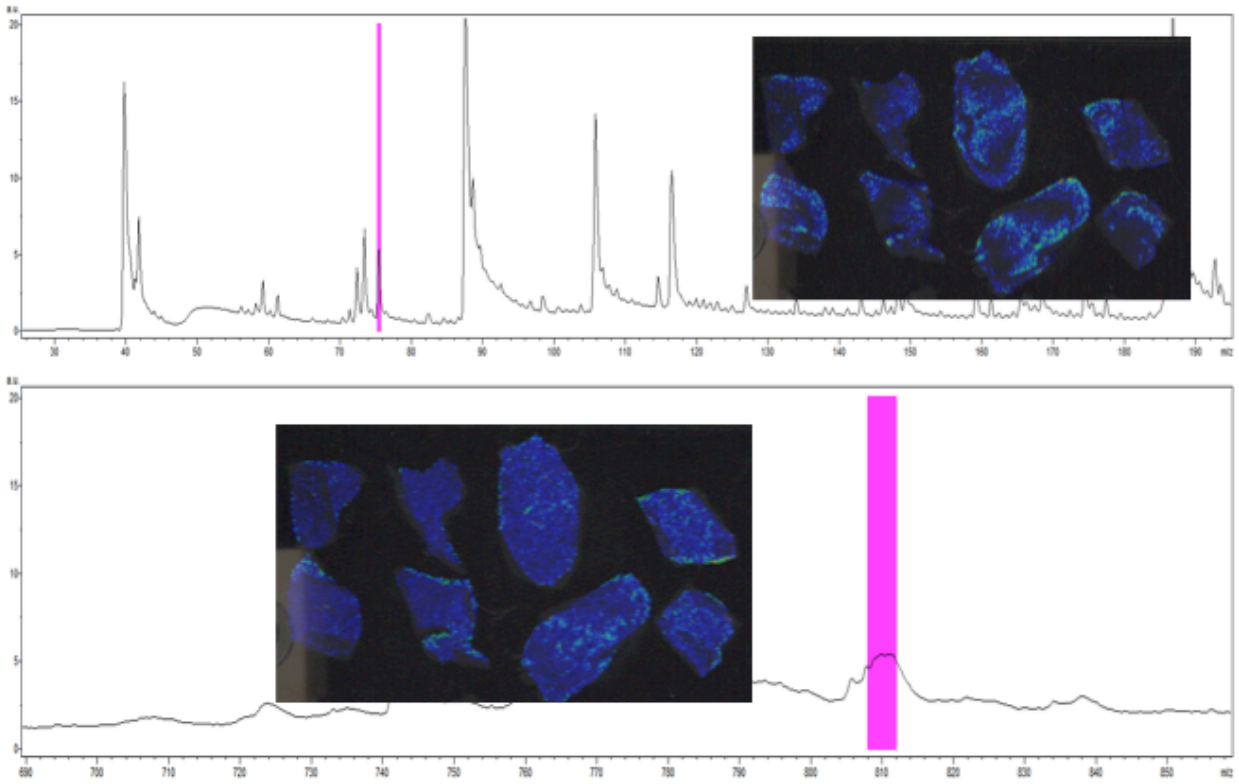

Figure 38. Several unique peaks were observed in brain excised from BZ16-treated SCID mice. (A) Shows the average spectrum from a washed cerebellum section, with the unique peak at 75 m/z highlighted in pink, and the virtual image shown to the right. (B) Shows the average spectrum from a washed cerebellum section, with the unique peak at 810 m/z highlighted in pink, and the virtual image shown to the right.

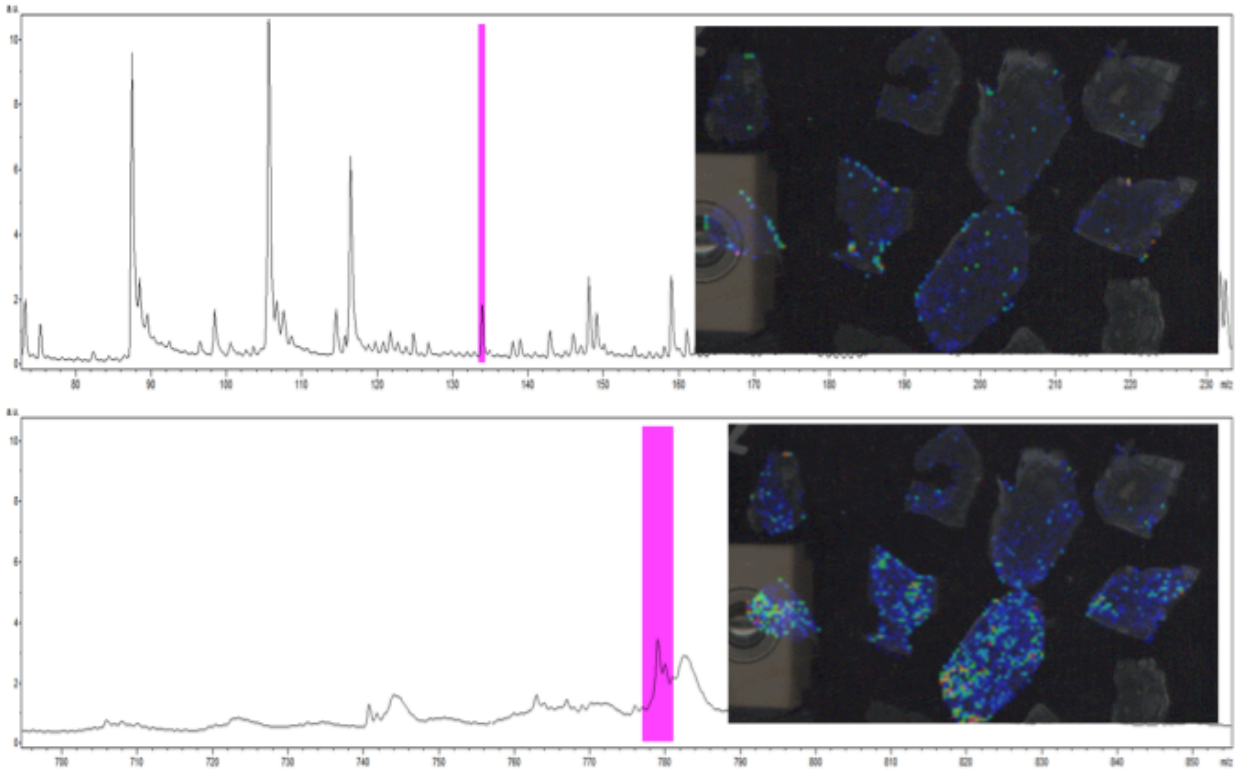

Figure 39. Several unique peaks were observed in brain excised from BZ16-treated SCID mice. (A) Shows the average spectrum from an unwashed cerebellum section, with the unique peak at 133 m/z highlighted in pink, and the virtual image shown to the right. (B) Shows the average spectrum from an unwashed cerebellum section, with the unique peak at 779 m/z highlighted in pink, and the virtual image shown to the right.

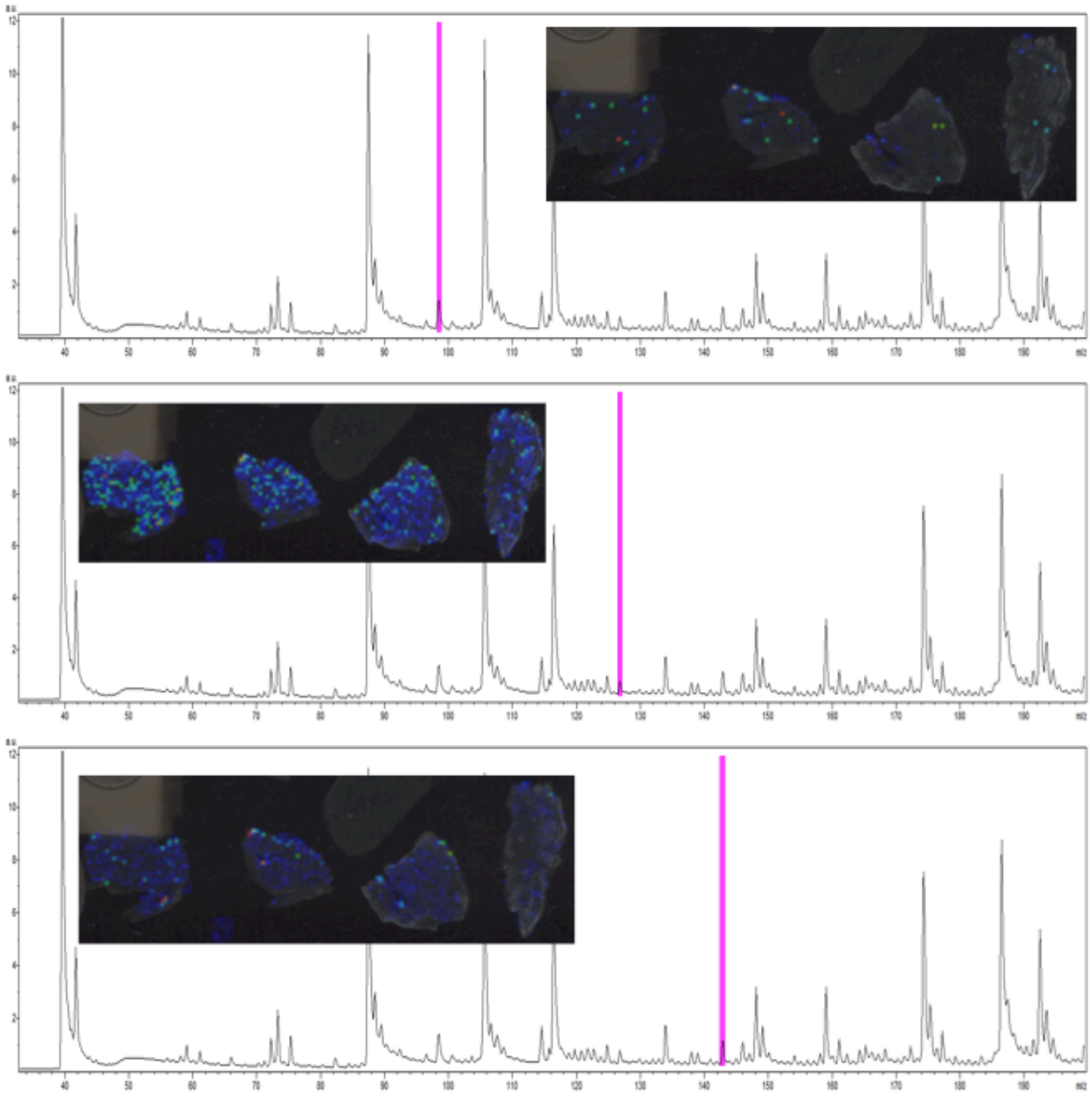

Figure 40. Several unique peaks were observed in brain excised from BZ16-treated SCID mice. (A) Shows the average spectrum from an unwashed cerebrum section, with the unique peak at 98 m/z highlighted in pink, and the virtual image shown to the right. (B) Shows the average spectrum from an unwashed cerebrum section, with the unique peak at 126 m/z highlighted in pink, and the virtual image shown to the right. (B) Shows

the average spectrum from an unwashed cerebrum section, with the unique peak at 142 m/z highlighted in pink, and the virtual image shown to the right.

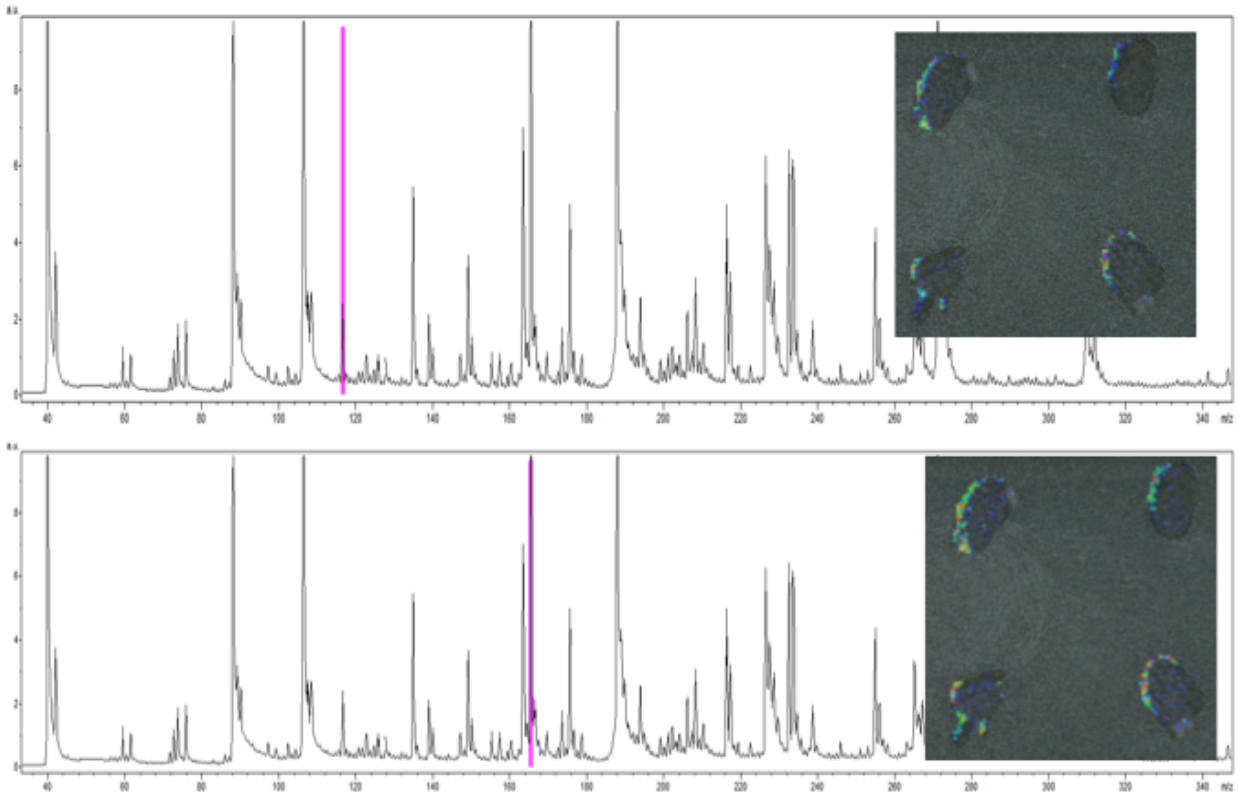

Figure 41. Several unique peaks were observed in heart excised from BZ16-treated SCID mice. (A) Shows the average spectrum from an unwashed heart section, with the unique peak at 116 m/z highlighted in pink, and the virtual image shown to the right. (B) Shows the average spectrum from an unwashed heart section, with the unique peak at 165 m/z highlighted in pink, and the virtual image shown to the right.

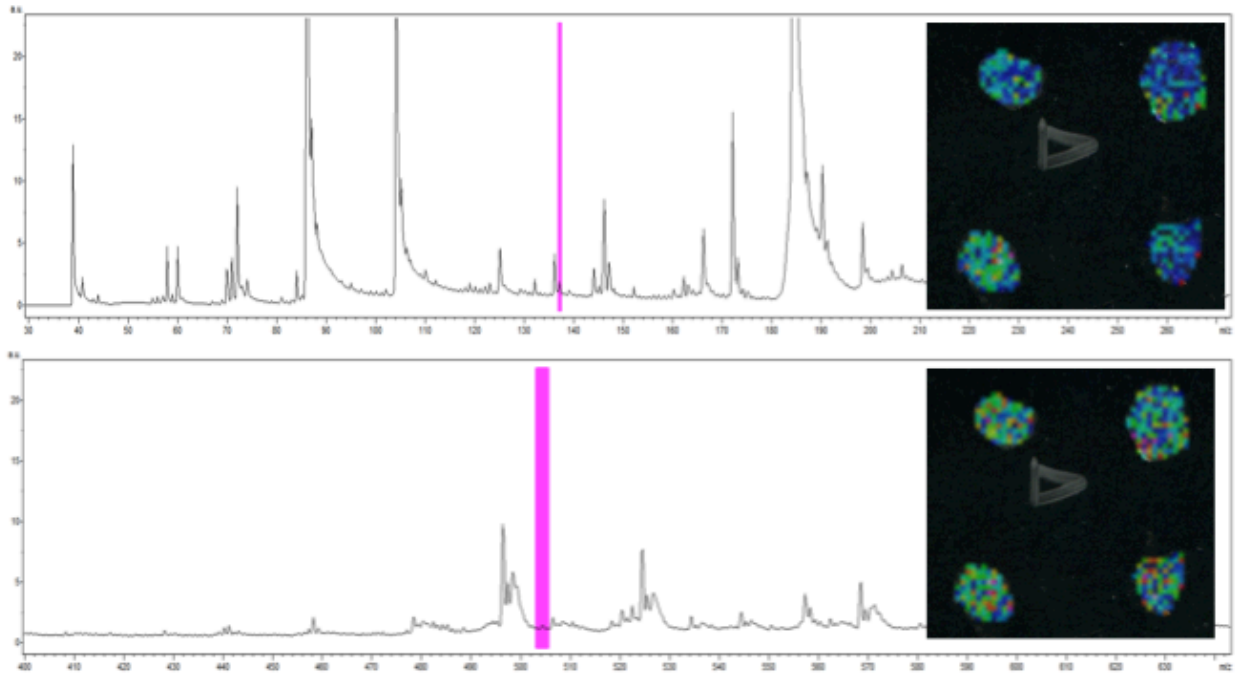

Figure 42. Several unique peaks were observed in heart excised from BZ16-treated SCID mice. (A) Shows the average spectrum from a washed heart section, with the unique peak at 138 m/z highlighted in pink, and the virtual image shown to the right. (B) Shows the average spectrum from a washed heart section, with the unique peak at 504 m/z highlighted in pink, and the virtual image shown to the right.

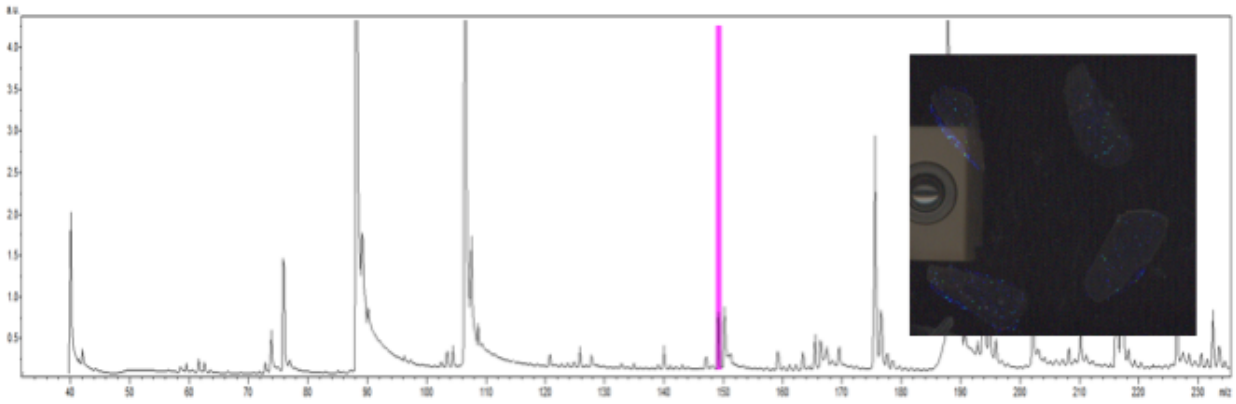

Figure 43. One unique peak was observed in kidney excised from BZ16-treated SCID mice. The average spectrum from an unwashed kidney section, with the unique peak at 149 m/z highlighted in pink is shown, and the virtual image shown to the right.

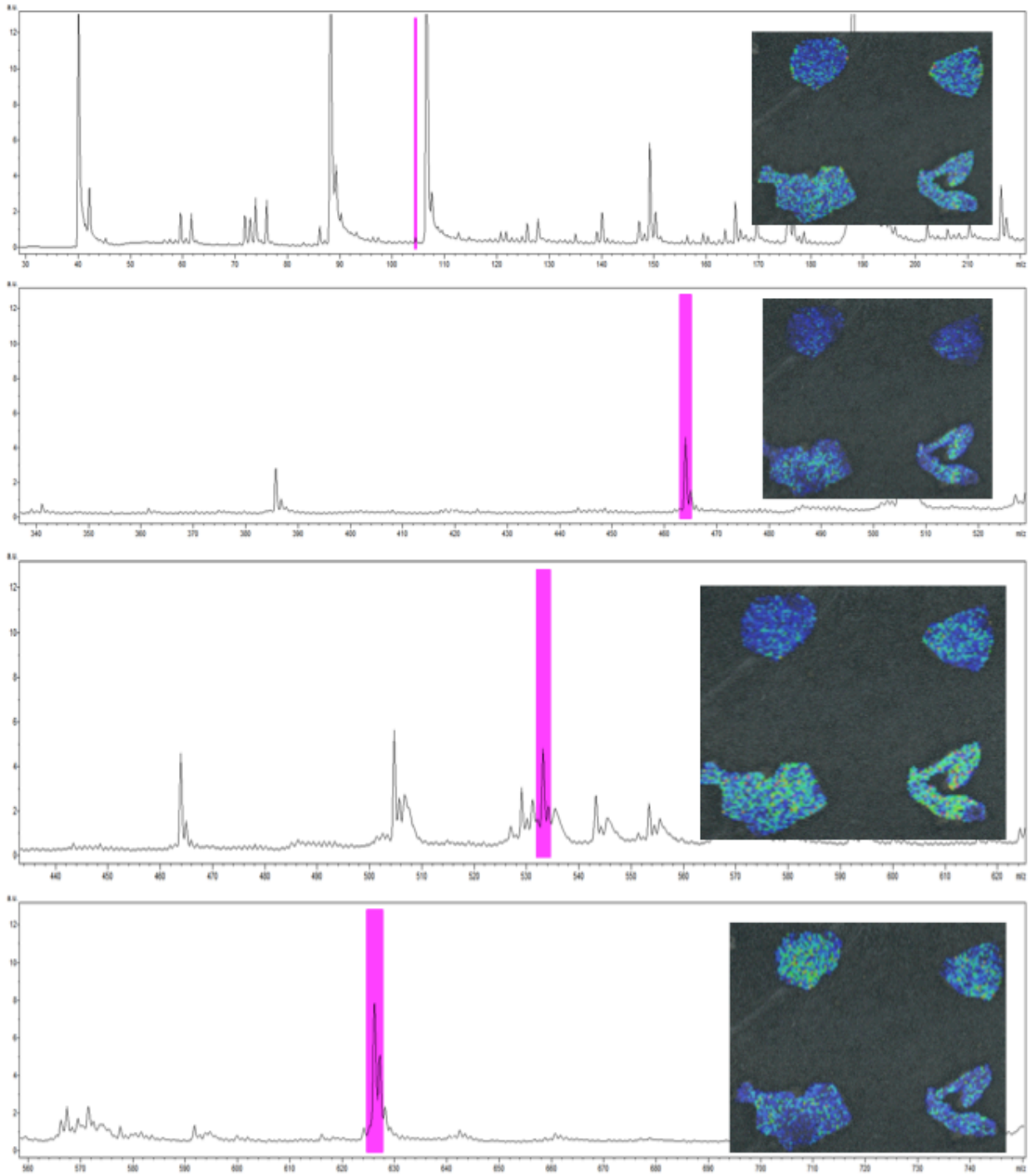

Figure 44. Several unique peaks were observed in liver excised from BZ16-treated SCID mice. (A) Shows the average spectrum from an unwashed liver section, with the unique peak at 104 m/z highlighted in pink, and the virtual image shown to the right. (B) Shows the average spectrum from an unwashed liver section, with the unique peak at

463 m/z highlighted in pink, and the virtual image shown to the right. (C) Shows the average spectrum from an unwashed liver section, with the unique peak at 533 m/z highlighted in pink, and the virtual image shown to the right. (D) Shows the average spectrum from an unwashed liver section, with the unique peak at 626 m/z highlighted in pink, and the virtual image shown to the right.

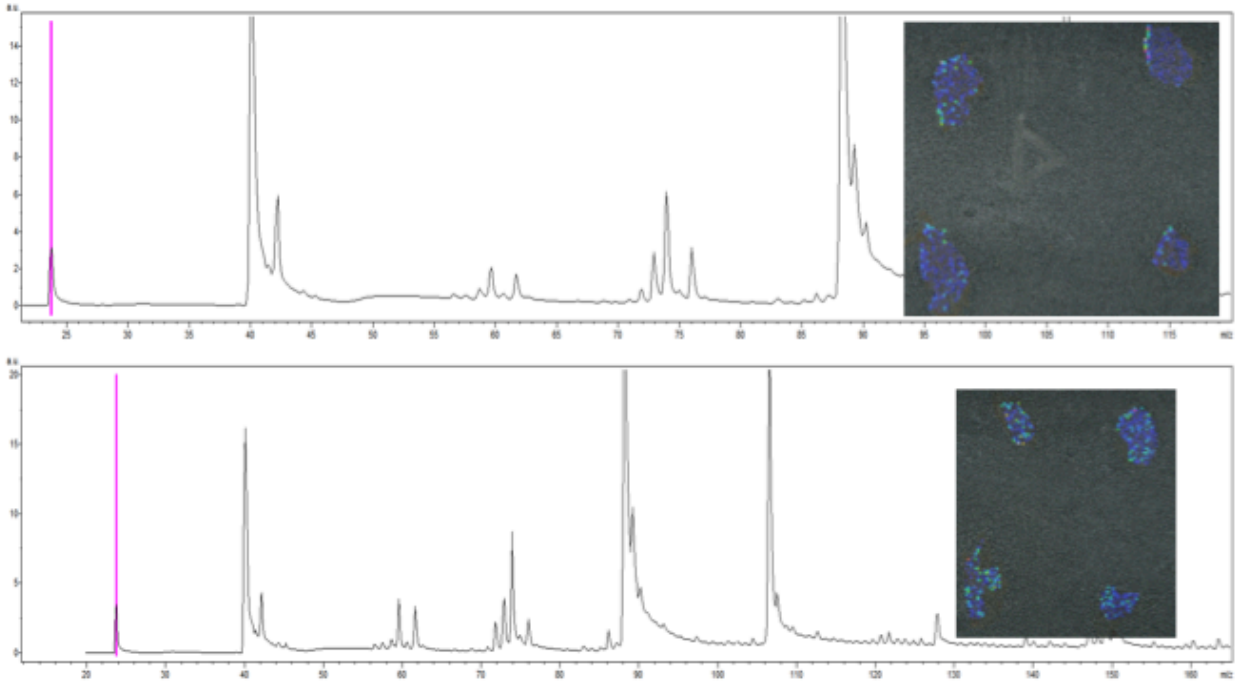

Figure 45. Several unique peaks were observed in lung excised from BZ16-treated SCID mice. (A) Shows the average spectrum from an unwashed lung section, with the unique peak at 23 m/z highlighted in pink, and the virtual image shown to the right. (B) Shows the average spectrum from a washed lung section, with the unique peak at 23 m/z highlighted in pink, and the virtual image shown to the right.

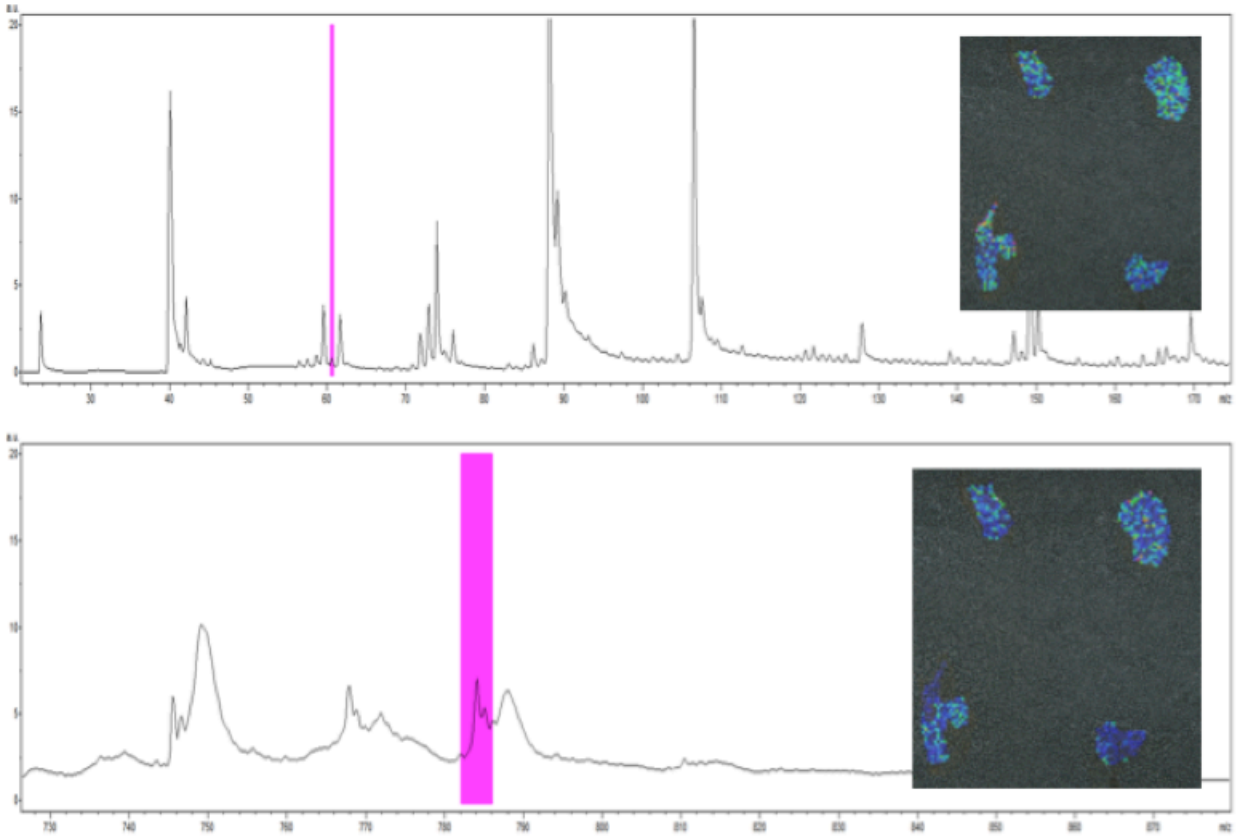

Figure 46. Several unique peaks were observed in lung excised from BZ16-treated SCID mice. (A) Shows the average spectrum from a washed lung section, with the unique peak at 60 m/z highlighted in pink, and the virtual image shown to the right. (B) Shows the average spectrum from a washed lung section, with the unique peak at 784 m/z highlighted in pink, and the virtual image shown to the right.

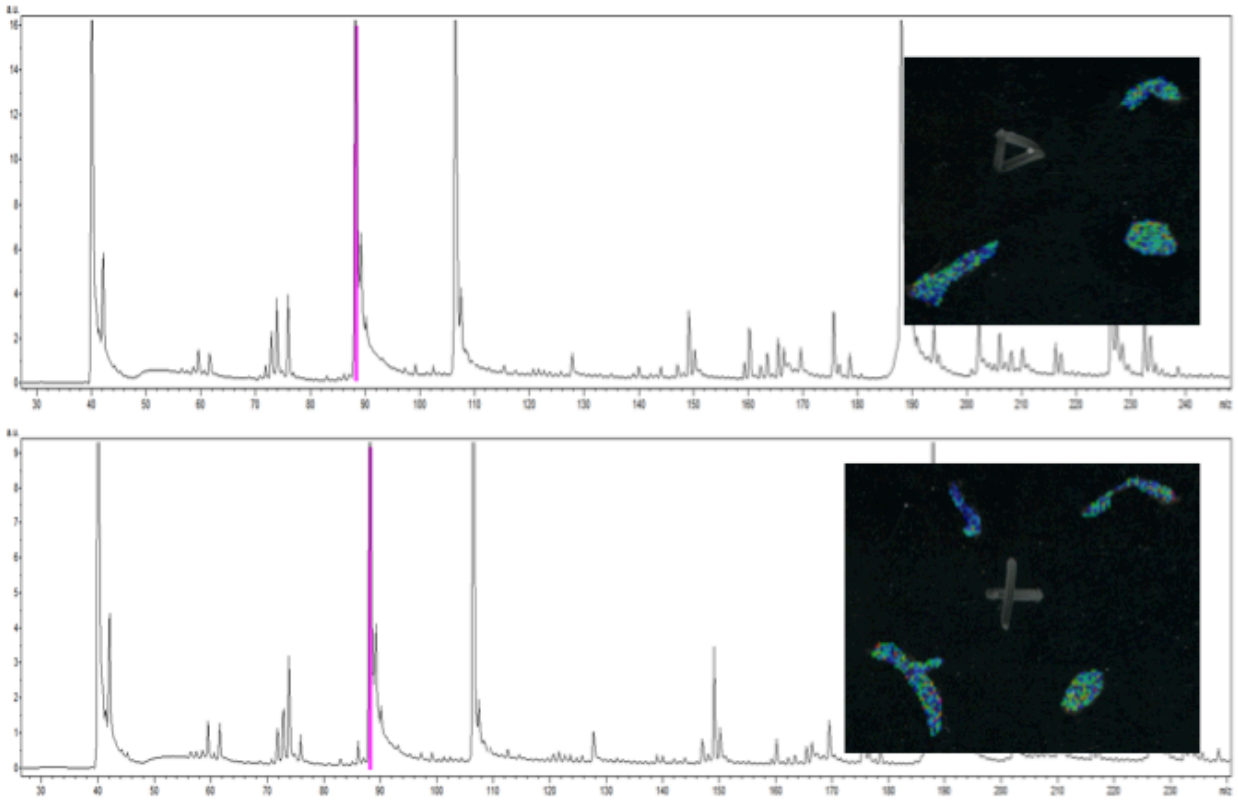

Figure 47. Several unique peaks were observed in spleen excised from BZ16-treated SCID mice. (A) Shows the average spectrum from an unwashed spleen section, with the unique peak at 88 m/z highlighted in pink, and the virtual image shown to the right. (B) Shows the average spectrum from a washed spleen section, with the unique peak at 88 m/z highlighted in pink, and the virtual image shown to the right.

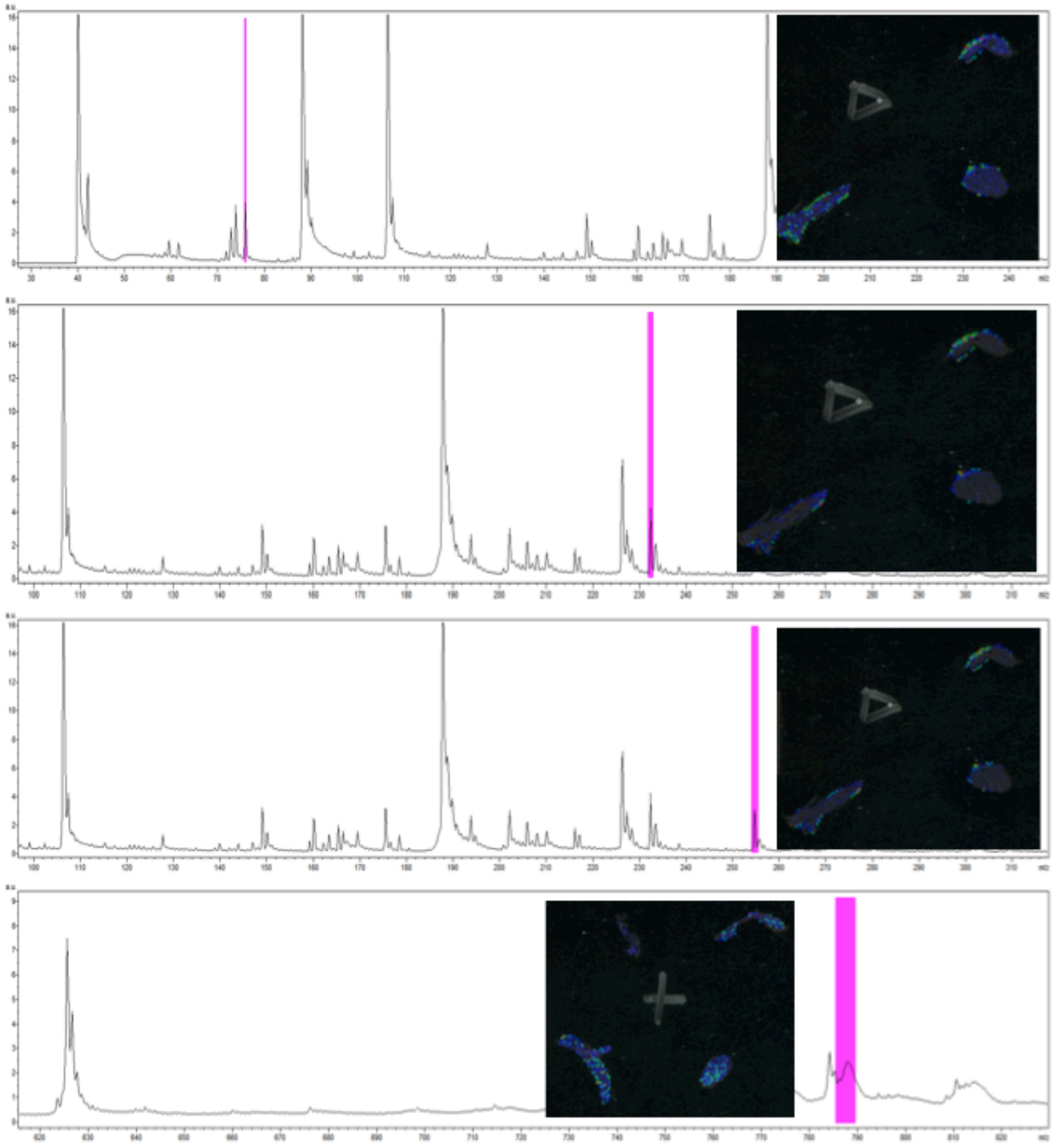

Figure 48. Several unique peaks were observed in spleen excised from BZ16-treated SCID mice. (A) Shows the average spectrum from an unwashed spleen section, with the unique peak at 75 m/z highlighted in pink, and the virtual image shown to the right. (B) Shows the average spectrum from an unwashed spleen section, with the unique peak at 232 m/z highlighted in pink, and the virtual image shown to the right. (C) Shows

the average spectrum from an unwashed spleen section, with the unique peak at 254 m/z highlighted in pink, and the virtual image shown to the right. (D) Shows the average spectrum from a washed spleen section, with the unique peak at 786 m/z highlighted in pink, and the virtual image shown to the right.

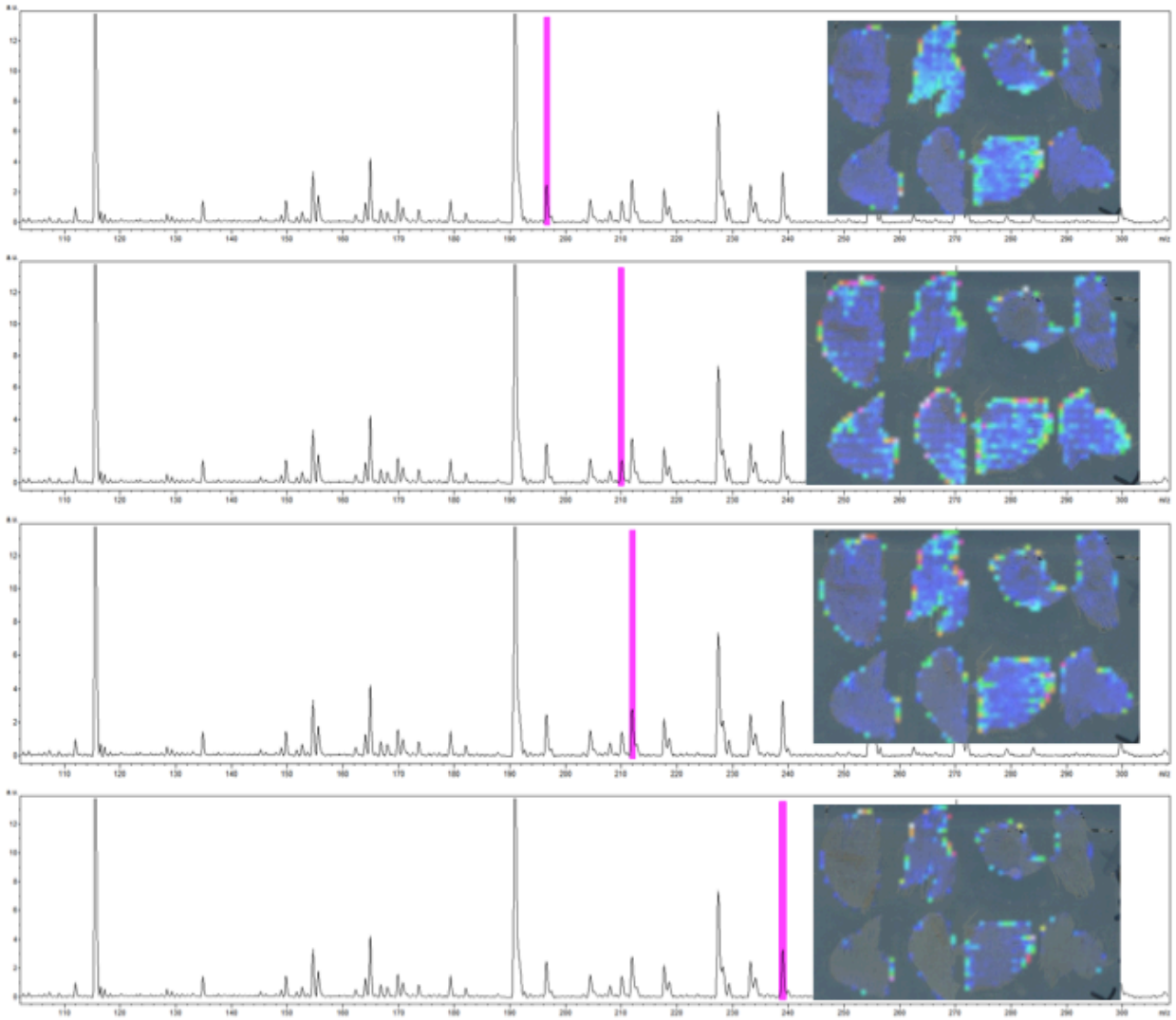

Figure 49. Several unique peaks were observed in liver excised from RTC13-treated C57BL/6 mice. (A) Shows the average spectrum from a liver section, with the unique peak at 196 m/z highlighted in pink, and the virtual image shown to the right (present in 2 h and 8 h timepoints). (B) Shows the average spectrum from a liver section, with the unique peak at 209 m/z highlighted in pink, and the virtual image shown to the right (present in 2 h, 8 h, and 24 h timepoints). (C) Shows the average spectrum from a liver section, with the unique peak at 212 m/z highlighted in pink, and the virtual image shown to the right (present in 2 h and 8 h timepoints). (D) Shows the average spectrum

from a liver section, with the unique peak at 239 m/z highlighted in pink, and the virtual image shown to the right (present in 2 h and 8 h timepoints).

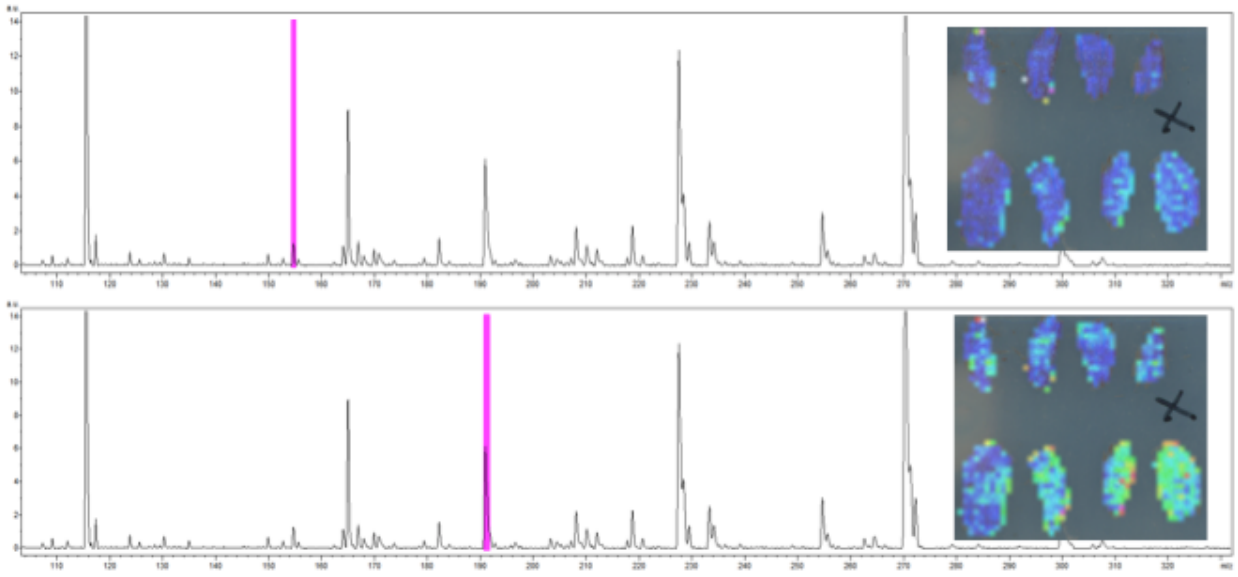

Figure 50. Several unique peaks were observed in spleen excised from RTC13-treated C57BL/6 mice. (A) Shows the average spectrum from a spleen section, with the unique peak at 154 m/z highlighted in pink, and the virtual image shown to the right (present in the 2 h timepoint). (B) Shows the average spectrum from a spleen section, with the unique peak at 191 m/z highlighted in pink, and the virtual image shown to the right (present in 2 h, 8 h, and 24 h timepoints).

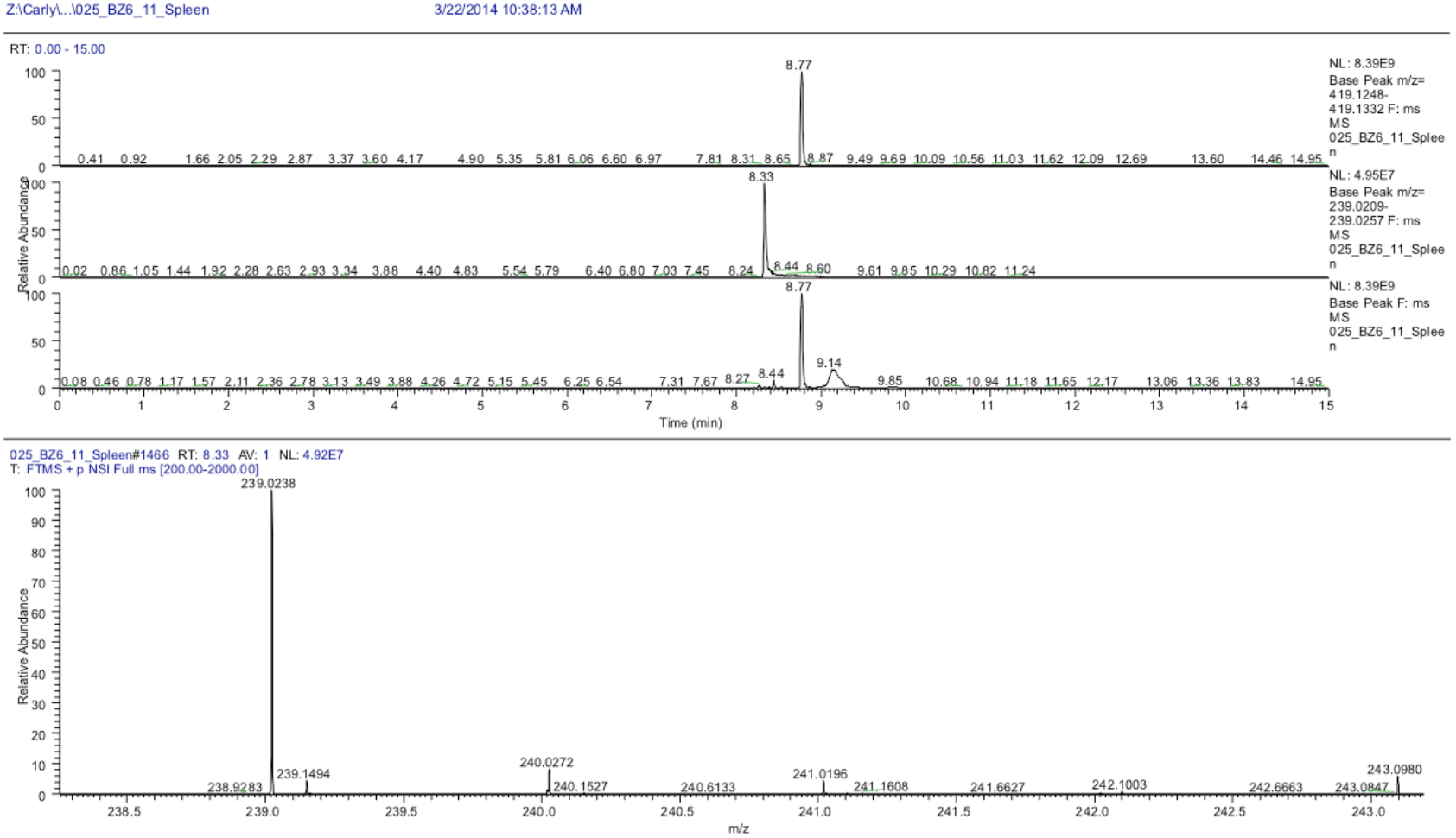
Z:\Carly\...\025_BZ6_11_Spleen 3/22/2014 10:38:13 AM
RT: 0.00 - 15.00
NL: 8.39E9
Base Peak m/z= 419.1248-419.1332 F: ms MS 025_BZ6_11_Spleen
NL: 4.95E7
Base Peak m/z= 239.0209-239.0257 F: ms MS 025_BZ6_11_Spleen
NL: 8.39E9
Base Peak F: ms MS 025_BZ6_11_Spleen
Relative Abundance
Time (min)
025_BZ6_11_Spleen#1466 RT: 8.33 AV: 1 NL: 4.92E7
T: FTMS + p NSI Full ms [200.00-2000.00]
239.0238
239.1494
240.0272
240.1527
240.6133
241.0196
241.1608
241.6627
242.1003
242.6663
243.0847
243.0980
m/z

Figure 51. BZ6 was detected in an extracted spleen homogenate from a BZ6-treated C57BL/6 mouse. (A) XIC of a 216-5 spiked standard. (B) XIC of BZ6. (C) TIC of the extracted spleen homogenate (mouse 11). (D) Mass spectrum of BZ6.

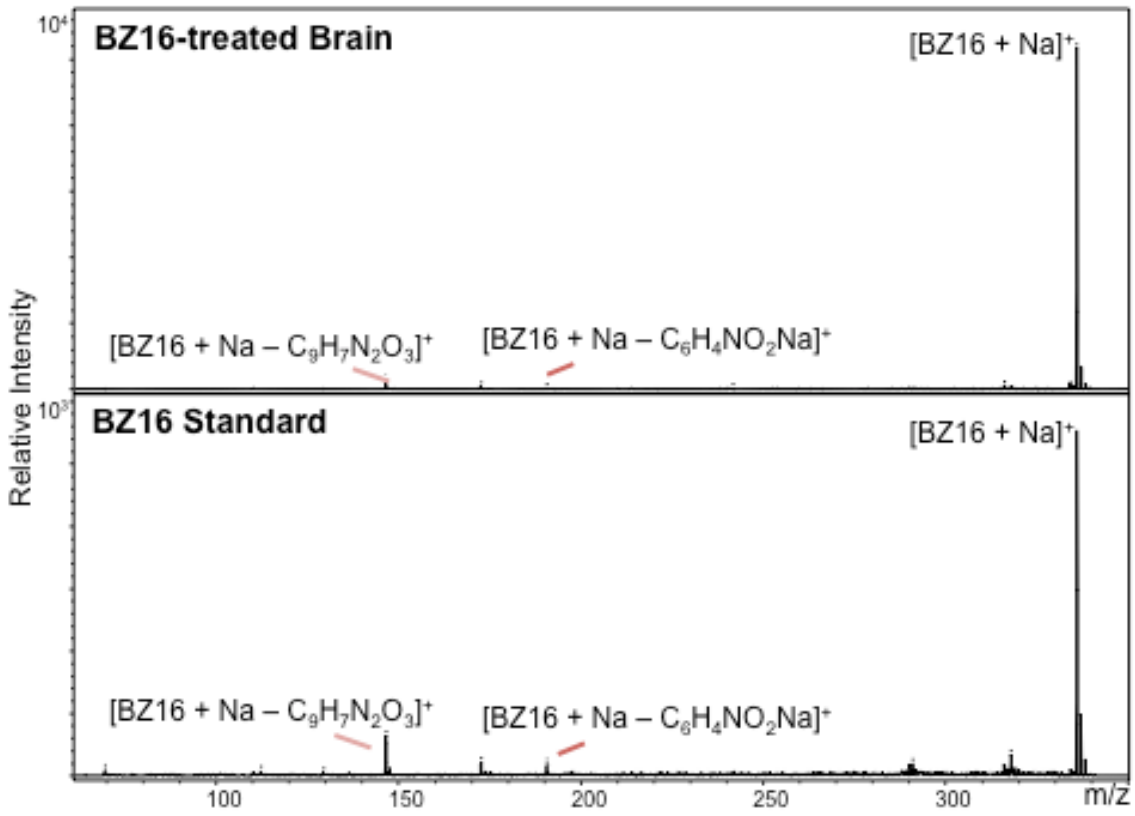

Figure 52. An MS/MS spectrum was collected using a MALDI-TOF/TOF, fragmenting peak 338 m/z from a washed section of BZ16-treated C57BL/6 mouse cerebellum. When compared to the BZ16 standard, this fragmentation confirmed this peak's identity as the monosidated form of BZ16.

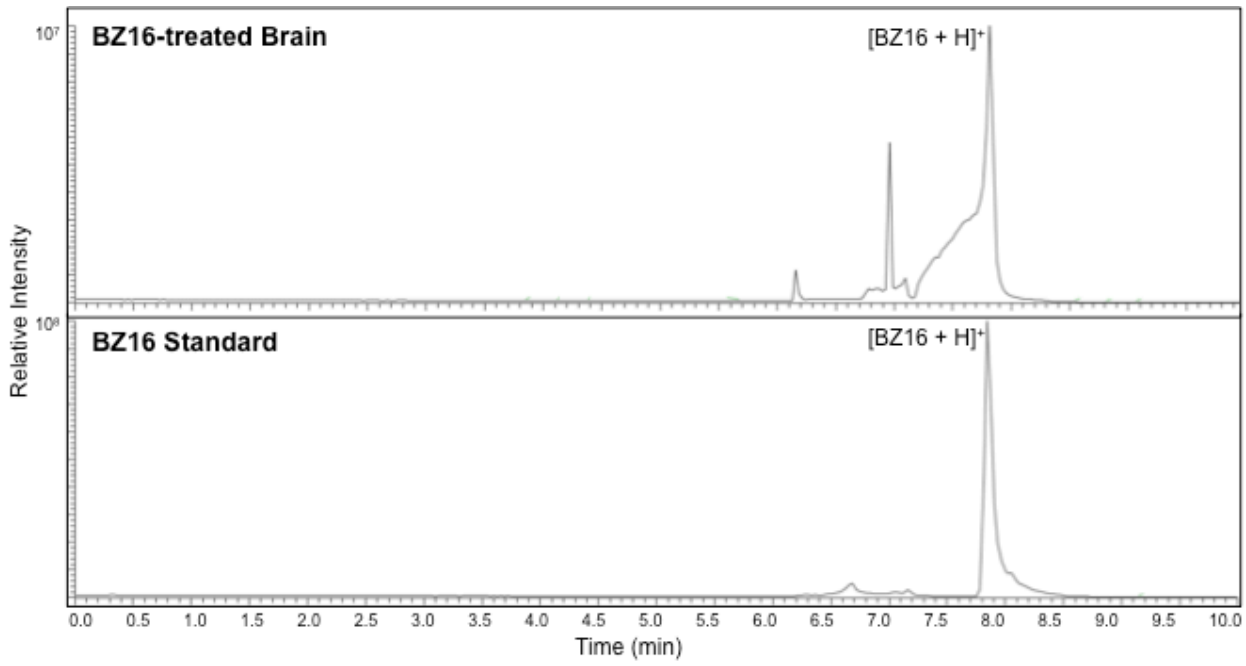

Figure 53. A chromatographic run shows the presence of BZ16 in an extracted brain homogenate of BZ16-treated C57BL/6 mouse brain when compared to a standard BZ16 run.

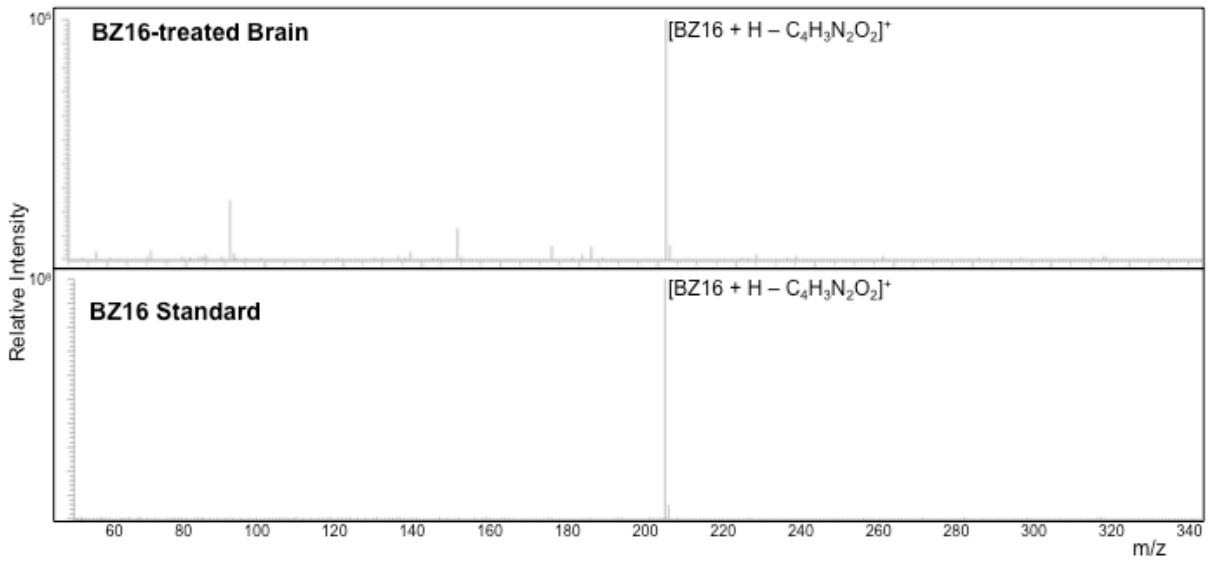

Figure 54. An LC-MS/MS spectrum shows the presence of BZ16 in an extracted brain homogenate of BZ16-treated C57BL/6 mouse brain when compared to a standard BZ16 MS/MS experiment.

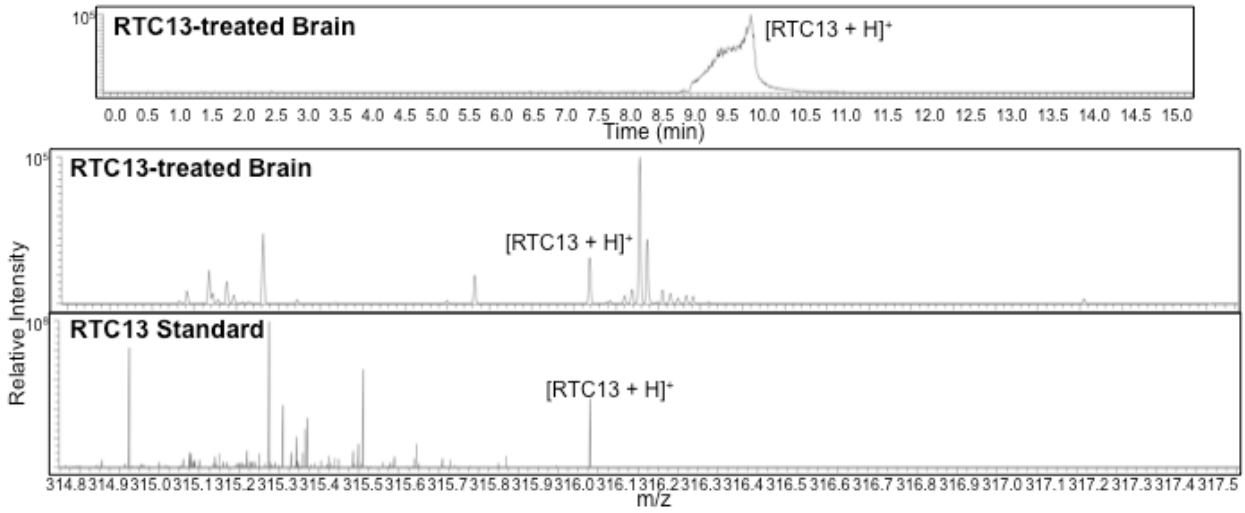

Figure 55. RTC13 was detected in an extracted brain homogenate from a RTC13-treated C57BL/6 mouse sacrificed at 2 h. (A) XIC of RTC13. (B) Mass spectrum of RTC13 in extracted brain homogenate. (C) Mass spectrum of RTC13 standard.

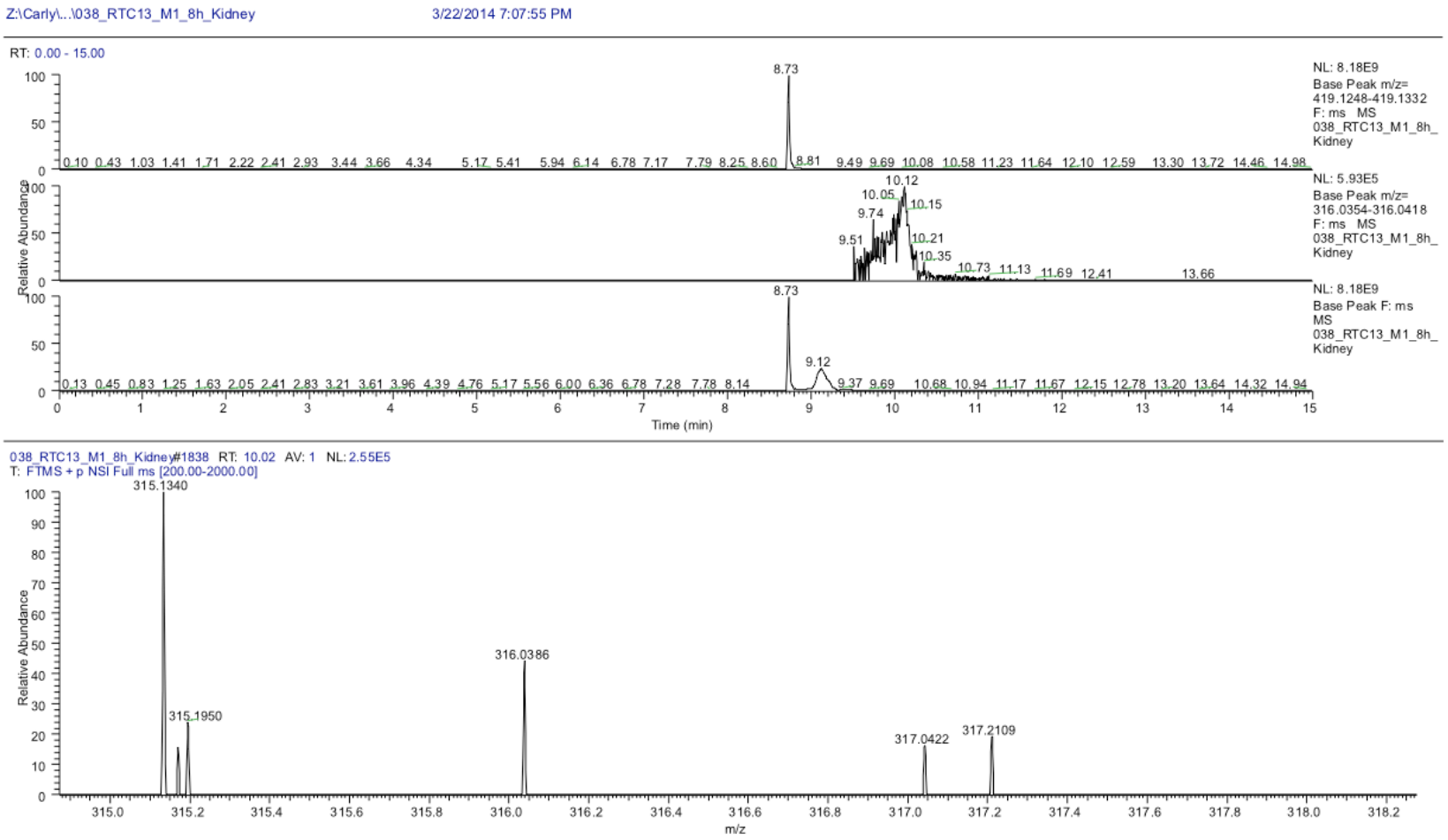
Z:\Carly\...\038_RTC13_M1_8h_Kidney 3/22/2014 7:07:55 PM
RT: 0.00 - 15.00
NL: 8.18E9
Base Peak m/z= 419.1248-419.1332 F: ms MS 038_RTC13_M1_8h_ Kidney
NL: 5.93E5
Base Peak m/z= 316.0354-316.0418 F: ms MS 038_RTC13_M1_8h_ Kidney
NL: 8.18E9
Base Peak F: ms MS 038_RTC13_M1_8h_ Kidney
Relative Abundance
Time (min)
038_RTC13_M1_8h_Kidney#1838 RT: 10.02 AV: 1 NL: 2.55E5
T: FTMS + p NSI Full ms [200.00-2000.00]
315.1340
316.0386
315.1950
317.0422
317.2109
Relative Abundance
m/z

Figure 56. RTC13 was detected in an extracted kidney homogenate from a RTC13-treated C57BL/6 mouse sacrificed at 8 h. (A) XIC of a 216-5 spiked standard. (B) XIC of RTC13. (C) TIC of the extracted kidney homogenate (8hM1). (D) Mass spectrum of RTC13.

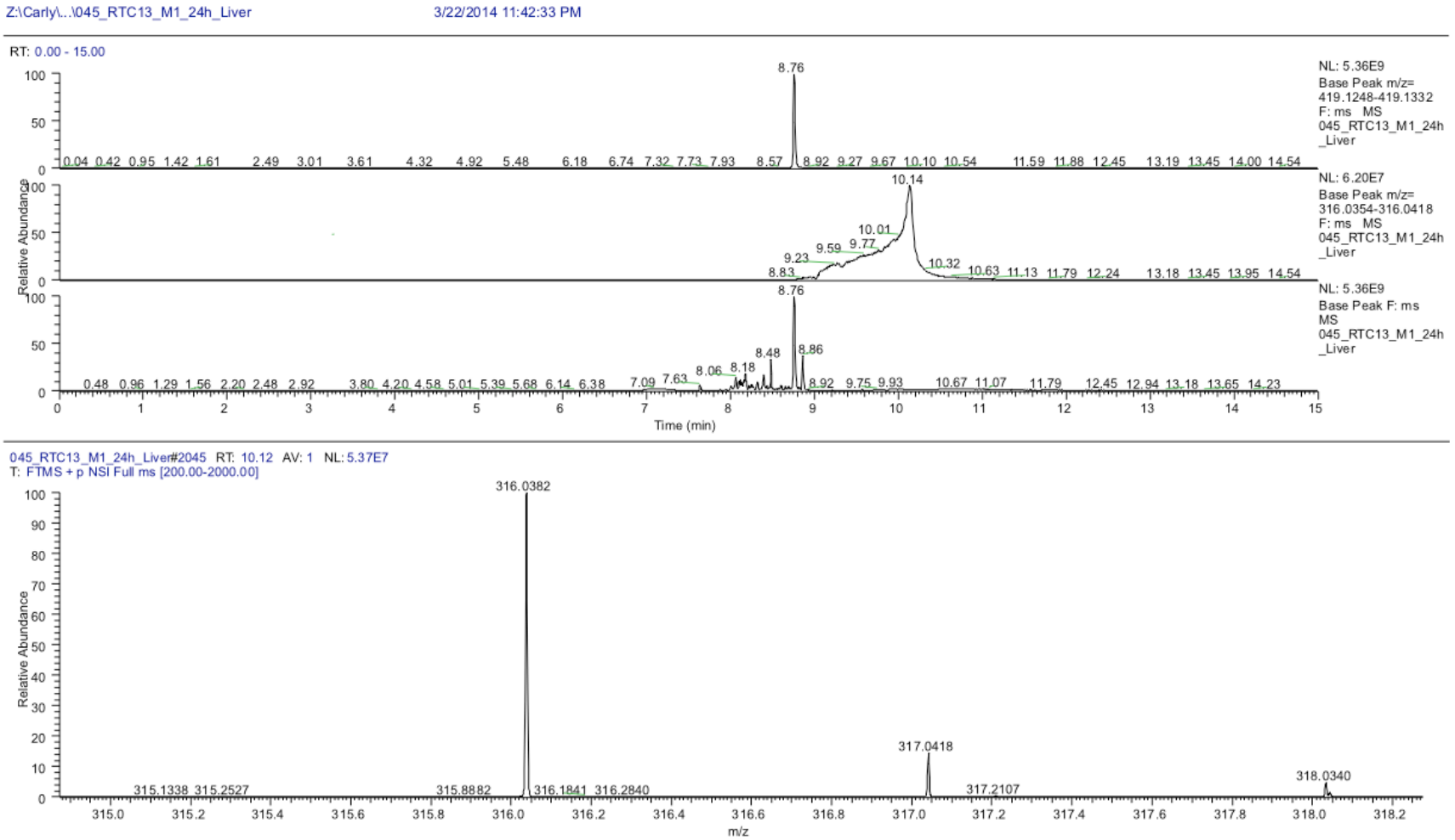
Z:\Carly\...\045_RTC13_M1_24h_Liver 3/22/2014 11:42:33 PM
RT: 0.00 - 15.00
NL: 5.36E9
Base Peak m/z= 419.1248-419.1332 F: ms MS 045_RTC13_M1_24h _Liver
NL: 6.20E7
Base Peak m/z= 316.0354-316.0418 F: ms MS 045_RTC13_M1_24h _Liver
NL: 5.36E9
Base Peak F: ms MS 045_RTC13_M1_24h _Liver
Relative Abundance
Time (min)
045_RTC13_M1_24h_Liver#2045 RT: 10.12 AV: 1 NL: 5.37E7
T: FTMS + p NSI Full ms [200.00-2000.00]
316.0382
317.0418
318.0340
315.1338
315.2527
315.8882
316.1841
316.2840
317.2107
m/z

Figure 57. RTC13 was detected in an extracted liver homogenate from an RTC13-treated C57BL/6 mouse sacrificed at 24 h. (A) XIC of a 216-5 spiked standard. (B) XIC of RTC13. (C) TIC of the extracted liver homogenate (24hM1). (D) Mass spectrum of RTC13.

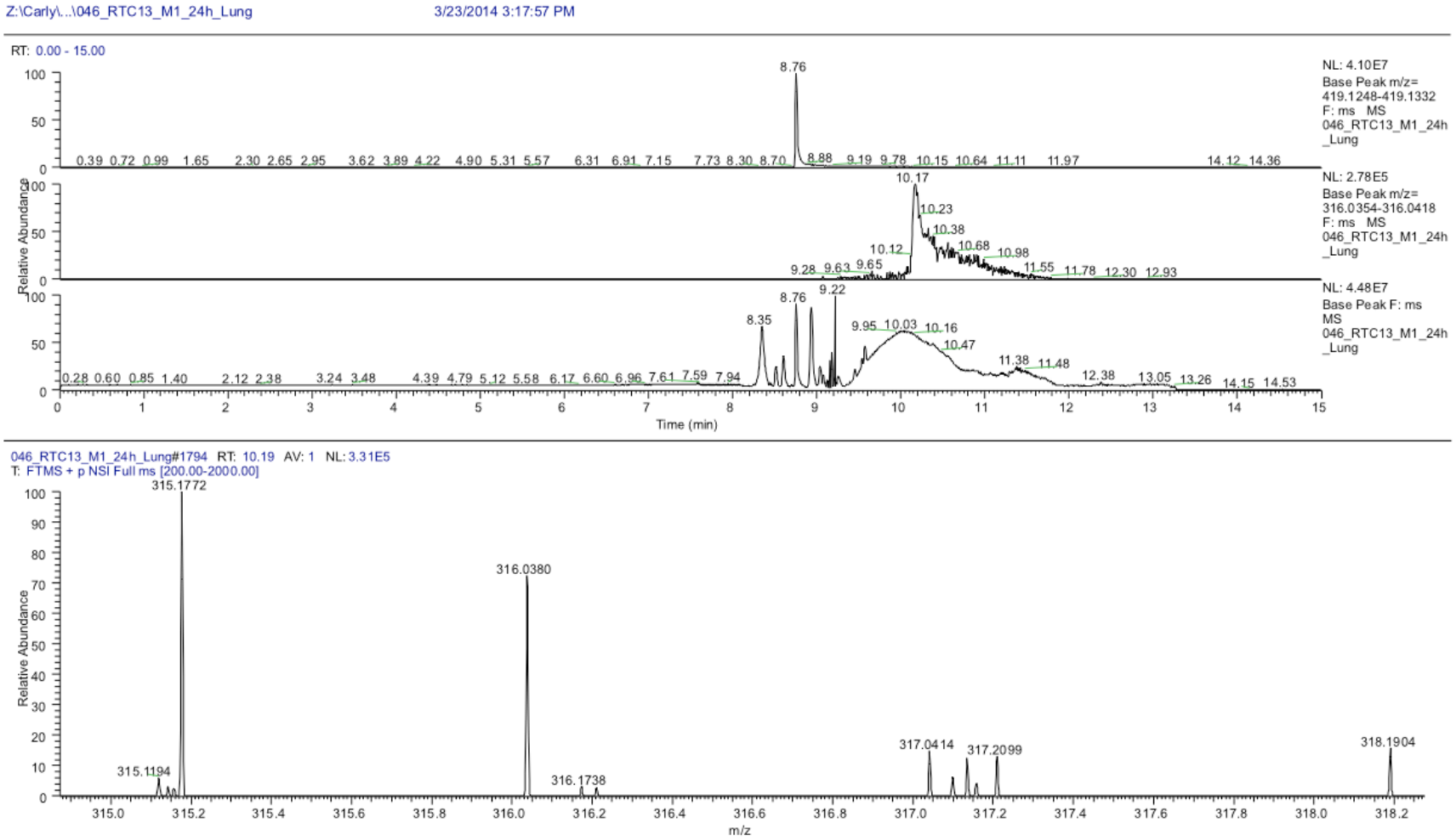
Z:\Carly\...\046_RTC13_M1_24h_Lung 3/23/2014 3:17:57 PM
RT: 0.00 - 15.00
NL: 4.10E7
Base Peak m/z= 419.1248-419.1332 F: ms MS 046_RTC13_M1_24h _Lung
NL: 2.78E5
Base Peak m/z= 316.0354-316.0418 F: ms MS 046_RTC13_M1_24h _Lung
NL: 4.48E7
Base Peak F: ms MS 046_RTC13_M1_24h _Lung
Relative Abundance
Time (min)
046_RTC13_M1_24h_Lung#1794 RT: 10.19 AV: 1 NL: 3.31E5
T: FTMS + p NSI Full ms [200.00-2000.00]
315.1772
316.0380
315.1194
316.1738
317.0414
317.2099
318.1904
Relative Abundance
m/z

Figure 58. RTC13 was detected in an extracted lung homogenate from a RTC13-treated C57BL/6 mouse sacrificed at 24 h. (A) XIC of a 216-5 spiked standard. (B) XIC of RTC13. (C) TIC of the extracted lung homogenate (24hM1). (D) Mass spectrum of RTC13.

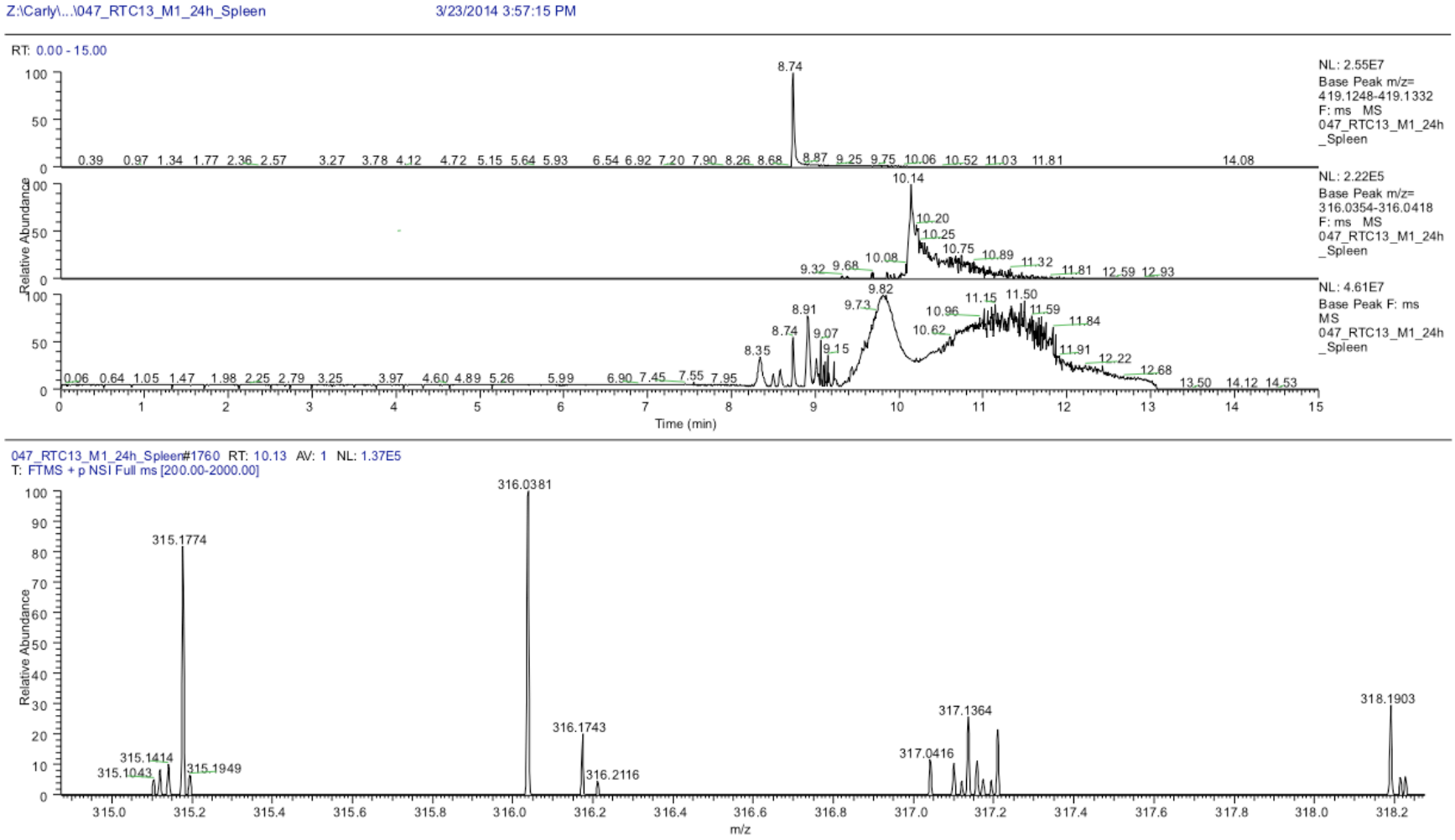
Z:\Carly\...\047_RTC13_M1_24h_Spleen 3/23/2014 3:57:15 PM
RT: 0.00 - 15.00
NL: 2.55E7
Base Peak m/z= 419.1248-419.1332
F: ms MS
047_RTC13_M1_24h_Spleen
NL: 2.22E5
Base Peak m/z= 316.0354-316.0418
F: ms MS
047_RTC13_M1_24h_Spleen
NL: 4.61E7
Base Peak F: ms
MS
047_RTC13_M1_24h_Spleen
Relative Abundance
Time (min)
047_RTC13_M1_24h_Spleen#1760 RT: 10.13 AV: 1 NL: 1.37E5
T: FTMS + p NSI Full ms [200.00-2000.00]
316.0381
315.1774
316.1743
317.1364
318.1903
315.1414
315.1043
315.1949
316.2116
317.0416
m/z

Figure 59. RTC13 was detected in an extracted spleen homogenate from a RTC13-treated C57BL/6 mouse sacrificed at 24 h. (A) XIC of a 216-5 spiked standard. (B) XIC of RTC13. (C) TIC of the extracted spleen homogenate (24hM1). (D) Mass spectrum of RTC13.

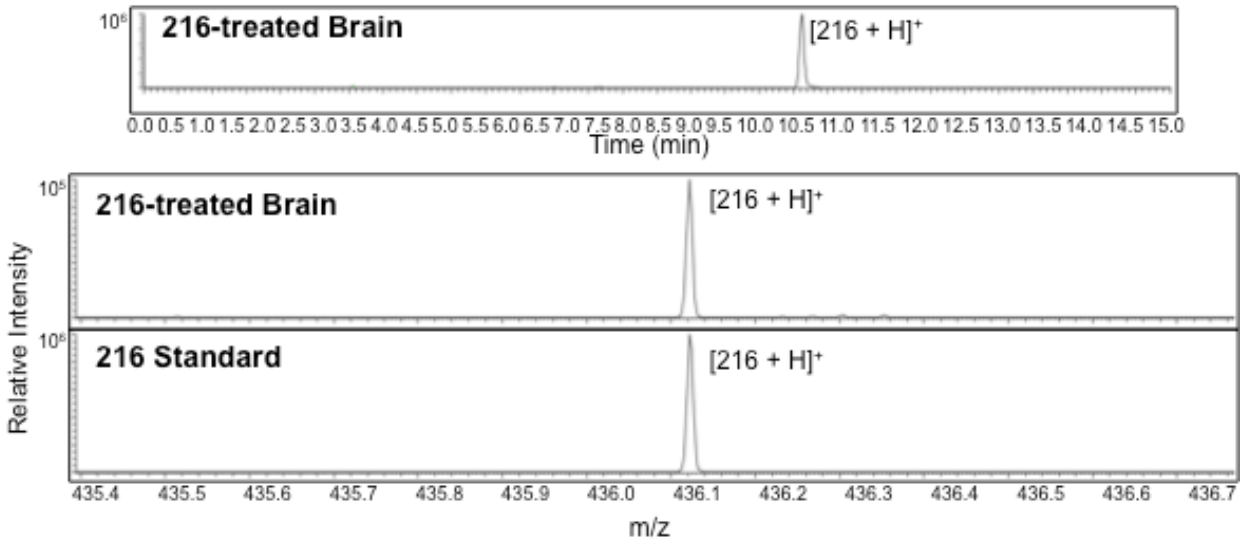

Figure 60. 216 was detected in an extracted brain homogenate from a 216-treated C57BL/6 mouse sacrificed at 2 h. (A) XIC of 216. (B) Mass spectrum of 216 in extracted brain homogenate. (C) Mass spectrum of 216 standard.

REFERENCES

1. Kellermayer, R. *European journal of medical genetics* **2006**, *49*, 445.

2. Byers, P. H. *The Journal of clinical investigation* **2002**, *109*, 3.

3. Lai, C. H.; Chun, H. H.; Nahas, S. A.; Mitui, M.; Gamo, K. M.; Du, L.; Gatti, R. A. *Proceedings of the National Academy of Sciences of the United States of America* **2004**, *101*, 15676.

4. Holbrook, J. A.; Neu-Yilik, G.; Hentze, M. W.; Kulozik, A. E. *Nature genetics* **2004**, *36*, 801.

5. Zingman, L. V.; Park, S.; Olson, T. M.; Alekseev, A. E.; Terzic, A. *Clinical pharmacology and therapeutics* **2007**, *81*, 99.

6. Lukacs, G. L.; Durie, P. R. *The New England journal of medicine* **2003**, *349*, 1401.

7. Luzzatto, L.; Apirion, D.; Schlessinger, D. *Proceedings of the National Academy of Sciences of the United States of America* **1968**, *60*, 873.

8. Ogle, J. M.; Brodersen, D. E.; Clemons, W. M., Jr.; Tarry, M. J.; Carter, A. P.; Ramakrishnan, V. *Science* **2001**, *292*, 897.

9. Recht, M. I.; Douthwaite, S.; Puglisi, J. D. *The EMBO journal* **1999**, *18*, 3133.

10. Yoshizawa, S.; Fourmy, D.; Puglisi, J. D. *The EMBO journal* **1998**, *17*, 6437.

11. Barton-Davis, E. R.; Cordier, L.; Shoturma, D. I.; Leland, S. E.; Sweeney, H. L. *The Journal of clinical investigation* **1999**, *104*, 375.

12. Howard, M. T.; Shirts, B. H.; Petros, L. M.; Flanigan, K. M.; Gesteland, R. F.; Atkins, J. F. *Annals of neurology* **2000**, *48*, 164.

13. Keeling, K. M.; Bedwell, D. M. *J Mol Med (Berl)* **2002**, *80*, 367.

14. Perlman, S.; Becker-Catania, S.; Gatti, R. A. *Seminars in pediatric neurology* **2003**, *10*, 173.

15. Bakkenist, C. J.; Kastan, M. B. *Nature* **2003**, *421*, 499.

16. Telatar, M.; Wang, Z.; Udar, N.; Liang, T.; Bernatowska-Matuszkiewicz, E.; Lavin, M.; Shiloh, Y.; Concannon, P.; Good, R. A.; Gatti, R. A. *American journal of human genetics* **1996**, *59*, 40.

17. Schroers, A.; Kley, R. A.; Stachon, A.; Horvath, R.; Lochmuller, H.; Zange, J.; Vorgerd, M. *Neurology* **2006**, *66*, 285.

18. Wagner, K. R.; Hamed, S.; Hadley, D. W.; Gropman, A. L.; Burstein, A. H.; Escolar, D. M.; Hoffman, E. P.; Fischbeck, K. H. *Annals of neurology* **2001**, *49*, 706.

19. Neuwelt, E. A.; Baker, D. E.; Pagel, M. A.; Blank, N. K. *Journal of neurosurgery* **1984**, *61*, 430.

20. Du, L.; Damoiseaux, R.; Nahas, S.; Gao, K.; Hu, H.; Pollard, J. M.; Goldstine, J.; Jung, M. E.; Henning, S. M.; Bertoni, C.; Gatti, R. A. *The Journal of experimental medicine* **2009**, *206*, 2285.

21. Mendell, J. R.; Buzin, C. H.; Feng, J.; Yan, J.; Serrano, C.; Sangani, D. S.; Wall, C.; Prior, T. W.; Sommer, S. S. *Neurology* **2001**, *57*, 645.

22. Kayali, R.; Ku, J. M.; Khitrov, G.; Jung, M. E.; Prikhodko, O.; Bertoni, C. *Human molecular genetics* **2012**, *21*, 4007.

23. Chaurand, P.; Norris, J. L.; Cornett, D. S.; Mobley, J. A.; Caprioli, R. M. *Journal of proteome research* **2006**, *5*, 2889.

24. McDonnell, L. A.; Heeren, R. M. *Mass spectrometry reviews* **2007**, *26*, 606.

25. Gatti, R. A. *Ann N Y Acad Sci* **2012**, *1250*, 33.

CHAPTER 4

Protein Coronae Composition of Mesoporous Silica Nanoparticles Dependent Upon Surface Modifications and Biological Material

Protein Coronae Composition of Mesoporous Silica Nanoparticles Dependent Upon Surface Modifications and Biological Material

Carly N. Ferguson, Rolando E. Yanes, Angela A. Hwang, Jie Lu, Dyna I. Shirasaki, Jeffrey I. Zink, Joseph A. Loo, Fuyu Tamanoi

ABSTRACT

Diagnostic medicine is a major factor in preventative medicine, often made difficult by conflicting symptoms and invasive tests. Successful cancer treatments largely rely on early, reliable diagnoses; however, early warning signs are not always readily apparent. Recently, we as well as others have developed mesoporous silica nanoparticle (MSNs) drug delivery vehicles that are targeted specifically to cancer cells.[1] Studies have shown promise of MSNs as potent drug systems; however, the MSNs cancer cell-targeting abilities are being further explored as a method of diagnosis. We are utilizing a proteomic approach to analyze MSNs-bound proteins extracted from cancer cells in order to develop these nanoparticles as a diagnostic tool. Four particle surface modifications were studied: polyethylene imine (PEI), phosphonate (Phos), amine, and non-modified. MSNs with an iron oxide core (for collection by a magnet) were endocytosed by three different cell lines (A549, HFF, or MCF7), isolated, and subjected to a modified trypsin digest. UPLC-MS/MS was used to analyze the samples. Negatively charged particles possess a more extensive network of proteins within their protein corona regions when incubated with cancerous cell lines. This is beneficial when designing differential diagnoses, allowing for a more complex and specific profile. The greater negative charge on the surface of Phos-MSNP particles is likely responsible for the larger number of bound proteins, and this was shown to contribute to a greater

propensity for exocytosis. While positively charged MSNs-Amine particles maintained an extensive corona, the highly positive PEI-MSNP particles were not shown to have a significant corona in cancerous cell lines. This may be an issue of steric hindrance, as shown to occur for PEG-coated particles. MSNs coated in smaller, covalently bonded surface modifiers may be more useful as diagnostic tools. Unique proteins were identified from MSNs incubated with cancer cell lines (A549 and MCF7) versus MSNs incubated with normal cell lines (HFF). Ultimately, these data indicate the promising potential of MSNs as diagnostic tools due to the varying composition of their protein coronas attributed to the different cell lines.

INTRODUCTION

The field of nanotechnology has expanded and overlapped with multiple areas of science over recent years, spanning such diverse areas from computer science to medicine. Within medicine, particular interest lies in the utilities of nanoparticles (NP), small inorganic molecules on the nanometer scale. They possess many promising features, including highly customizable synthesis reactions, biocompatibility, and efficient clearance. Manipulation of NP chemical properties via customized synthesis, as well as the variety of inorganic materials used to create NP, allow for alteration of physical and biological properties that provide NP unique advantages as potential drug delivery vehicles.

Mesoporous silica nanoparticles (MSNs) are a particularly exciting nanotechnology and have thus far been shown effective in many applications. MSNs chemistry has been well developed to allow the customization of both MSNs surface and internal packaging, yielding marked success as drug delivery vehicles. The use of multiple surface modifications, such as phosphonate and polyethylenimine (PEI) have allowed for dual-delivery functions: internal packaging of anti-cancer drugs and surface-tethering of siRNA to target multi-drug resistant cancer cells.[55] MSNs utility as drug delivery vehicles has been shown effective *in vitro* and *in vivo* in multiple studies ranging from tumor suppression to treatment of multi-drug resistant cancers.[55,94] Surface modifications also allow for cell-specific targeting of MSNs, as shown by Lu *et al* in folate receptor-targeting of cancer cells by conjugation of MSNs and folic acid.[94] Additionally, unique packaging and release chemistries allow for incorporation of molecules, such as membrane-impenetrable proteins and DNA, for delivery across

previously unreachable areas of the cell.[95,96] MSNs have also been employed as imaging markers due to their easily modified surface chemistry, allowing the inclusion of fluorescent dyes such as fluorescein isothiocyanate.[97]

As MSNs are further developed for clinical use, interest in their uptake pathway, release, and overall biological effects has increased. Of particular interest is the idea of a protein corona, or the layer(s) of proteins that interact and bind to the nanoparticle surface upon introduction to a biological sample.[98] There is existing concern that this corona may interfere with nanoparticle functions, such as cell targeting and drug delivery.[99] Other groups have addressed these concerns, and it was observed that protein binding does have an effect on nanoparticle distribution.[100] Whether these effects are positive or negative is still under debate. Positive effects such as enhanced blood-brain barrier (BBB) crossing abilities have been identified, but consequences such as more rapid clearance by filtering and excretory organs are known to exist, as well.[100-103] Further studies have looked at myriad of NP types and probed corona composition in correspondence with nanoparticle size and surface composition, finding significant effects on corona composition attributed to differences in each of these properties. Gref *et al* observed that increasing the length (or MW) of poly(ethylene glycol) (PEG) chains on the surface of NPs resulted in a reduction in protein adsorption, prevention of uptake by cells, and overall, changing the wt % PEG resulted in some alteration in protein corona composition.[104] Lundqvist *et al* (2008) found that increasing the diameter of the nanoparticle itself can alter the protein corona.[105]

Recently, groups have suggested differences in the layers within the protein corona when a nanoparticle is exposed to multiple biological fluids, identifying a longer-

lived “hard” corona as well as a loosely attached layer of proteins.[106,107] This hard corona contains information from the biological fluid the NP is first exposed to, while proteins from the second biological fluid are identified as well.[107] These studies have indicated the potential importance of these findings in terms of uptake pathway and efficacy effects; however, we propose an alternative use for protein corona composition analysis that takes advantage of these distinct differences.

In this study, MSNs of varied surface modifications were incubated with distinct human cell lines. Proteomic analyses confirmed that, while many proteins are present in the coronas of MSNs incubated with different cell lines, there are clear differences in the protein coronas composition that are unique to each cell line. Additionally, we found that there are differences in corona composition dependent upon surface modification (both specific modifications and generalized zeta-potential classes) within a given cell line.

METHODS

Materials. Acetonitrile (ACN), ammonium bicarbonate (ABC), anhydrous toluene, cetyltrimethylammonium bromide (CTAB), deoxycholic acid (DCA), dithiothreitol (DTT), ethanol, ethyl acetate (EA), fetal bovine serum (FBS), formic acid (FA), iodoacetamide (IAN), L-glutamine, methanol, penicillin, phosphate-buffered saline (PBS), polyethylene imine (PEI 1.8 kDa), streptomycin, tetraethyl orthosilicate (TEOS), and 3-(trihydroxysilypropyl)methylphosphonate were purchased from Sigma-Aldrich. Ammonium nitrate and hydrochloric acid (HCl) were purchased from Fisher Scientific. Trypsin (Porcine) was purchased from Promega. N-(2-aminoethyl)3-aminopropyl trimethoxysilane was purchased from Gelest.

Synthesis of Magnetic MSNs (Mag@MSNs). As previously reported by Yanes *et al,* silica nanoparticles with zinc-doped iron oxide cores were synthesized (Mag@MSNs). Briefly, CTAB (25 mg) was dissolved in NaOH solution (85 µL, 2 M) and H_2O (11 mL).[108] Once the mixture was heated to 80 °C, TEOS (100 µL) was added and aged for 2 h. The particles were collected by centrifugation and washed with ethanol. The surfactant was subsequently removed by refluxing in a solution of ammonium nitrate (15 mg) and ethanol (5 mL) for 30 min, and washed with ethanol.

Synthesis of Amine Mag@MSNs. Mag@MSNs (100 mg) were suspended in anhydrous toluene and N-(2-aminoethyl)3-aminopropyl trimethoxysilane (55 µL) was added. The solution was heated to 80 °C and left to react overnight. Materials were washed twice with each toluene, methanol, and water.

Synthesis of Phosphonate Mag@MSNs. For the phosphonate coating, nanoparticles (100 mg) were suspended in water and (trihydroxysilylpropyl)methylphosphonate (300

μL) was added to the solution to react overnight. The particles were collected via centrifugation and washed in water.

Synthesis of Polyethylenimine (PEI) Mag@MSNs. For the electrostatic PEI coating, as-synthesized nanoparticles (30 mg) were suspended in a 3 mL solution of PEI (weight 1.8 kD) and ethanol (2.5 mg/mL). Particles were stirred for 30 min and washed three times with ethanol to remove excess PEI.

Cell Culture. Human fibroblast cell line HFF, human lung cancer cell line A549, and human breast cancer cell line MCF7 were purchased from American Type Culture Collection. Each line was grown and maintained in Culbecco's modified Eagle's medium (DMEM; GIBCO) with 10% FBS, 1% L-glutamine, 1% penicillin, and 1% streptomycin.

Nanoparticle-Cell Incubation. Cells were seeded at a confluency of 400,000 cells in 2 mL of media per well in 6-well plates and incubated overnight. Zn-doped iron oxide core MSNs (bare, amine, phosphonate or PEI coated) were added to the cells at 80 μg/mL and incubated for 2 h. Media was removed and treated for nanoparticle isolation. Cells were washed twice with PBS, suspended in fresh growth media, and further incubated for 24 h to allow nanoparticle exocytosis. Media was collected, with three 6-well plates used for each MSNs coating within each of the three cell lines for a total of 36 mL. Mag@MSNs isolation was conducted by utilizing a neodymium magnet in a 25 mL cell culture flask for each sample condition. From each 36 mL solution, 6 mL were incubated with the magnet for 1 h, followed by careful extraction of media, avoiding perturbance of the magnet. This was repeated until nanoparticle isolation was completed on all 36 mL of media. Nanoparticles were washed two times with PBS, resuspended in 1 mL PBS, isolated with a magnetic rack, and resuspended in 50 μL PBS.

Protein Digest. Samples of Mag@MSNs in 50 μL PBS were placed in a magnetic rack to isolate protein-bound particles at room temperature (RT). After 20 min, 50 μL PBS were pipetted out, avoiding disturbance of isolated particles. Particles were resuspended in 90 μL mass spectrometry (MS)-grade H_2O for further washing, and placed into a magnetic rack for 20 min at RT. After 20 min, 90 μL MS-grade H_2O were pipetted out, avoiding disturbance of isolated particles. Particles were resuspended in 90 μL 200 mM ABC and 0.1% DCA in MS-grade H_2O.

Reducing agent DTT, at a concentration of 30 mM in 200 mM ABC and 0.1% DCA, was added to particle solutions to a final concentration of 3 mM DTT, and sample solutions were incubated at 95 ^{o}C for 30 min in the dark with moderate mixing (300 rpm). Alkylating agent IAN, at a concentration of 100 mM in 200 mM ABC and 0.1% DCA, was added to particle solutions to a final concentration of 7.4 mM IAN, and sample solutions were incubated at 37 ^{o}C for 1 h in the dark with moderate mixing (300 rpm). To quench the reaction, 30 mM DTT in 200 mM ABC and 0.1% DCA was added to the solutions to a final concentration of 4 mM DTT. A quantity of 200 mM ABC and 0.1% DCA was added to bring the final reaction concentrations to 3.7 mM DTT and 6.5 mM IAN. Lyophilized trypsin was suspended in 10 mM HCl to a final concentration of 0.5 μg/μL Trypsin. Trypsin was added to sample solutions in a ratio of 1 μg trypsin : 100 μg protein and incubated overnight at 37 ^{o}C in the dark with moderate mixing (300 rpm). Sample solution tubes were placed into a magnetic rack at RT for 20 min to isolate particles from the digested peptide mixture. Digest volume without Mag@MSNs was pipetted into a new tube.

Prior to MS analysis, DCA was removed from sample solutions. A volume of 125 μL 95.5% EA and 0.5% FA was added to the sample solution, lightly vortexed for 5 s, and a subsequent volume of 800 μL 100% EA was added. The solution was strongly vortexed for 10 s and centrifuged at 13,200 rpm for 10 min at RT. The top organic layer was removed, avoiding disturbance of the bottom aqueous layer. This procedure was repeated twice. The residual aqueous solution was dried down under vacuum at RT for 10 min in a Thermo Scientific SpeedVac®. Samples were subsequently resuspended in 50 μL 50% methanol in MS-grade H_2O. This procedure was repeated twice. Samples were resuspended in 40 μL 0.5% FA in MS-grade H_2O.

Mass Spectrometry. All samples were run on a Waters nanoACQUITY nano ultra-performance liquid chromatography (nanoUPLC) system (Manchester, UK). Separation was conducted with a UPLC symmetry C18 180 μm x 20 mm trap column and a nanoACQUITY UPLC BEH C18 75 μm x 150 mm reversed phase (RP) analytical column. MS-grade H_2O and 0.1% FA comprised the aqueous mobile phase (A). ACN and 0.1% FA comprised the organic mobile phase (B). A total of 5 μL per sample were injected onto the trap column, subjected to a 97% A and 3% B wash for 5 min, followed by injection onto the analytical column in 3% B. A 70 min 3-50% B gradient was used, followed by a 3 min 50-95% B gradient. A 15 min rinse with 95% B was followed by a 20 min re-equilibration period with 97% A.

The nanoACQUITY unit was interfaced with a Waters Xevo quadruopole time-of-flight (QTOF) mass spectrometer. Data acquisition was conducted in a data-independent (MS^E), positive ion mode over a 100-8000 m/z range. MSE involves a non-selective and continuous process alternating between low and high collisional energies

per second, allowing for observation of resulting precursor and associated fragment ion spectra and maximizing protein identification.

Data Analysis. Waters ProteinLynx Global Server 2.5.2 (PLGS) was used to process data. All data were searched against UniProtKB-SwissProt *Homo sapiens* (Human) database for protein identifications. Parameters were set to a minimum of 7 peptides per protein identification, 2 missed cleavages, 4% false positive rate, fixed carbamidomethyl modification of cysteine residues, and variable modifications, including: oxidation of methionine residues, deamidation of asparagine and glutamine residues, and acetylation of lysine residues and the N-terminus.

Western Blot. HFF, A549 and MCF7 Cells incubated in appropriate media were collected and cell lysates were separated with gel electrophoresis on a polyacrylamide gel containing sodium dodecyl sulfate and then transferred to nitrocellulose membranes. The membranes were blocked with Tris-buffered saline (TBS) containing 5% (w/v) skimmed milk. After being washed with TBS containing 0.1% Tween 20 (Sigma), the membranes were incubated overnight at room temperature with MAPK125 antibody (santa cruz Biotechnology) diluted with TBS. After being washed, the membranes were incubated for 2 h at room temperature with the second antibody (Santa Cruz Biotechnology). Bands were detected with an ECL system (Amersham Pharmacia Biotech).

RESULTS AND DISCUSSION

Surface Modification Effects on Protein Binding. Particles were grouped based on the overall surface charge, or ζ-potential. Bare MSNs have a negative ζ-potential of 16 mV. Phosphonate-coated MSNs (phos-MSNP) have a negative ζ-potential of 33 mV. Amine-coated MSNs (amine-MSNP) have a positive ζ-potential of 31 mV. Polyethylenimine-coated MSNs (PEI-MSNP) have a positive ζ-potential of 50 mV.

Bare MSNs. A total of 30 proteins were identified from negatively charged bare MSNs incubated with HFF cells, as shown in Table 1. A total of 68 proteins were identified from negatively charged bare MSNs incubated with A549 cells, as shown in Table 2. A total of 31 proteins were identified from negative charged bare MSNs incubated with MCF7 cells, as shown in Table 3.

Phos-MSNP. A total of 44 proteins were identified from negatively charged phos-MSNP incubated with HFF cells, as shown in Table 1. A total of 97 proteins were identified from negatively charged phos-MSNP incubated with A549 cells, as shown in Table 2. A total of 1 protein was identified from negative charged phos-MSNP incubated with MCF7 cells, as shown in Table 3.

amine-MSNP. A total of 39 proteins were identified from positively charged amine-MSNP incubated with HFF cells, as shown in Table 1. A total of 49 proteins were identified from positively charged amine-MSNP incubated with A549 cells, as shown in Table 2. A total of 2 proteins were identified from positively charged amine-MSNP incubated with MCF7 cells, as shown in Table 3.

PEI-MSNP. A total of 94 proteins were identified from positively charged PEI-MSNP incubated with HFF cells, as shown in Table 1. A total of 6 proteins were identified from

positively charged PEI-MSNP incubated with A549 cells, as shown in Table 2. A total of 3 proteins were identified from positively charged PEI-MSNP incubated with MCF7 cells, as shown in Table 3.

HFF Cells. A total of 82 unique proteins were identified from positively charged amine- and PEI-coated MSNs incubated with HFF cells. A total of 20 unique proteins were identified from negatively charged bare and phos-MSNP incubated with HFF cells. A total of 34 proteins were identified from both positively and negatively charged MSNs incubated with HFF cells. These data are shown in Table 1.

Several actin, hemoglobin, and histone isoforms were identified bound to all four MSNs types, with no apparent difference in histone identification from positively versus negatively charged particles. Several elongation factors were found buond to three MSNs types (amine-, bare-, and phos- MSNs); and, two POTE ankyrin isoforms (E and F) were found bound to amine- and phos- MSNs.

A549 Cells. A total of 8 unique proteins were identified from positively charged amine- and PEI-coated MSNs incubated with A549 cells. A total of 61 unique proteins were identified from negatively charged bare and phos-MSNP incubated with A549 cells. A total of 47 proteins were identified from both positively and negatively charged MSNs incubated with A549 cells. These data are shown in Table 2.

Several actin and histone isoforms were identified bound to three MSNs types (amine-, bare-, and phos- MSNs). Only one protein was identified from PEI-MSNP incubated with A549 cells. While actin was equally present on each of the three surface modified particles, histones were much more abundant on the negatively charged nanoparticles. This is likely due to the positively charged characteristics of the histone

proteins. Lactate dehydrogenase, pyruvate kinase, and glyceraldehyde-3-phosphate dehydrogenase were detected in digests from both positively and negatively charged particles. Additionally, several elongation factors and POTE ankyrin protein isoforms were detected in all three particle types as well. These POTE isoforms were not the same as those identified from HFF cells.

MCF7 Cells. A total of 2 unique proteins were identified from positively charged amine- and PEI-coated MSNs incubated with MCF7 cells. A total of 30 unique proteins were identified from negatively charged bare and phos-MSNP incubated with MCF7 cells. A total of 3 proteins were identified from both positively and negatively charged MSNs incubated with MCF7 cells. These data are shown in Table 3.

Protein Localization. A subcellular localization prediction database, WoLF PSORT was used to determine potential locations of identified proteins within the cell. The percentage of proteins identified in each of the subcellular locations (cytoplasm, cytoskeleton, endoplasmic reticulum, mitochondrion, nucleus, secreted, and transmembrane) were calculated. Isoelectric point (pI) was also examined, however, no significant difference in average protein pI was found between the various particle types or cell types.

HFF Cells. Cytoplasmic proteins comprised 38% of total identified proteins from positively charged amine-MSNP and PEI-MSNP incubated with HFF cells. Cytoskeletal proteins comprised 20% of total identified proteins from positively charged amine-MSNP and PEI-MSNP incubated with HFF cells. Endoplasmic reticulum-associated proteins comprised 2% of total identified proteins from positively charged amine-MSNP and PEI-MSNP incubated with HFF cells. Mitochondrial proteins comprised 2% of total identified

proteins from positively charged amine-MSNP and PEI-MSNP incubated with HFF cells. Nuclear proteins comprised 20% of total identified proteins from positively charged amine-MSNP and PEI-MSNP incubated with HFF cells. Secretory proteins comprised 18% of total identified proteins from positively charged amine-MSNP and PEI-MSNP incubated with HFF cells. No transmembrane proteins were identified from positively charged amine-MSNP and PEI-MSNP incubated with HFF cells. These data are shown in Table 1.

Cytoplasmic proteins comprised 21% of total identified proteins from negatively charged bare MSNs and Phos-MSNP incubated with HFF cells. Cytoskeletal proteins comprised 21% of total identified proteins from negatively charged bare MSNs and Phos-MSNP incubated with HFF cells. Mitochondrial proteins comprised 1.9% of total identified proteins from negatively charged bare MSNs and Phos-MSNP incubated with HFF cells. Nuclear proteins comprised 27% of total identified proteins from negatively charged bare MSNs and Phos-MSNP incubated with HFF cells. Secretory proteins comprised 23% of total identified proteins from negatively charged bare MSNs and Phos-MSNP incubated with HFF cells. No endoplasmic reticulum-associated proteins or transmembrane proteins were identified from negatively charged bare MSNs and Phos-MSNP incubated with HFF cells. These data are shown in Table 1.

A549 Cells. Cytoplasmic proteins comprised 38% of total identified proteins from positively charged amine-MSNP and PEI-MSNP incubated with A549 cells. Cytoskeletal proteins comprised 20% of total identified proteins from positively charged amine-MSNP and PEI-MSNP incubated with A549 cells. Endoplasmic reticulum-associated proteins comprised 2% of total identified proteins from positively charged amine-MSNP and PEI-

MSNP incubated with A549 cells. Mitochondrial proteins comprised 2% of total identified proteins from positively charged amine-MSNP and PEI-MSNP incubated with A549 cells. Nuclear proteins comprised 20% of total identified proteins from positively charged amine-MSNP and PEI-MSNP incubated with A549 cells. Secretory proteins comprised 18% of total identified proteins from positively charged amine-MSNP and PEI-MSNP incubated with A549 cells. No transmembrane proteins were identified from positively charged amine-MSNP and PEI-MSNP incubated with A549 cells. These data are shown in Table 2.

Cytoplasmic proteins comprised 46% of total identified proteins from negatively charged bare MSNs and Phos-MSNP incubated with A549 cells. Cytoskeletal proteins comprised 12% of total identified proteins from negatively charged bare MSNs and Phos-MSNP incubated with A549 cells. Mitochondrial proteins comprised 2% of total identified proteins from negatively charged bare MSNs and Phos-MSNP incubated with A549 cells. Nuclear proteins comprised 32% of total identified proteins from negatively charged bare MSNs and Phos-MSNP incubated with A549 cells. Secretory proteins comprised 7% of total identified proteins from negatively charged bare MSNs and Phos-MSNP incubated with A549 cells. Transmembrane proteins comprised 0.7% of total identified proteins from negatively charged bare MSNs and Phos-MSNP incubated with A549 cells. No endoplasmic reticulum-associated proteins were identified from negatively charged bare MSNs and Phos-MSNP incubated with A549 cells. These data are shown in Table 2.

MCF7 Cells. Cytoplasmic proteins comprised 40% of total identified proteins from positively charged amine-MSNP and PEI-MSNP incubated with MCF7 cells.

Cytoskeletal proteins comprised 20% of total identified proteins from positively charged amine-MSNP and PEI-MSNP incubated with MCF7 cells. Secretory proteins comprised 40% of total identified proteins from positively charged amine-MSNP and PEI-MSNP incubated with MCF7 cells. Endoplasmic reticulum-associated proteins, mitochondrial proteins, nuclear proteins, and transmembrane proteins were not identified from positively charged amine-MSNP and PEI-MSNP incubated with MCF7 cells. These data are shown in Table 3.

Cytoplasmic proteins comprised 56% of total identified proteins from negatively charged bare MSNs and Phos-MSNP incubated with MCF7 cells. Cytoskeletal proteins comprised 6% of total identified proteins from negatively charged bare MSNs and Phos-MSNP incubated with MCF7 cells. Mitochondrial proteins comprised 6% of total identified proteins from negatively charged bare MSNs and Phos-MSNP incubated with MCF7 cells. Nuclear proteins comprised 6% of total identified proteins from negatively charged bare MSNs and Phos-MSNP incubated with MCF7 cells. Secretory proteins comprised 25% of total identified proteins from negatively charged bare MSNs and Phos-MSNP incubated with MCF7 cells. Endoplasmic reticulum-associated proteins and transmembrane proteins were not identified from negatively charged bare MSNs and Phos-MSNP incubated with MCF7 cells. These data are shown in Table 3.

A549 Cell Line Associated Proteins. A total of 116 proteins were identified from all particles incubated with A549 cells. A total of 12 proteins were identified only in particles incubated with A549 cells. Of these 12 proteins, 3 were found to be disease-associated based on literature searches: organic solute carrier partner protein (OSCP1), POTE ankyrin protein (POTEI and POTEJ), and pyruvate kinase (KPYM).

Though preliminary, OSCP1 has been indicated to be involved in interactions associated with several cancer types.[109] POTEI and POTEJ (POTE2β) have both been found to be expressed in lung cancer, though no mechanism has be implicated.[110] KPYM, a glycolytic enzyme, has been shown to be upregulated in lung tumors.[111] This indicated overactive glycolysis processes, a hallmark of cancerous cells. Though none of these have been indicated as prognostic markers, their differential identification from A549 cells over other cell types indicate their potential.

MCF7 Cell Line Associated Proteins. A total of 34 proteins were identified from all particles incubated with MCF7 cells. A total of 15 proteins were identified only in particles incubated with MCF7 cells. Of these 15 proteins, 4 were found to be disease-associated based on literature searches: ADP/ATP translocase (ADT2 and ADT3), anterior gradient protein (AGR2), phosphatidylinositol kinase (PI4K2A), and vimentin (VIME).

ADT2 and ADT3 are ADP/ATP translocase enzymes, facilitating ADP/ATP exchange across the inner membrane of the mitochondria. ADT2, or ANT2, has been specifically shown as indicative of levels of cancer aggression, with increased levels associated with enhanced glycolysis.[112] This leads to proliferation, unlike the overexpression of ADT3, which leads to apoptosis.[113,114] ADT2 was found to be upregulated in MCF7 cell lines, and knockdown of this enzyme resulted in cell death.[115] AGR2 has been previously shown to be associated with breast cancer tumors as well as many other cancers, specifically with lower grade, less aggressive tumors.[116] It was also shown to induce metastasis, and is present in higher concentrations in malignant tumors versus benign tumors.[116] Previous studies have suggested AGR2 as a

prognostic marker in breast cancer due to its association with unfavorable patient survival.[117] PI4K2A has previously been shown to be upregulated in many cancer cell lines, including MCF7.[118] Though not conducted in breast cancer patients, a recent study detected upregulation of PIK42A in liver cancer patients and has been suggested as a prognosis marker.[119] VIME has been shown to be associated with breast cancer, as well, and is suggested to be involved in enhancement of invasive capabilities.[120,121]

Mitogen-Activated Protein Kinase. One protein was identified in MSNs incubated with both A549 and MCF7 cells. This protein was mitogen-activated protein kinase 12 (MAPK12), identified from amine-MSNP in A549 cells and phos-MSNP in MCF7 cells. A Western blot analysis confirmed the presence of MAPK12 in both A549 and MCF7 cells, with a higher intensity band in MCF7 cells indicating it is present in higher concentrations, as shown in Figure 2. Also of note, MAPK12 was detected by Western blot analysis in HFF cells; however, MAPK12 was not identified from MSNs incubated with HFF cells.

MAP kinases in general are involved in complex signaling cascades, involving p38, ERK1, and ERK2.[122] They have largely been associated with cancer processes, and points along the MAPK pathway have been targeted in cancer therapeutic development.[123,124] MAPK12 upregulation has been implicated as an effector in gastric, pancreatic, breast, and bladder cancers, among others; and, other MAP kinases have been suggested to be included as part of prognostic panels in various types of cancers.[125-128] The selective binding of MAPK12 by MSNs incubated with A549 and MCF7 cells suggests further exploration is necessary, as this could be a promising prognostic marker.

Fetal Bovine Serum Protein Identification. Previous studies have suggested nanoparticles can be incubated with one biological sample, transferred to another biological medium, further incubated, and analyzed for protein content that will yield identifications characteristic of both the first and second sample.[106,107] Digested protein coronae from MSNs incubated with HFF cells were found to contain 163 proteins (amine-MSNP), 44 proteins (bare-MSNP), and 66 proteins (PEI-MSNP). No FBS-associated proteins were identified from phos-MSNP incubated with HFF cells. Digested protein coronae from MSNs incubated with A549 cells were found to contain 9 proteins (amine-MSNP), 20 proteins (bare-MSNP), 19 proteins (phos-MSNP), and 17 proteins (PEI-MSNP). Digested protein coronae from MSNs incubated with MCF7 cells were found to contain 74 proteins (amine-MSNP) and 1 protein (phos-MSNP). No FBS-associated proteins were identified from bare-MSNP or PEI-MSNP incubated with MCF7 cells. These data are shown in Table 4.

CONCLUSIONS

MSNs incubated with varied cell types resulted in the identification of several cell line-specific proteins. When compared to MSNs incubated with normal cells (HFF), those MSNs incubated with two diseased cell lines (A549 and MCF7) were found to contain distinct protein coronae. These data suggest that cell lines are distinguishable based on the proteins that adhere to endocytosed nanoparticles. Previous experiments have shown that, when incubated with two different biological samples sequentially, nanoparticles retain proteins from both the first and second medium. This was observed due to the presence of FBS-associated proteins in protein coronae analyzed from MSNs incubated with various cell lines.

The presence of disease-associated proteins in the protein coronae of nanoparticles incubated with A549 and MCF7 cell lines suggests that particles are able to bind to a large number of proteins, not just those that are most abundant. Furthermore, these data indicate MSNs as promising tools for prognostic and diagnostic tests. Biocompatibility and fast clearance from the body have been shown in animal models when utilizing MSNs as drug delivery vehicles, thus MSNs utility as diagnostic tools should be further explored.

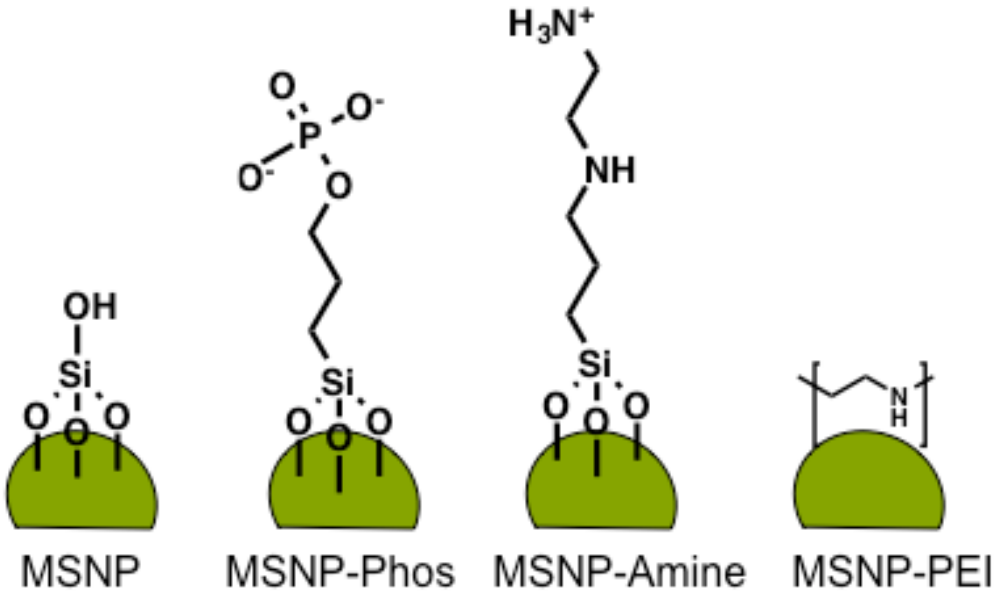

Figure 1. Structures of MSNs (A) Bare (B) Phos-MSNP (C) amine-MSNP (D) PEI-MSNP.

Particle Type	Protein ID	Protein Name	Subcellular Localization
amine-MSNP	ACTA	Actin_ aortic smooth muscle	Cytoplasm
amine-MSNP	ACTB	Actin_ cytoplasmic 1	Cytoplasm
amine-MSNP	ACTBL	Beta-actin-like protein 2	Cytoplasm
amine-MSNP	ACTBM	Putative beta-actin-like protein 3	Cytoplasm
amine-MSNP	ACTC	Actin_ alpha cardiac muscle 1	Cytoplasm
amine-MSNP	ACTG	Actin_ cytoplasmic 2	Cytoplasm
amine-MSNP	ACTH	Actin_ gamma-enteric smooth muscle	Cytoplasm
amine-MSNP	ACTS	Actin_ alpha skeletal muscle	Cytoplasm
amine-MSNP	ATPA	ATP synthase subunit alpha_ mitochondrial	Cytoskeleton
amine-MSNP	CEP89	Centrosomal protein of 89 kDa	Cytoskeleton
amine-MSNP	DESM	Desmin	Cytoskeleton
amine-MSNP	EF1A1	Elongation factor 1-alpha 1	Cytoskeleton
amine-MSNP	EF1A2	Elongation factor 1-alpha 2	Cytoskeleton
amine-MSNP	EF1A3	Putative elongation factor 1-alpha-like 3	Cytoskeleton
amine-MSNP	ENPL	Endoplasmin	Cytoskeleton
amine-MSNP	H4	Histone H4	Nucleus
amine-MSNP	HBA	Hemoglobin subunit alpha	Nucleus
amine-MSNP	HS71L	Heat shock 70 kDa protein 1-like	Cytoplasm
amine-MSNP	HS90A	Heat shock protein HSP 90-alpha	Cytoplasm
amine-MSNP	HS90B	Heat shock protein HSP 90-beta	Cytoplasm
amine-MSNP	HSP71	Heat shock 70 kDa protein 1A/1B	Cytoplasm
amine-	HSP72	Heat shock-related 70 kDa protein 2	Cytoplasm

MSNP			
amine-MSNP	HSP76	Heat shock 70 kDa protein 6	Cytoplasm
amine-MSNP	HSP77	Putative heat shock 70 kDa protein 7	Cytoplasm
amine-MSNP	HSP7C	Heat shock cognate 71 kDa protein	Cytoplasm
amine-MSNP	NUCL	Nucleolin	Secretory
amine-MSNP	POTEE	POTE ankyrin domain family member E	Secretory
amine-MSNP	POTEF	POTE ankyrin domain family member F	Secretory
amine-MSNP	RL40	Ubiquitin-60S ribosomal protein L40	Secretory
amine-MSNP	RS27A	Ubiquitin-40S ribosomal protein S27a	Secretory
amine-MSNP	TBA1A	Tubulin alpha-1A chain	Secretory
amine-MSNP	TBA1B	Tubulin alpha-1B chain	Secretory
amine-MSNP	TBA1C	Tubulin alpha-1C chain	Secretory
amine-MSNP	TBA3C	Isoform 2 of Tubulin alpha-3C/D chain	Secretory
amine-MSNP	TBA3E	Tubulin alpha-3E chain	Secretory
amine-MSNP	TBB5	Tubulin beta chain	Secretory
amine-MSNP	UBB	Polyubiquitin-B	Secretory
amine-MSNP	UBC	Polyubiquitin-C	Secretory
amine-MSNP	VTNC	Vitronectin	Secretory
bare-MSNP	ACTA	Actin_ aortic smooth muscle	Cytoplasm
bare-MSNP	ACTB	Actin_ cytoplasmic 1	Cytoplasm
bare-MSNP	ACTBL	Beta-actin-like protein 2	Cytoplasm
bare-MSNP	ACTBM	Putative beta-actin-like protein 3	Cytoplasm
bare-MSNP	ACTC	Actin_ alpha cardiac muscle 1	Cytoplasm

bare-MSNP	ACTG	Actin_ cytoplasmic 2	Cytoplasm
bare-MSNP	ACTH	Actin_ gamma-enteric smooth muscle	Cytoplasm
bare-MSNP	ACTS	Actin_ alpha skeletal muscle	Cytoplasm
bare-MSNP	AL3A2	Isoform 2 of Fatty aldehyde dehydrogenase	Cytoskeleton
bare-MSNP	APOA1	Apolipoprotein A-I	Cytoskeleton
bare-MSNP	APOE	Apolipoprotein E	Cytoskeleton
bare-MSNP	EF1A1	Elongation factor 1-alpha 1	Cytoskeleton
bare-MSNP	EF1A2	Elongation factor 1-alpha 2	Cytoskeleton
bare-MSNP	EF1A3	Putative elongation factor 1-alpha-like 3	Cytoskeleton
bare-MSNP	GELS	Gelsolin	Cytoskeleton
bare-MSNP	H4	Histone H4	Nucleus
bare-MSNP	HBA	Hemoglobin subunit alpha	Nucleus
bare-MSNP	HBAZ	Hemoglobin subunit zeta	Nucleus
bare-MSNP	HBB	Hemoglobin subunit beta	Nucleus
bare-MSNP	HBD	Hemoglobin subunit delta	Nucleus
bare-MSNP	HBE	Hemoglobin subunit epsilon	Nucleus
bare-MSNP	HBG1	Hemoglobin subunit gamma-1	Cytoplasm
bare-MSNP	HBG2	Hemoglobin subunit gamma-2	Cytoplasm
bare-MSNP	IBP2	Insulin-like growth factor-binding protein 2	Secretory
bare-MSNP	POTEE	POTE ankyrin domain family member E	Secretory
bare-MSNP	POTEF	POTE ankyrin domain family member F	Secretory
bare-MSNP	QCR7	Cytochrome b-c1 complex subunit 7	Mitochondria
bare-	SNAI3	Zinc finger protein SNAI3	Secretory

MSNP			
bare-MSNP	VTNC	Vitronectin	Secretory
bare-MSNP	WIPF3	WAS/WASL-interacting protein family member 3	Secretory
PEI-MSNP	ACTA	Actin_ aortic smooth muscle	Cytoplasm
PEI-MSNP	ACTB	Actin_ cytoplasmic 1	Cytoplasm
PEI-MSNP	ACTBL	Beta-actin-like protein 2	Cytoplasm
PEI-MSNP	ACTBM	Putative beta-actin-like protein 3	Cytoplasm
PEI-MSNP	ACTC	Actin_ alpha cardiac muscle 1	Cytoplasm
PEI-MSNP	ACTG	Actin_ cytoplasmic 2	Cytoplasm
PEI-MSNP	ACTH	Actin_ gamma-enteric smooth muscle	Cytoplasm
PEI-MSNP	ACTS	Actin_ alpha skeletal muscle	Cytoplasm
PEI-MSNP	ALBU	Serum albumin	Cytoskeleton
PEI-MSNP	ANR35	Ankyrin repeat domain-containing protein 35	Cytoskeleton
PEI-MSNP	APOA1	Apolipoprotein A-I	Cytoskeleton
PEI-MSNP	APOE	Apolipoprotein E	Cytoskeleton
PEI-MSNP	GOG8I	Golgin subfamily A member 8I	Cytoskeleton
PEI-MSNP	H2A1	Histone H2A type 1	Cytoskeleton
PEI-MSNP	H2A1A	Histone H2A type 1-A	Cytoskeleton
PEI-MSNP	H2A1B	Histone H2A type 1-B/E	Cytoskeleton
PEI-MSNP	H2A1C	Histone H2A type 1-C	Nucleus
PEI-MSNP	H2A1D	Histone H2A type 1-D	Nucleus
PEI-MSNP	H2A1H	Histone H2A type 1-H	Nucleus
PEI-MSNP	H2A1J	Histone H2A type 1-J	Nucleus
PEI-MSNP	H2A2A	Histone H2A type 2-A	Nucleus
PEI-MSNP	H2A2B	Histone H2A type 2-B	Nucleus
PEI-MSNP	H2A2C	Histone H2A type 2-C	Nucleus
PEI-MSNP	H2A3	Histone H2A type 3	Nucleus
PEI-MSNP	H2AJ	Histone H2A.J	Nucleus
PEI-MSNP	H2AV	Isoform 2 of Histone H2A.V	Nucleus
PEI-MSNP	H2AX	Histone H2A.x	Nucleus
PEI-MSNP	H2AZ	Histone H2A.Z	Nucleus
PEI-MSNP	H2B1A	Histone H2B type 1-A	Nucleus
PEI-MSNP	H2B1B	Histone H2B type 1-B	Nucleus
PEI-MSNP	H2B1C	Histone H2B type 1-C/E/F/G/I	Nucleus
PEI-MSNP	H2B1D	Histone H2B type 1-D	Nucleus
PEI-MSNP	H2B1H	Histone H2B type 1-H	Nucleus
PEI-MSNP	H2B1J	Histone H2B type 1-J	Nucleus
PEI-MSNP	H2B1K	Histone H2B type 1-K	Nucleus

PEI-MSNP	H2B1L	Histone H2B type 1-L	Nucleus
PEI-MSNP	H2B1M	Histone H2B type 1-M	Nucleus
PEI-MSNP	H2B1N	Histone H2B type 1-N	Nucleus
PEI-MSNP	H2B1O	Histone H2B type 1-O	Nucleus
PEI-MSNP	H2B2E	Histone H2B type 2-E	Nucleus
PEI-MSNP	H2B2F	Histone H2B type 2-F	Nucleus
PEI-MSNP	H2B3B	Histone H2B type 3-B	Nucleus
PEI-MSNP	H2BFS	Histone H2B type F-S	Nucleus
PEI-MSNP	H31	Histone H3.1	Nucleus
PEI-MSNP	H31T	Histone H3.1t	Nucleus
PEI-MSNP	H32	Histone H3.2	Nucleus
PEI-MSNP	H33	Histone H3.3	Nucleus
PEI-MSNP	H4	Histone H4	Nucleus
PEI-MSNP	HBA	Hemoglobin subunit alpha	Nucleus
PEI-MSNP	HBB	Hemoglobin subunit beta	Nucleus
PEI-MSNP	HBD	Hemoglobin subunit delta	Nucleus
PEI-MSNP	HBE	Hemoglobin subunit epsilon	Nucleus
PEI-MSNP	HBG1	Hemoglobin subunit gamma-1	Cytoplasm
PEI-MSNP	HBG2	Hemoglobin subunit gamma-2	Cytoplasm
PEI-MSNP	ITIH2	Inter-alpha-trypsin inhibitor heavy chain H2	Secretory
PEI-MSNP	KCD18	BTB/POZ domain-containing protein KCTD18	Secretory
PEI-MSNP	MBB1A	Myb-binding protein 1A	Secretory
PEI-MSNP	NPM	Nucleophosmin	Secretory
PEI-MSNP	NUSAP	Nucleolar and spindle-associated protein 1	Secretory
PEI-MSNP	PGS1	Biglycan	Secretory
PEI-MSNP	POTEE	POTE ankyrin domain family member E	Secretory
PEI-MSNP	POTEF	POTE ankyrin domain family member F	Secretory
PEI-MSNP	PRRX2	Paired mesoderm homeobox protein 2	Secretory
PEI-MSNP	RED	Protein Red	Secretory
PEI-MSNP	RL40	Ubiquitin-60S ribosomal protein L40	Secretory
PEI-MSNP	RLA1	60S acidic ribosomal protein P1	Secretory
PEI-MSNP	RLA2	60S acidic ribosomal protein P2	Secretory
PEI-MSNP	RN214	RING finger protein 214	Secretory
PEI-MSNP	RS27A	Ubiquitin-40S ribosomal protein S27a	Secretory
PEI-MSNP	TBA1A	Tubulin alpha-1A chain	Secretory
PEI-MSNP	TBA1B	Tubulin alpha-1B chain	Secretory
PEI-MSNP	TBA1C	Tubulin alpha-1C chain	Secretory
PEI-MSNP	TBA4A	Tubulin alpha-4A chain	Secretory

PEI-MSNP	THRB	Prothrombin	Secretory
PEI-MSNP	UBB	Polyubiquitin-B	Secretory
PEI-MSNP	UBC	Polyubiquitin-C	Secretory
PEI-MSNP	VTNC	Vitronectin	Secretory
PEI-MSNP	VWA3A	von Willebrand factor A domain-containing protein 3A	Secretory
PEI-MSNP	ZBT25	Zinc finger and BTB domain-containing protein 25	Secretory
PEI-MSNP	ZC3HD	Isoform 2 of Zinc finger CCCH domain-containing protein 13	Secretory
Phos-MSNP	ACTA	Actin_ aortic smooth muscle	Cytoplasm
Phos-MSNP	ACTB	Actin_ cytoplasmic 1	Cytoplasm
Phos-MSNP	ACTC	Actin_ alpha cardiac muscle 1	Cytoplasm
Phos-MSNP	ACTG	Actin_ cytoplasmic 2	Cytoplasm
Phos-MSNP	ACTH	Actin_ alpha cardiac muscle 1	Cytoplasm
Phos-MSNP	ACTS	Actin_ cytoplasmic 2	Cytoplasm
Phos-MSNP	AL3A2	Actin_ gamma-enteric smooth muscle	Cytoskeleton
Phos-MSNP	APOE	Actin_ alpha skeletal muscle	Cytoskeleton
Phos-MSNP	CCD50	Coiled-coil domain-containing protein 50	Cytoskeleton
Phos-MSNP	CLIC2	Chloride intracellular channel protein 2	Cytoskeleton
Phos-MSNP	EF1A1	Elongation factor 1-alpha 1	Cytoskeleton
Phos-MSNP	EF1A2	Elongation factor 1-alpha 2	Cytoskeleton
Phos-MSNP	EF1A3	Putative elongation factor 1-alpha-like 3	Cytoskeleton
Phos-MSNP	GELS	Gelsolin	Cytoskeleton
Phos-MSNP	H2A1	Histone H2A type 1	Cytoskeleton
Phos-MSNP	H2A1B	Histone H2A type 1-B/E	Cytoskeleton
Phos-MSNP	H2A1C	Histone H2A type 1-C	Nucleus
Phos-	H2A1D	Histone H2A type 1-D	Nucleus

MSNP			
Phos-MSNP	H2A1H	Histone H2A type 1-H	Nucleus
Phos-MSNP	H2A1J	Histone H2A type 1-J	Nucleus
Phos-MSNP	H2A2A	Histone H2A type 2-A	Nucleus
Phos-MSNP	H2A2C	Histone H2A type 2-C	Nucleus
Phos-MSNP	H2A3	Histone H2A type 3	Nucleus
Phos-MSNP	H2AJ	Histone H2A.J	Nucleus
Phos-MSNP	H33	Histone H3.3	Nucleus
Phos-MSNP	HBA	Hemoglobin subunit alpha	Nucleus
Phos-MSNP	HBB	Hemoglobin subunit beta	Nucleus
Phos-MSNP	HBD	Hemoglobin subunit delta	Nucleus
Phos-MSNP	HBE	Hemoglobin subunit epsilon	Nucleus
Phos-MSNP	HBG1	Hemoglobin subunit gamma-1	Cytoplasm
Phos-MSNP	HBG2	Hemoglobin subunit gamma-2	Cytoplasm
Phos-MSNP	HRG	Histidine-rich glycoprotein	Cytoplasm
Phos-MSNP	IBP2	Insulin-like growth factor-binding protein 2	Secretory
Phos-MSNP	PDE9A	High affinity cGMP-specific 3'_5'-cyclic phosphodiesterase 9A	Secretory
Phos-MSNP	POTEE	POTE ankyrin domain family member E	Secretory
Phos-MSNP	POTEF	POTE ankyrin domain family member F	Secretory
Phos-MSNP	SEMG1	Semenogelin-1	Secretory
Phos-MSNP	SSH1	Protein phosphatase Slingshot homolog 1	Secretory
Phos-MSNP	VTNC	Vitronectin	Secretory
Phos-MSNP	ZNHI2	Zinc finger HIT domain-containing protein 2	Secretory

Table 1. Human proteins identified from MSNs incubated with HFF cells.

Particle Type	Protein ID	Protein Name	Subcellular Localization
amine-MSNP	ACTA	Actin_ aortic smooth muscle	Cytoplasm
amine-MSNP	ACTB	Actin_ cytoplasmic 1	Cytoplasm
amine-MSNP	ACTBL	Beta-actin-like protein 2	Cytoplasm
amine-MSNP	ACTC	Actin_ alpha cardiac muscle 1	Cytoplasm
amine-MSNP	ACTG	Actin_ cytoplasmic 2	Cytoplasm
amine-MSNP	ACTH	Actin_ gamma-enteric smooth muscle	Cytoplasm
amine-MSNP	ACTS	Actin_ alpha skeletal muscle	Cytoplasm
amine-MSNP	AL1A1	Retinal dehydrogenase 1	Cytoplasm
amine-MSNP	ALDH2	Aldehyde dehydrogenase_ mitochondrial	Mitochondria
amine-MSNP	ANXA1	Annexin A1	Nucleus
amine-MSNP	EF1A1	Elongation factor 1-alpha 1	Cytoskeleton
amine-MSNP	EF1A2	Elongation factor 1-alpha 2	Cytoskeleton
amine-MSNP	EF1A3	Putative elongation factor 1-alpha-like 3	Cytoskeleton
amine-MSNP	ENOA	Alpha-enolase	Cytoplasm
amine-MSNP	ENOA	Alpha-enolase	Cytoplasm
amine-MSNP	G3P	Glyceraldehyde-3-phosphate dehydrogenase	Cytoplasm
amine-MSNP	H12	Histone H1.2	Nucleus
amine-MSNP	H13	Histone H1.3	Nucleus
amine-MSNP	H14	Histone H1.4	Nucleus
amine-MSNP	KPYM	Pyruvate kinase isozymes M1/M2	Cytoplasm
amine-MSNP	LDHA	L-lactate dehydrogenase A chain	Mitochondria
amine-	MK12	Mitogen-activated protein kinase 12	Cytoplasm

MSNP			
amine-MSNP	OSCP1	Protein OSCP1	Transmembrane
amine-MSNP	POTEE	POTE ankyrin domain family member E	Secretory
amine-MSNP	POTEF	POTE ankyrin domain family member F	Secretory
amine-MSNP	POTEI	POTE ankyrin domain family member I	Secretory
amine-MSNP	POTEJ	POTE ankyrin domain family member J	Secretory
amine-MSNP	PROF1	Profilin-1	Cytoplasm
amine-MSNP	TBA1A	Tubulin alpha-1A chain	Secretory
amine-MSNP	TBA1B	Tubulin alpha-1B chain	Secretory
amine-MSNP	TBA1C	Tubulin alpha-1C chain	Secretory
bare-MSNP	ACTA	Actin_ aortic smooth muscle	Cytoplasm
bare-MSNP	ACTB	Actin_ cytoplasmic 1	Cytoplasm
bare-MSNP	ACTBL	Beta-actin-like protein 2	Cytoplasm
bare-MSNP	ACTBM	Putative beta-actin-like protein 3	Cytoplasm
bare-MSNP	ACTC	Actin_ alpha cardiac muscle 1	Cytoplasm
bare-MSNP	ACTG	Actin_ cytoplasmic 2	Cytoplasm
bare-MSNP	ACTH	Actin_ gamma-enteric smooth muscle	Cytoplasm
bare-MSNP	ACTS	Actin_ alpha skeletal muscle	Cytoplasm
bare-MSNP	AK1BA	Aldo-keto reductase family 1 member B10	Cytoplasm
bare-MSNP	AL1A1	Retinal dehydrogenase 1	Cytoplasm
bare-MSNP	ALDH2	Aldehyde dehydrogenase_ mitochondrial	Mitochondria
bare-MSNP	ANXA1	Annexin A1	Nucleus
bare-MSNP	ANXA2	Annexin A2	Nucleus

bare-MSNP	AXA2L	Putative annexin A2-like protein	Nucleus
bare-MSNP	EF1A1	Elongation factor 1-alpha 1	Cytoskeleton
bare-MSNP	EF1A2	Elongation factor 1-alpha 2	Cytoskeleton
bare-MSNP	EF1A3	Putative elongation factor 1-alpha-like 3	Cytoskeleton
bare-MSNP	ENOA	Alpha-enolase	Cytoplasm
bare-MSNP	G3P	Glyceraldehyde-3-phosphate dehydrogenase	Cytoplasm
bare-MSNP	H2B1A	Histone H2B type 1-A	Nucleus
bare-MSNP	H2B1B	Histone H2B type 1-B	Nucleus
bare-MSNP	H2B1C	Histone H2B type 1-C/E/F/G/I	Nucleus
bare-MSNP	H2B1D	Histone H2B type 1-D	Nucleus
bare-MSNP	H2B1H	Histone H2B type 1-H	Nucleus
bare-MSNP	H2B1J	Histone H2B type 1-J	Nucleus
bare-MSNP	H2B1K	Histone H2B type 1-K	Nucleus
bare-MSNP	H2B1L	Histone H2B type 1-L	Nucleus
bare-MSNP	H2B1M	Histone H2B type 1-M	Nucleus
bare-MSNP	H2B1N	Histone H2B type 1-N	Nucleus
bare-MSNP	H2B1O	Histone H2B type 1-O	Nucleus
bare-MSNP	H2B2E	Histone H2B type 2-E	Nucleus
bare-MSNP	H2B2F	Histone H2B type 2-F	Nucleus
bare-MSNP	H2BFS	Histone H2B type F-S	Nucleus
bare-MSNP	H4	Histone H4	Nucleus
bare-MSNP	H90B3	Putative heat shock protein HSP 90-beta-3	Cytoplasm
bare-	HS71L	Heat shock 70 kDa protein 1-like	Cytoplasm

MSNP			
bare-MSNP	HS90A	Heat shock protein HSP 90-alpha	Cytoplasm
bare-MSNP	HS90B	Heat shock protein HSP 90-beta	Cytoplasm
bare-MSNP	HSP71	Heat shock 70 kDa protein 1A/1B	Cytoplasm
bare-MSNP	HSP72	Heat shock-related 70 kDa protein 2	Cytoplasm
bare-MSNP	HSP7C	Heat shock cognate 71 kDa protein	Cytoplasm
bare-MSNP	KPYM	Pyruvate kinase isozymes M1/M2	Cytoplasm
bare-MSNP	KPYR	Pyruvate kinase isozymes R/L	Cytoplasm
bare-MSNP	LDHA	L-lactate dehydrogenase A chain	Mitochondria
bare-MSNP	LDHB	L-lactate dehydrogenase B chain	Mitochondria
bare-MSNP	POTEE	POTE ankyrin domain family member E	Secretory
bare-MSNP	POTEF	POTE ankyrin domain family member F	Secretory
bare-MSNP	POTEI	POTE ankyrin domain family member I	Secretory
bare-MSNP	POTEJ	POTE ankyrin domain family member J	Secretory
bare-MSNP	PROF1	Profilin-1	Cytoplasm
bare-MSNP	TBA1A	Tubulin alpha-1A chain	Secretory
bare-MSNP	TBA1B	Tubulin alpha-1B chain	Secretory
bare-MSNP	TBA1C	Tubulin alpha-1C chain	Secretory
bare-MSNP	TBB5	Tubulin beta chain	Secretory
bare-MSNP	UBB	Polyubiquitin-B	Secretory
bare-MSNP	UBC	Polyubiquitin-C	Secretory
bare-MSNP	VIME	Vimentin	---
PEI-MSNP	ALBU	Serum albumin	Cytoskeleton
Phos-	4F2	Isoform 4 of 4F2 cell-surface antigen	Secretory

MSNP		heavy chain	
Phos-MSNP	ACTA	Actin_ aortic smooth muscle	Cytoplasm
Phos-MSNP	ACTB	Actin_ cytoplasmic 1	Cytoplasm
Phos-MSNP	ACTBL	Beta-actin-like protein 2	Cytoplasm
Phos-MSNP	ACTBM	Putative beta-actin-like protein 3	Cytoplasm
Phos-MSNP	ACTC	Actin_ alpha cardiac muscle 1	Cytoplasm
Phos-MSNP	ACTG	Actin_ cytoplasmic 2	Cytoplasm
Phos-MSNP	ACTH	Actin_ gamma-enteric smooth muscle	Cytoplasm
Phos-MSNP	ACTN1	Alpha-actinin-1	Cytoplasm
Phos-MSNP	ACTN4	Alpha-actinin-4	Cytoplasm
Phos-MSNP	ACTS	Actin_ alpha skeletal muscle	Cytoplasm
Phos-MSNP	AK1BA	Aldo-keto reductase family 1 member B10	Cytoplasm
Phos-MSNP	AK1C3	Aldo-keto reductase family 1 member C3	Cytoplasm
Phos-MSNP	AN36A	Ankyrin repeat domain-containing protein 36A	Cytoplasm
Phos-MSNP	AN36C	Ankyrin repeat domain-containing protein 36C	Cytoplasm
Phos-MSNP	ANXA1	Annexin A1	Nucleus
Phos-MSNP	CA173	Uncharacterized protein C1orf173	---
Phos-MSNP	CCD30	Coiled-coil domain-containing protein 30	Secretory
Phos-MSNP	CEP89	Centrosomal protein of 89 kDa	Cytoplasm
Phos-MSNP	DAAM2	Disheveled-associated activator of morphogenesis 2	---
Phos-MSNP	DAPLE	Protein Daple	Cytoplasm
Phos-MSNP	EF1A1	Elongation factor 1-alpha 1	Cytoskeleton
Phos-MSNP	EF1A2	Elongation factor 1-alpha 2	Cytoskeleton

Phos-MSNP	EF1A3	Putative elongation factor 1-alpha-like 3	Cytoskeleton
Phos-MSNP	EGFLA	Pikachurin	Secretory
Phos-MSNP	ENPL	Endoplasmin	Secretory
Phos-MSNP	F184A	Protein FAM184A	---
Phos-MSNP	FYCO1	FYVE and coiled-coil domain-containing protein 1	Secretory
Phos-MSNP	G3P	Glyceraldehyde-3-phosphate dehydrogenase	Cytoplasm
Phos-MSNP	GRIN1	G protein-regulated inducer of neurite outgrowth 1	Transmembrane
Phos-MSNP	GRP78	78 kDa glucose-regulated protein	Mitochondria
Phos-MSNP	GSTA4	Glutathione S-transferase A4	Cytoplasm
Phos-MSNP	GUAD	Isoform 2 of Guanine deaminase	---
Phos-MSNP	H12	Histone H1.2	Nucleus
Phos-MSNP	H13	Histone H1.3	Nucleus
Phos-MSNP	H14	Histone H1.4	Nucleus
Phos-MSNP	H2A1	Histone H2A type 1	Cytoskeleton
Phos-MSNP	H2A1A	Histone H2A type 1-A	Cytoskeleton
Phos-MSNP	H2A1B	Histone H2A type 1-B/E	Cytoskeleton
Phos-MSNP	H2A1C	Histone H2A type 1-C	Nucleus
Phos-MSNP	H2A1D	Histone H2A type 1-D	Nucleus
Phos-MSNP	H2A1H	Histone H2A type 1-H	Nucleus
Phos-MSNP	H2A1J	Histone H2A type 1-J	Nucleus
Phos-MSNP	H2A2A	Histone H2A type 2-A	Nucleus
Phos-MSNP	H2A2B	Histone H2A type 2-B	Nucleus
Phos-	H2A2C	Histone H2A type 2-C	Nucleus

MSNP			
Phos-MSNP	H2A3	Histone H2A type 3	Nucleus
Phos-MSNP	H2AJ	Histone H2A.J	Nucleus
Phos-MSNP	H2AV	Isoform 2 of Histone H2A.V	Nucleus
Phos-MSNP	H2AX	Histone H2A.x	Nucleus
Phos-MSNP	H2AZ	Histone H2A.Z	Nucleus
Phos-MSNP	H2B1A	Histone H2B type 1-A	Nucleus
Phos-MSNP	H2B1B	Histone H2B type 1-B	Nucleus
Phos-MSNP	H2B1C	Histone H2B type 1-C/E/F/G/I	Nucleus
Phos-MSNP	H2B1D	Histone H2B type 1-D	Nucleus
Phos-MSNP	H2B1H	Histone H2B type 1-H	Nucleus
Phos-MSNP	H2B1J	Histone H2B type 1-J	Nucleus
Phos-MSNP	H2B1K	Histone H2B type 1-K	Nucleus
Phos-MSNP	H2B1L	Histone H2B type 1-L	Nucleus
Phos-MSNP	H2B1M	Histone H2B type 1-M	Nucleus
Phos-MSNP	H2B1N	Histone H2B type 1-N	Nucleus
Phos-MSNP	H2B1O	Histone H2B type 1-O	Nucleus
Phos-MSNP	H2B2E	Histone H2B type 2-E	Nucleus
Phos-MSNP	H2B2F	Histone H2B type 2-F	Nucleus
Phos-MSNP	H2B3B	Histone H2B type 3-B	Nucleus
Phos-MSNP	H2BFS	Histone H2B type F-S	Nucleus
Phos-MSNP	H31	Histone H3.1	Nucleus
Phos-MSNP	H31T	Histone H3.1t	Nucleus

Phos-MSNP	H32	Histone H3.2	Nucleus
Phos-MSNP	H33	Histone H3.3	Nucleus
Phos-MSNP	H3C	Histone H3.3C	Nucleus
Phos-MSNP	H90B2	Putative heat shock protein HSP 90-beta 2	Cytoplasm
Phos-MSNP	H90B3	Putative heat shock protein HSP 90-beta-3	Cytoplasm
Phos-MSNP	H90B4	Putative heat shock protein HSP 90-beta 4	Cytoplasm
Phos-MSNP	HS71L	Heat shock 70 kDa protein 1-like	Cytoplasm
Phos-MSNP	HS90A	Heat shock protein HSP 90-alpha	Cytoplasm
Phos-MSNP	HS90B	Heat shock protein HSP 90-beta	Cytoplasm
Phos-MSNP	HSP72	Heat shock-related 70 kDa protein 2	Cytoplasm
Phos-MSNP	HSP7C	Heat shock cognate 71 kDa protein	Cytoplasm
Phos-MSNP	KIF15	Kinesin-like protein KIF15	Nucleus
Phos-MSNP	KIF5C	Kinesin heavy chain isoform 5C	Nucleus
Phos-MSNP	KIZ	Centrosomal protein kizuna	Nucleus
Phos-MSNP	KPYM	Pyruvate kinase isozymes M1/M2	Cytoplasm
Phos-MSNP	KPYR	Pyruvate kinase isozymes R/L	Cytoplasm
Phos-MSNP	MAP2	Microtubule-associated protein 2	Cytoplasm
Phos-MSNP	MYH7B	Myosin-7B	Cytoplasm
Phos-MSNP	PCM1	Pericentriolar material 1 protein	Cytoplasm
Phos-MSNP	PLIN4	Perilipin-4	---
Phos-MSNP	POTEE	POTE ankyrin domain family member E	Secretory
Phos-MSNP	POTEF	POTE ankyrin domain family member F	Secretory
Phos-	POTEI	POTE ankyrin domain family member I	Secretory

MSNP			
Phos-MSNP	POTEJ	POTE ankyrin domain family member J	Secretory
Phos-MSNP	PRDX1	Peroxiredoxin-1	Cytoplasm
Phos-MSNP	RL40	Ubiquitin-60S ribosomal protein L40	Cytoplasm
Phos-MSNP	RRBP1	Ribosome-binding protein 1	Cytoplasm
Phos-MSNP	RS27A	Ubiquitin-40S ribosomal protein S27a	Cytoplasm
Phos-MSNP	RS6	40S ribosomal protein S6	Cytoplasm
Phos-MSNP	SPRR3	Small proline-rich protein 3	Cytoplasm
Phos-MSNP	SREK1	Splicing regulatory glutamine/lysine-rich protein 1	---
Phos-MSNP	TARA	Isoform 4 of TRIO and F-actin-binding protein	---
Phos-MSNP	TBA1A	Tubulin alpha-1A chain	Secretory
Phos-MSNP	TBA1B	Tubulin alpha-1B chain	Secretory
Phos-MSNP	TBA1C	Tubulin alpha-1C chain	Secretory
Phos-MSNP	TBA3C	Isoform 2 of Tubulin alpha-3C/D chain	Secretory
Phos-MSNP	TBA3E	Tubulin alpha-3E chain	Secretory
Phos-MSNP	TBA4A	Tubulin alpha-4A chain	Secretory
Phos-MSNP	TBA8	Tubulin alpha-8 chain	Secretory
Phos-MSNP	TBB2A	Tubulin beta-2A chain	Secretory
Phos-MSNP	TBB2B	Tubulin beta-2B chain	Secretory
Phos-MSNP	TBB3	Tubulin beta-3 chain	Secretory
Phos-MSNP	TBB4A	Tubulin beta-4A chain	Secretory
Phos-MSNP	TBB4B	Tubulin beta-4B chain	Secretory
Phos-MSNP	TBB5	Tubulin beta chain	Secretory

Phos-MSNP	TBB6	Tubulin beta-6 chain	Secretory
Phos-MSNP	THOC2	THO complex subunit 2	Nucleus
Phos-MSNP	UBB	Polyubiquitin-B	Secretory
Phos-MSNP	UBC	Polyubiquitin-C	Secretory
Phos-MSNP	XXLT1	Xyloside xylosyltransferase 1	---
Phos-MSNP	ZC3HD	Isoform 2 of Zinc finger CCCH domain-containing protein 13	Secretory

Table 2. Human proteins identified from MSNs incubated with A549 cells.

Particle Type	Protein ID	Protein Name	Subcellular Localization
amine-MSNP	ALBU	Serum albumin	Secretory
amine-MSNP	FETUA	Alpha-2-HS-glycoprotein	Cytoskeleton
bare-MSNP	ACTA	Actin_ aortic smooth muscle	Cytoplasm
bare-MSNP	ACTB	Actin_ cytoplasmic 1	Cytoplasm
bare-MSNP	ACTC	Actin_ alpha cardiac muscle 1	Cytoplasm
bare-MSNP	ACTG	Actin_ cytoplasmic 2	Cytoplasm
bare-MSNP	ACTH	Actin_ gamma-enteric smooth muscle	Cytoplasm
bare-MSNP	ACTS	Actin_ alpha skeletal muscle	Cytoplasm
bare-MSNP	ADT2	ADP/ATP translocase 2	Cytoplasm
bare-MSNP	ADT3	ADP/ATP translocase 3	Cytoplasm
bare-MSNP	AGR2	Anterior gradient protein 2 homolog	Secretory
bare-MSNP	ALBU	Serum albumin	Secretory
bare-MSNP	BIRC5	Isoform 2 of Baculoviral IAP repeat-containing protein 5	Cytoskeleton
bare-MSNP	CH10	10 kDa heat shock protein_ mitochondrial	Cytoskeleton
bare-MSNP	CH60	60 kDa heat shock protein_ mitochondrial	Mitochondria
bare-MSNP	HBB	Hemoglobin subunit beta	Cytoplasm
bare-MSNP	HBD	Hemoglobin subunit delta	Cytoplasm
bare-MSNP	HBE	Hemoglobin subunit epsilon	Cytoplasm
bare-MSNP	HBG1	Hemoglobin subunit gamma-1	Cytoplasm
bare-MSNP	HBG2	Hemoglobin subunit gamma-2	Cytoplasm
bare-MSNP	HS902	Putative heat shock protein HSP 90-alpha A2	Cytoplasm
bare-	HXD9	Homeobox protein Hox-D9	Cytoplasm

MSNP			
bare-MSNP	PI4K2A	Phosphatidylinositol 4-kinase type 2-alpha	Secretory
bare-MSNP	PODN	Isoform 2 of Podocan	Secretory
bare-MSNP	RL40	Ubiquitin-60S ribosomal protein L40	Secretory
bare-MSNP	RS27A	Ubiquitin-40S ribosomal protein S27a	Secretory
bare-MSNP	S2546	Solute carrier family 25 member 46	Mitochondria
bare-MSNP	UBB	Polyubiquitin-B	Secretory
bare-MSNP	UBC	Polyubiquitin-C	Secretory
bare-MSNP	UHMK1	Isoform 2 of Serine/threonine-protein kinase Kist	Cytoplasm
bare-MSNP	VIME	Vimentin	Cytoplasm
bare-MSNP	ZN616	Zinc finger protein 616	Nucleus
bare-MSNP	ZN655	Isoform 3 of Zinc finger protein 655	Nucleus
PEI-MSNP	HBB	Hemoglobin subunit beta	Cytoplasm
PEI-MSNP	HBD	Hemoglobin subunit delta	Cytoplasm
PEI-MSNP	VTNC	Vitronectin	Secretory
Phos-MSNP	MK12	Mitogen-activated protein kinase 12	Cytoplasm

Table 3. Human proteins identified from MSNs incubated with MCF7 cells.

Cell Line	Particle Type	Protein ID	Protein Name
A549	amine-MSNP	A5D7M6	KRT5 protein
A549	amine-MSNP	A6QNZ7	Keratin 10 (Epidermolytic hyperkeratosis; keratosis palmaris et plantaris)
A549	amine-MSNP	ALBU	Serum albumin
A549	amine-MSNP	B0JYQ0	ALB protein
A549	amine-MSNP	E1B991	Uncharacterized protein
A549	amine-MSNP	G3MXL3	Uncharacterized protein (Fragment)
A549	amine-MSNP	G3MYU2	Uncharacterized protein
A549	amine-MSNP	G3MZ71	Uncharacterized protein
A549	amine-MSNP	G3N0V2	Uncharacterized protein
A549	bare-MSNP	A0JNH4	Breast carcinoma amplified sequence 1
A549	bare-MSNP	A4IFP6	GIMAP1 protein
A549	bare-MSNP	A5D7M6	KRT5 protein
A549	bare-MSNP	A6QNZ7	Keratin 10 (Epidermolytic hyperkeratosis; keratosis palmaris et plantaris)
A549	bare-MSNP	ALBU	Serum albumin
A549	bare-MSNP	APOA1	Apolipoprotein A-I
A549	bare-MSNP	B0JYK1	BCAS1 protein
A549	bare-MSNP	B0JYN6	Alpha-2-HS-glycoprotein
A549	bare-MSNP	B0JYQ0	ALB protein
A549	bare-MSNP	E1B822	Uncharacterized protein
A549	bare-MSNP	F1MNI3	Uncharacterized protein
A549	bare-	F2Y907	Zinc finger protein 507 (Fragment)

	MSNP		
A549	bare-MSNP	F6QP30	Uncharacterized protein
A549	bare-MSNP	FETUA	Alpha-2-HS-glycoprotein
A549	bare-MSNP	G3MXL3	Uncharacterized protein (Fragment)
A549	bare-MSNP	G3MYU2	Uncharacterized protein
A549	bare-MSNP	G3N0V2	Uncharacterized protein
A549	bare-MSNP	HBBF	Hemoglobin fetal subunit beta
A549	bare-MSNP	Q0VBY4	Tumor protein D52-like 1
A549	bare-MSNP	RANDOM1653	Random Sequence 1653
A549	PEI-MSNP	A5D792	DCK protein
A549	PEI-MSNP	A5D7M6	KRT5 protein
A549	PEI-MSNP	ALBU	Serum albumin
A549	PEI-MSNP	B0JYN6	Alpha-2-HS-glycoprotein
A549	PEI-MSNP	B0JYQ0	ALB protein
A549	PEI-MSNP	E1B7N2	Histone H4
A549	PEI-MSNP	E1B9M9	Histone H4
A549	PEI-MSNP	E1BBP7	Histone H4
A549	PEI-MSNP	E1BLC2	Histone H4
A549	PEI-MSNP	FETUA	Alpha-2-HS-glycoprotein
A549	PEI-MSNP	G3MXL3	Uncharacterized protein (Fragment)
A549	PEI-MSNP	G3MYX0	Histone H4
A549	PEI-MSNP	G3N081	Histone H4
A549	PEI-MSNP	G3N2B8	Histone H4
A549	PEI-MSNP	G3X807	Histone H4 (Fragment)
A549	PEI-MSNP	H4	Histone H4
A549	PEI-MSNP	RANDOM29734	Random Sequence 29734
A549	Phos-MSNP	A5D7M6	KRT5 protein
A549	Phos-MSNP	A6QNZ7	Keratin 10 (Epidermolytic hyperkeratosis; keratosis palmaris et plantaris)
A549	Phos-MSNP	A7YK65	Toll-like receptor 1
A549	Phos-MSNP	A7YK67	Toll-like receptor 1

A549	Phos-MSNP	ALBU	Serum albumin
A549	Phos-MSNP	APOA1	Apolipoprotein A-I
A549	Phos-MSNP	B0JYN6	Alpha-2-HS-glycoprotein
A549	Phos-MSNP	B0JYQ0	ALB protein
A549	Phos-MSNP	B5TYW4	Toll-like receptor
A549	Phos-MSNP	F1N566	Uncharacterized protein (Fragment)
A549	Phos-MSNP	F6PRB5	Uncharacterized protein
A549	Phos-MSNP	FETUA	Alpha-2-HS-glycoprotein
A549	Phos-MSNP	G3MXL3	Uncharacterized protein (Fragment)
A549	Phos-MSNP	G3N0V2	Uncharacterized protein
A549	Phos-MSNP	Q3T172	ECH1 protein (Fragment)
A549	Phos-MSNP	Q4TU52	Toll-like receptor 1 (Fragment)
A549	Phos-MSNP	Q5EBY8	ECH1-like protein (Fragment)
A549	Phos-MSNP	Q6GV21	Toll-like receptor 1
A549	Phos-MSNP	RANDOM18029	Random Sequence 18029
HFF	amine-MSNP	1433F	14-3-3 protein eta
HFF	amine-MSNP	A3KN00	DUSP23 protein
HFF	amine-MSNP	A4FUB9	ACIN1 protein (Fragment)
HFF	amine-MSNP	A4IFM8	Actin_ alpha 1_ skeletal muscle
HFF	amine-MSNP	A5D792	DCK protein
HFF	amine-MSNP	A5D7J0	ACTA2 protein
HFF	amine-	A5D7M6	KRT5 protein

	MSNP		
HFF	amine-MSNP	A5D7N2	Histone H2B
HFF	amine-MSNP	A6QP97	E3 ubiquitin-protein ligase RNF220
HFF	amine-MSNP	A7E3E1	HSPCA protein (Fragment)
HFF	amine-MSNP	A7E3Q2	Heat shock 70kDa protein 1A
HFF	amine-MSNP	A7Z082	ACIN1 protein
HFF	amine-MSNP	ACTA	Actin_ aortic smooth muscle
HFF	amine-MSNP	ACTB	Actin_ cytoplasmic 1
HFF	amine-MSNP	ACTC	Actin_ alpha cardiac muscle 1
HFF	amine-MSNP	ACTG	Actin_ cytoplasmic 2
HFF	amine-MSNP	ACTH	Actin_ gamma-enteric smooth muscle
HFF	amine-MSNP	ACTS	Actin_ alpha skeletal muscle
HFF	amine-MSNP	AINX	Alpha-internexin
HFF	amine-MSNP	ALBU	Serum albumin
HFF	amine-MSNP	APOA1	Apolipoprotein A-I
HFF	amine-MSNP	ATPA	ATP synthase subunit alpha_ mitochondrial
HFF	amine-MSNP	B0JYQ0	ALB protein
HFF	amine-MSNP	CH10	10 kDa heat shock protein_ mitochondrial
HFF	amine-MSNP	CSH1	Chorionic somatomammotropin hormone 1
HFF	amine-MSNP	D3U796	Nucleophosmin
HFF	amine-MSNP	D4QBB3	Hemoglobin beta
HFF	amine-MSNP	D4QBB4	Hemoglobin beta

HFF	amine-MSNP	E1B7J1	Elongation factor 1-alpha
HFF	amine-MSNP	E1B8G9	Histone H2B
HFF	amine-MSNP	E1B8K6	Uncharacterized protein
HFF	amine-MSNP	E1B9F6	Elongation factor 1-alpha
HFF	amine-MSNP	E1B9K1	Polyubiquitin-C
HFF	amine-MSNP	E1B9M9	Histone H4
HFF	amine-MSNP	E1BBP7	Histone H4
HFF	amine-MSNP	E1BDE9	Uncharacterized protein
HFF	amine-MSNP	E1BED8	Elongation factor 1-alpha (Fragment)
HFF	amine-MSNP	E1BEL8	Uncharacterized protein
HFF	amine-MSNP	E1BGW2	Histone H2B
HFF	amine-MSNP	E1BK75	Histone H2B
HFF	amine-MSNP	E1BKX5	Uncharacterized protein
HFF	amine-MSNP	E1BLC2	Histone H4
HFF	amine-MSNP	E1BLK2	Uncharacterized protein
HFF	amine-MSNP	E1BPF4	Elongation factor 1-alpha (Fragment)
HFF	amine-MSNP	E1BPK0	Uncharacterized protein
HFF	amine-MSNP	E3SAZ8	Nucleophosmin
HFF	amine-MSNP	EF1A1	Elongation factor 1-alpha 1
HFF	amine-MSNP	EF1A2	Elongation factor 1-alpha 2
HFF	amine-MSNP	ENPL	Endoplasmin
HFF	amine-	F1MBN8	Uncharacterized protein

	MSNP		
HFF	amine-MSNP	F1MJW1	Uncharacterized protein (Fragment)
HFF	amine-MSNP	F1MKC4	Uncharacterized protein
HFF	amine-MSNP	F1MKC4	Uncharacterized protein
HFF	amine-MSNP	F1MLB8	ATP synthase subunit alpha
HFF	amine-MSNP	F1MLB8	ATP synthase subunit alpha
HFF	amine-MSNP	F1MM88	Uncharacterized protein (Fragment)
HFF	amine-MSNP	F1MNF8	Uncharacterized protein
HFF	amine-MSNP	F1MQG6	Uncharacterized protein
HFF	amine-MSNP	F1MRD0	Actin_ cytoplasmic 1
HFF	amine-MSNP	F1MTV9	Uncharacterized protein
HFF	amine-MSNP	F1MUB8	Uncharacterized protein
HFF	amine-MSNP	F1MUD2	Histone H2B
HFF	amine-MSNP	F1MUU9	Uncharacterized protein (Fragment)
HFF	amine-MSNP	F1MV26	Uncharacterized protein
HFF	amine-MSNP	F1MYF0	Chorionic somatomammotropin hormone 2
HFF	amine-MSNP	F1MYL0	E3 ubiquitin-protein ligase RNF220
HFF	amine-MSNP	F1N453	Histone H2B
HFF	amine-MSNP	F1N614	Uncharacterized protein
HFF	amine-MSNP	F2Z4C1	Uncharacterized protein
HFF	amine-MSNP	F2Z4E8	Histone H2B
HFF	amine-MSNP	F2Z4F9	Histone H2B

HFF	amine-MSNP	F2Z4K0	Uncharacterized protein
HFF	amine-MSNP	F6RP72	Uncharacterized protein (Fragment)
HFF	amine-MSNP	G3MWH4	Uncharacterized protein
HFF	amine-MSNP	G3MX03	Uncharacterized protein
HFF	amine-MSNP	G3MXG1	Uncharacterized protein
HFF	amine-MSNP	G3MXL3	Uncharacterized protein (Fragment)
HFF	amine-MSNP	G3MXT4	Uncharacterized protein
HFF	amine-MSNP	G3MY27	Uncharacterized protein
HFF	amine-MSNP	G3MYJ0	Uncharacterized protein
HFF	amine-MSNP	G3MYV4	Histone H2B
HFF	amine-MSNP	G3MZ21	Uncharacterized protein
HFF	amine-MSNP	G3MZL8	Uncharacterized protein (Fragment)
HFF	amine-MSNP	G3MZR4	Histone H2B
HFF	amine-MSNP	G3N011	Uncharacterized protein
HFF	amine-MSNP	G3N053	Histone H2B
HFF	amine-MSNP	G3N068	Histone H2B
HFF	amine-MSNP	G3N080	Histone H2B (Fragment)
HFF	amine-MSNP	G3N081	Histone H4
HFF	amine-MSNP	G3N0L9	Uncharacterized protein
HFF	amine-MSNP	G3N0V2	Uncharacterized protein
HFF	amine-MSNP	G3N1C9	Histone H2B
HFF	amine-	G3N1R5	Uncharacterized protein

	MSNP		
HFF	amine-MSNP	G3N1Y3	Uncharacterized protein (Fragment)
HFF	amine-MSNP	G3N2B8	Histone H4
HFF	amine-MSNP	G3N2F0	Elongation factor 1-alpha
HFF	amine-MSNP	G3N2V5	Heat shock protein HSP 90-beta
HFF	amine-MSNP	G3N3L9	Uncharacterized protein
HFF	amine-MSNP	G3P	Glyceraldehyde-3-phosphate dehydrogenase
HFF	amine-MSNP	G3X7M4	Uncharacterized protein
HFF	amine-MSNP	G3X807	Histone H4 (Fragment)
HFF	amine-MSNP	G5E507	Heat shock protein HSP 90-beta
HFF	amine-MSNP	G5E6I9	Histone H2B
HFF	amine-MSNP	G8JKX4	Actin_ aortic smooth muscle
HFF	amine-MSNP	G8JL06	Histone H2B
HFF	amine-MSNP	GRP78	78 kDa glucose-regulated protein
HFF	amine-MSNP	H2B1	Histone H2B type 1
HFF	amine-MSNP	H2B1K	Histone H2B type 1-K
HFF	amine-MSNP	H2B1N	Histone H2B type 1-N
HFF	amine-MSNP	H4	Histone H4
HFF	amine-MSNP	HBB	Hemoglobin subunit beta
HFF	amine-MSNP	HBBF	Hemoglobin fetal subunit beta
HFF	amine-MSNP	HBE2	Hemoglobin subunit epsilon-2
HFF	amine-MSNP	HBE4	Hemoglobin subunit epsilon-4

HFF	amine-MSNP	HS71A	Heat shock 70 kDa protein 1A
HFF	amine-MSNP	HS71L	Heat shock 70 kDa protein 1-like
HFF	amine-MSNP	HS90A	Heat shock protein HSP 90-alpha
HFF	amine-MSNP	HS90B	Heat shock protein HSP 90-beta
HFF	amine-MSNP	HSP72	Heat shock-related 70 kDa protein 2
HFF	amine-MSNP	HSP7C	Heat shock cognate 71 kDa protein
HFF	amine-MSNP	HSP7C	Heat shock cognate 71 kDa protein
HFF	amine-MSNP	M5FJZ9	Heat shock protein 75 kDa_ mitochondrial
HFF	amine-MSNP	NPM	Nucleophosmin
HFF	amine-MSNP	O18787	Elongation factor 1 alpha (Fragment)
HFF	amine-MSNP	Q0QES8	Glyceraldehyde-3-phosphate dehydrogenase (Fragment)
HFF	amine-MSNP	Q28163	Placental lactogen (Fragment)
HFF	amine-MSNP	Q2KII5	Histone H2B
HFF	amine-MSNP	Q2QJG3	Beta-actin (Fragment)
HFF	amine-MSNP	Q32S29	Histone H2B
HFF	amine-MSNP	Q3SZD6	HSP90AB1 protein (Fragment)
HFF	amine-MSNP	Q3T007	HSPCA protein (Fragment)
HFF	amine-MSNP	Q3ZBS7	Uncharacterized protein
HFF	amine-MSNP	Q58D76	Proteasome 26S non-ATPase subunit 4 isoform 1
HFF	amine-MSNP	Q58DT9	Alpha 2 actin
HFF	amine-MSNP	Q5JB60	Nucleolin (Fragment)
HFF	amine-	Q712W6	Glyceraldehyde-3-phosphate dehydrogenase

	MSNP		(Fragment)
HFF	amine-MSNP	Q861V2	Similar to 7O kDa heat shock cognate protein (Fragment)
HFF	amine-MSNP	Q862L2	Similar to alpha-tubulin isoform 1 (Fragment)
HFF	amine-MSNP	Q862L7	Similar to elongation factor 1 alpha (Fragment)
HFF	amine-MSNP	Q862P9	Similar to beta actin (Fragment)
HFF	amine-MSNP	Q862R6	Similar to elongation factor 1 alpha (Fragment)
HFF	amine-MSNP	Q865A1	Heat shock protein 90 beta (Fragment)
HFF	amine-MSNP	Q9TTW4	Beta actin (Fragment)
HFF	amine-MSNP	RANDOM11686	Random Sequence 11686
HFF	amine-MSNP	RANDOM12679	Random Sequence 12679
HFF	amine-MSNP	RANDOM1273	Random Sequence 1273
HFF	amine-MSNP	RANDOM1653	Random Sequence 1653
HFF	amine-MSNP	RANDOM25591	Random Sequence 25591
HFF	amine-MSNP	RANDOM28104	Random Sequence 28104
HFF	amine-MSNP	RANDOM450	Random Sequence 450
HFF	amine-MSNP	RANDOM4902	Random Sequence 4902
HFF	amine-MSNP	RL40	Ubiquitin-60S ribosomal protein L40
HFF	amine-MSNP	RN220	E3 ubiquitin-protein ligase RNF220
HFF	amine-MSNP	RS27A	Ubiquitin-40S ribosomal protein S27a
HFF	amine-MSNP	TBA1B	Tubulin alpha-1B chain
HFF	amine-MSNP	TBA1C	Tubulin alpha-1C chain
HFF	amine-MSNP	TBA1D	Tubulin alpha-1D chain

HFF	amine-MSNP	TBA3	Tubulin alpha-3 chain
HFF	amine-MSNP	TBB5	Tubulin beta-5 chain
HFF	amine-MSNP	TRAP1	Heat shock protein 75 kDa_ mitochondrial
HFF	amine-MSNP	UBB	Polyubiquitin-B
HFF	amine-MSNP	UBC	Polyubiquitin-C
HFF	amine-MSNP	VIME	Vimentin
HFF	bare-MSNP	A4IFM8	Actin_ alpha 1_ skeletal muscle
HFF	bare-MSNP	A5D7J0	ACTA2 protein
HFF	bare-MSNP	A5D7M6	KRT5 protein
HFF	bare-MSNP	A6QNZ7	Keratin 10 (Epidermolytic hyperkeratosis; keratosis palmaris et plantaris)
HFF	bare-MSNP	ACTA	Actin_ aortic smooth muscle
HFF	bare-MSNP	ACTB	Actin_ cytoplasmic 1
HFF	bare-MSNP	ACTC	Actin_ alpha cardiac muscle 1
HFF	bare-MSNP	ACTG	Actin_ cytoplasmic 2
HFF	bare-MSNP	ACTH	Actin_ gamma-enteric smooth muscle
HFF	bare-MSNP	ACTS	Actin_ alpha skeletal muscle
HFF	bare-MSNP	APOA1	Apolipoprotein A-I
HFF	bare-MSNP	B0JYN6	Alpha-2-HS-glycoprotein
HFF	bare-MSNP	D4QBB3	Hemoglobin beta
HFF	bare-MSNP	D4QBB4	Hemoglobin beta
HFF	bare-MSNP	E1B7N8	Uncharacterized protein
HFF	bare-	E1B991	Uncharacterized protein

	MSNP		
HFF	bare-MSNP	E1B9M9	Histone H4
HFF	bare-MSNP	E1BBP7	Histone H4
HFF	bare-MSNP	E1BEL8	Uncharacterized protein
HFF	bare-MSNP	E1BLC2	Histone H4
HFF	bare-MSNP	F1MHL1	Uncharacterized protein (Fragment)
HFF	bare-MSNP	F1MIM6	Uncharacterized protein (Fragment)
HFF	bare-MSNP	F1MKC4	Uncharacterized protein
HFF	bare-MSNP	F1MM88	Uncharacterized protein (Fragment)
HFF	bare-MSNP	F1MRD0	Actin_ cytoplasmic 1
HFF	bare-MSNP	FETUA	Alpha-2-HS-glycoprotein
HFF	bare-MSNP	G3MXL3	Uncharacterized protein (Fragment)
HFF	bare-MSNP	G3MYU2	Uncharacterized protein
HFF	bare-MSNP	G3MZ71	Uncharacterized protein
HFF	bare-MSNP	G3N0V2	Uncharacterized protein
HFF	bare-MSNP	G3N1Y3	Uncharacterized protein (Fragment)
HFF	bare-MSNP	G3N2B8	Histone H4
HFF	bare-MSNP	G3X807	Histone H4 (Fragment)
HFF	bare-MSNP	G8JKX4	Actin_ aortic smooth muscle
HFF	bare-MSNP	H4	Histone H4
HFF	bare-MSNP	HBB	Hemoglobin subunit beta
HFF	bare-MSNP	HBBF	Hemoglobin fetal subunit beta

HFF	bare-MSNP	Q58DT9	Alpha 2 actin
HFF	bare-MSNP	Q862P9	Similar to beta actin (Fragment)
HFF	bare-MSNP	Q9TTW4	Beta actin (Fragment)
HFF	bare-MSNP	RANDOM16097	Random Sequence 16097
HFF	bare-MSNP	RANDOM1653	Random Sequence 1653
HFF	bare-MSNP	RANDOM17625	Random Sequence 17625
HFF	bare-MSNP	RT31	28S ribosomal protein S31_ mitochondrial
HFF	PEI-MSNP	A4IFM8	Actin_ alpha 1_ skeletal muscle
HFF	PEI-MSNP	A5D7J0	ACTA2 protein
HFF	PEI-MSNP	A5D7M6	KRT5 protein
HFF	PEI-MSNP	A6QNZ7	Keratin 10 (Epidermolytic hyperkeratosis; keratosis palmaris et plantaris)
HFF	PEI-MSNP	ACTA	Actin_ aortic smooth muscle
HFF	PEI-MSNP	ACTB	Actin_ cytoplasmic 1
HFF	PEI-MSNP	ACTC	Actin_ alpha cardiac muscle 1
HFF	PEI-MSNP	ACTG	Actin_ cytoplasmic 2
HFF	PEI-MSNP	ACTH	Actin_ gamma-enteric smooth muscle
HFF	PEI-MSNP	ACTS	Actin_ alpha skeletal muscle
HFF	PEI-MSNP	ALBU	Serum albumin
HFF	PEI-MSNP	APOA1	Apolipoprotein A-I
HFF	PEI-MSNP	B0JYQ0	ALB protein
HFF	PEI-MSNP	CDN2D	Cyclin-dependent kinase 4 inhibitor D
HFF	PEI-MSNP	DRG2	Developmentally-regulated GTP-binding protein 2
HFF	PEI-MSNP	E1B7J1	Elongation factor 1-alpha
HFF	PEI-MSNP	E1B991	Uncharacterized protein
HFF	PEI-MSNP	E1B9F6	Elongation factor 1-alpha
HFF	PEI-MSNP	E1B9G8	Uncharacterized protein
HFF	PEI-MSNP	E1B9K1	Polyubiquitin-C
HFF	PEI-MSNP	E1BCU2	Uncharacterized protein
HFF	PEI-MSNP	E1BED8	Elongation factor 1-alpha (Fragment)
HFF	PEI-MSNP	E1BPF4	Elongation factor 1-alpha (Fragment)
HFF	PEI-MSNP	EF1A1	Elongation factor 1-alpha 1
HFF	PEI-MSNP	EF1A2	Elongation factor 1-alpha 2
HFF	PEI-MSNP	F1MC11	Keratin_ type I cytoskeletal 14

HFF	PEI-MSNP	F1MIM6	Uncharacterized protein (Fragment)
HFF	PEI-MSNP	F1MJ66	Uncharacterized protein (Fragment)
HFF	PEI-MSNP	F1MKC4	Uncharacterized protein
HFF	PEI-MSNP	F1MM88	Uncharacterized protein (Fragment)
HFF	PEI-MSNP	F1MNF8	Uncharacterized protein
HFF	PEI-MSNP	F1MRD0	Actin_ cytoplasmic 1
HFF	PEI-MSNP	F1MYV1	Uncharacterized protein (Fragment)
HFF	PEI-MSNP	F2Z4C1	Uncharacterized protein
HFF	PEI-MSNP	F2Z4K0	Uncharacterized protein
HFF	PEI-MSNP	F6RP72	Uncharacterized protein (Fragment)
HFF	PEI-MSNP	G3MXL3	Uncharacterized protein (Fragment)
HFF	PEI-MSNP	G3MYU2	Uncharacterized protein
HFF	PEI-MSNP	G3MZ71	Uncharacterized protein
HFF	PEI-MSNP	G3N0V2	Uncharacterized protein
HFF	PEI-MSNP	G3N1Y3	Uncharacterized protein (Fragment)
HFF	PEI-MSNP	G3N2F0	Elongation factor 1-alpha
HFF	PEI-MSNP	G3N3B9	Uncharacterized protein (Fragment)
HFF	PEI-MSNP	G8JKX4	Actin_ aortic smooth muscle
HFF	PEI-MSNP	HBBF	Hemoglobin fetal subunit beta
HFF	PEI-MSNP	O18787	Elongation factor 1 alpha (Fragment)
HFF	PEI-MSNP	Q17QL7	KRT15 protein
HFF	PEI-MSNP	Q3ZBS7	Uncharacterized protein
HFF	PEI-MSNP	Q58DT9	Alpha 2 actin
HFF	PEI-MSNP	Q862L7	Similar to elongation factor 1 alpha (Fragment)
HFF	PEI-MSNP	Q862P9	Similar to beta actin (Fragment)
HFF	PEI-MSNP	Q862R6	Similar to elongation factor 1 alpha (Fragment)
HFF	PEI-MSNP	Q9TTW4	Beta actin (Fragment)
HFF	PEI-MSNP	RANDOM1549	Random Sequence 1549
HFF	PEI-MSNP	RANDOM17853	Random Sequence 17853
HFF	PEI-MSNP	RANDOM2905	Random Sequence 2905
HFF	PEI-MSNP	RANDOM697	Random Sequence 697
HFF	PEI-MSNP	RANDOM7813	Random Sequence 7813
HFF	PEI-MSNP	RL40	Ubiquitin-60S ribosomal protein L40
HFF	PEI-MSNP	RS27A	Ubiquitin-40S ribosomal protein S27a
HFF	PEI-MSNP	TAGL2	Transgelin-2
HFF	PEI-MSNP	TBA1B	Tubulin alpha-1B chain
HFF	PEI-MSNP	TBA1C	Tubulin alpha-1C chain
HFF	PEI-MSNP	TBA1D	Tubulin alpha-1D chain
HFF	PEI-MSNP	UBB	Polyubiquitin-B
HFF	PEI-MSNP	UBC	Polyubiquitin-C

MCF7	amine-MSNP	A1A4M3	KRT86 protein (Fragment)
MCF7	amine-MSNP	A1AT	Alpha-1-antiproteinase
MCF7	amine-MSNP	A3KMY1	KRT82 protein
MCF7	amine-MSNP	A3KN26	KRT33B protein
MCF7	amine-MSNP	A3KN26	KRT33B protein
MCF7	amine-MSNP	A4FV94	KRT6A protein
MCF7	amine-MSNP	A4IFP2	KRT4 protein
MCF7	amine-MSNP	A5D7M6	KRT5 protein
MCF7	amine-MSNP	A5PJJ1	KRT33A protein
MCF7	amine-MSNP	A5PJL3	MAPK12 protein
MCF7	amine-MSNP	A6H7D3	KRT18 protein (Fragment)
MCF7	amine-MSNP	A6QNZ7	Keratin 10 (Epidermolytic hyperkeratosis; keratosis palmaris et plantaris)
MCF7	amine-MSNP	A6QP32	KRT85 protein
MCF7	amine-MSNP	A6QP90	KRT32 protein
MCF7	amine-MSNP	ALBU	Serum albumin
MCF7	amine-MSNP	APOA1	Apolipoprotein A-I
MCF7	amine-MSNP	B0JYN6	Alpha-2-HS-glycoprotein
MCF7	amine-MSNP	B0JYQ0	ALB protein
MCF7	amine-MSNP	D4QBB4	Hemoglobin beta
MCF7	amine-MSNP	E1B898	Uncharacterized protein
MCF7	amine-MSNP	E1B991	Uncharacterized protein
MCF7	amine-	E1BFG1	Uncharacterized protein

	MSNP		
MCF7	amine-MSNP	E1BIL2	Uncharacterized protein (Fragment)
MCF7	amine-MSNP	E1BPW6	Keratin_ type I cuticular Ha5
MCF7	amine-MSNP	F1MC11	Keratin_ type I cytoskeletal 14
MCF7	amine-MSNP	F1MDL7	Uncharacterized protein (Fragment)
MCF7	amine-MSNP	F1MFW9	Uncharacterized protein (Fragment)
MCF7	amine-MSNP	F1MI98	Uncharacterized protein
MCF7	amine-MSNP	F1MJ66	Uncharacterized protein (Fragment)
MCF7	amine-MSNP	F1MKE7	Uncharacterized protein (Fragment)
MCF7	amine-MSNP	F1MM88	Uncharacterized protein (Fragment)
MCF7	amine-MSNP	F1MNI3	Uncharacterized protein
MCF7	amine-MSNP	F1MSA6	Uncharacterized protein
MCF7	amine-MSNP	F1MUY2	Uncharacterized protein
MCF7	amine-MSNP	F1MV92	Uncharacterized protein (Fragment)
MCF7	amine-MSNP	F1MXG6	Uncharacterized protein
MCF7	amine-MSNP	F1N362	Uncharacterized protein
MCF7	amine-MSNP	F1N566	Uncharacterized protein (Fragment)
MCF7	amine-MSNP	F2Y907	Zinc finger protein 507 (Fragment)
MCF7	amine-MSNP	F6S1Q0	Uncharacterized protein
MCF7	amine-MSNP	FETUA	Alpha-2-HS-glycoprotein
MCF7	amine-MSNP	G3MXL3	Uncharacterized protein (Fragment)
MCF7	amine-MSNP	G3MYU2	Uncharacterized protein

MCF7	amine-MSNP	G3MZ71	Uncharacterized protein
MCF7	amine-MSNP	G3N0V2	Uncharacterized protein
MCF7	amine-MSNP	G3N0W8	Uncharacterized protein
MCF7	amine-MSNP	G3N1Y3	Uncharacterized protein (Fragment)
MCF7	amine-MSNP	G3X6C0	Inositol oxygenase
MCF7	amine-MSNP	G3X6N3	Serotransferrin
MCF7	amine-MSNP	G3X7W8	Uncharacterized protein (Fragment)
MCF7	amine-MSNP	HBB	Hemoglobin subunit beta
MCF7	amine-MSNP	HBBF	Hemoglobin fetal subunit beta
MCF7	amine-MSNP	M0QVY0	Uncharacterized protein
MCF7	amine-MSNP	MIOX	Inositol oxygenase
MCF7	amine-MSNP	O62659	Hair keratin A1 (Fragment)
MCF7	amine-MSNP	PI42C	Phosphatidylinositol 5-phosphate 4-kinase type-2 gamma
MCF7	amine-MSNP	Q0VD04	Keratin 85
MCF7	amine-MSNP	Q148I8	Keratin 31
MCF7	amine-MSNP	Q148J0	Keratin 34
MCF7	amine-MSNP	Q17QL7	KRT15 protein
MCF7	amine-MSNP	Q1HDH9	LOC507184 (Fragment)
MCF7	amine-MSNP	Q862F9	Similar to vimentin (Fragment)
MCF7	amine-MSNP	Q9TRP4	Fetuin (Fragment)
MCF7	amine-MSNP	RANDOM10786	Random Sequence 10786
MCF7	amine-	RANDOM12682	Random Sequence 12682

	MSNP		
MCF7	amine-MSNP	RANDOM15146	Random Sequence 15146
MCF7	amine-MSNP	RANDOM16097	Random Sequence 16097
MCF7	amine-MSNP	RANDOM19162	Random Sequence 19162
MCF7	amine-MSNP	RANDOM19634	Random Sequence 19634
MCF7	amine-MSNP	RANDOM20132	Random Sequence 20132
MCF7	amine-MSNP	RANDOM28556	Random Sequence 28556
MCF7	amine-MSNP	RANDOM29734	Random Sequence 29734
MCF7	amine-MSNP	TRFE	Serotransferrin
MCF7	amine-MSNP	VIME	Vimentin
MCF7	Phos-MSNP	Q8HY43	Early growth response protein 1 (Fragment)

Table 4. Bovine proteins identified from MSNs incubated with A549, HFF, and MCF7 cells.

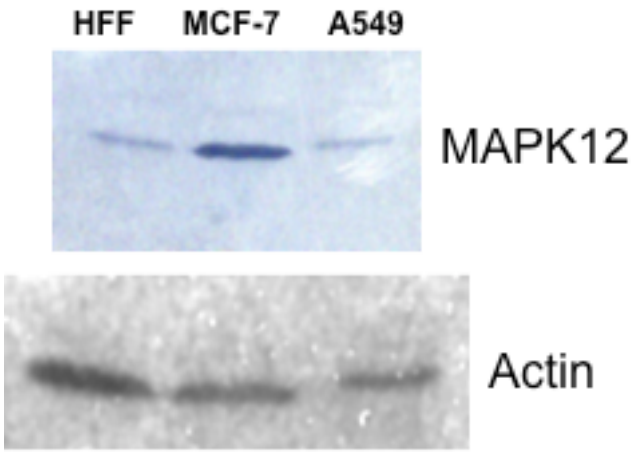

Figure 2. A Western Blot of HFF, MCF7, and A549 cell lysates shows that (A) MAPK12 is present in all three cell lines. (B) Actin control.

REFERENCES

1. Meng, H.; Liong, M.; Xia, T.; Li, Z.; Ji, Z.; Zink, J. I.; Nel, A. E. *ACS nano* **2010**, *4*, 4539.

2. Lu, J.; Li, Z.; Zink, J. I.; Tamanoi, F. *Nanomedicine : nanotechnology, biology, and medicine* **2012**, *8*, 212.

3. Slowing, II; Trewyn, B. G.; Lin, V. S. *Journal of the American Chemical Society* **2007**, *129*, 8845.

4. Qin, F.; Zhou, Y.; Shi, J.; Zhang, Y. *Journal of biomedical materials research. Part A* **2009**, *90*, 333.

5. Kim, J.; Kim, H. S.; Lee, N.; Kim, T.; Kim, H.; Yu, T.; Song, I. C.; Moon, W. K.; Hyeon, T. *Angew Chem Int Ed Engl* **2008**, *47*, 8438.

6. Nel, A. E.; Madler, L.; Velegol, D.; Xia, T.; Hoek, E. M.; Somasundaran, P.; Klaessig, F.; Castranova, V.; Thompson, M. *Nature materials* **2009**, *8*, 543.

7. Aggarwal, P.; Hall, J. B.; McLeland, C. B.; Dobrovolskaia, M. A.; McNeil, S. E. *Advanced drug delivery reviews* **2009**, *61*, 428.

8. Owens, D. E., 3rd; Peppas, N. A. *International journal of pharmaceutics* **2006**, *307*, 93.

9. Goppert, T. M.; Muller, R. H. *Journal of drug targeting* **2005**, *13*, 179.

10. Kreuter, J. *Advanced drug delivery reviews* **2001**, *47*, 65.

11. Olivier, J. C. *NeuroRx : the journal of the American Society for Experimental NeuroTherapeutics* **2005**, *2*, 108.

12. Gref, R.; Luck, M.; Quellec, P.; Marchand, M.; Dellacherie, E.; Harnisch, S.; Blunk, T.; Muller, R. H. *Colloids and surfaces. B, Biointerfaces* **2000**, *18*, 301.

13. Lundqvist, M.; Stigler, J.; Elia, G.; Lynch, I.; Cedervall, T.; Dawson, K. A. *Proceedings of the National Academy of Sciences of the United States of America* **2008**, *105*, 14265.

14. Casals, E.; Pfaller, T.; Duschl, A.; Oostingh, G. J.; Puntes, V. *ACS nano* **2010**, *4*, 3623.

15. Lundqvist, M.; Stigler, J.; Cedervall, T.; Berggard, T.; Flanagan, M. B.; Lynch, I.; Elia, G.; Dawson, K. *ACS nano* **2011**, *5*, 7503.

16. Yanes, R. E.; Tarn, D.; Hwang, A. A.; Ferris, D. P.; Sherman, S. P.; Thomas, C. R.; Lu, J.; Pyle, A. D.; Zink, J. I.; Tamanoi, F. *Small* **2013**, *9*, 697.

17. Nikas, J. B.; Low, W. C. *Cancer informatics* **2012**, *11*, 1.

18. Bera, T. K.; Saint Fleur, A.; Lee, Y.; Kydd, A.; Hahn, Y.; Popescu, N. C.; Zimonjic, D. B.; Lee, B.; Pastan, I. *Cancer Res* **2006**, *66*, 52.

19. Kami, K.; Fujimori, T.; Sato, H.; Sato, M.; Yamamoto, H.; Ohashi, Y.; Sugiyama, N.; Ishihama, Y.; Onozuka, H.; Ochiai, A.; Esumi, H.; Soga, T.; Tomita, M. *Metabolomics : Official journal of the Metabolomic Society* **2013**, *9*, 444.

20. Chevrollier, A.; Loiseau, D.; Chabi, B.; Renier, G.; Douay, O.; Malthièry, Y.; Stepien, G. *J Bioenerg Biomembr* **2005**, *37*, 307.

21. Le Bras, M.; Borgne-Sanchez, A.; Touat, Z.; El Dein, O. S.; Deniaud, A.; Maillier, E.; Lecellier, G.; Rebouillat, D.; Lemaire, C.; Kroemer, G.; Jacotot, E.; Brenner, C. *Cancer Research* **2006**, *66*, 9143.

22. Yang, Z.; Cheng, W.; Hong, L.; Chen, W.; Wang, Y.; Lin, S.; Han, J.; Zhou, H.; Gu, J. *Molecular biology of the cell* **2007**, *18*, 4681.

23. Jang, J.-Y.; Choi, Y.; Jeon, Y.-K.; Kim, C.-W. *Breast Cancer Research* **2008**, *10*, R11.

24. Fritzsche, F. R.; Dahl, E.; Pahl, S.; Burkhardt, M.; Luo, J.; Mayordomo, E.; Gansukh, T.; Dankof, A.; Knuechel, R.; Denkert, C.; Winzer, K. J.; Dietel, M.; Kristiansen, G. *Clinical cancer research : an official journal of the American Association for Cancer Research* **2006**, *12*, 1728.

25. Barraclough, D. L.; Platt-Higgins, A.; de Silva Rudland, S.; Barraclough, R.; Winstanley, J.; West, C. R.; Rudland, P. S. *The American journal of pathology* **2009**, *175*, 1848.

26. Li, J.; Lu, Y.; Zhang, J.; Kang, H.; Qin, Z.; Chen, C. *Oncogene* **2010**, *29*, 2550.

27. Ilboudo, A.; Nault, J. C.; Dubois-Pot-Schneider, H.; Corlu, A.; Zucman-Rossi, J.; Samson, M.; Le Seyec, J. *BMC cancer* **2014**, *14*, 7.

28. Fu, C. H.; Lin, R. J.; Yu, J.; Chang, W. W.; Liao, G. S.; Chang, W. Y.; Tseng, L. M.; Tsai, Y. F.; Yu, J. C.; Yu, A. L. *Stem cells* **2014**.

29. Sommers, C. L.; Heckford, S. E.; Skerker, J. M.; Worland, P.; Torri, J. A.; Thompson, E. W.; Byers, S. W.; Gelmann, E. P. *Cancer Res* **1992**, *52*, 5190.

30. Wagner, E. F.; Nebreda, A. R. *Nature reviews. Cancer* **2009**, *9*, 537.

31. Lord, C. J.; Ashworth, A. *Current opinion in pharmacology* **2008**, *8*, 363.

32. Sebolt-Leopold, J. S.; Herrera, R. *Nature reviews. Cancer* **2004**, *4*, 937.

33. Tao, K.; Fang, M.; Alroy, J.; Sahagian, G. G. *BMC cancer* **2008**, *8*, 228.

34. Zhao, Y. H.; Wang, T.; Yu, G. F.; Zhuang, D. M.; Zhang, Z.; Zhang, H. X.; Zhao, D. P.; Yu, A. L. *Asian Pacific journal of cancer prevention : APJCP* **2013**, *14*, 5513.

35. Mitra, A. P.; Pagliarulo, V.; Yang, D.; Waldman, F. M.; Datar, R. H.; Skinner, D. G.; Groshen, S.; Cote, R. J. *Journal of clinical oncology : official journal of the American Society of Clinical Oncology* **2009**, *27*, 3929.

36. Xie, X. T., X.; Wieland, A.; Zhou, S.; Bachem, M.; Henne-Bruns, D.; Kornmann, M. *Zeitschrift für Gastroenterologie* **2010**, *48*, 1.

CHAPTER 5

Direct Ionization of Large Proteins and Protein Complexes by Desorption Electrospray Ionization-Mass Spectrometry

analytical chemistry

ACCELERATED ARTICLE

pubs.acs.org/ac

Direct Ionization of Large Proteins and Protein Complexes by Desorption Electrospray Ionization-Mass Spectrometry

Carly N. Ferguson,[†] Sabrina A. Benchaar,[†] Zhixin Miao,[§] Joseph A. Loo,[*,†,‡] and Hao Chen[*,§]

[†]Department of Chemistry and Biochemistry and [‡]Department of Biological Chemistry, David Geffen School of Medicine, University of California-Los Angeles, Los Angeles, California 90095, United States

[§]Center for Intelligent Chemical Instrumentation, Department of Chemistry and Biochemistry, Ohio University, Athens, Ohio 45701, United States

Supporting Information

ABSTRACT: Desorption electrospray ionization-mass spectrometry (DESI-MS) has advantages for rapid sample analysis with little or no sample pretreatment, but performance for large biomolecules has not been demonstrated. In this study, liquid sample DESI, an extended version of DESI used for analysis of liquid samples, was shown to have capabilities for direct ionization of large noncovalent protein complexes (>45 kDa) and proteins (up to 150 kDa). Protein complex ions (e.g., superoxide dismutase, enolase, and hemoglobin) desorbed from solution by liquid sample DESI were measured intact, indicating the capability of DESI for preserving weak noncovalent interactions. Doping the DESI spray solvent with supercharging reagents resulted in protein complex ions having increased multiple charging without complex dissociation. Ion mobility measurements of model protein cytochrome *c* showed that the supercharging reagent favored the more compact conformation for the lower charged protein ions. Liquid sample DESI of hydrophobic peptide gramicidin D suggests that the ionization mechanism involves a droplet pick-up mixing process. Measurement of liquid samples significantly extends the mass range of DESI-MS, allowing the analysis of high-mass proteins such as 150 kDa immunoglobulin G (IgG) and thus represents the largest protein successfully ionized by DESI to date.

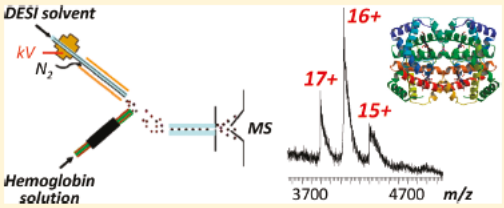

Protein complexes, such as those formed by noncovalent protein−protein and protein−ligand interactions, are the cornerstone of many biological processes and together they form various types of molecular machines that perform a vast array of biological functions. Because of their biological significance, the ability to structurally characterize protein complexes is of great importance. In this regard, mass spectrometry (MS) has demonstrated its utility for characterizing noncovalent protein complexes, particularly with the development of electrospray ionization (ESI).[1] MS measurements of biomolecular assemblies provide information on binding partners, binding stoichiometries, and binding affinities.[2−6] With the more recent development of tandem mass spectrometry (MS/MS) tools to interrogate intact protein−ligand complexes (i.e., top-down MS), the spatial or positional information on ligand binding sites can be assessed directly.[7−9] The conceptual simplicity of this ESI-MS method, along with its speed, sensitivity, and low sample consumption makes MS an attractive tool compared to other spectroscopic techniques for monitoring binding and probing protein conformation.

A recent breakthrough in the MS field is the advent of ambient mass spectrometry techniques, such as desorption electrospray ionization (DESI)[10] and direct analysis in real time (DART),[11] which provide direct ionization of analytes with little or no sample preparation. It has been shown that DESI promotes the rapid analysis of a wide variety of analytes, ranging from pharmaceuticals to imaging small molecules directly from tissue.[10,12−15] However, previous investigations using traditional DESI have been limited to the examination of small proteins (≤25 kDa)[14] and small protein−substrate complexes (≤15 kDa, e.g., lysozyme with its natural hexa-*N*-acetyl chitohexaose substrate),[10] while large protein complexes have not been extensively explored by DESI.

Recently, in addition to being used regularly for solid sample analysis on surfaces, DESI has been extended to the direct analysis of liquid samples.[16−20] In this "liquid sample DESI" technique, analyte desorption/ionization occurs via interactions of the liquid sample with charged microdroplets generated by a pneumatically assisted DESI spray with subsequent desolvation of the resulting secondary microdroplets containing the sample analyte. It was found that liquid sample DESI can be used for the analysis of a wide range of compounds including amino acids, peptides, protein digests, and intact proteins directly from solution without extensive sample pretreatment. Several analytically useful

Received: June 1, 2011
Accepted: July 20, 2011
Published: July 20, 2011

features of liquid sample DESI have been uncovered, such as an increased tolerance to salt and other matrixes that allows direct analysis of biological samples, e.g., raw urine. The direct sampling capability of liquid sample DESI allows electrolyzed samples from an electrochemical cell to be directly probed, enabling a convenient online coupling of MS with electrochemistry.[17,21] Liquid sample DESI is amenable for analysis of very small volume samples (e.g., nanoliter size)[20,22] and continuous-flow samples eluting from a chromatographic column.[23] The capability of integrating ionic reactions with the ionization event, i.e., reactive DESI,[17,20,24−29] in which a chemical reagent is doped with the spray solvent to react with analytes, allows online post-column chromatographic derivatization for enhanced detection specificity.[23]

The present study focuses on the direct ionization of protein complexes and large proteins under ambient conditions by liquid sample DESI. The motivations for this study are multifold. Previously reported traditional DESI-MS studies of proteins and protein complexes dried on a surface demonstrated a molecular mass limit of less than 25 kDa.[14] Interestingly, liquid sample DESI has been found to increase the mass range, as evidenced by the ionization of 66 kDa bovine serum albumin (BSA). Given this likelihood that DESI of proteins from solution is easier than from dried samples on a surface and the significance of mass spectrometric characterization of protein complexes, it is of interest to further explore the application of DESI to the analysis of larger proteins and protein complexes.

DESI has the aforementioned capability to combine ionic reactions with its ionization process. This would allow one to increase the multiple charging of the resulting protein-complex ions by performing a variant form of reactive DESI[17,20,24−26,28−30] in which the DESI spray solvent is conveniently doped with "supercharging" reagents.[31−38] Increasing multiple charging for MS analysis of large proteins could be of significant value to further structural analysis via top-down proteomic approaches using electron-based tandem mass spectrometry techniques, such as electron capture dissociation (ECD)[7] and electron transfer dissociation (ETD).

In the present study, several protein complexes and large proteins were examined using liquid sample DESI analysis and a quadrupole time-of-flight (QTOF) mass spectrometer with a broad m/z range, as well as an ion mobility function. In addition, by doping the DESI spray solvent or protein sample with supercharging reagents, the supercharging effect can be observed for protein-complex ions. This study demonstrates the potential of liquid sample DESI for protein-complex and large protein characterization.

EXPERIMENTAL SECTION

Materials. Cytochrome *c* (cytc, bovine), manganese superoxide dismutase (MnSOD from *E. coli*), enolase (from yeast), gramicidin D, antibody IgG1 kappa murine myeloma (IgG), *m*-nitrobenzyl alcohol (*m*-NBA), sulfolane, formic acid (FA), ammonium acetate (NH_4OAc), and acetonitrile (ACN) were purchased from Sigma-Aldrich. Human hemoglobin (Hb) was provided by Professor Robert Clubb (UCLA Department of Chemistry and Biochemistry).

Apparatus. The liquid sample DESI source has been described previously,[17,21] in which a beam of charged microdroplets from the DESI spray probe is directed at the outlet of a sample introduction capillary for desorption and ionization. The sample introduction capillary outlet was positioned between the DESI spray probe and the mass spectrometer interface (Figure S-1 in the Supporting Information). A quadrupole-ion mobility-TOF instrument (Synapt HDMS, Waters Corporation, Milford, MA) was used for MS measurements. The standard nanoelectrospray source was removed to accommodate the liquid sample DESI source. The DESI spray probe was supplied with a high voltage of +5 kV and high-pressure nebulizing nitrogen gas (120 psi) to generate the charged microdroplet beam for sample desorption and ionization. The DESI spray solvent was altered between ACN/H_2O/FA acid (49.5:49.5:1 v/v/v) or 20 mM NH_4OAc and was pumped at a flow rate of 10 μL/min through a gastight Hamilton syringe.

The Synapt HDMS parameters were: sampling cone voltage 80 V, extraction cone voltage 5 V, source temperature 80 °C, trap collisional energy 4, and transfer collisional energy 6. Data were analyzed using MassLynx 4.1 and Driftscope v2.0 (Waters Corporation).

Sample Preparation. For protein-complex samples, the following conditions were implemented: MnSOD in 20 mM NH_4OAc (or in 1% acetic acid for comparison); enolase in H_2O; Hb in 20 mM NH_4OAc, IgG in H_2O/ACN/FA (90:10:0.1 v/v/v), and gramicidin D in methanol. The solutions were introduced into the DESI source through a deactivated fused silica capillary at a flow rate of 2 μL/min. Ion mobility measurements were exclusively conducted with cytochrome *c*, utilizing sample solvents of either H_2O or 4% acetic acid both with and without the supercharging reagents. DESI spray solvents were kept at ACN/H_2O/FA 49.5:49.5:1 (v/v/v), both with and without the supercharging reagents.

RESULTS AND DISCUSSION

Liquid sample DESI allows proteins in solution (e.g., water) to be directly desorbed and ionized with high sensitivity without addition of acids or organic solvents into sample solutions to generate native protein ions (e.g., cytochrome *c*, ubiquitin, etc).[39] Such a direct sampling feature could be advantageous for probing changes in protein conformation[40] and provides a complementary method for detecting noncovalent protein complexes to the well-known native ESI-MS.[3,41]

The added flexibility of having different solvent systems tailored for the analyte and the DESI spray is a unique feature for liquid sample DESI. Analytes do not need to be soluble in the DESI spray solvent system. Gramicidin D is a mixture of linear, hydrophobic pentadecapeptides (gramicidin A, B, and C) with alternating D- and L-amino acids. The Val^1-gramicidin A variety is the most abundant species (1881 Da). The peptides are not soluble in water but can be dissolved in organic solvents (e.g., methanol). Gramicidin D (10 μM in methanol) was analyzed by liquid sample DESI using a spray solvent of 20 mM aqueous NH_4OAc or a solvent spray comprised of 50:50 ACN/H_2O, 0.1% FA. Both the singly and doubly charged ions were observed for both spray solvent systems (Figure S-2 in the Supporting Information). This suggests that the methanolic droplets containing the analyte were picked up by the aqueous charged droplets from the DESI solvent spray probe, resulting in secondary fused microdroplets (as methanol and water are miscible) that subsequently enter the mass spectrometer for analysis.[17] This droplet pick-up mechanism appears to be plausible for liquid sample DESI analyses, suggesting that ionization occurs

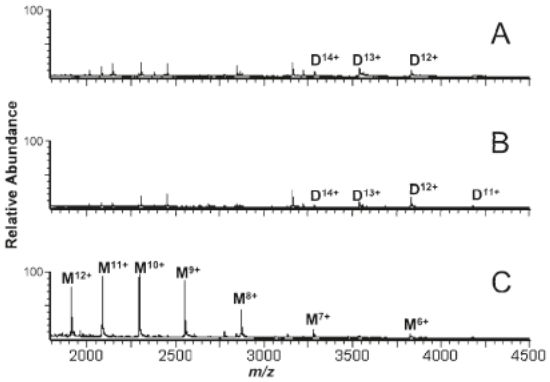

Figure 1. Mass spectra showing liquid sample DESI analysis of MnSOD: (A) MnSOD (30 μM) in 20 mM NH_4OAc sampled by a DESI solvent composed of 20 mM NH_4OAc aqueous solution, (B) MnSOD (30 μM) in 20 mM NH_4OAc sampled by a DESI solvent of ACN/H_2O/FA, and (C) MnSOD (15 μM) in 1% HOAc sampled by a DESI solvent of 1:1 ACN/H_2O with 1% FA.

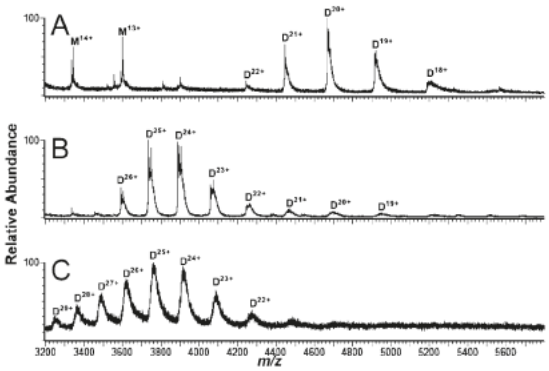

Figure 2. Liquid sample DESI mass spectra of enolase (10 μM in water) with the DESI solvent composed of (A) 20 mM NH_4OAc (aq), (B) 1:1 ACN/H_2O with 1% FA, and (C) 1:1 ACN/H_2O with 1% FA and 40 mM *m*-NBA supercharging reagent.

after mixing of charged droplets with the liquid sample at the DESI source silica capillary.

Liquid Sample DESI of Noncovalent Protein Complexes. Protein complexes, some larger than 45 kDa, were tested using the quadrupole-ion mobility-TOF instrument equipped with a home-built liquid sample DESI source.

Superoxide Dismutase. Manganese superoxide dismutase (MnSOD from *E. coli*; monomer apoprotein, 22 966 Da), the SOD isoform found in the mitochondrial matrix of eukaryotes as well as a variety of prokaryotes, is a metalloenzyme that plays an important role in immune defense by eliminating oxidative stress.[42] In this study, 30 μM MnSOD in 20 mM NH_4OAc (pH 6.8) was desorbed/ionized by the DESI source using a 20 mM aqueous NH_4OAc spray solvent. The 11+ to 14+ charged noncovalent 46 kDa dimer ions of MnSOD with two Mn ions bound per dimer (Mn_2−MnSOD) were clearly detected (Figure 1A), confirming the soft ionization nature of liquid sample DESI. Interestingly, changing the DESI spray solvent to ACN/H_2O/FA (49.5:49.5:1.0 v/v) also generated 11+ to 14+ charged MnSOD dimer ions (Figure 1B). This result is somewhat surprising, as the newly introduced spray contained a high fraction of organic solvent and acid that typically denature proteins and disrupt noncovalent interactions. It is most likely that only a limited interaction (i.e., partial mixing) or transient interaction (estimated to be less than 1 ms[40]) occurs between the DESI spray solvent and the analyte solution in liquid sample DESI analyses. This observation is also consistent with our previous observation of holo-myoglobin ions using denaturing DESI spray solvent conditions.[40] An added advantage of including the organics and acid in the spray solvent is the gain in sensitivity when compared with those experiments conducted using ammonium acetate as the spray solvent. Using the ACN/H_2O/FA DESI spray solvent (Figure 1B) increased the signal-to-noise ratio (S/N) of the MnSOD dimer ions by a factor of 2−3 relative to using NH_4OAc (Figure 1A). This is also in-line with our previously reported data on cytochrome *c*[40] that showed that increased sensitivity can be achieved with nondenaturing analyte solutions by using a denaturing solvent system (methanol/H_2O/acetic acid) for the DESI spray solvent. Using both a denaturing solvent in the analyte solution (1% acetic acid) with the ACN/H_2O/FA DESI spray solvent resulted in the observation of the denatured 22.9 kDa apo-SOD monomer (Figure 1C).

Enolase. Enolase is a metalloenzyme involved in the glycolytic pathway, catalyzing the dehydration of 2-phospho-D-glycerate. Enolase derived from yeast is a 93 kDa homodimeric complex (apo-monomer mass 46671 Da) that requires divalent metal ions, such as Mg^{2+}, and first row divalent transition metals (e.g., Mn^{2+}) for activity.[5,43] In this liquid sample DESI analysis, 10 μM enolase in H_2O was analyzed with various DESI spray solvents. When a DESI solvent of 20 mM aqueous NH_4OAc was used, ions for the enolase 93 kDa noncovalent dimer were observed (93 342 Da, theory; 93 339 ± 6 Da, measured; 18+ to 22+ charge states) as well as protein monomer ions (Figure 2A). However, with the use of a potentially denaturing solvent composition (49.5:49.5:1.0 ACN/H_2O/FA), the sensitivity was improved when compared to the 20 mM aqueous NH_4OAc solution (Figure 2A,B). Moreover, using the ACN/H_2O/FA spray solvent generated a noticeable increase in charge state for the dimer to 19+ to 26+. Although the acetonitrile/formic acid mixture did not cause complete denaturation to disrupt the noncovalent dimer, it may have caused partial unfolding of the enolase dimer exhibited by the higher degree of charging. In comparison to the MnSOD dimer, the enolase dimer appears to be more sensitive to unfolding in the presence of organic solvent and acid.

Currently, minimum protein concentrations of 1−10 μM have been analyzed using liquid sample DESI.[17] For the protein enolase noncovalent dimer complex (Figure 2), a S/N ratio of ~9 was measured (for the 20+ dimer ion) from 4 pmol of protein injected. However, future experiments will explore the absolute sensitivity of the method for large protein analysis.

Hemoglobin. Human hemoglobin (Hb, 64.5 kDa) is a noncovalent tetrameric protein composed of two distinct polypeptide chains, two identical α subunits (141 amino acids, 15126 Da), and two identical β subunits (146 amino acids, 15 867 Da), in addition to a heme molecule (protoporphyrin IX; 616 Da) noncovalently bound to each chain. The Hb tetramer associates from two $\alpha_h\beta_h$ heterodimers (where α_h and β_h represent the heme-bound α and β chains, respectively).[44] Previous ESI-MS studies have shown that the intact Hb tetramer can be observed.[44−48] The liquid DESI mass spectrum from 50 μM

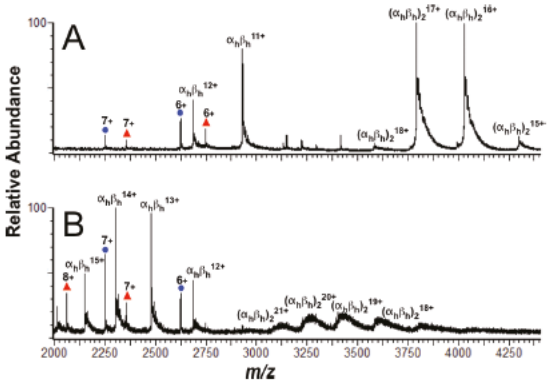

Figure 3. Liquid sample DESI mass spectra of human hemoglobin (50 μM) in 20 mM NH_4OAc and a DESI spray solvent of (A) 20 mM NH_4OAc and (B) 20 mM NH_4OAc with 40 mM *m*-NBA. The "$\alpha_h\beta_h$" notation refers to the heme-bound α and β polypeptide chains. The free heme-bound α-chain is represented by the blue ●, and the red ▲ denote the heme-bound β-chain.

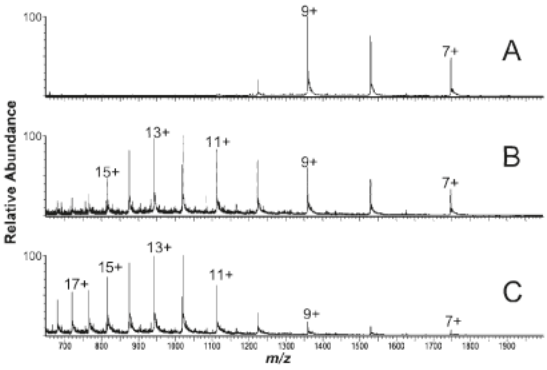

Figure 4. Supercharging liquid sample DESI mass spectra of 50 μM cytochrome *c* in water with DESI spray solvents of (A) 1:1 ACN/H_2O and 0.1% FA, (B) 1:1 ACN/H_2O and 0.1% FA with 40 mM *m*-NBA, and (C) 1:1 ACN/H_2O and 0.1% FA with 200 mM sulfolane.

Hb in 20 mM NH_4OAc and spraying a "native" solvent system (20 mM NH_4OAc) enabled the observation of the intact Hb $(\alpha_h\beta_h)_2$ protein tetramer with charge states 15+ to 18+ (64 451 Da, theory; 64 449 ± 2 Da, measured) as well as the 32.2 kDa $\alpha_h\beta_h$ dimer (32 226 Da, theory; 32 225 ± 1 Da, measured; 11+ and 12+ charge states), with minor contributions from the α_h and β_h species (Figure 3). Changing the spray solvent system to one that contains acid (49.5:49.5:1 ACN/H_2O/FA) and the Hb remaining in 20 mM NH_4OAc resulted in the complete disruption of the noncovalent tetramer (data not shown). Thus, although the interaction between the spray solvent and the analyte is relatively short (likely less than 1 ms), the Hb tetramer appears to be the most sensitive to acid denaturation among the proteins studied.

Supercharging of Protein Complexes by Reactive Liquid DESI. As the mass range of macromolecular mass spectrometry has increased, exemplified by use of ESI-TOF and ESI-quadrupole-TOF instruments, new methods to supplement the analysis of large molecules have been developed, e.g., ion mobility. Another such development is the incorporation of supercharging reagents for ESI-MS that effectively increase the overall charge on a protein and thus lowers the observed mass-to-charge ratio to a value well within the detectable range of most analyzers.[34] Recent experiments have identified a number of reagents that produce this supercharging phenomenon when applied in an ESI setting, such as *m*-nitrobenzyl alcohol (*m*-NBA) and tetramethylene sulfone (sulfolane).[31,32] These reagents have characteristics of low solution-phase basicity and nonvolatility compared to water as well as the ability to directly interact with proteins in solution (and possibly in the gas phase) to stabilize charging in the gas phase and to promote the supercharging phenomenon. These supercharging reagents are effective in both denaturing and native solution conditions.[33−37] When paired with DESI,[38] supercharging becomes a useful tool that drives the threshold of high molecular weight protein analysis toward ever-increasing limits. Recently, a novel method, continuous flow-extractive desorption electrospray ionization (CF-EDESI), has been used to control the protein charge state distributions using different additives, such as acetic acid and sulfolane, in the analysis of small proteins such as cytochrome *c* and lysozyme.[38]

Cytochrome c. To investigate the integration of supercharging with liquid sample DESI, bovine cytochrome *c* (cytc, 12231 Da) was selected as a sample specimen. The protein (50 μM) prepared in water with a spray solvent of 50:50 ACN/H_2O and 0.1% FA (v/v) showed a native-type charge state distribution (7+ to 10+) that is consistent with previous work (Figure 4A).[40] The supercharging reagent *m*-NBA (40 mM) was doped into the ACN/H_2O/FA spray solvent, resulting in higher charging, ranging from 7+ to 17+ and centered at 12+ (Figure 4B). Using sulfolane (200 mM) in a similar fashion generated a cytc charge distribution with slightly higher charging than observed for *m*-NBA (Figure 4C). The introduction of supercharging agents and the resulting increase in charging for liquid DESI mimic the data observed for electrospray-assisted laser desorption/ionization (ELDI),[49,50] another ambient MS technique.

The effect of the addition of *m*-NBA to the liquid DESI spray on the structure of cytc was probed by ion mobility-mass spectrometry. Figure 5 shows the ion mobility data obtained for the 7+ to 9+ charge states of cytc. The protein dissolved in 4% acetic acid and coupled with a spray solvent of 50:50 ACN/H_2O and 0.1% FA (v/v) served as a control to represent the denatured protein. The Driftscope ion mobility plots are shown in Figure 5 for the various cytc charge states generated from different solution and DESI spray solvent systems. A longer drift time is associated with a less compact or more unfolded conformation. The ion mobility profiles for the 7+ to 9+ charge states are similar for cytc in either H_2O or 4% acetic acid, with perhaps a slight increase in the more native or compact conformer present with cytc in H_2O (represented by the blue trace and the small reduction of the extended conformer peak for the 8+ ion and the increase in the compact conformer for the 9+ ion). Adding 40 mM *m*-NBA to the DESI spray solvent (cytc in H_2O) resulted in an increase in the more native, compact conformation of the protein (red trace in Figure 5). This trend was observed in triplicate measurements. Taken together, this trend suggests that, rather than causing unfolding and denaturation, the *m*-NBA supercharging reagent in the spray solvent aids in stabilization of the native conformation of a protein. However, additional experiments with many different proteins are needed to more firmly establish the effects of supercharging agents on protein conformation.

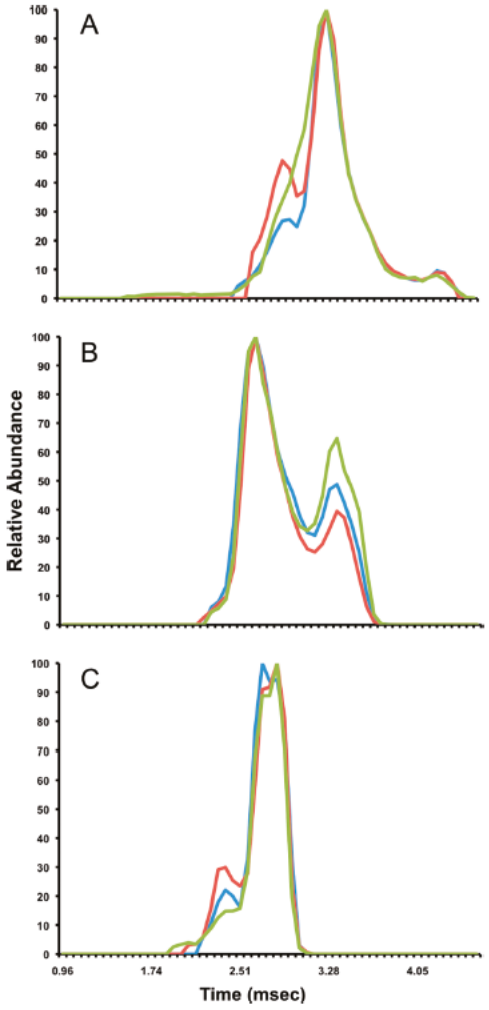

Figure 5. Ion mobility drift time plots of the (A) 7+, (B) 8+, and (C) 9+ charged ions of cytochrome *c* (50 μM). The green and blue traces represent the ion mobility of cytc in 4% and 0% acetic acid (in water), respectively, and the DESI solvent of 1:1 ACN/H_2O with 0.1% FA. The red line represents the data from cytc in water and the DESI solvent of 1:1 ACN/H_2O with 0.1% FA and 40 mM *m*-NBA.

Enolase and Hemoglobin. To further test the ability of liquid sample DESI to enable supercharging of larger proteins and protein complexes, 10 μM enolase in H_2O was reacted with a spray solvent consisting of 40 mM *m*-NBA in 50:50 ACN/H_2O and 0.1% FA. Figure 2C shows that the enolase dimer shift to higher charge, moving from the range 19+ to 26+ to the 23+ to 29+ range. (Note that the observed ions also have increased peak width, probably caused by the formation of adduct ions with *m*-NBA due to insufficient desolvation conditions used in the experiments). Similarly, with 40 mM *m*-NBA sprayed in 20 mM NH_4OAc, a charge increase was observed for both the Hb $(\alpha_h\beta_h)_2$ tetramer and $\alpha_h\beta_h$ dimer when compared to DESI lacking the supercharging reagent. Figure 3B shows a charge state

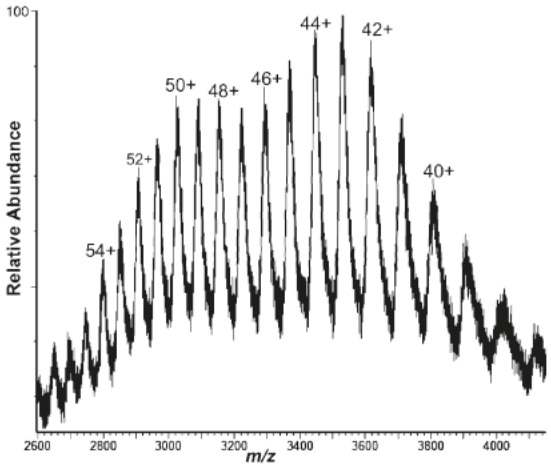

Figure 6. Liquid sample DESI mass spectrum of IgG (6 μM) in H_2O/ACN/FA (90:10:0.1 by volume) with a DESI spray solvent composition the same as the analyte solvent.

distribution shift for the tetramer from a range of 15+ to 18+ to a range of 18+ to 21+; additionally, the dimer shifts from 11+ to 12+ to a higher range of 12+ to 16+. This further demonstrates that reactive DESI can be easily carried out using supercharging reagents to increase charging of proteins and protein complexes.

Immunoglobulin G (IgG) Measurement by Liquid Sample DESI. Traditional DESI of proteins desorbed from a dried state on a solid surface has molecular mass limits within the range of 25 kDa,[14] whereas liquid sample DESI of proteins in a solution state, to date, have pushed this molecular mass limit to approximately 66 kDa (BSA).[17] With the liquid sample DESI apparatus coupled to the higher mass range Q-TOF ion mobility mass spectrometer, this range for observable protein and protein-complex maximum molecular weights was extended to 150 kDa.

Immunoglobulin G (IgG) antibodies consist of four polypeptide chains: two identical heavy chains and two identical light chains all linked together by disulfide bonds that comprise the tetrameric quaternary structure. IgG (6 μM in 90/10 H_2O/ACN, 0.1% FA) was analyzed using a DESI spray solvent of 90:10 H_2O/ACN, 0.1% FA, resulting in IgG ions ranging from 38+ to 55+ (Figure 6). Similar mass spectra were acquired with aqueous 20 mM NH_4OAc as the spray solvent, albeit at a slightly reduced signal-to-noise and charging (36+ to 51+) (data not shown).

CONCLUSIONS

As demonstrated in this series of liquid sample DESI studies, noncovalent interactions among protein complexes can be detected. Sensitivity for measuring protein complexes is improved slightly by using a denaturing spray solvent (i.e., containing organic solvent and acids). In addition, the inclusion of supercharging reagents in the DESI spray solvent produced the desired effect by increasing multiple charging of proteins and protein complexes without disrupting their structure and conformation, further expanding the capabilities of liquid sample DESI. Proteins as large as 150 kDa IgG and with low micromolar concentrations can be successfully ionized by DESI. Additional refinement to the DESI system in the future should further improve the sensitivity for large molecule analysis. Because of its flexibility

and its compatibility with an unlimited range of spray solvents and sample solvents as well as its useful conjunction with supercharging compounds, liquid sample DESI is emerging as a useful tool for mass spectrometric monitoring of conformational changes in solution for proteins, both small and large.

■ ASSOCIATED CONTENT

Supporting Information. Additional information as noted in text. This material is available free of charge via the Internet at http://pubs.acs.org.

■ AUTHOR INFORMATION

Corresponding Author

*Dr. Joseph A. Loo: address, Molecular Biology Institute, University of California-Los Angeles, Los Angeles, CA 90095; e-mail, JLoo@chem.ucla.edu; phone, 310-794-7023. Dr. Hao Chen: address, Department of Chemistry and Biochemistry, Clippinger Laboratories, Ohio University, Athens, OH 45701; e-mail, chenh2@ohio.edu; phone, 740-593-0719.

■ ACKNOWLEDGMENT

This work was supported by the National Science Foundation (Grant CHE-0911160 to H.C.), the Ruth L. Kirschstein National Research Service Award (Grant GM007185, UCLA Cellular and Molecular Biology Training Grant, for C.N.F.), and the National Institutes of Health (Grant R01 RR20004 to J.A.L.).

■ REFERENCES

(1) Fenn, J. B.; Mann, M.; Meng, C. K.; Wong, S. F.; Whitehouse, C. M. *Science* **1989**, *246*, 64–71.
(2) Barrera, N. P.; Bartolo, N. D.; Booth, P. J.; Robinson, C. V. *Science* **2008**, *321*, 243–246.
(3) Heck, A. J. R.; van den Heuvel, R. H. H. *Mass Spectrom. Rev.* **2004**, *23*, 368–389.
(4) Loo, J. A. *Mass Spectrom. Rev.* **1997**, *16*, 1–23.
(5) Loo, J. A. *Int. J. Mass Spectrom.* **2001**, *204*, 113–123.
(6) van Duijn, E. *J. Am. Soc. Mass Spectrom.* **2010**, *21*, 971–978.
(7) Xie, Y.; Zhang, J.; Yin, S.; Loo, J. A. *J. Am. Chem. Soc.* **2006**, *128*, 14432–14433.
(8) Yin, S.; Loo, J. A. *J. Am. Soc. Mass Spectrom.* **2010**, *21*, 899–907.
(9) Yin, S.; Loo, J. A. *Int. J. Mass Spectrom.* **2011**, *300*, 118–122.
(10) Takats, Z.; Wiseman, J. M.; Gologan, B.; Cooks, R. G. *Science* **2004**, *306*, 471–473.
(11) Cody, R. B.; Laramee, J. A.; Durst, H. D. *Anal. Chem.* **2005**, *77*, 2297–2302.
(12) Denes, J.; Katona, M.; Hosszu, A.; Czuczy, N.; Takats, Z. *Anal. Chem.* **2009**, *81*, 1669–1675.
(13) Kauppila, T.; Wiseman, J. M.; Ketola, R. A.; Kotiaho, T.; Cooks, R. G.; Kostiainen, R. *Rapid Commun. Mass Spectrom.* **2006**, *20*, 387–392.
(14) Shin, Y. S.; Drolet, B.; Mayer, R.; Dolence, K.; Basile, F. *Anal. Chem.* **2007**, *79*, 3514–3518.
(15) Cotte-Rodriguez, I.; Chen, H.; Cooks, R. G. *Chem. Commun.* **2006**, 953–955.
(16) Miao, Z.; Chen, H. *Proceedings of the 56th ASMS Conference on Mass Spectrometry and Allied Topics*, June 1−5, 2008, Denver, CO, 2008.
(17) Miao, Z.; Chen, H. *J. Am. Soc. Mass Spectrom.* **2009**, *20*, 10–19.
(18) Ma, X.; Zhao, M.; Lin, Z.; Zhang, S.; Yang, C.; Zhang, X. *Anal. Chem.* **2008**, *80*, 6131–6136.
(19) Chipuk, J. E.; Brodbelt, J. S. *J. Am. Soc. Mass Spectrom.* **2008**, *19*, 1612–1620.
(20) Zhang, Y.; Chen, H. *Int. J. Mass Spectrom.* **2010**, *289*, 98–107.
(21) Li, J.; Dewald, H. D.; Chen, H. *Anal. Chem.* **2009**, *81* 9716–9722.
(22) Sun, X.; Miao, Z.; Yuan, Z.; Harrington, P. B.; Colla, J.; Chen, H. *Int. J. Mass Spectrom.* **2011**, *301*, 102–108.
(23) Zhang, Y.; Yuan, Z.; Dewald, H. D.; Chen, H. *Chem. Commun.* **2011**, *47*, 4171–4173.
(24) Chen, H.; Talaty, N.; Takats, Z.; Cooks, R. G. *Anal. Chem.* **2005**, *77*, 6915–6927.
(25) Cotte, R. I.; Chen, H.; Cooks, R. G. *Chem. Commun.* **2006** 953–955.
(26) Cotte-Rodriguez, I.; Hernandez-Soto, H.; Chen, H.; Cooks, R. G. *Anal. Chem.* **2008**, *80*, 1512–1519.
(27) Chen, H.; Cotte-Rodriguez, I.; Cooks, R. G. *Chem. Commun.* **2006**, 597–599.
(28) Nyadong, L.; Green, M. D.; De Jesus, V. R.; Newton, P. N.; Fernandez, F. M. *Anal. Chem.* **2007**, *79*, 2150–2157.
(29) Huang, G.; Chen, H.; Zhang, X.; Cooks, R. G.; Ouyang, Z. *Anal. Chem.* **2007**, *79*, 8327–8332.
(30) Chen, H.; Venter, A.; Cooks, R. G. *Chem. Commun.* **2006** 2042–2044.
(31) Lomeli, S. H.; Yin, S.; Ogorzalek Loo, R. R.; Loo, J. A. *J. Am. Soc. Mass Spectrom.* **2009**, *20*, 593–596.
(32) Lomeli, S. H.; Peng, I. X.; Yin, S.; Ogorzalek Loo, R. R.; Loo, J. A. *J. Am. Soc. Mass Spectrom.* **2010**, *21*, 127–131.
(33) Iavarone, A. T.; Jurchen, J. C.; Williams, E. R. *J. Am. Soc. Mass Spectrom.* **2000**, *11*, 976–985.
(34) Iavarone, A. T.; Jurchen, J. C.; Williams, E. R. *Anal. Chem.* **2001**, *73*, 1455–1460.
(35) Iavarone, A. T.; Williams, E. R. *Int. J. Mass Spectrom.* **2002**, *219* 63–72.
(36) Iavarone, A. T.; Williams, E. R. *J. Am. Chem. Soc.* **2003**, *125* 2319–2327.
(37) Iavarone, A. T.; Williams, E. R. *Anal. Chem.* **2003**, *75* 4525–4533.
(38) Yang, S. H.; Wijeratne, A. B.; Li, L.; Edwards, B. L.; Schug, K. A. *Anal. Chem.* **2011**, *83*, 643–647.
(39) Miao, Z.; Chen, H.; Liu, P.; Liu, Y. *Anal. Chem.* **2011**, *83*, 3994–3997.
(40) Miao, Z.; Wu, S.; Chen, H. *J. Am. Soc. Mass Spectrom.* **2010**, *21*, 1730–1736.
(41) Kaddis, C. S.; Lomeli, S. H.; Yin, S.; Berhane, B.; Apostol, M. I.; Kickhoefer, V. A.; Rome, L. H.; Loo, J. A. *J. Am. Soc. Mass Spectrom.* **2007**, *18*, 1206–1216.
(42) Qiujano, C.; Hernandez-Saavedra, D.; Castro, L.; McCord, J. M.; Freeman, B. A.; Radi, R. *J. Biol. Chem.* **2001**, *276*, 11631–11638.
(43) Zhang, E.; Brewer, J. M.; Minor, W.; Carreira, L. A.; Lebioda, L. *Biochemistry* **1997**, *36*, 12526–12534.
(44) Light−Wahl, K. J.; Schwartz, B. L.; Smith, R. D. *J. Am. Chem. Soc.* **1994**, *116*, 5271–5278.
(45) Apostol, I. *Anal. Biochem.* **1999**, *272*, 8–18.
(46) Ofori-Acquah, S. F.; Green, B. N.; Davies, S. C.; Nicolaides, K. H.; Sarjeant, G. R.; Layton, D. M. *Anal. Biochem.* **2001**, *298*, 76–82.
(47) Schmidt, A.; Karas, M. *J. Am. Soc. Mass Spectrom.* **2001**, *12*, 1092–1098.
(48) Simmons, D. A.; Wilson, D. J.; Lajoie, G. A.; Doherty-Kirby, A.; Konermann, L. *Biochemistry* **2004**, *43*, 14792–14801.
(49) Peng, I. X.; Ogorzalek Loo, R. R.; Shiea, J.; Loo, J. A. *Anal. Chem.* **2008**, *80*, 6995–7003.
(50) Peng, I. X.; Ogorzalek Loo, R. R.; Margalith, E.; Little, M. W.; Loo, J. A. *Analyst* **2010**, *135*, 767–772.

Supporting Information

Direct Ionization of Large Protein Complexes and Proteins by Desorption Electrospray Ionization-Mass Spectrometry

Carly N. Ferguson[1], Sabrina A. Benchaar[1], Zhixin Miao[3], Joseph A. Loo[1,2*] and Hao Chen[3*]

[1]Department of Chemistry and Biochemistry, [2]Department of Biological Chemistry, David Geffen School of Medicine, University of California, Los Angeles, CA, USA

[2]Center for Intelligent Chemical Instrumentation, Department of Chemistry and Biochemistry, Ohio University, Athens, OH, USA

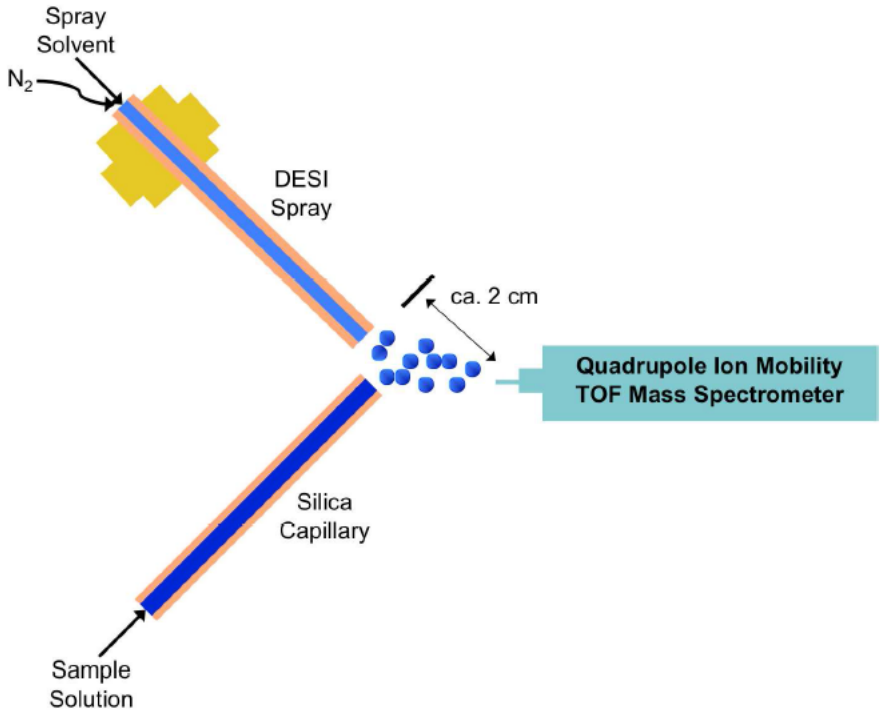

Figure S-1. Schematic of the liquid sample DESI source coupled to the quadrupole-ion mobility-TOF instrument (Synapt HDMS).

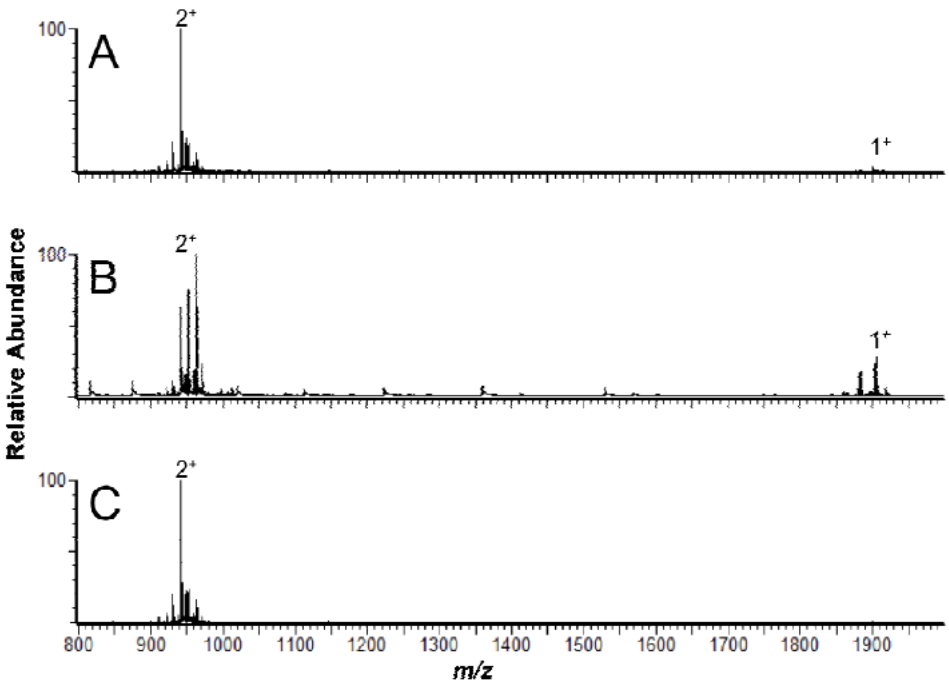

Figure S-2. Liquid sample DESI mass spectra of gramicidin D (10 µM) in MeOH with different DESI spray conditions: (A) 20 mM NH_4OAc, (B) 1:1 ACN/H_2O with 0.1% FA, (C) 1:1 ACN/H_2O with 0.1% FA and 40 mM *m*-NBA.

CHAPTER 6

Measuring Protein-Ligand Interactions Using Liquid Sample Desorption Electrospray Ionization Mass Spectrometry

analytical chemistry

Article

pubs.acs.org/ac

Measuring Protein–Ligand Interactions Using Liquid Sample Desorption Electrospray Ionization Mass Spectrometry

Pengyuan Liu,[§] Jiang Zhang,[†] Carly N. Ferguson,[†] Hao Chen,*[,§] and Joseph A. Loo*[,†,‡]

[†]Department of Chemistry and Biochemistry and [‡]Department of Biological Chemistry, David Geffen School of Medicine, University of California-Los Angeles, Los Angeles, California 90095, United States

[§]Center for Intelligent Chemical Instrumentation, Department of Chemistry and Biochemistry, Ohio University, Athens, Ohio 45701, United States

Supporting Information

ABSTRACT: We have previously shown that liquid sample desorption electrospray ionization-mass spectrometry (DESI-MS) is able to measure large proteins and noncovalently bound protein complexes (to 150 kDa) (Ferguson et al., *Anal. Chem.* **2011**, *83*, 6468–6473). In this study, we further investigate the application of liquid sample DESI-MS to probe protein–ligand interactions. Liquid sample DESI allows the direct formation of intact protein–ligand complex ions by spraying ligands toward separate protein sample solutions. This type of "reactive" DESI methodology can provide rapid information on binding stiochiometry, selectivity, and kinetics, as demonstrated by the binding of ribonuclease A (RNaseA, 13.7 kDa) with cytidine nucleotide ligands and the binding of lysozyme (14.3 kDa) with acetyl chitose ligands. A higher throughput method for ligand screening by liquid sample DESI was demonstrated, in which different ligands were sequentially injected as a segmented flow for DESI ionization. Furthermore, supercharging to enhance analyte charge can be integrated with liquid sample DESI-MS, without interfering with the formation of protein–ligand complexes.

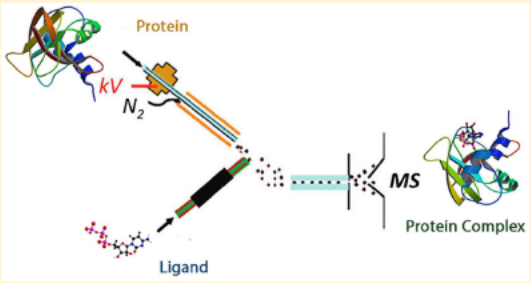

Protein–protein and protein–ligand interactions provide the basis for the formation of molecular assemblies and machines that perform a vast array of biological functions. Because of the biological significance of protein complexes, the ability to probe and measure protein complexes held together by noncovalent interactions in a sensitive and selective manner would have great utility. To this end, mass spectrometry (MS) coupled with electrospray ionization (ESI)[1] has demonstrated its applicability for measuring noncovalent protein complexes. ESI-MS measurements of biomolecular assemblies provide information on binding partners, binding stoichiometries, and solution binding affinities.[2−7] The conceptual simplicity of this method, along with its speed, sensitivity, and low sample consumption makes ESI-MS an attractive tool relative to other spectroscopic techniques for monitoring binding.

The recent development of ambient mass spectrometry techniques, such as desorption electrospray ionization (DESI)[8] and direct analysis in real time (DART),[9] has provided new capabilities and the means to provide direct ionization of analytes with little-to-no sample preparation required. In particular, DESI has been successfully used for the rapid analysis of a variety of different analytes, ranging from pharmaceuticals to tissue samples.[8,10−15] For proteins, however, previous investigations of DESI from dried samples on surfaces have been limited to the small proteins (≤27 kDa)[12] and small protein–substrate complexes (≤15 kDa, e.g., lysozyme with its natural substrate hexa-*N*-acetyl chitohexaose).[8] Recently, DESI has been extended to allow for the direct analysis of liquid samples;[16−19] ionization of the liquid sample occurs via interactions of the sample with charged microdroplets generated in a pneumatically assisted DESI spray and subsequent desolvation of the resulting secondary microdroplets containing the sample analyte. Several useful features of liquid sample DESI were uncovered in our previous studies. For instance, its increased tolerance to salt allows direct measurement of raw urine samples. Electrolyzed samples from an electrochemical cell can be directly desorbed into the gas phase for MS detection, enabling convenient online coupling of MS with electrochemistry.[18,20−27] Very small volume samples (e.g., nL size)[19,28] or at extreme solution pHs,[29] as well as the effluent from high flow-rate liquid chromatography columns[21,30] can be measured by liquid sample DESI. It also allows for the development of submillisecond time-resolved mass spectrometry for the study of fast reaction kinetics.[31] Results from protein analysis by Julian's group[32] and our lab[33] suggests that protein measurements by DESI can be enhanced

Received: September 11, 2013
Accepted: November 15, 2013
Published: November 15, 2013

by the liquid sample DESI option, especially for the analysis of native proteins because an acidic spray solvent can be used without denaturation of the protein structure.

Integration of a chemical reaction with DESI ionization, known as reactive DESI,[10,18,19,34−39] is a further development that exploits the potential for coupling specific ion/molecule reactions[40,41] with the ionization event and so greatly improves the selectivity and efficiency with which compounds with specific functionalities can be detected. It involves the use of a spray solution containing reagents intended to allow specific ionic and molecular reactions to proceed during the sampling process. An analytical advantage of reactive DESI, in contrast to traditional protocols[10] employing solution phase derivatization followed by ESI, is that online derivation during reactive DESI is much faster, thereby speeding up the analytical process. In addition, by taking advantage of the short timescale during DESI ionization (<2 ms),[42] transient reaction intermediates can be intercepted and detected in reactive DESI experiments.[39,43]

The focus of the present study is to exploit the special advantages of liquid sample DESI and reactive DESI for the mass spectrometric characterization of protein−ligand complexes. Monitoring protein−ligand binding reactions by reactive DESI could be of value as a high throughput method for screening of potent protein-binding ligands, a process that is important for drug discovery research. Previously, we demonstrated that liquid sample DESI's capabilities to directly desorb/ionize noncovalent complexes such as the protein dimers of manganese superoxide dismutase and 93 kDa enolase, the 65 kDa hemoglobin (Hb) tetramer, and large proteins such as 150 kDa monoclonal antibodies.[33] The results are consistent with the soft ionization nature of DESI and suggest the possibility of examining protein−ligand interaction events by DESI.

Reactive liquid sample DESI was used to measure the noncovalent complexes formed between ribonuclease A (RNaseA) and cytidine nucleotide ligands and between lysozyme and *N*-acetylglucosamine ligands. The protein target and the ligands were combined by either having the protein or the ligand in the DESI spray (and the other component resided in the "liquid sample" droplet), and the noncovalent complexes were formed during the brief time of DESI desorption/ionization. Liquid sample DESI-MS measurements of solution phase binding constants were compared to previously reported values using other biophysical methods. The effects of increasing analyte charge by "supercharging" on measuring protein−ligand complexes were investigated as well.

EXPERIMENTAL SECTION

Materials. Ribonuclease A (bovine pancreas), lysozyme (chicken egg white), cytidine 2′-monophosphate (2′-CMP), cytidine 5′-diphosphate disodium salt (CDP), cytidine 5′-triphosphate disodium salt (CTP), sulfolane, formic acid (FA), ammonium acetate (NH_4OAc), and acetonitrile (ACN) were all purchased from Sigma-Aldrich (St. Louis, MO). *N*,*N*′,*N*″-triacetylchitotriose (NAG3) and *N*,*N*′,*N*″,*N*‴,*N*′′′′,*N*′′′′′-hexaacetylchitohexaose (NAG6) were purchased from Santa Cruz Biotechnology (Dallas, TX).

Apparatus. The liquid sample DESI source, in which a beam of charged microdroplets from the DESI spray probe is directed at the outlet of a sample introduction capillary for desorption and ionization, has been described previously.[18,33] The sample introduction capillary outlet was positioned between the DESI spray probe and the mass spectrometer interface. A quadrupole-ion mobility-time-of-flight (TOF) instrument (Synapt HDMS G1, Waters Corporation, Milford, MA) was used for the MS measurements. The standard nanoelectrospray source was removed to accommodate the liquid sample DESI source. The DESI spray probe was supplied with a voltage of +5 kV and high-pressure nebulizing nitrogen gas (120 psi) to generate the charged microdroplet beam. The Synapt HDMS parameters were sampling cone voltage 80 V, extraction cone voltage 5 V, source temperature 80 °C, trap collisional energy 6, and transfer collisional energy 4. Data were analyzed using MassLynx 4.1 and Driftscope v2.0 (Waters Corporation).

Mixing of the proteins and the ligands to form the protein−ligand complexes were accomplished in either of two modes of the liquid sample DESI source. One mode was to introduce the ligand solution (in water with 20 mM NH_4OAc, pH 6.5) into the DESI spray probe at a flow rate of 5 μL min^{-1}. The protein solutions were introduced through the sample introduction capillary at a flow rate of 5 μL min^{-1}, as shown in Figure 1. The other mode was to introduce the protein solution into the DESI spray probe, and the ligand solution was pumped through the sample introduction capillary.

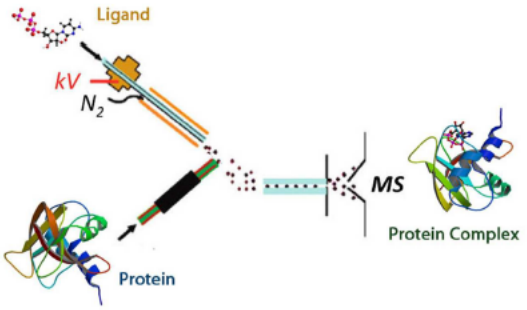

Figure 1. Schematic showing the reactive liquid sample DESI source for analysis MS of protein−ligand complexes. As depicted, a protein solution is infused through a sample transfer capillary, and the emerging droplet containing the protein is exposed to the charged droplets containing ligand molecules from the DESI probe. The sampling can be reversed, with the ligand solution introduced via the sample transfer capillary and the protein sprayed through the DESI probe.

RESULTS AND DISCUSSION

Probing Protein−Ligand Interactions Using Reactive DESI-MS. Figure 1 shows the scheme for the reactive liquid sample DESI-MS platform. The solutions containing the protein and the ligand(s) are infused from the sample introduction capillary and DESI probe, respectively (or vice versa). Desorption/ionization occurs immediately after the solution mixing and complex formation may occur during the initial mixing and/or after the microdroplets leave the surface.

To test the performance of reactive liquid sample DESI for measuring protein−ligand complexes formed in this manner, the binding of RNaseA with cytidine nucleotide ligands was investigated. RNaseA is an enzyme that catalyzes the cleavage of the P−O 5′-bond of single-stranded ribonucleic acids on the 3′-side of cytidine and uridine residues. The complexation of mono- and oligonucleotide ligands with ribonuclease A has been measured using ESI-MS by many laboratories.[44−48]

RNaseA (13,682 Da, 5 μM) was prepared in 20 mM NH_4OAc aqueous solution and the cytidine nucleotide ligands (2′-CMP, CDP, and CTP) were dissolved in 20 mM NH_4OAc (aq) and infused into the DESI spray probe. Multiply charged ions for both the free protein (apo-form) and the ligand-bound protein (holo-form) were detected (Figure 2, panels a–c), but

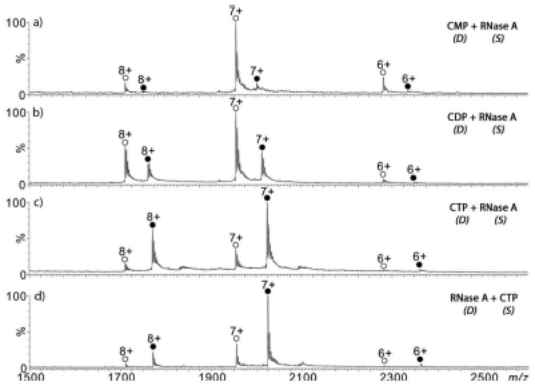

Figure 2. Reactive liquid sample DESI-MS spectra of RNaseA (5 μM in 20 mM NH_4OAc aqueous solution, pH 6.5) in the sample transfer capillary (designated as "S" in the figure) with the DESI probe (designated as "D" in the figure) spraying reagents containing (a) 50 μM 2′-CMP, (b) 50 μM CDP, and (c) 50 μM CTP in 20 mM NH_4OAc. (d) Reactive DESI-MS spectrum of CTP (50 μM in 20 mM NH_4OAc aqueous solution) in the sample transfer capillary ("S") with the DESI probe ("D") spraying 5 μM RNaseA (20 mM NH_4OAc). ○ represents free protein ions (apo) and ● represents protein–ligand complex ions (holo).

with [holo]/[apo] ratios that were dependent on the nature of the nucleotide ligand. As expected from previous studies, a protein–ligand stoichiometry of 1:1 was the dominant form of the complex measured.[44] The total ion chromatograms (TICs) and extracted ion chromatograms (EICs) for the 7+ charge apo- and holo-ions (Figures S6–S8 of the Supporting Information) showed very good stability and reflected the reproducibility of this method. Moreover, the relative abundance of the holo-complex was higher with an increasing number of phosphate groups for the same concentration of ligand; with 5 μM protein and 50 μM ligand, the measured [holo]/[apo] ratio was 0.13 ± 0.017, 0.37 ± 0.04, and 3.21 ± 0.22 (based on 5 replicate measurements) for 2′-CMP, CDP, and CTP, respectively, which agreed well with their solution phase binding trends.[44]

Similar results were obtained when the RNaseA solution was infused from the DESI probe, and the ligand solution was injected through the sample introduction capillary. For the CTP ligand, the measured [holo]/[apo] ratio was 3.12 (Figure 2d), which is similar to the value measured by introducing the ligand solution through the DESI spray probe (Figure 2c).

Their relative solution binding affinities can be tested directly also using liquid sample DESI by performing a competitive binding experiment,[49] in which equimolar mixtures of ligands are presented to the protein target. The rank order of ligand binding can be determined if the total ligand concentration is higher than the total protein concentration. A noncompetitive binding experiment in which the protein concentration is greater than the total ligand concentration showed ions for the protein–ligand complexes for each of the ligands (data not shown). Figure 3a shows the mass spectrum resulting from a

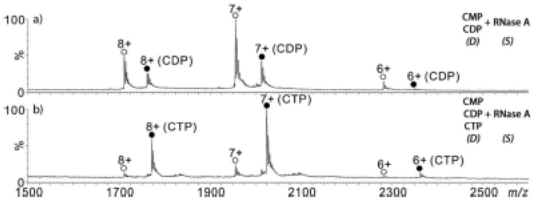

Figure 3. Reactive DESI-MS spectra of RNaseA (5 μM in 20 mM NH_4OAc aqueous solution) in the sample transfer capillary ("S") and the DESI probe ("D") spraying a mixture of (a) 50 μM CDP and 50 μM 2′-CMP (20 mM NH_4OAc) and (b) 50 μM CTP, 50 μM CDP, and 50 μM 2′-CMP (20 mM NH_4OAc). (apo, ○; holo, ●).

mixture of 50 μM CDP and 50 μM 2′-CMP sprayed toward a RNaseA (5 μM) sample solution. Only ions for the RNaseA-CDP complex (and the apoprotein) could be measured, which is consistent with the data collected from the individual ligands (Figure 2) that suggests that CDP has a higher affinity to RNase-A than does 2′-CMP. Similarly, only RNaseA-CTP complex ions were observed when a mixture of 50 μM each of the CMP, CDP, and CTP mixture was sprayed at the protein (Figure 3b). Thus, the rank order of binding affinities to RNaseA is CTP > CDP > 2′-CMP.

The solution phase dissociation constant (K_d) of the protein–ligand binding reaction can be measured using the liquid sample DESI apparatus by monitoring the formation of the complex as a function of ligand concentration. A solution of 5 μM RNaseA (20 mM NH_4OAc) was infused through the sample transfer capillary at a flow rate of 5 μL min^{-1}. Solutions of CTP ligand with different concentrations (from 1 to 15 μM in 20 mM NH_4OAc) were sprayed at a flow rate of 5 μL min^{-1} by the DESI probe. The liquid sample DESI-based K_d was determined based on the relative abundance of the holo- and apo-forms of the protein, according to the method previously described by Daniel et al.[50] The measured K_d was 1.91 μM (see Supporting Information), which is slightly higher than a value of 0.72 μM reported in an earlier ESI-MS study[48] and 1.6 μM from a more recent study,[51] but it is also consistent with other values using other biophysical methods.[52,53]

Liquid Sample DESI-MS of Lysozyme–Acetyl Chitose Complexes. Our reactive liquid sample DESI-MS platform was used to measure another protein–ligand system previously studied by ESI-MS, lysozyme binding with oligoacetyl chitose ligands.[54–56] An aqueous solution of lysozyme (5 μM in 20 mM NH_4OAc) was infused through the sample transfer capillary at a flow rate of 5 μL min^{-1}. The ligands, *N*, *N*′, *N*″, *N*‴, *N*⁗, *N*⁗′-hexaacetylchitohexaose (NAG6) and *N*, *N*′, *N*″-triacetylchitotriose (NAG3) were dissolved in 20 mM NH_4OAc (aq) at a concentration of 200 μM and were infused through the DESI spray capillary at 5 μL min^{-1}. A protein–ligand stoichiometry of 1:1 was measured by reactive liquid sample DESI-MS (Figure 4). The [holo]/[apo] ratios for NAG3 and NAG6 were 0.28 and 0.31, suggesting that their binding affinities are similar and consistent with earlier work.[57] The calculated K_d of the lysozyme-NAG3 system is 169.1 μM, which is also larger than the ESI-MS measured value (59.8 μM) reported before.[56] This may be due to relatively poor mixing efficiency between the protein solution and ligand-containing

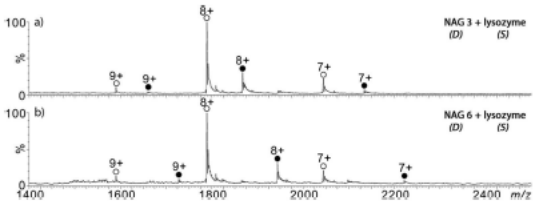

Figure 4. Reactive DESI-MS spectra of lysozyme in the sample transfer capillary ("S") and the DESI probe ("D") spraying (a) 200 μM NAG3 and (b) 200 μM NAG6 in 20 mM NH_4OAc aqueous solution. (apo, ○; holo, ●).

droplets and/or weaker gas phase avidity compared to the RNaseA-nucleotide complexes (see the Supporting Information).

High Throughput Ligand Screening Using Segment Flow Infusion. Potentially, liquid sample DESI could be an effective method for high-throughput monitoring of protein–ligand binding by rapidly switching the ligand composition. To test this, we employed a segmented flow technique[58–60] coupled to liquid sample DESI. RNaseA (5 μM) in 20 mM NH_4OAc aqueous solution was sprayed through the DESI probe (5 μL min^{-1}). The three different nucleotide ligands (20 μM in 20 mM NH_4OAc aqueous solution) were packed in a syringe as segmented plugs separated by air (Figure 5a). The packed segmented ligands were infused using the syringe at a flow rate of 10 μL min^{-1}, and the resulting MS spectra were recorded continuously. The extracted ion chromatograms (EIC) of the 7+-charged protein–ligand complex ions are shown in Figure 5b, with the y axis representing the relative abundance of the holo-complex compared to that of the apoprotein. In this example, a sample plug of 2′-CMP was eluted first, followed by CDP and CTP (Figure 5a). From the EIC, the complexes with different ligands were observed in the order of their packing in the syringe. Consistent with the previously discussed measurements, CTP has the greatest affinity toward RNaseA of the 3 ligands tested. In this example, the total screening time for the three ligands was only 3 min, but one could easily envision segmenting many more ligands over a similar time period.

Supercharging and Reactive Liquid Sample DESI. For protein and peptide analysis by MS, there is value to increase analyte multiple charging:[61] (a) structural analysis via top-down MS approaches using electron-based ion activation/dissociation techniques, such as electron capture dissociation (ECD)[62] and electron transfer dissociation (ETD)[63], is more effective with higher charging. (b) Signal-to-noise (S/N) ratio, mass resolution, and mass accuracy are enhanced at lower mass-to-charge (m/z) ratio and higher z for most mass analyzers, including orbitrap[64] and ion cyclotron resonance[65,66] systems.

Variables such as solution pH and solvent composition affect ESI-based multiple charging of peptides and proteins. Another approach to enhance multiple charging is by addition of so-called "supercharging" reagents, such as m-nitrobenzyl alcohol (m-NBA), which has been systematically studied by Williams' group.[67–70] Our lab has introduced new supercharging reagents, including sulfolane, and we have studied the supercharging effects on proteins (and protein complexes) under native and denaturing solution environments.[33,71,72]

Previously, we demonstrated the ability to incorporate supercharging with electrospray laser desorption ionization (ELDI)[73] and liquid sample DESI;[33] for DESI, increased multiple charging was observed for proteins and protein complex ions when the supercharging reagent was sprayed from the DESI probe. In the present study, RNaseA was mixed with 200 mM sulfolane and infused into the sample introduction capillary. The DESI spray solution was composed of the nucleotide ligand in the NH_4OAc aqueous solution (Figure 6, panels a–c). With the supercharging reagent doped into the protein solution, multiple charging increased from 8+ to 12+ for both the apo- and holo-protein states. The measured [holo]/[apo] ratios of the complex ions for 2′-CMP and CDP were 0.06 and 0.58, respectively, and similar to the data generated without the presence of supercharging reagents (Figure 2).

The supercharging agent can be introduced by premixing with the small molecule ligand instead of with the protein. Figure 6d also shows the result of this method for RNaseA binding to CTP. Sulfolane and CTP were mixed together and sprayed through the DESI spray probe toward the RNaseA solution, which was infused from sample introduction capillary. The measured [holo]/[apo] ratio of 3.37 is similar to the 3.21

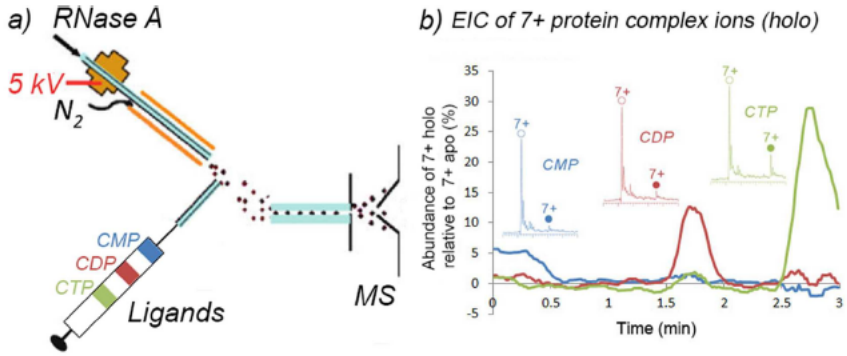

Figure 5. (a) Scheme showing the segmented flow experiment apparatus and (b) EICs of the 7+ complex ions. The three different traces represent the three different complexes (blue, 2′-CMP; red, CDP; green, CTP). The recorded mass spectra of the different complexes are shown in the inset (apo, ○; holo, ●).

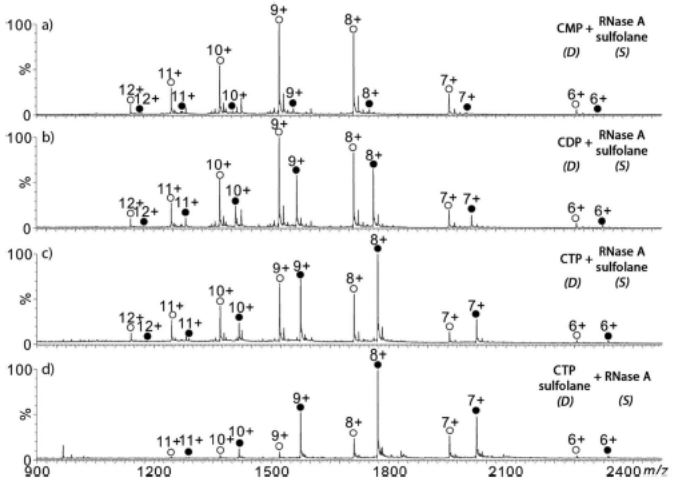

Figure 6. Reactive DESI-MS spectra of mixture composed of 5 μM RNase A and 200 mM sulfolane (in 20 mM NH_4OAc aqueous solution; 5 μL min^{-1}) in the sample transfer capillary ("S") and the DESI probe ("D") spraying (5 μL min^{-1}) 50 μM of (a) CMP, (b) CDP, and (c) CTP in 20 mM NH_4OAc aqueous solution. (d) Sulfolane (200 mM) was mixed with CTP and sprayed through the DESI probe (apo, O; holo, ●).

value measured without supercharging (Figure 2). However, we note that the [holo]/[apo] ratio in Figure 6c is smaller. We suspect that some change in the DESI probe position or sample capillary position occurred, and this has some effect on the [holo]/[apo] ratio. Ideally, both DESI probe and sample capillary positions should be well-controlled for each experiment.

Similar results with the addition of sulfolane supercharging agent were observed for the lysozyme–NAG complex system. Ions for the complex were shifted to higher charge state, and the measured [holo]/[apo] ratio was similar to results without the addition of the supercharging agent (see the Supporting Information).

The results are consistent with our previous data that showed that the addition of supercharging agents at the concentrations used allowed the protein to retain a structure that is sufficient for recognizing and binding to small molecule ligands,[71,72,74] and the measured affinities are similar to previous measurements without the addition of supercharging agents. Even for the example in which sulfolane is added to the protein solution and the supercharged protein reacts with the ligand (Figure 6, panels a–c), no alteration of binding affinities were noted.

Mechanism of Liquid Sample DESI as it Relates to Protein–Ligand Complex Measurements. The results described in this study are consistent with the previously proposed droplet pick-up mechanism for DESI.[75] As the protein (or ligand) is sprayed out of the DESI probe, the charged microdroplet carrying the protein (or ligand) will pick up the sample containing its binding partner.

In principle, there are several factors that could preclude the utility of this method for measuring solution phase binding constants. We assumed that the efficiency for mixing of the DESI probe solution and sample introduction capillary solution is high under the experimental conditions explored for this study. However, the effect of gas and solution flow, temperature, spray voltage, and geometry may play a role in the mixing efficiency (and will be the subject of a future study).

The kinetics of protein–ligand association and dissociation may govern the type of complexes that can be probed by our method. As the DESI ionization timescale is around 1–2 ms, the on-rate for formation of the RNaseA and lysozyme complexes should fall in this time regime. However, the reaction rate for complex formation may be driven further from a concentration effect that might occur as the final droplet containing the complex is evaporating, potentially raising the concentration of the reactants prior to desorption/ionization into the gas phase complex. Previous work with ELDI-MS showed that reduction of disulfide bonds can occur in the millisecond timescale for reactions that take many minutes in solution.[73]

■ CONCLUSIONS

Liquid sample DESI was used as a method to separately introduce reactants and mix to form noncovalent protein–ligand complexes to be measured by mass spectrometry. For RNaseA binding to cytidine nucleotides and lysozyme binding to saccharides, the measured binding affinities using this ambient ionization method with MS were consistent with other measurements using conventional MS and biophysical tools.

Liquid sample DESI-MS offers some sample handling convenience, as the protein does not need to be mixed with the ligand (or ligand mixture) prior to the measurement. Further, a potentially higher throughput method of sample introduction was tested by using a segmented flow arrangement. A library of ligand compounds can be introduced in a single flow, and each compound can be tested for binding and measured sequentially using MS detection. The results described in this study agree well with the previously proposed droplet pick-up mechanism for DESI.[75] The fast mixing of two partners of a protein/ligand pair in liquid sample DESI may allow for the monitoring of the early stages of a binding event in solution.

■ ASSOCIATED CONTENT

Supporting Information

Supercharging spectra of lysozyme−NAG_n complex data and the K_d calculations are provided. This material is available free of charge via the Internet at http://pubs.acs.org.

■ AUTHOR INFORMATION

Corresponding Authors

*E-mail: chenh2@ohio.edu.
*E-mail: jloo@chem.ucla.edu.

Notes

The authors declare no competing financial interest.

■ ACKNOWLEDGMENTS

This work was supported by the National Science Foundation (Grant CHE-0911160), NSF Career (Grant CHE-1149367), the ASMS Research Award (Thermo Scientific), and the National Natural Science Foundation of China (NNSFC; Grant 21328502) to H.C., the Ruth L. Kirschstein National Research Service Award (Grant GM007185, UCLA Cellular and Molecular Biology Training Grant to C.N.F.), and the National Institutes of Health (Grant R01 GM103479 to J.A.L.).

■ REFERENCES

(1) Fenn, J. B.; Mann, M.; Meng, C. K.; Wong, S. F.; Whitehouse, C. M. *Science* **1989**, *246*, 64−71.
(2) Loo, J. A. *Mass Spectrom. Rev.* **1997**, *16*, 1−23.
(3) Loo, J. A. *Int. J. Mass Spectrom.* **2000**, *200*, 175−186.
(4) Loo, J. A. *Int. J. Mass Spectrom.* **2001**, *204*, 113−123.
(5) van den Heuvel, R. H.; Heck, A. J. R. *Curr. Opin. Chem. Biol.* **2004**, *8*, 519−526.
(6) Benesch, J. L. P.; Ruotolo, B. T.; Simmons, D. A.; Robinson, C. V. *Chem. Rev.* **2007**, *107*, 3544−3567.
(7) Li, J. X.; Shefcheck, K.; Callahan, J.; Fenselau, C. *Int. J. Mass Spectrom.* **2008**, *278*, 109−113.
(8) Takats, Z.; Wiseman, J. M.; Gologan, B.; Cooks, R. G. *Science* **2004**, *306*, 471−473.
(9) Cody, R. B.; Laramee, J. A.; Durst, H. D. *Anal. Chem.* **2005**, *77*, 2297−2302.
(10) Cotte-Rodriguez, I.; Chen, H.; Cooks, R. G. *Chem. Commun.* **2006**, 953−955.
(11) Kauppila, T. J.; Wiseman, J. M.; Ketola, R. A.; Kotiaho, T.; Cooks, R. G.; Kostiainen, R. *Rapid Commun. Mass Spectrom.* **2006**, *20*, 387−392.
(12) Shin, Y. S.; Drolet, B.; Mayer, R.; Dolence, K.; Basile, F. *Anal. Chem.* **2007**, *79*, 3514−3518.
(13) Denes, J.; Katona, M.; Hosszu, A.; Czuczy, N.; Takats, Z. *Anal. Chem.* **2009**, *81*, 1669−1675.
(14) Douglass, K. A.; Venter, A. R. *J. Mass Spectrom.* **2013**, *48*, 553−560.
(15) Harris, G. A.; Galhena, A. S.; Fernandez, F. M. *Anal. Chem.* **2011**, *83*, 4508−4538.
(16) Miao, Z.; Chen, H. Proceedings of the 56th ASMS Conference on Mass Spectrometry and Allied Topics, Denver, CO, June 1−5, 2008.
(17) Ma, X.; Zhao, M.; Lin, Z.; Zhang, S.; Yang, C.; Zhang, X. *Anal. Chem.* **2008**, *80*, 6131−6136.
(18) Miao, Z. X.; Chen, H. *J. Am. Soc. Mass Spectrom.* **2009**, *20*, 10−19.
(19) Zhang, Y.; Chen, H. *Int. J. Mass Spectrom.* **2010**, *289*, 98−107.
(20) Li, J. W.; Dewald, H. D.; Chen, H. *Anal. Chem.* **2009**, *81*, 9716−9722.
(21) Zhang, Y.; Yuan, Z.; Dewald, H. D.; Chen, H. *Chem. Commun.* **2011**, *47*, 4171−4173.
(22) Zhang, Y.; Dewald, H. D.; Chen, H. *J. Proteome Res.* **2011**, *10*, 1293−1304.
(23) Lu, M.; Wolff, C.; Cui, W.; Chen, H. *Anal. Bioanal. Chem.* **2012**, *403*, 355−365.
(24) Zhang, Y.; Cui, W.; Zhang, H.; Dewald, H. D.; Chen, H. *Anal. Chem.* **2012**, *84*, 3838−3842.
(25) Liu, P.; Lanekoff, I. T.; Laskin, J.; Dewald, H. D.; Chen, H. *Anal. Chem.* **2012**, *84*, 5737−5743.
(26) Liu, P.; Lu, M.; Zheng, Q.; Dewald, H. D.; Zhang, Y.; Chen, H. *Analyst* **2013**, *138*, 5519−5539.
(27) Zheng, Q.; Zhang, H.; Chen, H. *Int. J. Mass Spectrom.* **2013**, *353*, 84−92.
(28) Sun, X.; Miao, Z.; Yuan, Z.; Harrington, P. d. B.; Colla, J.; Chen, H. *Int. J. Mass Spectrom.* **2011**, *301*, 102−108.
(29) Pan, N.; Liu, P.; Chen, H.; Cui, W.; Tang, B.; Shi, J. *Analyst* **2013**, *138*, 1321−1324.
(30) Liu, Y.; Miao, Z. X.; Lakshmanan, R.; Ogorzalek Loo, R. R.; Loo, J. A.; Chen, H. *Int. J. Mass Spectrom.* **2012**, *325*, 161−166.
(31) Miao, Z.; Chen, H.; Liu, P.; Liu, Y. *Anal. Chem.* **2011**, *83*, 3994−3997.
(32) Moore, B. N.; Hamdy, O.; Julian, R. R. *Int. J. Mass Spectrom.* **2012**, *330*−*332*, 220−225.
(33) Ferguson, C. N.; Benchaar, S. A.; Miao, Z. X.; Loo, J. A.; Chen, H. *Anal. Chem.* **2011**, *83*, 6468−6473.
(34) Chen, H. W.; Talaty, N. N.; Takats, Z.; Cooks, R. G. *Anal. Chem.* **2005**, *77*, 6915−6927.
(35) Chen, H.; Cotte-Rodriguez, I.; Cooks, R. G. *Chem. Commun.* **2006**, 597−599.
(36) Huang, G.; Chen, H.; Zhang, X.; Cooks, R. G.; Ouyang, Z. *Anal. Chem.* **2007**, *79*, 8327−8332.
(37) Nyadong, L.; Green, M. D.; De Jesus, V. R.; Newton, P. N.; Fernandez, F. M. *Anal. Chem.* **2007**, *79*, 2150−2157.
(38) Cotte-Rodriguez, I.; Hernandez-Soto, H.; Chen, H.; Cooks, R. G. *Anal. Chem.* **2008**, *80*, 1512−1519.
(39) Perry, R. H.; Splendore, M.; Chien, A.; Davis, N. K.; Zare, R. N. *Angew. Chem., Int. Ed.* **2011**, *50*, 250−254.
(40) O'Hair, R. A. J. *Chem. Commun.* **2006**, 1469−1481.
(41) Schröder, D.; Schwarz, H. *Proc. Natl. Acad. Sci. U.S.A.* **2008**, *105*, 18114−18119.
(42) Miao, Z. X.; Wu, S. Y.; Chen, H. *J. Am. Soc. Mass Spectrom.* **2010**, *21*, 1730−1736.
(43) Perry, R.; Cahill, T., III; Roizen, J.; Du Bois, J.; Zare, R. N. *Proc. Natl. Acad. Sci. U.S.A.* **2012**, *109*, 18295−18299.
(44) Yin, S.; Xie, Y. M.; Loo, J. A. *J. Am. Soc. Mass Spectrom.* **2008**, *19*, 1199−1208.
(45) Benkestock, K.; Sundqvist, G.; Edlund, P.-O.; Roeraade, J. *J. Mass Spectrom.* **2004**, *39*, 1059−1067.
(46) Camilleri, P.; Haskins, N. J. *Rapid Commun. Mass Spectrom.* **1993**, *7*, 603−604.
(47) Sundqvist, G.; Benkestock, K.; Roeraade, J. *Rapid Commun. Mass Spectrom.* **2005**, *19*, 1011−1016.
(48) Zhang, S.; Van Pelt, C. K.; Wilson, D. B. *Anal. Chem.* **2003**, *75*, 3010−3018.
(49) Loo, J. A.; Hu, P.; McConnell, P.; Mueller, W. T. *J. Am. Soc. Mass Spectrom.* **1997**, *8*, 234−243.
(50) Daniel, J. M.; McCombie, G.; Wendt, S.; Zenobi, R. *J. Am. Soc. Mass Spectrom.* **2003**, *14*, 442−448.
(51) Jaquillard, L.; Saab, F.; Schoentgen, F.; Cadene, M. *J. Am. Soc. Mass Spectrom.* **2012**, *23*, 908−922.
(52) Cathou, R. E.; Hammes, G. G. *J. Am. Chem. Soc.* **1965**, *87*, 4674−4680.
(53) Plotnikov, V.; Rochalski, A.; Brandts, M.; Brandts, J. F.; Williston, S.; Frasca, V.; Lin, L.-N. *Assay Drug Dev. Technol.* **2002**, *1*, 83−90.
(54) Ganem, B.; Li, Y. T.; Henion, J. D. *J. Am. Chem. Soc.* **1991**, *113*, 7818−7819.
(55) Cubrilovic, D.; Zenobi, R. *Anal. Chem.* **2013**, *85*, 2724−2730.
(56) Jecklin, M. C.; Touboul, D.; Bovet, C.; Wortmann, A.; Zenobi, R. *J. Am. Soc. Mass Spectrom.* **2008**, *19*, 332−343.
(57) Holler, E.; Rupley, J. A.; Hess, G. P. *Biochem. Biophys. Res. Commun.* **1970**, *40*, 166−170.

(58) Gunther, A.; Jhunjhunwala, M.; Thalmann, M.; Schmidt, M. A.; Jensen, K. F. *Langmuir* **2005**, *21*, 1547−1555.
(59) Hatakeyama, T.; Chen, D. L.; Ismagilov, R. F. *J. Am. Chem. Soc.* **2006**, *128*, 2518−2519.
(60) Li, Q.; Pei, J.; Song, P.; Kennedy, R. T. *Anal. Chem.* **2010**, *82*, 5260−5267.
(61) Valeja, S. G.; Tipton, J. D.; Emmett, M. R.; Marshall, A. G. *Anal. Chem.* **2010**, *82*, 7515−7519.
(62) Zubarev, R. A.; Kelleher, N. L.; McLafferty, F. W. *J. Am. Chem. Soc.* **1998**, *120*, 3265−3266.
(63) Syka, J. E. P.; Coon, J. J.; Schroeder, M. J.; Shabanowitz, J.; Hunt, D. F. *Proc. Natl. Acad. Sci. U.S.A.* **2004**, *101*, 9528−9533.
(64) Hu, Q. Z.; Noll, R. J.; Li, H. Y.; Makarov, A.; Hardman, M.; Cooks, R. G. *J. Mass Spectrom.* **2005**, *40*, 430−443.
(65) Marshall, A. G.; Hendrickson, C. L.; Jackson, G. S. *Mass Spectrom. Rev.* **1998**, *17*, 1−35.
(66) Marshall, A. G.; Hendrickson, C. L. *Rapid Commun. Mass Spectrom.* **2001**, *15*, 232−235.
(67) Iavarone, A. T.; Jurchen, J. C.; Williams, E. R. *Anal. Chem.* **2001**, *73*, 1455−1460.
(68) Iavarone, A. T.; Williams, E. R. *Int. J. Mass Spectrom.* **2002**, *219*, 63−72.
(69) Iavarone, A. T.; Williams, E. R. *J. Am. Chem. Soc.* **2003**, *125*, 2319−2327.
(70) Iavarone, A. T.; Williams, E. R. *Anal. Chem.* **2003**, *75*, 4525−4533.
(71) Lomeli, S. H.; Yin, S.; Ogorzalek Loo, R. R.; Loo, J. A. *J. Am. Soc. Mass Spectrom.* **2009**, *20*, 593−596.
(72) Lomeli, S. H.; Peng, I. X.; Yin, S.; Ogorzalek Loo, R. R.; Loo, J. A. *J. Am. Soc. Mass Spectrom.* **2010**, *21*, 127−131.
(73) Peng, I. X.; Ogorzalek Loo, R. R.; Shiea, J.; Loo, J. A. *Anal. Chem.* **2008**, *80*, 6995−7003.
(74) Yin, S.; Loo, J. A. *Int. J. Mass Spectrom.* **2011**, *300*, 118−122.
(75) Takats, Z.; Wiseman, J. M.; Cooks, R. G. *J. Mass Spectrom.* **2005**, *40*, 1261−1275.

Supporting Information

Measuring Protein-Ligand Interactions Using Liquid Sample Desorption Electrospray Ionization Mass Spectrometry

Pengyuan Liu,[†,§] Jiang Zhang,[†] Carly N. Ferguson,[†] Hao Chen,[*,§] Joseph A. Loo[*,†,‡]

[†]Department of Chemistry and Biochemistry and [‡]Department of Biological Chemistry, [‡]David Geffen School of Medicine, University of California-Los Angeles, Los Angeles, California 90095, United States

[§]Center for Intelligent Chemical Instrumentation, Department of Chemistry and Biochemistry, Ohio University, Athens, Ohio 45701, United States

Supercharging effects of lysozyme-NAG_n complex

Lysozyme was dissolved in 20 mM NH_4OAc aqueous solution and diluted to 5 µM. The diluted protein solution was infused into the sample infusing capillary at a flow rate of 5 µL/min. The DESI spray solution was 20 mM NH_4OAc aqueous solution containing 200 µM ligand and 200 mM sulfolane (5 µL/min). Figure S1 shows the results for NAG3 and NAG6 ligands. The charge states of the protein complex ions increased from +7~+9 (see Figure 4) to +7~+11. From the spectra for the NAG_3 and NAG_6 ligands, the holo/apo ratio was measured to be 0.27 and 0.31, respectively. These ratios are similar to values measured without the addition of supercharging reagents, and thus protein-ligand binding was not affected by supercharging.

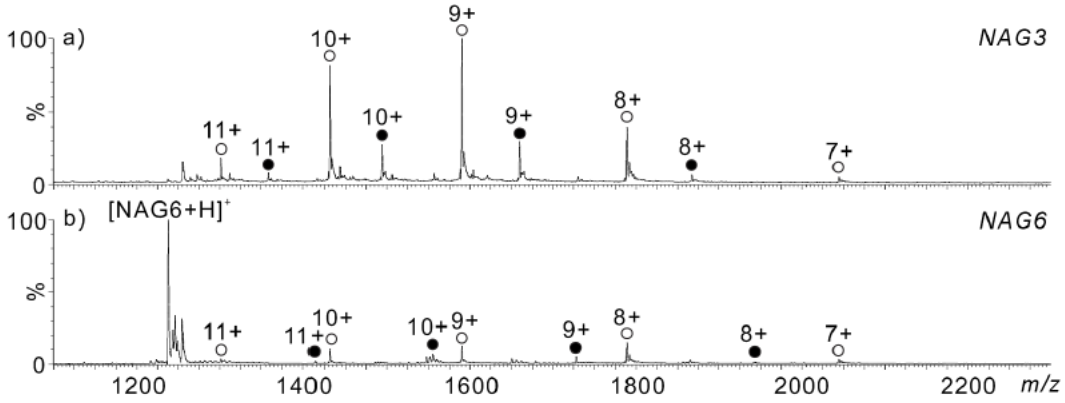

Figure S1. Reactive liquid sample DESI-MS spectra of lysozyme in the sample transfer capillary ("S") and the DESI probe ("D") spraying 200 mM sulfolane and a) 200 µM NAG3 and b) 200 µM NAG6 in 20 mM NH_4OAc aqueous solution. (apo – open circles; holo – filled circles)

MS/MS of RNase A-cytidine complex

To better confirm the results acquired by reactive DESI-MS, collisionally activated dissociation (CAD) mass spectra were recorded for each of the multiply charged complex ions to compare the stability of RNase A-cytidine nucleotide ligand complexes with previous studies done by ESI-MS/MS.[1] The CAD spectra are shown in Figure S2. Consistent with the ESI-MS/MS results, CAD of the $(RNaseA+CMP+7H)^{7+}$ complex yields the complementary product ion pair, $(RNaseA+6H)^{6+}$ and $(CMP+H)^{+}$, and the protein ion $(RNaseA+7H)^{7+}$ by loss of neutral 2'-CMP (Figure S2a). Similarly, dissociation of the $(RNaseA+CDP+7H)^{7+}$ complex yields the complementary product ion pair $(RNaseA+6H)^{6+}$ and $(CDP+H)^{+}$. A minor dissociation pathway gives rise to $(RNaseA+7H)^{7+}$ by loss of neutral CDP. A predominant dissociation pathway, which is the cleavage of a covalent phosphate bond within the diphosphate group of CDP and the subsequent release of charged CMP, yields the complementary $(RNaseA+phosphate+6H)^{6+}$ and $(CMP+H)^{+}$. This phenomenon, cleavage of a covalent bond prior to non-covalent bonds, is also consistent with the ESI-MS/MS result we published before,[1] indicating the strong gas phase interaction of the protein with the ligand. Another similar pathway produces $(RNaseA+phosphate+7H)^{7+}$ complex with loss of neutral CMP (Figure S2b). For dissociation of $(RNaseA+CTP+7H)^{7+}$, both $(CMP+H)^{+}$ and $(CDP+H)^{+}$ along with their complementary fragment ions $(RNaseA+di\text{-}phosphate+6H)^{6+}$ and $(RNaseA+phosphate+6H)^{6+}$ were observed (Figure S2c). Likewise, one and two phosphate binding to RNaseA in +7 charged products was observed, too. However, no loss of intact CTP was observed (Figure S2c). These observations agree well with previously reported ESI-MS/MS results.

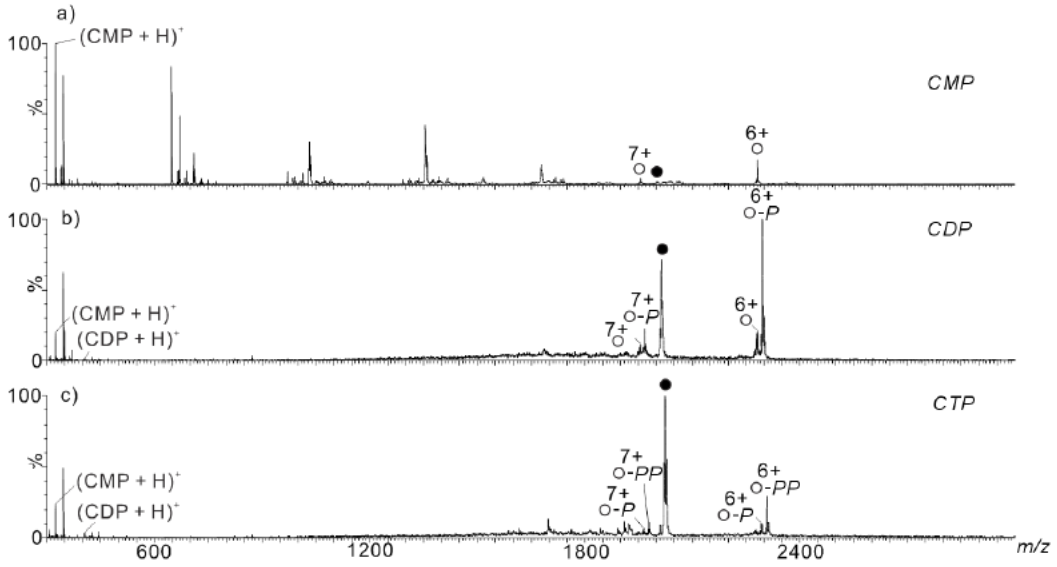

Figure S2. CAD MS/MS spectra of the +7 charged complex ions of RNase A and (a) CMP, (b) CDP, and (c) CTP generated by reactive DESI. The 7+-charged precursor ions are labeled with filled circles. Product ions for the apo-protein are labeled with open circles. "P" represents the retention of one phosphate group and "PP" represents the retention of two phosphates.

Dissociation constant measurement

The dissociation constant (K_d) of the protein-ligand complex was determined by performing tiration experiements with the liquid sample DESI appratus. For the titration experiments, 5 μM RNase A solution was infused through the sample infusion capillary. The ligand was prepared in a series of solutions with different concentrations (1 μM, 2 μM, 3 μM, 5 μM, 7 μM, 10 μM, and 15 μM) and sprayed by the DESI probe. A series of mass spectra were obtained and the K_d was calculated following the method previously described.[2] The relative abundances of both holo- and apo-protein were determined from the mass spectra and used to determine their relative concentrations (assuming that the free protein and the protein complex have similar ionization efficiencies). The K_d was calculated by the following equation:

$$K_d = \frac{[R][L]}{[RL]} \quad (1)$$

In Equation 1, [R] represents the concentration of remaining apo-protein in the resulting secondary droplets; [RL] represents the concentration of protein complex; [L] represents the concentration of unbound ligand. The reactive-DESI process is shown in Figure S3. During the desorption/ionization process, the ligand solution that is sprayed by the DESI probe first picks up the protein solution flowing from the sample introduction capillary. Subsequently the ligand binds with the protein and the complex is transferred to the mass spectrometer for detection. All of the free protein, free ligand and protein-ligand complex will be detected by the mass spectrometer. The concentration and volume changes of both the protein and ligand solutions are marked in Figure S3. The initial concentration and volume of the ligand solution infused from DESI probe are $[L_i]$ and V_{Li}, respectively; the initial concentration and volume of the protein solution infused from sample introduction capillary are $[R_i]$ and V_{Ri}, respectively. After the "pick-up" step, the volume of the secondary droplet is V_M and in the secondary droplet the concentration of the ligand and protein becomes $[L_M]$ and $[R_M]$, respectively. At the point of detection, the final concentration of the free protein, free ligand and protein-ligand complex are [R], [L], and [RL], respectively.

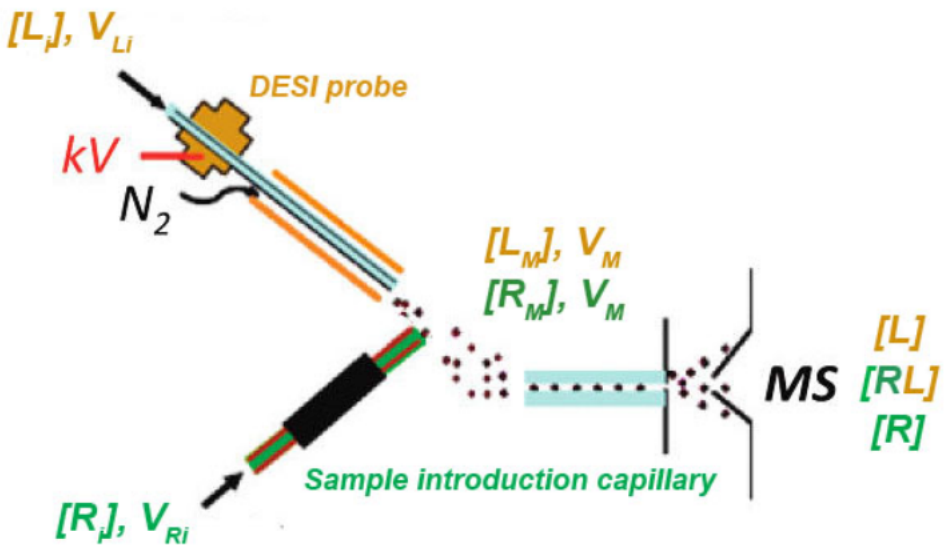

Figure S3. Reactive liquid sample DESI-MS scheme for measuring protein complex formation.

From the figure, the relationship of the concentrations can be determined, shown in Equations 2-4. In Equation 4, r represents the holo/apo concentration ratios.

$$[L_M] = [L] + [RL] \tag{2}$$

$$[R_M] = [R] + [RL] \tag{3}$$

$$r = \frac{[RL]}{[R]} \tag{4}$$

From Equations 1-4, the concentration of free protein, free ligand, and protein-ligand complex in the gas phase can be determined.

$$[R_M] = [R] + [RL] = [R] + r[R] \tag{5}$$

$$[R] = \frac{[R_M]}{r+1} \tag{6}$$

$$[RL] = \frac{r \cdot [R_M]}{r+1} \tag{7}$$

$$[L] = [L_M] - [RL] = [L_M] - \frac{r \cdot [R_M]}{r+1} \tag{8}$$

Therefore, Equation 1 can be converted to Equation 9 from the relationships described in Equations 6-8.

$$K_d = \frac{[R][L]}{[RL]} = \frac{[L_M] - \frac{r \cdot [R_M]}{r+1}}{r} \quad (9)$$

And based on Equation 9:

$$r = f_{([L_M])} = \frac{-(K_d - [L_M] + [R_M]) + \sqrt{(K_d - [L_M] + [R_M])^2 + 4 \cdot K_d \cdot [L_M]}}{2 \cdot K_d} \quad (10)$$

Equation 10 is represents the concentration of ligand used in the titration experiment. In this Equation 10, $[R_M]$ is a constant in one single titration experiment. By plotting r versus $[L_M]$, the K_d can be determined.

However, determination of $[L_M]$ is difficult. It can be calculated by Equations 11 and 12.

$$[L_M] = \frac{[L_i] \cdot V_{Li}}{V_M} = \alpha \cdot [L_i] \quad (11)$$

$$[R_M] = \frac{[R_i] \cdot V_{Ri}}{V_M} = \beta \cdot [R_i] \quad (12)$$

In the equations, α and β are defined as the dilution ratio of ligand and the protein during the desorption/ionization.

$$\alpha = \frac{V_{Li}}{V_M};\ \beta = \frac{V_{Ri}}{V_M} \quad (13)$$

In reactive DESI, the reaction takes place after the "pick-up" of the DESI process. Therefore, the concentration of the protein (receptor) and ligand could change during the process of the reaction. The changed concentration depends on the dilution ratio of the two solutions, which is unknown. The difficulty of the designed measurements originates from the process of liquid sample DESI.

Two issues affect the dilution ratio. The first one is that the mixing might not be even when the two injection rates are the same. The reason is that one capillary has a high voltage applied and a high flow rate nebulizing gas flow, which may affect the mixing, which might cause $\alpha \neq \beta$.

Taking consideration of the dilution ratio, the K_d can be calculated by plotting Equation 14.

$$r = \frac{-(K_d - \alpha \cdot [L_i] + (1-\alpha) \cdot [R_i]) + \sqrt{(K_d - \alpha \cdot [L_i] + (1-\alpha)[R_i])^2 + 4 \cdot K_d \cdot \alpha \cdot [L_i]}}{2 \cdot K_d} \quad (14)$$

In Equation 14, r can be determined from the relative holo/apo ratios. Ideally, the dilution factor is 50% when A) the infusion rates of both the DESI probe and sample

introduction are the same, and B) no volume loss is in the ionization process. Then the K_d can be determined as

$$r = \frac{-(K_d - 0.5 \cdot [L_i] + 0.5 \cdot [R_i]) + \sqrt{(K_d - 0.5 \cdot [L_i] + 0.5[R_i])^2 + 2 \cdot K_d \cdot [L_i]}}{2 \cdot K_d} \quad (15)$$

Two systems, RNase A-CTP and lysozyme-NAG_3 were chosen as illustration of the method. For the RNase A-CTP system, 7 solutions with different concentrations of CTP were used for the titration. The concentration of the CTP solutions and the relevant holo/apo ratios are listed in the table below.

Table S1. Titration of 5 μM RNase A with CTP

$[L_i]$ (μM)	r ($\frac{[RL]}{[R]}$)
1	0.1976
2	0.2276
3	0.4314
5	1.1980
7.5	1.4684
10	2.1038
15	2.4703

The correlation of ligand concentrations and holo/apo ratios is plotted in Figure S4. The points are fitted with the Equation 15. The fitted K_d is 1.91 μM, slightly larger than the reported ESI value (0.72 μM).[3]

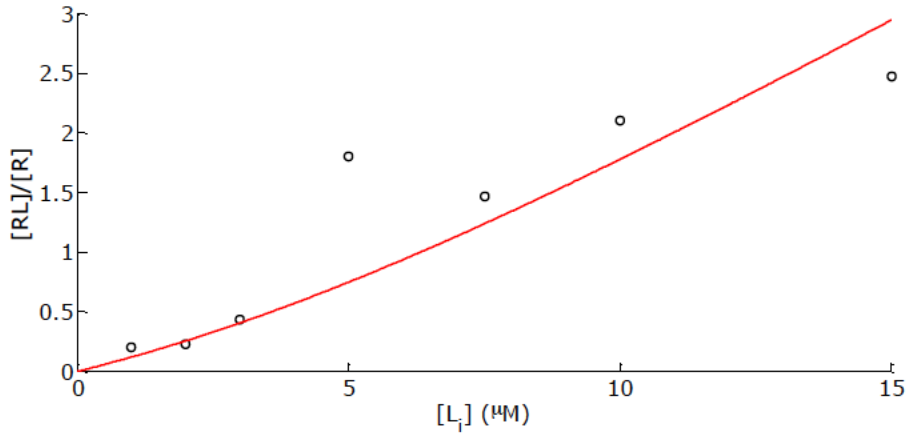

Figure S4. Plot of holo/apo ratios of RNase A as a function of the CTP concentrations.

In the case of lysozyme-NAG3, 7 solutions with different concentrations of NAG_3 were used for the titration. The concentration of the NAG_3 solution and the relevant holo/apo ratios are listed in the table below.

Table S2. Titration of 5 μM lysozyme with NAG3

$[L_i]$ (μM)	r ($\frac{[RL]}{[R]}$)
20	0.082548
30	0.030796
50	0.128424
75	0.196644
100	0.400301
200	0.550419
300	0.88052

The correlation of ligand concentrations and holo/apo ratios is plotted in Figure S5. The points are fitted with the Equation 15. The fitted K_d is 169.06 μM, larger than the reported ESI value (59.8 μM).[4]

However, the actual dilution ratio may not be 0.5 in the reality, and this may be a source of discrepancy for the measurement of K_d. We have preliminary data that suggests that the relative positions of the DESI probe, sample introduction capillary, and MS inlet capillary may affect the dilution ratio. This will be a focus of a future study.

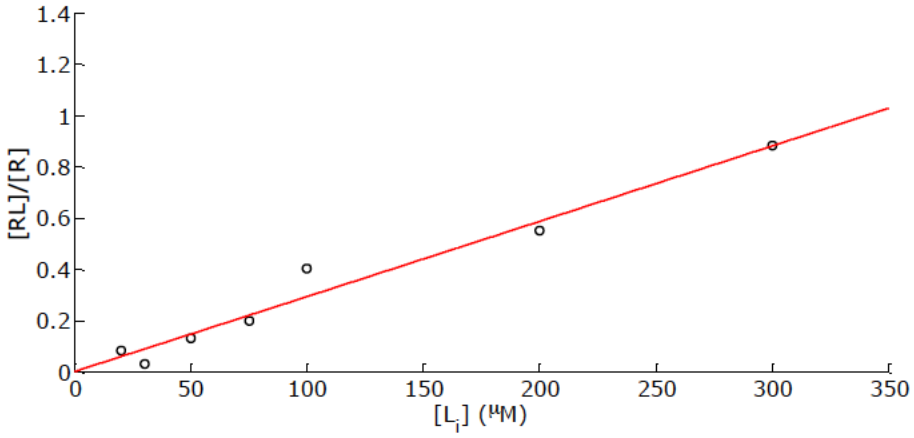

Figure S5. Plot of holo/apo ratios of lysozyme as a function of NAG3 concentrations.

EIC of RNaseA – cytidine complex

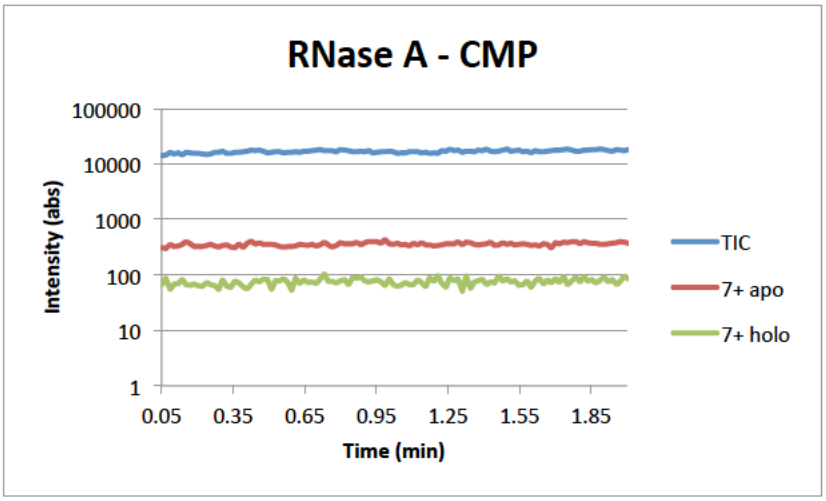

Figure S6. The total ion chromatogram (TIC, blue curve) and extracted ion chromatograms (EICs) of +7 apo-ion (red curve) and +7 holo-ion (green curve) recorded in the reactive liquid sample DESI-MS spectrum of RNaseA (5 μM in 20 mM NH_4OAc aqueous solution, pH 6.5) in the sample transfer capillary with the DESI probe spraying reagents containing 50 μM 2'-CMP in 20 mM NH_4OAc.

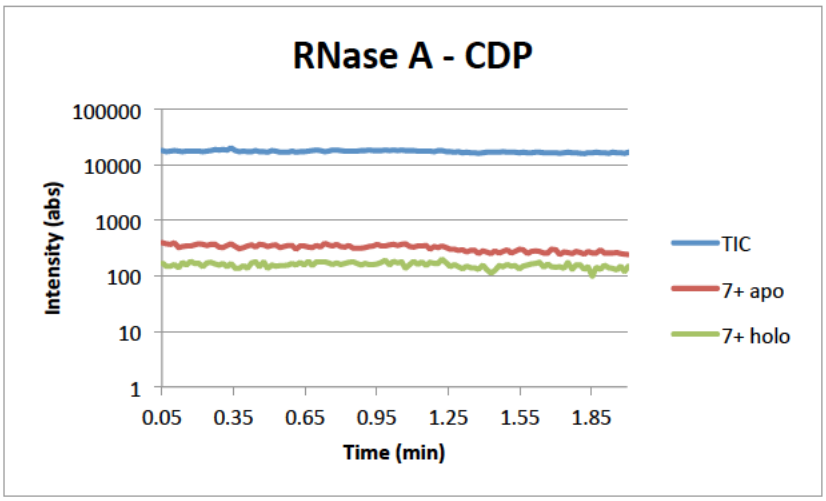

Figure S7. The TIC (blue curve) and EICs of +7 apo-ion (red curve) and +7 holo-ion (green curve) recorded in the reactive liquid sample DESI-MS spectrum of RNaseA (5 μM in 20 mM NH_4OAc aqueous solution, pH 6.5) in the sample transfer capillary with the DESI probe spraying reagents containing 50 μM CDP in 20 mM NH_4OAc.

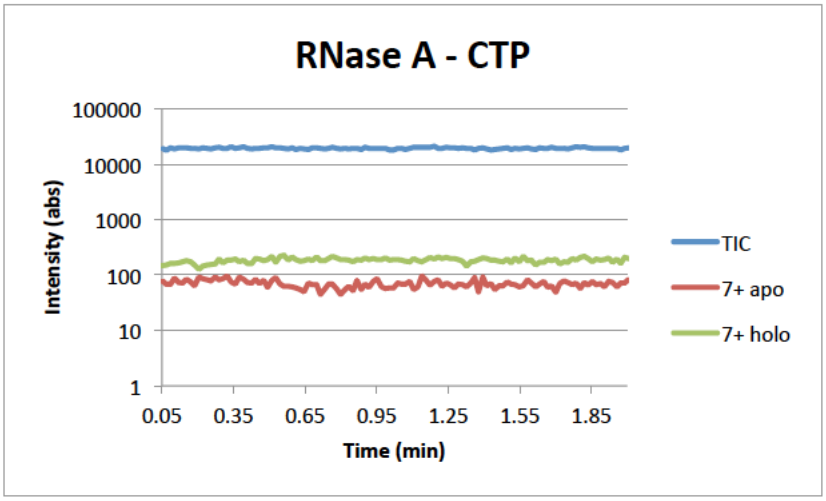

Figure S8. The TIC (blue curve) and EICs of +7 apo-ion (red curve) and +7 holo-ion (green curve) recorded in the reactive liquid sample DESI-MS spectrum of RNaseA (5 μM in 20 mM NH_4OAc aqueous solution, pH 6.5) in the sample transfer capillary with the DESI probe spraying reagents containing 50 μM CTP in 20 mM NH_4OAc.

References

1. Yin, S.; Xie, Y.; Loo, J. A. *J. Am. Soc. Mass Spectrom.* **2008**, *19*, 1199-1208.
2. Daniel, J. M.; McCombie, G.; Wendt, S.; Zenobi, R. *J. Am. Soc. Mass Spectrom.* **2003**, *14*, 442–448.
3. Zhang, S.; Van Pelt, C. K.; Wilson, D. B., *Anal. Chem.* **2003,** *75*, 3010-3018.
4. Jecklin, M. C.; Touboul, D.; Bovet, C.; Wortmann, A.; Zenobi, R. *J. Am. Soc. Mass Spectrom.* **2008**, *19*, 332–343.

CHAPTER 7

Conclusions

Conclusions

Mass spectrometry imaging (MSI) of tissue specimens is a promising technique due to its versatility and limited necessity of sample preparation.[1] We have shown its utility for targeted detection of small molecules, eliminating the need for a tagging or labeling process and allowing for the detection of all potential metabolites. This analytical platform could be especially valuable to pre-clinical biodistribution studies and drug development efforts.

While small molecule MSI has several unique advantages, there are challenges that we encountered during its development and application. Matrix-assisted laser desorption/ionization (MALDI), and especially MALDI of tissue sections, results in signal suppression of lower abundance peaks by more highly abundant ions. This is compounded by the molecular complexity of tissue sections, with several endogenous molecules, such as salts, lipids, and metabolites, present in large quantities.[2] We utilized a solvent wash test as a potential pre-treatment protocol to enhance signal intensity and decrease ion suppression effects. This technique was successful in the study of SMRT compound BZ16, as demonstrated by the enhancement of analyte signal intensity with no observable compound spatial delocalization. However, this sample preparation process is not universally applicable. Other small molecules studied, such as BZ6, RTC13, and compound 216 were unable to be detected by MSI, even after employing a wash step. Relative quantification by LC-MS/MS suggested these compounds were present at levels two orders of magnitude below the level of BZ16. Because the signal attributed to BZ16 via MSI was already low, it is likely that the remaining compounds were below the MSI limit of detection. Ion suppression was also

observed with compound RM512. Although the solution containing the standard compound that was spotted onto tissue ionized efficiently, a mixture of RM512 with other molecules resulted in the complete suppression of RM512 signal.

Despite the challenges associated with MALDI-MSI of small molecules, the future remains bright for MSI as a whole. Further improvements to sample preparation, in addition to polarity-based wash solvent selection, such as pH-specific cleanup protocols, suggest the potential for a universally applicable, optimized method for small molecule analysis.[3] MALDI is not considered to be a universal desorption/ionization technique for all classes of compounds. Other ionization techniques, such as liquid extraction surface analysis (LESA), laser ablation electrospray ionization (LAESI), and desorption electrospray ionization (DESI), may provide the biggest promise for MSI of small analyte molecules.[4-6] The enhanced sensitivity due to incorporation of electrospray solvent or organic extraction circumvents the ionization inefficiencies exhibited by MALDI, although spatial resolution can be compromised. Additionally, the use of ESI-based ionization techniques allow for the possibility of quantitative-based imaging. Multi-modal capabilities and serial sectioning allow for the coupling of complimentary techniques, thus enabling the utilization of the spatial resolution of MALDI and the sensitivity of ESI-based methodologies, a powerful combination for the future of mass spectrometry-based imaging studies. It may be possible in the future to see widespread application of MSI in the hospital operating room to provide real-time clinical assessment of tissue state and perhaps even treatment response.[7,8]

REFERENCES

1. McDonnell, L. A.; Heeren, R. M. A. Imaging mass spectrometry. *Mass Spectrometry Reviews* **2007**, *26***,** 606-643.
2. Reyzer, M. L.; Hsieh, Y.; Ng, K.; Korfmacher, W. A.; Caprioli, R. M., Direct analysis of drug candidates in tissue by matrix-assisted laser desorption/ionization mass spectrometry. *Journal of Mass Spectrometry* **2003,** *38* (10), 1081-1092.
3. Shariatgorji, S.; Kallback, P.; Gustavsson, L.; Schintu, N.; Svenningsson, P.; Goodwin, R. J. A.; Andren, P. E. Controlled-pH tissue cleanup protocol for signal enhancement of small molecule drugs analyzed by MALDI-MS imaging. *Analytical Chemistry* **2012**, *84* (10), 4603-4607.
4. Eikel, D.; Vavrek, M.; Smith, S.; Bason, C.; Yeh, S.; Korfmacher, W. A.; Henion, J. D., Liquid extraction surface analysis mass spectrometry (LESA-MS) as a novel profiling tool for drug distribution and metabolism analysis: the terfenadine example. *Rapid Communications in Mass Spectrometry* **2011,** *25* (23), 3587-3596.
5. Nemes, P.; Woods, A. S.; Vertes, A., Simultaneous imaging of small metabolites and lipids in rat brain tissues at atmospheric pressure by laser ablation electrospray ionization mass spectrometry. *Analytical Chemistry* **2010,** *82* (3), 982-988.
6. Wiseman, J. M.; Ifa, D. R.; Zhu, Y.; Kissinger, C. B.; Manicke, N. E.; Kissinger, P. T.; Cooks, R. G., Desorption electrospray ionization mass spectrometry: Imaging

drugs and metabolites in tissues. *Proceedings of the National Academy of Sciences of the United States of America* **2008,** *105* (47), 18120-18125.

7. Pope, W. B., Intraoperative mass spectrometry of tumor metabolites. *Proceedings of the National Academy of Sciences of the United States of America* **2014,** *111* (30), 10906–10907.
8. Santagata, S.; Eberlin, L. S.; Norton, I.; Calligaris, D.; Feldman, D. R.; Ide, J. L.; Liu, X.; Wiley, J. S.; Vestal, M. L.; Ramkissoon, S. H.; Orringer, D. A.; Gill, K. K.; Dunn, I. F.; Dias-Santagata, D.; Ligon, K. L.; Jolesz, F. A.; Golby, A. J.; Cooks, R. G.; Agar, N. Y. R., Intraoperative mass spectrometry mapping of an onco-metabolite to guide brain tumor surgery. *Proceedings of the National Academy of Sciences of the United States of America* **2014,** *111* (30), 11121–11126.